JAERI-M
91-081

CONCEPT STUDY OF THE STEADY STATE TOKAMAK REACTOR (SSTR)

June 1991

Fusion Reactor System Laboratory

日本原子力研究所
Japan Atomic Energy Research Institute

JAERI-Mレポートは，日本原子力研究所が不定期に公刊している研究報告書です。
入手の問合わせは，日本原子力研究所技術情報部情報資料課（〒319-11茨城県那珂郡東海村）あて，お申しこしください。なお，このほかに財団法人原子力弘済会資料センター（〒319-11 茨城県那珂郡東海村日本原子力研究所内）で複写による実費頒布をおこなっております。

JAERI-M reports are issued irregularly.
Inquiries about availability of the reports should be addressed to Information Division Department of Technical Information, Japan Atomic Energy Research Institute, Tokai-mura, Naka-gun, Ibaraki-ken 319-11, Japan.

編集兼発行　日本原子力研究所
印　　刷　いばらき印刷㈱

JAERI-M 91-081

Concept Study of the Steady State Tokamak Reactor (SSTR)

Fusion Reactor System Laboratory

Department of Large Tokamak Research
Naka Fusion Research Establshment
Japan Atomic Energy Research Institute
Naka-machi, Naka-gun, Ibaraki-ken

(Received April 11, 1991)

The Steady State Tokamak Reactor (SSTR) concept has been proposed as a realistic fusion power reactor to be built in the near future. An overall concept of SSTR is introduced which is based on a small extension of the present day physics and technologies. The major feature of SSTR is the maximum utilization of a bootstrap current in order to reduce the power required for the steady state operation. This requirement leads to the choice of moderate current (12 MA), and high βp (2.0) for the device, which are achieved by selecting high aspect ratio (A=4) and high toroidal magnetic field (16.5 T). A negative-ion-based neutral beam injection system is used both for heating and central current drive. Notable engineering features of SSTR are: the use of a uniform vacuum vessel and periodical replacements of the first wall and blanket layers and significant reduction of the electromagnetic force with the use of functionally gradient material. It is shown that a tokamak machine comparable to ITER in size can become a power reactor capable of generating about 1 GW of electricity with a plant efficiency of ~30%.

This work has been conducted under the research theme of the Fusion Reactor System Laboratory with the cooperation of the researchers from other laboratories in the Naka Fusion Research Establishment, a university and Industries. Names of the design contributors are shown in a separate sheet.

Keywords: SSTR, Steady State Tokamak Reactor, Fusion Power Reactor, Toroidal Field Coil, Poloidal Field Coil, Vacuum Vessel, First Wall, Divertor, Blanket, Shield, Neutral Beam Injector, ECH, Pellet Injector

定常トカマク型動力炉（SSTR）の概念検討

日本原子力研究所那珂研究所臨界プラズマ研究部
炉設計研究室

（1991年4月11日受理）

定常トカマク型動力炉（SSTR：Steady State Tokamak Reactor）を，近い将来実現可能な核融合動力炉概念として提案する。SSTRは現在知られている物理と工学の僅かな外挿に基づいており，本報告書ではSSTRのプラント全体の検討結果を紹介する。SSTRの最も大きな特徴は定常運転に必要な所内電力をできるだけ減らすために，プラズマ中に自発的に流れるブートストラップ電流を最大限に利用している点である。そのために高いアスペクト比（プラズマ主半径／プラズマ小半径：A＝4）と強いトロイダル磁場（Bt＝16.5T）を選択した。その結果プラズマ電流は適度な大きさ（Ip ＝12MA）となり，高いプラズマの安定性（βp＝2.0）が得られた。プラズマの加熱と中心部分の電流駆動はともに，負イオン源中性粒子入射により達成される。また，SSTRの工学面での特徴は，均一抵抗型真空容器の使用，第1壁とブランケット前半部の定期交換，傾斜機能材料の利用による電磁力の大幅な軽減等である。国際熱核融合実験炉ITERとそれほど変わらぬ寸法のSSTRが，総合熱効率約30％で，約100万kWの電気出力を出せることを示した。

那珂研究所：〒311－01　茨城県那珂郡那珂町大字向山801－1

本概念検討は，炉設計研究室の研究テーマのもとに，臨界プラズマ研究部，核融合研究部の関連課室，核融合実験炉特別チーム，大学，メーカーの研究者の協力を得て行われた。設計協力者の氏名リストを別紙に示す。

List of Design Contributors

Japan Atomic Energy Research Institute
Yasushi Seki, Mitsuru Kikuchi, Satoshi Nishio, Akira Oikawa, Toshinari Ando, Yoshihiro Ohara, Masahiro Seki, Tomonori Takizuka, Keiji Tani, Takahisa Ozeki, Kouichi Koizumi, Yuuji Matsuda, Masashi Azumi, Yoshikazu Okumura, Makoto Mizuno, Shinji Nakajima, Masanori Araki

University of Tokyo
Haruki Madarame

Hitachi Limited
Tadanori Mizoguchi, Munetsugu Kajiura, Takashi Watanabe, Yoshihide Shizuoka, Hideo Tukamoto, Kouzou Matsumoto, Fumio Iida, Michio Ohtuka, Yoshihiro Ozawa

Kawasaki Heavy Industries
Seiji Mori, Seiichiro Yamazaki, Jun-ichi Adachi, Shingo Hirata, Hidenori Miura, Tatuaki Sawai, Tatsushi Suzuki, Kensuke Mohri, Takeshi Yamada, Takeshi Kobayashi

Mitsubishi Group
Noriaki Ueda, Bunkoh Ikeda, Yoshika Hosoda, Shigeru Tado, Minoru Yamane, Ryuta Saito, Yutaka Suzuki, Masao Yamada, Kimihiro Ioki, Teruhisa Kageyama, Michio Iimura, Mituru Tomita, Katsusuke Simizu, Yasushi Oda, Kazuhiro Miyamoto, Kunihiko Nakashima, Haruhiko Tomita

Sumitomo Heavy Industries Ltd.
Masaji Asahara, Nobuhisa Yokogawa, Kazumasa Konishi, Takayuki Aoki, Akihiko Matsumoto, Keijou Takahashi

Nisshin Denki Ltd.
Kiyoshi Nakata, Hiroshi Nakazato, Yuu, Kawakita, Masahiro Tanii, Shuuiti Taniguchi, Keizou Hayashi

Toshiba Corporation
Ken'iti Kakizawa, Katsuyuki Ebisawa, Shigetada Kobayashi, Akiyoshi Hatayama, Nobuo Tachikawa, Satoshi Nakagawa, Akira Ozaki, Yukio Watanabe, Kichiro Shin'ya, Haruhiko Takase,

ＳＳＴＲ設計協力者リスト

日本原子力研究所

関　泰、菊池　満、西尾　敏、及川　晃、安藤俊就、小原祥裕、関　昌弘、滝塚知典、谷　啓二、小関隆久、小泉興一、松田祐二、安積正史、奥村義和、水野　誠、中島信治、荒木　政則

東京大学

斑目春樹

㈱日立製作所

溝口忠憲、梶浦宗次、渡辺　隆、静岡義秀、塚本英雄、松本孝三、飯田文雄、大塚道夫、小澤義弘

川崎重工㈱

森　誠治、山崎誠一郎、安達潤一、平田慎吾、三浦秀徳、沢井達明、鈴木達志、毛利憲介、山田　猛、小林武司

三菱グループ

上田憲照、池田文構、細田佳加、田戸　茂、山根　実、斉藤龍太、鈴木　優、山田政男、伊尾木公裕、影山輝久、飯村道夫、富田　充、清水克祐、小田泰嗣、宮元和弘、中島国彦、冨田晴彦

住友重機械工業㈱

浅原政治、横川伸久、小西一正、青木高之、松本昭彦、高橋慶丞

日新電気㈱

中田　清、中里　宏、川北　有、谷井正博、谷口周一、林　啓三

㈱東芝

柿澤憲一、海老澤克之、小林重忠、畑山明聖、立川信夫、中川　敏、尾崎　章、渡辺幸夫、新谷吉郎、高瀬治彦

Acknowledgment

Authors deeply thank Dr. Hiroshi Kishimoto of JAERI for the large support and helpful comments throughout this design study. They are thankful to Dr. Akimichi Hishinuma for informations on ferritic steels and CAD Team members of FER Design Team for numerous drawings, three dimensional drawings and interaction studies. For the discussions on negative-ion-based NBI, they thank Drs. Masaya Hanada, Takashi Inoue, Shigeru Tanaka and Kazuhiro Watanabe. They deeply thank members of a Power Reactor Physics Evaluation Committee namely, Drs. Masayuki Nagami, Yasuo Shimomura, Noboru Fujisawa, Toshihide Tsunematsu, Masayoshi Sugihara, Toshio Hirayama, Michiya Shimada and Masahiro Mori for precious comments. They also thank Drs. Masaji Yoshikawa, Tsutomu Iijima, Sanae Tamura, Susumu Shimamoto, Yuuji Tanaka, Shinzaburo Matsuda, Masashi Tsuji, Tatsuoki Takeda and Yuuju Naruse for their understanding and support for this work.

Contents

目　　次

1. Executive Summary

1.1 Introduction

A conceptual design of a fusion power reactor has been carried out in order to clarify the aim of nuclear fusion research and development. The previous power reactor study in the Japan Atomic Energy Research Institute was carried out in 1983 on the SPTR-P concept.[1] Therefore, the concept study of the SSTR (Steady State Tokamak Reactor) was carried out utilizing 1) the new experimental data obtained in the Large Tokamaks such as JT-60, 2) the progress in the fusion reactor technology, 3) recently developed design methodologies and database through the conceptual design studies for ITER and FER.

Specifically, the observation[2] of the bootstrap current driving about 80% of the plasma current in JT-60 lead us to a tokamak reactor concept with the possibility of overcoming a pulse mode operation to achieve a steady state operation. This observation gave the motivation for the proposal of the basic concept[3] of the SSTR.

A realistic power reactor concept has been attained based on the technological progress based on the recent achievements such as the substantial progress in the negative-ion-based NBI development in JAERI and the development of 16.5 T high field superconductor filaments in the industries.

From the ITER/FER conceptual designs, many useful ideas such as the "twin loop concept" to enhance the vertical stability of the plasma and the use of hydraulic pressure cotter for easy coupling and de-coupling of the blanket modules have been employed. That this study has been essentially completed in a remarkably short period of about a half year is owning to the utilization of the experience and the methodology developed in the conceptual designs of ITER/FER. The ITER and FER designs are not always referenced in this report. Their detailed informations could be obtained in the references (4) and (5).

The main objectives of the SSTR concept design[6] is to establish a power reactor concept which can be built in the near future based on the above new informations. So that the concept is made to be as realistic as possible sometimes not optimized in terms of safety and economics. Now that we have established the basic concept of the realistic SSTR, we plan to improve the safety and economics of the reactor concept to make it more acceptable to the society.

References

(1) T. Tone et al.,The Swimming Pool Type Tokamak Power Reactor (SPTR-P), JAERI-M83-120 (1983) (in Japanese)
(2) M. Kikuchi, et al., Nuclear Fusion 30 (1990) 343-355
(3) M. Kikuchi, Nuclear Fusion 30 (1990) 265-276
(4) K. Tomabechi et al., 13-th Int. Conf. Plasma Physics and Controlled Nuclear Fusion Research, IAEA-CN-53/F-1-1 (1990), and ITER Conceptual Design Report, to be published
(5) M. Matsuda et al., 13-th Int. Conf. Plasma Physics and Controlled Nuclear Fusion Research, IAEA-CN-53/G-2-2 (1990), and FER Conceptual Design Report, to be published
(6) Y. Seki et al., 13-th Int. Conf. Plasma Physics and Controlled Nuclear Fusion Research, IAEA-CN-53/G-1-2 (1990), to be published

1.2 Concept of the SSTR and its History

The Steady State tokamak reactor , SSTR, is the original and promising fusion reactor concept with a high fusion output ,which is derived from the result of the bootstrap experiment with JT-60 , and is designed taking account of the current data base for plasma physics and fusion reactor technology.

Since tokamak is superior in a plasma confinement capability, the research and development have proceeded steadily . But, since tokamak drives a plasma current inductively, it is necessary to enhance the research on a steady state operation to overcome its pulsed operation so that it can provide the fusion energy as the practical power reactor.

To establish a steady state operation without an inductive current, an injection power is necessary to actively drive the current of charged particles in one direction. For this purpose, high energy injections with neutral beams and a low hybrid resonance frequency wave are tried. Nevertheless, it is conceived an inefficient large power is necessary for the ways of such an active current drive according to the theoretical estimation and calculation . Therefore, the reduction of net power and energy efficiency as power plant is concerned and the remarkable improvement of the current drive efficiency are desired.

Recently, large tokamaks have conducted high power heating experiment and TFTR and JET consequently exemplified the presence of bootstrap current respectively which was predicted theoretically by Dr.Bickerton etc. of UK in 1971. Especially, JT-60 exemplified the bootstrap current of up to 80% of the plasma current appeared in proportion as βp increased. These result made it possible to overcome its pulsed operation, so-called

tokamak`s destiny, and ensure the steady state operation with tokamak foreseeable.

To put tokamak into practical use as a power reactor,which produce electricity , it should fulfilled to produce a high fusion output at high efficiency and to make the cost of generated electricity comparable to an existing power plant system. To increase fusion output , the ways of increasing plasma current have been generally explored on the base of empirical scaling laws. However, it is necessary to improve the active current drive efficiency in proportional as plasma current increases and consequently the steady state operation become difficult . Also, a successful engineering design considering a large electrical magnetic force induced by disruption become concerned.

On these concerns, SSTR applies a high toroidal field and a large aspect ratio of plasma so that it can produce a high fusion output and efficiently generate electricity as a power reactor. Also SSTR applies a moderate plasma current to reduce the required injection power for an active current drive so that it can easily operate in steady state and to

have a large safety factor in electromagnetic hydrodynamics so that it is viable as the power reactor hard to cause disruption, which has been the subject to be overcome.

On the base of the fundamental consideration described above and an extrapolation from the current data base for plasma physics and reactor engineering, a feasible tokamak reactor concept, which can produce a net power of 1000MW, is preliminary designed.

1.3 Major characteristics on physics of SSTR

Core plasma of SSTR applies the moderate plasma current to enhance a βp value and the ratio of bootstrap current to plasma current. Furthermore SSTR applies a high toroidal field and a high aspect ratio of plasma to enhance the plasma confinement capability and to attain a high fusion output. And also, it can form the stable plasmas with a high safety factor and with a current profile control .Such a characteristics on plasma physics are summarized bellows.

(1) Since the bootstrap current spontaneously causes in proportional to a plasma pressure gradient in a high plasma temperature, comparatively high βp , that is the ratio of plasma pressure to magnetic pressure, of 2 is adopted. Consequently, bootstrap current of around 75% are produced in the high plasma temperature and density. Besides,toroidal B is reduced with a high toroidal field and a moderate plasma current according to the relation of Troyon limit of plasma pressure. However, the plasma center where is no presence of pressure gradient is necessary to be driven with a high power NBI . The improving of B limit and the stabilization of plasma formation are also expected with it .

(2) Based on the empirical scaling laws on a plasma energy confinement (Goldston law, ITER-89 Power law etc.) , which have a weak dependency of stored plasma energy on a minor plasma radius , and on the experimental results with TFTR,PLT,JT-60 (lower divertor configuration) and JET, the high aspect ratio (major radius to minor radius) of 4 extends a fusion power and improve the energy multiplication factor (Q= fusion out put power / plasma heating power),supplementing its moderate plasma current. Consequently , even if such a moderate plasma current , a high energy multiplication factor of around 50 necessary for the power reactor, will be attained within 2 times energy confinement time of so-called L mode.

The injection power for current drive can be minimized due to the large fraction of bootstrap current in SSTR. The plasma with high toroidal field and low current is also stable in the electromagnetic hydrodynamics so that the plasma can avoid an occurrence of disruption due to an instability in m=2. Furthermore a current profile control with NBI is very effective for the control of disruption. A lower single null divertor configuration will be also effective for the suppress of disruption due to inject some pieces of impurities from the upper first wall . Besides, in case of occurrence of disruption,there are many merits in designing, operating and maintenance of SSTR since a low plasma current induce a low electromagnetic force.

1.4 Engineering characteristics of SSTR

SSTR with the characteristics of plasma physics as fusion reactor described above is also distinguished with the engineering characteristics shown below. SSTR extends the engineering feasibility taking account of simplicity and rationality in power reactor system.

(1) Superconductive toroidal field coils (SC TF coils) , made of Ti doped Nb3Sn , produce a maximum field of 16.5 T and 9 T in the center of plasma.
(2) Large aspect ratio of plasma provides a moderate electromagnetic force on the SC TF coils and facilitate those designing
(3) High power neutral beam injection systems play the all roles of the current drive in the center of plasma , the control of current profile and a plasma heating.Those systems applies a Cockcroft Walton accelerator type which is suitable for a continuous injection with a high energy conversion factor (the ratio of injected beam power to the total injection system power) of 50% .
(4) Vacuum vessel is made of uniformed resistive double thin plates embodied the shielding and ensure the mechanical strength against the variable force induced at plasma rump up and disruption.
(5) A lower single null divertor configuration gives birth to a simple reactor structure . Gas

injection into the divertor region is applied to form a dense and cold divertor plasma to protect the divertor plate.

(6) Blanket consists of a solid breeder in pebble bed structure and the low activation ferritic steel pipe panel of F82H. A thin layer of functionally gradient material (FGM) made of ceramics is employed to reduce an electromagnetic force.The blanket consisting of the first wall and the breeder section with the total thickness of about 20 cm in the radial direction , which is mainly facing plasma and radiated,is replaceable periodically.

(7) The generated heat is removed out with a pressurized water in the blanket and employs for a generation of electricity through a steam generator of an existing PWR turbine plant system.

1.5 Design parameter of SSTR

SSTR applies a moderate plasma current of 12 MA and a high βp of 2 so that it can facilitate the steady state operation of a dense plasma with a large fraction of bootstrap current 75 % and a current drive in the center of plasma with a negative ion source based NBI. Furthermore, SSTR applies a major plasma radius of 7 m , a plasma aspect of 4 and a toroidal field of 9 T so that it can extend a fusion output. Accordingly,SSTR can generate a net power of 1000MW at a high efficiency.

Major design parameters of SSTR are shown in the Table 1.5.1. Reactor core structure of SSTR is depicted in Fig.1.5.1.

Table 1.5.1 Major parameters of SSTR

Major Radius	Rp	7.0m	Bootstrap Current	Ibootstrap	9 MA
Minor Radius	ap	1.75m	Beam Driven Current	Ibeam	3 MA
Elongation	κ	1.8	NBI Power	P_{NBI}	60 MW
Triangularity	δ	0.3	Beam Energy	Ebeam	2MeV
Aspect Ratio	A	4.0	Fusion Power	Pfusion	3000MW
Plasma Volume	V	760m^3	Power Gain	Q	50
Plasma Current	Ip	12MA	Total Thermal Output	P_{th}	3710MW
Toroidal Field	Bt	9T	Max. Neutron Wall Load	P_n	5MW/m^2
Safety Factor	q(95%)	5.0	Gross Electric Power	P_{eG}	1280MWe
Safety Factor	q(0)		Net Electric Power	P_{enet}	1080MWe
Toroidal Beta	βt	2.52%			
Poloidal Beta	βp	2.0			
Troyon Factor	g	3.3			
Average Density	$\langle n_e \rangle$	1.45x10^{20}m^{-3}			
Average Temperature	$\langle nT \rangle / \langle n \rangle$	17keV			
Effective Charge	Z_{eff}	1.8			
He Concentration	f(He)	0.05			

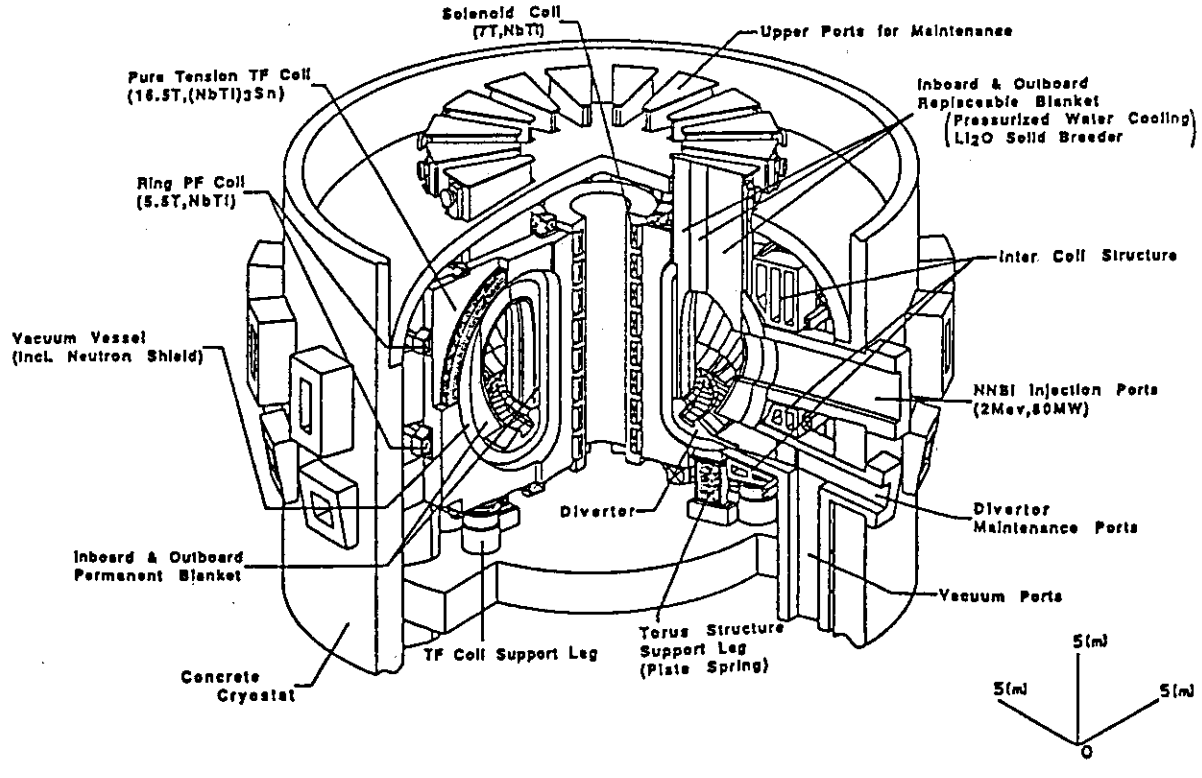

Fig. 1.5.1 Bird's-eye view of SSTR

1.6 Significance of SSTR concept

In case of the realization of a practical use of a fusion energy , since there are an abundant energy resources , people can stably attain an inexhaustible energy . Consequently, its effect is significant enough to give birth to a steady international relation in politics , economics and various fields. Furthermore a fusion reactor system secure the desirable environment not to exhaust an oxide gas supposed to give birth to a green house and also ensure to be a desirable energy resources if only to pay attention to an appropriate tritium handling and a neutron shielding. From such a point of view, major developed nations has proceeded the R & D for the practical use of fusion energy as " the promising alternative energy resources" from early days and the realization of fusion reactor is significantly desired in current days.

By the way, both a steady high fusion output and a desirable economic potential are necessary characteristics for a candidate of a fusion reactor. However , since a steady state operation of tokamak should be compatible with producing a high fusion output , it remains "a difficult home work" to be solved in the future.

On the other hand, the concept of SSTR,which was derived from the verification of large fraction of bootstrap current exemplified with JT-60, is promised to be able to produce a high fusion output steadily with a moderate plasma current, a high βp ,a large fraction of bootstrap current , a high toroidal field and a high aspect ratio of plasma . Furthermore, an application of current engineering enhances its feasibility and ensure the high efficiency of around 30% as the realistic power plant. Consequently SSTR stands for the reference of the realistic reactor through a small extension of current data base of plasma physics and fusion reactor engineering . Additionally its economical potential is foreseeable to be able to compatible with an existing power plant systems according to a preliminary estimation.

It is very significant for the concept of SSTR to provide the realistic image of tokamak power reactor to appear in near future .

2. Major Design Selections

2.1 Operation mode

In a tokamak power reactor, the operation mode could be either pulsed as the most present day tokamaks are, or of a steady state. As a pulsed operation, the pulse length of about eight hours to cover the electricity power peak load has been selected for the comparison. (The pulse operation to cover the base electricity load with a large heat storage to smooth out the electric power output during the dwell time for poloidal magnetic field recharging is believed to be less attractive because of economical drawback and low thermal efficiency.) The merits and demerits of the two operation modes are shown in Table 2.1.1. In a power reactor, the reliability improvement is particularly important so that the steady state operation mode with lower thermal cycle fatigue has been selected.

Table 2.1.1 Merits and demerits of a power reactor operation modes

Items	Steady state operation	Merit or demerit		Pulsed operation
1. Number of thermal cycle fatigue	Thermal cycle is ~50 in the lifetime	M	D	One pulse a day sums up to more than 10,000 cycles in the lifetime
2. Space for magnetic flux swing	The space for plasma ramp up and ramp down will be sufficient	M	D	Additional space of about 2 m thickness is required at inboard side of torus for sustaining plasma current for 8 hours
3. Current drive power	Depends upon the current drive efficiency , 60 MW in case of SSTR	D	M	Small for the inductive current drive
4. Energy balance	Energy multiplication Q in the plasma is ~50 is sufficient for SSTR	-	M	Energy required for the plasma ramp up and ramp down is negligible compared with the energy generated in one pulse

2.2 Reactor power and power density

The unit electricity generating cost becomes lower as the reactor power becomes larger because of the scale merit effect. However, considering the stability in the electric power supply grid and to enable easy comparison with the conventional power generating stations, the net electric power is chosen to be 1 GW.

As for the power density, the unit electricity generating cost becomes lower as the power density can be made higher. Some of the most critical factors limiting the power density are the heat removal capability of the divertor plate and the first wall, and the lifetime of the first wall caused by the neutron wall loading. The heat removal capability of the divertor plate is the limiting factor in most cases. In case of SSTR, the peaking of the heat flux at the divertor plate was lowered by the remote radiative cooling in the divertor region. So that the first wall neutron loading became the limiting condition. The maximum neutron loading at the first wall is 2 MW/m^2 and the first wall is scheduled to be replaced every 2 years.

2.3 High aspect ratio and H-mode confinement

Merits and demerits of high aspect ratio are shown in Table 2.3.1. From this table, we selected high aspect ratio of 4, because we considered it most important for a power reactor to have large energy multiplication in the plasma by having high bootstrap current fraction. As for the confinement, H-mode confinement is assumed. Although present database are mainly obtained in the tokamak devices with aspect ratio less than 3.5, SSTR core plasma characteristics are based on the extrapolation of high aspect ratio data such as in JT-60 bottom X-point configuration.

Table 2.3.1 Merits and demerits of high aspect ratio

Items	High aspect ratio	Merit or demerit		Low aspect ratio
1. Reliability of confinement database	Low	D	M	High
2. Space for magnetic flux swing	Easy to obtain	M	D	Difficult to obtain
3. Bootstrap current fraction	Large 75% in case of SSTR	M	D	Small
4. Plasma current	Relatively small	M	D	Need to be large
5. Divertor particle flux	Low temperature	M	D	High temperature
6. Toroidal field	High Bt required	D	M	Relatively low Bt is sufficient
7. Poloidal field	Stored magnetic energy can be relatively low	M	D	Relatively large stored energy is required

2.4 Plasma beta value

Troyon coefficient of 3.3 is adopted expecting technological and physics progress in future. Plasma confinement is considered in the first stability regime as the data for the second stability regime are considered to be insufficient.

2.5 Plasma vertical elongation

Plasma vertical elongation coefficient k is determined as 1.85. Merits and demerits of large or small elongation are shown in Table 2.5.1. As we considered it important to make the radial size to be as small as possible and selected vertical replacement scheme for the in vessel components such as blankets, large elongation was desired. On the other hand, from the requirement of vertical stabilization of the plasma, upper limit of the elongation was determined to be 1.85.

Table 2.5.1 Merits and demerits of large and small plasma elongation

Items	Large plasma elongation	Merit or demerit		Small plasma elongation
1. Beta value	Can be made larger	M	D	Relatively small
2. Vertical stabilization of the plasma	Stabilization control is more difficult	D	M	Relatively stable
3. Maintenance	Suitable for vertical replacements of in-vessel components. Poloidal field magnet stored energy becomes large for horizontal replacements	-	M	Possibility exists for horizontal replacements

2.6 Divertor scheme

Merits and demerits of single null and double null divertors are shown in Table 2.6.1. Based on the assumption that the divertor heat flux can be lowered by the remote radiative cooling in the divertor region, single null divertor is selected.

Table 2.6.1 Merits and demerits of single null and double null divertors

Items	Single null divertor	Merit or demerit		Double null divertor
1. Peak heat flux in divertor	High	D	M	Low .
2. Effect of plasma vertical movement	Relatively small	M	D	Large
3. Maintenance space allocation	Relatively mote space	M	D	Smaller space
4. Plasma exhaust	Relatively difficult	D	M	Better
5. Exhaust from the upper divertor port	Not necessary	M	D	If exhaust pump is placed on top, it is undesirable from seismic design.
6. Divertor particle flux	Low temperature	M	D	Relatively high temperature
7. Divertor characteristics	Relatively uncertain	D	M	Relatively known

2.7 Current drive method

Negative-ion-based neutral beam injection (NNBI) is selected for the plasma current drive because the physics is best known and also it is planned to be installed in JT-60U. NNBI is particularly suitable for the current drive in the central part of the plasma where bootstrap current is not existing. It can also be used to heat up the plasma. A small amount (5MW) of electron cyclotron heating (ECH) is used for the plasma ramp up. In consequence, a simple mix of 80 MW of NNBI and 5 MW of ECH constitute the plasma heating and current drive system for the SSTR.

2.8 Toroidal field

In order to fully utilize the merits of high aspect ratio plasma, high toroidal magnetic field (with the maximum field of 16.5 T at the conductor) has been adopted for SSTR. This value is selected because 16.5 T superconducting filament has already been developed and the progress in the superconducting magnet technology is very rapid that with appropriate R&D effort, the toroidal field coil used in SSTR has been judged to be realizable 10 years from now.

2.9 Blanket

Water cooled solid breeder material blanket is selected. Merits and demerits of solid and liquid breeder materials are shown in Table 2.9.1. Major reason for selecting solid breeder material is in safety advantages.

Table 2.9.1 Merits and demerits of solid and liquid breeder materials

Items	Solid breeding material	Merit or demerit		Liquid breeding material
1. Safety	High	M	D	Low
2. Database	Relatively large	M	D	Relatively small
3. MHD pressure loss	None	M	D	Large
4. Irradiation damage	Relatively problematic	D	M	No problem
5. Tritium inventory	Small if in case of Li_2O	M	D	Larger
6. Neutron multiplier	Required	D	M	Not required
7. Purge gas for tritium recovery	Required	D	M	Not required

2.10 Cooling scheme

Merits and demerits of water cooling and helium cooling are shown in Table 2.10.1. In order to use the vast experience on water cooling in fission reactors, water cooling has been selected.

Table 2.10.1 Merits and demerits of water cooling and helium cooling

Items	Water cooling	Merit or demerit		Helium cooling
1. User experience	High	M	D	Low
2. Energy conversion efficiency	Relatively low	D	M	Possibility exists for high efficiency
3. Consequence of pressurization accident	Relatively severe	D	M	Relatively less severe
4. Corrosion products	Relatively problematic	D	M	Less problematic
5. BOP cost	Low	M	D	Larger
6. Shielding capability	Large	M	D	None
7. In case of loss of flow	Natural convection can be expected	M	D	Not much can be expected
8. Coolant cost	Relatively low	M	D	High

2.11 Structural materials

For the most highly activated structural materials for the first wall and blanket of SSTR, low activation ferritic steel called F82H jointly developed by NKK and JAERI have been adopted. Merits and demerits of ferritic steels are as follows:

Merits

1)Relatively high thermal conductivity is effective in reducing thermal stress
2)Irradiation swelling is relatively small.
3)Creep rate change at irradiation is small.
4)Reduction of elongation at irradiation is small.
5)Relatively easy to have low activation composition.
6)Relatively inexpensive.

Demerits

1)DBTT increase with irradiation
2)Embrittlement under high temperature, long term irradiation
3)Corrosion under water cooling.
4)Poor fabricability and weldability.
5)Relatively low high temperature strength

Comparison of four ferritic steels, HT-9, F82H, PNC FMS, MA 957 are made in Table 2.11.1. PNC FMS is a carbon dispersion strengthened wrapper tube material and MA 957 is a oxide (Y_2O_3) dispersion strengthened steel.

Table 2.11.1 Comparison of 4 ferritic steels

Item	Temperature	HT-9	F82H	PNC FMS	MA 957
Ultimate tensile strength (MPa)	R.T. 400°C 600°C	770 600 380	700 550 380	880 450	
Creep fracture characteristics		M	G	G	E
DBTT(°C)		-20	-70	~-20	-20
Low activation		M	G	M	M
Material cost		G	G	G	M
Fabricability		G	G	G	M

M:medium G:good E:excellent

2.12 Vacuum vessel scheme

Two types of torus vacuum vessel structures have been considered. One is the concentrated resistance type with a thick, rigid structure with electric resistance concentrated in high resistance part such as made of bellows and the other is a uniform resistance structure vacuum vessel. Their merits and demerits are shown in Table 2.12.1. In SSTR we employed a uniform double walled structure type integrated with shielding so that it became simple and rigid. The use of such a uniform structure became possible because the one turn resistance could be made as small as 4mW when the plasma ramp up scenario based on the recent experiment in DIII-D in which plasma was successfully ramped up assisted by ECH pre-ionization.

Table 2.12.1 Merits and demerits of vacuum vessel structures

Items	Uniform resistance type	Merit or demerit		Concentrated resistance type
1. Structure	Simple	M	D	Complex
2. Electrical resistance	Relatively low but it is allowed when ECH assisted plasma ramp up scenario is adopted.	-	M	Relatively high resistance is possible
3. Experience	Small	D	M	Large
4. Cost	Relatively low	M	D	Relatively high
5. Reliability	High	M	D	Low

2.13 Remote maintenance scheme

Three types of remote maintenance schemes for the in-vessel components of a fusion reactor are compared in Table 2.13.1. In case of SSTR, putting weight on reducing the radial dimension of the reactor room, vertical replacement scheme has been selected for the blanket replacement and horizontal replacement scheme for the divertor plate replacement which needs to be replaced more frequently. Minor repair of the first wall is to be done by in-situ maintenance.

Table 2.13.1 Comparison of remote maintenance schemes

Item	Vertical access	Horizontal access	In-situ maintenance
1. Blanket replacement and replacement time	Crane operation is required. One sector must be divided into parts and both radial and vertical movement are required	Straight motion in the horizontal direction is sufficient so that it is most time efficient	It takes most time because only a limited amount (~1ton?) could be removed at a time by a remote device.
2. Unit of repair and maintenance	Usually by a part of a sector. Another remote maintenance device should be provided for minor blanket repairs.	Usually by a sector. Another remote maintenance device should be provided for minor blanket repairs.	A partial repair of a blanket is possible.
3. Pipings cut and re-connection	Conducted for the whole sector at the connection part above the upper shield plug.	Conducted for the whole sector at the connection part outside the access door.	Pipings are cut or re-connected for each replacement unit.
4. Preparation before replacement	Transport cask must be placed for a sector removal.	Port structures must be removed before placing transport casks.	Remote maintenance devices are placed at the ports and casks for storing removed blankets must be provided.
5. Dependence on remote operations	Miniscule swaying must be controlled.	Least dependence	Largest dependence
6. Requirement for in-vessel sensors, armor tile replacement device	Required	Required	In-situ replacement device may used for such purpose.
7. Possibility of sticking and counter measures	Least possibility and counter measures are easy	Largest possibility and reliable counter measure required.	Relatively low possibility but counter measure should be provided.
8. Earthquake resistant design	Most vulnerable to earthquake	Locking mechanism against earthquake required.	Damage caused by earthquake should be relatively mild.
9. Effect on reactor building	Radial dimension becomes small but height becomes tall.	Radial dimension becomes large.	Reactor building becomes smallest.

10. Overall evaluation	Removal by crane will have large freedom and will be extrapolation of present experience. A clearance of about 2 cm will be required between the blanket sectors.	Freedom is small as sectors are moved along the rails. Possibility for automatic control is largest . Highest possibility for sticking so that counter measure is required.	Minimum preparatory work is required for in-situ maintenance by inserting remote maintenance device through the ports. Since maximum weight handled at a time is small many operations are required. Highest degree of remote maintenance technology is required.

2.14 Reactor containment building

A reactor containment building capable of withstanding 3-4 Atm is employed in SSTR because pressurized water is used for the primary cooling . The reactor building will serve as the final confinement barrier of tritium and activation products in the reactor. Although the hazard potential of a fusion reactor is much less than a fission reactor of comparable power, a reactor building similar to fission reactor will be employed until it is clearly shown by safety analysis to be not necessary.

3. Overview of the SSTR

3.1 Introduction

There are many important subjects to be solved in order to mature tokamak system as a power producing reactor. SSTR(The Steady State Tokamak Reactor) is proposed and designed[1,2] as a power reactor in which basic physics and technology will be established around ten years of proper R&D efforts. In this section, requirements for the fusion power reactor are given and it is described how these requirements will be met with the SSTR design. It is intended to clarify physics and technology R&D items leading to the realization of fusion power reactor. In this section, an overall picture of the design is described.

There are many conditions on the reactor core plasma to realize tokamak system as a power producing reactor and they are called reactor plasma condition. As typical conditions, there are the energy confinement condition, the steady state condition, the magneto-hydrodynamic stability condition and the particle control condition, etc. On the other hand, technical specifications are defined through the selection of the technology basis to realize reactor plasma conditions. The rational for the design selections are given in the previous section.

The plasma equilibrium configuration of the SSTR is shown in Fig.3.1.1. And the plasma parameters are given in Table 3.1.1. Major feature of the plasma are that the plasma minor radius a is relatively small at 1.7m and the plasma volume V is 730m^3 (relatively compact) although the plasma major radius R is large at 7m. And the plasma elongation κ is chosen at 1.85 to be sure on the vertical stability. One of important differences of the design from the previous reactor designs is the use of high magnetic field (9T at the plasma center) and the high surface safety factor (q=5) in order to increase the bootstrap current fraction (high poloidal beta) keeping magneto hydrodynamic stability. Maximum magnetic field at the coil is 16.5T. High toroidal beta is not necessary in such a high magnetic field and it is relatively low at 2.5%. The Troyon factor as a measure of the magneto hydrodynamic stability is high at 3.3. However, enhancement of the Troyon factor in high q regime is reported through current profile control, experimentally and theoretically.

The average temperature of the reactor is 17kev to get high current drive efficiency. The average electron density is chosen at $1.4 \times 10^{20} m^{-3}$. This high density is required to enhance remote radiative cooling in the divertor plasma and to reduce heat flux to the divertor plate. The use of the high magnetic field enables to use dense and high

temperature core plasma. The plasma current is chosen at 12MA to realize efficient steady state operation by the use of bootstrap current. The aspect ratio A is chosen at 4.1 and the safety factor is chosen at 5 to get high confinement Q (=50) with such a moderate plasma current. The current drive power is 60MW due to large bootstrap fraction (75%). Summation of the current drive power and α heating power is 660MW and the required energy confinement time is 1.4 sec. Required confinement enhancement factors for Goldston scaling and ITER power law are 1.8 and 2.0, respectively.

The thermal output from the core plasma and the blanket is 3710MW and the net electric output (after subtraction of circulating power) is 1080MW with the turbine generator for the light water reactor.

Table 3.1.1 Major parameters of the SSTR

Major Radius	Rp	7.0m	Bootstrap Current	$I_{bootstrap}$	9MA
Minor Radius	ap	1.70m	Beam Driven Current	I_{beam}	3MA
Elongation	κ	1.85	NBI Power	P_{NBI}	60MW
Triangularity	δ	0.3	Beam Energy	E_{beam}	2MeV
Aspect Ratio	A	4.1	Fusion Power	P_{fusion}	3000MW
Plasma Volume	V	730m³	Power Gain	Q	50
Plasma Current	Ip	12MA	Total Thermal Output	P_{th}	3710MW
Toroidal Field	Bt	9T	Max. Neutron Wall Load	P_n	5MW/m²
Safety Factor	q(95%)	5.0	Gross Electric Power	P_{eG}	1280MWe
Safety Factor	q(0)	2.0	Net Electric Power	P_{enet}	1080MWe
Toroidal Beta	βt	2.52%	Cost of Electricity	COE	16yen/kWh
Poloidal Beta	βp	2.0			
Troyon Factor	g	3.3			
Average Density	<Πe>	1.4x10²⁰m⁻³			
Average Temperature	≤nT≥ / <n>	17keV			
Effective Charge	Z_{eff}	1.8			
He Concentration	f(He)	0.05			

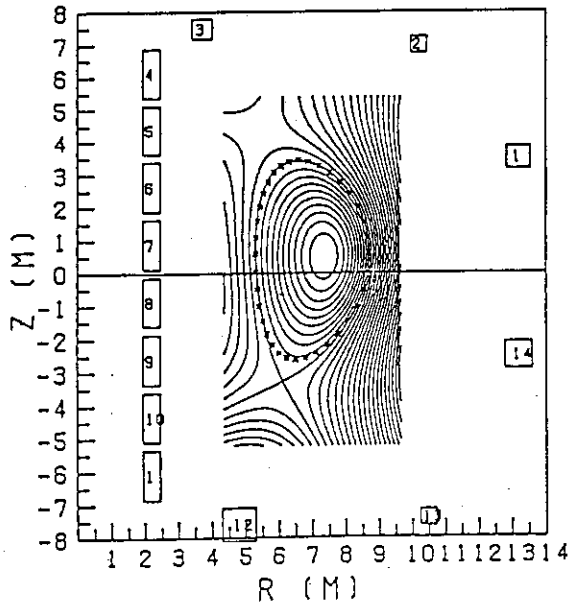

Fig. 3.1.1 Equilibrium configuration of the SSTR

3.2 Energy balance of the fusion reactor

Tokamak fusion reactor as a power reactor should produce more electric power than that for the operation. It is necessary for the efficient power reactor to reduce the operation power to about 20% of the gross electric power including the current drive power. The plant efficiency η_{plant} is defined as a ratio of P_{net} (net electric power output) to P_{th} (total thermal output of fusion reactor) which is an important parameter as a power plant. The plant efficiency depends on the type of power conversion system (steam turbine, water cooling in SSTR) and the required operation power. Basic energy flow of the SSTR fusion reactor is shown in Fig. 3.2.1. Current drive power P_{CD}(60MW) is injected into the reactor core plasma and the fusion power P_f (3GW) is produced. The ratio of P_f to P_{CD} is called as an energy multiplication factor Q(=50). Kinetic energy of fusion α is 20% of the total fusion power. This α power together with current drive power is transferred to the coolant (high pressure water in the SSTR) through the first wall and the divertor plate. On the other hand, 80% of the fusion power is produced as a kinetic energy of neutron (14.06MeV). 90% of the neutron goes to the blanket through the first wall and it reacts with the Be neutron multiplier or it reacts with Li producing tritium and energy. Total thermal power produced in the blanket is $0.72\gamma_{blanket}P_f$ (2930MW) where $\gamma_{blanket}$ is the local neutron energy multiplication factor at the blanket (1.36). A part of the neutron power will be lost to the shield, divertor duct and neutral beam injection ports (P_{loss}=120MW). On the other hand, the neutron energy to the divertor plate is collected without energy multiplication (P_d=120MW).

These thermal output together with the kinetic energy of α particles P_α(=600MW) and the current drive power P_{CD}(60MW) becomes total thermal output P_{th}(1.24P_f). This thermal energy is collected by the high temperature pressurized water (inlet temperature 285°C,outlet temperature 325°C) and is converted to the electric energy with the turbine generator through the steam generator. The energy conversion efficiency η_{th} is ~0.345 achieved in the usual light water reactor. The gross electric power from turbine generator P_{gross} is 1280MWe and about 20% (200MWe) is recirculated as the operating power of the fusion reactor. Largest part of the recirculating power comes from the current drive power. The power conversion efficiency of the NBI system up to 50% is expected and the electric power to the NBI system becomes 120MWe to inject 60MW NBI power. Other recirculating electric power requirements are pressurized water pumping power (50MW), cryogenic system power for superconducting coils(SC) (20MW for cryogenic load 16kW) and the power consumption of the power supply for the SC (10MW).

We understand that the fusion reactor system capable to deliver net electricity more

than 1GWe is basically possible with the tokamak system using the reliable pressurized water as a coolant although the tokamak fusion reactor has a defect in which power required for the steady state operation is relatively large. The plant efficiency η_{plant} is 29% and is 5.5% smaller than the turbine efficiency. Improvement of the energy conversion efficiency of the turbine generator is desirable. But it requires to increase the operating temperature. It should be noticed that the increase of the operating temperature reduce the reliability due to burn out.

Fig. 3.2.2 shows the plant efficiency as a function of the energy gain Q. The plant efficiency becomes positive at about Q~7 and is insensitive to Q for Q>30 as seen from this figure. Thus the achievement of Q=30-50 is important to improve the plant efficiency due to current drive power.

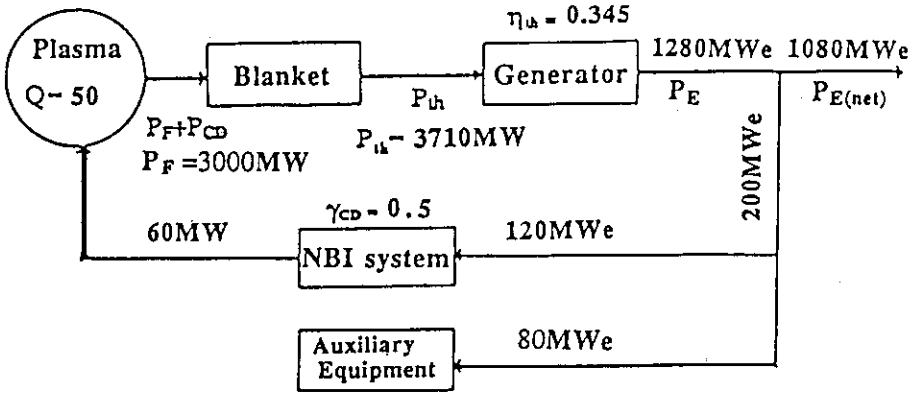

Fig. 3.2.1 Basic energy flow in the SSTR

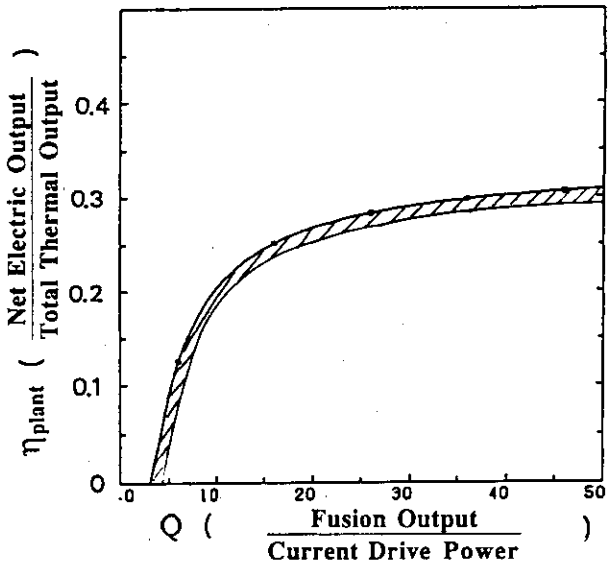

Fig. 3.2.2 Plant efficiency η_{plant} as a function of energy gain Q

3.3 Overview of the Core Plasma

3.3.1 Energy Confinement Condition

Sustainment of the D-T fusion reaction requires following condition,

$$\frac{W_P}{\tau_E} = P_\alpha + P_{CD} \qquad (3.3.1)$$

where W_p, τ_E, P_α and P_{CD} are plasma stored energy, energy confinement time (including radiation loss), α heating power and current drive power, respectively. The α heating power $P\alpha$ is expressed by $P_\alpha = E_\alpha V_p \overline{n_d n_t \langle\sigma v\rangle}$ where E_α=3.52MeV and $\langle\sigma v\rangle$ is the D-T fusion reaction rate and $\overline{A}$ is the volume average of A. The P_α is 20% of the total fusion output. The fusion product $n_i(0)T_i(0)\tau_E$ is expressed as follows with the definition of the energy multiplication factor $Q = P_f/P_{CD}$.

$$n_i(0)T_i(0)\tau_E = \frac{1.5(1+\tau)\alpha_p n_i^2(0)T_i^2(0)}{E_\alpha(1+5/Q)\overline{n_D n_T\langle\sigma v\rangle}} \qquad (3.3.2)$$

where $\tau=\langle n_e T_e\rangle/\langle n_i T_i\rangle$, $\alpha_p=\langle n_i T_i\rangle/n_i(0)T_i(0)$.

The right hand side of equation (3.3.2) is a function of temperature. And, the required fusion product is given as a function of Q. Fig. 3.3.1 shows the operation point of the SSTR in ($n_i(0)T_i(0)\tau_E$, $T_i(0)$) plane. Maximum achieved parameters of three large tokamaks are also shown in the figure.

Figure 3.3.2 shows the history of the record fusion product since 1955. As shown in the figure, the fusion product is improved 100 times in 10 years. Thus the achievement of the energy confinement condition in a fusion reactor will be optimistic if we construct next large tokamak device.

3.3.2 Scaling Laws of Energy Confinement Time

Prediction of the energy confinement is usually made by the extrapolation of the the empirical law. As a representative energy confinement scaling, Goldston scaling [3] which is established based on the experimental data from the medium size tokamaks (R~1m) predicted L & H mode data of large tokamaks (R~3m) quite well. This scaling is expressed as follows,

$$\tau_E = 0.037 I_p R_p^{1.75} a_p^{-0.37} (\kappa A_I/1.5)^{0.5} P_{abs}^{-0.5} \text{ (sec,MA,m,MW)} \qquad (3.3.3)$$

where I_p, R_p, a_p, κ, A_i, P_{abs} are plasma current, major radius, minor radius, ellipticity, mass number and the heating power, respectively.

The ITER design team assessed the confinement data base and established new L mode scaling, called ITER power law(1988).

$$\tau_E = 0.048 I_p^{0.85} R_p^{1.2} a_p^{0.3} B_t^{0.2} n_e^{0.1} (\kappa A_i)^{0.5} P_{abs}^{-0.5} \ (\mathrm{sec, MA, m, 10^{20} m^{-3}, MW}) \quad (3.3.4)$$

Because $n_i(0)T_i(0)\tau_E \sim \langle nT \rangle \tau_E \sim W_p \tau_E / V_p = P_{abs} \tau_E^2 / V_p$,

$n_i(0)T_i(0)\tau_E \sim I_p^2 R_p^{2.5} a_p^{-2.74}$ (Goldston scaling)

$n_i(0)T_i(0)\tau_E \sim I_p^{2.1} R_p^{1.8} a_p^{-2.2} q^{0.4}$ (ITER power law scaling)

From this relation, we see two possibilities to get fusion product required for the power reactor. One is to increase plasma current and the other is to increase the aspect ratio of the device. If the maximum field of the toroidal field coil is limited, we must reduce the aspect ratio to increase the plasma current which reduces the degree of confinement improvement. Thus the high field and high aspect ratio design is an attractive option for the steady state tokamak reactor with moderate plasma current. Fig.3.3.3 shows the plasma current dependence of the fusion product parameter $\tau_E P_{abs}^2 / V_p$ for medium size tokamaks. As is clear from the figure, low aspect ratio tokamaks such as JET and DIII-D reached relatively low fusion product parameter for the same plasma current compared with the high aspect ratio tokamaks such as ASDEX and DoubletIII. SSTR is designed based on such a database. It is important to study the confinement scaling to confirm this SSTR concept.

The confinement enhancement factor over L mode scalings around 1.5-2 is required for the power reactor with low plasma current. This enhancement factor is that obtained in between ELMY H mode and ELM free H mode. These H modes have different characteristics in the impurity accumulation observed in present experimental database.

3.3.3 Current Drive

Inductive (or transformer) current drive method is used in present tokamak devices. So it is required to develop non inductive current drive method for the steady state operation. There are two non inductive current drive methods, namely the passive method such as bootstrap current drive and the active current drive method such as RF and NB current drive. Experimental progresses in JT-60 in this field are significant , for example, in bootstrap current drive and the lower hybrid current drive.

The current drive methods are based on the physics of the momentum exchange along the magnetic field line. So the theoretical calculations are basically consistent with the experimental results which is in contrast to the energy and particle transports (significant deviation from the classical calculation).

3.3.4 Active Current Drive method

Neutral beam current drive and RF current drive methods are well known as active current drive method. The active current drive efficiency $\eta_{CD}=I_p^{CD}R_p\langle n_e\rangle/P_{CD}$ (I_p^{CD}; driven current, $\langle n_e\rangle$; average density,R_p; plasma major radius) of ~ 0.5×10^{20}MA/m^2/MW is expected. The current drive efficiency up to 3.4×10^{19}MA/m^2/MW is realized with the lower hybrid current drive in JT-60(1989).

Summation of the ion current and the electron shielding current is the beam driven current ($J_{BD}=J_{beam}^{i} - J_{shield}^{e}$). The beam driven current is almost cancelled in a uniform magnetic field due to large electron shielding current. But the existence of the trapped electron helps to reduce the shielding current and net beam driven current can flow even in the hydrogen plasma in a toroidal plasma. The beam driven current increases with the electron temperature because the ion current increases with the slowing down time of the fast ion (τ_s~$T_e^{1.5}$). Thus the beam current drive is most effective in high temperature plasma such as SSTR.

On the other hand, there are many kinds of RF current drive such as lower hybrid current drive, fast wave current drive and EC current drive, depending on the driver wave. The lower hybrid current drive was adopted in the STARFIRE[5] but the wave is fairly difficult to penetrate into the plasma center when T_{e0} >10keV due to strong wave damping in the plasma periphery. The central current drive is desirable when we realize high efficiency steady state with the bootstrap current. And the current drive efficiency in ITER is ~0.3×10^{20}MA/m^2/MW due to collisions between trapped and passing electrons. High frequency is also required to reduce power absorption through α particle.

The fast wave can penetrate into the core plasma due to weak damping. But the current drive efficiency decreases due to strong wave absorption by α particles if the wave frequency is higher than ion cyclotron frequency. Thus the fast wave frequency below ion cyclotron frequency is considered as a driver wave. Then the large antenna area (reduce TBR) and the low current drive efficiency (~3×10^{19}MA/m^2/MW) are not quite desirable. But the system may be cheaper than the NBI system. The efficiency of the electron cyclotron current drive is relatively low and EC system is fairly expensive at present. From these considerations, the NB current drive system is adopted for the active current driver in the SSTR.

Steady state tokamak reactor based only on the active current drive requires large current drive power and the net electric output is significantly reduced. For example, current drive of R=7m, $\langle n_e\rangle$ =1.5×10^{20}m^{-3}, Ip=12MA plasma requires net injection

power of 252MW. Assuming the total energy conversion efficiency of the current drive system as 50%, the circulating power is more than 504MW. This power corresponds to >42% of the gross electric power in the 3GW fusion reactor. Basic feasibility of the steady state reactor may be lost in such a situation. On the other hand, a spontaneous plasma current (bootstrap current) exists in a tokamak plasma and it is possible to excess 50% of the total plasma current. In this case, it is possible to get efficient steady state with present level of current drive efficiency. The existence of such a passive current and its experimental confirmation enable the conceptual design of this steady state tokamak reactor.

3.3.5 Passive Current Drive Method (Bootstrap Current)

Extremely important scientific achievement is made on the passive current drive method in these two years, namely the existence of the bootstrap current. Dr. R.J. Bickerton of the United Kingdom proposed a theory of the bootstrap current [6] (1971) in which he pointed out the existence of a large natural current proportional to the pressure gradient in a collisionless plasma. The theory predicts that the plasma current can be dominated by the bootstrap current when the poloidal beta defined as a ratio of the plasma pressure to the magnetic pressure of the poloidal field is large. The definition of the poloidal beta is given as follows,

$$\beta_p = \frac{4}{\mu_o R_p I_p^2} \int P dV \qquad (3.3.5)$$

where, P and dV are the plasma pressure and the volume element, respectively. Most of the plasma current is carried by the bootstrap current when the poloidal beta defined by equation (3.3.5) reaches ~2. Many scientists intended to confirm its existence since then. But it becomes possible in three large tokamaks(JT-60, TFTR and JET) in which high temperature and high βp plasma is produced with intense NB heating. Since the existence of the bootstrap current is reported in the TFTR tokamak (1988), it is confirmed in JET (1988) and in JT-60 (1990). Especially in JT-60 [7], 80% of the total plasma current is carried by the bootstrap current which is extremely important for the realization of the steady state tokamak reactor. The mechanism responsible for the bootstrap current is fairly complicated but it comes from the parallel momentum balance equation. A simple form of the bootstrap current fraction is proposed by Fujisawa and Mizoguchi [8] as follows,

$$f_{bootstrap} = \frac{I_p^{bootstrap}}{I_p^{total}} = 0.75(\sqrt{\frac{a}{R}}\beta_p)^{1.3} \qquad (3.3.6)$$

It is easily shown 75% of the total plasma current is the bootstrap current for the tokamak with the aspect ratio of 4 and βp of 2. Detailed calculations with the current drive code predict similar values depending on the current profile. Figure 3.3.4 shows the

(Ip,A) diagram and the equi fusion product contours for ITER power law and Goldston scaling. Equi bootstrap current fraction (75%) line is also shown by the broken line for constant fusion power(3GW) and constant surface area (constant neutron flux). As is seen from this figure, higher aspect ratio regime is easier to get compromise between high bootstrap current fraction and high fusion product for the same fusion output. Low aspect ratio tokamaks may become an efficient fusion reactor in cases of higher fusion output, better confinement and current drive efficiency.

3.3.6 Plasma Pressure Limit

Progress of theory and experiment on the magneto hydrodynamic stability is one of remarkable scientific achievements in the fusion research in 1980's. Magneto hydrodynamic instabilities are categorized into current driven modes and pressure driven modes. Typical examples of the current driven mode are magnetic island formation by the tearing mode and the low beta disruption (m=2 mode plays an important role) and those for the pressure driven modes are the high n ballooning mode and the internal kink mode. These instabilities may result in the loss of confinement geometry (destruction of the magnetic surface or disruption) or the degradation of the plasma confinement. So careful attention must be paid on the magneto hydrodynamic stability in a design of a tokamak reactor plasma. Requirement from the current driven instability is $q95 > 3$ in a standard reactor design. On the other hand, plasma pressure is limited for the reactor design within following Troyon limit from the pressure driven MHD stability. This scaling of the pressure limit is shown by F. Troyon in 1984 and it is beautifully checked in the DoubletIII and DIII-D experiments.

$$<\beta_t> (\%) = g \frac{I_p(MA)}{a_p(m)B_t(T)} \qquad (3.3.7)$$

where g is called Troyon factor and is ~3.5. Combination with previous definition of the poloidal beta gives following relation between β_t and β_p,

$$\beta_p <\beta_t>(\%) = \frac{g^2\kappa}{4} \qquad (3.3.8)$$

This relation is shown in Fig.3.3.5. The operation points for the experimental reactors (FER,ITER,NET) and the power reactor (SSTR) are shown in the figure. As is seen from eq. (3.3.6), poloidal beta must be increased to increase passive current (bootstrap current) fraction. So the toroidal beta must be decreased to meet Troyon limit ($<\beta_t>$=2.5% in SSTR). Thus the operation point of the steady state power reactor is fairly different from that of the experimental reactor whose direction is to reach high fusion product regime by increasing plasma current. Presently, DIII-D has produced g=3.5 quasi steady discharges. So the selection of the Troyon factor g=3.3 in the SSTR is fairly good assumption from the

experimental point of view.

3.3.7 Current Profile Control and Pressure Limit Improvement

Active control of the plasma current profile is important for the reactor to operate near the pressure limit. Passive plasma current (bootstrap current) reached up to 75% of the total plasma current. The bootstrap current is zero at the plasma center and hollow current profile is formed. So it is required to drive the plasma current near the center actively and to keep MHD stability. To drive plasma current near the plasma center, we have NB (high energy beam) and RF (low frequency fast wave) current drive methods. We think low frequency RF current drive requires large antenna area which may not be desirable for the reactor. On the other hand, efficiency of the NB current drive is proportional to the electron temperature which is suitable for the central current drive. The beam energy of 2MeV is required for the central current drive in the SSTR taking into account of the multi step ionization process. Plasma equilibrium and NB cross section are shown in Fig.3.3.6. The bootstrap current profile is calculated assuming that the density profile $n_e \sim (1-x^2)^{0.5}$ and the temperature profile $T_e \sim (1-x^2)^{1.5}$. The calculated current profile is shown in Fig. 3.3.7. The bootstrap current profile is hollow and total current profile is monotonic as a function of minor radius. In this calculation, the total bootstrap current is 10MA and the beam driven current is only 2MA. This situation comes from high central q value ($q_o \sim 2$)
which resulted in the low poloidal field near the center and is effective in enhancing bootstrap current. So the required NBI power is only 45MW which is less than the design value of the NBI system in the SSTR. Ballooning stability is calculated for this profile as shown in Fig.3.3.7. In this figure, critical pressure gradient against ballooning mode is shown together with the assumed pressure gradient. The pressure gradient is less than the critical one. So the pressure profile assumed in the SSTR is stable to the ballooning mode.

The MHD stability against low n kink-ballooning modes is also investigated using the ERATO-J code. Fig.3.3.8 shows the growth rate of low n ideal MHD modes as a function of the central q value. Here we use the boundary condition, namely the location of the conducting wall at 1.2 times the plasma surface taking into account that the first wall of the SSTR is made of conductive ferritic steel. As is clear from the figure, low n ideal MHD modes are stabilized when $q_o > 2$.

The improvement of the MHD stability with such a current profile control comes from the compromise between the pressure gradient (driving force of the instability which is determined by the plasma transport process) and the magnetic shear (depending on the current profile). In the present calculation the pressure profile P~(1-x2)2 is assumed and the

broader current profile is stable. If the pressure profile is much broader, then peaked current profile may be better in improving Troyon limit. In such a case, we expect slight decrease of the bootstrap current. So we adopted the NBI power of 60MW in a reference design.

3.3.8 Dense and Cold Divertor and Remote Radiative Cooling

The heat and particle removals from the fusion reactor with the poloidal divertor are made in the divertor room. So the heat and neutral fluxes to the first wall becomes small. Synchrotron and bremsstrahlung radiations in the main plasma are 10-20 % (effective power reflection coefficient of the synchrotron radiation of the first wall is assumed at 85%) and the rest of the power goes to the divertor plasma through the scrape off layer (SOL) plasma. This power reaches up to 600MW and the heat flux to the divertor plate is ~100MW/m^2 if total power is transferred to the divertor plate. With this heat flux, we can not obtain any realistic solution of the power reactor even if we include significant progresses in the high heat flux components. On the other hand, it is possible to have low temperature plasma in front of the divertor plate and large temperature gradient along the magnetic field line due to finite electron parallel thermal conductivity for the high recycling divertor. Low temperature plasma in front of the divertor plate is high density plasma due to pressure continuity along the magnetic field line. Sputtering erosion from the divertor plate is negligibly small for the low temperature plasma (~10eV) even if we take into account of the acceleration in the plasma sheath. The formation of the dense divertor plasma enhances the remote radiative cooling and reduces the heat flux to the divertor plate because the line radiation and the recombination radiation is proportional to the square of the plasma density. Thus the cold and dense divertor plasma has favorable aspects for the tokamak fusion reactor.

3.3.9 Dense and Cold Divertor Plasma

We use two point divertor plasma model to understand the formation of the cold and dense divertor plasma. Particle, momentum and heat balance equations along magnetic field line are expressed as follows,

$$\text{Particle} \quad ; \frac{\partial}{\partial s}(nv_s) = S_i$$

$$\text{Momentum} \; ; \frac{\partial}{\partial s}\left(n\left(v_s^2+\frac{2T}{m}\right)\right) = 0$$

$$\text{Heat} \quad ; \frac{\partial}{\partial s}\left(-\kappa_{//o}T^{2.5}\frac{\partial T}{\partial s}\right) = -W_R \qquad (3.3.9)$$

where s is the length along the magnetic field line, n is the plasma density, Vs is the parallel flow velocity, Si is the ionization rate, T is the temperature, $\kappa_{//o}$ is the parallel thermal conduction coefficient ($12.5 W/cm/ev^{3.5}$), W_R is the radiation power density. From these equations, temperature, density and flow velocity near the divertor plate and SOL are given as follows,

Near divertor plate;

$$n_d = \frac{R\Gamma_s}{u_{//d}}, \quad T_d = (q_{//s} - \int_0^{L_D} W_R ds)/(\gamma R \Gamma_s), \quad u_{//d} = \sqrt{\frac{2T_d}{m}} \qquad (3.3.10)$$

SOL;

$$n_s = \frac{\Gamma_s}{(R - \sqrt{R^2 - T_s/T_d})u_{//d}}, \quad T_s = (T_d^{3.5} + \frac{3.5 L_D q_{//s}}{\kappa_{//o}})^{2/7}, \quad u_{//s} = \frac{\Gamma_s}{n_s} \qquad (3.3.11)$$

where R is the flux multiplication factor near the divertor plate, Γs is the particle flux from the SOL, γ is the heat transmission coefficient (~7.8), $q_{//s}$ is the heat flux from the SOL. As is clear from equation (3.3.10), the temperature near the divertor plate is proportional to the ratio of the heat flux to the particle flux. The SOL temperature can be high compared with the temperature near the divertor plate due to finite $\kappa_{//o}$. Flux multiplication factor R is a strong function of plasma density and it depends on the divertor geometry. As an example, plasma parameters are calculated in Fig.3.3.9 as a function of Γs for the model $R=1+(R_m-1)(1-\exp(-2\times10^{20} n_d))$ with the assumption of 80% radiation of the total heating power (660MW). As is clear from the figure, cold and dense divertor plasma condition can be satisfied by increasing particle flux from the main plasma. This flux is determined from the particle confinement time of the main plasma and will be limited especially in the H mode. Strong gas puff along the separatrix line between X point and the divertor plate is effective to enhance the particle flux to the divertor plate. This point will be described later. Temperature and density profiles along the poloidal projection of the field line is shown in Fig.3.3.10 in the case of $\Gamma=2\times10^{23}$/sec. As is clear from the figure, the temperature is less than 10eV near the divertor plate but is more than 100eV at ~10cm away from the plate. The temperature is more than 200eV near X point and ~400eV around the main plasma with the electron density $n_e \sim 7\times10^{19} m^{-3}$.

It is required to have small impurity near the divertor plate to enhance remote radiative cooling and hence to reduce the heat flux to the divertor. But impurity injection to SOL may result in the accumulation of the impurity in the main plasma. So some methods to localize the impurity near the divertor plate is needed. Thus the active control of the particle flux and the remote radiative cooling of the divertor plasma is required to protect erosion of the divertor plate during one year of operation before the annual replacement of the divertor plate. We call such an actively controlled divertor plasma as Active Cooled Divertor.

3.3.10 Active Cooled Divertor

As described above, it is required to produce cold and dense divertor plasma actively and we adopted 1) divertor gas puff and 2) radiative cooling with impurity injection. Formation of the cold and dense divertor plasma is determined by the balance between particle flux and heat flux from the main plasma. Qualitatively speaking, high particle flux and low net heat flux is favorable for the formation of cold and dense divertor plasma. Gas puffing to SOL plasma is one of the candidates to enhance particle flux. However, gas puffing to the SOL plasma around the main plasma produces energetic neutrals which produce the sputtering erosion of the first wall. So the gas puffing is applied to the SOL plasma near the divertor plate which is effective in reducing the energy of the charge-exchange neutrals. The heat flux to the divertor plate is usually highest near the separatrix. In order to reduce the heat flux in such a region, the gas puffing is applied from the inner side of the separatrix line (private region) which is effective for the gas to penetrate into the high heat flux zone (see Fig.3.3.11). The applied gas puff rate of 6×10^{23}/sec is selected which is three times the particle flux from the main plasma (particle confinement time of 0.5sec is assumed). As a simple estimate, total hydrogen radiation becomes 115MW if the flux multiplication factor R=30 and the radiation per ionization of 30eV are assumed. It is clear that hydrogen radiation is not enough to reduce the heat flux to the divertor. So remote radiative cooling through the impurity injection is required. The medium Z impurity is effective which has large radiative cooling rate around a few 100eV. The radiative cooling rate from the impurity is calculated by D. Post et al.[10]. The radiative cooling rate is shown for Ar and Fe in Fig.3.3.12. Here we calculated the effect of remote radiative cooling (radiative cooling rate $W_R=n_e n_{Fe} L(T_e)$) for Fe. Fig.3.3.13 shows radiation cooling rate expected from the coronal model in the case of Fe inclusion of 0.8% of the total electron. The total radiation from the SOL reaches up to 490MW and the heat flux to the divertor plate is significantly reduced. In this case, the impurity backflow to the main plasma due to the thermal force is most serious issue. The momentum balance equation along the magnetic field is expressed as follows,

$$\rho_z\left(\frac{\partial}{\partial t} + V_z\frac{\partial}{\partial z}\right)V_z = \nabla_{//}P_z + eZn_zE + \rho_z(v-v_z)/\tau_z + n_z[\alpha_z\nabla_{//}(kT_e) + \beta_z\nabla_{//}(kT_i)] \qquad (3.3.12)$$

where third term of the right hand side is the friction force between fuel particles and the impurity. The fourth term is the backflow term due to the thermal force. It is possible to get a solution in which the impurity is condensed near the divertor plate with the strong friction force. Fig.3.3.14 shows typical example of temperature, density profiles along the poloidal projection of the magnetic field line calculated from the two dimensional divertor code.

3.3.11 Heat Load Control Condition

From the above discussions, the design condition of the heat flux to the divertor and the first wall is selected as follows,

Radiation in the core plasma = 90MW
(mainly synchrotron radiation)
Edge and SOL radiations = 490MW
Conduction to divertor plate = 80MW

Fig.3.3.15 shows the heat flux distribution along the first wall. As is clear from the figure, the heat flux at the outboard midplane is ~0.4MW/m^2 where the neutron flux is maximized. Fig.3.3.16 shows the heat flux distribution along the divertor plate. The maximum heat flux to the divertor plate is 7MW/m^2 for the outboard plate and 5MW/m^2 for the inboard plate. Table 3.3.1 shows design conditions of the heat flux in the SSTR. The key point is the dense plasma operation and the use of active cooled divertor. (Preliminary two dimensional divertor code analysis gives the heat flux ~10MW/m^2. But we hope further reduction of the heat flux with careful optimization.)

It is possible to separate the high heat flux zone and the high neutron flux zone with the use of the poloidal divertor configuration. So the blanket mainly controls the neutron load and the divertor room mainly control the heat load. Such a function sharing is effective to relieve the technical design specification.

3.3.12 Particle Control Condition

Fuelling and the He ash exhaust are important in the particle balance. The D/T burn up rate is 2.0×10^{21}/sec for the fusion output of 3GW. The net particle flux from the main plasma (assumption) is 2×10^{23}/sec (100 times the D/T burn up rate). So the required fuelling rate with the pellet injection system is 100 times the D/T burn up rate. So the injection rate is not determined from the fuelling but from the formation of cold and dense divertor plasma with strong friction force to the impurity. So peripheral ablation of the pellet is favorable. If we can reduce the particle flux without sacrificing impurity control, we can adopt much smaller pellet injection rate. But it should be verified from the numerical analysis and the experiments).

Presently, two types of pellet injectors are available, namely the centrifugal injector with the injection velocity ~1km/sec and the pneumatic injector with the injection velocity ~2km/sec. In either case, it is possible to penetrate ~20cm into the plasma. In the present design, we adopt the centrifugal injector system which is suitable for the continuous

injection. (Although an ultra high speed injector (~50km/sec) can penetrate deeply into the core plasma and is favorable for the effective fuelling, the reduction of the pellet size is required to reduce the parameter change. Furthermore, ultra high speed injector requires extensive R&D to be used as a continuous injector.

If the particle confinement time is much longer than 0.5 sec, plasma density will increase with such a large particle fuelling rate. In this case, particle fuelling should be reduced and the divertor gas puff is important for the particle flux enhancement which has low fuelling efficiency for the main plasma. In this case, it is required to check the impurity control with friction force. The particle confinement time data base is not established for the H mode. This is an important research subject of the tokamak experiment. As a simple estimate, we calculate here required particle diffusion coefficient in the periphery to get a particle flux of 2×10^{23}/sec. We assume that the pellet ablation occurs at 20cm from the plasma edge and the plasma density is $1.6\times10^{20}m^{-3}$. Using the relation $\Gamma = -SDdn/dr$, the diffusion coefficient D at the plasma edge is $0.7m^2$/sec for $S=700m^2$ and $dn/dr=(1.6-0.7)\times10^{20}m^{-3}/0.2$. It is well known that the particle diffusivity in the H mode is much lower than that in the L mode. So the fuelling rate to the main plasma should be reduced in the case of $D_{edge} < 0.7m^2$/sec. Moreover, such a high fuelling may result in the over cooling of the edge plasma. So the optimum fuelling rate with the pellet injector should be determined by the experiment and the simulation. The pellet injection may influence the structure of the edge plasma and be a possible tool for the edge plasma control of the H mode plasma. Preliminary results of the two dimensional divertor code analysis show that a strong divertor gas puff (1.75×10^{24}(D/T)/sec) is required even with the large particle outflux from the main plasma (2.5×10^{23}(D/T)/sec) to form a cold and dense divertor plasma. Total fuelling of 2×10^{24}(D/T)/sec should be pumped with the He ash. In the SSTR, the pumping is made from the outboard divertor and no pumping duct is connected to the inboard divertor. The neutral pressure near the pumping port becomes fairly high (>1Pa). It should be noted that the particles from the main plasma flow into the divertor room and neutralize at the divertor plate. So the neutral pressure around the first wall is low enough to reduce the sputtering erosion.

3.3.13 Low Voltage Inductive Current Build Up

Design of the vacuum vessel as a fundamental component of the fusion reactor is influenced by the breakdown voltage required for the plasma current build up. The design values of the applied voltage and the one turn resistance in JT-60 are 300V and 1.3mΩ, respectively. Similar values are adopted in the TFTR and JET. On the other hand, DIII-D and JT-60U adopted the uniform and low resistance vacuum vessel taking account of the

experimental results of the applied voltage during the plasma break down. Table 3.3.2 shows design and achieved values of the one turn resistance and the applied voltage for various tokamaks. Recent results from DIII-D tokamak shows that the surface voltage required for the plasma current build up is as low as 2V. The voltage required for the current build up with the intense preionization is determined from the electron confinement characteristics. The energy balance is expressed by using the Neo Alcator law as follows,

$$\frac{3n_eT_eV}{P_{ECH}} = cR^2an_eq \qquad (3.3.13)$$

This relation gives T~(R/a)PECE. The minimum one turn voltage required for the current build up in the SSTR is calculated for the ECH power of 5MW as ~0.1V_L(DIII-D) ~0.2V. This value together with the inductive voltage $V_I=L_pdI_p/dt$~1V is the minimum required voltage for the plasma current build up. The externally applied voltage is chosen at 4V with some margin and the maximum induced plasma current in the vacuum vessel is 1MA for the one turn resistance of 4μΩ. The poloidal field induced by the eddy current in the vacuum vessel is nearly vertical field and can be cancelled by the pre bias. For such a low one turn resistance , very simple structure of the vacuum vessel can be adopted. Moreover, low resistance vacuum vessel can shield the time variation of the magnetic field during the plasma disruption and reduce the AC loss of the superconductor. The low resistance vacuum vessel improves the vertical stability in the low frequency regime and reduces the power supply for the feedback control system.

We adopted the pure inductive current build up. This is because non inductive current drive with 2MeV beam is adopted in the SSTR and is not suitable for the current drive in the low density and low temperature plasma during the start up phase, due to large shine through and low current drive efficiency. Moreover, use of the non inductive current drive during the start up phase do not save the EMF of the center solenoid coil.

3.3.14 Vertical Stability

The vertically elongated plasma has good properties in increasing the plasma current and the pressure limit. So this shape becomes a standard of the tokamak fusion reactor. But the counterplan for the vertical instability should be made in the vertically elongated plasma. The vertical stability is maintained by the repulsive force between plasma current and the eddy current induced in the stabilizing shell. It is also determined by the balance between curvature index of the magnetic field (n index) and the index of the passive shell ($n_s(\gamma)$). So the stability condition is expressed as follows,

$$n + n_s(\gamma) > 0 \qquad (3.3.14)$$

The low resistance vacuum vessel is adopted in the SSTR. And the time constant of

the eddy current in the passive shell is large which is effective to stabilize the mode in the low frequency regime. This reduces the capacity of the power supply of the feedback control system.

3.3.15 Plasma Disruption Condition

It is highly desirable that the plasma is free from the disruption in the fusion reactor. The SSTR is characterized by its high q operation and the probability of the plasma disruption is expected to be small. But it is very dangerous from the present database to design the fusion reactor to be free from the disruption. In the present design, a disruption of 12MA plasma within 20ms is used for the designs of the blanket and the vacuum vessel. We adopted plasma disruptions without movement and 2m movement toward the X point for the design.

References

(1) M. Kikuchi, Nuclear Fusion **30** (1990)265.
(2) Y. Seki, M. Kikuchi, T. Ando, Y. Ohara, et al., 13th Int. Conf. Plasma Physics and Controlled Nuclear Fusion Research, IAEA-CN-53/G-1-2,(1990)
(3) R. J. Goldston, Plasma Physics and Controlled Fusion, **26**(1984)87.
(4) P. N. Yushimanov, T. Takizuka, et al., Nuclear Fusion,**30**(1990)1990.
(5) C. Baker, et al., "STARFIRE - A commercial tokamak fusion power plant study", ANL/PFF-80-1,(1980).
(6) R. J. Bickerton, et al., Nat. Phys. Sci.,**229**(1971)110.
(7) M. Kikuchi, M. Azumi, et al., Nuclear Fusion,**30**(1990)343.
(8) N. Fujisawa, T. Mizoguchi, ITER Rep. IL-6-9-J-4.
(9) F. Troyon et al., Plasma Physics and Controlled Fusion,**26**(1984)209.
(10) D.E. Post, R.V. Jensen et al., Atomic Data and Nuclear Tables, **20** (1977) 397.

Table 3.3.1 Heat load condition

Item	Value
Total fusion power	3000MW
α heating power	600MW
NBI power	60MW
Main radiation	90MW
SOL/divertor radiation power	490MW
Heat conduction	
inboard plate	27MW
outboard plate	53MW
Peak heat load	
inboard	7MW/m^2
outboard	5MW/m^2

Table 3.3.2 Plasma initiation voltages and one turn resistances of tokamaks

Name	major radius	minor radius	one turn resistance	design/achieved loop voltage
JFT-2	1.05m	0.30m	~5mΩ	(~12V)
DoubletIII	1.43m	0.45m	0.2mΩ	256V
DIII-D	1.67m	0.60m	0.18mΩ	(~2V)
JT-60	3.0m	0.90m	1.3mΩ	300V(20V)
JET	2.96m	1.2m		140V(10-20V)
JT-60U	3.3m	1.0m	0.2mΩ	36V
ITER	6.0m	2.15m	20μΩ	25V
SSTR	7.0m	1.70m	4μΩ	4V

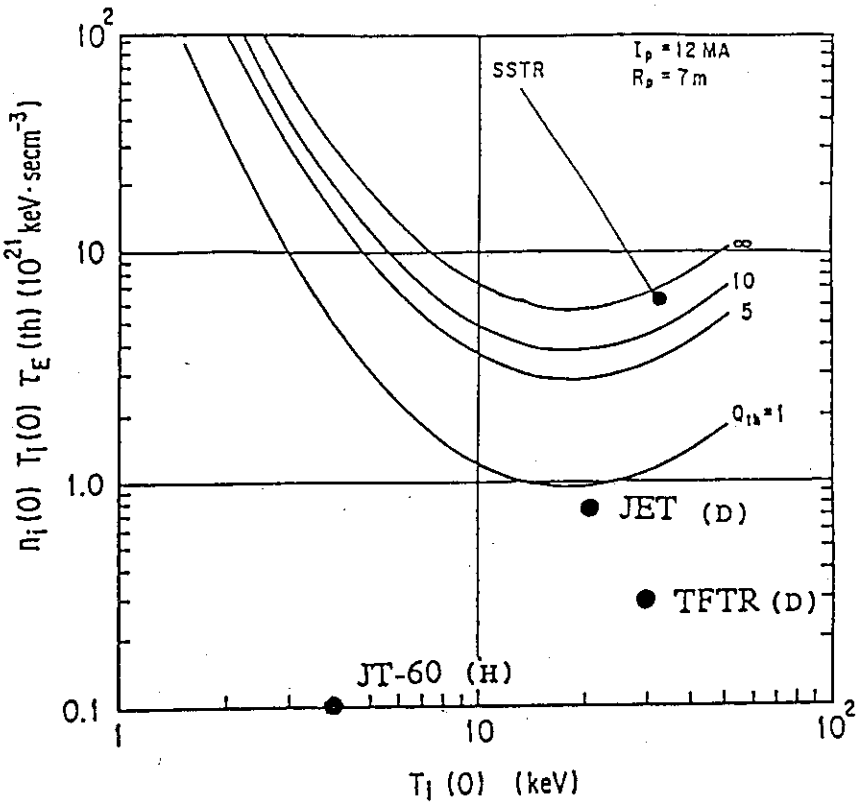

Fig. 3.3.1 $(n_i(0)T_i(0)\tau_E, T_i(0))$ diagram and the operation point of the SSTR Maximum performances of 3 large tokamaks are also shown.

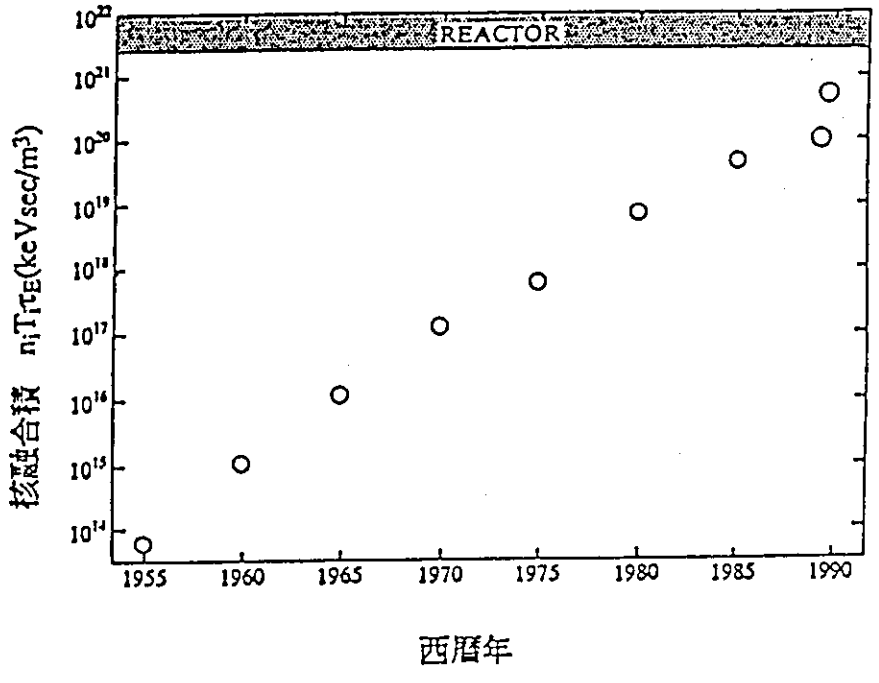

Fig. 3.3.2 Progress of the fusion product achieved in tokamaks

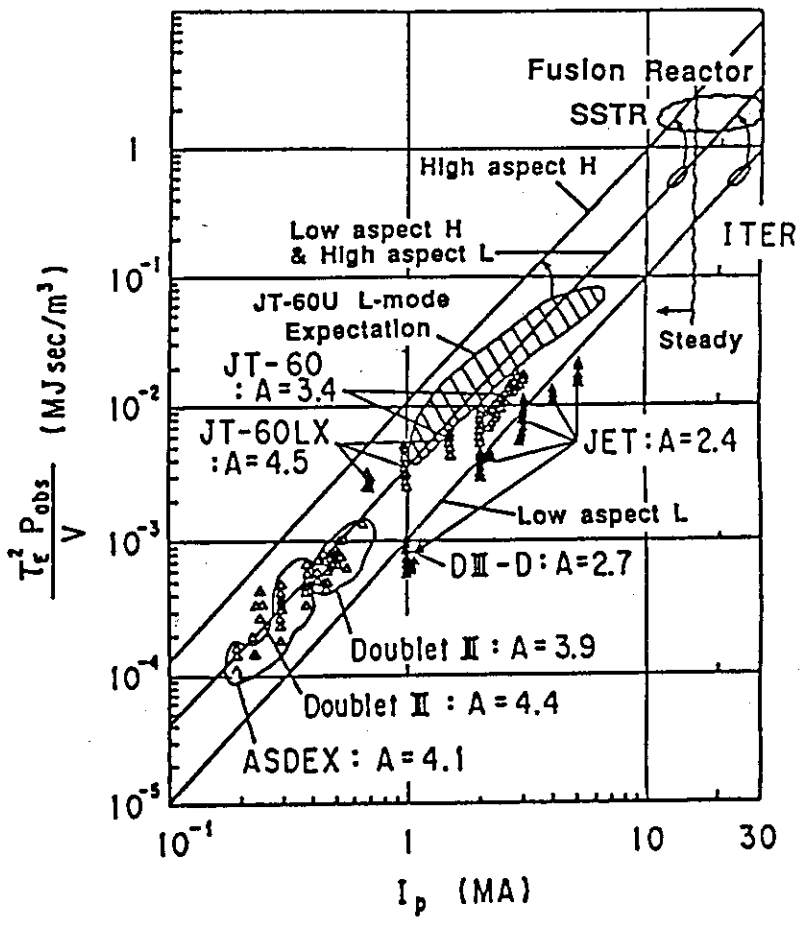

ITER L mode Database

Fig. 3.3.3 Fusion product parameter $P_{abs}\tau_E^2/V$ as a function of plasma current Ip for various tokamak L mode database. Solid lines show Ip^2 dependence of $P_{abs}\tau_E^2/V$ expected from empirical scalings.

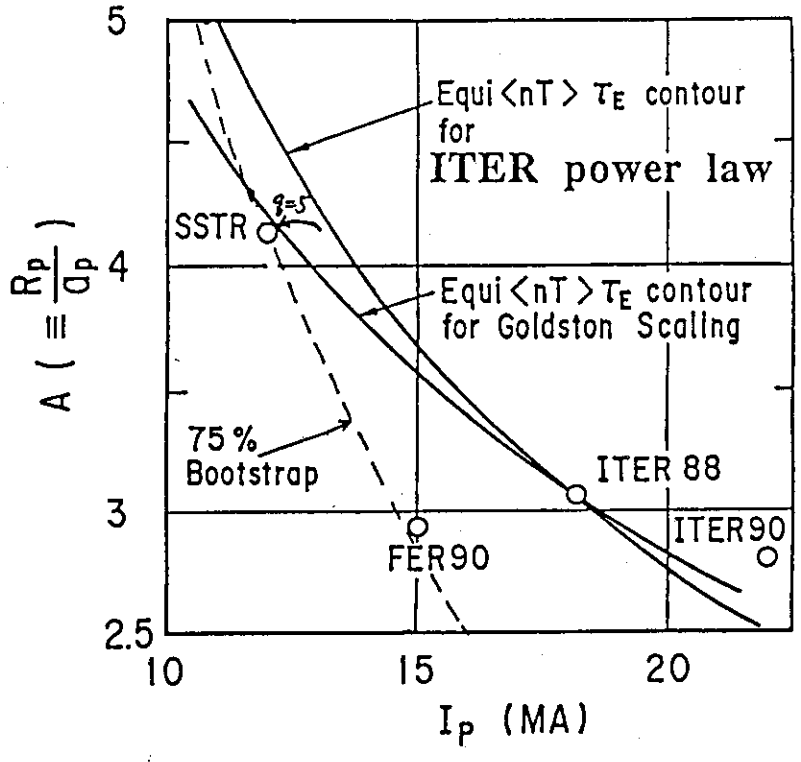

Fig. 3.3.4 Equi fusion product contours from Goldston and ITER power scalings. Design points for experimental reactors (FER and ITER) and the SSTR are shown in the figure.

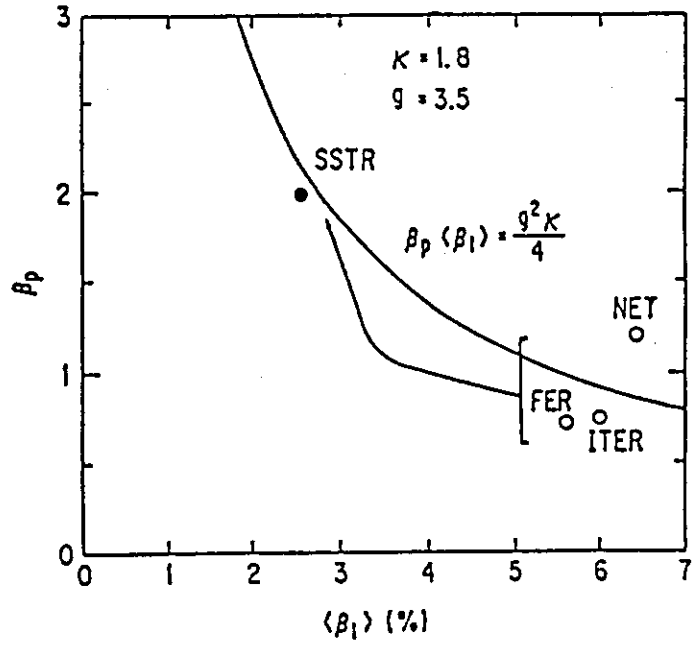

Fig. 3.3.5 (βp,βt) diagram showing g=3.5 contour and various design points of FER, ITER and the SSTR

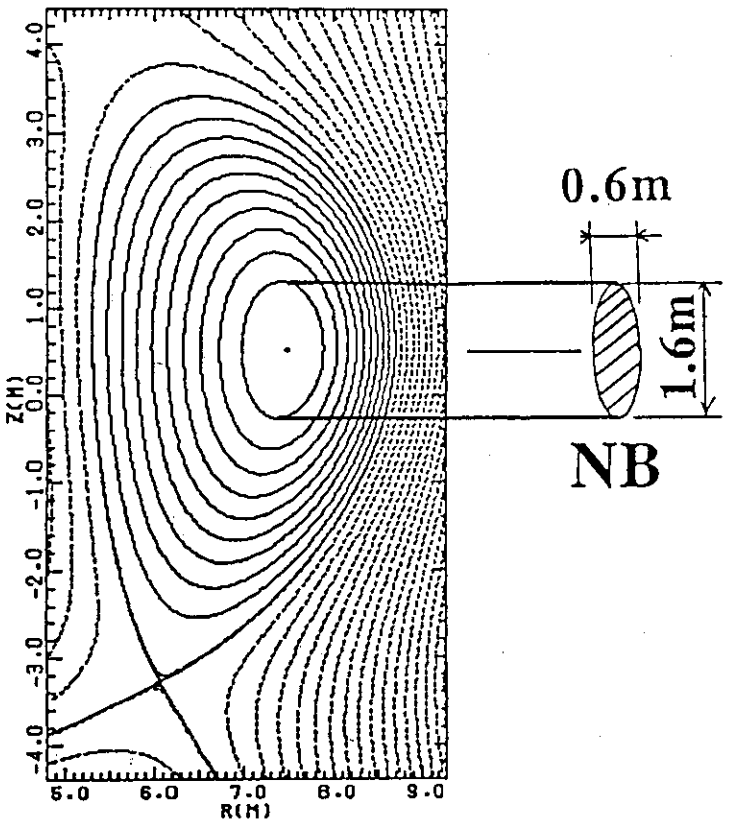

Fig. 3.3.6 NBI injection geometry into the SSTR quilibrium

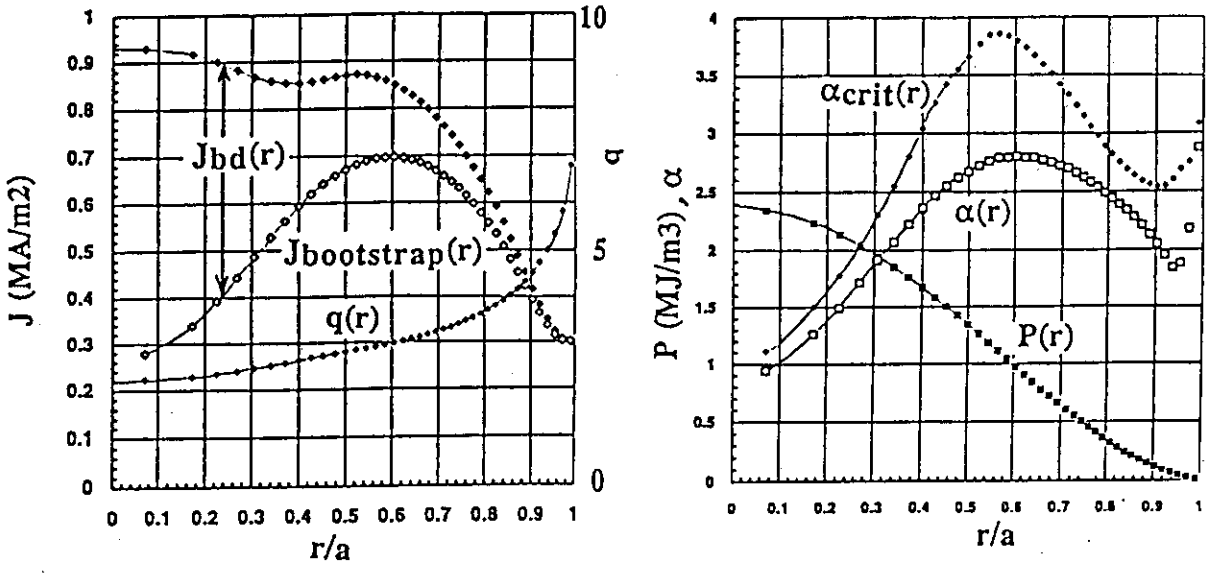

Fig. 3.3.7 Current profile and the ballooning stability of the SSTR equilibrium. J_{bd}(beam driven current), $J_{bootstrap}$(bootstrap current) and q are shown in the left figure. P(pressure profile), $\alpha(=-2Rq^2dp/dr/B^2)$ and $\alpha_{crit.}$(critical a for stability) are shown in the right figure.

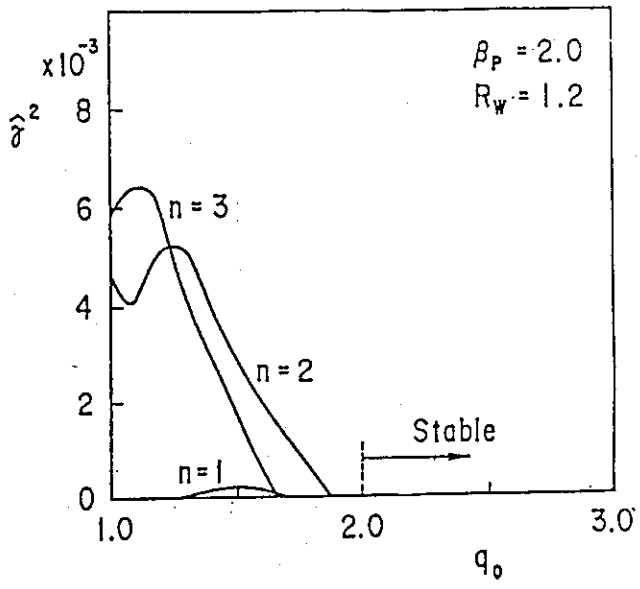

Fig. 3.3.8 Low n ideal MHD mode growth rate as a function of central q value. It was found n=1,2,3,5 modes are stable in $q_0>2$ regime, $J_{//}\sim(1-\Psi)^2$, $dP/d\Psi\sim 1-\Psi$ are assumed for the calculation.

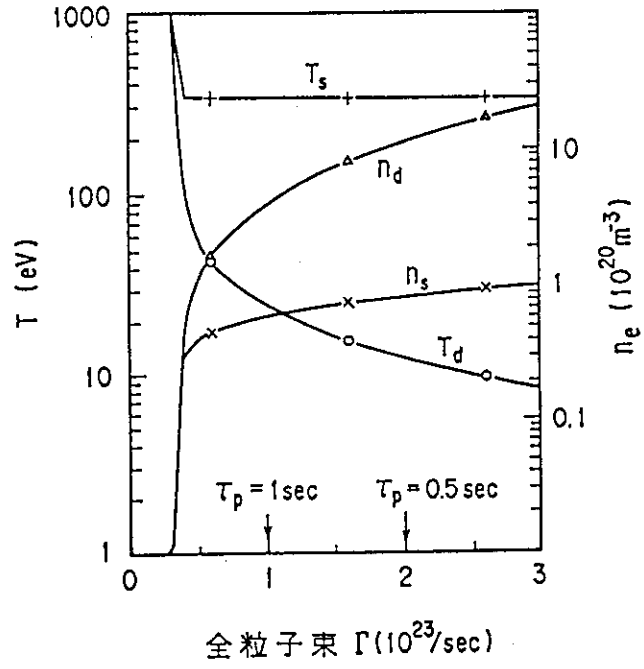

Fig. 3.3.9 Divertor and SOL plasma parameters for the SSTR as a function of particle flux G. Calculation is made for outboard divertor leg. Major radius R=7m, SOL width d=0.04m, total heat flux Q=350MW, maximum flux multiplication factor Rm=30, radiative loss fraction fr=0.73, divertor length L_D=76m and field line pitch Bt/Bp=16.

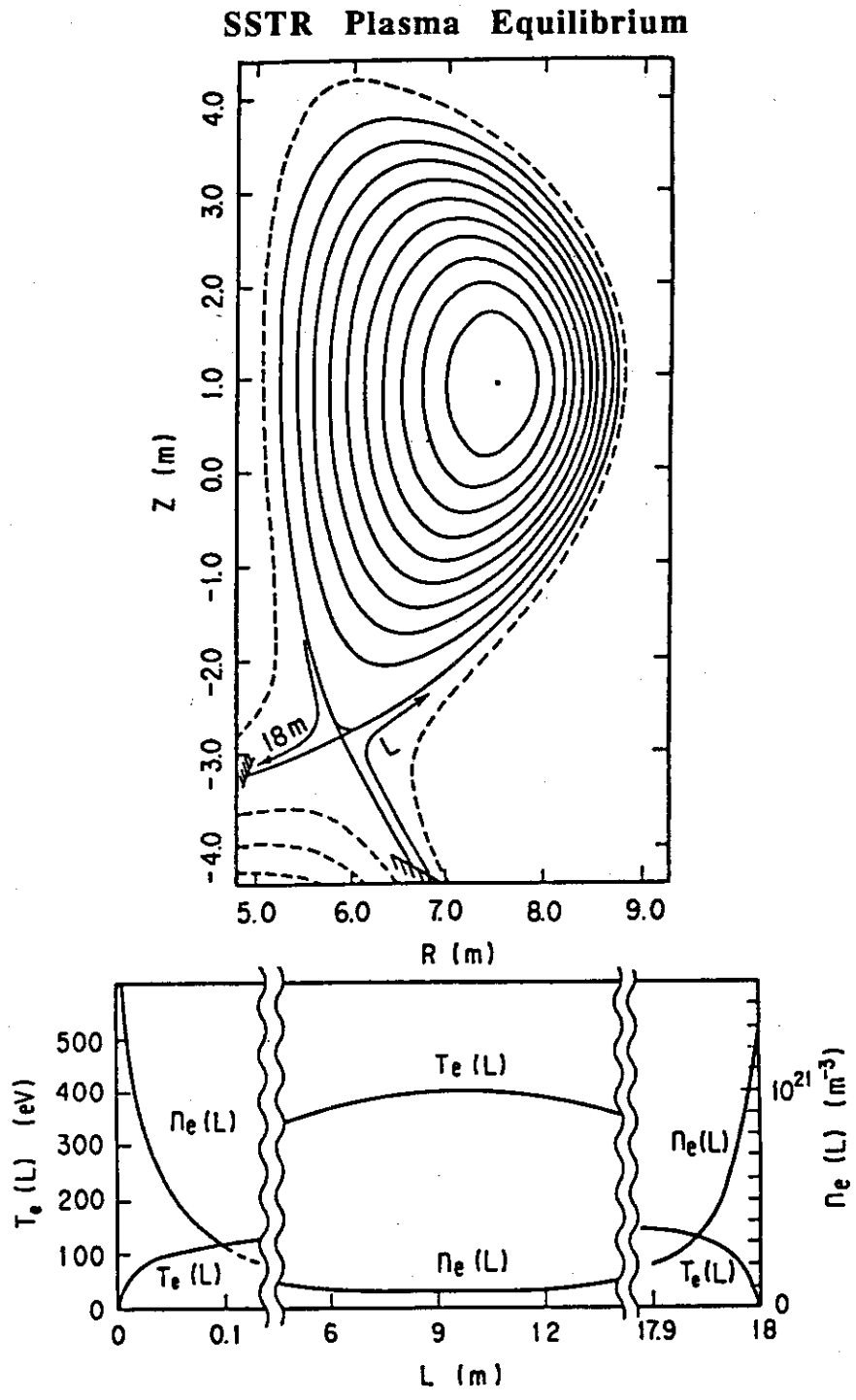

Fig. 3.3.10 Density and temperature along the field line in the SSTR calculated from two point divertor model.

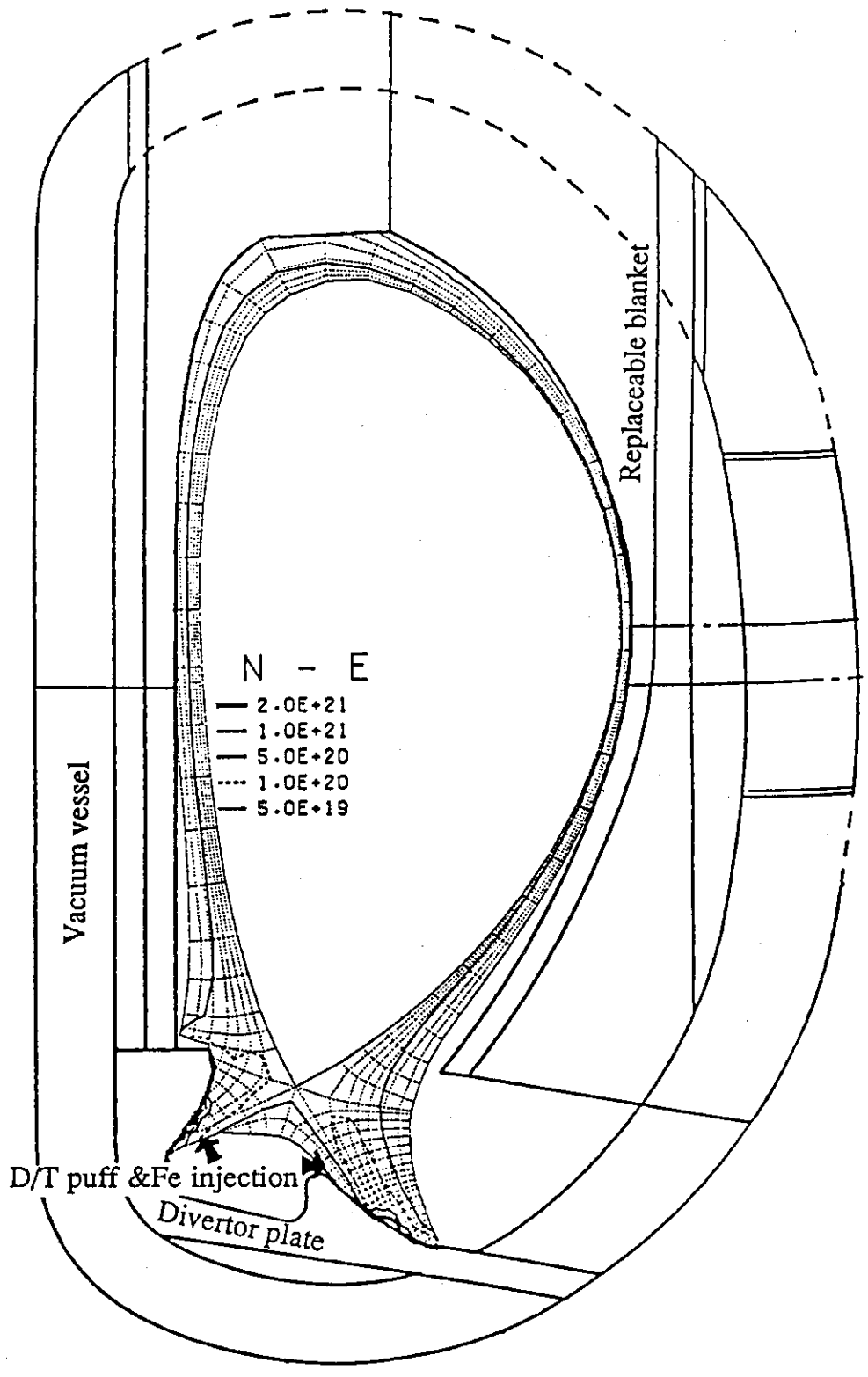

Fig. 3.3.11 Divertor geometry and the active cooling of the SSTR.

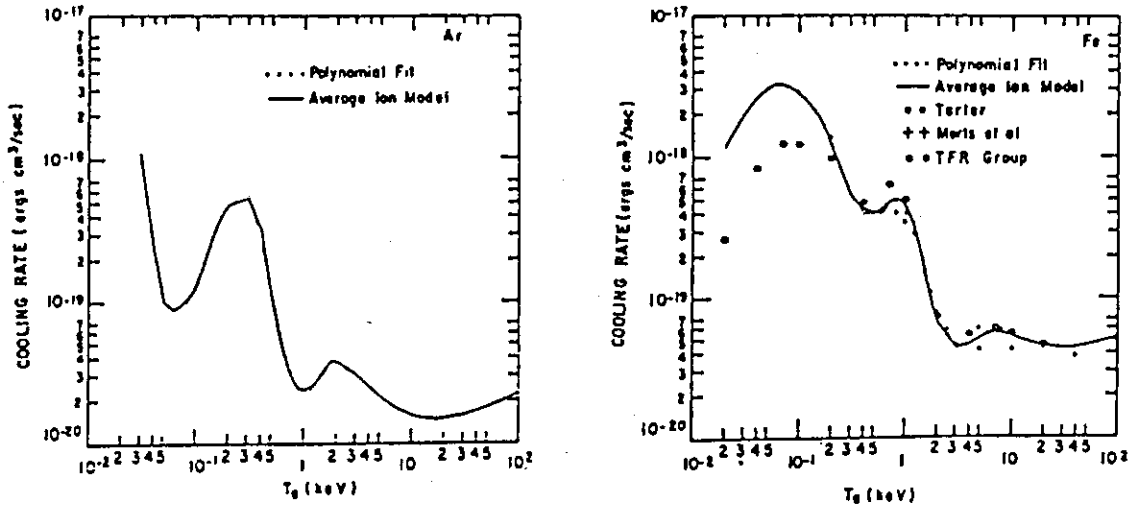

Fig. 3.3.12 Radiative cooling rates L(T) of Ar and Fe. (after Post, Jensen et al.,)

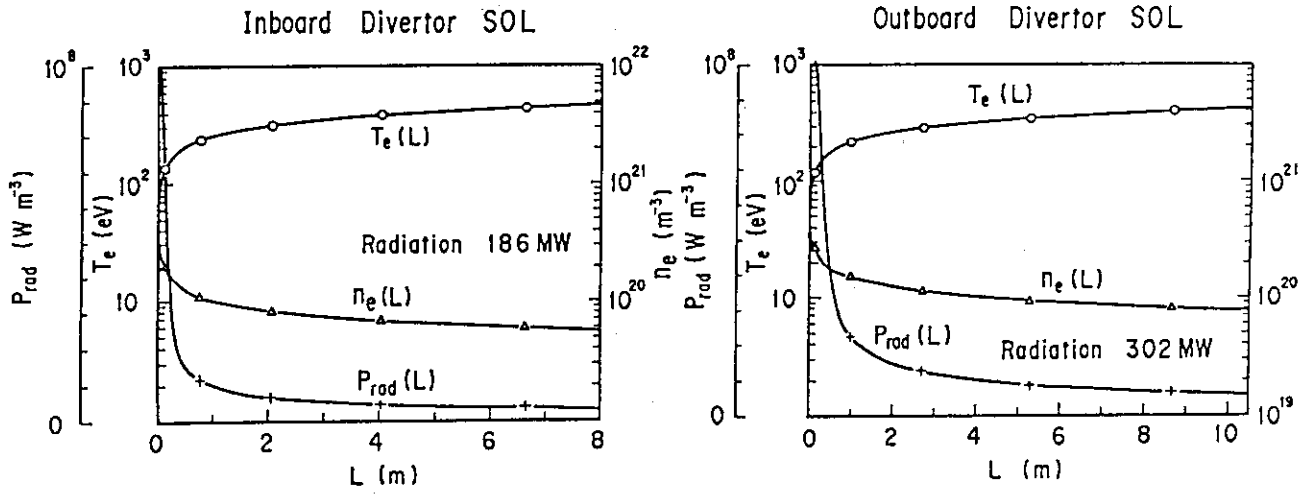

Fig. 3.3.13 Impurity radiation along the field line in case of n_{Fe}/n_e=0.8%. Calculation conditions (two point divertor model) are same as in Fig. 3.3.9.

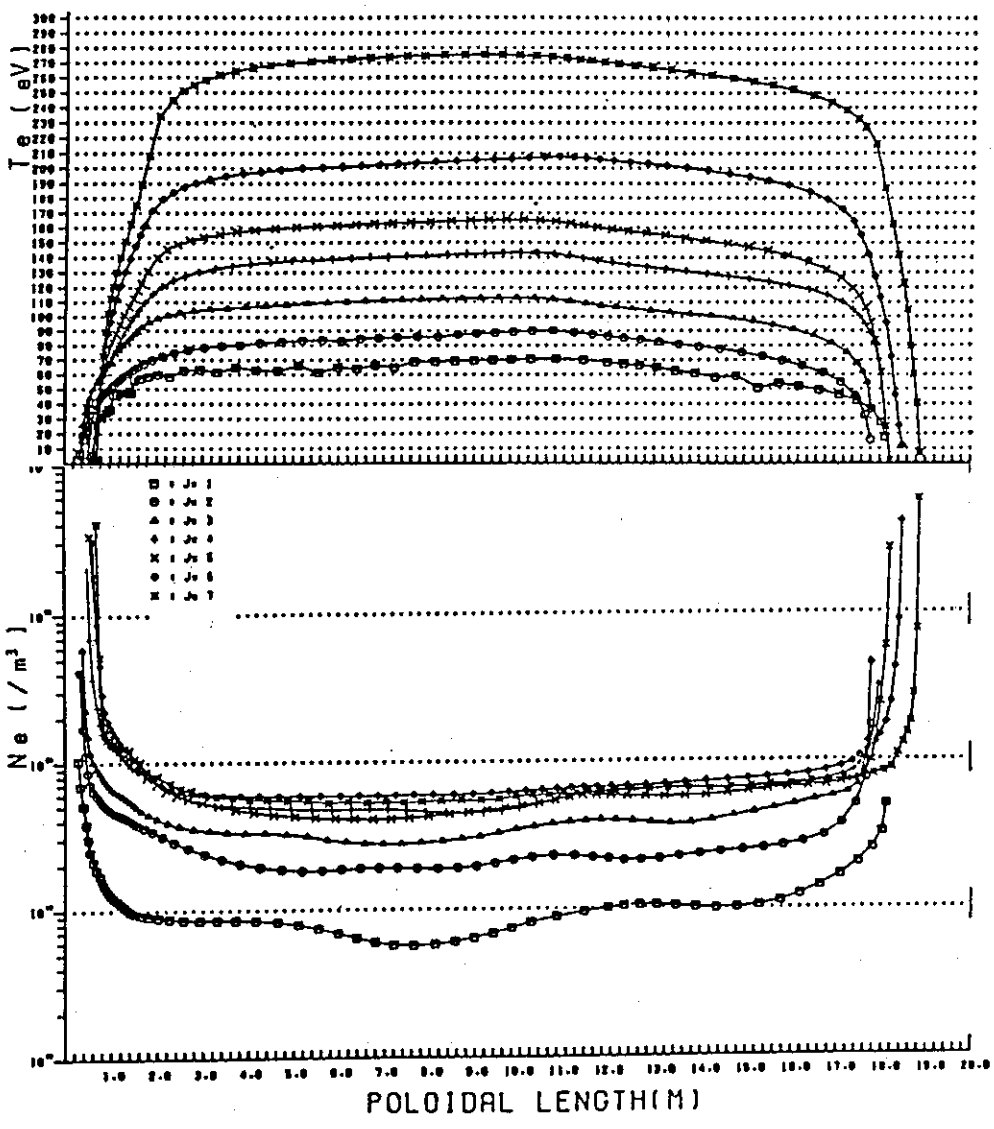

Fig. 3.3.14 Density and temperature along the field line calculated from two dimensional divertor code.

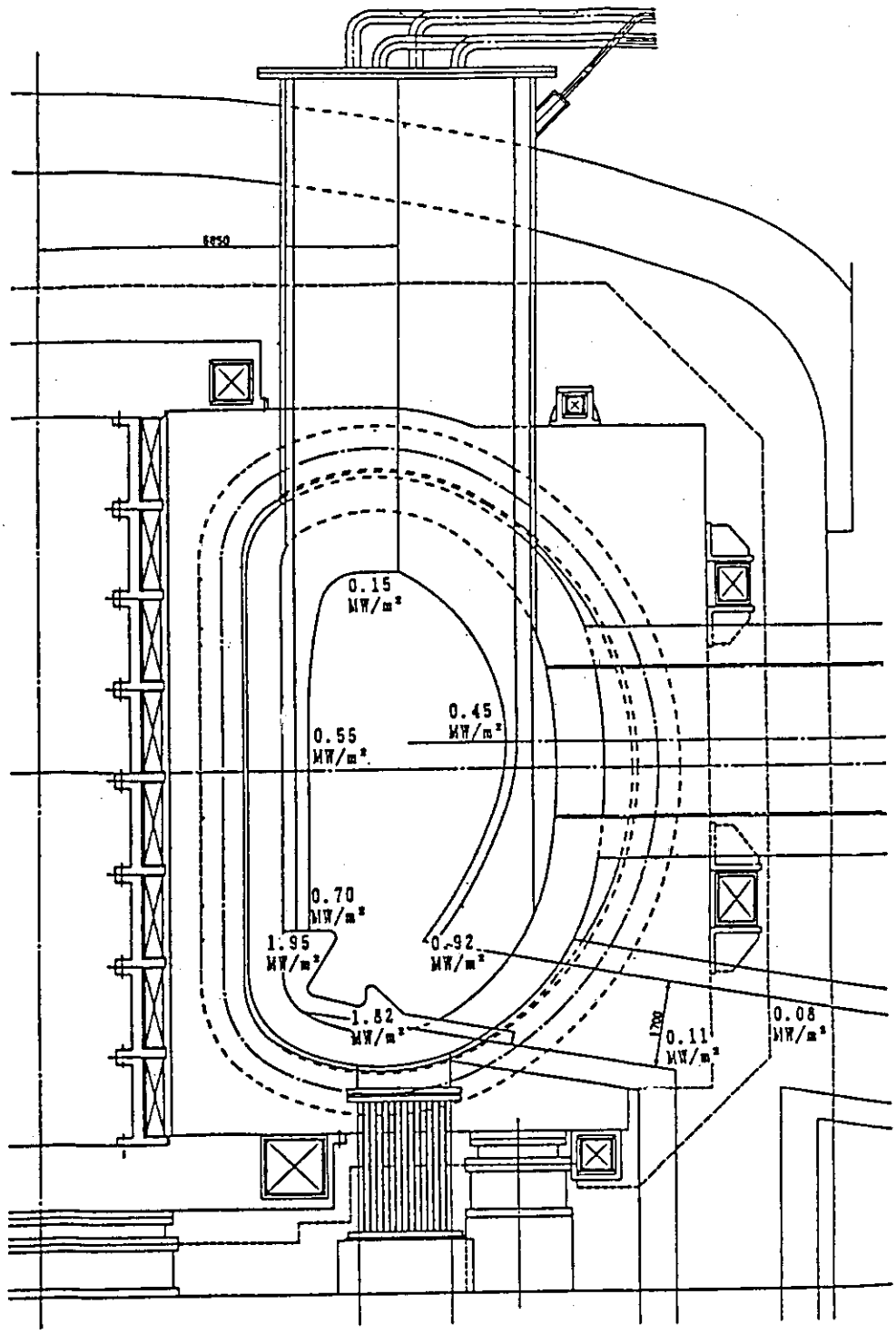

Fig. 3.3.15 Heat flux to the blanket first wall assuming P_{rad}(main)=90MW, P_{rad}(SOL)=490MW.

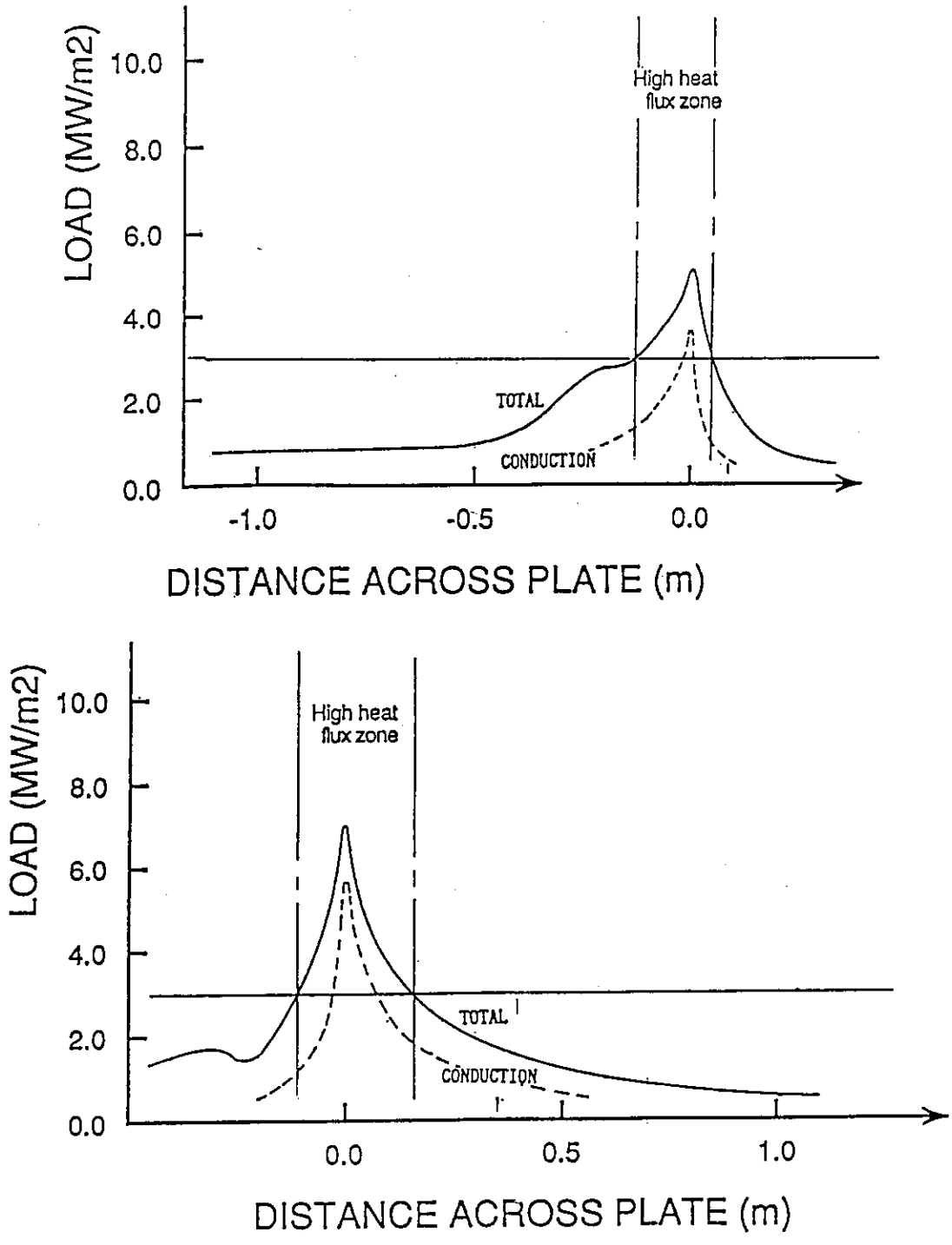

Fig. 3.3.16 Heat flux to the divertor first wall assuming P_{rad}(main)=90MW, P_{rad}(SOL)=490MW, P_{cnd}(divertor)=80MW.

3.4 Overview of the Reactor Machine

3.4.1 Overall Design Philosophy

Technical specifications of the fusion power reactor are categorized into those from the reactor plasma conditions, those from the technical feasibility and those from the economical feasibility. The reactor size to satisfy reactor plasma conditions and the technical feasibility changes with the maximum toroidal field. Rather compact reactor becomes possible with higher field. But the maximum field of the superconductor and the strength of the structural material have some limits. Moreover, shield thickness of the 14MeV neutron is almost constant for any design and some maintenance space is required. So an extremely compact reactor may not be practical. To realize high efficiency steady state with the bootstrap current, the major radius of the 1GWe power reactor is ~9m with 12T superconductor and is ~7m with 16T superconductor. Further increase of the magnetic field may reduce the reactor size slightly but it requires higher magnet technology and material development for higher neutron flux. The benefit should be compared with the cost of R&D. Relatively compact reactor is favorable from the economical point of view. In this study, we decided to use the near term technologies to be realized with ~10 years of proper R&D efforts. With this choice, we intended to show that a proto type fusion reactor can be constructed without extremely innovative technology development. The reason for this is that the reactor plasma conditions designed from the present confinement scalings and the current drive physics is not far from the initial intuition. And recent progresses of the superconductor and heating technologies make 16T superconductor and 2MeV NBI fairly realistic which are key technologies for this reactor concept.

3.4.2 Overall Structure

The SSTR is a fusion reactor with the major radius of 7m, maximum neutron wall load of 5MW/m^2 and the thermal output of 3710MW. Fig.3.4.1 shows a bird's eye view of the SSTR reactor body. The reactor body consists of toroidal/poloidal superconducting coil system, vacuum vessel integrated with neutron shield, blanket, divertor, ports, various cooling pipes and supports. Fig.3.4.2 and Fig.3.4.3 shows horizontal and vertical views of the tokamak. The tokamak has sixteen toroidal field coils and the periodic replacements of the blanket and the piping are made through the vertical ports between coils. The thermal energy produced in the blanket is transferred to the high temperature pressurized water around 300°. The high temperature pressurized water is collected to the ring header by way of piping from each blanket module. And it is led to four steam generators in the

reactor hall. Maintenance equipments, ECH system, D/T pellet injector are placed in the reactor hall. The neutral beam injector for current drive is placed in the NBI room near the reactor hall. A crane system for the maintenance and the construction of the blanket and the divertor is also set up in the hall. Fig. 3.4.4 and Fig. 3.4.5 are plan and side views of the reactor hall and the NBI room showing rough arrangements.

Main components of the tokamak machine except for the replaceable blankets and the divertor plates will be used until the end of the reactor life (~30years) and will be disposed.

3.4.3 Superconducting Coil System

The toroidal field coil system of the SSTR produces 9T at the plasma center (R=7m) and the maximum field at the coil is 16.5T. On the other hand, the maximum field of the equilibrium field coil is only 7T due to high aspect ratio and low plasma current (12MA). The superconducting wire for the toroidal magnet is $(N_bT_i)_3S_n$ conductor manufactured by the N_b tube method and that for the poloidal magnet is N_bT_i conductor. The shape of the toroidal field coil is close to pure tension shape and the maximum toroidal field ripple is chosen at 1% at the plasma edge. The poloidal field coil consists of 14 blocks. The electromagnetic forces on the toroidal and the poloidal coils are internally supported and total coil system is supported by the common support legs. The centering force (140kton/coil) is supported by the wedge and the out of plane force is supported by the shear key and the shear panel.

3.4.4 Toroidal Field Coil

Fig. 3.4.6 shows (B, J_c) curve for the recently developed Ti doped N_b3S_n superconductor with N_b tube method and the inner cross section of the toroidal field coil. As is clear from the figure, high field superconductor required for the SSTR already exists. And the demonstration of the large coil is the remaining subject. The toroidal field coil has 9 layers of double pancake. The superconductor consists of two gradings in which 16.5T $(N_bT_i)_3S_n$ conductor and 5T N_bT_i conductor are connected with modified three in hand. The total stored energy of the toroidal field coil reaches up to 137GJ and good mechanical properties are required. So the coil structure is a circular cable-in-conduit conductor in the advanced disk by which the electromagnetic force in the conductor is transferred to the structural material effectively. And the conductor is wound by a semi-wind-and-react method in which the annealed conductor can be wound inside the hard disk. So the bending strain of the conductor is reduced significantly which is a critical issue of the high field conductor. Table 3.4.1 shows the design parameters of the SSTR superconductor.

This toroidal field coil is a high field coil and the large stress operates on the structural materials. The maximum stress operates at nose of the coil at the mid plane. For example, tensile force at the midplane is 40kton per coil and the average hoop stress is 30kg/mm^2 with the cross section S=1.32m^2 of the structural materials. The average compression stress at the wedge is 32kg/mm^2 for the centering force of 140kton/coil. Detailed stress pattern of the structural materials is analyzed using the FEM method. The hoop stress of the coil is 80kg/mm^2 and the total stress including the bending stress due to the out of plane force is 107kg/mm^2. These values are consistent with the strength of the new cryogenic steel JN-1. Fig.3.4.7 shows the displacement pattern for the inplane and out of plane forces.

3.4.5 Poloidal Field Coil

Poloidal superconducting coil system consists of center solenoid and equilibrium field coils. Circular cable-in-conduit conductors are sandwiched by the cryogenic steel JN-1 similar to that for the toroidal coil. Fig.3.4.8 shows the arrangement of the poloidal field coils and the conductor shapes of CS and EF coils. The maximum field of the CS conductor is 7T whose operating current is 40kA. The maximum field of the EF conductor is 5.5T whose operating current is 40kA. NbTi conductors are used for CS and EF conductors. Table 3.4.2 shows basic parameters of the poloidal field coils. The magnetic shielding effect of the low resistance vacuum vessel reduces the AC loss during the plasma disruption and the long coupling time constant can be used for the poloidal field coil. Moreover, the up down force of the center solenoid is fairly small. Fig. 3.4.9 shows the structure of the center solenoid.

3.4.6 Low Resistance Vacuum Vessel and Shield

As structural components of the tokamak reactor, there are vacuum vessel, neutron shield, blanket and divertor. In the previous designs such as the experimental reactor, there are a few resistive parts in the toroidal direction to increase the one turn resistance of the vacuum vessel. In such a design, the resistive parts must withstand the joule heating during plasma disruption and the nuclear heating during burn. So the structure is relatively complicated. On the other hand, the structure becomes simpler for the uniform thin double-walled vacuum vessel adopted in JT-60U. However, the vacuum vessel and the shield is separated and the support will be fairly complicated. A simple structure of the vacuum vessel with good quality for manufacturing is proposed in the SSTR. We consider it is possible to build up the plasma current with the applied voltage of 4V considering the recent ECH pre ionization experiments. In this case, induced current in the vacuum vessel

is less than 1MA for the one turn resistance of 4μΩ and the induced poloidal field can be cancelled with the pre bias. It is possible to integrate the vacuum vessel with the shield and it is possible to form the vacuum vessel with uniform double-thin-wall SUS skins (50mm) and the reinforcement plates welded between two skins. And the electrically isolated SUS/water shield is placed between skins.

Fig.3.4.10 shows the basic structure of this uniform resistance vacuum vessel including the neutron shield. Efficient neutron shield is required for the inboard shield and the weight ratio of SUS/water is chosen at 85/15. On the other hand, there is large space in the outboard side and the SUS/water ratio of 50/50 is adopted. The vacuum vessel is divided into 16 section and is welded at the port center during the assembly. The vacuum vessel is cooled with the water at the room temperature and with low flow velocity. The vacuum vessel is isolated electrically and thermally from the high temperature blanket. This type of vacuum vessel is fairly rigid uniformly around the torus and the stress due to the eddy current is fairly low. This is also favorable for the support. The port of the SSTR consists of 16 vertical ports for the maintenance of the blanket modules, 16 divertor ports for pumping and the maintenance of the divertor plates, 2 tangential ports for the current drive, 2 maintenance ports, ECH pre ionization port and pellet injection port. Uniform resistance and shield-integrated vacuum vessel of the SSTR simplifies the manufacturing processes and improves the quality of manufacturing and the reliability (hence reduces the cost). Moreover, it has beneficial effects on the vertical stability,AC loss of the superconductor and the power supplies.

3.4.7 Stabilizing Shell and the Control Coil

The curvature of the equilibrium field n= -R(dBz/dr)/Bz is negative to produce vertically elongated plasma. Then the plasma is unstable to the vertical displacement without feedback control. In order to stabilize this mode, passive shell is introduced with the vacuum vessel and the mode is stabilized with the repulsive force by the eddy current. There are two types of passive shells. One is saddle loop adopted in INTOR and the other is twin loop adopted in ITER. Twin loop is adopted as a passive shell considering the advantage of the low resistance vacuum vessel. Fig.3.4.11 shows structure of the SSTR and the location of the twin loop and the feedback control loops.

Integration of the Z component of the equation of motion $\rho_m d\vec{V}/dt = \vec{J} \times \vec{B} - \nabla P$ over the plasma volume with the assumption of the rigid displacement gives $M_p \partial^2 Z/\partial t^2 = \int [J_\phi B_R - \partial P/\partial z] dv$. The perturbation expansion including the shell current Is

gives $I_p<\partial B_z/\partial z>Z_p+I_p<b_R^s>I_s=M_p d^2z/dt^2$. Here, $<f>=\int J_\phi f dv/I_p$ and b_R^s is the horizontal field from the unit eddy current in the shell. On the other hand, circuit equation for the eddy current in the shell is given by, $I_p<b_R^s>dz/dt + L_s dI_s/dt + \Omega_s I_s = 0$. So the growth rate of the vertical instability g is given as follows,

$$\frac{\gamma^2}{\Gamma_a^2} = -\left(\bar{n} + \bar{n_s}\frac{\gamma\tau_s}{1+\gamma\tau_s}\right) \qquad (3.4.1)$$

where $\bar{n} = -<\partial B_z/\partial R>/<B_z/R>$, $\bar{n_s} = I_p<b_R^s>^2/(L_s<B_z/R>)$, $\Gamma_A^2=<B_z/R>/M_p$, $\tau_s=L_s/\Omega_s$.
Second term of the right hand side of the equation (3.4.1) represents the shell stabilizing effect. The shell stabilization is not effective for the slow displacement whose time constant is longer than that of the eddy current. In the actual system, there are many eigen modes and the frequency characteristics is fairly complicated. Fig.3.4.12 shows the eddy current analysis model of the vacuum vessel and the twin loop. The shell stabilizing index (second term of the right hand side of equation (3.4.1)) is also shown in the figure. The average n index of the standard equilibrium is -1.11 and the growth rate of the vertical instability γ~5/sec. So the vertical displacement is ~1.5cm associated with the 10cm horizontal displacement. And the capacity of the power supply is only 2MW.

The feedback control coil is made of the normal conductor. And the continuous high current operation is not favorable. So the slow control of the vertical plasma position is required with the poloidal superconductor to reduce the joule loss of the normal conductor. In such a case, the power loss of the feedback control coil is negligibly small in the energy balance of the power reactor.

3.4.8 Blanket and First Wall

Tritium is one of fusion reactor fuels and is rare in the nature. So the blanket is placed around the reactor plasma to produce tritium by the reaction between ^6Li and the neutron. The first wall of the blanket is exposed to the 14MeV neutron and the heat and particle fluxes from the main plasma. In the SSTR, the Li_2O is chosen as the tritium breeding material and the water cooling which has abundant experiences in the light water reactor. Table 3.4.3 shows major parameters of the blanket/first wall. As a structural material, low activation ferritic steel F82H is adopted. The merits of the ferritic steel are that the thermal conductivity is relatively high and the thermal stress can be reduced and that the swelling and the changes of the creep speed and the toughness are relatively small and that the activation can be reduced by the material selection and finally its low price.

Fig.3.4.13 shows the overall structure of the blanket. The blanket is composed of a replaceable blanket and a permanent blanket. The reason is that the maximum tolerable neutron fluence of the low activation ferritic steel F82H is ~10MWa/m^2 and periodic replacement is required every two years. And the ^{6}Li burn up in the first breeding zone just behind the first wall becomes large and the effective tritium breeding becomes possible with the periodic replacement. This situation is very similar to that in the LWR(light water reactor) in which one third of the fuel rods are annually replaced. Fig.3.4.14 shows the poloidal variation of the first wall neutron wall load. As is clear from this figure, the neutron wall load of the inboard blanket is less than half of the maximum neutron flux in the outboard blanket. So the replacement is required every four years for the inboard blanket. The replaceable blanket is composed of the first wall, the first breeding zone, the Be neutron multiplier zone and the second breeding zone. Natural Li is used as the breeding material in which ^{6}Li fraction is 7.5%. In this case, ^{6}Li burn up fraction of the first breeding zone (~10mm thick) reaches up to 70% after two years of operation with the maximum neutron flux of 5MW/m^2 which results in a slight decrease of the tritium breeding ratio (TBR). The thickness of the Be is 10cm to realize high TBR (=1.21). Cooling water pipes in the blanket run in the poloidal direction and their density is chosen according to the heat generation density. And the cooling pipes have a layer of solid insulator by which an operation temperature is kept between 450-950 degree. The cooling pipes of the first wall run in the toroidal direction and the tube panel form is adopted because of its reliability.

The neutral flux to the first wall is estimated using the two dimensional divertor code and it is ~10^{16}/sec/cm^2 with the average energy of 50eV. So the sputtering erosion of the first wall by D/T is negligibly small. And we expect that the self sputtering is small due to the low Fe concentration in the SOL as shown by the two dimensional divertor code. But the ferritic steel has high tritium permeation coefficient. And the tritium permeation rate becomes ~20g/day, so a protection film for the tritium permeation is required. Replaceable blanket is divided into three modules (one center module and two side modules) for inboard and outboard blankets for every section (total 16 sections). The inboard center module is used to fix the side modules and does not have a function as a blanket. Vertical maintenance scheme is adopted for the replacement of the replaceable blankets. In order to extract the inboard replaceable blanket, replaceable and upper permanent blankets of the outboard center module is extracted during the maintenance and re-installed after changing the replaceable blanket. The permanent blanket consists of Li_2O pebbles and the cooling pipes without neutron multiplier. The inboard and outboard permanent blankets of each section are divided into three modules, respectively. The number of blanket modules becomes large to release the thermal expansion during the temperature change from room

temperature and 500°. Water cotter system proposed in the FER design is adopted to fix the modules.

3.4.9 Divertor Room

Most of the heat and particle fluxes from the main plasma should be controlled in the divertor room which is exposed to very severe circumstances. Especially, the divertor plate to which high heat and particle fluxes flow along the separatrix field line requires highest technical specifications among plasma facing components. As shown in Fig.3.3.16, maximum heat flux to the divertor plate is 7MW/m^2 and the plasma temperature near the divertor plate is ~10eV due to high remote radiative cooling with the impurity. But the neutron flux to the divertor plate is only 1MW/m2. High melting point metals such as Mo and W are primary candidate materials for the divertor plate. Here we adopted Mo-Re alloy.

The net plant efficiency is decreased by about 1% if the high temperature pressurized water can not be used for the divertor plate coolant. However, the burn out heat flux of the high temperature (285°/325°) pressurized water in a smooth tube is ~10MW/m^2 for the flow velocity of 15m/sec. So the upper limit of the heat flux is only 3MW/m^2 for the safety. The swirl tube is one of the most promising candidates to improve the burn out heat flux (Burn out heat flux up to 41MW/m^2 is achieved for the room temperature, the pressure of 0.9MPa and the flow velocity of 13m/sec[1]). There seems to be few data on the burn out heat flux of the swirl tube under high temperature pressurized water cooling applied to the divertor plate condition. Here we assumed that the burn out heat flux up to 20MW/m2 is possible with the swirl tube for 290°,15MPa water cooling conditions. It is assumed that the swirl tape of 50cm length is inserted to the high heat flux zone of the divertor plate. The primary cooling water (285°) from the steam generator is led to the high heat flux zone (~10° increase of the water temperature). And the water is heated up to 325° in the low heat flux zone which is led to the primary cooling water ring header. If such a high heat flux can not be removed with the high temperature water, low temperature (~200°) water having high subcool should be used for the high heat flux zone. This warm water is used for the feed water heating system.

As shown in the two dimensional divertor code analysis, the neutral particle density is highest where the neutral is reflected by the divertor plate. The angles between the separatrix line and the plate are 150° and 15° for inboard and outboard divertor plates, respectively. So the neutrals near the inboard plate tends to be reflected back to the divertor plasma and reionized. On the other hand, the neutrals near the outboard plate are reflected

to the pumping port and the neutral pressure near the port is fairly high. The SOL density should be ~ $7x10^{19}m^{-3}$ to form cold and dense divertor plasma and to enhance remote radiative cooling and to prevent impurity back flow with the friction force. So the large pumping conductance tends to increase the D/T puff rate near the divertor plate (We think that large D/T puff rate required in the two dimensional analysis described in section 4.5 may be caused by relatively large port area).

The heat flux except for the high heat flux zone in the divertor plate is the radiative heat flux from the SOL and the core plasma and is less than $1MW/m^2$. So the reduced activation ferritic steel can be used for the first wall material. But the neutral pressure in the divertor chamber is fairly high. So the large neutral influx to the first wall causes the tritium permeation to the primary coolant water. A tritium transport barrier should be added to the divertor first wall if we use the ferritic steel.

3.4.10 High Temperature Pressurized Water Cooling System

Total thermal output of the SSTR is 3820MW. But the net thermal output to the steam generator is 3710MW due to the power loss to the port and the shield. Here we assumed that the high heat flux zone is also cooled by the high temperature pressurized water. The thermal energy transferred to the $285^{o}/325^{o}$ pressurized water is collected to the ring header at the top of the tokamak. The primary cooling water is supplied to four steam generators where the secondary steam with 6 MPa is produced. The secondary steam is transferred to the large turbine generator used in the conventional nuclear fission reactors. This turbine has high pressure and low pressure turbines by which thermal efficiency is improved. Fig.3.4.15 shows the arrangement of the high temperature pressurized water cooling system of the SSTR. As described in the previous section, low temperature divertor cooling water will be introduced for the feed water heating system when the low temperature (~200^{o}) water should be used to cool the high heat flux zone of the divertor plate.

3.4.11 Negative-ion-based NBI

High energy tangential NBI is adopted for the heating and current drive of the SSTR. The SSTR operates at high density and the beam energy of 2MeV is required to obtain favorable current profile if we consider the multi step ionization processes. On the other hand, as described in section 3.3.4, the power required for the steady state operation is only 60MW and the beam current is only 30A. Table 3.4.4 shows the list of the design parameters of the NBI system. The NBI system has two beam lines, each of which

consists of eight ion sources. Each ion source provides a net injection power of 5MW. Two of eight ion sources are installed as a back up in case of the accident.

Most significant characteristics of this NBI system is its high power conversion efficiency (>50%) by the use of the electrostatic acceleration and the plasma neutralizing cell. The Cockcroft-Walton acceleration system is adopted which has many experiences in this energy range. The ion beam extracted from the ion source is bended by the bending magnet and is introduced into the plasma neutralizing cell. The merit of this system is that many small ion sources can be installed in the beam line to reduce the probability of the plasma quench in case of the ion source accident and that the ion sources are not exposed to the neutron flux directly from the main plasma. Moreover, the R&D risk is relatively small because only the acceleration current should be increased by an order from the present commercial level of 2MeV, 0.5A. Fig.3.4.16 and Fig.3.4.17 shows the plan and side views of the N-NBI system.

3.4.12 ECH System

Preionization/heating by the ECH is adopted to reduce the one turn voltage required during the current build up phase. RF power source with source frequency of 250GHz is required because of its high toroidal field. The ECH is only used during the break down phase and the current build up phase. But the duration is 100 second and design for the steady state is required. Torus input power of 5MW is adopted. The injection mode is outside launching O mode. Fig.3.4.18 shows the plan and side views of the ECH system. Injection line is chosen to match the plasma position (-1m) during the current build up phase.

3.4.13 Pellet Injection System

As described in section 3.3.10, the pellet injection is most desirable to maintain the quality of the first wall avoiding the sputtering erosion due to the fast neutrals. From the viewpoint of the formation of the cold and dense divertor plasma by the enhanced particle flux, intensive injection of the low speed pellets is adopted. A centrifugal injector is adopted for this use. Major parameters of the pellet injector are pellet size of 5mmϕ x 5mmL, injection rate of 45Hz and pellet speed of 1km/sec. Fig.3.4.19 shows a cross sectional view of the device. As shown in the table, a continuous injector with high reliability is required. The development of the mixed pellet injector is required with the composition ratio of D/T=1/1.

3.4.14 Fuel System

The fuel system of the SSTR consists of plasma exhaust system, fuel clean up system, isotope separation system, fuel storage system, fuel gas injection system and tritium recovery system. The plasma exhaust system consists of a set of turbo molecular pumps (four units of $25m^3$/sec pump in each ports). Effective pumping speed is reduced to $68m^3$/sec/port due to the port conductance. The pressure near the exhaust port reaches up to 2Pa. The compositions of the exhaust gas from the plasma exhaust system are D/T fuel of 3300 mol/hr, He as an ash and various impurities. On the other hand, deuterium gas and Xe gas used in the plasma neutralizing cell are exhausted from the NBI exhaust system. These exhaust gases are supplied to the fuel clean up system and the impurities except helium are removed by the cryogenic adsorption method. Most of this clean up D/T fuel (+He) is sent to the gas injection system to be used for the divertor gas puff. On the other hand, a part of the processed fuel (~900mol/hr) is sent to the isotope separation system to separate H/D/T using the cryogenic distillation method. Here, the atomic ratio of D/T=1/1 is adopted for the D/T fuel to the pellet injector in order to reduce the tritium inventory. With this method, the tritium inventory of the isotope separation system is significantly reduced and is ~1.5kg including the tritium gas in the piping. The total tritium inventory is only 5kg including those in the blanket (~1200g) and the pellet injector (~230g) and the storage(~2kg). The fuel cycle for this case is shown in Fig.3.4.20.

If the high purity of the divertor gas puff and the pellet injector is required, the tritium inventory reaches more than 15kg and the tritium release during the large scale accident is increased. Such a situation is not desirable to improve the safety aspect of the fusion reactor. Thus a careful attention has been paid in the SSTR design.

3.4.15 Power Supply and Control System

The power supplies of the SSTR consist of those for superconducting coils, NNBI and ECH. Here we describe the power supply for the superconducting coils.

The power supplies of the superconducting coils consist of those for toroidal coils and poloidal coils. The capacity of the toroidal power supply is relatively small (39V,81kA,3.2MW) in contrast to its large stored energy (137GJ) due to its steady state operation. On the other hand, large capacity of quench protection circuit is required (DC circuit breaker DC20kV, 81kA,16units, protection resistor 0.247Ω,81kA, 8.53GJ, 16units). Large forcing voltage is required for the current lump up and the plasma control for the poloidal power supply. So the capacity of poloidal coil power supply becomes

large in spite of its relatively small stored energy (7GJ). The maximum coil currents of 14 coil units are determined by the equilibrium configuration. Then the total capacity is determined by the required voltages determined by its operation scenario. As is seen in Fig.3.4.21, a pure inductive current build up with 100 seconds is adopted in the SSTR. The applied voltage during the break down phase is chosen at 4V. The capacity of the poloidal power supply is then ~900MW. This capacity is strongly affected by the break down voltage and can be reduced to ~400MW if we use the DC circuit breaker to produce initial voltage. In this design, we decided not to use DC circuit breaker for the initial break down. The capacity of the power supply can be reduced to ~200MW for the condition of $d\beta p/dt$~0.1/2sec. So two motor generators having 3GJ each are connected during initial 100 seconds and only the commercial line power is used after the flat top phase. By pass pair operation is adopted to reduce the resistive power losses in the thyristor convertors. Then it is possible to reduce the power loss to ~10MW.

Thus the toroidal and poloidal power supplies are fairly different in its specifications. So the choice of low current and high field has a significant advantage from the view point of the optimization including the power supplies. The control system is basically same as previous designs. So, the design of the control system has been neglected.

3.4.16 Cryogenic system

The capacity of the He refrigeration system in the fusion reactor is the summation of those required for the superconducting coils and the pellet injector. The He refrigeration capacity required for the superconductors is larger during the current rump up phase than that required in a steady state operation. The refrigeration load of the tokamak is 46kW during the current build up phase and is 16kW during the steady state operation. Reduction of the total capacity of the cryogenic system is made by a preparation of the liquid He storage tank for the current build up phase. Even with this optimization, the total power consumption of the cryogenic system reaches up to 20MWe including the cryogenic loads of the ultra low temperature pump and of the He evaporation in the current leads.

Table 3.4.1 TFC design parameters

Design Specification of SSTR TFC

Major characteristics	
Shape of coil	Pure Tension
Coil structure	Advanced Disk
Conductor concept	Cable in Conduit
Winding concept	Semi Wind&React
Bore radius	7.35mx11.52m
Number of coils	16
Cooling method	Forced flow
Superconductor	(NbTi)3Sn/NbTi
Peak field	16.5T
Operating current	81kA
Coil current density	20.8A/mm^2
Number of turns	244
Number of D-pancake	9
Number of grading	2
Magnetomotive force	315MAT
Total inductance	41.6H
Total stored energy	136.5GJ
Hoop force	3788MN/COIL
Centering force	-1378MN/COIL
Quench temp. rise	150K
Quench τ & V_{max}	10s & 20kV
Toroidal field ripple	1%

	16T	5T
strand dia.	1.05mm	0.86mm
filament dia	5μm	20μm
no. of filaments in strand	4065	363
Cu/nonCu	2.1	4.1
No of strands	972	972
SC area/cond.	272mm^2	111mm^2
Cu area/cond.	570mm^2	454mm^2
total area/cond.	842mm^2	565mm^2
ope. current	81kA	81kA
crit. current	162kA	244kA
void fraction	0.34	0.332
conductor L	720m	160m
cooling path L	360m	160m
max. He flow	13.6g/s	12.5g/s
pressure drop	1atm	1atm

Table 3.4.2 Design parameters of poloidal coils

Basic parameters

No	R	Z	dR	dZ	pair	turn	total
1(7U)	13.2	3.5	0.430	0.632	14	10	140
2(6U)	10.2	7.0	0.258	0.272	6	6	36
3(5U)	3.7	7.5	0.602	0.632	14	14	196
4(4U)	2.2	6.125	0.430	1.352	30	10	300
5(3U)	2.2	4.375	0.430	1.352	30	10	300
6(2U)	2.2	2.625	0.430	1.352	30	10	300
7(1U)	2.2	0.875	0.430	1.352	30	10	300
8(1L)	2.2	-0.875	0.430	1.352	30	10	300
9(2L)	2.2	-2.625	0.430	1.352	30	10	300
10(3L)	2.2	-4.375	0.430	1.352	30	10	300
11(4L)	2.2	-6.125	0.430	1.352	30	10	300
12(5L)	4.8	-7.600	1.032	0.992	22	24	300
13(6L)	10.5	-7.400	0.430	0.542	12	10	120
14(7L)	13.2	-2.500	0.645	0.812	18	15	270

Item	CS	EF
SC	NbTi	NbTi
Strand D	0.84mm	2.2mm
Filament D	10μm	10μm
No of Fil.	2803	5660
Cu/nonCu	1.5	7.5
No of Strand	972	108
A(sc)	214mm2	48mm2
A(Cu)	324mm2	362mm2
A(strand)	538mm2	410mm2
A(He)	266mm2	205mm2
A(CuNi)	104mm2	91mm2
1st conduit		
A(JN1)	856mm2	1057mm2
2nd conduit		
Void frac.	0.33	0.33
Critical Jc	1400A/mm^2 (7T)	2120A/mm^2 (5.5T)
Ope. I	40kA	40kA
Critical Ic	300kA	101kA

Table 3.4.3 Basic design parameters of SSTR blanket

Structural material	Ferritic steel (F82H)
Maximum temperature	< 500 ℃
Coolant	Water (H_2O)
Inlet/Outlet Temperature	～285/325 ℃
Pressure	15 MPa
Breeding material	Lithium oxide (Li_2O)
Shape	Pebble (1 and 0.2mmφ)
Density	85 % T.D.
Packing fraction	70 %
^6Li enrichment	natural
Temperature range	450 ～ 950 ℃
Neutron multiplier	Berrylium (Be) small blocks
Temperature range	< 400 ℃
Blanket concept	BOT (Tube-in-shell)
First wall concept	Tube-panel
Breeder tempe.control	
Maximum temperature	Cooling tube arrangement
Minimum temperature	Solid insulator around tube
Coolant flow direction	
First wall	Toroidal
Breeding region	Poloidal
Torus segmentation	16 toroidal sectors 3 modules /sector Inboard center replaceable module : Non-reeding blanket to fix side modules
Poloidal segmentation	Replaceable banket
Outboard	1 unit
Inboard	1 unit
	Permanent blanket
Outboard	6 units (side modules) 1 unit (ceter module)
Inboard	1 unit
Blanket thickness	
Outboard	Replaceable blanket 20 cm Permanent blanket 30 cm
Inboard	Replaceable blanket 20 cm Permanent blanket 30 cm

Table 3.4.4 NBI system design parameters

N NBI System Design Spec.

Beam energy	2MeV	Ext. electrode	12cmx30cm
Beam power	60MW(max 80MW)	Electrode hall	12.3φIDx100
Beam species	D^0	Oper. Pres.	0.3Pa
Beam lines	2	Gas supply	0.6Pam3/s/u
No of units	8 units/beam line	Accelerator	ES accel.
Efficiency	50%	Accel. curr.	3.5A/u
Acceleration	90%	Beam divergence	3mrad
El.detach. loss	10%	Accel. stage	10stage
Neutralization	85%	Beam deflector	Magnet+QM
Geometric loss	5%	Neutralizer	plasma cell
Reionization	5%	Gas	Xe
Power supply	80%	Ionization	50%
Ion source	volume-surface	Oper. press.	0.03Pa
Extraction Curr.	5A	Accel. P/S	Cockcroft
Curr. density	50mA/cm2	Ripple	<1%
Pumping	25m³/sTMPx100	Frequency	10 kHz
Beam dump	swirl tube		

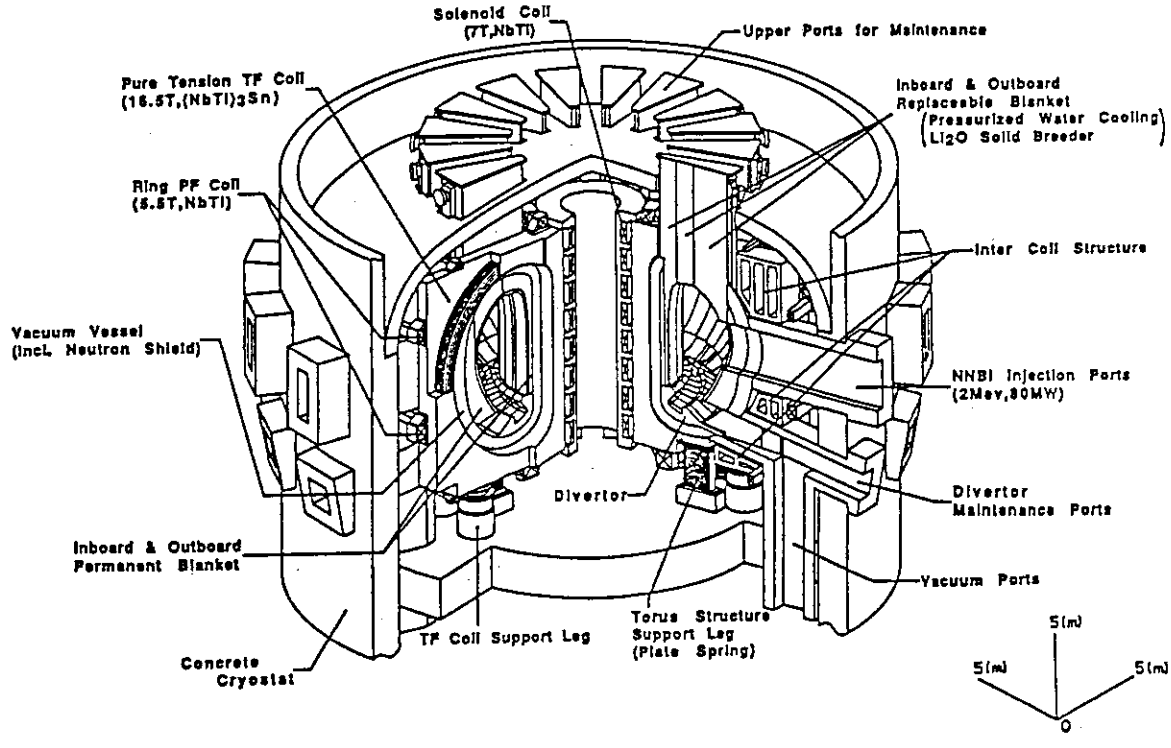

Fig. 3.4.1 Bird's eye view of the SSTR.

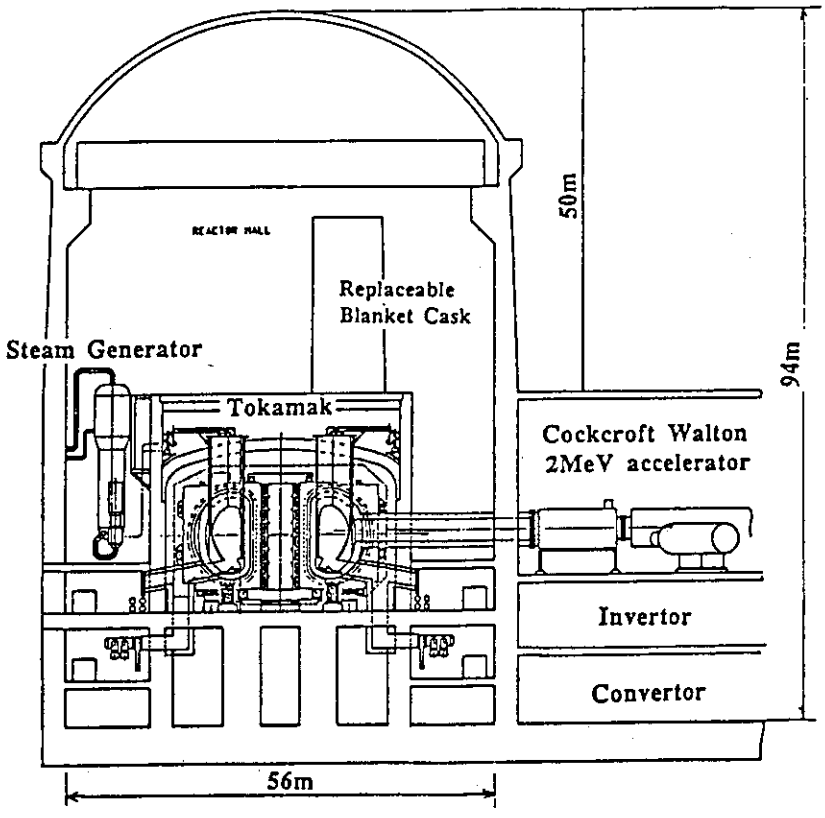

Fig. 3.4.4 Side view of the SSTR tokamak and NBI.

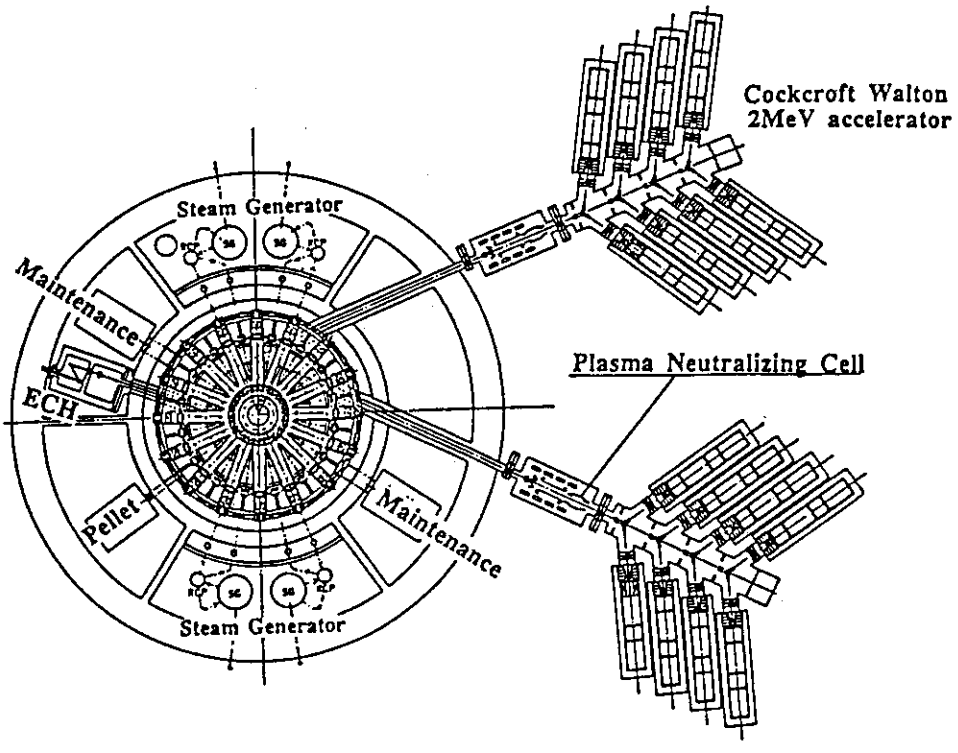

Fig. 3.4.5 Top view of the SSTR tokamak and NBI.

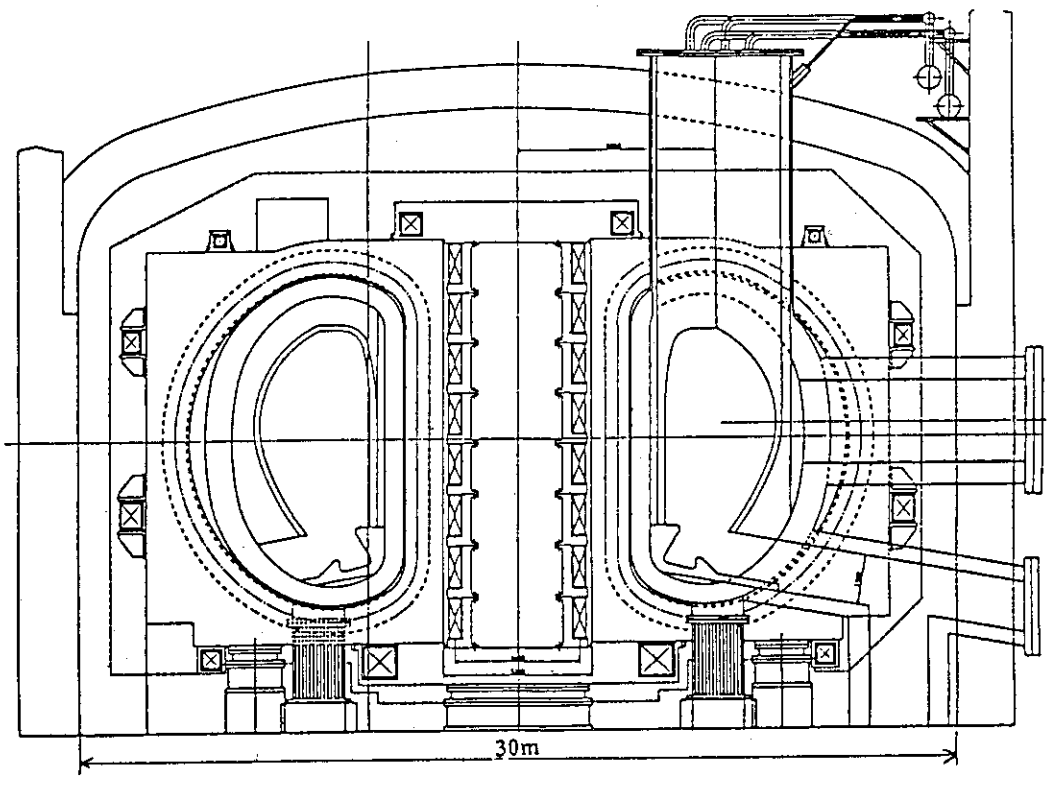

Fig. 3.4.2 Side view of the SSTR tokamak machine.

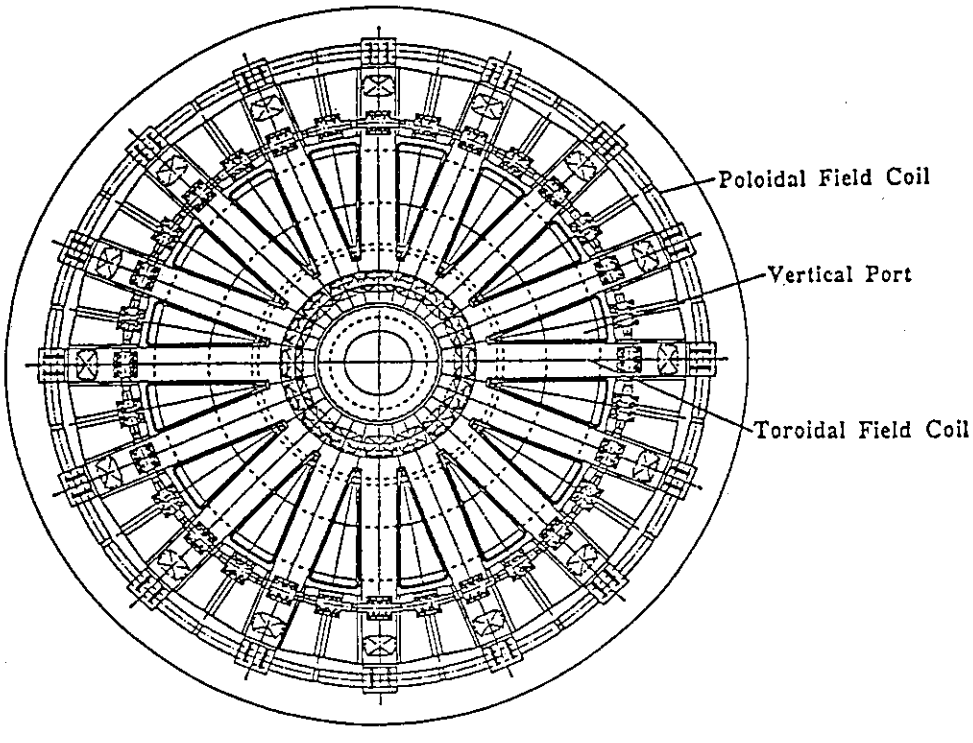

Fig. 3.4.3 Top view of the SSTR tokamak machine.

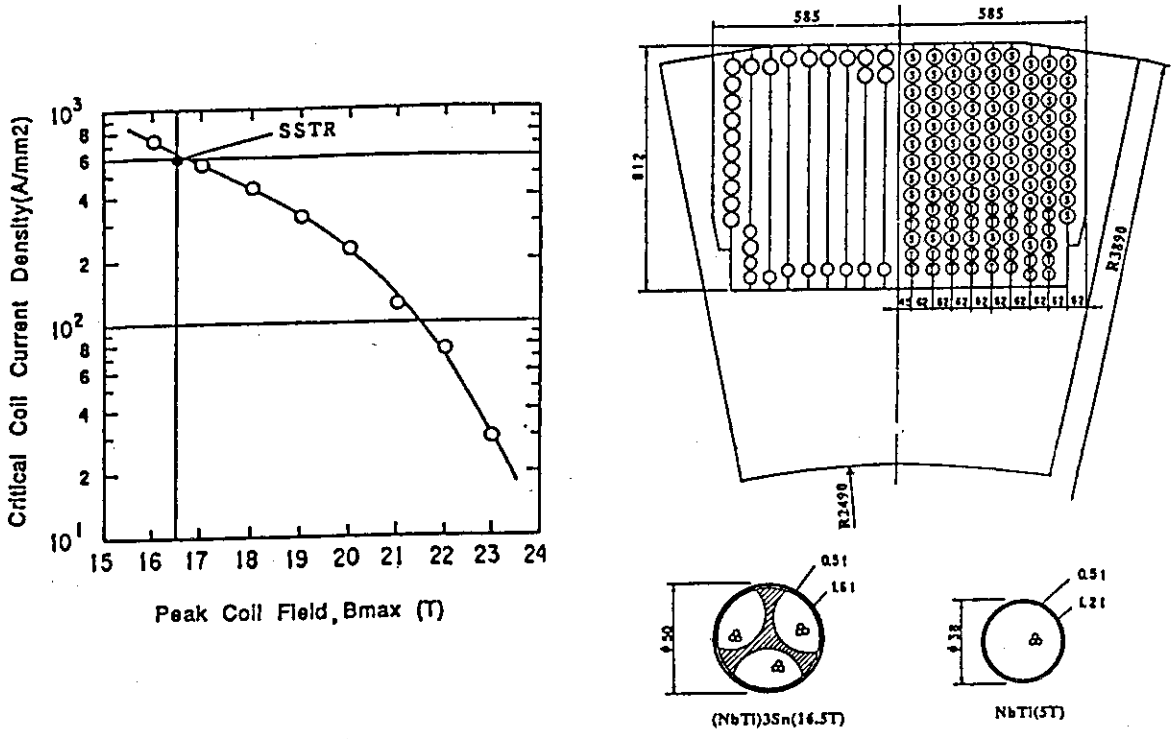

Fig. 3.4.6 (B,Jc) curve of the superconductor manufactured with Nb tube method and the inboard cross section of the TFC.

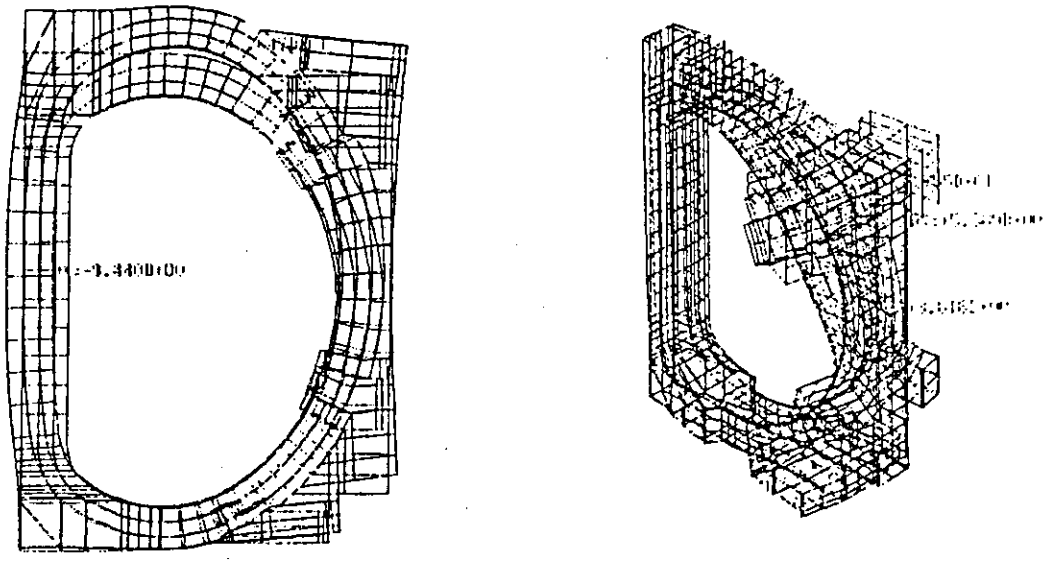

Displacement pattern for the self field
dX(max)=-9.4mm,dZ(max)= 28mm

Displacement pattern for the out of plane force
dY(max)=27.5mm,dX(max)=5.4mm

Fig. 3.4.7 Displacement patterns of the TFC. Left and right figures show displacements due to self field and out of plane force, respectively.

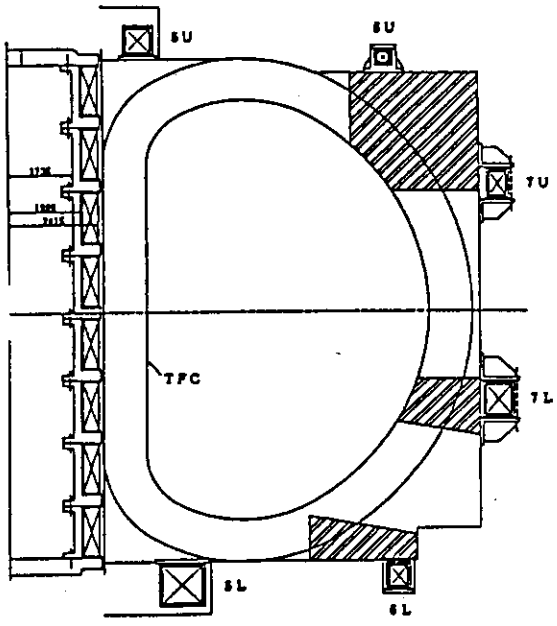

SSTR PFC configuration

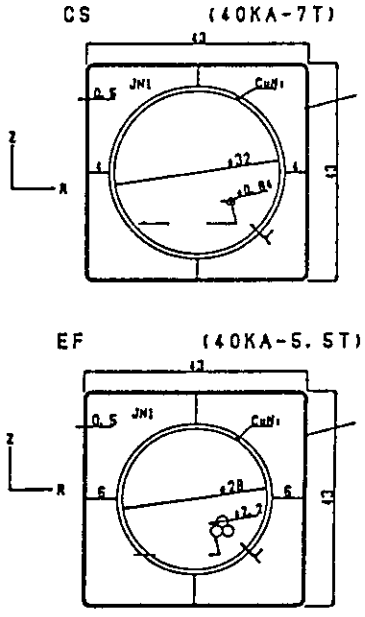

PFC conductor structure

Fig. 3.4.8 Arrangement of the PFC and the cross section of the conductors.

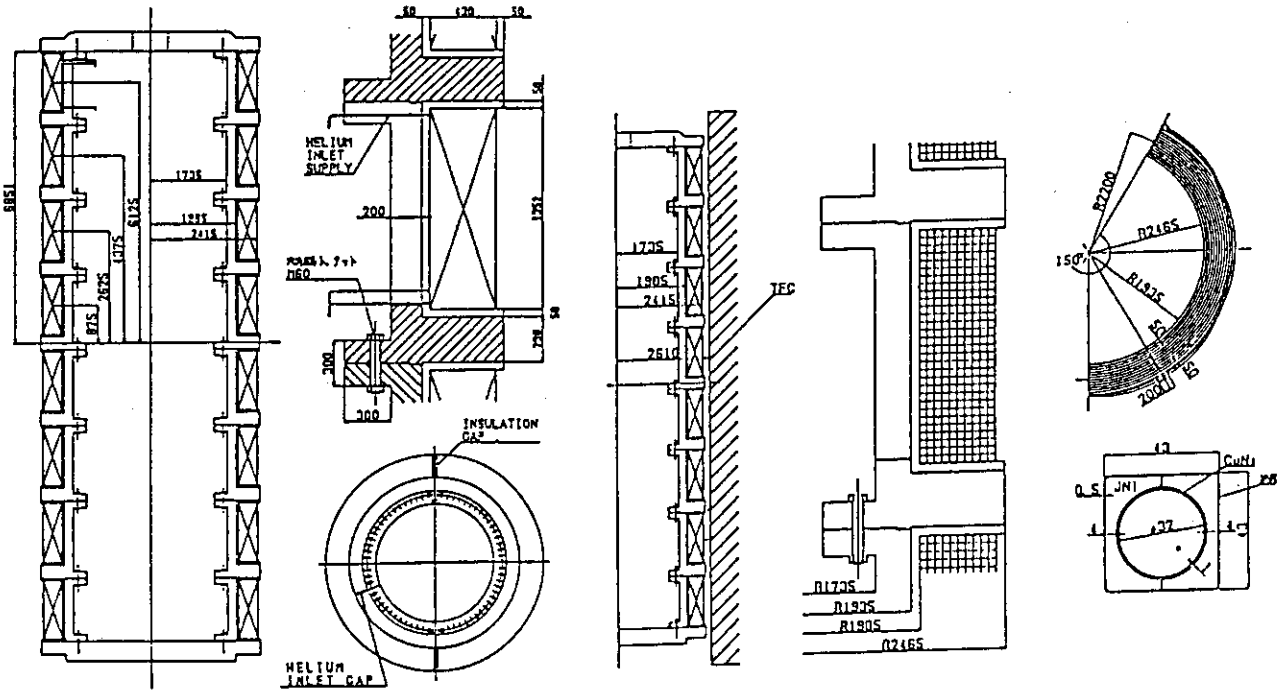

Fig. 3.4.9 Center solenoid structure of SSTR.

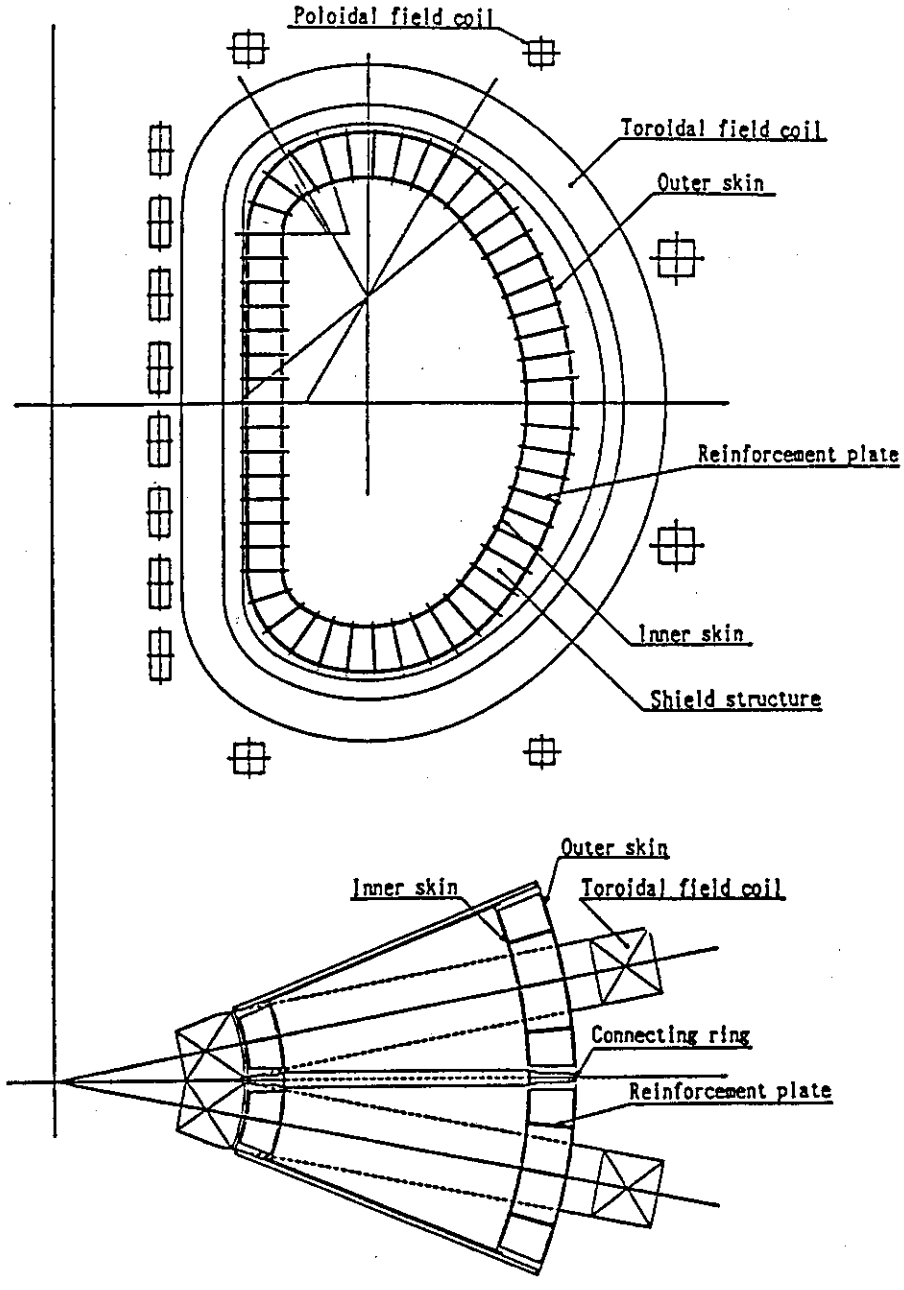

Fig. 3.4.10 Structure of the uniform low resistance vacuum vessel integrated with neutron shield.

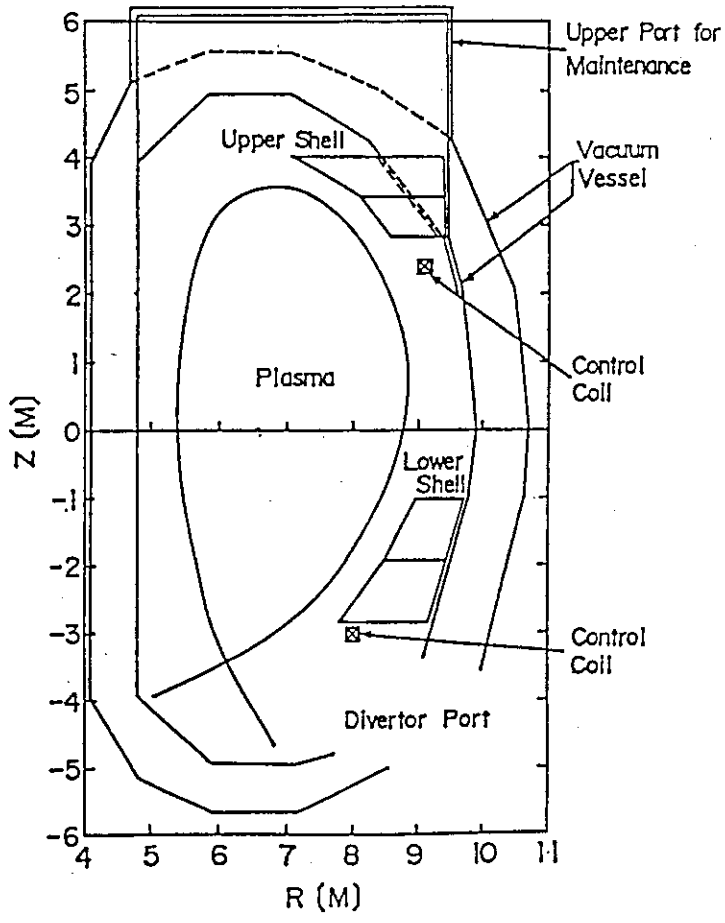

Fig. 3.4.11 Arrangement of the passive shell and active coil.

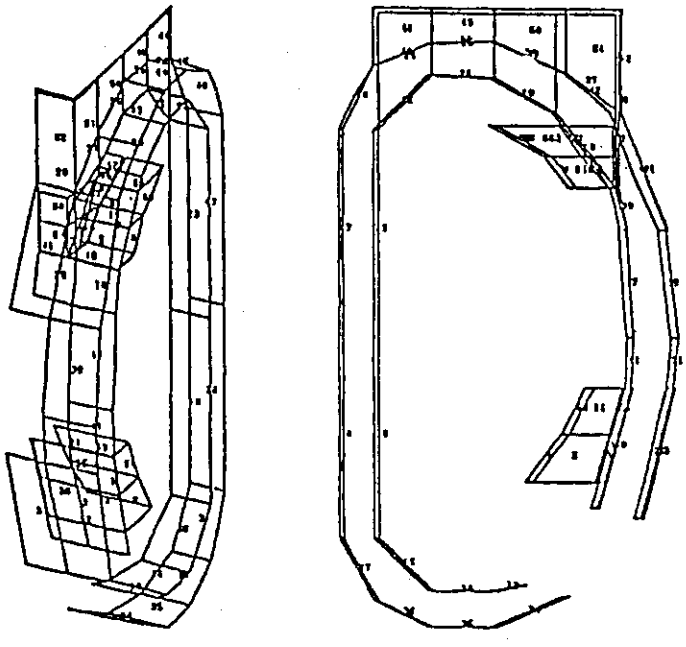

Fig. 3.4.12 Structural model for eddy current analysis on the vertical stability.

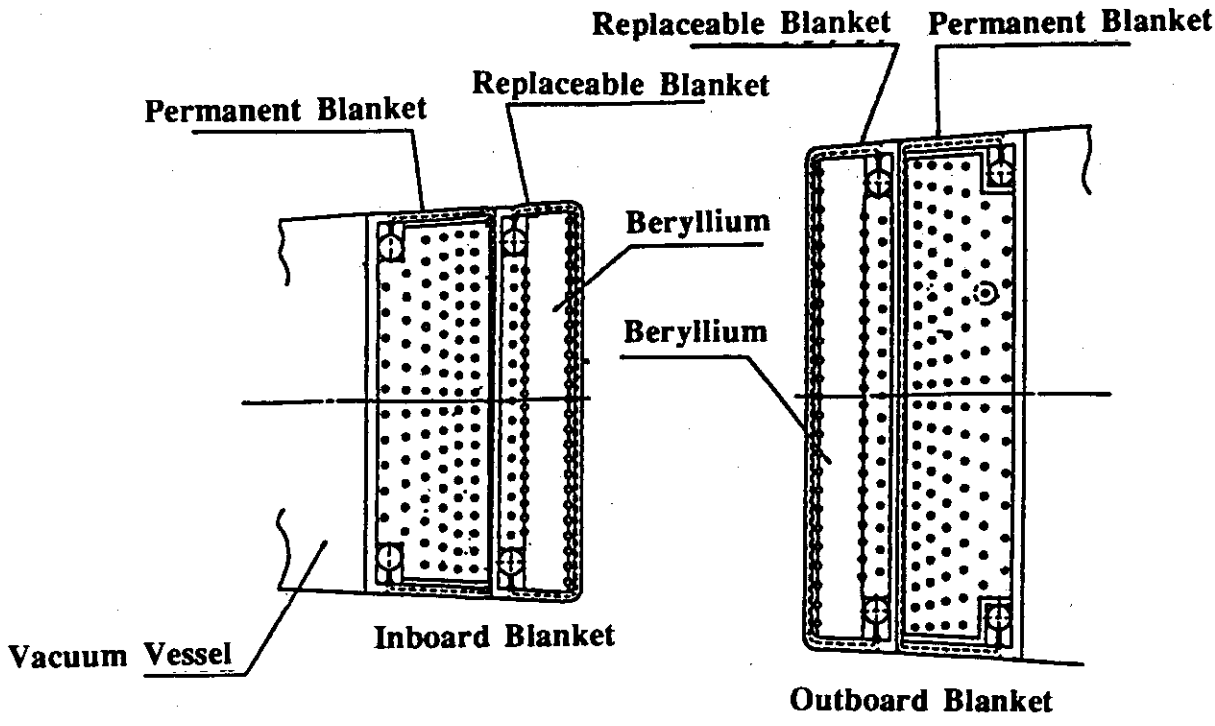

Fig. 3.4.13 Cross sectional view of the blanket.

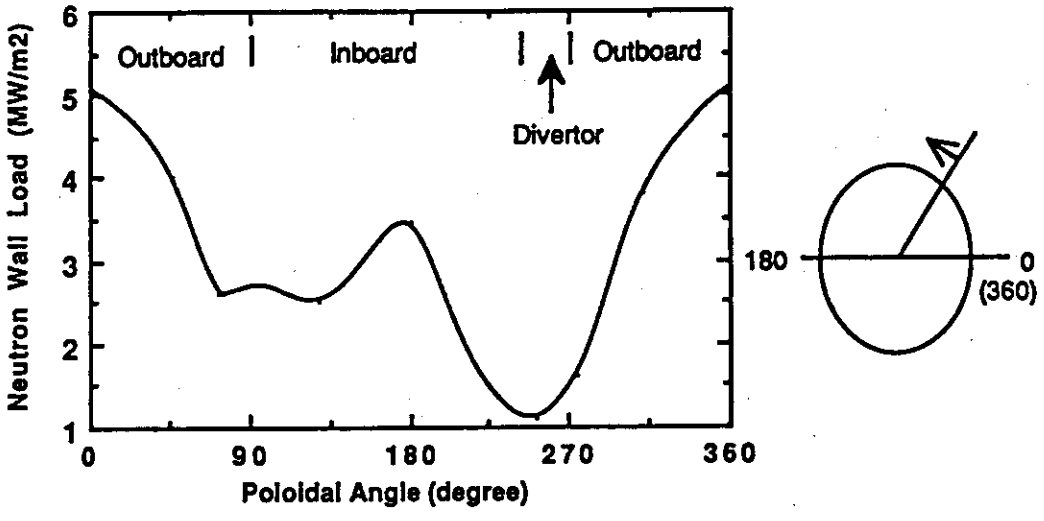

Fig. 3.4.14 Poloidal distribution of neutron wall load.

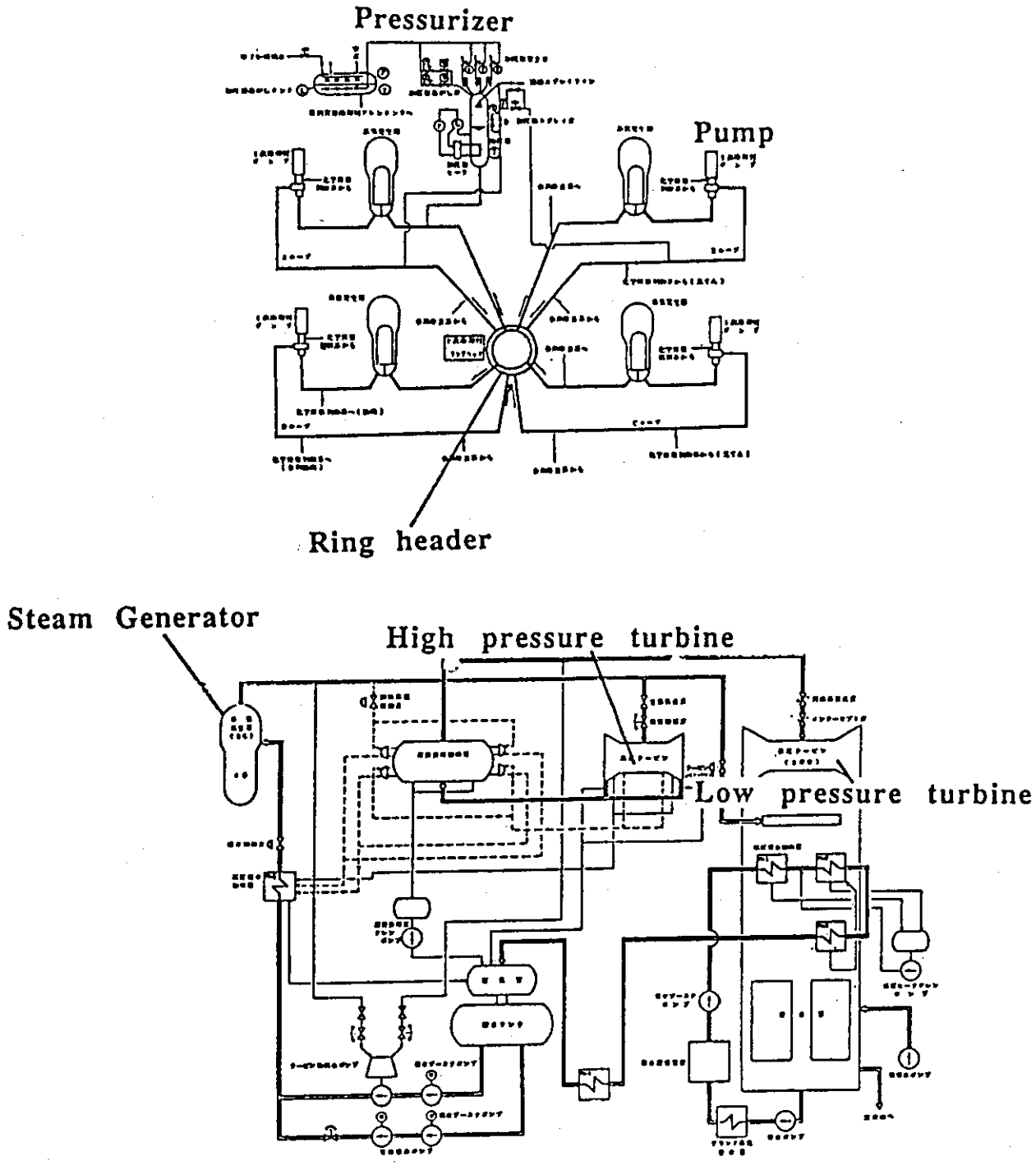

Fig. 3.4.15 Primary cooling/turbine generator system in SSTR.

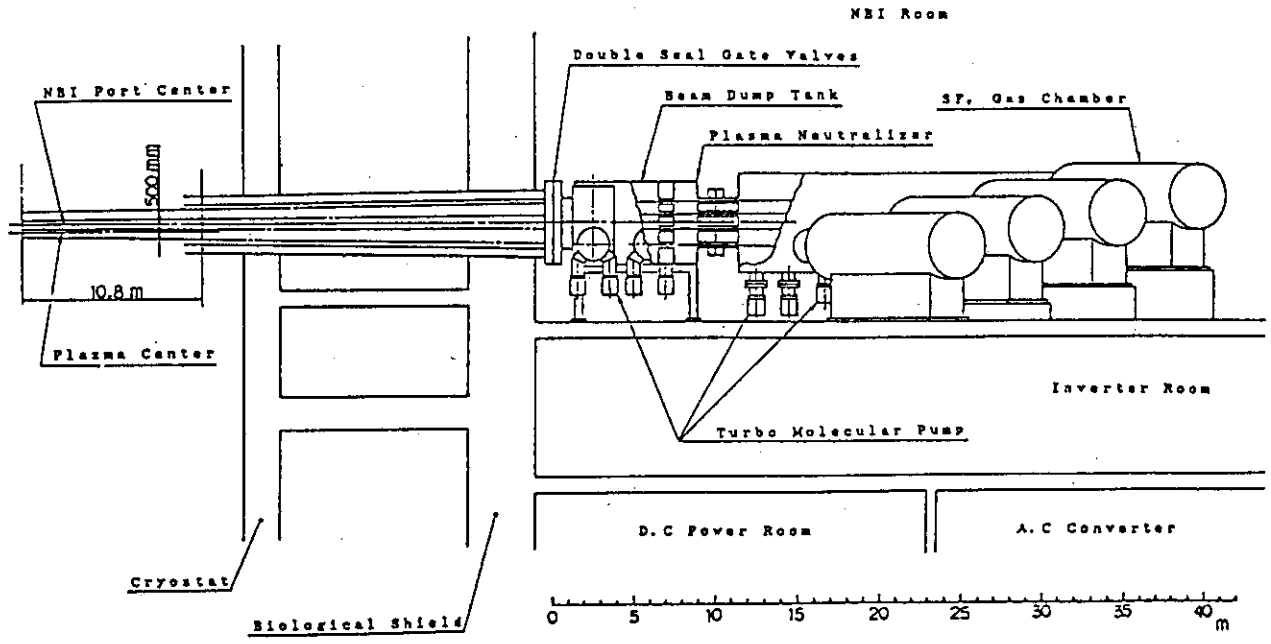

Fig. 3.4.16 Side view of SSTR NBI system.

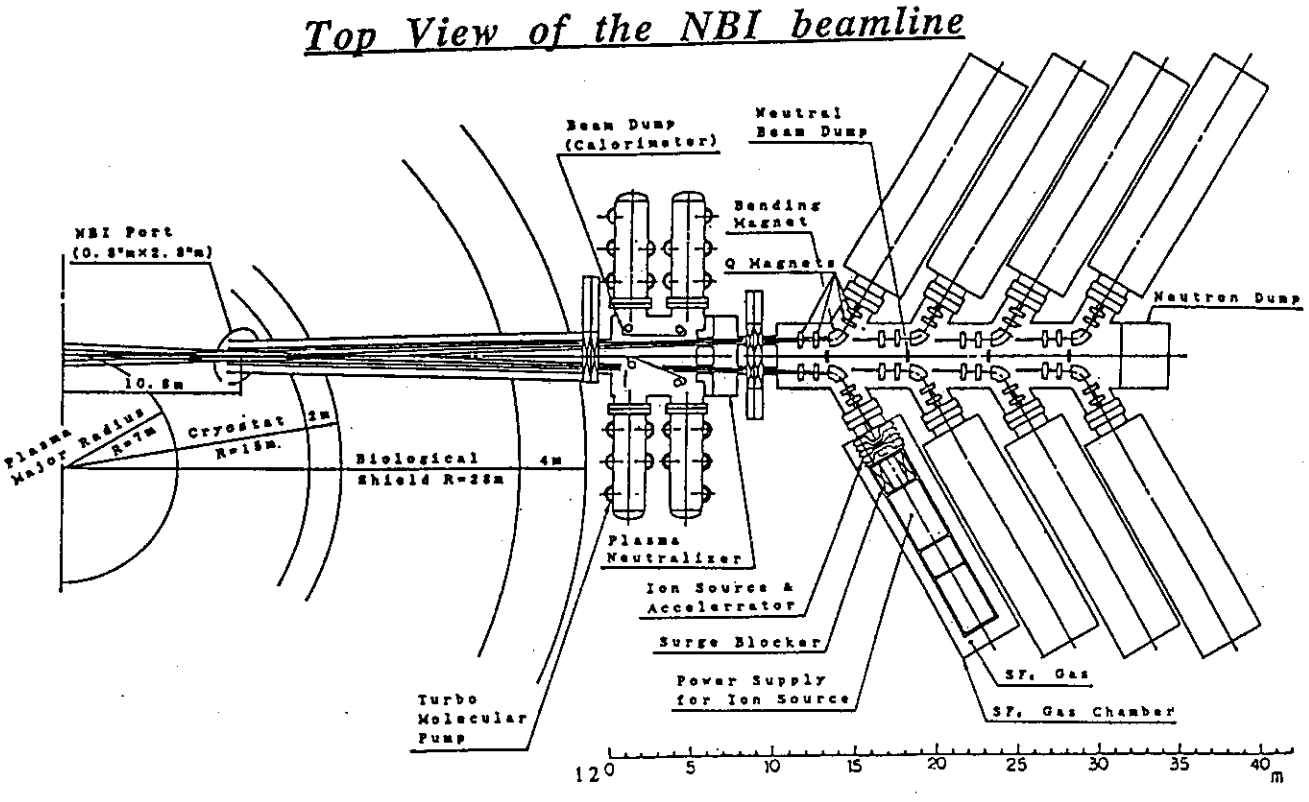

Fig. 3.4.17 Plan view of SSTR NBI system.

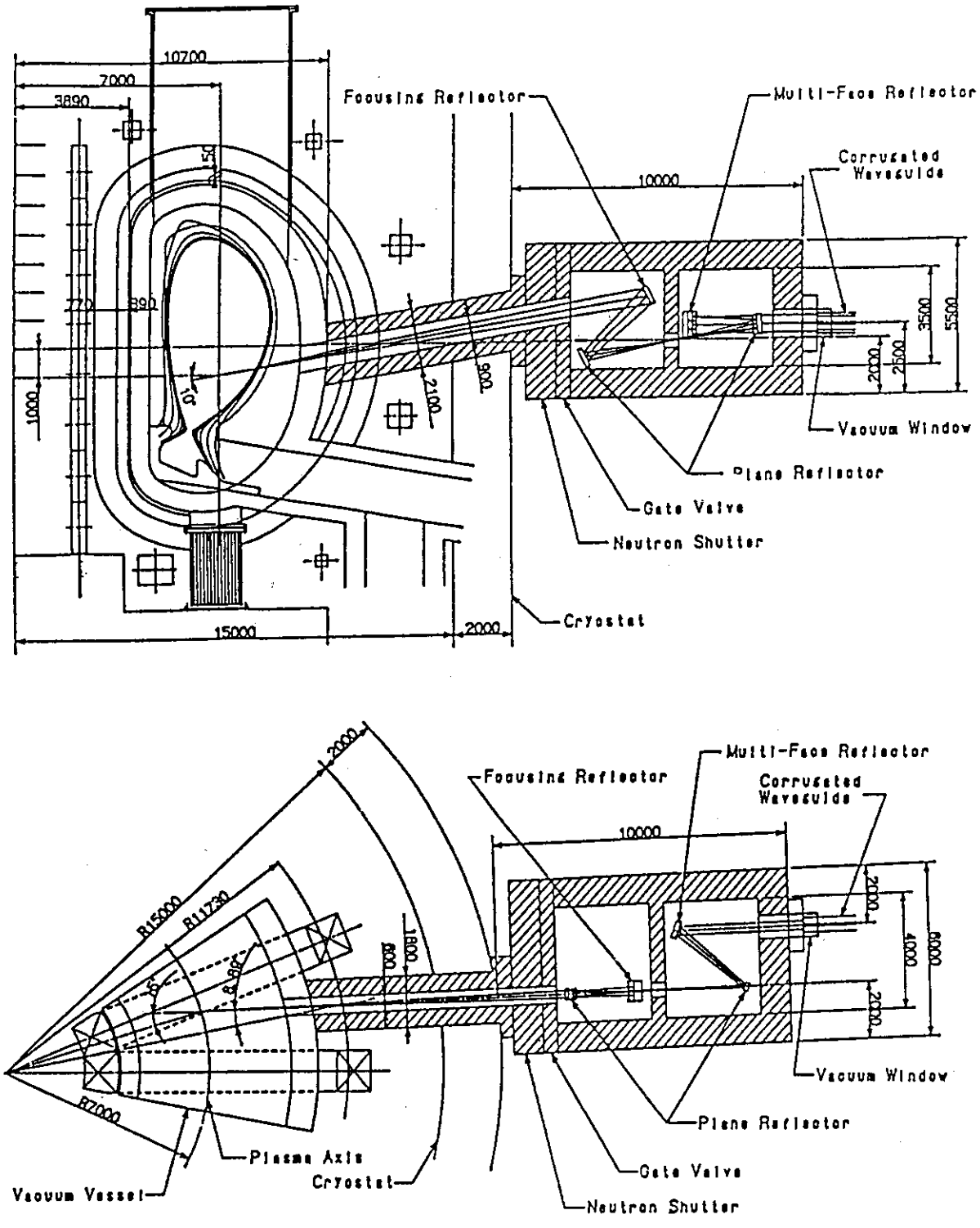

Fig. 3.4.18 Side and plan views of ECH system.

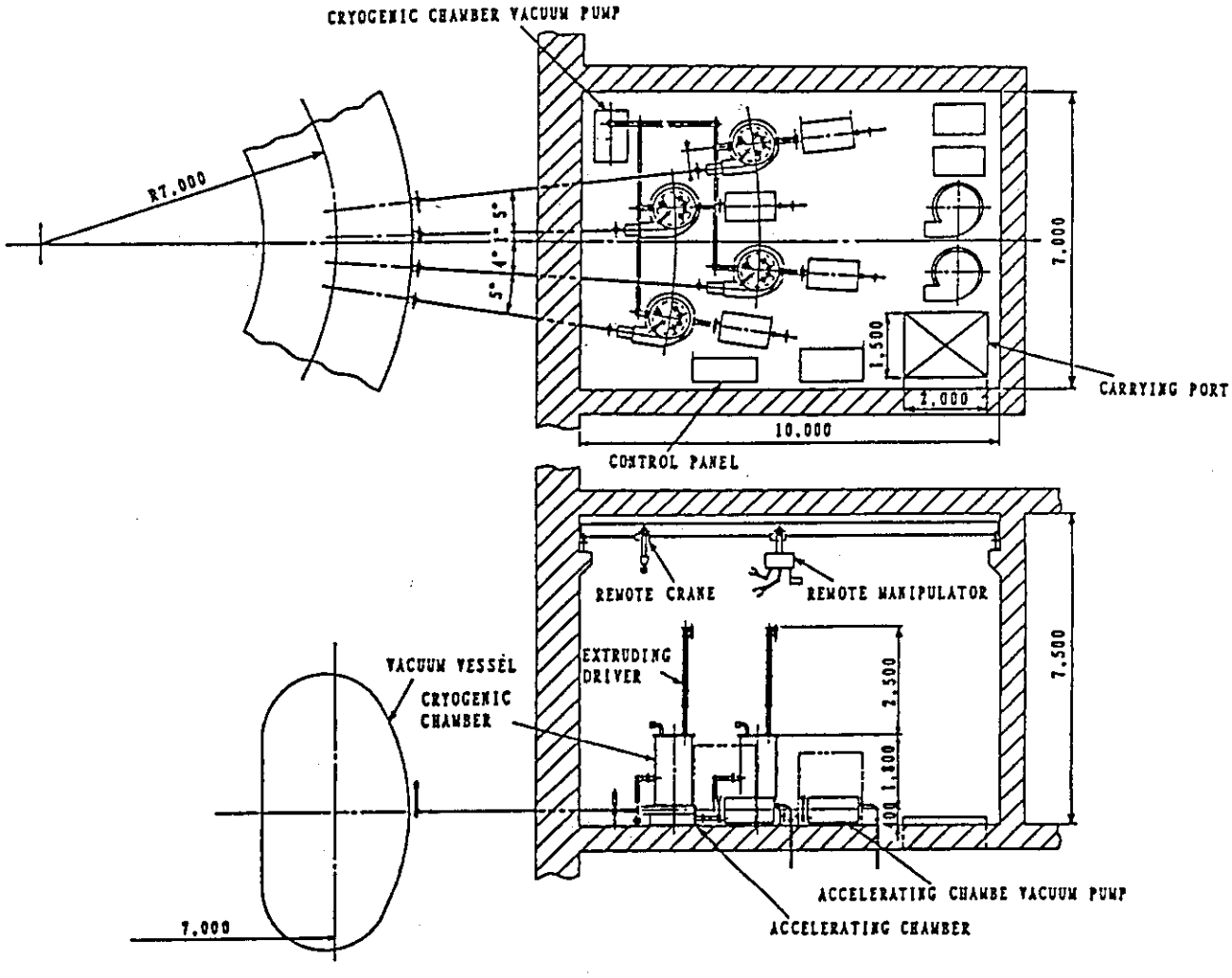

Fig. 3.4.19 Plan and side views of pellet injector.

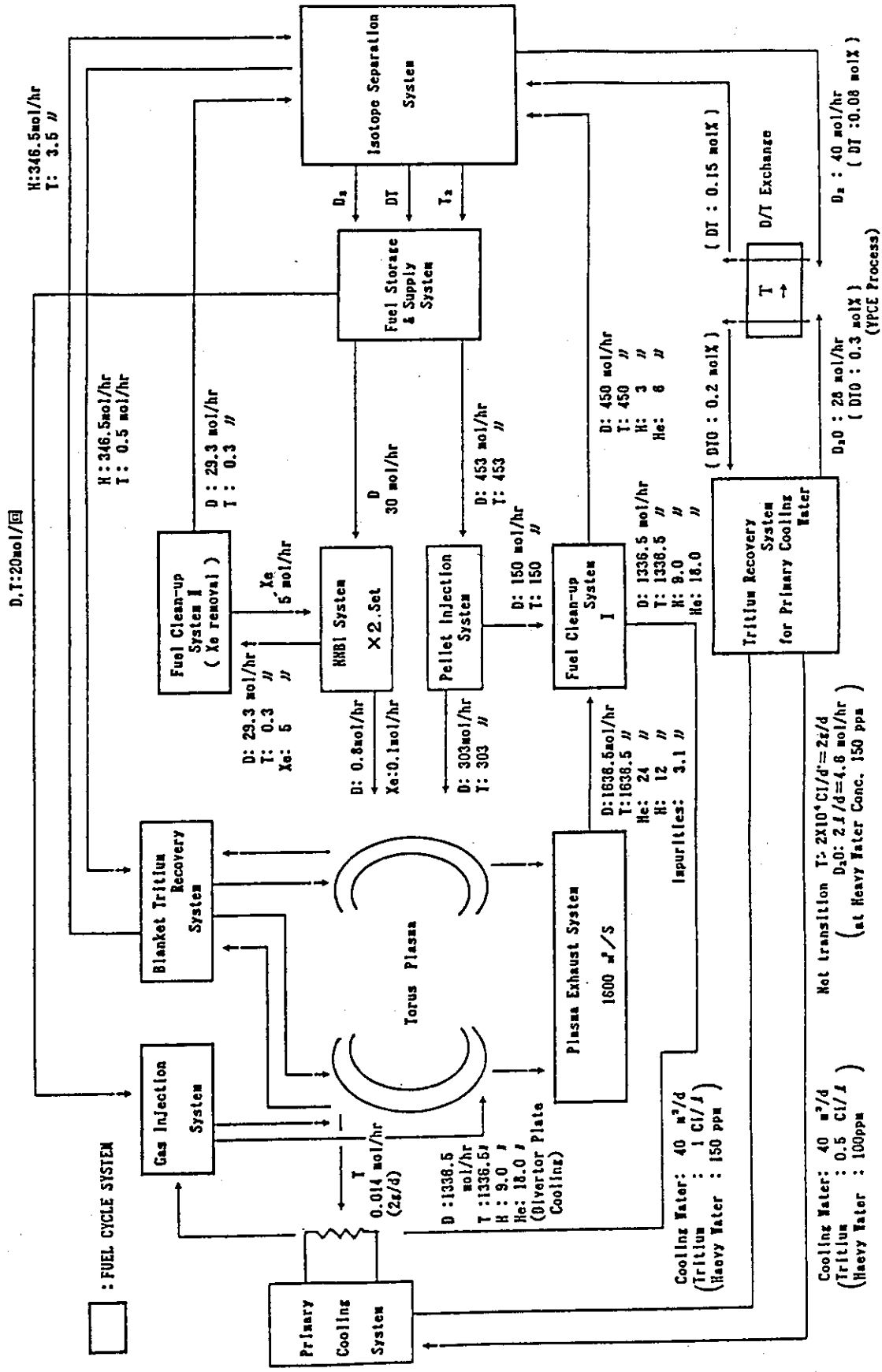

Fig. 3.4.20 Fuel cycle of SSTR.

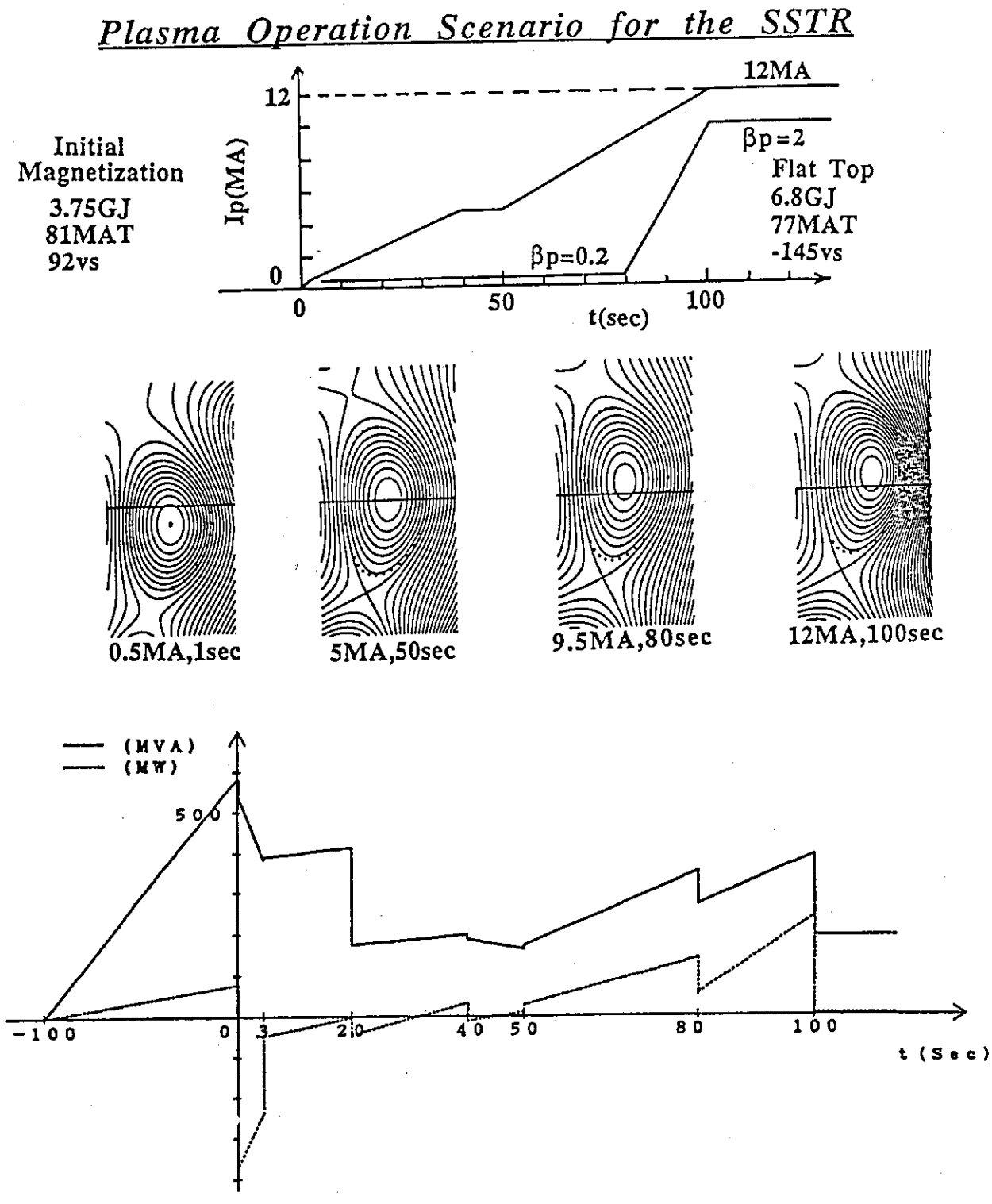

Fig. 3.4.21 Plasma current build up scenario and power supply requirement.

3.5 Overview of the plant

3.5.1 Site and buildings

Site arrangement of the buildings of the fusion power reactor is shown in Fig.3.5.1. In the site, there are fusion reactor building, electrical building, turbine building, cryogenic building, blanket maintenance building, waste storage building and switch gear yard etc. The area of the site is 450m x 400m including some open spaces. In the fusion reactor building shown in Fig.3.5.2, reactor hall, NBI room and fuel clean up room are the hot area and the air conditioning system (HVAC) for these rooms are separated from that for other rooms. There is no construction room in the SSTR taking into account of the reliability of the major components of the tokamak and the cost merit as a DEMO reactor. The major components of the tokamak are constructed with the large side crane during the construction phase of the fusion reactor building similar to the fission reactor. In the DEMO phase, we can expect high reliability on the superconductors and there is few possibility for the coil failure. Moreover, the shield integrated vacuum vessel proposed in the SSTR has large reliability and the probability of the severe damage is quite few. Thus, we can adopt simple reactor building structure similar to the commercial light water reactor. So a significant reduction of the volume of the reactor building becomes possible.

3.5.2 Operation and Maintenance

Steady state operation is adopted in the SSTR and the availability of 70% which has been attained in the commercial fission reactors could be attainable when the disruption probability is reduced. Here, the disruption probability could be very low because of its high edge safety factor. Major replaced elements during the maintenance are the divertor plates and the replaceable blankets. The damage rate of the divertor tiles is supposed to be high and the annual replacement is assumed. The divertor plates are extracted from the divertor port and is transported to the blanket maintenance building. Replacement of the damaged components and careful checking procedures are made in the maintenance building. Spare divertor units are used for the reactor until next maintenance. On the other hand, Outboard replaceable blankets are changed every two years (half torus every year) and inboard replaceable blankets are changed every four years (quarter torus every year). With this maintenance scheme, it is possible to reduce the shut down period to keep 70% availability.

3.5.3 Construction and construction schedule

As described above, major components of the tokamak are assembled by large side cranes during the construction of the reactor building. By this, reductions of the building volume and the capacity of the polar crane in the reactor hall are possible. Openable temporary dome is used for the dust control during the assembly. The construction experience of large tokamaks (for example JT-60 in Japan) is helpful in estimating the SSTR construction. Seven years were spent in JT-60 from the contract to the first plasma. On the other hand, five years are usually required until the start of its operation. Although it depends on the design level before the start of its construction, it may be possible to fire the first plasma with five and half years of the construction period by appropriate sharing of the manufacturing between heavy industries. A construction schedule of the SSTR is shown in Fig.3.5.3.

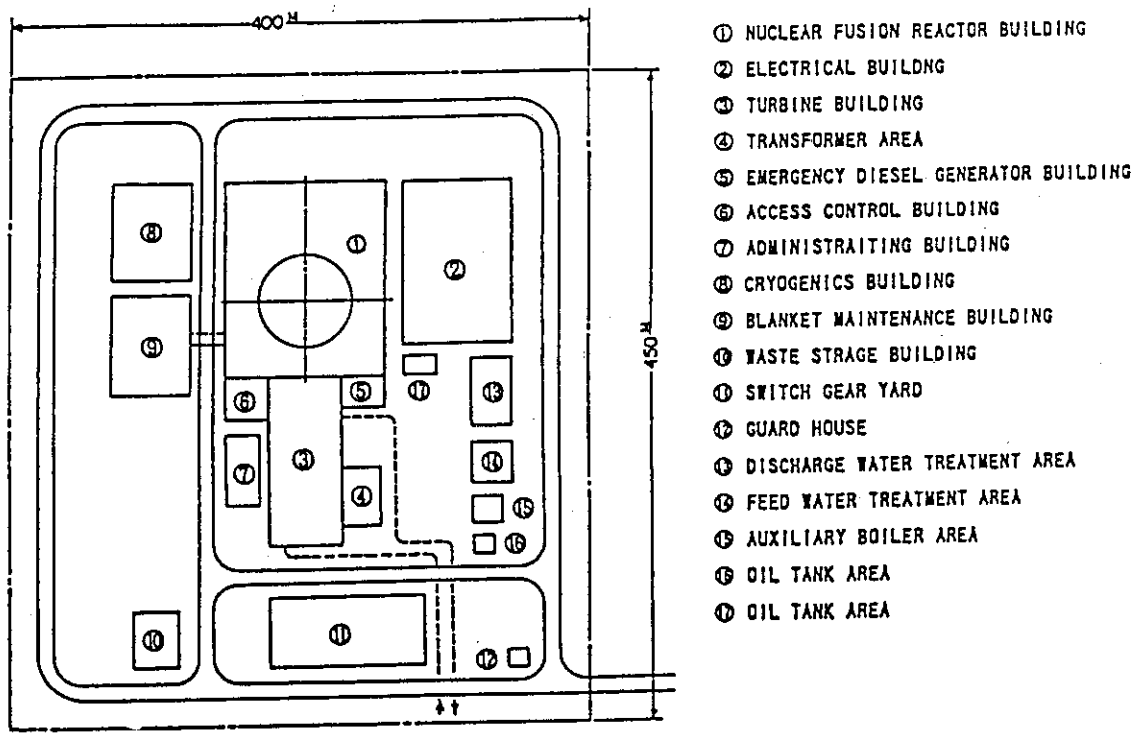

Fig. 3.5.1 SSTR site plan.

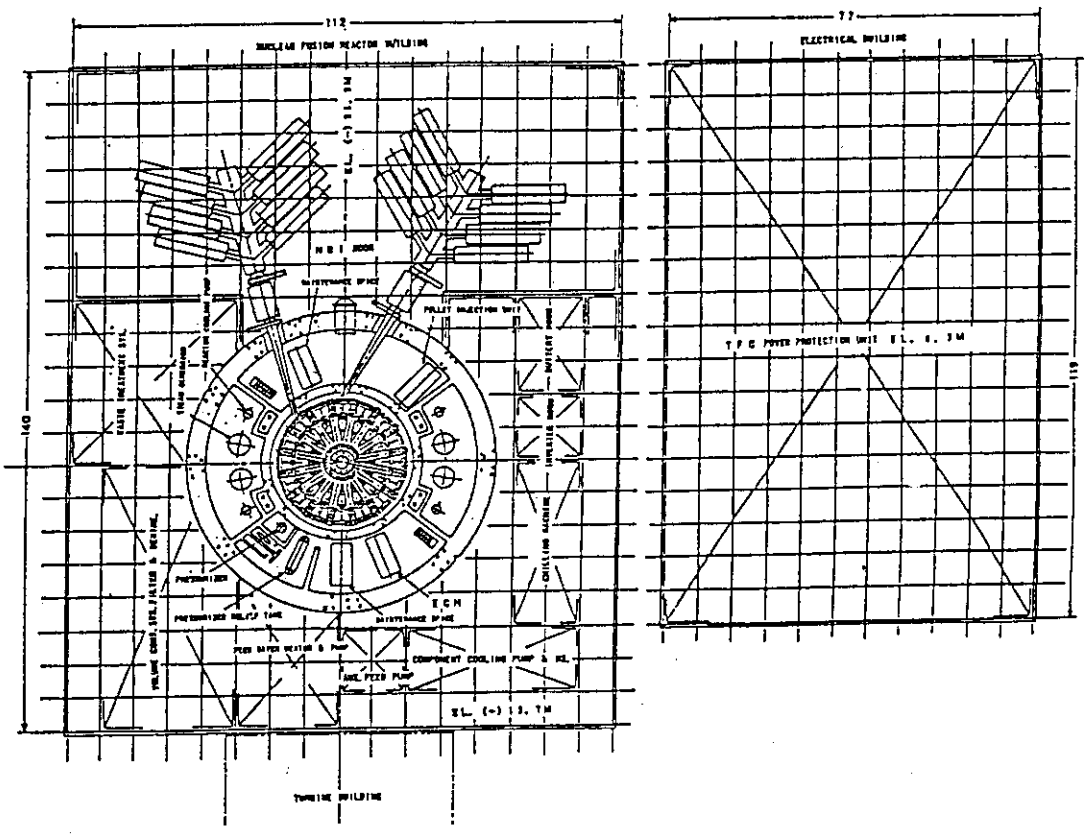

Fig. 3.5.2 Reactor building layout (plan view).

year	1	2	3	4	5	6
Work	Contract				Power	Test/Plasma Ope
SC Magnet		TFC			Assemble	
		PFC(L)		Assemble		
			PFC(U)		Assemble	
VV/Div.					Assemble	
Blanket Fuel					Assemble	
NBI					Assemble	
Power Supply					Assemble	
SG/ Turbine					SG Assemble	Turbine Assemble
Building		Reactor Building				
		Electrical Building				
		Cryo Building				

Fig. 3.5.3 Construction schedule of SSTR.

3.6 Economical Prospects

The cost of electricity in the fusion reactor is evaluated for example in the STARFIRE designed in the USA. The cost of electricity is a summation of those from the capital cost, the operation cost and the fuel cost. In the fusion reactor, the capital cost is fairly high compared with that in other electricity sources. However, the operation and fuel costs are relatively low. And it is possible to have an economical competitiveness against other electricity sources. Fig.3.6.1 shows construction unit cost and cost of electricity for major electric energy sources in Japan, light water reactor and coal/oil/LNG fired reactors, compared with those for the SSTR. As is clear in the figure, it is estimated that the SSTR can produce electricity with the cost of electricity of 1.5 times that of light water reactor (16yen/kWh). Here we used 16 years as the service life for the capital cost (same as that defined by the government law for the light water reactor). If we use 30 years as the service life taking into account of the technical life limit or the realistic operation period of the reactor and higher availability up to 85%, the cost of electricity is lowered to 11.5 yen/kWh.

For the assessment of the economical feasibility of fusion, local situations on the electricity supply for various countries should be considered. For example, the economical competitiveness of fusion is poor for developing countries which has large rivers and hydro power stations. Even in the developed countries which have large amount of coal, fusion may have poor competitiveness. But in the developed countries which have no large rivers and few coal, it may be much easier to have better competitiveness with relatively high cost of electricity. The fusion reactor is an electric power source which requires large investment. And the large interest for the capital cost becomes a severe load even for the large electric power companies in Japan. So a long term budget supply with low interest rate is required for the development of fusion.

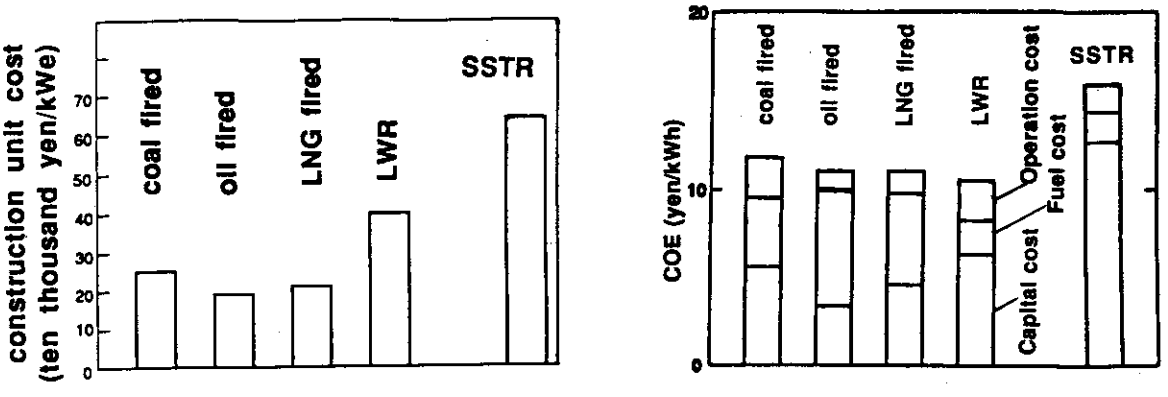

Fig. 3.6.1 Cost of electricity for various energy sources.

4. Plasma Engineering

4.1 Equilibrium Configuration and Operation Scenario

4.1.1 Plasma Configuration and Parameters during Burn

(1) Triangularity and null point location

Since single null (SN) divertor plasma was employed in SSTR, plasma configuration is up-down asymmetric and any combinations of both the elongation and triangularity between null and non-null sides can be selected, though the average values are constant. According to the previous design studies on ITER and FER, it can be concluded that the ratio of the elongation and triangularity should be about 1.1/0.9 between null and non-null sides to minimize total stored electromagnetic energy of the poloidal field coil (PFC) system. Basically, this value is employed for the elongation in present the SSTR design, but for the triangularity the other factor, such as separation between active and passive separatrices, dominates to decide the ratio.

Elongation of the SSTR plasma was selected as 1.85 based on the trade-off study between energy confinement property, beta limit, controllability of positional instability, etc. On the contrary, reactor structure dominates the triangularity of the plasma through the size and shape of the toroidal field coil, ripple distribution of the toroidal magnetic field, position of the port for the remote maintenance, required length between null point and divertor plate, etc. Values of 0.3-0.4 are still recommended for the triangularity to maximize available volt-second for appropriate value of the internal inductance (~0.65 in the ITER definition of $l_i(3)$ which roughly corresponds to parabolic plasma current profile) within the engineering constraint for the center solenoid. Radial position of the null point can be decided straightforward, once the the triangularity was decided, and vice versa.

Plasma position is shifted upward by about 0.6 m from the mid-plane of the torus structure to assure adequate space for the divertor, since the divertor is located in the lower half of the torus. Allowable maximum shift should be decided from the viewpoint of the toroidal field ripple at the upper half of the plasma, maintenance port width requirement, space required for shear panel to support over-turning force at the upper half of the toroidal coil, etc.

Location of the null point was selected as (6.1 m, -3.272 m) which results in the combinations of the elongation and triangularity at null and non-null sides are (2.3, 0.36) and (1.7, 0.23) on 95% flux surface. Average value is still (1.85, 0.29).

(2) Flux linkage dependence of total ampere-turns and stored energy

Since SSTR assumes that all the plasma current in the burn phase can be sustained by non-inductive current drive by negative neutral beam injection (NNBI) and bootstrap current, no flux change is required for the poloidal field coils during burn. This suggests the optimum design of the poloidal field coil system will be attained if the flux linkage is selected so that the total ampere-turns or stored energy can be minimum at burn phase.

Figure 4.1.1 shows the flux linkage dependence which indicates choosing flux linkage around -100 to -120 Vs minimizes both total ampere-turns and stored energy of the poloidal field coil system. The location of PF coils is summarized in Table. 4.1.1. The ITER physics guideline for the volt-second requirement claims flux swing of 237 Vs for SSTR, while initial magnetization for the maximum poloidal magnetic field of 7 T is only 92 Vs. This value of initial magnetization requires flux linkage of -145 Vs at burn phase and additional ampere-turns of about 10%, while the total stored energy remains almost the same amount.

(3) K index

The equilibrium magnetic field for the single null divertor plasma is up-down asymmetric due to the up-down asymmetry of plasma cross section. This asymmetry induces vertical movement of the plasma if the plasma position shifted horizontally. Strength of the coupling between vertical and horizontal movements can be represented by K index which is defined by the following equation.

$$K = - \frac{R}{B_z} \frac{\partial B_z}{\partial z}$$

Using <n>, <K> and $\langle B_Z \rangle$ averaged by weighting plasma current distribution, motive force of the positional instability for the coupled mode can be represented as follows;

$$\begin{pmatrix} \delta F_R \\ \delta F_Z \end{pmatrix} = - 2\pi I_p \langle B_Z \rangle \begin{pmatrix} \langle n \rangle - 1 & \langle K \rangle \\ \langle K \rangle & -\langle n \rangle \end{pmatrix} \begin{pmatrix} \delta R \\ \delta Z \end{pmatrix}$$

It is preferable to decrease absolute value of K index for minimizing coupling between vertical and horizontal motions and then for attaining easy control of the positional instability. In the present design of 1.1/0.9 elongation rate, the value of <K> is 0.1. Because of the positive <K> value, plasma shifted radially inward moves downward, i.e., to the divertor plate, and the plasma, therefore, deposits its thermal energy on the divertor plate without touching any first wall during disruption.

4.1.2 Magnetic Field Structure

Information about the precise magnetic field configuration near plasma surface is required for designing divertor structure in detail. Magnetic line of force was traced on the separatrix and neighboring several magnetic surfaces for plasmas of both high (β_p=2.0) and low (β_p=0.1) poloidal betas. Distances of these magnetic surface from the plasma surface measured at the points on the outside equatorial plane with same height as the magnetic axis are 0.01, 0.1, 0.2, 0.5, 1, 2, 5 and 10 cm, respectively. Magnetic line of force with 0.01 cm separation was considered as separatrix in the analysis. Hitting points of the inside and outside separatrices on the divertor plate are separated from the null point by 1.2 and 1.3 m, respectively.

Figure 4.1.2 shows the results of magnetic line tracing for both high and low βp plasmas along with the position of the divertor plate and the first wall. Location of the characteristic points shown in Fig. 4.1.2 are summarized in Table 4.1.2. At low poloidal beta the first wall clears magnetic lines up to 10 cm flux tube, but magnetic lines apart from more than 7.5 cm intercept the top and inside first walls at burn phase in the present design.

Besides the active separatrix which determines the plasma surface, there exist another separatrix outside the active separatrix, so called passive separatrix. Plasma particles existing between two separatrices can flow to the divertor plate without hitting the first wall as long as the first wall is separated from the plasma surface adequately. For the SSTR plasma configuration, separation between two separatrices is 10 cm at burn phase and is 19 cm before additional heating.

Magnetic surface expands near the null point and then shrinks gradually toward the divertor plate. For the designed distance between the null point and divertor plate, expansion at the outside hitting point is 4.5 cm on the 1 cm flux tube and 23 cm on the 10 cm tube. Ratio between the toroidal and poloidal magnetic fields is about 20 at the outside hitting point during burn.

DIII-D experiments showed that width of the heat flow is 1 cm or less at the B point for L- and quiescent H-mode plasmas, while the width expands twice for the giant ELM plasma [1]. The results indicate that heat flow in the scrape-off layer can safely be deposited on the divertor plate in the present SSTR design. Particle flow seems to be much wider than heat flow. In the present design the width was assumed as 7.5 cm.

4.1.3 Poloidal Field Coil Layout

Hybrid poloidal field coil system was employed in SSTR in which individual coil functions as both the OH and EF coils resulting in decrease in the number of the coil and simplification of the torus structure. Fourteen coils (seven coils in the upper and lower halves of the torus, respectively) build up a whole PFC system, in which 8 coils form a center solenoid. This idea of the layout is same as ITER and FER.

Length of the center solenoid is same as the height of the toroidal coils and is equally divided into 8 coils. Plasma extends up to 4 coils which can easily control plasma shape for changes in β_p and l_i. Coil locations are shown in Table 4.1.1. In spite of the hybrid coil employment, multiple coils are controlled in the same way as described in the operation scenario. Maximum ampere-turns of each coil are determined by studying operation scenario and the result is summarized in Table 4.1.3 and Fig. 4.1.3.

4.1.4 Operation Scenario

Since SSTR is a steady state reactor, start-up and shutdown are rare occurrences and the operation scenario should be constructed so that during these phases the electric power remains in the appropriate extension from the steady state burn phase. Furthermore, magnetic field experience and ampere-turns should basically not attain maximum during these phases because of maximum utilization of the PFC ability at burn phase.

Based on the above description the following start-up scenario was fixed.

(1) Full inductive start-up with ECH assist to attain adequately slow ramp-up of the plasma current.
(2) Current initiation with limiter configuration and transition to divertor configuration at appropriate plasma current
(3) Gradual increase of plasma size, elongation and triangularity
(4) Locate limiter at the apex of the divertor throat to be extracted easily for maintenance
(5) Concurrent heating and plasma current ramp-up at final stage of start-up to avoid ampere-turns maximum at low β_p

Required volt second was decided on the basis of the ITER physics guideline, i.e.,

$$\Psi_{req} = L_p I_p + 0.4\mu_0 R_p I_p + 1.42 + 10.0 \qquad (Vs)$$

The last term of the right hand side corresponds to flux consumption during heating. Flux consumption at breakdown can not be decided accurately and was assumed to be 1.42 Vs to round the total flux swing to 247 Vs without decimals. The second term was obtained

from compilation of the large tokamak experiments and is explained as resistive flux consumption during the time constant decided by internal inductance and resistance of the plasma. Initial magnetization for the maximum poloidal field of 7 T is 92 Vs. Flux linkage at any time can be obtained by subtracting flux calculated by the above equation from the initial magnetization flux.

Limiter to divertor transition is done by keeping plasma current at 5 MA for 10 s. Flux linkage was assumed, for simplicity, to be constant during the transition by canceling resistive consumption with change in inductive storage. It is not exactly correct but net change in the flux linkage during this phase does not affect the ampere-turns of the coil.

Heating starts at 9.5 MA plasma current, so that the increase in solenoid coil current due to plasma current increase can be canceled by decrease in coil current due to increase of β_p. Location of null point is fixed at (7.0 m, -3.2 m) throughout the heating. Time evolution of the plasma parameters and ampere-turns of the coils are summarized in Table 4.1.4.

Figure 4.1.4 depicts time evolution of the plasma configuration for typical time slices which correspond the times in Table 4.1.4. Stray magnetic field into the plasma region at the initial magnetization of 92 Vs is 17 G in average, while maximum field is 42 G. These small amount of stray magnetic field will not prevent the successful breakdown. At limiter configuration (b, c and d in Fig. 4.1.4) separatrix gradually approaches the final location as time proceeds. Note that plasma surface does not always clear the first wall in the present operation scenario. This point should be studied in the future.

Time evolutions of major and minor radii, height of the magnetic axis and plasma current are shown in Fig. 4.1.5. Elongation and triangularity of the plasma cross section gradually increase as shown in Fig. 4.1.6. Plasma heating starts at I_p=9.5 MA described before and β_p increases rapidly during heating, while ramp-up rate of the plasma current is rather constant (~0.1 MA/s) as shown in Fig. 4.1.7.

Figure 4.1.8 shows time evolution of the coil ampere-turns. Fundamentally changes are monotonic and smooth which suggests moderate electric power is required during start-up. Discussion of the electric power supply will be made in detail in Chapter 14.

Safety factors at magnetic axis, q(0), and 95 % flux surface, q(95), are shown in Fig. 4.1.9. Safety factor on the magnetic axis always remains more than unity and reaches 1.5 at burn phase. This fact together with the large value of q(95) assures good MHD stability

of the SSTR plasma. Changes in <n> and <K> are shown in Fig. 4.1.10 which indicates low β_p plasma will be critical for the positional instability control. The <n>-<K> diagram is shown in Fig. 4.1.11.

4.1.5 Flexibility

Tokamak reactor should have adequate flexibility for changes in plasma pressure and current profile. Figures 4.1.12 and 4.1.13 show the variation of the PF coil current distribution for the 0.1 deviation of both the β_p and l_i, respectively. Peaked plasma current profile requires much currents for PF5L, PF6L and PF7L coils. Effect of the β_p deviation is smaller than that of l_i. Disruption does not affect so much because most of the coil currents except divertor coil (PF5L) tend to decrease in the absolute value. Increase of the divertor coil current of 750kA is within the increase for the l_i deviation. It must be concluded that only PF5L, PF6L and PF7L should have supplementary capability for the flexible operation.

4.1.6 Future tasks

The following tasks should be studied.

(1) Plasma behavior and equilibrium during disruption
(2) Plasma start-up scenario which does not interrupt the first wall
(3) Study of shutdown scenario
(4) Study of flexibility in more detail

Reference

[1] HILL D.N.,PETRIE T.,Ali MAHDAVI M.,et al.,Nucl. Fusion **28** (1988) 902

Table 4.1.1 Poloidal coil position

Coil No.	Rc (m)	Zc (m)
PF7U	13.2	3.5
PF6U	10.2	7.0
PF5U	3.7	7.5
PF4U	2.2	6.125
PF3U	2.2	4.375
PF2U	2.2	2.625
PF1U	2.2	0.875
PF1L	2.2	-0.875
PF2L	2.2	-2.625
PF3L	2.2	-4.375
PF4L	2.2	-6.125
PF5L	4.8	-7.6
PF6L	10.5	-7.4
PF7L	13.2	-2.5

Table 4.1.2(a) Characteristic point of magnetic line of force at SOL (βp=2.0)

unit : m

Separation (cm)		Separatrix		5.0		10.0	
Outside hitting	A	6.719	-4.396	7.046	-4.614	7.288	-4.775
Null	X	6.098	-3.272	-----	-----	-----	-----
Outermost	B	8.696	0.573	8.746	0.573	8.796	0.573
Top	C	6.585	3.411	6.171	3.642	5.756	4.136
Innermost	D	5.302	0.738	5.174	0.821	5.040	1.071
Inside hitting	E	4.998	-3.796	5.260	-3.240	5.120	-2.838

Table 4.1.2(b) Characteristic point of magnetic line of force at SOL (βp=0.1)

unit : m

Separation (cm)		Separatrix		5.0		10.0	
Outside hitting	A	6.615	-4.327	6.811	-4.6457	6.963	-4.559
Null	X	6.099	-3.273	-----	-----	-----	-----
Outermost	B	8.692	0.573	8.742	0.655	8.792	0.655
Top	C	6.585	3.412	6.502	3.556	6.420	3.731
Innermost	D	5.299	0.655	5.241	0.821	5.182	0.821
Inside hitting	E	4.982	-3.762	5.140	-3.500	5.300	-3.120

Table 4.1.3 Operation range

Coil No.	Max. (MAT)	Min. (MAT)
PF7U	0.39	-6.37
PF6U	1.50	-1.69
PF5U	7.59	3.58
PF4U	8.43	1.42
PF3U	8.43	-1.35
PF2U	9.42	-6.51
PF1U	9.21	-9.75
PF1L	8.43	-10.67
PF2L	9.02	-8.58
PF3L	8.43	-1.25
PF4L	9.91	2.50
PF5L	14.42	4.12
PF6L	0.66	-4.71
PF7L	0.32	-9.77

Table 4.1.5 Decay indices

Time (sec)	⟨D⟩	⟨K⟩
3.0	-1.926	0.260
20.0	-1.982	-0.001
40.0	-2.061	0.185
50.0	-1.919	0.182
80.0	-1.960	0.152
100.0	-1.112	0.094

Table 4.1.6 Coil currents for flexible operation

Coil No.	βp=2.0	βp=2.1	li(3)=0.75
PF7U	-6.363	-6.555	-6.985
PF6U	-0.089	0.062	0.881
PF5U	5.897	5.930	5.236
PF4U	1.676	1.698	1.596
PF3U	-0.950	-0.883	-0.692
PF2U	-5.995	-5.775	-6.309
PF1U	-8.549	-8.129	-10.980
PF1L	-10.210	-9.817	-10.910
PF2L	-8.165	-8.003	-6.021
PF3L	-0.855	-0.878	-0.130
PF4L	2.767	2.720	2.143
PF5L	13.760	13.700	10.310
PF6L	-0.909	-0.652	1.738
PF7L	-9.677	-9.869	-10.470

Table 4.1.4 Time evolution of plasma parameters and coil currents

Time (sec)	0.0	3.0	20.0	40.0	50.0	80.0	100.0
Ip (MA)	0.0	0.5	2.0	5.0	5.0	9.5	12.0
Rp (m)	6.6	6.6	6.9	6.9	6.9	7.0	7.0
a (m)	1.25	1.25	1.6	1.6	1.7	1.7	1.7
Zmag (m)	-1.67	-1.67	-0.72	-0.59	0.04	0.48	0.5
Elongation	1.3	1.3	1.6	1.7	1.8	1.85	1.85
Triangularity	0.1	0.1	0.2	0.25	0.3	0.3	0.3
βp	-----	0.01	0.02	0.05	0.05	0.1	2.0
Ψp (Vs)	92.0	80.5	54.7	3.5	3.5	-72.8	-145.0
Lp (μH)	-----	16.09	14.27	14.07	13.38	13.64	15.28
PF7U	0.10	0.39	-1.54	-2.50	-1.87	-2.35	-6.37
PF6U	0.99	1.17	1.50	0.47	0.19	-1.69	-0.13
PF5U	6.28	3.58	6.42	7.59	6.10	7.12	5.50
PF4U	8.43	4.47	4.34	4.62	3.65	3.01	1.42
PF3U	8.43	7.62	7.18	5.45	4.95	1.56	-1.35
PF2U	8.43	9.42	8.15	5.12	3.46	-4.09	-6.51
PF1U	8.43	9.21	4.45	-0.05	-0.70	-9.75	-9.08
PF1L	8.43	5.17	3.08	-4.16	-2.18	-10.63	-10.67
PF2L	8.43	9.02	6.55	1.57	0.85	-4.82	-8.58
PF3L	8.43	7.61	6.89	5.04	4.56	3.10	-1.25
PF4L	9.91	6.16	3.99	4.25	4.34	4.80	2.50
PF5L	4.12	4.92	6.04	7.96	10.27	14.42	13.27
PF6L	0.66	0.46	-0.68	-2.69	-3.40	-4.71	-0.77
PF7L	0.32	-0.26	-0.02	-1.13	-1.23	-4.40	-9.77
q(95%)	-----	32.80	18.20	7.97	9.65	5.18	4.52
q(0)	-----	21.50	9.70	3.87	4.43	2.31	1.50
Et (GJ)	3.75	2.65	2.11	1.82	1.84	4.08	6.83
∫Idt (MAT)	81.5	69.45	60.82	52.59	47.74	76.44	77.17
⟨D⟩	-----	-1.93	-1.98	-2.06	-1.92	-1.96	-1.11
⟨K⟩	-----	0.26	-0.0	0.18	0.18	0.15	0.09

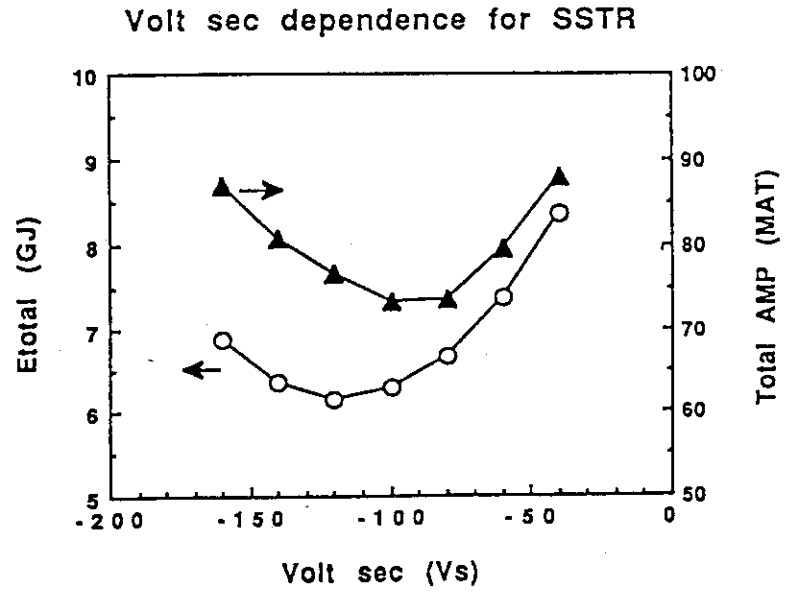

Fig. 4.1.1 Dependence of total ampere-turns and total stored energy of poloidal coils on external flux linkage.

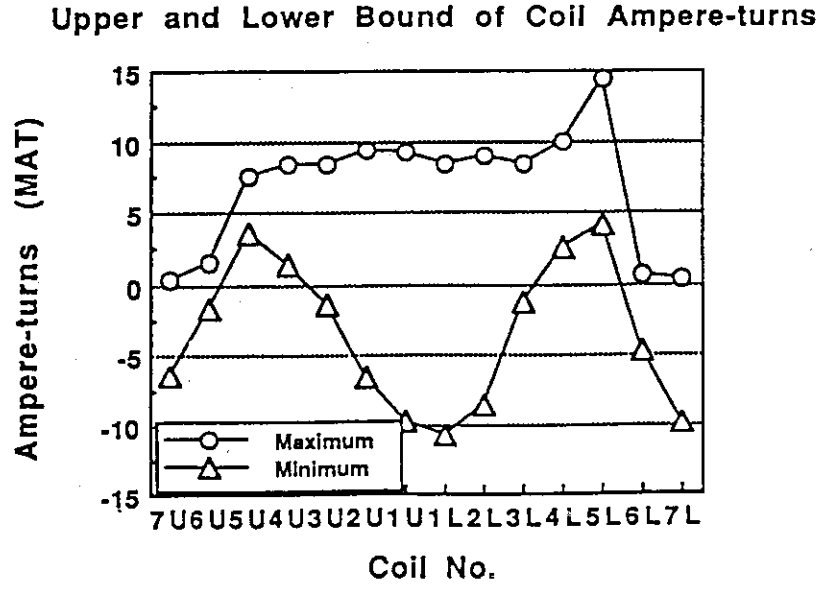

Fig. 4.1.3 Upper and lower bounds of ampere-turns of poloidal coils for reference operation scenario. Practically, the lower bounds for the PF5U, PF4U, PF4L and PF5U are zero.

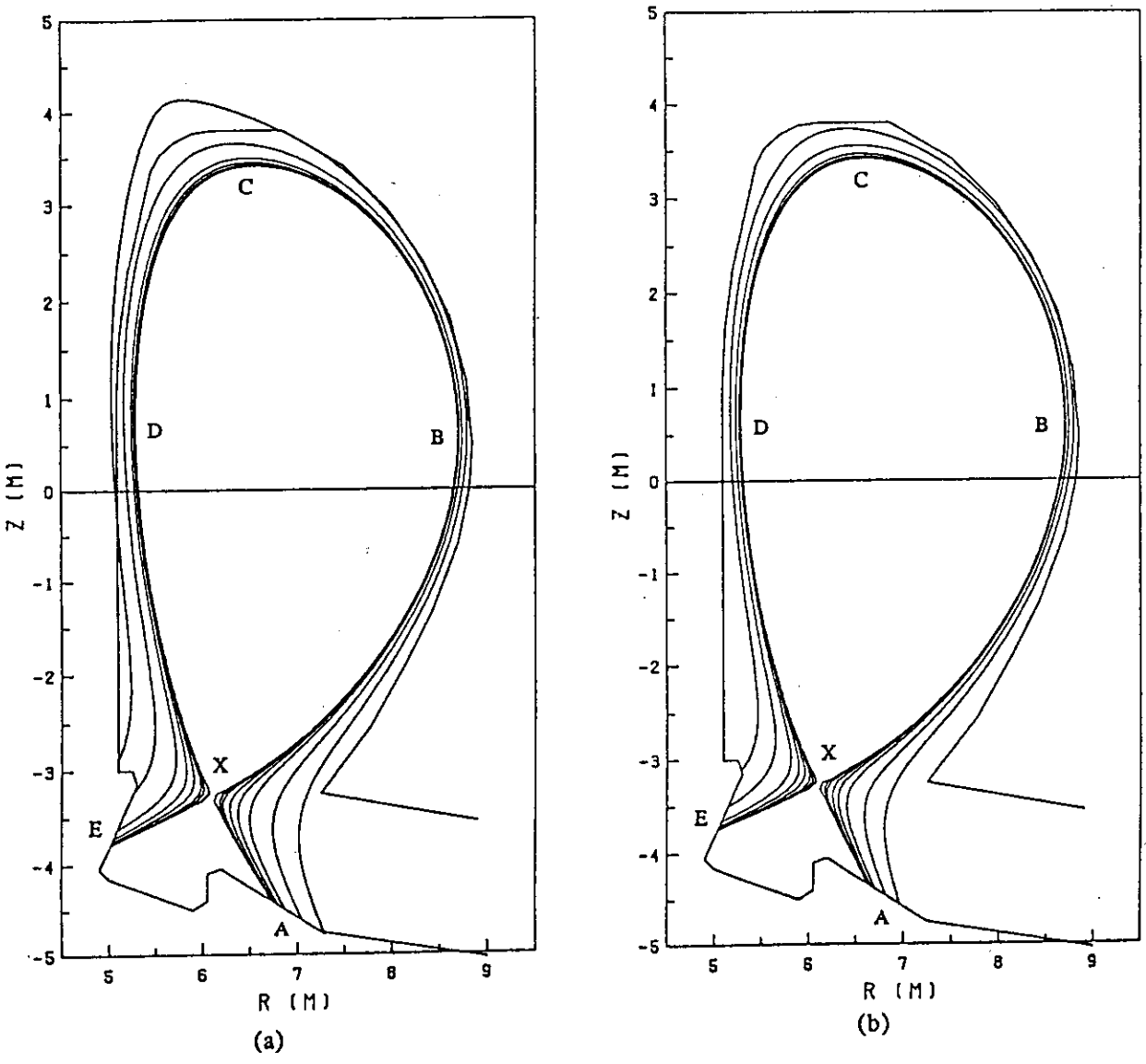

Fig. 4.1.2 Magnetic line tracing for (a) βp=2.0 and (b) βp=0.1 plasmas. Eight lines with distances from the outer plasma surface at horizontal plane located on the magnetic axis are displayed. Distances are 0.01, 0.1, 0.2, 0.5, 1, 2, 5 and 10 cm.

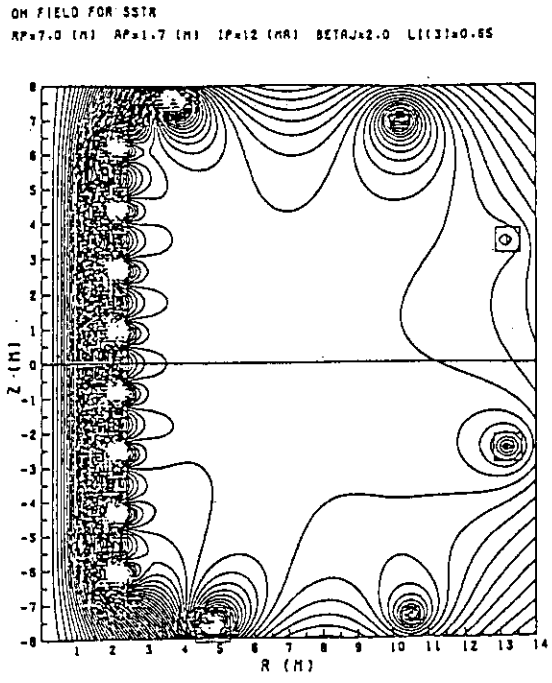

(a) t=0.0 sec

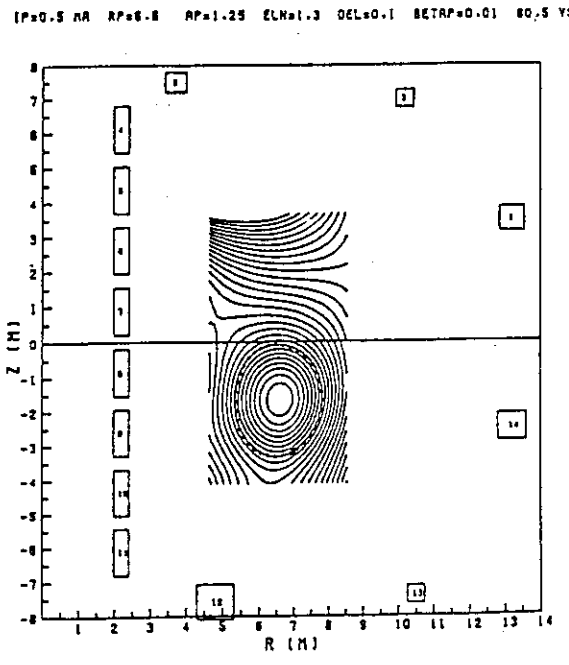

(b) t=3.0 sec

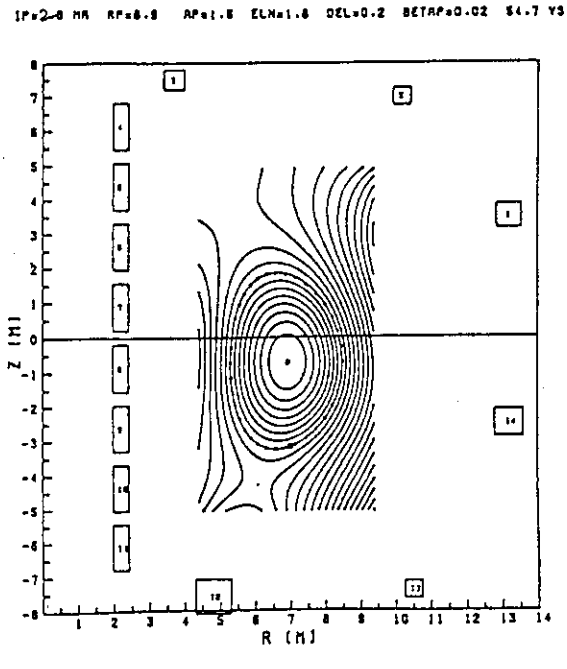

(c) t=20.0 sec

Fig. 4.1.4 Plasma equilibria during start-up. Size, elongation and triangularity of the plasma cross section increase with plasma current. Null point gradually approaches the location of the null point for the final divertor plasma.

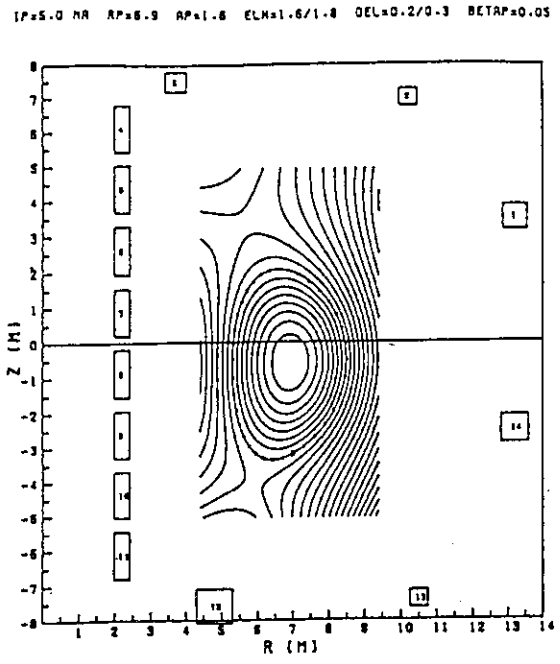

(d) t=40.0 sec

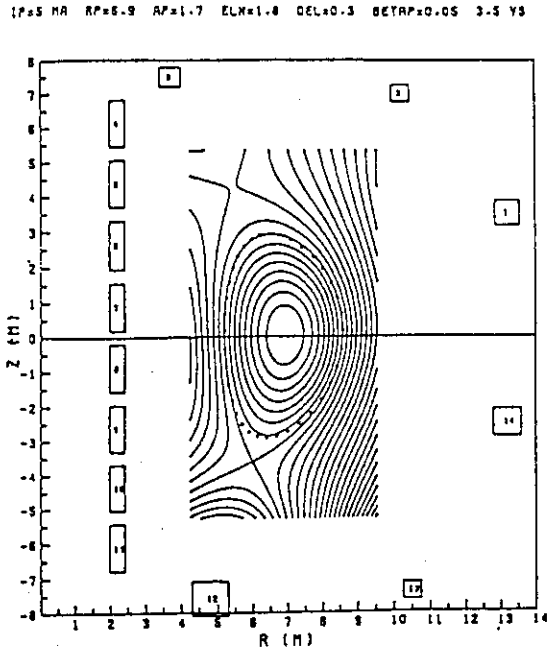

(e) t=50.0 sec

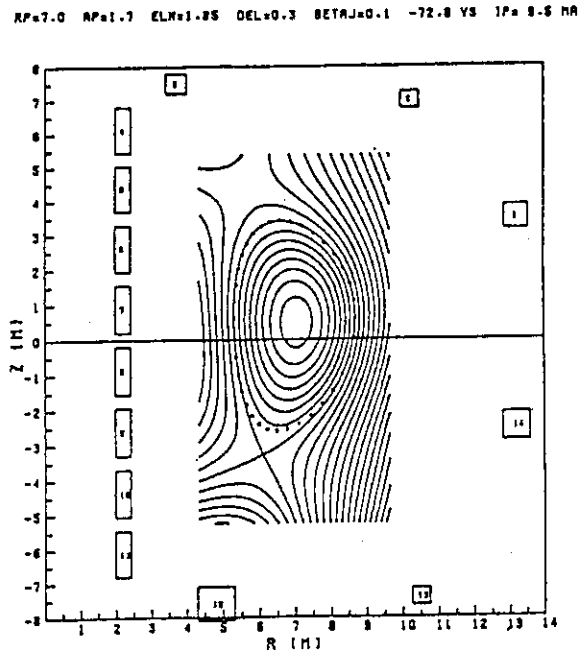

(f) t=80.0 sec

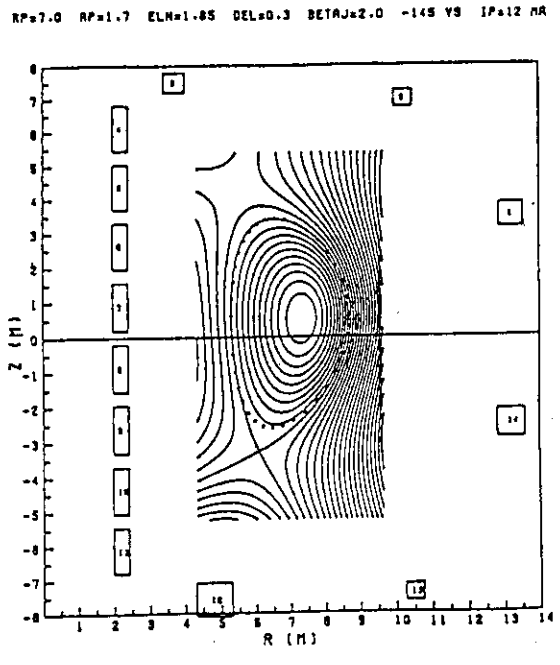

(g) t=100.0 sec

Fig. 4.1.4 (Continued)

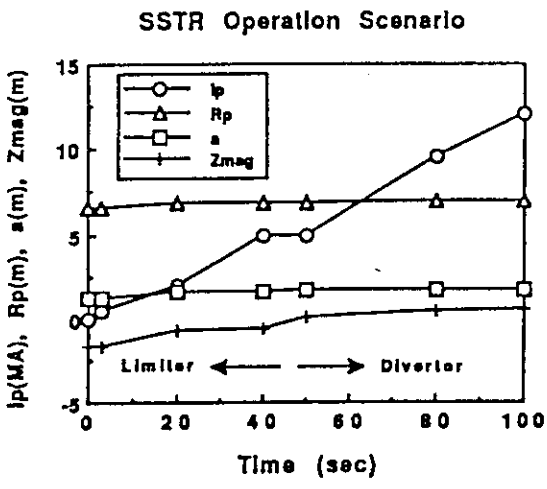

Fig. 4.1.5 Time evolution of plasma current, major and minor radii and height of magnetic axis.

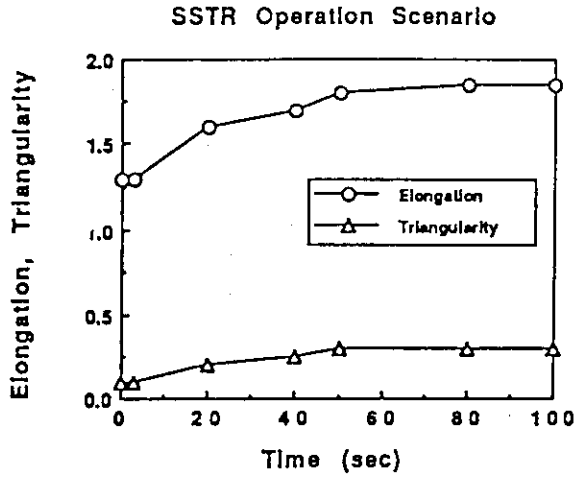

Fig. 4.1.6 Time evolution of elongation and triangularity. The values are measured at the 95% magnetic surface.

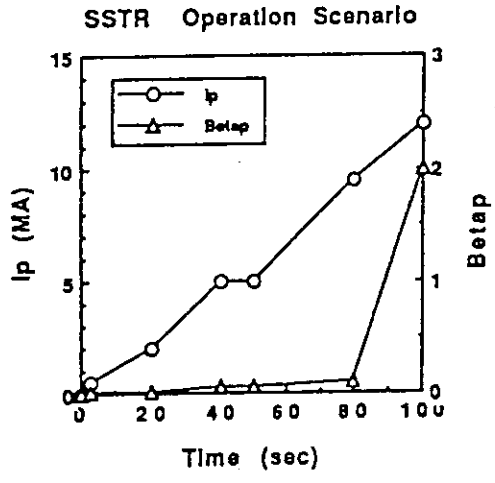

Fig. 4.1.7 Timing of plasma heating. Concurrent heating with plasma current ramp-up avoid excessive ampere-turns of the solenoid coil at low βp.

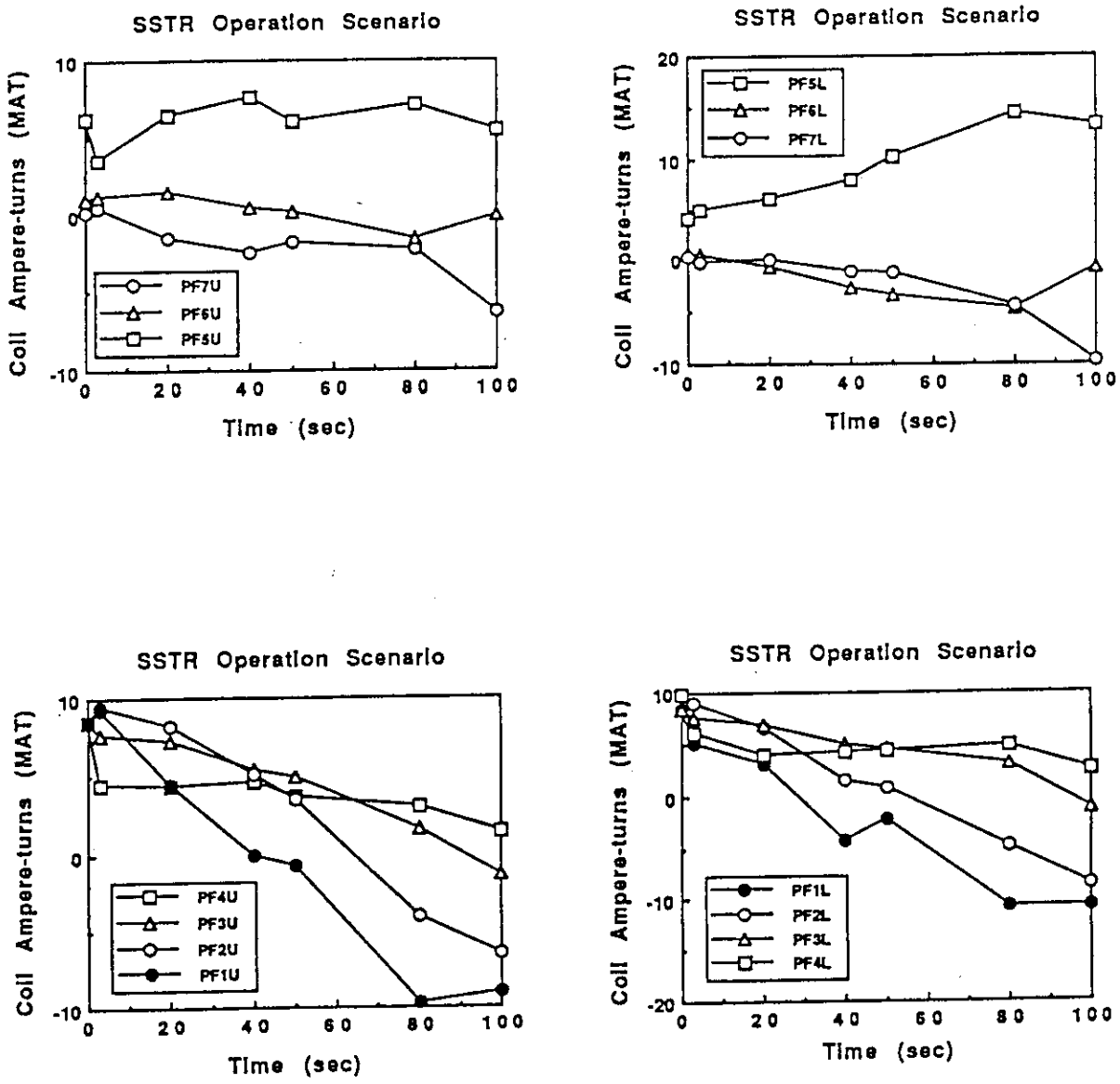

Fig. 4.1.8 Changes in coil ampere-turns. Basically changes are monotonic and smooth which suggest moderate electric power is attained.

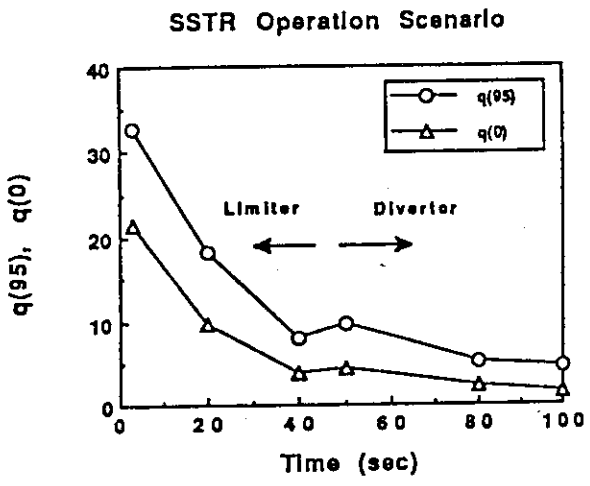

Fig. 4.1.9 Changes in safety factor at plasma surface, q(95), and magnetic axis, q(0). For the limiter plasma q(95) is measured on the limited plasma surface.

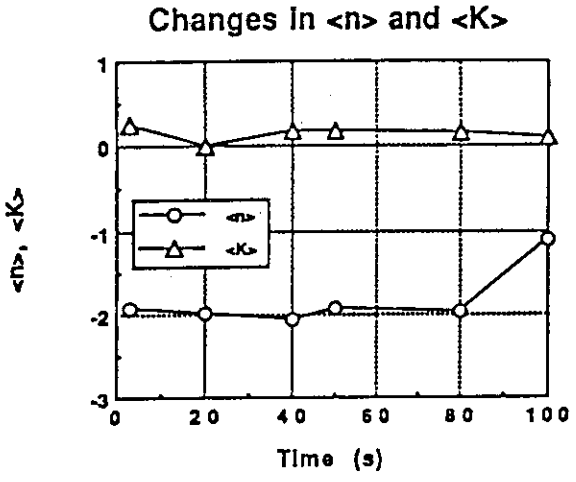

Fig. 4.1.10 Changes in n and K induces which are averaged by weighing plasma current distribution.

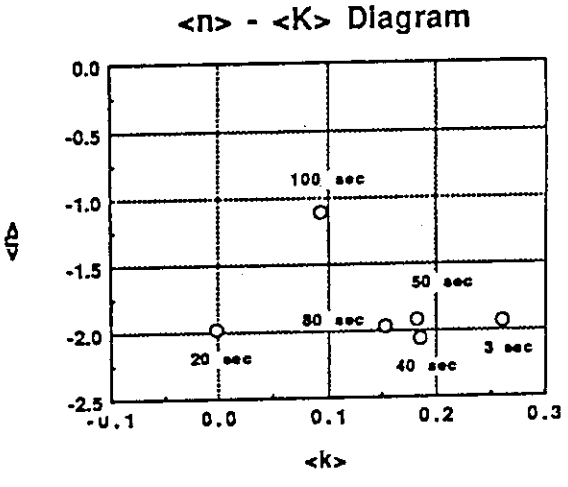

Fig. 4.1.11 <n>-<K> diagram for plasma start-up. Positional instability at initial stage of the start-up seems to be severe to control.

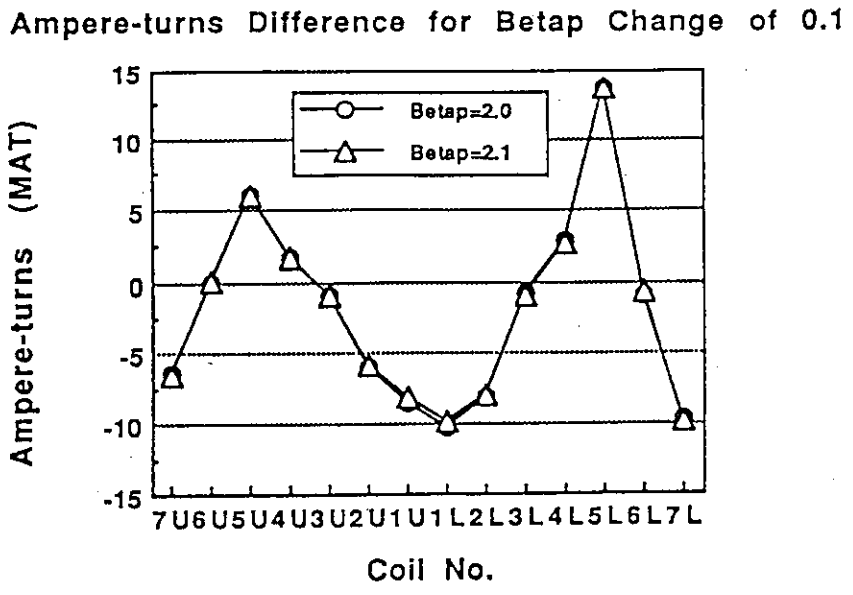

Fig. 4.1.12 Ampere-turns difference for 0.1 deviation of the poloidal beta value.

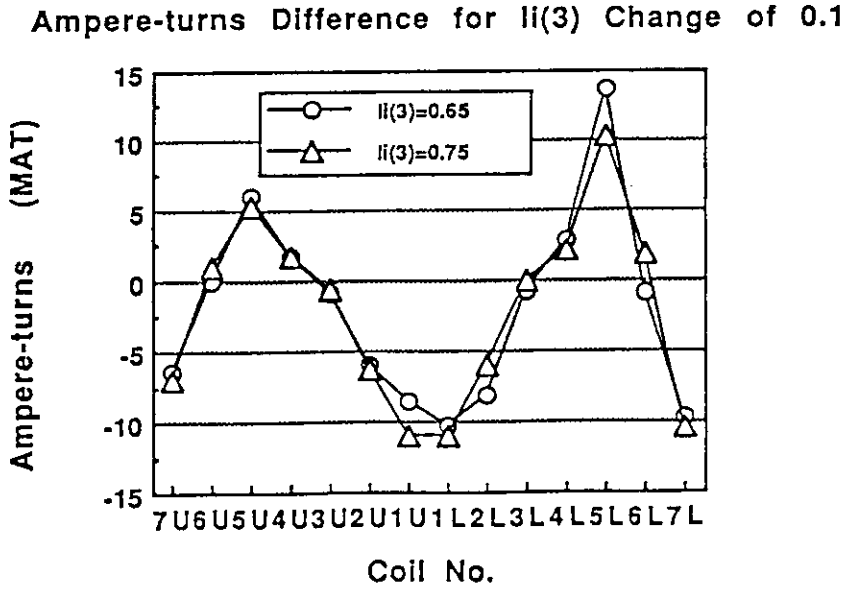

Fig. 4.1.13 Ampere-turns difference for 0.1 deviation of the internal inductances. For the flexible operation Ampere-turns rating of PF5L should be increased.

4.2 Vertical position control

4.2.1 Design of conducting shell and eddy current analysis

SSTR plasma is essentially unstable for vertical plasma motion since the plasma has a vertically elongated cross section. Therefore, it is necessary to stabilize instability with fast growth rate by conducting shell and instability with slow growth rate by feedback control coil. The design of conducting shell and the frequency response characteristics of the stability index n_S in the plasma current ramp up for SSTR are discussed in this subsection.

SSTR has 16 ports at the upper of the reactor since it is necessary to repair or exchange blankets that are equipped inside of the reactor. In addition, the blanket is divided into one center module and two side modules at each port. Although the conducting shell must be located at the plasma surface as nearly as possible for improvement of stabilization effect of conducting shell, it is necessary to design the conducting shell fitting these blanket modules. Furthermore, considering interference on the injection ports of neutral beams, the conducting shell must be divided into two parts, upper shell and lower shell. Only the effect by these divided conducting shells in the toroidal direction is not sufficient to stabilize the plasma positional instability since loop of eddy current is small in the conducting shell.

Since the structure of the vacuum vessel is uniform in the toroidal direction, the twin loop type concept proposed in the ITER activity is adopted for the stabilizing shell in which one turn current in the toroidal direction can be formed effectively by the electromagnetic induction between conducting shell and vacuum vessel. The structures of the upper shell and the lower shell are described as follows. The upper shell is divided into 48 parts since it is necessary to take out that with the blanket from the reactor. On the other hand, the lower shell has only to be divided into 16 parts since there is no interference by other devices if that is located behind the blankets.

As mentioned above, the conditions for the design of shell are as follows;
(1) The twin loop type concept is adopted in which effective one turn current near the plasma can flow in the toroidal direction. The one turn current is generated by combining the eddy current of the shell and that of the vacuum vessel.
(2) The conducting shell is composed of the upper shell (center and side modules, 48 parts) and the lower shell (16 parts).

Under these conditions, the conducting shell for SSTR is designed as shown in Fig. 4.2.1. Cross sections of the plasma, the vacuum vessel, the control coils and the shells are

shown in the figure. The figure is simply described to show the positional relation between each devices. The control coil is described in subsection 4.2.2. The ports for maintenance and divertor are equipped at the top and bottom of the vacuum vessel, respectively. It is assumed that the divertor ports are open in the toroidal direction. The results on the eddy current analysis are hardly affected by this assumption since eddy currents in the poloidal direction are small.

The vacuum vessel is made of SUS316 and has double structure. Although there are shelves for support between outer and inner vacuum vessel, in stead of considering them, calculations are carried out by increasing conductivity ρ ($\rho = 4 \times \rho_{SUS}$, ρ_{SUS} is conductivity of SUS316). Bird's-eye view of conducting shells and vacuum vessel is shown in Fig. 4.2.2. The figure shows only one of 32 parts in the toroidal direction. Although the conducting shell must be located at the plasma surface as nearly as possible for improvement of stabilization effect, they are located at 20 cm behind the blanket surface considering tritium breeding in the blanket.

On the other hand, for generating one turn current in the toroidal direction by formation of twin loop between the vacuum vessel and the shells, the shells approach the vacuum vessel and the effect is maximized as much as possible. The shells are made of copper with 25 mm thickness and the vacuum vessel is made of stainless steel with 50 mm thickness. Furthermore, the distance of conductor center on shell-shell and shell-vacuum vessel are 50 mm. The determination of the distance of conductor center depends on the generation of effective one turn current in the toroidal direction by cancelling the eddy currents of the vacuum vessel and these of outer region in the shells. In this report, this problem is not investigated in detail. However, we confirmed that the difference of n_S ($\omega \rightarrow \infty$) is about 3 % comparing with 25 mm and 50 mm of the distance of conductor center. Here, ω is the growth rate of the vertical instability.

T frequency response characteristics of n_S is investigated in plasma current ramp up by using eddy current analysis[1] code. From results of the eddy current analysis, n_S is calculated by next equation.

$$n_S(\omega) = \frac{I_P}{2\pi B_{V0}} \sum_i \frac{1}{\tau_{si}} \left(\frac{\partial M_{psi}}{\partial Z} \right)^2 \frac{\omega \tau_{si}}{\omega \tau_{si} + 1} \qquad (4.2.1)$$

Here, I_P is the plasma current, B_{V0} is the vertical field, Σ is the sum of eddy current mode, τ_{si} is the time constant of the i-th eddy current mode, and M_{psi} is the mutual inductance between the i-th eddy current mode and plasma current. τ_{si} and $(\partial M_{psi}/\partial Z)$ are obtained

from the results of eddy current analysis and B_{V0} is obtained from the results of equilibrium analysis. In this report, for reduction of CPU time and saving memory, plasma is represented by 18 filament currents which can obtain same magnetic surfaces as results of equilibrium analysis. The mutual inductances between plasma current and the i-th eddy current mode are approximated by one between these filament currents and the eddy currents.

Table 4.2.1 shows change of n-index of magnetic field in plasma current ramp up and if $n + n_S > 0$, then plasma vertical position is stable. Figs. 4.2.3 (a)_(d) show the frequency response characteristics of n_S (solid line) and reversed-sign n-index (dotted line) at typical plasma currents (limiter configuration $I_P = 0.5$, 5 MA and divertor configuration $I_P = 9.5$, 12 MA). Although plasma is stable under the condition of $\omega > 10$ sec^{-1} in all cases, considering load of control coil, controllable condition is estimated to be $\omega \geq 30$ sec^{-1}. Fig. 4.2.4 shows comparison of the frequency response characteristics of n_S between $r = 4$ ¥ r_{SUS} (solid line) and $r = r_{SUS}$ (dotted line) in the case of I_P =12 MA. n_S value of SSTR that adopts the vacuum vessel with low resistivity (solid line) is large even in the small ω region and the improvement of the characteristics became clear.

4.2.2 Numerical simulation of vertical position control

Numerical simulations of vertical position control have been carried out by using equations as below. The formulation employs R (horizontal direction) - Z (vertical direction) Cartesian co-ordinate system with the origin at the center of plasma current. If Z_p is the displacement from the center of plasma current, the equation of motion of plasma in the vertical direction is

$$m_P \frac{d^2 Z_P}{dt^2} = 2\pi I_P B_{V0} n Z_P + I_P \left(\sum_i \frac{\partial M_{psi}}{\partial Z} I_{si} + \sum_j \frac{\partial M_{pcj}}{\partial Z} I_{cj} \right) - 2\pi I_P B_d R_P , \qquad (4.2.2)$$

where m_P is the mass of plasma, M_{pcj} is the mutual inductance between the plasma and the j-th control coil, S in the second term of right hand means the sum of the control coil, R_P is the plasma major radius, and I_{Si} and I_{cj} are the eddy current and coil current, respectively. B_d is a disturbance magnetic field and is assumed as follows;

$$B_d = B_{d0} \{ 1 - \exp(-t/\tau_d) \} \qquad (4.2.3)$$

Here, B_{d0} is the value of the disturbance magnetic field at $\tau \rightarrow \infty$ and τ_d is the time constant. The circuit equations of the i-th eddy current mode ($i = 1 \sim N_m$; N_m is total mode number) in the shells or the vacuum vessel are

$$\tau_{si} \frac{dI_{si}}{dt} + I_{si} = - I_P \frac{\partial M_{psi}}{\partial Z} \frac{dZ_P}{dt} - \sum_j M_{csij} \frac{dI_{cj}}{dt}, \qquad (4.2.4)$$

where M_{csij} is the mutual inductance between the i-th eddy current mode and the j-th control coil current. The circuit equations of control coil ($j = 1 \sim N_c$; N_c is total coil number) are

$$\sum_k M_{ccjk} \frac{dI_{ck}}{dt} + R_{cj} I_{cj} = - I_P \frac{\partial M_{pcj}}{\partial Z} \frac{dZ_P}{dt} - \sum_i M_{csij} \frac{dI_{si}}{dt} + K_P Z_P + K_I \int Z_P \, dt, \qquad (4.2.5)$$

where M_{ccjk} is the mutual inductance between the j-th coil and the k-th coil and Σ before M_{ccjk} is the sum with respect to the control coil. R_{cj} is the resistance of the control coil, and K_P and K_I are the gain of proportional and integral controllers, respectively. Since it is sufficient to control the plasma position by PI controllers, differential controller is not especially considered in this report.

Simulations of position control in the case of steady state (I_P = 12MA, flat top) are discussed in this subsection. If it is assumed that the disturbance magnetic field is generated by movement of plasma in the horizontal direction as a result of change of plasma pressure in the vertically asymmetric equilibrium field, B_{d0} is represented by

$$B_{d0} = B_{V0} \, k \, \delta R / R_P \, ^{2)}. \qquad (4.2.6)$$

Here, k is the index with respect to asymmetry of magnetic field and is represented by following equation,

$$k = - \frac{1}{I_P B_{V0}} \int \int R \cdot \frac{\partial B_Z}{\partial Z} j_P(R,Z) dR dZ, \qquad (4.2.7)$$

where B_Z is the vertical component of magnetic field and j_p is the plasma current density in the toroidal direction. k is given by the equilibrium analysis. dR is the displacement of the

plasma position in the horizontal direction and its value is estimated about 10 cm by plasma disruption and so on. Therefore, B_{d0} is estimated about 10 Gauss since B_{V0} = - 0.676 T and k = 0.099 from the results of the equilibrium analysis on the steady state (I_P = 12 MA).

Neglecting plasma mass m_P, simulations have been carried out in the cases of τ_d = 0.1 msec and 1 msec. The eddy current mode which have the time constant τ_s more than 1 msec have been treated (with respect to the shells and the vacuum vessel in this report, N_m = 323). The two control coils are located under the the upper shell (R, Z) = (9.1 m, 2.4 m) and the lower shell (8.0 m, -3.0 m) and have the size of 0.1 × 0.1 m^2 in square cross section as shown in Fig. 4.2.1. In Fig. 4.2.1, the control coils are described more than the actual size. The two coils are connected in opposite direction each other and are divided into 16 parts in the toroidal direction as shown in Fig. 4.2.5. Since axial symmetry is assumed, in simulations, the equation of the control coils are approximately solved by model which circulates in the toroidal direction and the upper coil and the lower coil are connected in a series. PI feedback control is adopted and the gain parameters are fixed at $K_P = 6 \times 10^3$ V/m and $K_I = 6 \times 10^3$ V/m · sec, respectively.

In Fig. 4.2.6 (a)-(d), time evolution of the plasma vertical displacement and various quantities of the control coil in the case of τ_d = 1 msec are shown, respectively. In each figure, (a) is the vertical displacement Z_P, (b) is the coil voltage V, (c) is the coil current I_c and (d) is the coil power P, respectively. In the case of τ_d = 1 msec, the maximum displacement Z_{PMAX} is 1.2 cm and the maximum power P_{MAX} is 1.6 MW. In the case of τ_d = 0.1 msec, Z_{PMAX} is 1.3 cm and P_{MAX} is 1.7 MW. These values are enough small values for input power of SSTR and satisfy the design goal.

The results of various quantities are summarized in Table 4.2.2. In Table, V_{MAX} and I_{MAX} are the maximum coil voltage and the maximum coil current, respectively.

4. 2. 3 Electromagnetic forces on the shells and the control coils at plasma disruption

Since eddy currents are induced in the shells and the vacuum vessel at plasma disruption, electromagnetic forces are generated by these eddy currents and toroidal and poloidal magnetic fields. Since the force by toroidal field is main, it is simply investigated in this subsection.

It is assumed model of plasma disruption that the plasma position is unchanged and the plasma current decreases exponentially. Namely, $I_P = I_{P0} \times \exp(-t / \tau_{dis})$, where I_{P0} is plasma current at the steady state and its value is 12MA. τ_{dis} is the time constant of disruption and its value is assumed be 1 msec. In the case of disruption at which plasma disappears stationary, since eddy currents that circulate in the coil can be not induced basically in the saddle type control coil, there is no problem about electromagnetic forces. Therefore, in this subsection, only the shells are investigated.

If the shape of shell is assumed to be one as shown in Fig. 4.2.7 for simplicity, the eddy currents and the electromagnetic forces on the shells can be calculated analytically. In Fig. 4.2.7, h is the height of shell, a is the side length, b is the width and t is the thickness. The maximum eddy current $I_{EDDY\ MAX}$ in this case is approximately given by

$$I_{EDDY\ MAX} = h \cdot B_P / \mu_0. \qquad (4.2.8)$$

The eddy current flows the path that circulates in the shell. Here, m_0 is the vacuum magnetic permeability and B_P is the poloidal field at the shell. If the plasma current is assumed to be a filament current, then $B_P = m_0 I_{P0}/(2pr_S)$, where r_S is the distance between the center of plasma current and the shell. The electromagnetic force F generated by the toroidal magnetic field and the eddy current is

$$F = I_{EDDY\ MAX} \cdot B_T \cdot h. \qquad (4.2.9)$$

B_T is given by $R_P B_{T0}/R$, where R_P = 7 m and B_{T0} = 9 T. The electromagnetic force loads on the side of shell and gives the torque to the shell. From the above equations, $I_{EDDY\ MAX}$ and F of the upper shells (center and side modules) and the lower shells is estimated as follows;

Upper shell for the center module
$I_{EDDY\ MAX}$ = 660 kA, F = 5.75 $\times 10^5$ kgf,
Upper shell for the side module
$I_{EDDY\ MAX}$ = 690 kA, F = 6.30 $\times 10^5$ kgf,
Lower shell
$I_{EDDY\ MAX}$ = 1100 kA, F = 1.44 $\times 10^6$kgf.

Here, the averaged values are used on r_S, a and b since the model correspond to the actual shape of the shell. From the above results, although large eddy currents and electromagnetic forces are generated, these electromagnetic forces can be supported since the shells are located in the blankets.

4. 2. 4 Future study for research and development

1) Radial and vertical position control

Considering the radial movement, still more correct position control analysis should be carried out. Furthermore, the optimization on the gain parameters of feedback control should be also investigated.

References

1) A. Kameari, Transient Eddy Current Analysis on Thin Conductors with Arbitrary Connections and Shapes, J. Comput. Phys., Vol.42, pp. 124-140, 1981.
2) Conceptual Design Study of Quasi-Steady State Fusion Experimental Reactor (FER-Q) Part 1, JAERI-M85-177.

Table 4.2.1 n value in current ramp up

	limiter			divertor		
I_p (MA)	0.5	2.0	5.0	5.0	9.5	12.0
n	-1.926	-1.982	-2.061	-1.919	-1.960	-1.112

Table 4.2.2 Summary of simulation results

τ_d (msec)	0.1	1.0
Z_{PMAX} (cm)	1.3	1.2
P_{MAX} (MW)	1.7	1.6
V_{MAX} (V)	77	71
I_{MAX} (kA)	23	23

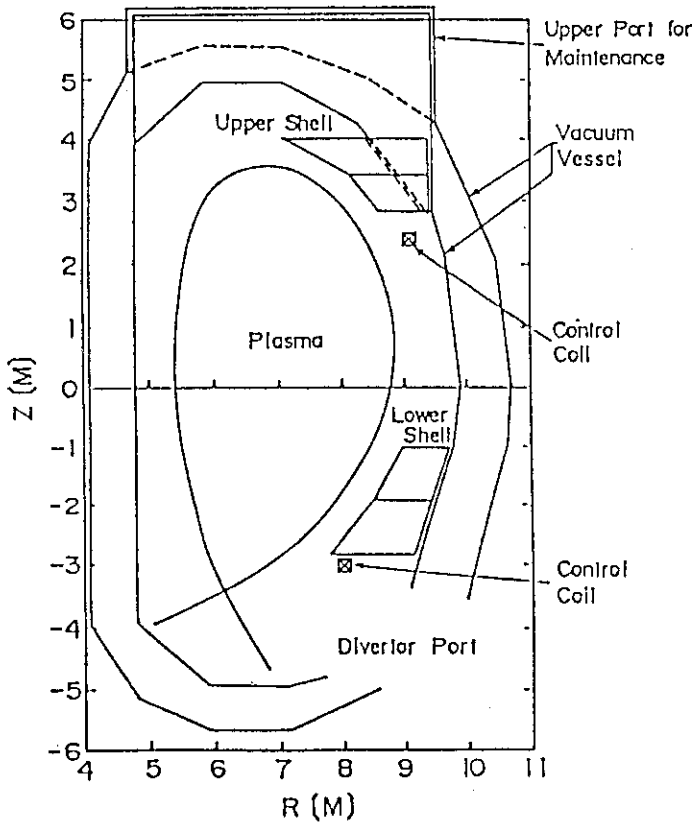

Fig. 4.2.1 Cross section of conducting shell and vacuum vessel.

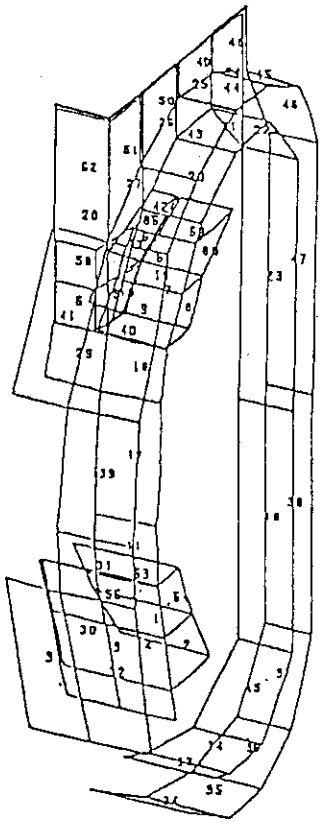

Fig. 4.2.2 Bird's-eye view of conducting shell and vacuum vessel.

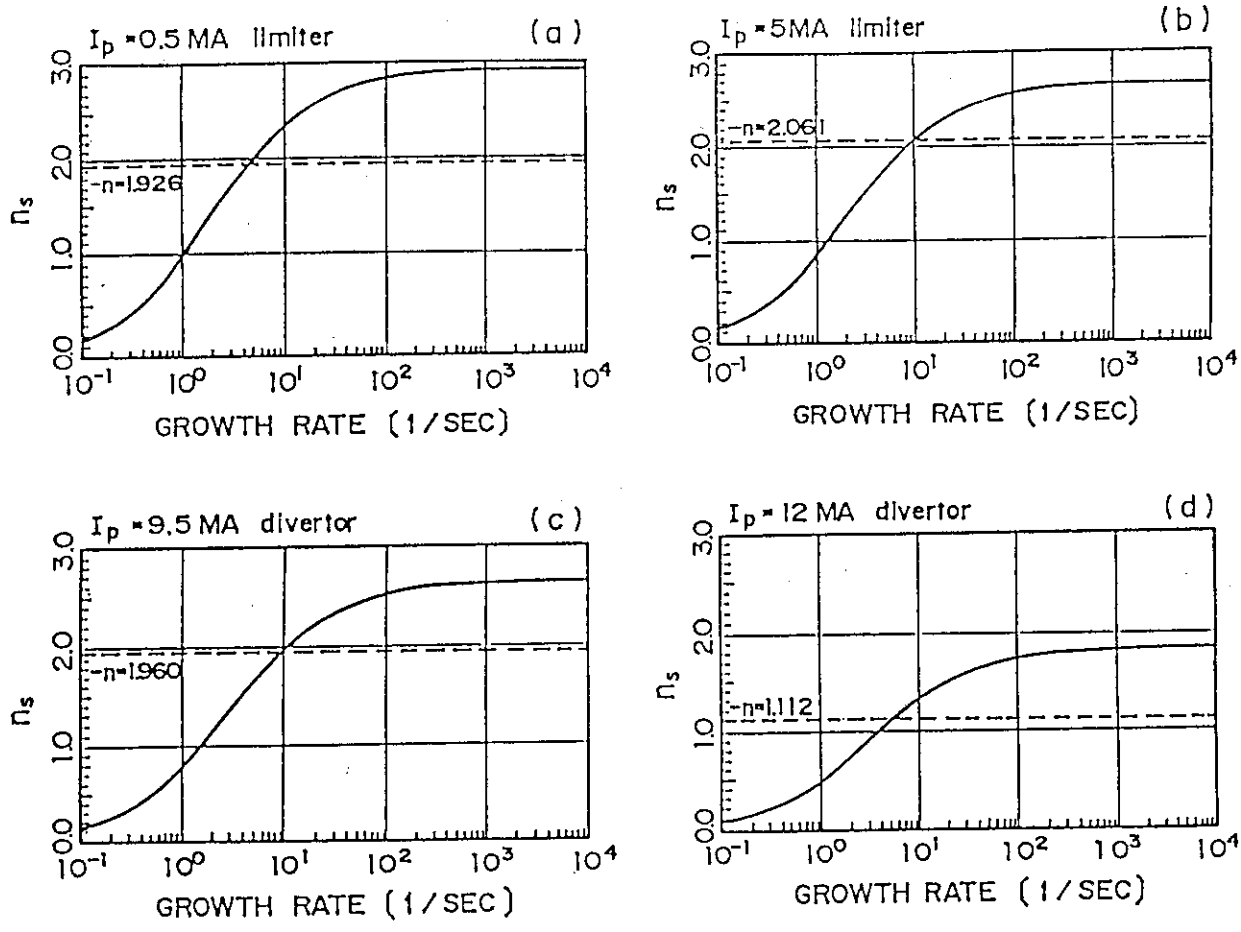

Fig. 4.2.3 Frequency response characteristics of n_s.

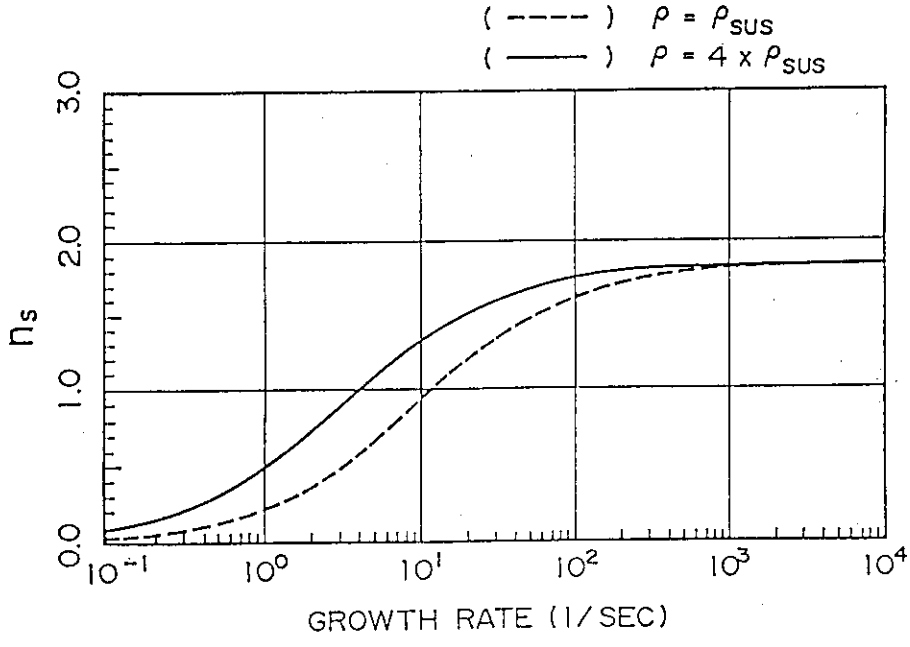

Fig. 4.2.4 Comparison with n_s of high and low resistivity vacuum vessel.

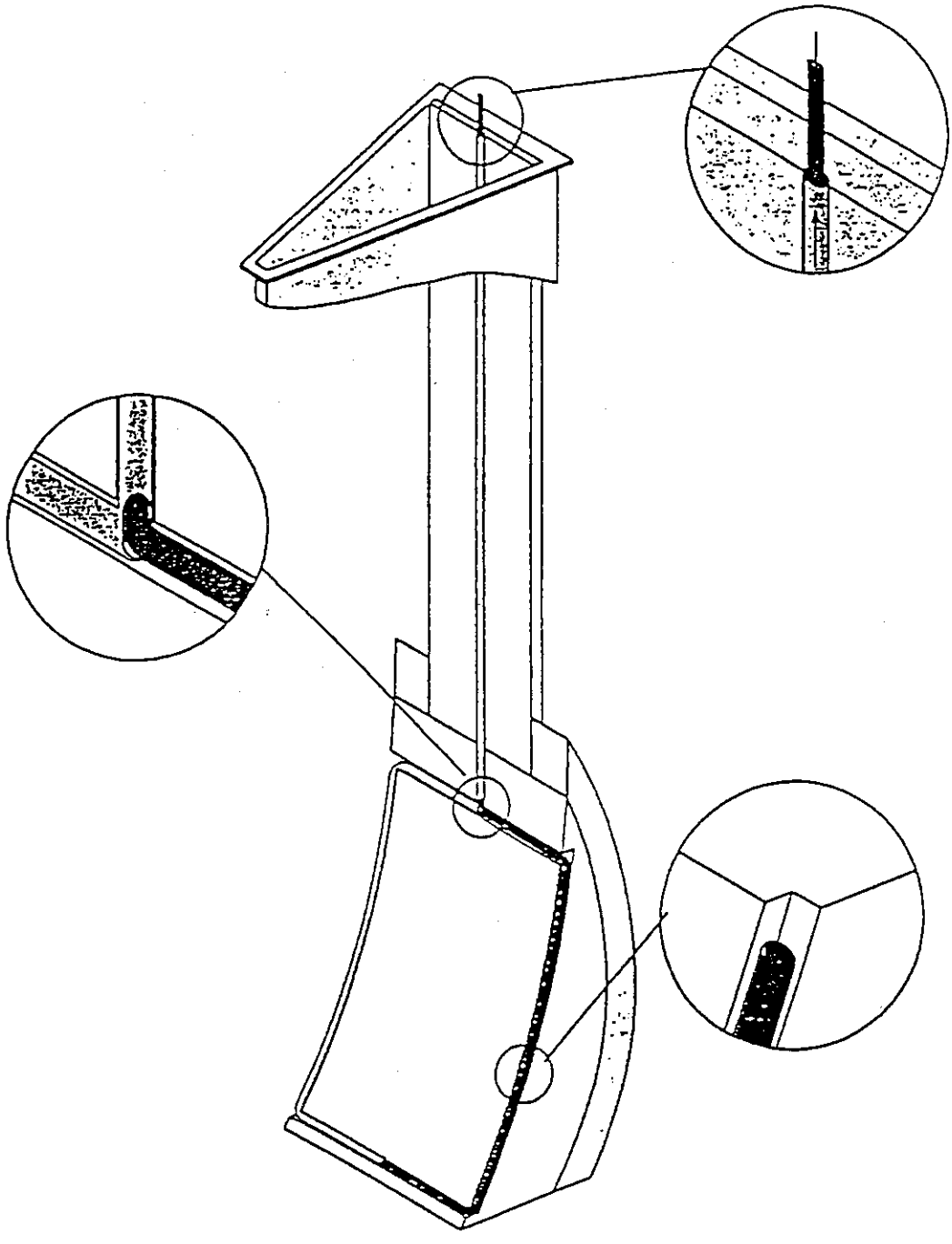

Fig. 4.2.5 Control coil.

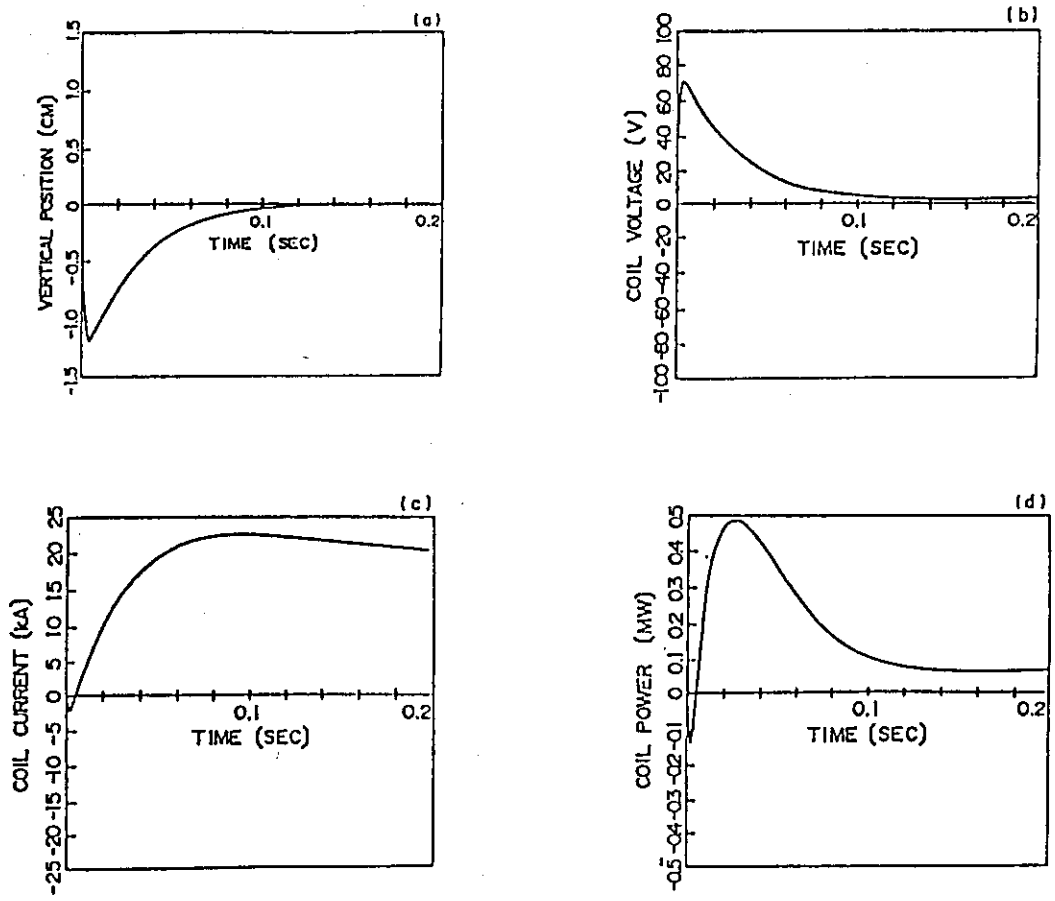

Fig. 4.2.6 Time evolution of (a) vertical position, (b) coil voltage, (c) coil current and (d) coil power.

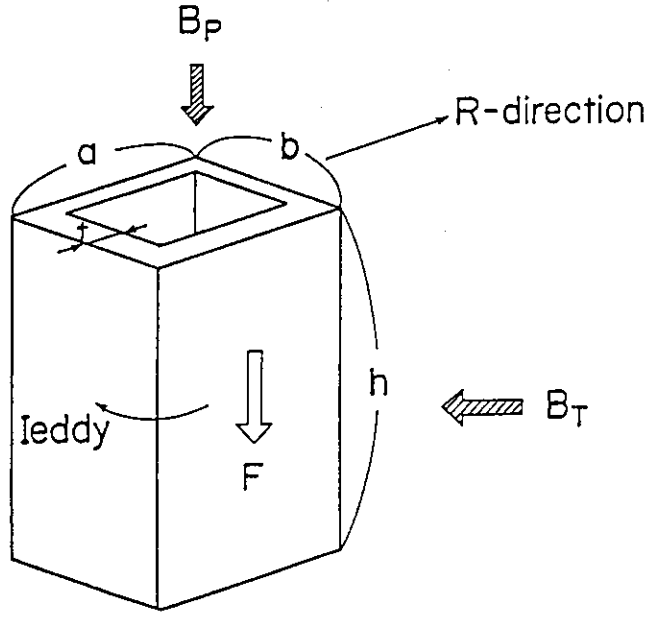

Fig. 4.2.7 Model of conducting shell for calculation of electro-magnetic force.

4.3 Current drive

In the SSTR, 75% of the total plasma current is driven by the bootstrap current and the rest is driven by the high energy neutral beam. The current profile is calculated by the ACCOME code[1] in which plasma equilibrium is solved self consistently. The ACCOME code is a steady state analysis code and it is possible to determine the current profile and the equilibrium in a burn phase. The plasma equilibrium is solved numerically. In this calculation, neoclassical bootstrap current and beam driven current are used for the equilibrium calculation. Fig.4.3.1 shows the plasma equilibrium and the injection geometry of the SSTR. Following momentum balance equations along magnetic field line are solved numerically for the evaluation of the bootstrap current.

$$\langle J^{BS}B\rangle = \sum_j e_j n_j \langle u_j B\rangle = -\sum_j (\hat{L}^j_{31} V_{1j} + \hat{L}^j_{32} V_{2j})$$

or,

$$\langle J^{BS}B\rangle = -RB_T p_e \sum_j \frac{T_j}{|Z_j|T_e}\left(L^j_{31}\frac{\partial ln p_j}{\partial \psi} + L^j_{31}\frac{\partial ln T_j}{\partial \psi}\right)$$

$$T_f = \frac{p_f}{n_f}\ ,\ V_{2f} = 0\ \left(\text{or},\ \frac{\partial ln T_f}{\partial \psi} = 0\right)$$

$$V_{1j} = -\frac{RB_T}{\psi'}\frac{T_j}{e_j B}\left(\frac{p'_j}{p_j} + \frac{e_j \Phi}{T_j}\right)\quad V_{2j} = -\frac{RB_T}{\psi'}\frac{T'_j}{e_j B}$$

parallel mometum balance equations

$$\sum_k \begin{pmatrix} l^{11}_{jk} & l^{12}_{jk} \\ l^{21}_{jk} & l^{22}_{jk} \end{pmatrix} \cdot \begin{bmatrix} \langle u_k \cdot B\rangle \\ \langle \hat{q}_k \cdot B\rangle \end{bmatrix} = \frac{3\langle (n\cdot B)^2\rangle}{\langle B^2\rangle} \begin{pmatrix} \mu^{11}_j & \mu^{12}_j \\ \mu^{21}_j & \mu^{22}_j \end{pmatrix} \cdot \begin{bmatrix} \langle u_j \cdot B\rangle - V_{1j}B \\ \langle \hat{q}_j \cdot B\rangle - V_{2j}B \end{bmatrix}$$

$$\langle \hat{q}_j \cdot B\rangle = \frac{2\langle q_j \cdot B\rangle}{5p_j}, \qquad + \begin{bmatrix} \langle E\cdot B\rangle\, \delta_{j=e} \\ 0 \end{bmatrix} + \begin{bmatrix} \langle M_j \cdot B\rangle \\ \langle Q_j \cdot B\rangle \end{bmatrix}$$

l^{mn}_{jk} : friction coefficient

μ^{mn}_j : viscosity coefficient

Here, left hand side and right hand side are friction and viscous forces on the j-th particle, respectively. Viscous and friction coefficients given by Hirshman and Sigmar[2] is used for the calculation. Only the viscous coefficients are given as follows,

Viscosity coefficients of Maxwellian particles

$$\mu_j^{11} = K_j^{11}$$

$$\mu_j^{12} = \mu_j^{21} = K_j^{12} - \frac{5}{2} K_j^{11}$$

$$\mu_j^{22} = K_j^{22} - 5\, K_j^{12} + \frac{25}{4} K_j^{11}$$

$$K_j^{mn} = \frac{f_t}{f_c} \frac{\langle B^2 \rangle}{3\langle (n\cdot B)^2 \rangle} \{ x_j^{2(m+n-2)} \nu_j^{tot}(v) \tau_{jj} \}$$

$$\{A(v)\} \equiv \frac{8}{3\sqrt{\pi}} \int_0^\infty dx_j e^{-x_j^2} x_j^4 A(x_j v_{Tj}) \quad , x_j = v/v_{Tj}$$

$$\nu_j^{tot}(v) = \nu_j^D(v)/[1+2.48\nu_{*j}\nu_j^D(v)\tau_{jj}/x_a]$$

$$f_c = (1-\varepsilon)^2 (1-\varepsilon^2)^{-1/2} (1+1.46\,\varepsilon^{1/2})^{-1}$$

where the effect of α particle is considered. Although the friction coefficient is correct but the viscous coefficient is not applicable for the α particle which gave a negative contribution to the bootstrap current. An improvement of the theory is required. Fig.4.3.2 shows the calculated current profile. As is seen from the figure, the bootstrap current does not flow at the plasma center and is a hollow current which is unstable to the MHD modes. So an active current drive near the plasma center is required to control the current profile. In the SSTR, a central current drive with 2MeV NBI is adopted. For this calculation, the beam driven current is 2MA and the NBI power is only 45MW. The central safety factor q_o is just above 2. Such a current profile is stable to the high n and low n kink/ballooning modes as shown in section 4.4. Here we assumed the pressure profile is a square of the parabolic. If the pressure profile is much broader, required NBI power may increase and the design value of 60MW is adopted.

(1) K. Tani, M. Azumi, R.S. Devote, Numerical analysis of 2-D MHD equilibrium with non-inductive current in tokamaks, to be published in J. Comput. Phys.
(2) S.P.Hirshman, D.J.Sigmar, Nuclear Fusion **21**(1981)1079.

Reduction of active driven current with bootstrap current & efficient current drive with energetic neutral beam

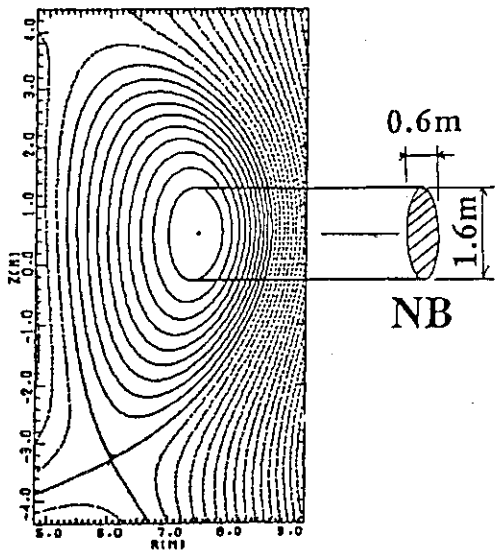

ACCOME Code

$\beta_p=\frac{4}{\mu_0 I_p^2 R_p}\int PdV=2$ for the SSTR

Bootstrap Current = 9 MA

Beam Driven Curr.= 3 MA

$\eta_{CD}=\frac{I_{CD}R_p<n_e>}{P_{CD}}=4.8\times10^{19}MAm^{-2}MW^{-1}$

P_{CD} =60MW

E_{beam}=2MeV

Fig. 4.3.1 SSTR plasma equilibrium and beam geometry.

Neutral Beam Current Profile Control

Hollow current profile unstable to kink/Ballooning mode is compensated by the central NB current drive.

Standard Case:
$T_e=32(1-(r/a)^2)^{1.5}$, $n_e=2.1\times10^{20}(1-(r/a)^2)^{0.5}$
$I_{bootstrap}$=10MA, βp=2, I_{bd}=2MA,
P_{NBI}=45MW, P_f=3GW, Q=67
(I_e=6.8MA, I_d=1.9MA, I_t=1.85MA,
I_{He+O}=0.35MA, Iα=-0.94MA)

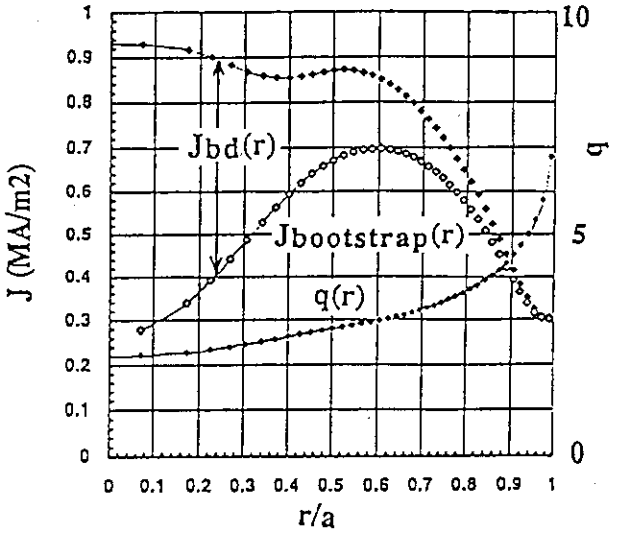

Fig. 4.3.2 Standard current profile with J_{bd} (beam driven current), $J_{bootstrap}$ (bootstrap current) and q(r).

4.4 MHD Stability

4.4.1 Introduction

High βp plasma (~2) is required in the Steady State Reactor (SSTR) in order to make a high ratio of bootstrap current to the total current. Therefore, MHD instability due to the increase of βp becomes a problem to realize the SSTR.

The important instabilities in the high βp plasma are high-n ballooning mode and low-n kink mode. In JT-60 high βp experiments, the rapid reduction of stored energy, called βp-collapses, are observed which is correlated with the low n MHD activities. The stability analysis of the low-n kink modes using the equilibrium of JT-60 high βp experiments clarifies the following results: The large bootstrap current induced by the perpendicular NBI heating makes the hollow current profile. The hollow current profile in the high βp plasma excited the kink-ballooning modes. This critical βp of kink-ballooning modes is consistent with the value of βp when the βp-collapse happened.

This βp-collapse could be suppressed by the current drive in the central plasma region, because the current profile is changed from the hollow to the monotonic profile. The SSTR employs the tangential NB injection to drive the plasma current in the central region, but, even if the monotonic current profile, the critical βp strongly depends on the central q-value (q is the safety factor), namely, the ratio of the beam driven current against the total current. Thus, in this section, we study the low-n kink-ballooning modes (n = 1,2,3,5) and high-n ballooning mode against the central q-value, q_0, fixing the surface q-value, q_s, (namely, fixing total current), and discuss the critical βp in the SSTR.

4.4.2 Calculation Procedure

Equilibria simulated SSTR plasma are produced by the MHD equilibrium code MEUDAS. For these equilibria, the nigh-n ballooning mode is analyzed by BETA code and the kink-ballooning mode is analyzed by ERATO-J code, which is the ideal linear stability code. Equilibrium of the SSTR is produced on the restriction of up-down symmetry due to the restriction of ERATO-J code. The main parameters are as follows;

Poloidal beta	$\beta p = 2.0$
Elongation	$\kappa \approx 1.8$
Triangularity	$\delta \approx 0.3$
Safety factor at 95%	$q_{95} \approx 5.0$

at center $q_0 \approx 1.0$ to 3.0

Axisymmetric free boundary equilibria are obtained by solving the Grad-Shafranov equation in the cylindrical coordinates (R, z, ϕ). In order to obtain the accuracy of a numerical calculation in ERATO-J, we employ the fine grids with 512 in the R-direction and 256 in the z-direction. The convergence of the solution is checked by the condition $\varepsilon<10^{-6}$, where $\varepsilon=\max|\psi_{ij}^{n} - \psi_{ij}^{n-1}| / \max|\psi_{ij}^{n}|$. ψ_{ij}^{n} is the poloidal flux at the ij-mesh in the n-th iteration step.

The current profile is assumed that a monotonic profile is produced by the beam driven current in the plasma center adding to the bootstrap current . Thus we employ the current profile of the following form,

$$<j B_{\parallel}> = j_0 B_0 (1- \tilde{\psi})^{\alpha} \quad (1)$$

where α is determined to adjust the central q_0 to the given value. The other unknown parameter of the equilibrium is the pressure profile, $dp/d\psi$. This profile is assumed to be relatively peak, thus, we employ

$$\frac{dp}{d\psi} = p_0 (1-\tilde{\psi}) \quad (2)$$

ERATO-J is ideal linear MHD stability code based on the energy principle. This two-dimensional code computes the ideal MHD spectrum by minimizing the potential energy in the flux coordinate (ρ, χ), where $\rho=\sqrt{\tilde{\psi}}$ and the poloidal angle χ is selected so that the magnetic field line are straight. To accuracy express the eigenfunction of the most unstable mode, the fine radial mesh (= 270) is employed. For the calculation of medium-n number mode ($n\geq3$), we used the eikonal transform since the high-m mode become unstable.

We consider to expect the wall stabilization for kink modes in the SSTR, so that we located the conduction wall at $\rho_{wall}/\rho_{plasma}$ ($=R_W$)= 1.2 in the following calculation. In this case, there is a possibility to destabilize the external kink modes. The external kink modes have a large perturbation at the plasma surface, so that the radial mesh are accumulated near the plasma surface.

4.4.3 Results

At first, we obtained the stability region for low-n kink-ballooning modes (n =1, 2,3,5). Figure 1 shows the growth rate of the unstable mode against q_0. Each low-n modes are unstable in the region of $q_0 < 1.8$, but the stable region is obtained in $q_0 \gtrsim 2$. In this q_0-scanning, as the q_0 increase, q profile becomes flat. Thus, resonance surfaces for low-n mode disappear near the plasma center and the magnetic well are

produced due to the large shafranov shift produced in high βp plasma. And the perturbation near the plasma surface is stabilized by the conducting wall close to the plasma surface. Therefore, low-n kink modes are stabilized in the high q_0 plasmas. This results are similar to the access to second stability region in a high q_0 (~2) and high shear plasma, as to be demonstrated by Genver et al.

Next, ballooning mode analysis are carried out for q_0-scanning in the similar way. Figure 2 shows the normalized pressure gradients against the plasma minor radius, $\tilde{\psi}$. The dotted line indicates the value of equilibrium and the solid line indicates the ballooning limit, where α is $-2Rq^2(dp/dr)/B^2$. In q_0=1.0 (Fig.2(c)), the normalized pressure gradients, α_{eq}, exceeds the ballooning limit, α_B. As the q_0 increases (Fig.2(b)), α_{eq} is nearly equal to α_B which is the marginally stable for the ballooning mode. In the plasmas with $q_0 \geq 1.8$ (Fig.(a)), α_{eq} is lower than α_B in the whole plasma region, thus, the ballooning mode is stable. This is because, as the q_0 increase, the current profile become flat near the plasma center, and the negative local shear is produced (right side figures on Fig.2), which stabilizes the ballooning modes.

4.4.4 Summary

Equilibrium simulated SSTR plasmas becomes stable against low-n kink-ballooning mode and high-n ballooning mode even in high βp (~2) by increasing q_0 up to 2.0. Thus, no βp-collapse would happen in the plasma with q_0>2.

Our calculation, however, carried out for the only typical parameter estimated in the SSTR. To obtain the final conclusion, the following discussion is necessary. First is the influence of the current and pressure profile on the stability boundary. In the reactor plasma, these profile are depends on burning, so that the wide stable region is required in the various pressure profiles. Next is the effect of the wall stabilization. In this calculation, the location of wall is fixed to 1.2 ($=R_W$). The low-n external kink

4.5 Power and Particle Control

4.5.1 Introduction

In future large tokamak fusion reactors, nearly 600 MW of fusion power (α heating power and NB injection power), even considering the radiation loss in the main plasma, would be delivered to the scrape-off layer (SOL). This power level is too high to extract by the usual poloidal divertor concept. Power of 120 MW is assumed, for example in ITER design, nevertheless it is believed the heat extraction is not so easy with the level of present day technology.

In the power and particle extraction in the poloidal divertor, it is expected to realize the high recycling plasma at the target plate and by this, to reduce the divertor temperature below the threshold value where no dominant erosion of the target plate would occur. For this, it is well known that the enough particle supply from the core to the SOL, which is uncontrollable parameter, is necessary for the open divertor configuration.

One of the effective solution to this problem may be an external fuel injection near the target plate and to enhance with it, the particle recycling at the target plate. This could solve the problem of the power extraction at least for the next step machine. Unfortunately, it seems not adequate for future large fusion reactors since an extremely high gas puff would be required.

We propose here one of the solution for the power extraction for the future large tokamak reactors. In the concept, active injection of heavy impurities near the target plate is employed expecting strong impurity radiation. It does depend on the behavior of the impurity ions whether the concept would succeed or not. Impurity ions are often said to flow up to the mid-plane from the divertor room by the thermal force and finally might be absorbed into the core plasma. Therefore, we must estimate the behavior of impurity ions in the SOL plasma.

The charge state distribution of impurities in the highly inhomogeneous tokamak boundary depends strongly on the location and composition of the impurity sources and is usually far from local coronal equilibrium. Therefore, a theoretical investigation of the impurity transport requires rather sophisticated models, the dominant physical effects being quite different for different collisionality. In the high recycling regime of present day tokamaks, the mean free path of all relevant particles is small compared with typical

system dimensions and a fluid description may be adequate. In view of the low impurity content measured in the present day experiments and the small tolerable impurity contamination in future fusion reactors, a test fluid approach seems to be justified.

The detailed numerical calculation of impurity radiation requires the treatment of several ionization states for each element in the plasma. For high Z impurities, this approach is very costly in terms of computer time. A useful approximation, which has been successfully employed at Livermore, is to replace the various ionic species with a single fictitious average ion. Using the average ion model, Jensen and Post calculated the steady state (coronal) radiation as a function of electron temperature for a variety of impurities in a hydrogen plasma.

In this paper, using a single average ion for the transport of impurity ions and coronal equilibrium value for radiated power and average charge Z, we solve the time dependent fluid equations in the SOL for both impurities and fuels simultaneously. By this, we estimate the possibility of the proposed heat extraction concept in large fusion reactors.

4.5.2 Computer model

Model geometry of the poloidal cross section of SSTR and its numerical mesh are shown in Fig. 4.5.1. The orthogonal Z(i)- ψ(j) co-ordinates is employed for the fluid equations where Z(i) and ψ(i) denotes the poloidal length of the magnetic line of force and the poloidal flux, respectively. The motion of the neutral particle is calculated on the real space.

The molybdenum target plate is assumed and Marlowe reflection model is employed. Section AB denotes the albedo surface. Neutral particles which are released when plasma ions impact upon the divertor plate first traverse the divertor plasma channels. A smaller fraction enter the pumping ducts and a still further reduced fraction enter the down-pipes which lead to the vacuum pumps. Even when within a down-pipe, the escaping neutral particles may be backscattered and return to the pumping ducts. The probability of return through the entrance of the down-pipe is quantified in this work by assigning an albedo whose magnitude "α" represents the effective reflectivity of the entrance of the down-pipe. The probability that a particle is pumped is therefore (1- α); α=0.96 is used in the simulation.

The behavior of plasmas and neutrals is calculated using the UEDA code. The code is a 2-D dynamic simulation code for transport processes both in the edge and divertor plasmas, coupled with a Monte Carlo method for neutral gas. The plasma behavior is delt with the fluid model which consists of the continuity equation for the density, the momentum conservation equation governing the parallel velocity $V_{//}$ the diffusion equation for the perpendicular velocity $V\psi$ and energy equations for the electron and ion temperatures. The explicit form of the equations are as follows;

$$\frac{\partial \rho_i}{\partial t}+\nabla\cdot(\rho_i v)=S_n\,, \tag{4.5.1}$$

$$\rho_i\left(\frac{\partial}{\partial t}+v\cdot\nabla\right)v_{11}=-\frac{B_\theta}{B}\cdot\frac{1}{h_z}\cdot\frac{\partial P}{\partial z}-S_n v_{11}\,, \tag{4.5.2}$$

$$v_\psi=-\frac{1}{h_\psi}\cdot\frac{D}{n_i}\cdot\frac{\partial n_i}{\partial \psi}\,, \tag{4.5.3}$$

$$\begin{aligned}&\rho_i\left(\frac{\partial}{\partial t}+v\cdot\nabla\right)\left(\frac{3}{2}\cdot\frac{kT_i}{m_i}+\frac{1}{2}v\cdot v\right)\\&=-\nabla\left(\frac{\rho_i kT_i}{m_i}v\right)-v\cdot\nabla\left(\frac{\rho_e kT_e}{m_e}\right)\\&\quad+\nabla\cdot\kappa^i\nabla(kT_i)-E_s^iS_n^i+Q_{ei}-Q_{rx}\,,\end{aligned} \tag{4.5.4}$$

$$\begin{aligned}&\rho_e\left(\frac{\partial}{\partial t}+v\cdot\nabla\right)\left(\frac{3}{2}\cdot\frac{kT_e}{m_e}+\frac{1}{2}v\cdot v\right)\\&=-\nabla\left(\frac{\rho_e kT_e}{m_e}v\right)+v\cdot\nabla\left(\frac{\rho_e kT_e}{m_e}\right)\\&\quad+\nabla\cdot\kappa^e\nabla(kT_e)-E_s^eS_n^e-Q_{ei}-Q_{\mathrm{rad}}\,,\end{aligned} \tag{4.5.5}$$

The mathematical model of the behavior of impurity ion in charge state Z consists of the momentum conservation equation in the parallel direction and the diffusion equation in the perpendicular direction with anomalous diffusion constant D. The equation for the average charge state "Z" in the average ion model is assumed as follows in the parallel direction.

$$\begin{aligned}&\rho_z\left(\frac{\partial}{\partial t}+v_z\cdot\nabla\right)v_z\\&=-\nabla_{11}P_z+n_z zeE+\rho_z\frac{v-v_z}{\tau_z}\\&\quad+n_z[\alpha_z\nabla_{11}(kT_e)+\beta_z\nabla_{11}(kT_i)]\end{aligned} \tag{4.5.6}$$

In the perpendicular direction, the following diffusion equation with a diffusion coefficient D

$$v_\phi = -\frac{1}{h_\phi}\cdot\frac{D}{n_z}\cdot\frac{\partial n_z}{\partial \phi}, \qquad (4.5.7)$$

is assumed. The temperature of impurity ion is set to that of field ion, i.e., the energy conservation equation for impurity ion is not solved.

Using the steady state average ion model, average charge state Z is calculated quickly from Fig. 4.5.2 once the electron temperature is given. Radiated power loss is also interpolated from Fig. 4.5.3.

At the plasma edge, the particle (mass) and the energy input to the SOL, i.e. the output from the core, are given. In the UEDA code, the total particle flux, Γ_{out}, and the total energy fluxes of electrons and ions, Q_e and Q_i, are parameters. (Γ_{out} and $Q_{e,i}$ are the values integrated on the plasma surface, and $P_{out}=Q_i+Q_e$.) We assign the mass and the energy to the boundary cells in the SOL. The method for the poloidal distribution of the power and particle input to the SOL at the separatrix is as follows; once the particle and energy inputs across this boundary is given, we assign values of the particle and energy flux to each cell "i" located adjacent to the boundary (called boundary cell) under the assumption that the diffusion equation is satisfied on that boundary.

Fig. 4.5.4 depicts the core/edge treatment. The procedures are as follows. Assuming the poloidal dependence of diffusion coefficient D is weak, the particle flux G(i) for the i-th boundary cell is calculated by the diffusion equation on the i-th boundary;

$$\Gamma(i) = -2D[\rho_m - \rho(i)]/h_\phi(i)\delta\phi, \qquad (4.5.8)$$

where $\rho(i)$ is the density of the boundary cell i and ρ_m is the uniform density of the fictitious cell as shown in the figure. After multiplication of Eq. (4.5.8) with the poloidal length of the cell i and summation over all boundary cell i, ρ_m can be written as follows, using the total mass input M per unit toroidal length,

$$\rho_m = \left(\sum_i \frac{\rho(i)h_z(i)\delta z}{h_\phi(i)\delta\phi} - \frac{M}{2D}\right)\Big/\left(\sum_i \frac{h_z(i)\delta z}{h_\phi(i)\delta\phi}\right), \qquad (4.5.9)$$

where $M = \sum_i h_z(i)\delta z\Gamma(i)$.

As a result, the distributed particle flux along the boundary of the core plasma can be obtained with Eqs. (4.5.8) and (4.5.9).

The distributed electron and ion energy flux to the edge region are also calculated in the same way mentioned above. For example, the electron energy flux to the boundary cell i is written.

$$q^e(i)=\frac{5}{2}\cdot\frac{k}{m_e}\Gamma^e(i)T^e_m-\kappa^e_\phi(i)k\frac{T^e_m-T^e(i)}{h_\phi\delta\phi/2}.$$

Here, the uniform electron temperature T^e_m of the fictitious cell is given as

$$T^e_m=\frac{Q^e-2k\sum_i\frac{h_z\delta z}{h_\phi\delta\phi}\kappa^e_\phi(i)T^e(i)}{\frac{5}{2}\cdot\frac{k}{m_e}M-2k\sum_i\frac{h_z\delta z}{h_\phi\delta\phi}\kappa^e_\phi(i)}.$$

In the above equation, Q^e(W/m) is the prescribed electron energy input to the edge region across the boundary per unit toroidal length.

4.5.3 Calculation Conditions

(1) Major input parameters

Major input parameters are listed in Table 4.5.1. Another important data in the calculation is the distribution of the pitch of the magnetic line of force $B\theta/B_t$. Fig. 4.5.5 shows $B\theta/B_t$ profiles in the poloidal direction for each flux tube (only for j=3 to j=9 flux tubes are shown in this figure).

(2) Gas puff condition

Impurity ion (Fe) is given at places shown in Fig. 4.5.6 with the rate of 0.01 x Γ_p for the outer divertor and 0.015 Γ_p for the inner divertor, respectively. Also, fuel gas is injected at the rate of $4\Gamma_p$ and $3\Gamma_p$ for outer and inner divertor, respectively.

4.5.4 Results

We show below the numerical results for the SOL plasma behavior in SSTR. Fig. 4.5.7 shows electron temperature (T_e) and electron density (n_e) profiles in the poloidal direction in the case of no impurity injection. This figure clearly shows the high divertor temperature and low electron density at the target plates. Namely, no dense and cold divertor plasma is established in this case and severe erosion of the plates would

occur. Therefore, it is required to inject the impurity atom expecting high radiation loss and resultant low power flux to the plates.

Te profiles with fuel and Fe ion injection is illustrated in Fig. 4.5.8. Divertor temperature decreased to considerably low values and no erosion of the molybdenum target plate is observed in this case. The maximum SOL temperature is about 270 eV at the mid-plane.

Fig. 4.5.9 shows T_i profiles in the poloidal direction for each flux tubes. T_i is also low at the divertor plates. Electron density (n_e) profiles in the poloidal direction is depicted in Fig. 4.5.10. High density at the divertor plates is clearly realized in this case. The maximum density is about $4x10^{21}/m^3$. The density at the mid-plane is also high ($\sim 7x10^{19}/m^3$) compared with that of no impurity injection. These data show that the dense and cold divertor plasma is established with fuel and impurity injection near the target plates.

Temperature and density along the plates T_{ed} and n_{ed}, respectively are shown in Fig. 4.5.11. T_{ed} at the position where the separatrix intersects is below 10eV (The power and particle is maximum in this flux tube). Fig. 4.5.12 illustrates the heat flux and radiation heat flux along the target plates. Total heat flux exceeds 1 KW/cm2 at the position mentioned above. This result means further optimization for the injection rate and injection point is required.

Contour plot for electron density n_e is shown in Fig. 4.5.13. Fig. 4.5.14 depicts the density contour for Fe ions. The maximum value of n_{Fe} is about $2x10^{19}/m^3$ and its position locates in front of the outer divertor plate. We can see the almost of all Fe ions remain in the inner and outer divertor region.Contour plot for neutral fuel gas is illustrated in Fig. 4.5.15. Neutrals also concentrate near the inner and outer plate.

2-D profile of the poloidal flow velocity is depicted in Fig. 4.5.16. The flow of the fuel ions directs to the divertor plate at least at the lower region than null point of j=7 flux tube. The flow of fuel ion suppress the impurity ion, i.e. the friction force between impurity and fuel ions stops the motion of impurity ion to flow up to the mid-plane.

Last figure (Fig. 4.5.17) shows 2-D radiation loss profile for Fe ions. The power loss concentrates at very narrow region in front of the plates. This is the reason for the high radiation heat flux to the plates. It seems to be required to scatter Fe ions. This is left open in this paper and is our near future problem.

4.5.5 Conclusion

We proposed here the heat extraction method by the usual poloidal divertor for the future large tokamak reactors. In the method, active injection of powdery iron near the divertor plate with fuel gas is employed. The numerical simulation for heat extraction properties in SSTR shows that the method could realize the dense and cold divertor plasma with injection rate of $7\Gamma_p$ for fuels and $0.02\Gamma_p$ for impurities.

Further optimization for injection rate and also injection point seems to be required and this is our near future problem.

Table 4.5.1 Major input parameters for the UEDA code

Q_T	:	600MW
Γp	:	2.5×10^{23} /sec
D	:	D_B (D_B : Bohm diffusion coefficient)
χ	:	$\chi e = \chi i = 2D_B$
$B_t(0)$	:	9T
R	:	7m
Albedo	:	$\beta = 4\%$
Wall temperature	:	50°C
Plate temperature	:	500°C
Absorbing factor	:	= 0 for D/T, = 1 for Fe ion
Molecular production rate	:	0.5
Ion reflection model	:	Marlowe model

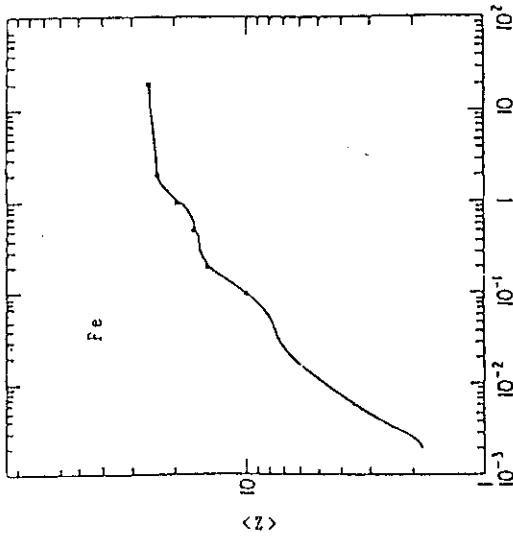

Fig. 4.5.2 Average charge state as a function of Te for Fe.

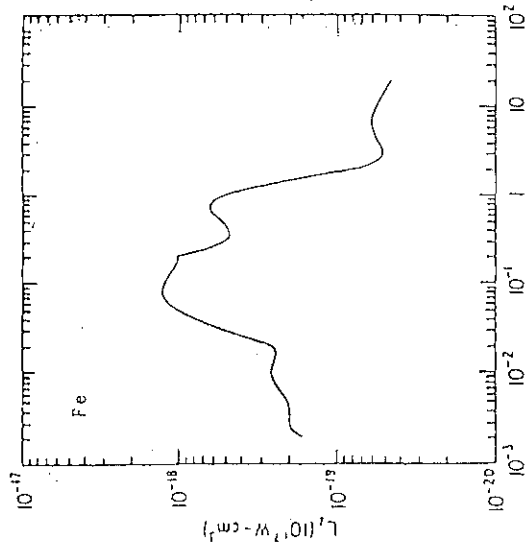

Fig. 4.5.3 Power loss rate of Fe as a function of Te.

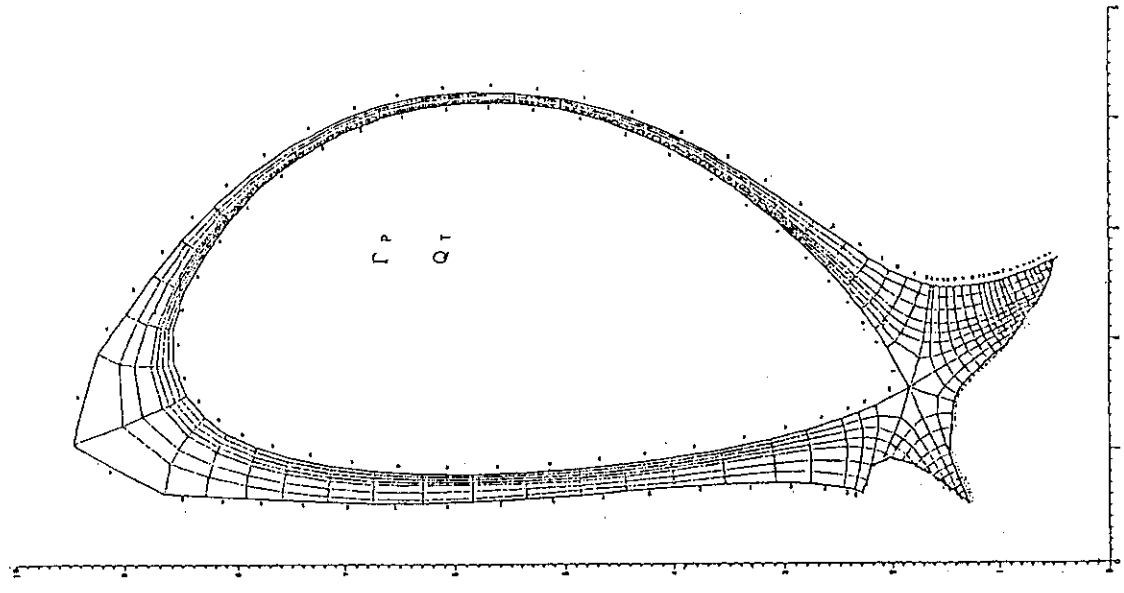

Fig. 4.5.1 Calculation mesh of SSTR.

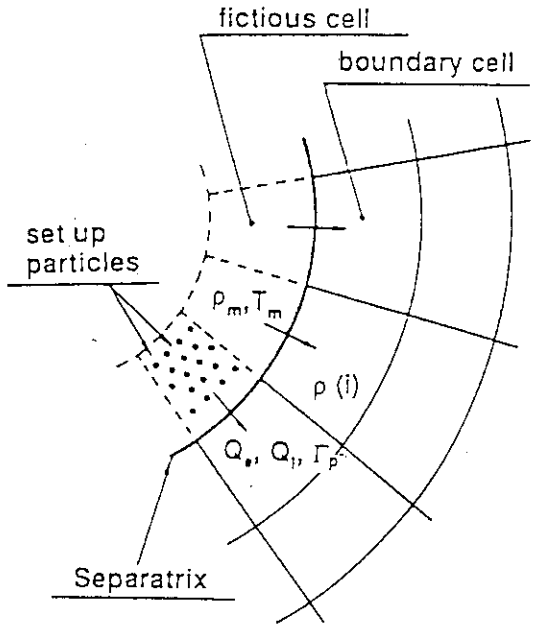

Fig. 4.5.4 Treatment of separatrix boundary.

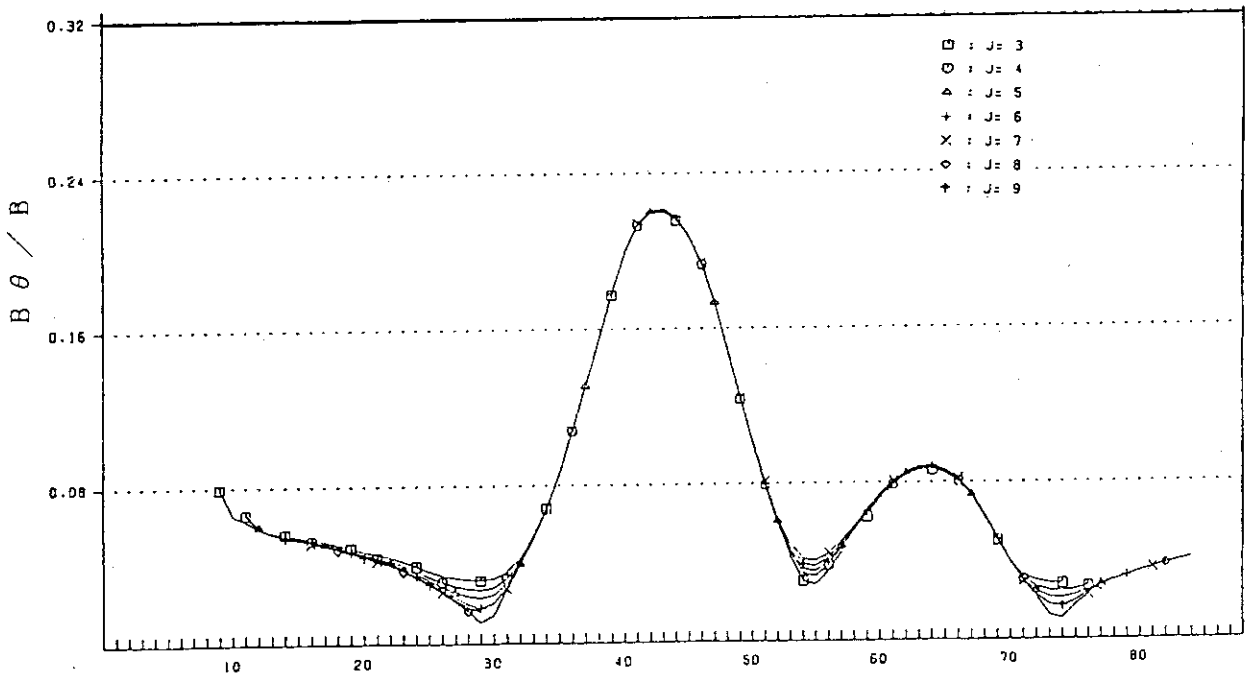

Fig. 4.5.5 Profiles of the pitch parameter for each flux tube.

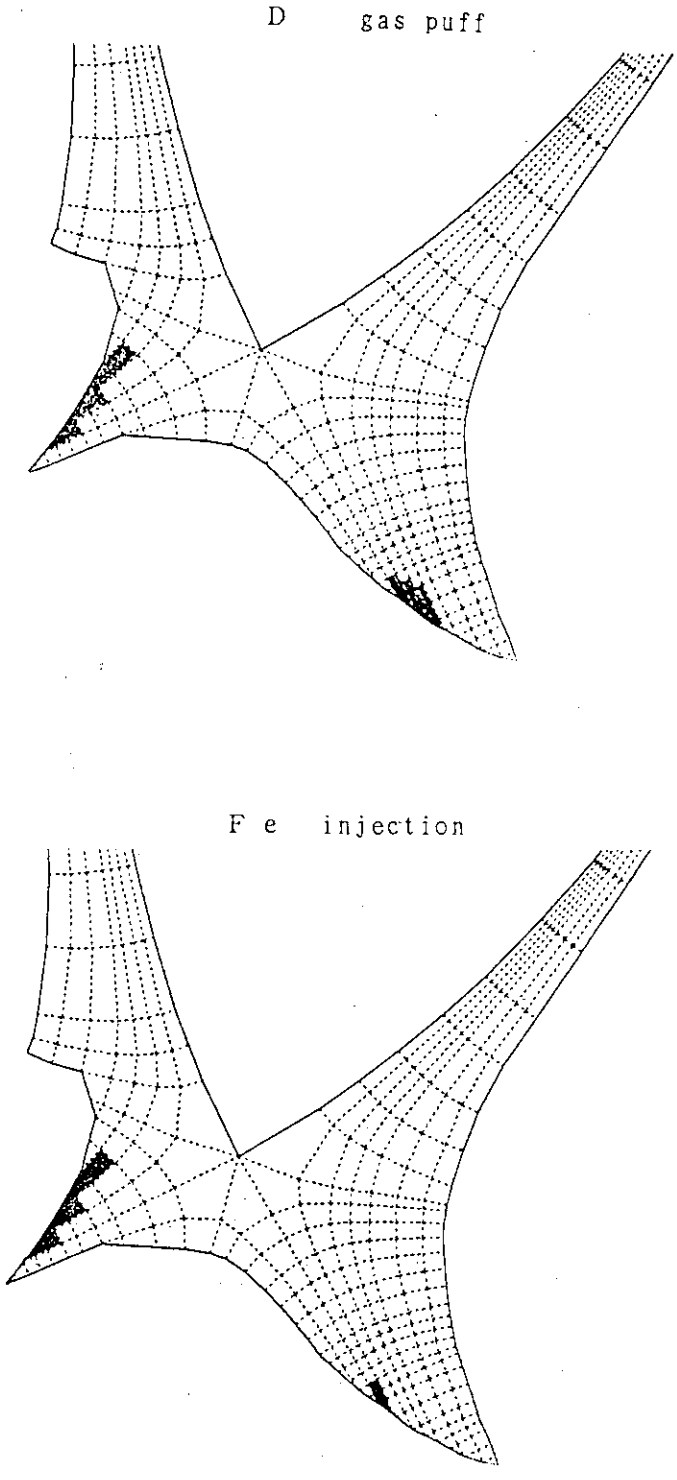

Fig. 4.5.6 Position of Fe and fuel injection.

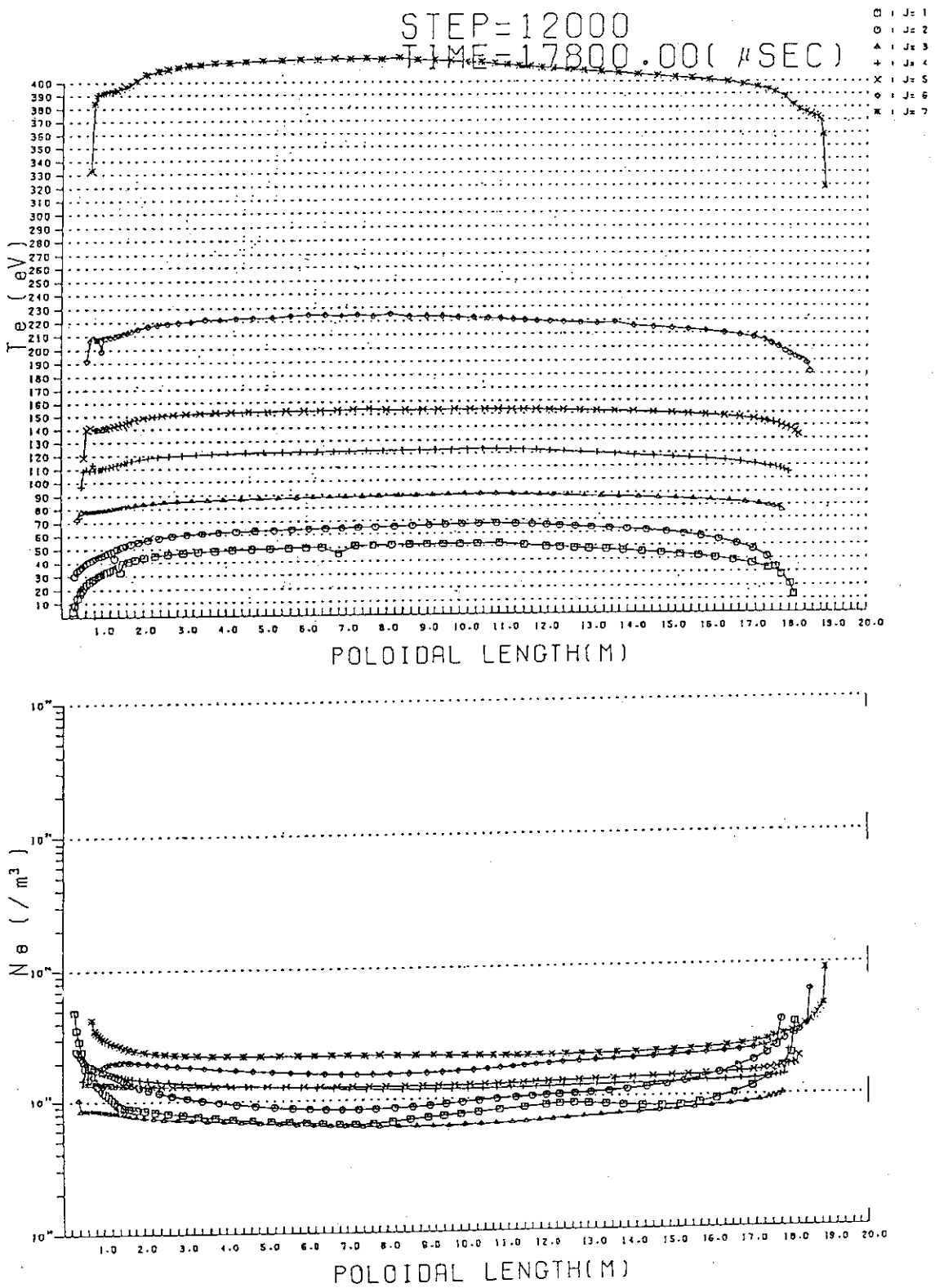

Fig. 4.5.7 Te and n_e profiles along the poloidal direction without Fe injection.

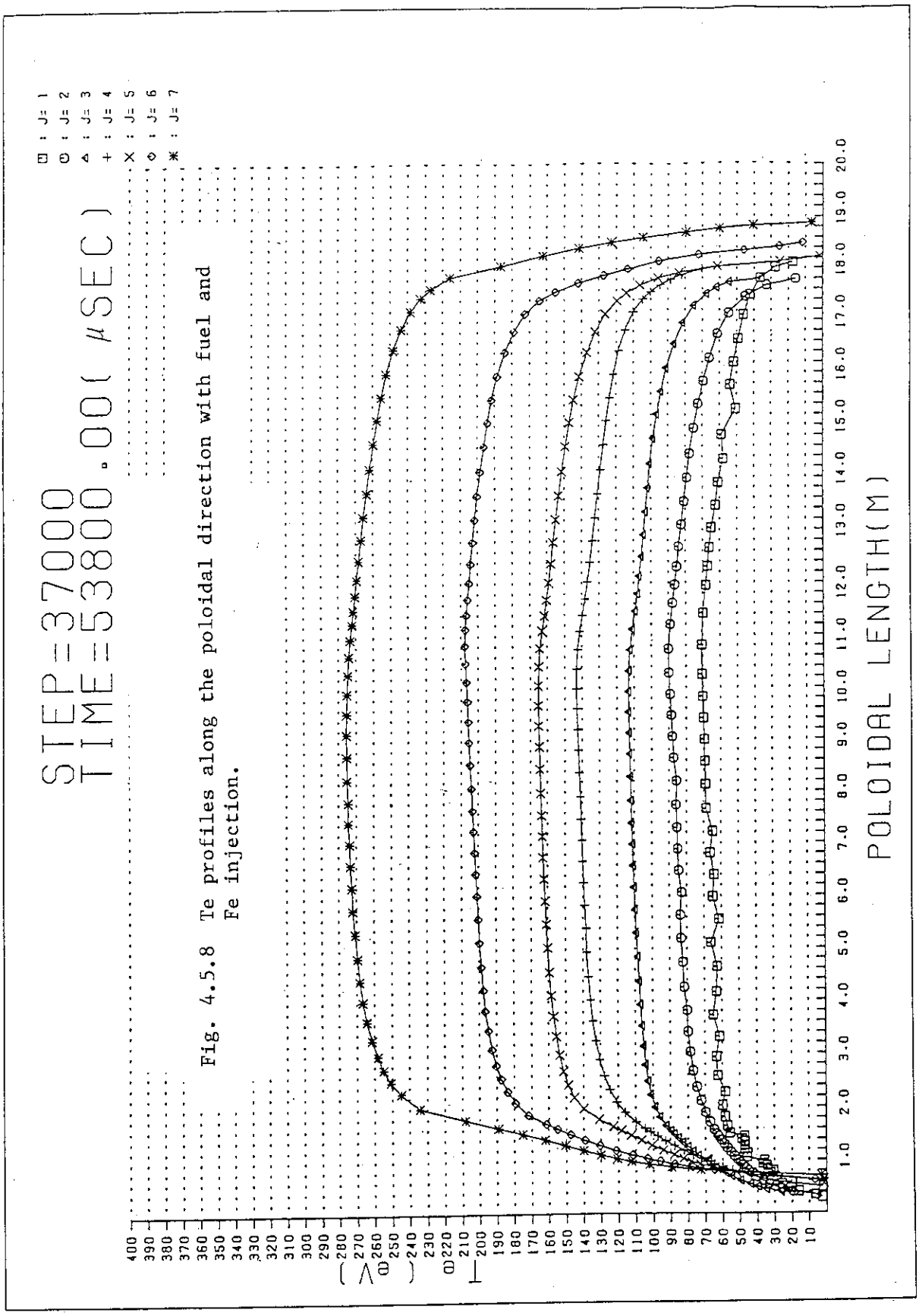

Fig. 4.5.8 Te profiles along the poloidal direction with fuel and Fe injection.

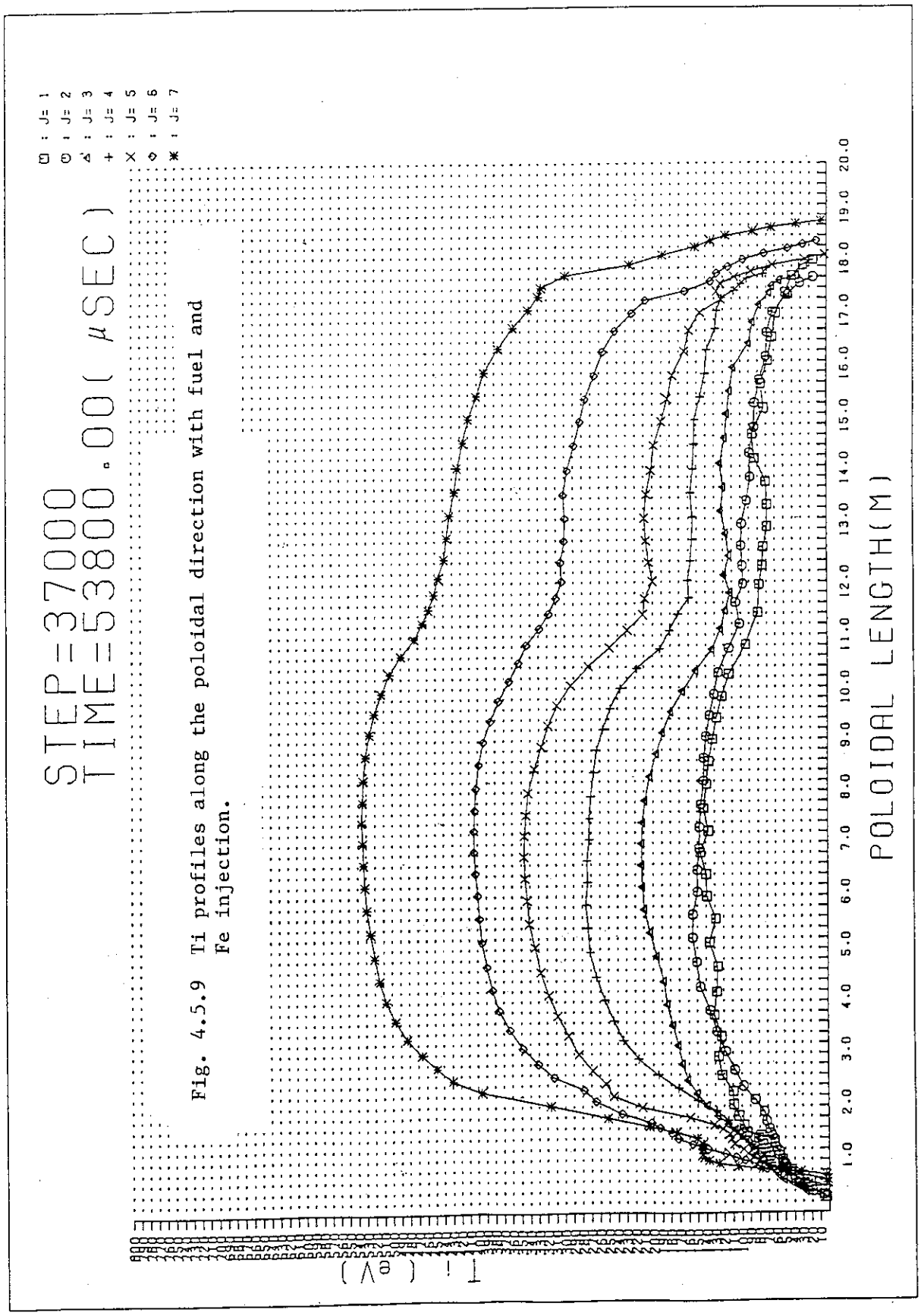

Fig. 4.5.9 Ti profiles along the poloidal direction with fuel and Fe injection.

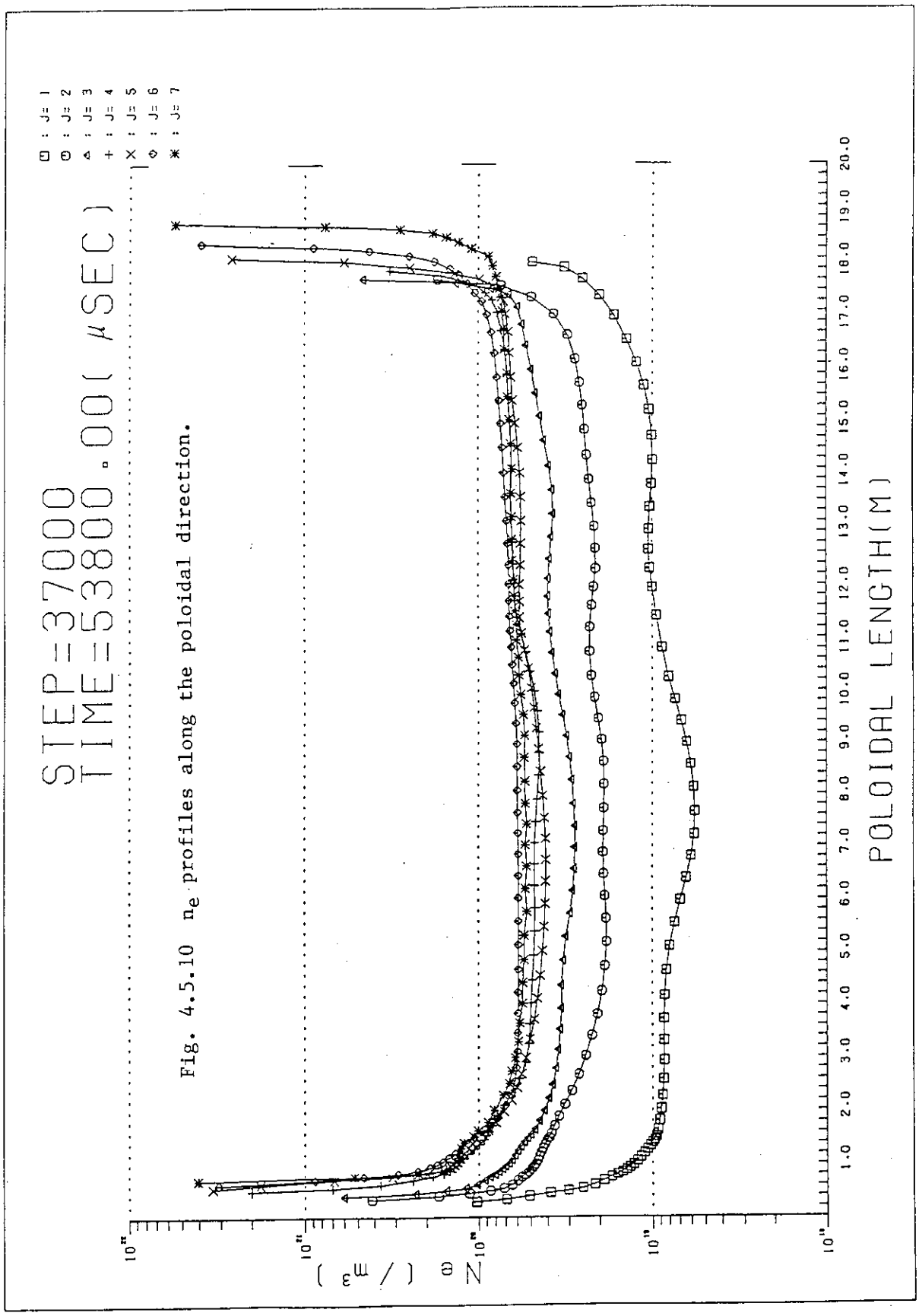

Fig. 4.5.10 n_e profiles along the poloidal direction.

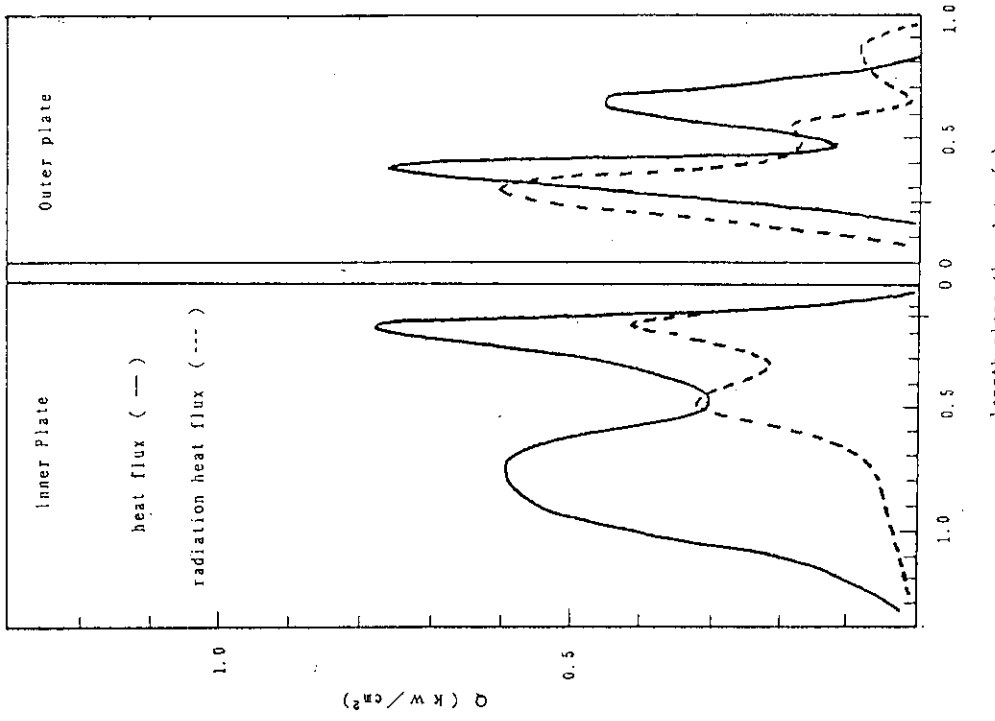

Fig. 4.5.12 Heat flux and radiation heat flux profiles along the divertor plate.

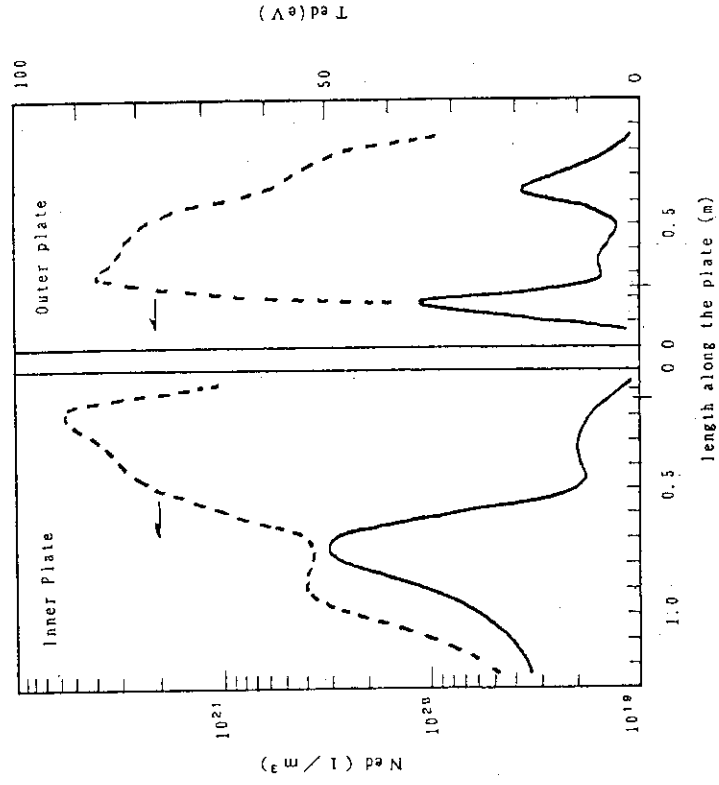

Fig. 4.5.11 T_{ed} and n_{ed} profiles along the divertor plates.

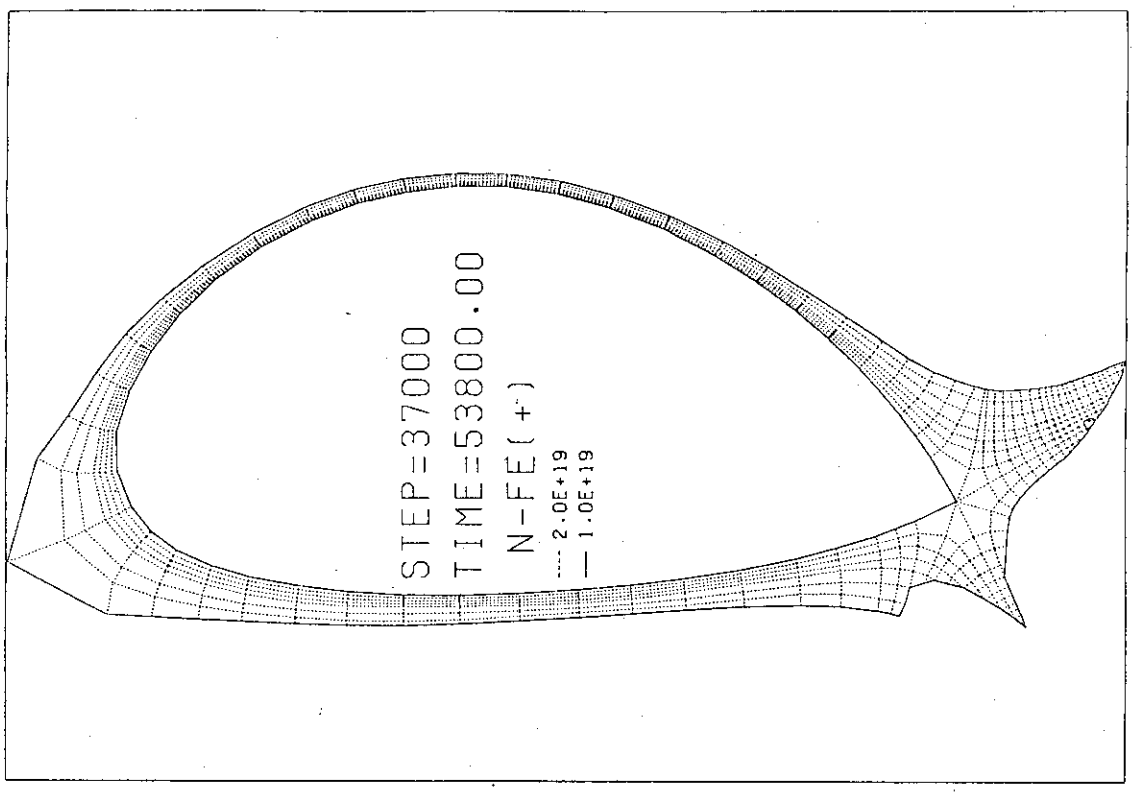

Fig. 4.5.14 Contour plot for Fe ion.

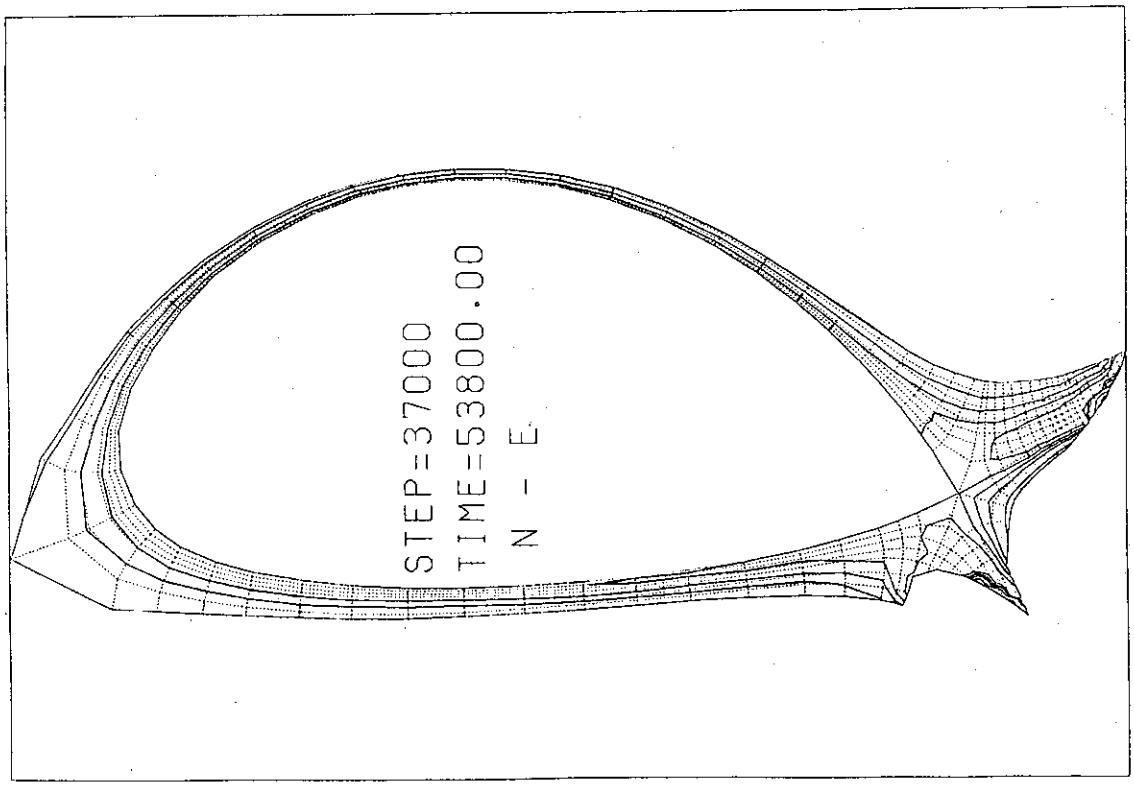

Fig. 4.5.13 Contour plot for n_e.

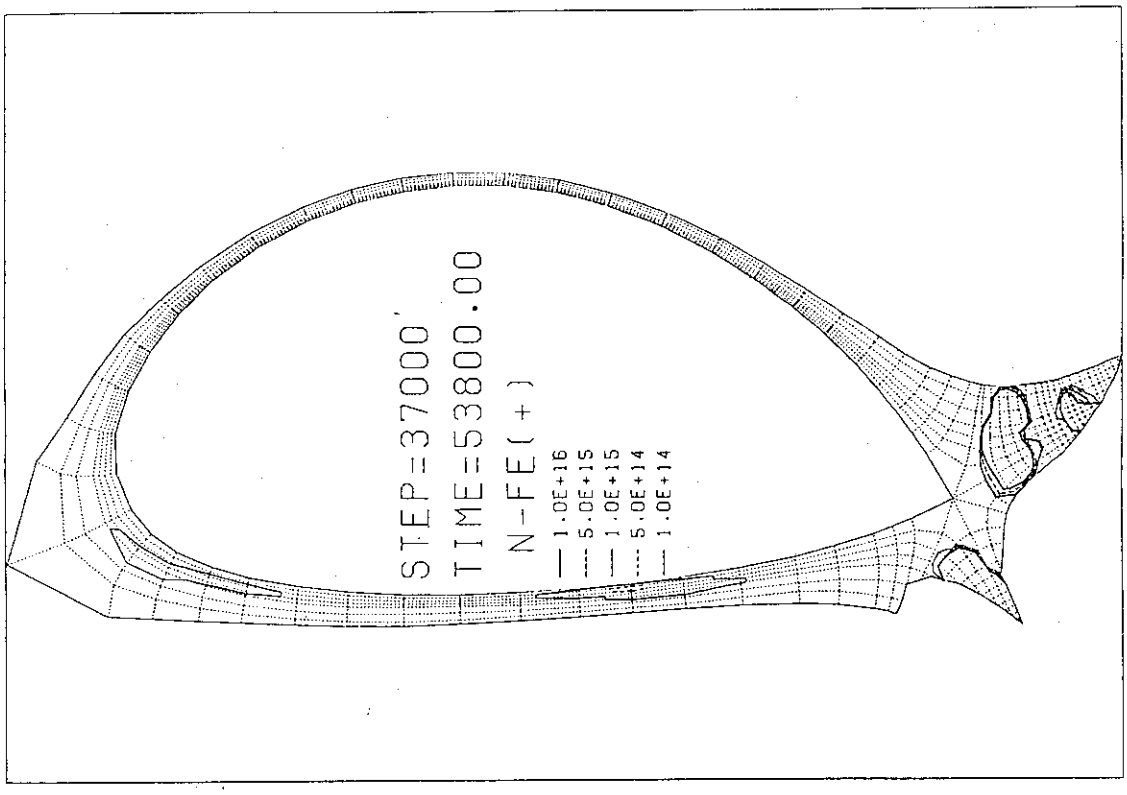

Fig. 4.5.14 (Continued)

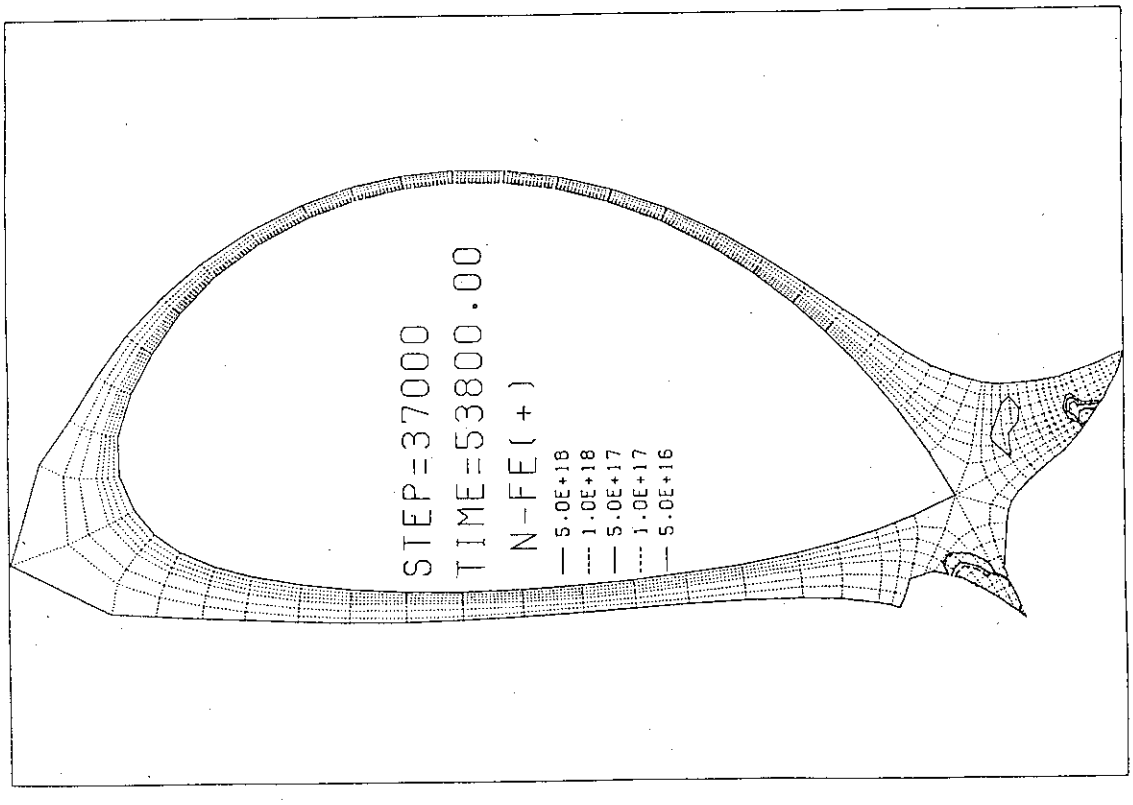

Fig. 4.5.14 (Continued)

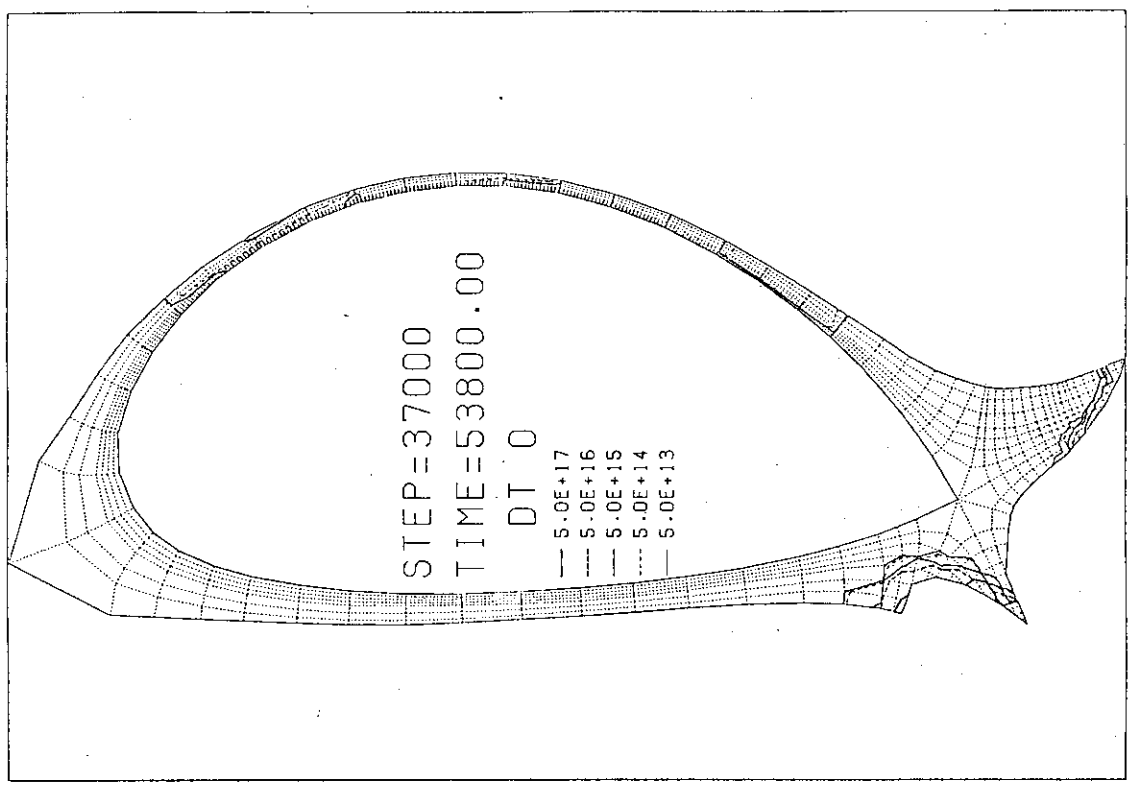

Fig. 4.5.15 (Continued)

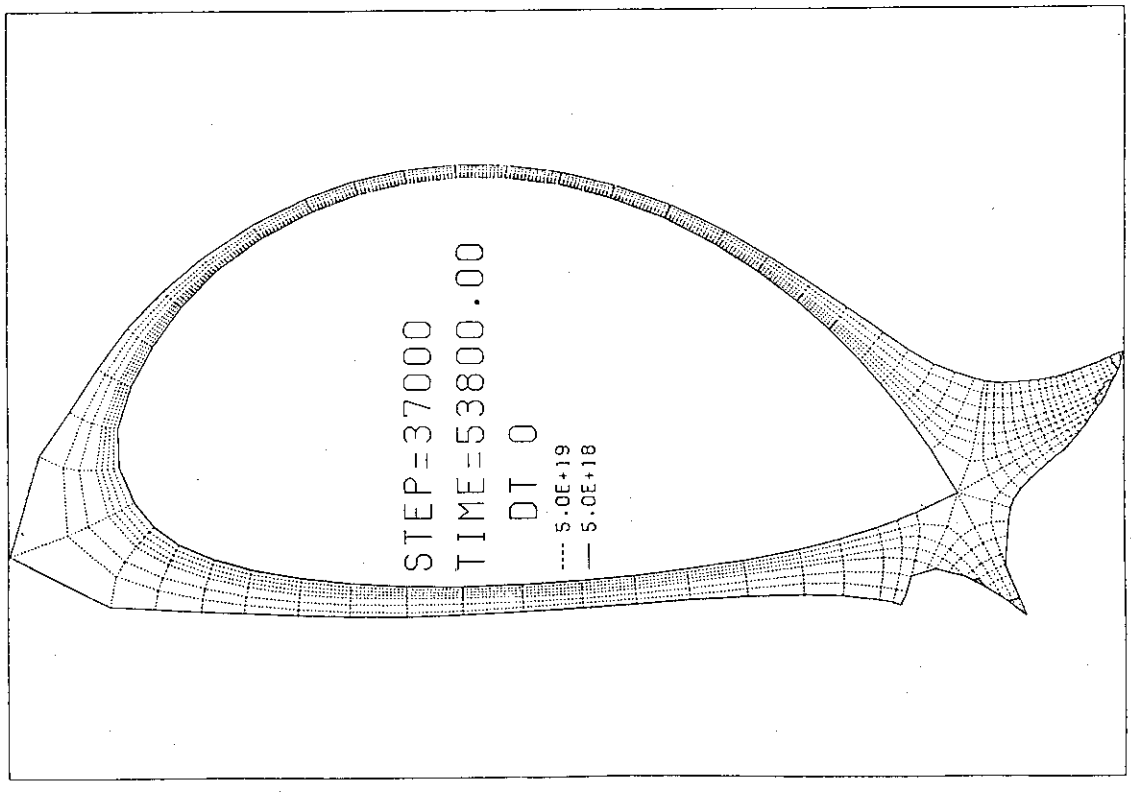

Fig. 4.5.15 Contour plot for neutrals of fuel.

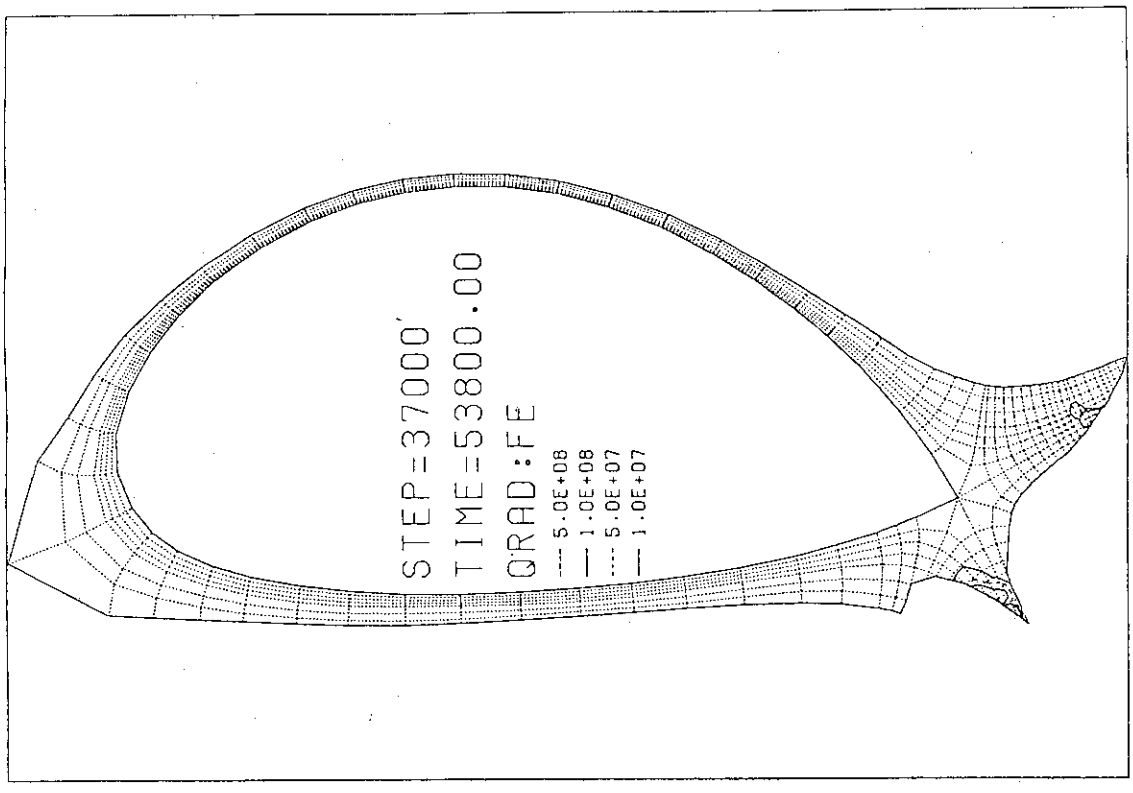

Fig. 4.5.16 Flow velocity for fuel ions.

Fig. 4.5.17 Radiation loss profile for Fe ion.

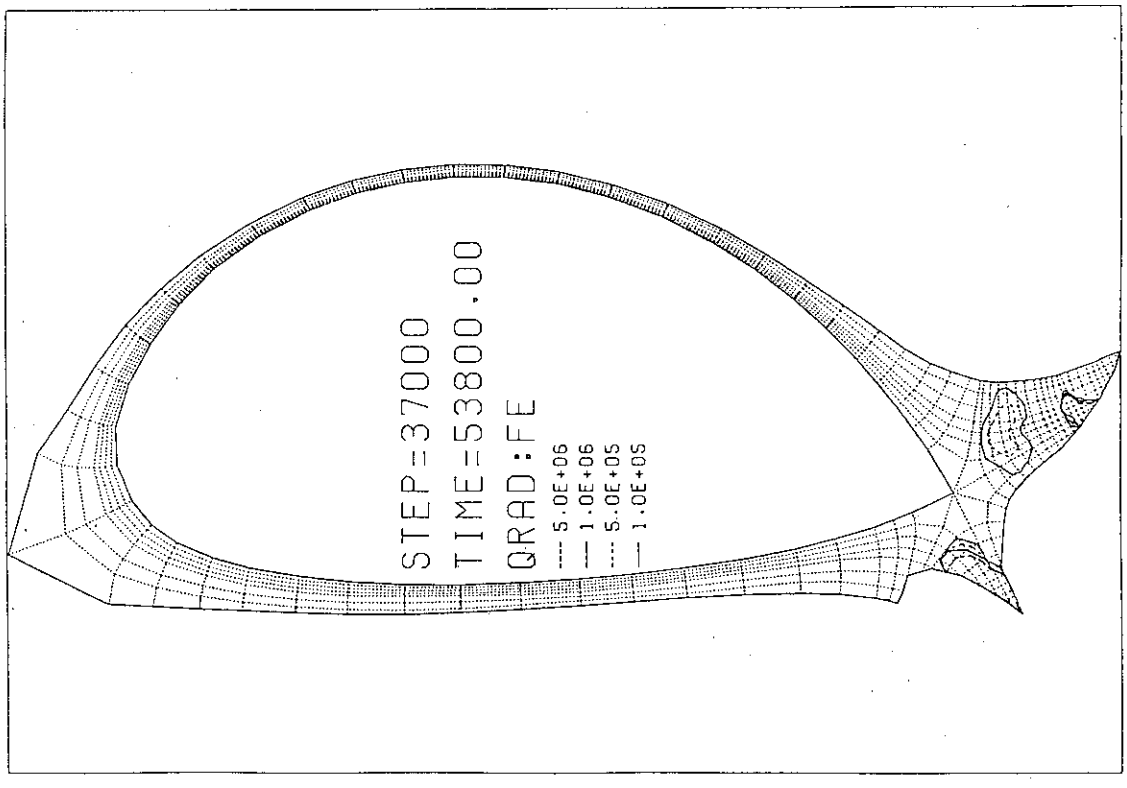

Fig. 4.5.17 (Continued)

5. Toroidal Field Coil

5.1 General

A toroidal field coil system of the SSTR consists of sixteen superconducting coils with a clear bore of 7.4 m x 12.4 m. The maximum magnetic field is 16.5 T and the total stored energy is about 140 GJ. These values are 1.4 - 3 times those of ignited machines such as FER and ITER. Though a very large size and high field coil, on one hand the toroidal field coil of the SSTR has a merit that the changing field rate and the nuclear heating for the coil are small in comparison with those for ignited machines.

The conceptual design for the toroidal field coil was carried out using data obtained by the cluster test coil program and the large coil task (LCT) program and by recent experiments. The characteristics of the designed SSTR toroidal field coil are as follows.

1) The advanced disk type which consists of plates enclosed in the case, was adopted as coil structure, with the advantage of high rigidity in winding pack.
2) Grading was provided with $(NbTi)_3Sn$ and NbTi conductors in order to to get high average current density in coil pack and easy coil construction.
3) A semi wind-and-react method proposed as a new technique to prevent a bending strain during winding was chosen.
4) A cable-in-conduit type conductor was selected.
5) A value of non-copper critical current density of a $(NbTi)_3Sn$ strand is 600 A/mm^2 at 16.5 T.
6) The operating current was 81 kA.
7) As cooling method, a forced flow cooling was selected.
8) As support of a centering force, a wedge method was chosen.

The toroidal field coil of the SSTR has the average current density in an inner leg of 12 A/mm^2 and the total weight of about 12,000 tons. The maximum stress was 850 MPa less than 1200 MPa which is 1.5 Sm of JN-1 structure material.

5.2 Conductor

The conductor of the toroidal coil is a cable-in-conduit type which has high stability and low ac losses and furthermore is low cost for its fabrication. The design of the conductor was performed as based on the condition shown in Table 5.2.1. The cross-section and the parameter of the conductor are Fig. 5.2.1 and Table 5.2.2, respectively. The characteristics of the conductor are as follows.

1) The operating current of 81 kA was decided from the limited temperature rise and the limited terminal voltage during quench.
2) The shape of the conductor is circular to get no damage of strand and high fitness into the plates with half circular grooves.
3) As conduit material, Ti was selected because thermal construction of Ti is almost equal to that of $(NbTi)_3Sn$.
4) The strand cable within the conductor is divided by a reinforcement bar with three grooves because of reducing stress on the strands and prehending strand motion.
5) Non-copper critical current density of a $(NbTi)_3Sn$ strand used in this design is 600 A/mm^2 at 16.5 T. This value is already obtained by a multifilamentary (NbTi)3Sn made by a tube method shown in Fig. 5.2.2.
6) As consideration of the stability for this conductor, the nominal operating current is designed to be less than the limiting current calculated by the following formula.

$$I_{lim} = (h\ P\ S\ (T_c - T_b))^{1/2}$$

where h is the thermal conductivity coefficient between superconductor and coolant helium. In this calculation, h = 0.1 mW/Kcm^2 is used. P is the cooling perimeter of conductor. S is the cross-section area of copper, T_c and T_b are the critical temperature and the cooling temperature.

Table 5.2.1 Design condition of superconducting coil for the SSTR

Inlet temperature	4.5 K
Inlet Pressure	0.6 MPa
Temperature difference between inlet and outlet	below 1.5 K
Pressure difference between inlet and outlet	below 0.2 MPa
Temperature margin	above 1.5 K
Limiting current	above operating current
Temperature rise during quench	below 150 K
Pressure rise during quench	below 20 MPa
Lag time of dump start	1.0 sec
Time constant of dump current	10.0 sec
Dump voltage	below 20 kV
Protection system of current circuit	Tore supra method
Strain limit on Nb_3Sn conductor	0.4 %
Transverse stress limit on Nb_3Sn conductor	100 MPa
Average heat load	below 22 kW

Table 5.2.2 Parameters of the superconductors for the toroidal coil

Item	High field region	Low field region
Size	50 mmm diameter	38 mm diameter
Maximum field	16.5 T	5 T
Operating current	81 kA	81 kA
Superconducting material	$(NbTi)_3Sn$	NbTi
Strand diameter	1.05 mm	0.86 mm
Filament diameter	5 μm	20 μm
Cu/Non Cu	2.33	4.4
NO of strands	972	972
Superconducting material area of strands	243 mm^2	103 mm^2
Copper area of strands	567 mm^2	454 mm^2
Total area of strands	810 mm^2	557 mm^2
Helium area	425 mm^2	287 mm^2
Internal reinforcement material area	412 mm^2	−
Conduit material area	238 mm^2	135 mm^2
Insulation thickness	0.5 mm	0.5 mm
Void fraction	0.34	0.34
Conductor unit length	720 m	160 m
Cooling path length	360 m	160 m
Critical current	146 kA	244 kA
Limiting current	98 kA	110 kA

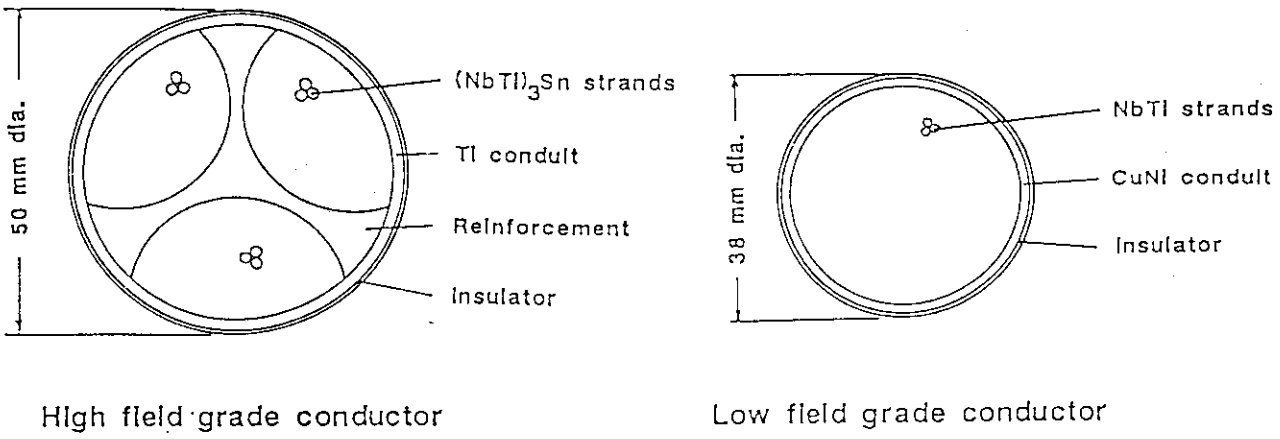

Fig. 5.2.1 Conductors of toroidal coil for the SSTR.

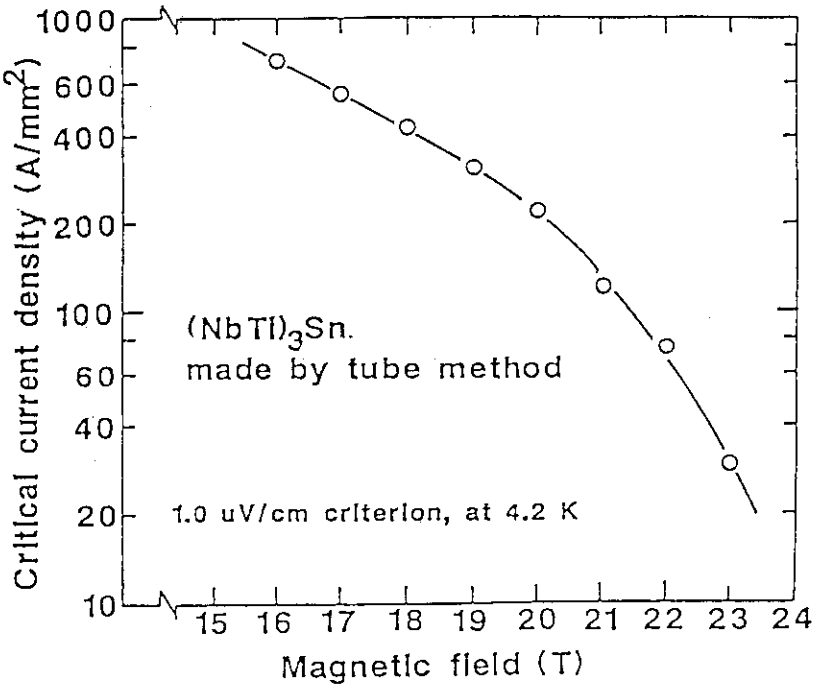

Fig. 5.2.2 Non-cu critical current density of a $(NbTi)_3Sn$ strand used in this design. (from H. Shiraki et al., MRS Int'l. Mtg. on Adv. Mats. Vol.6 1989)

5.3 Coil Structure

D-shaped coil configuration in the poloidal plane is adopted in order to minimize the coil stress by the electromagnetic force. As shone in Fig.5.3.1, it is made up of one straight line and three arcs, and is similar to the constant tension coil configuration . It is settled to make Bt-ripple value less than 1%.

The coil cross section configuration is determined as follows. The cross section of winding is rectangular. The average current density of winding section is rather high as 20.8 A/mm^2 (at 16.5T) to make the coil compact. In order to reduce stress of Nb_3Sn conductor from the LCT experiment result, the advanced disk type coil construction is adopted. One coil is composed of nine double pancake coils. Two grading conductors of Nb_3Sn and NbTi are used for the purpose of the manufacturing easiness and the cost reduction. The coil cross section is shown is Fig.5.3.2.

The length of the cooling channel is 360 m in Nb_3Sn, and 160 m in NbTi. The pressure drop in the cooling channel less than 2 bar. The shear panels in the outer section of coil and shear keys in the straight line of the coil are chose against overturning electromagnetic force. The shear panels are located in the upper and lower section on the coil, which is not space for drawing out of the reactor core equipment.

The outer configuration of TF coil is determined in consideration of the location and the supporting of PF coils. The weight of a coil is about 700 tons.

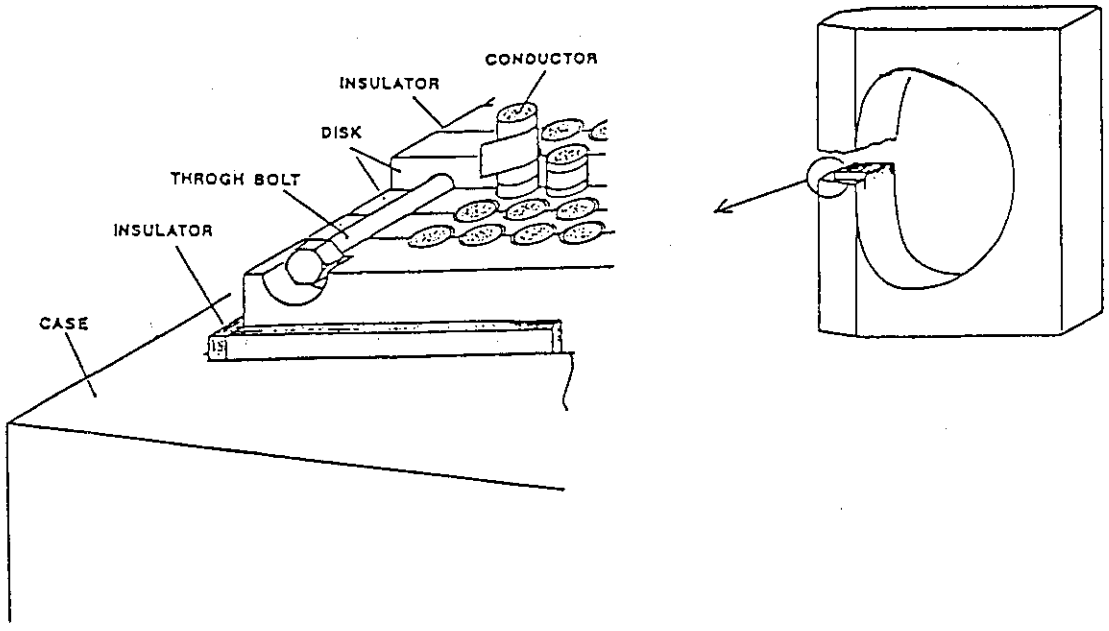

Fig. 5.3.2 Inner leg cross section of TF coil.

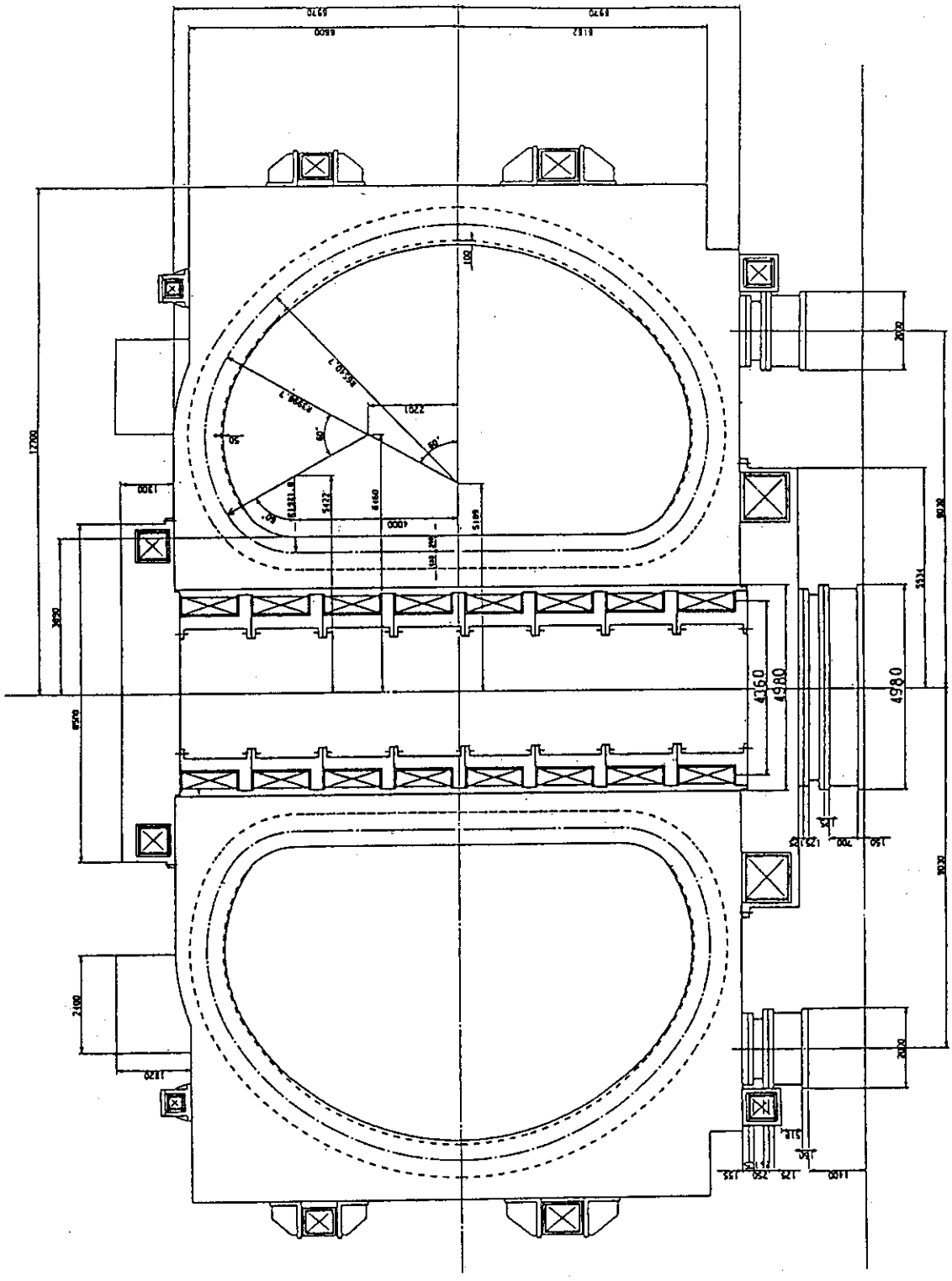

Fig. 5.3.1 Dimension of TF coil.

5.4 Electromagnetic Analysis

5.4.1 Electromagnetic quantities

We design electromagnetic quantities as follows.

(1) The conductor is cable in conduit forced flow type.

(2) The average current density of coil is 20.8 A/mm^2 at 16.5 T.

(3) The coil current is 81 KA.

(4) The electromagnetic force is determined as the toroidal magnetic field is 9.0 T at plasma major radius 7.0 m.

(5) Electromagnetic quantities of TF coil are shown in Table 5.4.1.

(6) The earth insulation voltage is 20 KV.

5.4.2 Magnetic Field Distribution

The magnetic field distribution in the mid plane is shown in Fig. 5.4.1. The solid line shows the magnetic field distribution in the toroidal directional central cross section of the TF coil, and the dotted line shows it in the central plane between two TF coils.

The maximum magnetic field at the winding section is 16.5 T, and is generated at the most inward part of the minimum winding radius section. We confirmed that the magnetic field was 9.0 T at the plasma center radius 7.0 m.

The toroidal magnetic field field ripple d is given as follows. The ripple at the plasma outer major radius 8.7 m is 1.04 %. The ripple is shown in Fig. 5.4.2.

$$\delta = \frac{B_{max}-B_{min}}{B_{max}+B_{min}} \times 100\%$$

Bmax : maximum magnetic field at radius R.

Bmin : minimum magnetic field at radius R.

5.4.3 Electromagnetic Force

(1) In-plane electromagnetic force

The electromagnetic force by the toroidal magnetic field is shown in Fig. 5.4.3. The total hoop force in the minor radius direction Fhoop is 3.8X10^3 MN/coil. The total centering force inward the torus center Fr is 1.4X10^3 MN/coil. The vertical force of upper half coil Fz is 7.6X10^3 MN/coil.

The centering force is supported by wedges of neighboring TF coils. The hoop force is supported by the conductor itself and the nonmagnetic steel casing which is located outside the winding.

(2) Overturning Force by Poloidal Field

As the magnetomotiy force of PF coils is changed at each time step for the plasma control, the overturning force of the TF coil is changed at each time step, too. So, we calculated the electromagnetic force distribution of the each part of the TF coil at each time step. The result is shown in Fig. 5.4.4. Figure 5.4.5 shows the overturning force with the plasma and without the plasma.

The overturning force is supported by the out-of-plane bonding rigidity of the casing, the shear panel, and the shear key between TF coils.

Table 5.4.1 Main characteristics of TF coils

ITEMS	UNIT	SSTR
BORE RADIUS	m	7.35×11.52
NUMBER OF COILS		16
COOLING METHOD		FORCED FLOW COOLING
WINDING CONCEPT		DOUBLE-PANCAKE WINDING + DISK
SHAPE OF COIL		D-SHAPE
SUPERCONDUCTOR		(NbTi)3Sn/NbTi
PEAK FIELD	T	16.5
OPERATING CURRENT	kA	81
CURRENT DENSITY IN WINDING	A/mm²	20.8
CURRENT DENSITY IN COIL	A/mm²	12.1
WINDING CAVITY	m²	0.95
NUMBER OF TURNS	TURNS	244
NUMBER OF DOUBLE-PANCAKES		9
NUMBER OF GRADINGS		2
MAGNETOMOTIVE FORCE	MAT	315
TOTAL INDUCTANCE	H	41.6
TOTAL STORED ENERGY	GJ	136.5
HOOP FORCE FH	MN/COIL	3788
CENTERING FORCE FR	MN/COIL	-1378
VERTICAL FORCE FZ	MN/COIL	764
TOROIDAL FIELD RIPPLE	%	1.04

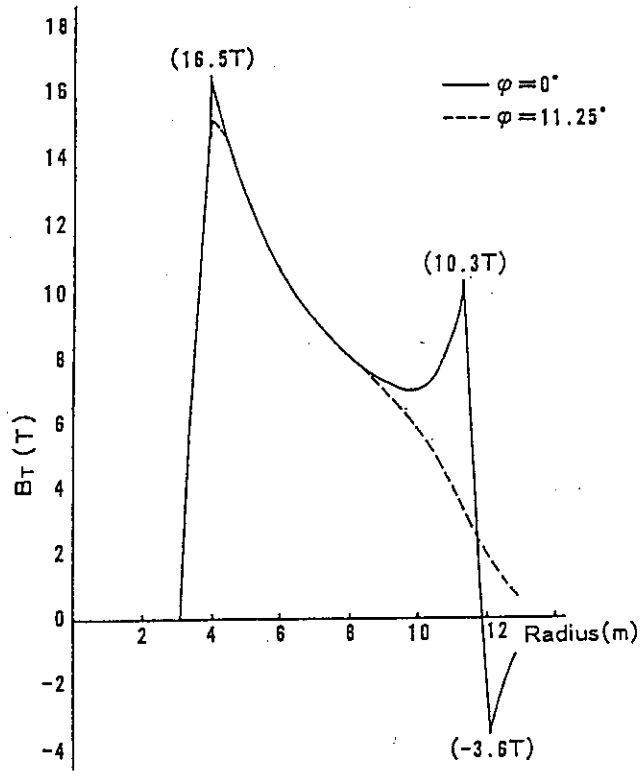

Fig. 5.4.1 Magnetic field distribution on the mid plane of TF coil.

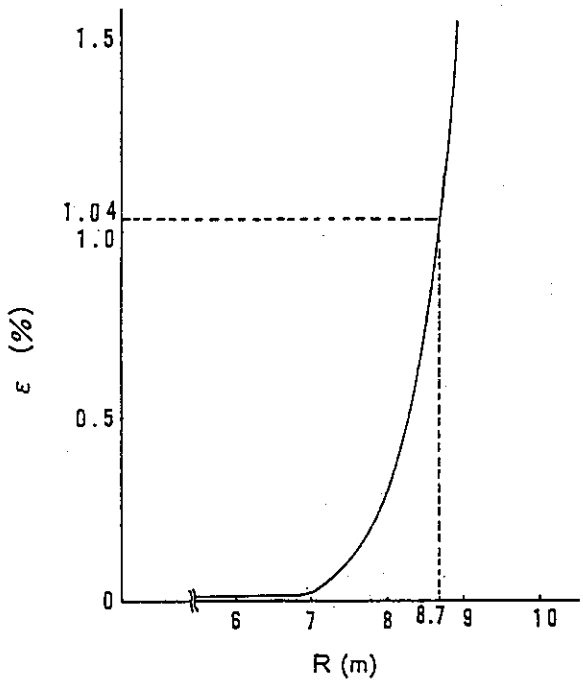

Fig. 5.4.2 Toroidal ripple.

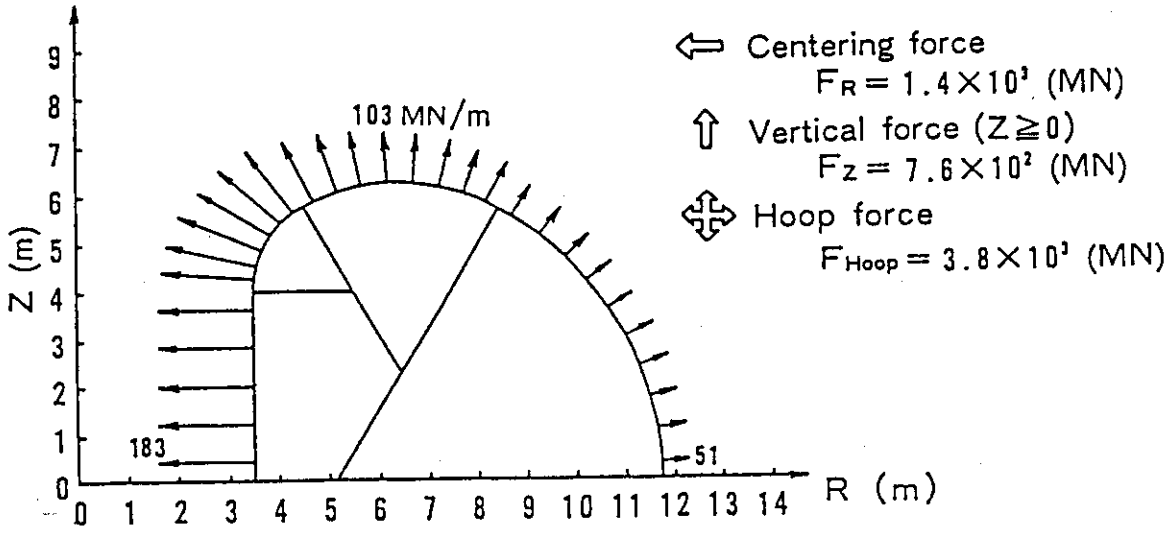

Fig. 5.4.3 In-plane force distribution along the coil mid-plane.

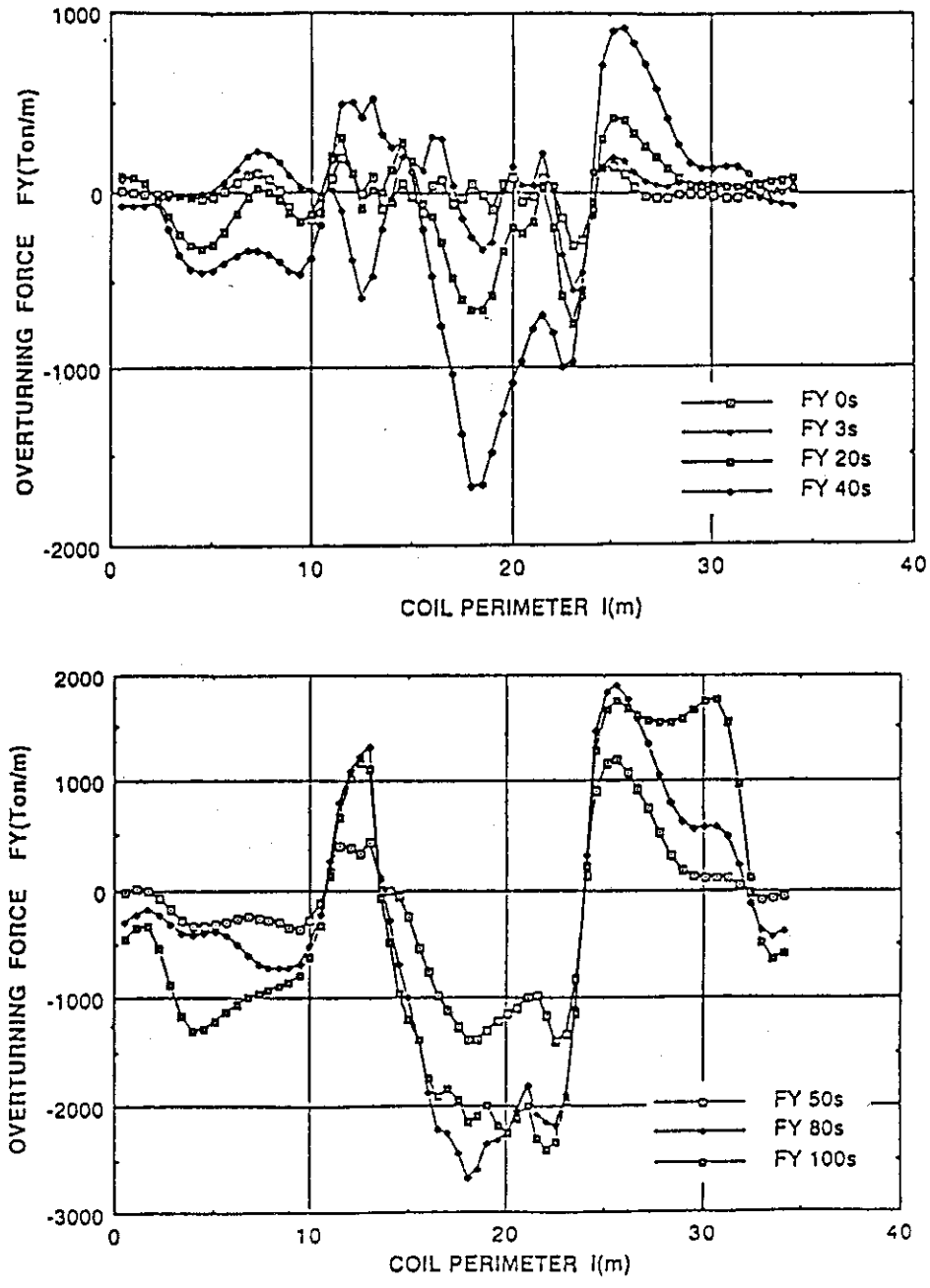

Fig. 5.4.4 Distribution of overturning force per unit length along the coil perimeter.

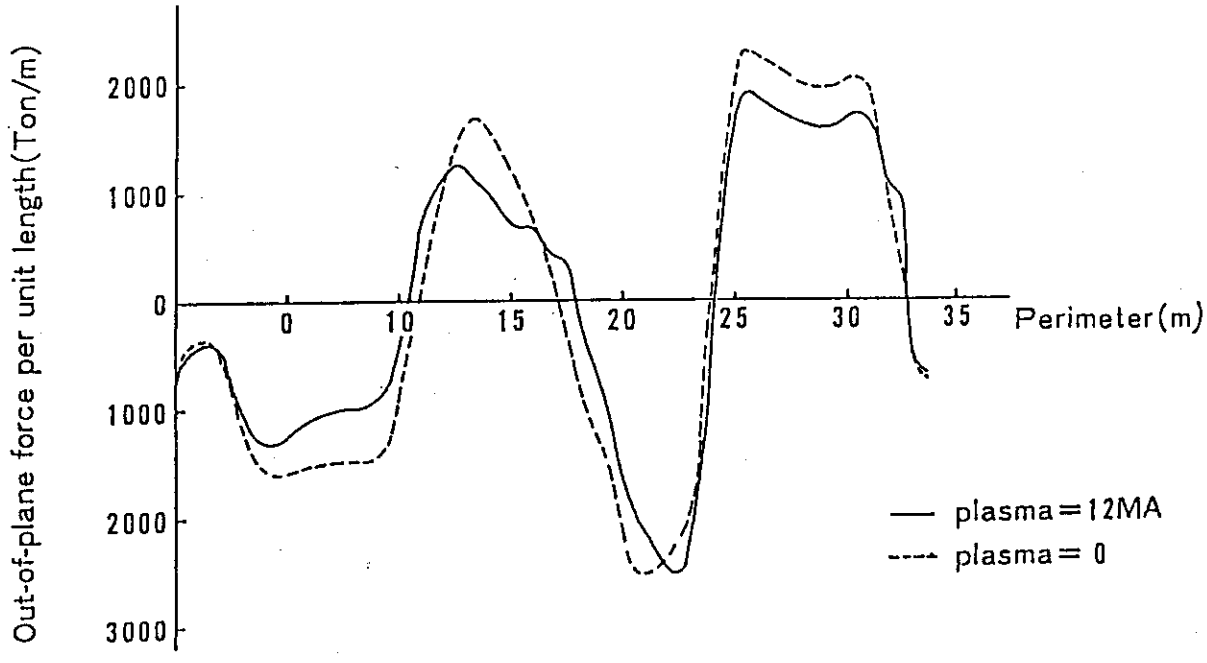

Fig. 5.4.5 Out-of-plane force distribution along the TF coil perimeter for the plasma equilibrium (t=100s).

5.5 Stress Analysis of TF Coils

The TF coils (troidal field coils) must have enough factors of mechanical safety with huge electromagnetic forces. In this paragraph, we are going to describe the model and the result for the stress analysis of TF coils. In this analysis, we use the loads which occur at the plasma disruption and at 100 sec from the plasma made up which is severest condition for TF coils. The coil case's material "JN1", which has high strength, will make the mechanical design of TF coils possible.

5.5.1 Making the Models

(1) The Element Type

- Winding Part
- Coil Case
- Back Support
- Shear Panel

} solid type elements (One solid has 20 nodes.)

(2) The Mesh Drawing

The mesh of a TF coil is shown in Fig. 5.5.1.

(3) The Strength of Elements

1) The Strength of Elements for the Inner-plane Force

· Winding Part

The effective strength members are the only flames (disks). As we agree the spring fixed number of the winding part model with the one of a real winding part, we calculate the equivalent Young's module E_M as follows.

$$K = \frac{EA}{l} = \frac{E_M A_M}{l_M} \quad (l=l_M)$$

$$E_M = \frac{A}{A_M} E = 1.1 \times 10^4 \ (kg/mm^2)$$

E : the Young's module of the flames (disks) 2.1×10^4 (kg/mm^2)

A : the cross-sectional area of the flames (disks) 5.0×10^5 (mm^2)

A_M : the cross-sectional area of the winding part model. 9.5×10^5 (mm^2)

Input data are E_M and ν (Poisson's ratio, 0.3), and they are used in three direction, X, Y, Z.

· Coil Case

The Young's module and the Poisson's ratio of the coil case model are shown as follows.

$E = 2.1 \times 10^4$ (kg/mm^2)

$\nu = 0.3$

· Back Support

As this part's effective strength for the Inner-plane force is small, we use a small value nealy zero to the Young's module of the back support model.

· Shear Panel

Shear panel's effective strength for the Inner-plane force is small as same as the back support, the Young's module of the shear panel model is small. However, the transformation of the model will be larger than that of a coil, because the Young's module of the shear panel model is smaller than that of a real coil.

2) The Strength of Elements for the Out-of plane Force

· Winding Part We agree the strength of the winding part model with that of a coil for the out-of-plane Force.Used formulas are as follows.

$E_i I_i = E_{iM} I_{iM}$

$E_i M = I_i E_i / I_{iM}$

E_i : the Young's module in i direction (i = X, Y, Z)

I_i : the moment of inertia of area in i direction (i = X, Y, Z)

I_{iM} : the moment of inertia of area of the model in i direction (i = X, Y, Z)

The model of a TF coil is on X-Z plane, so $E_X = E_Z$ and $I = I_Z$ and $I_{XM} = I_{ZM}$.

$I_X = I_Z = 1.76 \times 10^{10}$ (mm^4)

$I_Y = 4.97 \times 10^7$ (mm^4)

$E_X = E_Y = E_Z = 2.1 \times 10^4$ (kg/mm^2)

$$I_{xM} = I_{zM} = \frac{1170 \times 812^3}{12} = 5.22 \times 10^{18} (\text{mm}^4)$$

$$I_{YM} = \frac{812 \times 1170^3}{12} = 1.08 \times 10^{11} (\text{mm}^4)$$

so $E_{XM} = E_{ZM} = 7.08 \times 10^3$ (kg/mm^2)

$E_{YM} = 9.7$ (kg/mm^2)

As the Poisson's ratio must satisfy follow formulas, some of them has inappropriate value. But that's influence to the whole transformation is very small, because the strength of the winding is smaller than that of the coil case.

$\nu_{XY} E_X = \nu_{YX} E_Y$

$\nu_{YZ} E_Y = \nu_{ZY} E_Z$

$\nu_{ZX} E_Z = \nu_{XZ} E_X$

The shear module of elasticity of the winding part model is decided to agree the shear transformation of the model with that of a coil.

$$G = Go \frac{A}{A_M} = Go \frac{5.0x10^5}{9.5x10^5} = \frac{21000}{2(1+0.3)} x \frac{1}{1.9} = 4251 kg/mm^2$$

· Coil Case

$E = 2.1 \times 10^4$ (kg/mm^2)

$\nu = 0.3$

· Back support

Though the back support model is a block, we can't make it a block. So it's Young's module may be from $5.0X10^3$ to $2.1X10^4$ kg/mm^2.

$\nu = 0.3$

· Shear Panel

It is the same reason as the back support, and the Young's module may be as follows.

$E = 5.0 \times 10^3 \sim 2.1 \times 10^4$ (kg/mm^2)

$\nu = 0.3$

(4) Load Condition

1) In Case of Inner-plane Force

We use the force which is shown in Fig. 5.4.3, and give the force to the center plane of the winding part model as pressure.

2) In Case of Out-of plane Force

We use the force which is shown in Fig. 5.4.4 (no plasma current), and give the force to the center plane of the winding part model as pressure.

(5) Boundary Condition

1) Periodical Boundary Condition

A nose surface or a shear panel surface may adhere to the next because of inserted keys, so periodical boundary condition is used at nose surfaces in case of both inner-plane force and out-of-plane force, and used at shear panel surfaces in case of the out-of plane force. (see Fig. 5.5.2)

2) Support Condition

Supporting a point of a TF coil's leg, the motion of that point is stopped in upper and lower and troidal direction. And condition 1) is as same as the support condition in radial direction.

5.5.2 The Result of Stress Analysis

1) The Result of Stress Analysis in case of Inner-plane Force

·The drawing of tranceformation is shown in Fig.5.5.3. The maximum transformation occurs at the upper part of the coil, and is 27 mm upward.

The distribution of stress is shown in Fig. 5.5.4.

The maximum stress occurs at the coil case in the coil nose part, shown in Fig. 5.5.6, is 85 kg/mm^2.

The component of the stress is shown in Fig.5.5.5, so we can see the membrane stress is as follows.

y-y component of stress 46 kg/mm^2

(compressive stress by nose surface's pressure)

z-z component of stress 34 kg/mm^2

(tensile strain by foop force)

2) The Result of Stress Analysis in case of Out-of plane Force.

The drawing of transformation is shown in Fig. 5.5.7 and Fig. 5.5.8 on condition that the Young's module of the shear panel model is 2.1X10^4 kg/mm^2.

The maximum transformation occurs at the upper shear panel and is 28 mm in troidal direction.

The distribution of the shear stress is shown in Fig. 5.5.9.

The strength of stress in coil nose part will be less than 9 kg/mm^2.

3) Evaluation of the stress compared with an allowable stress.

We evaluate the stress at the center (Y=0, Z=0) of the coil case in the nose part, and obtaiin the following table.

		membrane stress	membrane stress + bending stress
Inner-plane force	y-y component	34	85
	z-z component	46	
out-of-plane force		—	* less than 9
sum		80	** 85.5
allowable stress		80	120

(unit : kg/mm^2)

* shear stress

** $\sqrt{85^2 + 4 \times (\frac{9}{2})^2} = 85.5$

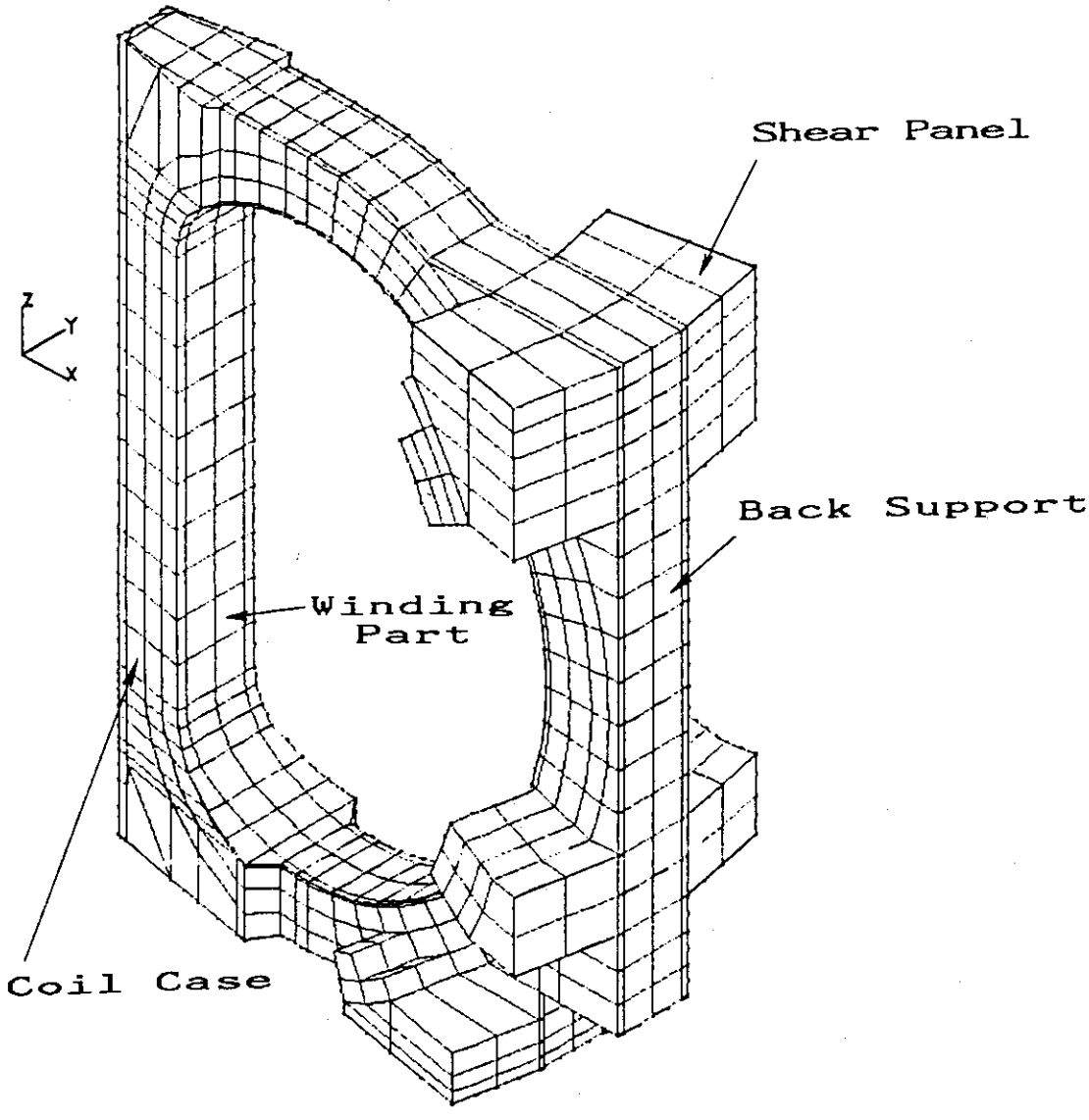

Fig. 5.5.1 Mesh drawing of a TF coil.

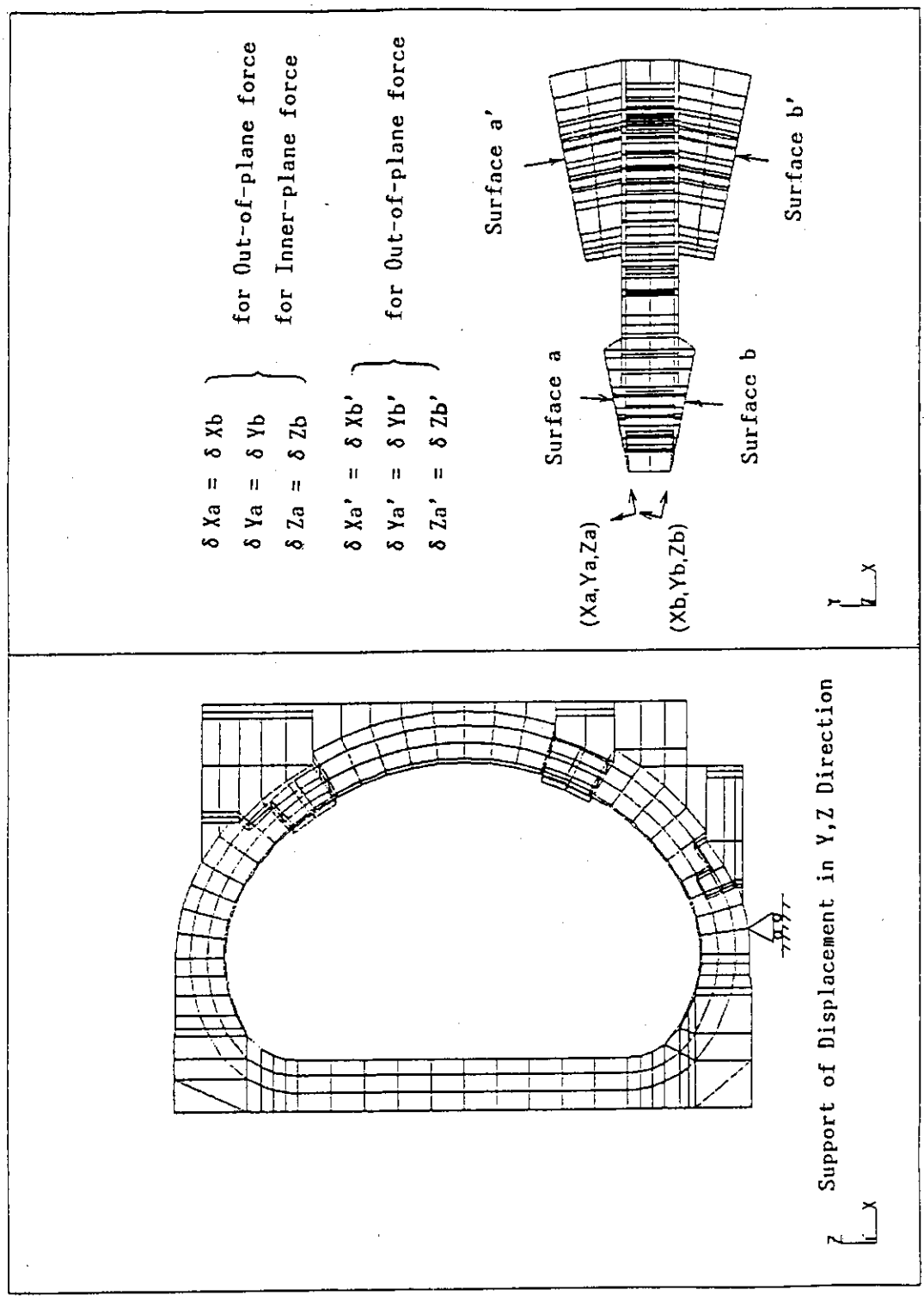

Fig. 5.5.2 Boundary condition.

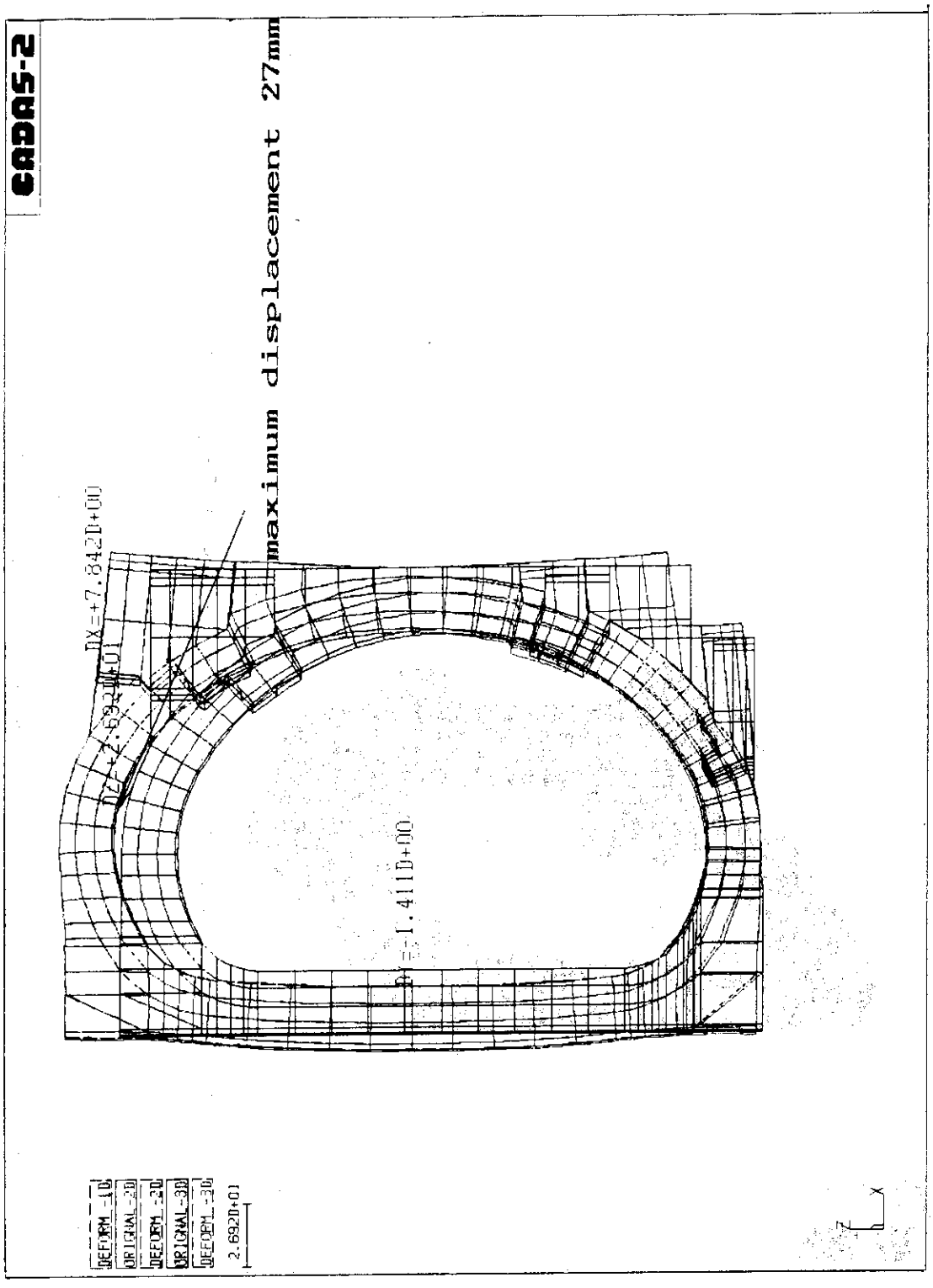

Fig. 5.5.3 Displacement by the inner-plane force.

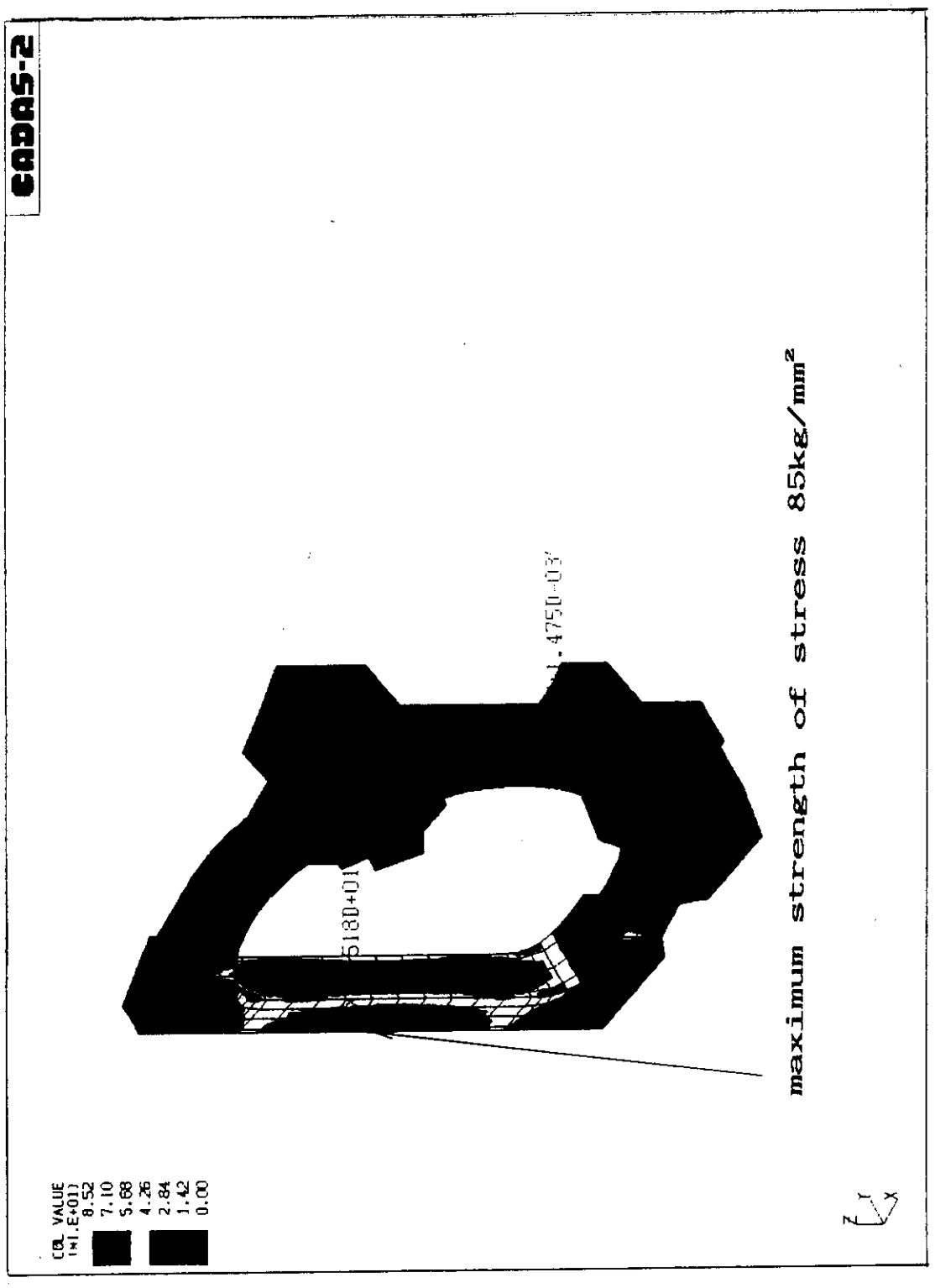

Fig. 5.5.4 Distribution of the strength of stress by the inner-plane force.

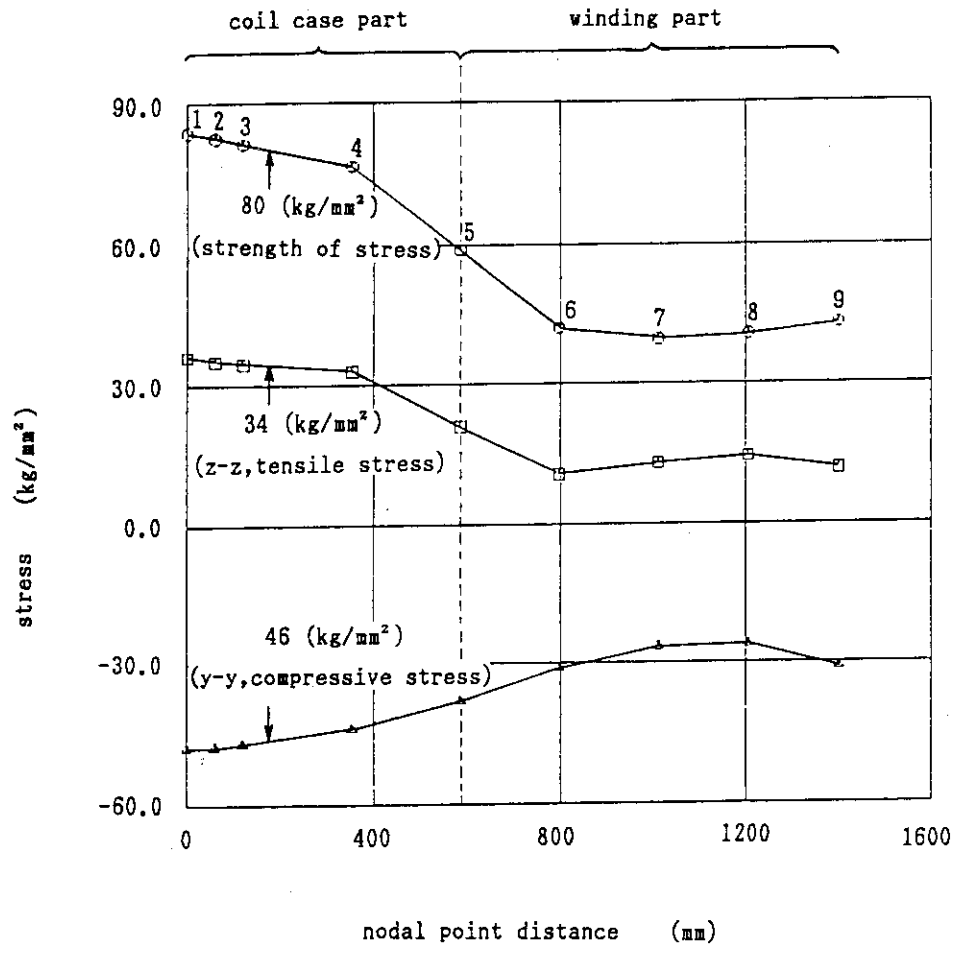

Fig. 5.5.5 Distribution of the stress at the center of a nose.

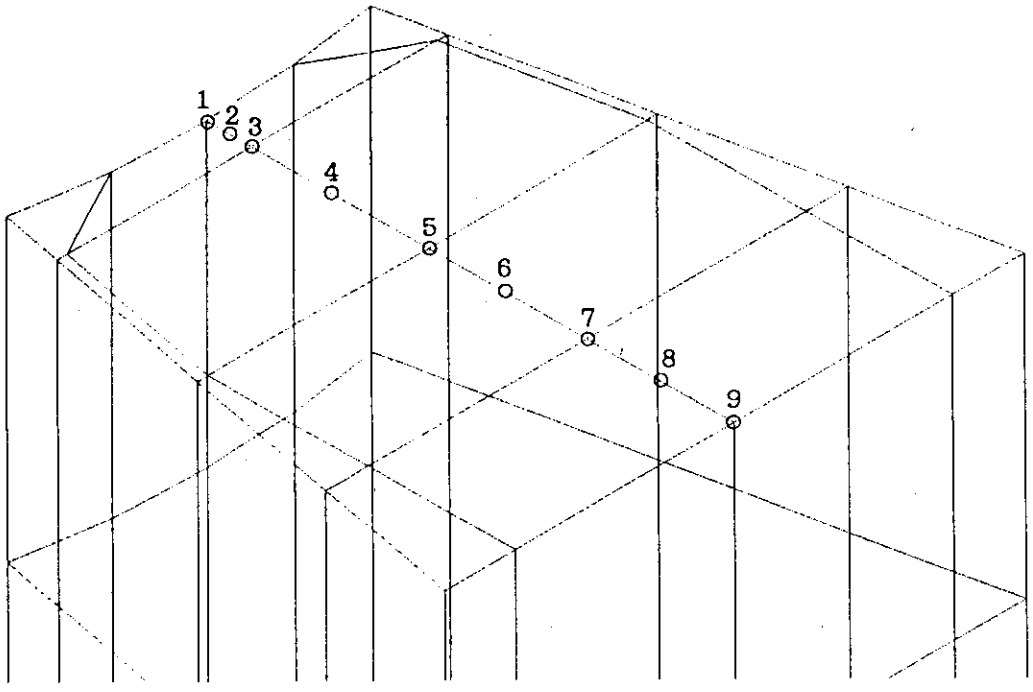

Fig. 5.5.6 Calculating point at the center of a nose.

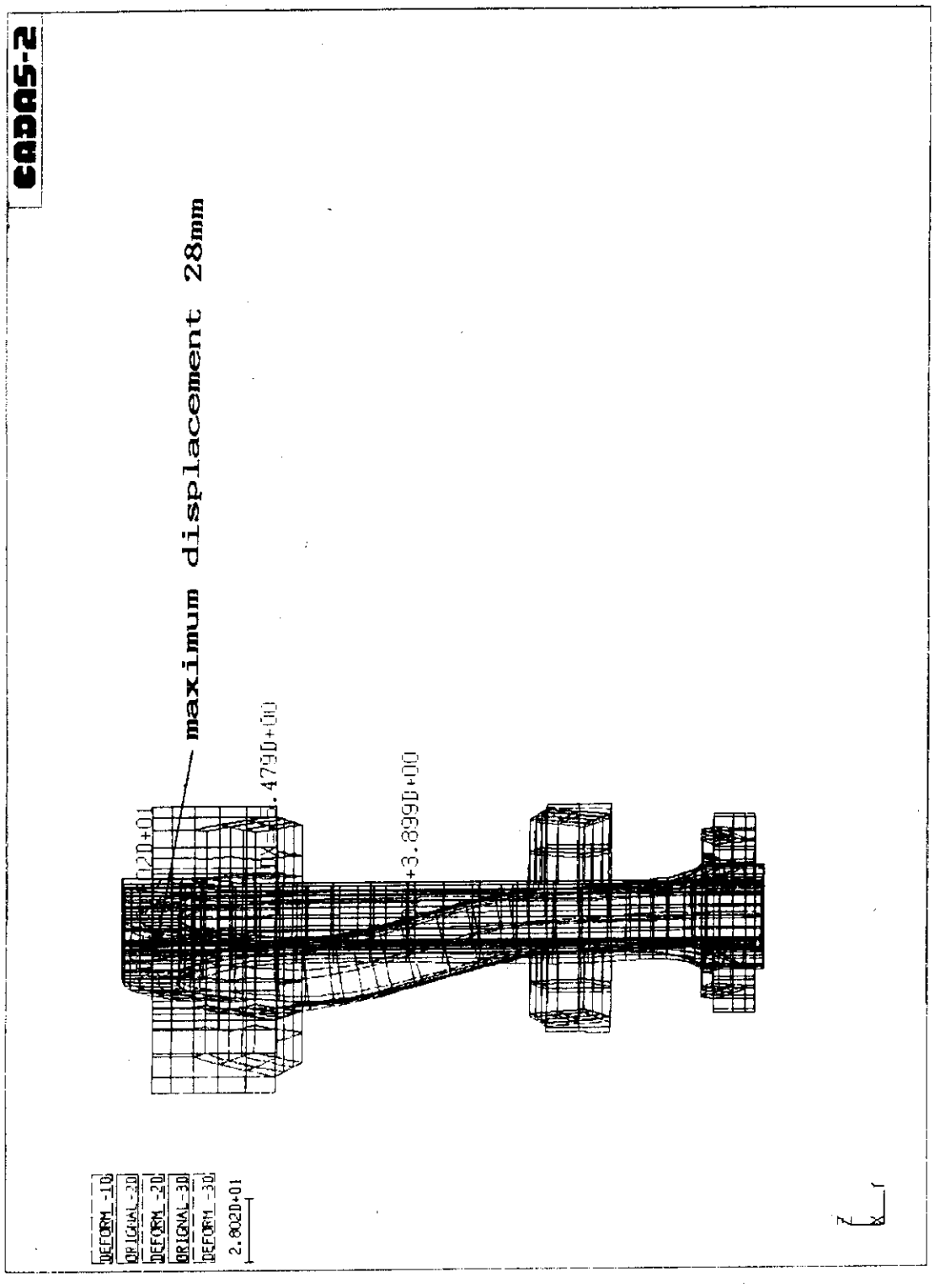

Fig. 5.5.7 Displacement by the out-of-plane force.

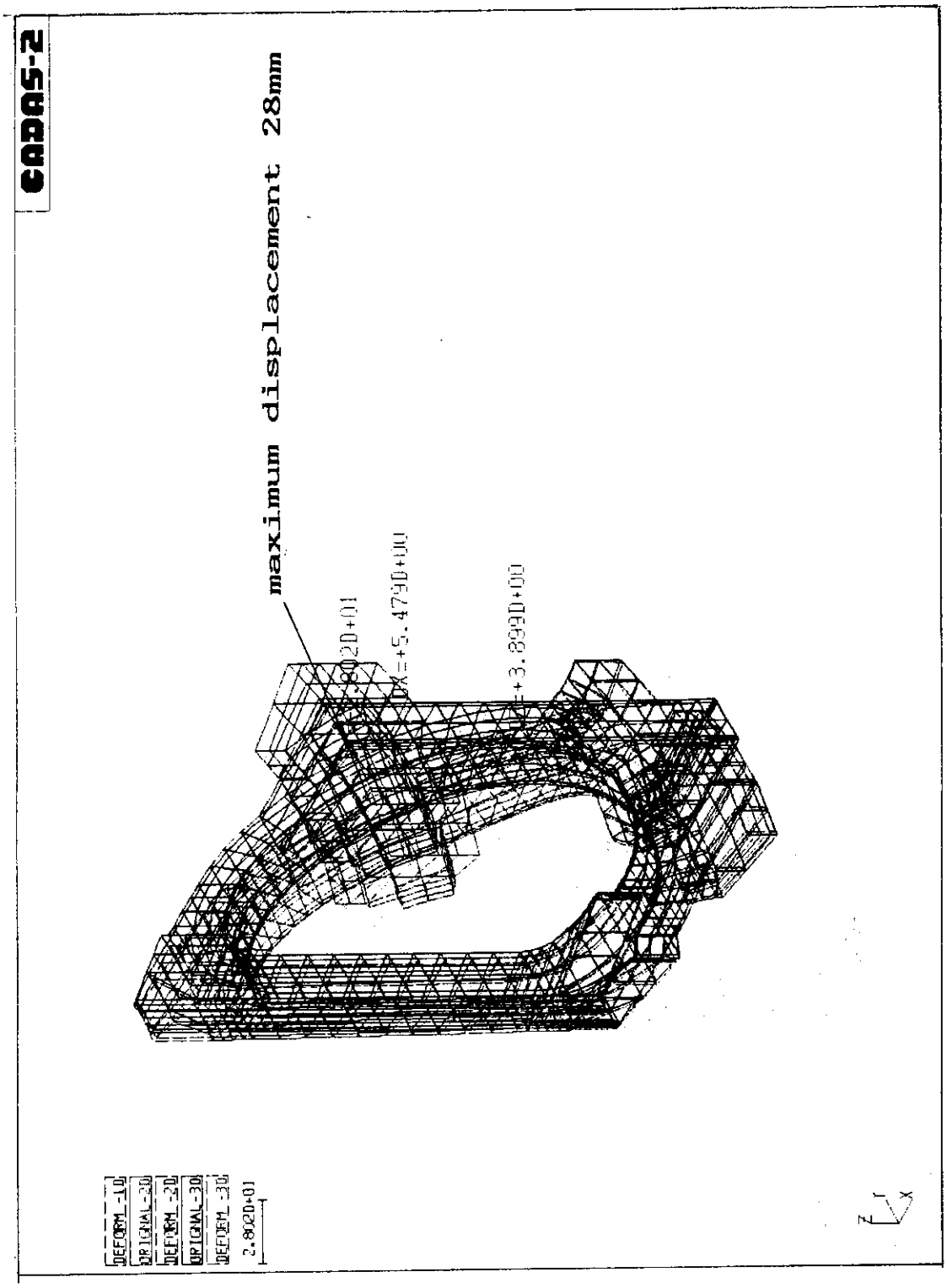

Fig. 5.5.8 Displacement by the out-of-plane force.

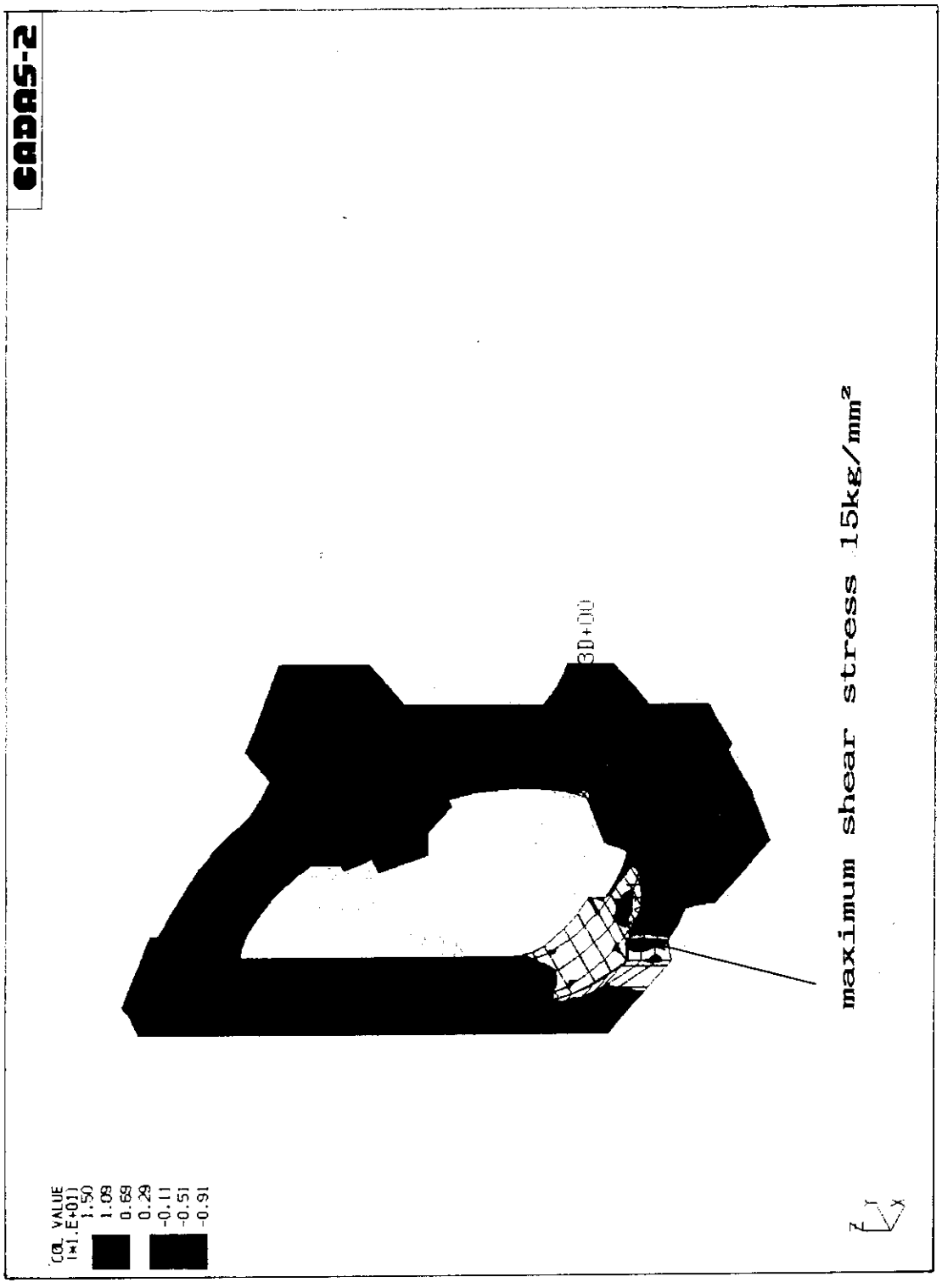

Fig. 5.5.9 Distribution of the shear stress by the out-of-plane force.

5.6 Thermal Analysis

The thermal loads that are generated on the toroidal field coil are important factors for deciding the capacity of cryogenic system.

The thermal loads are the following,

(1) AC loss : The toroidal field coil is subject to the AC loss due to the changing field. The superconductor AC loss is conveniently divided into three contributions, i.e. the hysteresis loss, the eddy current loss and the coupling loss.

(2) nuclear heating : The toroidal field coil is subject to the nuclear heating dou to the neutron of 14 MeV according to the nuclear fusion reaction.

(3) Thermal entrances : These are the thermal entrances from the adiabatic support, the feeder of the measuring instrument, the pipe and the power llead.

(4) Follwing loss of the helium : This is the loss according to the flowing helium in the coil.

Expressly the AC loss, the thermal entrance and the following loss of the helium are described in this chapter.

5.6.1 AC Loss

The AC loss-formulas are given by the Table 5.6.1 according to the JAFRI-M 88-110.

Fig. 5.6.1 and Fig 5.6.2 show the distribution of magnetic fields (BU and BP) along the perimeter on the toroidal field coil according to the operation scenario of SSTR.

where,

B_u : perpendicular magnetic field to the conductor

B_P : parallel magnetic field to the conductor

and Fig 5.6.3 show the distribution of dBv,dBp along the perimeter on the toroidal field coil in plasma disruption at the 100 second from rising up the plasma.

Where, the duration time is 400 msec, and it considers the shield effect of the vacuum vessel for the plasma dismption time (t=20 msec). The AC loss is most generated in the nose section of the toroidal field coil, and the AC loss is 3.5 MJ per a unit coil.

If the AC loss is almost consume in the superconductor, the amount of heat of the conductors unit volume is 0.2/3 J/cm^3 and this value is less than the stability margin (ΔH=0.7 J/m^3) of the conductor, the toroidal field coil does not quench.

Fig 5.6.4 shows the AC loss of the all toroidal field coil according to the operation scenario. The average thermal load is 0.94 kW. However, the AC loss of the toroidal field coil support structure is not included in this analysis.

5.6.2 Thermal Entrance

The thermal entrance for the toroidal field coil is estimated in this section.

The thermal entrances are following,

1) thermal conduction from the support leg.

2) radiation from the 80 K shield.

3) remaining gas conduction of the vacuum region

4) heat load of the power lead

5) joule loss of the connected part

1) Theramal conduction from the support leg.

a) Theramal conduction from the outside support leg.

This heat load is given the next equation according to the JAERI-M86-134 (P.351, 352, 371, 372).

$$Q_{cond} = \frac{A}{L}\int_{T1}^{T2}\lambda \; dT \; (W)$$

where,

A : thermal conduction area

L : distance between the temparature A_1 to and the temparature A2 (m^2)

λ : thermal conductinity (W/m · k)

A is 0.4084m^2, L is 0.2m^{-1} and

$\int_{T1}^{T2}\lambda \; dT = 20$ (W/m)

Therefor

$$Q_{cond} = \frac{4.084 \times 10^{-1}}{2.0 \times 10^{-1}} \times 20 \times 16 = 653 \; (W)$$

b) Thermal conduction from the inside support leg If the dimensions of the inside support leg are the external form 3.6 m, the depth 0.2 m the thermal conduction from the inside support leg is follow.

$$Q_{cond} = \frac{A}{L}\int_{T1}^{T2}\lambda \; dT = \frac{\pi \times 3.4 \times 0.2}{2.0 \times 10^{-1}} \times 20 = 214 \; (W)$$

There the tatal value is about 870 (W).

2) Radiation from the 80 K shield

$$Qrad = 5.76 \times 10^{-8} \cdot A \cdot Fe \cdot (T_2^4 - T_1^4)$$

where,

$$Fe = (\varepsilon_1^{-1} + \varepsilon_2^{-1} - 1)^{-1}$$

$$\varepsilon_1 = \varepsilon_2 = 0.1$$

Therefor

$$Qrad = 5.76 \times 10^{-8} \cdot A \cdot (10 + 10 - 1) \times (80^4 - 4.2^4)$$
$$= 0.12 \cdot A \ (W)$$

Here

Fe : geometrical factor

ε_1 ; ε_2 : each emissivity of the 80 K support structure and the 4.2 K support structure.

If the surface are of the toroidal field coil is about 1.5 times of the winding part of the toroidal field coil, the radiation from the 80 K shield is follow,

$$A = 1.5 \times 34.9 \times \{1.4 \times 2 + (3.89 - 2.61) \times 2\} \times 16 = 4490 \ (m^2)$$

Where the averave perimeter of the toroidal field coil is 34.9 (m)

Therefore

$$Q_{rad} = 540 \ (W)$$

3) Remaining gas conduction of the vacuum region.

The amount of the thermal conduction at the molecula flow region is given follow.

$$Q_{reg} = 3.32 \times 10^2 \frac{1}{\sqrt{M}} \frac{\gamma^{+1}}{\gamma^{-1}} F_2 \, P \, A \, (T_2 - T_1)$$

$$F_2 = (\alpha_1^{-1} + \alpha_2^{-1} + 1)^{-1} \quad (\alpha_1 = \alpha_2 \approx 1)$$

where

M	: molecular weight	28.8 (kg/mol)
g	: specific heat ratio	1.41
P	: pressure	1.33×10^{-5} (Pa)
A	: thermal conducion area	4490 (m^2)

α_1;α_2 : geometrical factor of the each temparature area.

Therefore

$$Q_{reg} = 520 \ (W)$$

4) Heat load of the power lead

The optimum structure of the power lead is given next equations.

$$\left(\frac{S}{LI}\right)_{opt} = 4.08 \times 10^{-5} \times \left(\frac{\rho_{300k}}{\rho_{4.2k}}\right)^{-0.574}$$

$$\left(\frac{Q}{I}\right)_{min} = 1.72 \times 10^{-3} \times \left(\frac{\rho_{300k}}{\rho_{4.2k}}\right)^{-0.0865}$$

wherer

f_{300k} : specific resistivity of the power lead at 300 K. (Ω-cm)

$f_{4.2k}$: specific resistivity of the power lead at 4.2 K (Ω-cm)

S : cross section area of the power lead (m^2)

L : length of the power lead (m)

I : rated current (A)

Therefore, the thermal entrance of the power lead at no current is given next equation.

$$Q = 0.058 \times \frac{S}{L} \int_{4.2k}^{300k} \lambda \, dT$$

where

$\int_{4.2k}^{300k}$: integration of the power leads thermal conductivity.

The structure of the power lead was decided by the above equation and we calculated for the confirmation.

The Table 5.6.2 shows the result.

5) Joule loss of the connected part

If the number of the connected part is 10 per a unit coil and the resistance of the connected part is $10^{-9}\Omega$, the safety factor is 2, the joule loss is given follow.

$$Q_{jou} = Ri^2 \times N \times f = 10^{-9} \times (81 \times 10^3)^2 \times 10 \times 16 \times 2 = 2100 \ (W)$$

5.6.3 Flowing Loss

The flowing loss of the holium is given the next equation.

$$Q_f = m \cdot \Delta P \cdot V \ (W)$$

where,

m : circulation mass flow rate (kg/s)

ΔP : head loss (Pa)

V : specific gravity of the helium

The flowing loss of the helium is given to substitute the each value for the above equation.

$$Q_f = 4.9 \times 2.026 \times 10^5 \times 6.72 \times 10^{-3} = 6671 \ (W)$$

However, we consider this loss on the chapter 5.8. The above result is put in the Table 5.6.3. The Table 5.6.4 shows the loss of the during operation.

Table 5.6.1 AC loss formulas

AC loss	No	Models	Formulas	Notes
Hysteresis loss	1	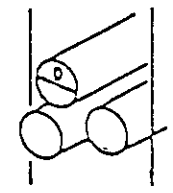	• $Q_\perp = \frac{B_m^2}{2\mu_0} \cdot 2\left\{\frac{2\beta}{3} - \frac{\beta^2}{3}\right\} \cdot Asc$ $(\beta \le 1)$ (J/cycle·m) • $Q_\perp = \frac{B_m^2}{2\mu_0} \cdot 2 \cdot \left\{\frac{2}{3\beta} - \frac{1}{3\beta^2}\right\} \cdot Asc$ $(\beta \ge 1)$ (J/cycle·m) • $\beta_\perp = \frac{\pi B_m}{2\mu_0 J_c D}$	Asc : Area of S.C material (m²) $\left[A_{sc} = N \cdot \pi D^2/4\right]$ N : No of filaments J : Critical current density (A/m²) D : Filament diameter (m) B_m : Oscillating field amplitude (T)
	2	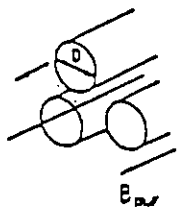	• $Q_\parallel = \frac{B_m^2}{2\mu_0} \cdot \left\{\frac{2\beta}{3} - \frac{\beta^2}{3}\right\} \cdot Asc$ $(\beta \le 1)$ (J/cycle·m) • $Q_\parallel = \frac{B_m^2}{2\mu_0} \cdot \left\{\frac{2}{3\beta} - \frac{1}{3\beta^2}\right\} \cdot Asc$ $(\beta \ge 1)$ (J/cycle·m) • $\beta_\parallel = \frac{B_m}{\mu_c J_c D}$	
Eddy current loss	1	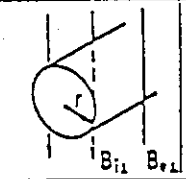	• $P_{e\perp} = 16 \cdot \frac{\dot{}}{n} \frac{\tau_n}{k_n^2} \cdot \frac{\dot{B}_{i\perp}^2}{2\mu_0} \cdot Ac$ (W/m) • $\tau_n = \frac{\mu_c r^2}{\rho k_n^2}$ (sec)	r : Conductor radius (m) Ac : πr^2 (m²) $J_0(k_n) = 0$: Bessel function $k_1 = 2.405$ $k_4 = 11.792$ $k_2 = 5.520$ $k_5 = 14.931$ $k_3 = 8.654$ $k_6 = 18.071$
	2	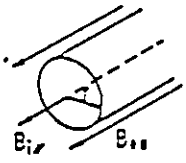	• $P_{e\parallel} = 8 \cdot \frac{\dot{}}{n} \frac{\tau_n}{k_n^2} \cdot \frac{\dot{B}_{i\parallel}^2}{2\mu_0} \cdot Ac$ (W/m) • $\tau_n = \frac{\mu_c r^2}{\rho k_n^2}$ (sec)	
	3	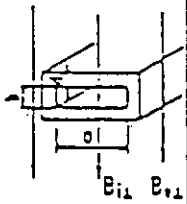	• $P_{e\perp} = \frac{a+2b}{4(a+b)} \cdot \frac{a}{d} \cdot \tau_\perp \cdot \frac{\dot{B}_{i\perp}^2}{2\mu_0} \cdot Ac$ (W/m) • $\tau_\perp = \frac{\mu_0 a d}{4\rho}$ (sec)	d : Conductor width (m) A : $2d(a+b)$ (m²)
	4	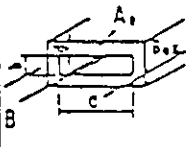	• $P_{e\parallel} = \frac{ab}{d(a+b)} \cdot \tau_M \cdot \frac{\dot{B}_{i\parallel}^2}{2\mu_0} \cdot Ac$ $(d \ll a, b)$ (W/m) • $\tau_\parallel = \frac{\mu_0 d a b}{2\rho(a+b)}$ (sec)	
	5	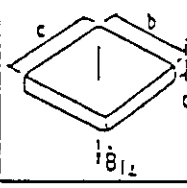	• $P = \frac{\sigma d}{8\pi} \cdot \dot{B}_{i\perp}^2 \cdot A^2 \cdot l$ (W) • $l = 0.6\pi\left(\frac{b}{c} + \frac{c}{b}\right)^{-1}$	A : $b \cdot c$ (m²)

Table 5.6.1 (Continued)

AC loss	No	Models	Formulas	Note
Filament Coupling loss	1	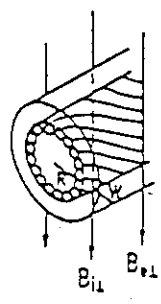	• $P_{c1} = 4 \cdot \tau_\perp \cdot \frac{\dot{B}_{i\perp}^2}{2\mu_0} \cdot A_{scs}$ (W/m) • $\tau_\perp = \frac{\mu_0}{2\rho_{ef}} \left(\frac{l_p}{2\pi}\right)^2$ (sec) • $\frac{1}{\rho_{ef}} = \frac{1}{\rho_\perp} + \frac{W}{R} \cdot \frac{1}{\rho}$ (1/Ωm) • $\rho_\perp = \frac{1+\lambda}{1-\lambda}\rho$	A_{scs} Cross section of S.C.area $\left[A_{scs} = \pi R^2\right]$ (m²) l_p : Twist pitch (m) R : Radius of SC area (m) W : Width of surrounding condactor (m) ρ_{ef} : Effective resistivity (Ωm) $\rho_\perp$: Perpendicular resistivity (Ωm) λ : Proportion of S.C. material
	2	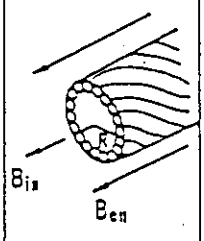	• $P_{c\parallel} = \frac{R}{D} \cdot \tau_\parallel \cdot \frac{B_{i\parallel}^2}{2\mu_0} \cdot A_{scs}$ (W/m) • $\tau_\parallel = \frac{\mu \cdot RD}{2\rho_\parallel} \left(\frac{2\pi R}{l_p}\right)^2$ (sec) • $\rho_\parallel \sim \rho_\perp$ $\left(P_{c\parallel} = \frac{1}{\rho_\parallel}\left(\frac{\pi}{l_p}R^2\right)^2 \cdot B_i^2\right)$	

Table 5.6.2 Heat load from power lead

	non exciting	exciting
heat load from a power lead	≃ 0 W (5.63 g/s)	23.7W (5.63 g/s)
heat load from all power leads	≃ 0 W (180 g/s)	≃ 760W (180 g/s)

( ) : He vaporization rate

Table 5.6.3 Heat load of TFC

item	loss(kW)
AC loss + joule loss of connected part	14.7 + 2.1
thermal conduction from support leg	0.87
radiation from 80K shield	0.54
remaining gas conduction of vacuum region	0.52
heat load of power leads	0.76
flowing loss of helium	6.67

Table 5.6.4 Heat load of TFC for the operation scenario

	normal operation	plasma starting-up	plasma disruption
heat load	7.8 kW	19.5 kW	1.44×10^5 kW
He flow rate	4900 g/s	4900 g/s	4900 g/s
vaporization rate	5200 ℓ/hr	5200 ℓ/hr	5200 ℓ/hr

flowing loss of helium is not included in this Table

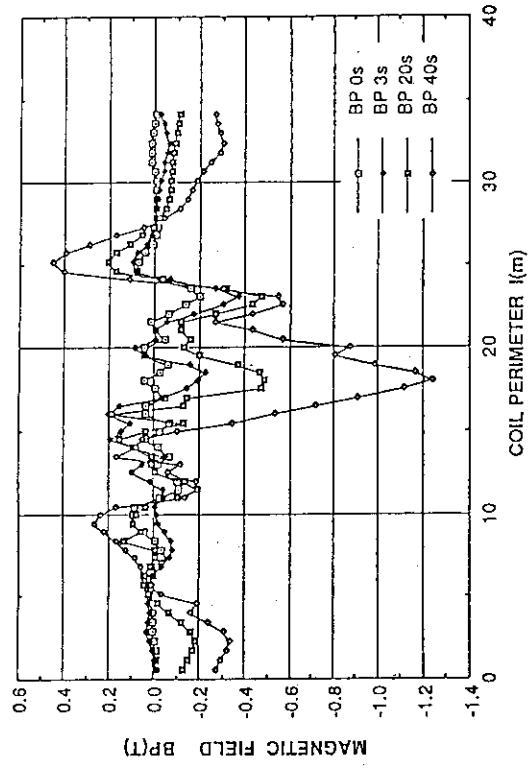

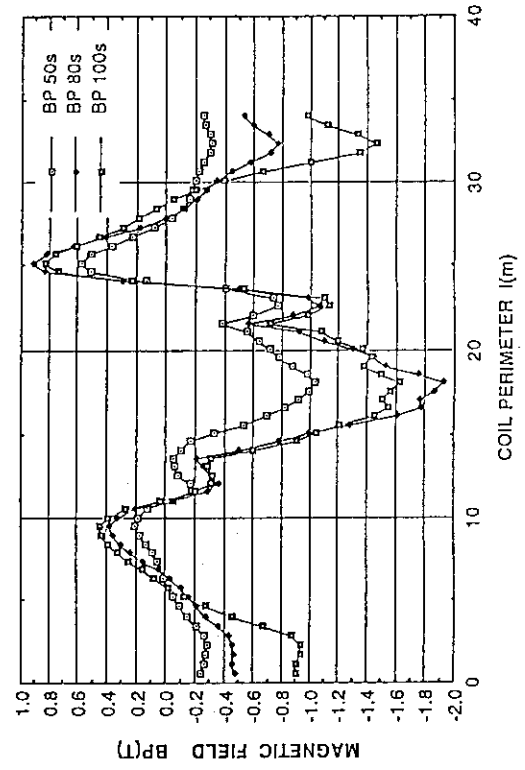

Fig. 5.6.2 Distribution of magnetic field BP along coil perimeter.

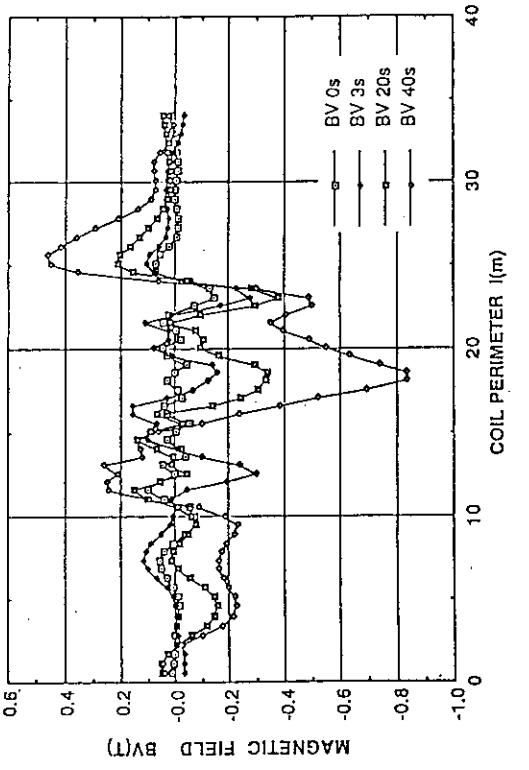

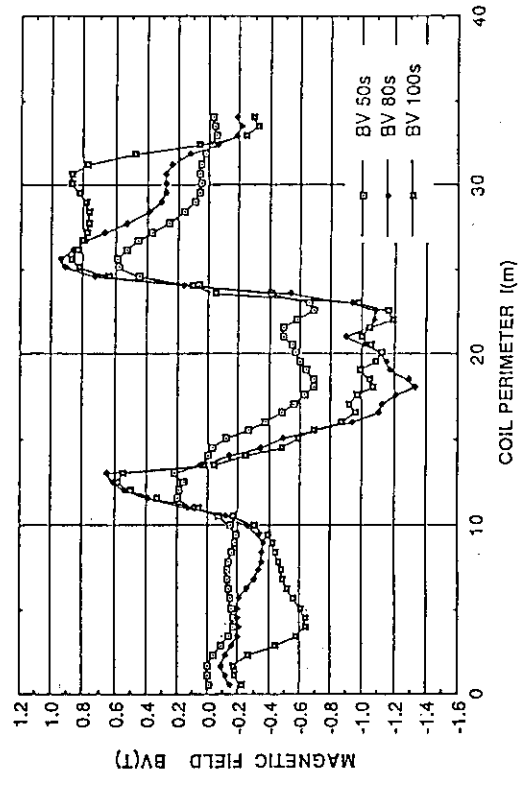

Fig. 5.6.1 Distribution of magnetic field BV along coil perimeter.

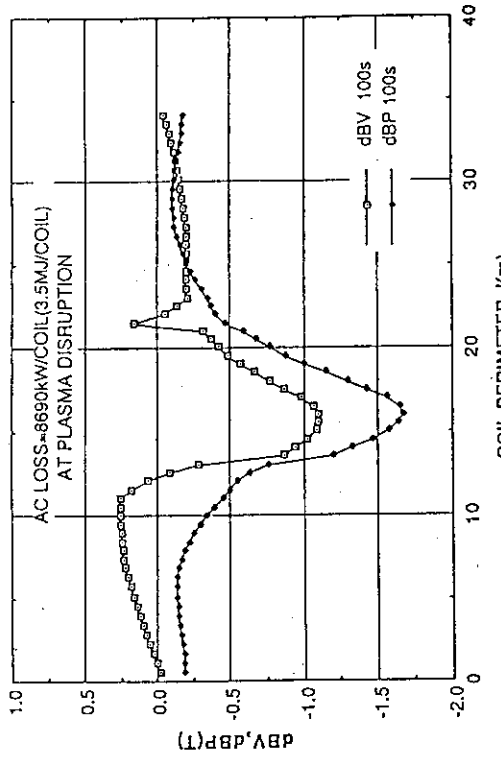

Fig. 5.6.3 Distribution of dBV, dBP along coil perimeter in plasma disruption.

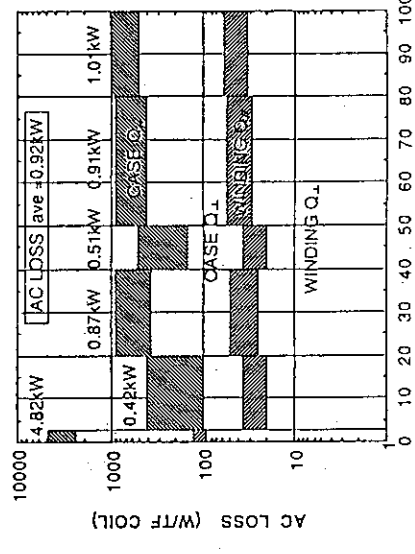

Fig. 5.6.4 AC loss in TF coils.

5.7 Electric Circuit and Protection Analysis

The protection analysis for the superconducting magnet in the quench is detailed in this section and the chapter 14 is described about the electric circuit more precisely. In the case of the quench, the stored energy of the superconducting coil is discharged through the dump resistor to protect the coil from such damages as a short circuit between turns and the coil case and a conductor breaks or melt down. Setting the dump resistivity higher keeps joule heat lower generated in the coil and makes the current decay time shorter, so that a brake down of the coil insulation due to thermal stress should be avoided. On the other hand, the sump resistivity is limited by an allowable coil insulation voltage. From the view point of the coil protection, the coil insulation voltage should be designed to keep the maximum temperature of the superconductor less than 70 K during the quench.

The maximum temperature of the toroidal field coil for the SSTR is calculated by a HOT SPOT MODEL (adiabatic analysis) and discussed the relationships between the stored energy, the dump voltage, and the current density of the Cu stabilizer in the superconductor. Following eqn.(5.7-1) gives the heat balance in the part of the superconductor where the quench is caused.

$$I^2Rdt = \sum \gamma i Ci(T) VidT \qquad \text{(5.7-1)}$$

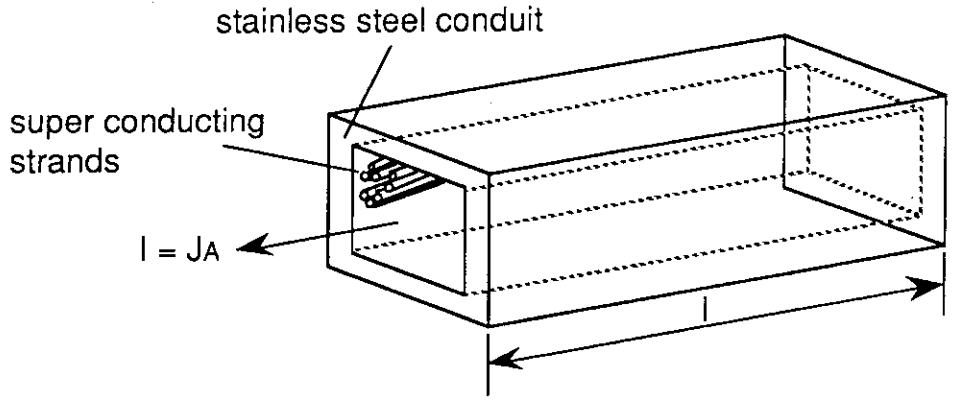

$$A = A_{cond} + A_{He} + A_{SUS} + A_{ins}$$

$$A_{cond} = A_{Cu} + A_{sc}$$

$$R = \rho_{cu} \cdot \frac{l}{A_{Cu}}$$

Where,

I	: rated current [A]
J	: current density of superconductor [A/m^2]
A	: cross section of super conductor [m^2]
A_{cond}	: cross section of superconducting strand [m^2]
A_{CU}	: cross section of CU stabilizer [m^2]
A_{SC}	: cross section of superconducting material [m^2]
A_{He}	: cross section of coolant path [m^2]
A_{SUS}	: cross section of stainless steel conduit [m^2]
A_{ins}	: cross section of conductor insulation [m^2]
γ	: specific gravity [kg/m^3]
C(T)	: specific heat [J/kg K]
V	: volume [m^3]
i	: components CU, SC, He, SUS, Insulator
ρ_{CU}	: specific resistivity of CU stabilizer

Eqn.(5.7-1) is transformed as follows.

$$\int_0^\infty J^2 A^2 \rho_{CU}(T) \frac{\ell}{A_{CU}} dt = \int_{Tb}^{Tm} \sum_i \gamma_i C_i(T) V_i dT$$

$$\therefore \int_0^\infty J^2 dt = \int_{Tb}^{Tm} \sum_i \frac{A_{CU} \cdot V_i}{\ell \cdot A^2} \cdot \frac{\gamma_i C_i(T)}{\rho_{CU}(T)} dT$$

$$= \sum_i \int_{Tb}^{Tm} \frac{A_{CU} \cdot A_i}{A^2} \cdot \frac{\gamma_i C_i(T)}{\rho_{CU}(T)} dT \quad ------(5.7\text{-}2)$$

Where,

T_b	: initial temperature of coolant [K]
T_m	: maximum temperature of superconductor during quench [K]

Following picture shows the fundamental electric circuit including the dump resistor for the superconducting magnet.

Where,

L	: coil inductance [H]
R	: dump resistivity [ohm]
t_{lag}	: time lag between coil dumping and start of quench

Decay of the coil current after opening the switch is expressed by the following eqn.(5.7-3).

$$\int_0^\infty J^2(t)\,dt = \int_0^\infty J^2 \exp\left[-\frac{2(t-t_{lag})}{\tau}\right] dt$$

$$= J^2\left(\frac{\tau}{2} + t_{lag}\right) \qquad \text{----------(5.7-3)}$$

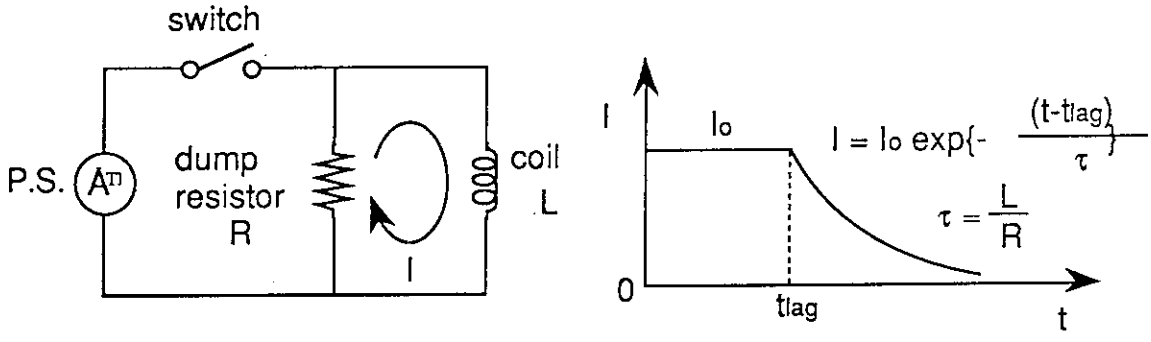

Where,

$\tau = L/R$: coil current decay time [sec]

$E=LI^2/2$: stored energy [J]

V : coil dump voltage during quench

$$\tau = \frac{L}{R} = \frac{2E}{RI^2} = \frac{2E}{V \cdot I} \qquad \text{----------(5.7-4)}$$

In the case of $t_{lag}=0$, the eqn.(5.7-2) is simplified as follows by the eqn.(5.7-3) and (5.7-4).

$$\frac{E}{V \cdot I} J^2 = \sum_i \frac{A_{CU} \cdot A_i}{A^2} \int_{Tb}^{Tm} \frac{\gamma_i C_i(T)}{\rho_{CU}(T)} dT$$

$$\therefore\ J = \left\{\frac{V \cdot I}{E} \sum_i \frac{A_{CU} \cdot A_i}{A^2} \int_{Tb}^{Tm} \frac{\gamma_i C_i(T)}{\rho_{CU}(T)} dT\right\}^{1/2} \qquad \text{----(5.7-5)}$$

Where $I_1 = \int_{Tb}^{Tm} \frac{\gamma\ C_{He}(T)}{\rho_{CU}(T)} dT$, $I_2 = \int_{Tb}^{Tm} \frac{\gamma_{CU} C_{CU}(T)}{\rho_{CU}(T)} dT$,

$I_3 = \int_{Tb}^{Tm} \frac{\gamma_{SC} C_{SC}(T)}{\rho_{CU}(T)} dT$, $I_4 = \int_{Tb}^{Tm} \frac{\gamma_{SUS} C_{SUS}(T)}{\rho_{CU}(T)} dT$,

$I_5 = \int_{Tb}^{Tm} \frac{\gamma_{ins} C_{ins}(T)}{\rho_{CU}(T)} dT$

The eqn.(5.7-5) is transformed to followings.

$$J = \left\{ \frac{V \cdot I}{E} \cdot \frac{A_{CU}}{A^2} \left(A_{He} \cdot I_1 + A_{CU} \cdot I_2 + A_{SC} \cdot I_3 + A_{SUS} \cdot I_4 + A_{ns} \cdot I_5 \right) \right\}^{1/2} \quad \text{----------} \quad (5.7\text{-}6)$$

Fig.5.7-1 shows the temperature dependence of I1(He), I2(CU), I3(SC), I4(SUS) and I5(INS).

The eqn.(5.7-6) shows the relationship between the maximum temperature T_m and current density J in the case superconducting magnet with he rated current I, the stored energy E and the dump voltage V.

Fig.5.7-2 depicts the relationship between T_m and J with the parameter of the dump voltage V for the toroidal coil the SSTR. As the coil surrent density J=41.25 A/mm^2 is designed, the dmp voltage should be selected V=20 kV in order to keep the maximum temperature T_m of the superconductor less than 70 K.

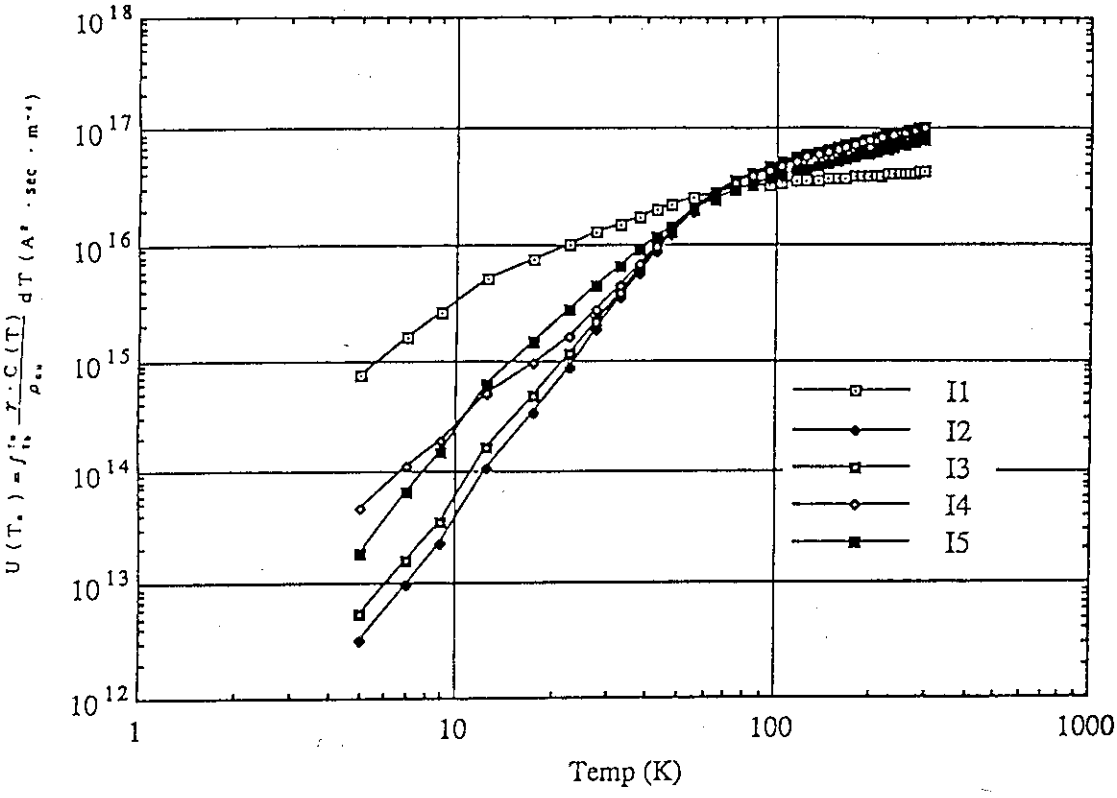

Fig. 5.7.1 Temperature-U (T_m).

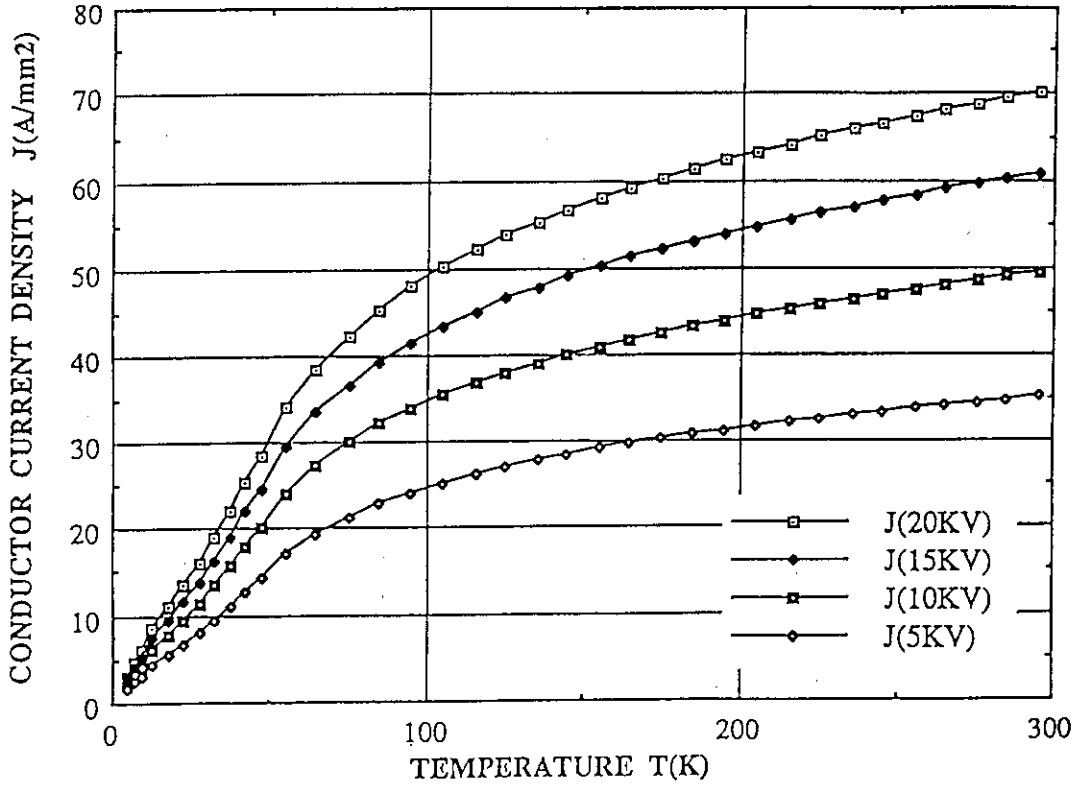

Fig. 5.7.2 Conductor current density vs maximum temperature.

5.8 Cryogenic System

5.8.1 Overview

The cryogenic system of SSTR is designed to supply cryogenic temperature helium to the superconducting coil system (ex. Troidal Field Coil), the coil structure, the fuel recirculation system, and the NBI plasma heating system. The cryogenic system is consist of large scale helium compressors, helium refrigeration cold boxes, and cryogenic helium circulation pumps.

In 1988, as the previous design documents, JAERI has designed another cryogenic system for Fusion Experimental Reactor (FER), on the title of "Cryogenic system design for FER".

Since the basic design condition of the SSTR cryogenic system is similar to the cryogenic design of FER this design has been investigated on the base of the FER system.

5.8.2 Design Specifications

(1) Basic condition

Required heat loads condition such as from Troidal Field Coils, are listed in table 5.8.1. Present report describes investigated cryogenic system design for the SSTR in accordance with this table.

(2) Design conception

(a) In order to satisfy different operational condition (ex. cool-down, steady state) and high system reliability, main components of cryogenic system are composed of several units.

(b) This conceptual design work has been investigated as the extension of the present technology, in spite of the possibility of technology development before the construction of SSTR. The main subjects of development for the SSTR is described in chapter 5.8.6.

(c) In the steady state mode, the cryogenic system is designed to be a closed cycle system. In case of the coil quench, plasma disruption, however, helium gas will be burst into the atmospheric air. The cryogenic system construction is planed to minimize the discharged helium gas.

5.8.3 Policy of System Design

(1) System construction

Basic construction of the cryogenic system is shown in figure 5.8.1.

(a) It will be essential to adopt the forced flow cooling with supercritical helium, together with enlargement of superconducting magnets, such as TFC. In the case of the refrigeration with the forced flow of supercritical helium, as shown in figure 5.8.2, an available heat loads of unit circulation fluid is only several watts. It is very small value compared with the sensible heat capacity of the liquid helium, about 20 watts. Therefore, mass flow rate of supercritical helium is required several times of pool-cooled syperconducting magnets. From the view point of thermal design, supplying supercritical helium directly from the helium refrigerator is not reasonable method. The cryogenic system of SSTR needs independent supercritical helium circulation loops.

From the view of energy efficiency, machine size, cryogenic pump system is adopted for the loop of supercritical helium.

(b) Generally speaking, the heat loads of 80 K shields in the cryostats is absorbed by liquid nitrogen, in case of SSTR. however, it should be absorbed in the helium refrigerator in order to prevent the radiation of nitrogen. Therefor, the helium refrigerator of SSTR is required both or the heat loads at 4 K regime and 80 K regime.

(c) In the system of purification, only a purifier is investigated. Gas bag, recovery compressors, and recovery storage tanks are not planned in this time, on the concept for common use of compressor and helium storage tanks of the refrigerator.

(d) Considering about the characteristics of the components, the arrangement of the each equipments are decided as followers.

* Large volume storage tanks which need recharging are planned to arrange in the outside of the room.
* Helium compressors which need to consider a countermeasure of mechanical noise, are arranged in the compressor room of the cryogenic system area.
* The helium refrigerator etc, are installed in the refrigerator room of the cryogenic system area.

* The cryogenic pump system is planned to arrange in a beside room of the refrigerator in the reactor area.

(2) System specifications

In this paragraph, design concept of each components consisting of the cryogenic system is described, such as cryogenic circulation pump system (cryogenic pump equipments), refrigeration system (Gas helium storage tank, helium compressors, helium refrigerator, liquid helium dewar), purification system (helium purifier), liquid nitrogen supply system (liquid nitrogen supplier).

As shown in table 5.8.1, though refrigeration loads at the plasma starting-up (average value of 100 seconds) in crease 2.5 or 3.9 times of the steady stats, required refrigeration capacity of 100 seconds including the cryogenic pump system, is estimated 4000 litters converted into the liquid helium. This capacity is able to be satisfied by the liquid helium dewar which is designed as a cold buffer. Therefore, cryogenic pump system id designed to have a capacity of plasma starting-up. The design basis of the cryogenic system, however, consists of the steady state operation.

1) Cryogenic pump system

In spite of the steady heat loads required from the cryostats (shown in table 5.8.1), supplied helium temperature and pressure conditions will be an important items for the optimum design of the cryogenic, pump system. Namely, under the same heat loads condition, the lower temperature of the helium and the higher pressure drop requires the larger refrigeration capacity of the cryogenic system.

$$Q = m \times (Ho - Hi)$$

where, Q : heat loads. (W)

m : circulation mass flow rate. (g/s)

Ho, Hi : helium enthalpy of outlet and inlet respectively, as a function of temperature and pressure. (J/g)

In case of the forced cooling with supercritical helium, as shown in this formula, circulation mass flow rate could not be fixed unless temperature and pressure condition of the helium was decided. Therefore, the total required refrigeration capacity for the cryogenic system is strongly dependent on the cooling specification.

On the other hand. the mass flow rate of liquefaction line (JT line) has an optimum condition, that is about

12 to 18 W/(g/s).

The requirement of the independent supercritical helium line, should be concluded from the comparison of heat loads of the unit mass flow rate. In case of SSTR, as shown in Figure 2.8.2, required mass flow rate from the superconducting magnets is specified to 2.2-5. 0W/(g/s). From the comparison with 17W/(g/s) on the refrigerator side, it is obviously that the cryogenic system should be designed to have the independent supercritical helium loop.

Though the heat loads of coil structure is not listed explicitly in Table 5.8.1, the basic construction of the cryogenic pump system based on the conceptual design of FER is listed in Figure 5.8.2.

Hereafter, every heat load conditions should be specified in detall and system optimization should be discussed from now on.

2) Refrigerator system

The refrigerator system is consist of several units of cold boxes. The specification of each unit is decided from that the number of the cold boxes is sepated about 4 units.

The design condition of the helium compressor system is decided from the thermal calculation of the refrigerator.

Generally speaking, the specification of the liquid helium dewar is decided from the condition of

* Total amount of liquid in the cryostats, and the amount of the liquid helium reserved in the cryogenic pump system.
* Required liquid helium for the made changing from the cool-down mode to the refrigeration mode.
* Sufficient liquid helium in order to keep the cryostats at the cryogenic temperature when the refrigerator stops by any fatal accident.

In case of SSTR, since the coil is cooled by forced flow with supercritical helium, the amount of required liquid helium is not large. For the emergency stop of the refrigerator, it is not necessary to consider about reserved liquid helium, because the refrigerator is planned to be several units cold boxes.

Therefore, required capacity of the liquid helium dewar is design to be a pair of 20,000 litters, as the same capacity as the conceptual design of FER.

The gas helium storage tanks should have the sufficient capacity to recover the total helium when the system is warmed up to the room temperature.

3) Purification system

For the cryogenic system, it is one of the most inportant problem to prevent the fatal accident by contaminations. The contamination is mainlycomes from remained impurities after the replacement of the system, and oil components which is not removed at the oil screw compressors. In the present, they are not cleared quantitatively. Therefore, the most reliable countermeasure in prescnce is to adopt the full flow purification system in spite of its large scale.

The SSTR system is designed to adopt the extraction gas purification system, because the evaluation of the impurities will be investigated more accurately and some technical improvements will be expected in the near future.

The helium flow rate into the purification system is estimated to the 10 % of the capacity of the helium compressors. This is under the same design concept of FER.

4) Liquid nitrogen system

In the cryogenic system of SSTR, liquid nitrogen is only used in the purification system. Liquid nitrogen is supplied from the liquid nitrogen storage tanks. Considering about the charging by liquid nitrogen tank-loader, the capacity of the liquid nitrogen tanks is designed to cover 5 days continuous operation.

5.8.4 Thermal Design

(1) Cryogenic pump system

Results of the thermal design of the cryogenic pump system in accordance with Figure 5.8.2 is shown in Table 5.8.2.

(2) Refrigerator system

As shown in Table 5.8.2, the total loads for the helium refrigerator is 8,630 litter/hour + 38 KW at 4.4 K. The equivalent total refrigeration loads which is converted the liquefaction loads with the 3 K/(litter/hour) is calculated into 64 KW. Considering about the back-up margin, the helium refrigerator is designed to be (35kW at 4.4 K + 100 kW at 80 K) X 3 units. 80-K heat loads is specified as 10 times of 4 K refrigeration loads of cryostat.

In case of the conceptual design of FER, which is specified not only the refrigeration capacity but also the liquefaction capacity from the cool-down time (400 to 500 hours), the expansion turbine would be required much performance, and the total efficiency of the

refrigerator would be deteriorated at the steady state operation.

For SSTR system, which is expected very long term operation, the cool-down time is not so critical condition. Therefore, the refrigerator is designed at the refrigeration mode in order to attain higher system efficiency.

1) Helium refrigerator cold box

Specification of unit 30 kW at 4.4 K + 100 kW at 80 K.

The results of thermal design is shown in Figure 5.8.3.

2) Helium compressor .

From the results of thermal design in the cold box,

3,148 g/s X 3 units = 9,440 g/s (= 190,000 Nm^3/hour)

Including the by-pass for the control and the pressure drop of the main line, the specification of the compressor system is decided as follows.

Flow rate	200,000 Nm^3 hour (= 9,920 g/s)
Inlet pressure	1.1 atm
Outlet pressure	18.5 atm

3) Gas helium storage tanks

The total storage capacity is specified to recover 45,000 litter liquid helium including the liquid dewar, pipe helium bath, and heat exchangers.

Pressure	3 to 16 atm
Temperature	313 K
Capacity	5,450 kg

Hence, the storage thank capacity should be planned as 2,800 m^3.

4) Energy efficiency

According to the results of the thermal design, the energy efficiency of the cycle become as follows.

a) Power calculation of helium refrigerator

Theoretical converted power at 310 K is

$$\left(35\text{kW}\,\frac{310 - 4.42}{4.42} + \frac{100\text{kW}}{40\text{K}}\int \frac{310-T}{T}dT\right)\times 3 = 8570\text{kW}$$

b) Power of helium compressor

The isothemal efficiency of the compressor is specified to be 55 %.

$$\frac{9.92\text{kg/s} \times 2.08\text{kJ/kgk} \times 310\text{k} \times \ln(18.5/1.1\text{atm})}{0.55} = 32800\text{kW}$$

c) Energy efficiency

Hence, the energy efficiency (percent CARNOT) is calculated into 26.1 %. The energy efficiency includes the following items.

* Cycle efficiency of helium refrigerator

Thecretical power 9.44x2.08x310x1n(18/1.2)=16,500 kW
Efficiency 8,570/16,500X100=52.0 %
(loss percent is 47 %)

* Helium compressor efficiency

As described above 55% (loss percent is 44 %)

* Others (pressure drop etc.)

0.261/0.520/0.55X100=91.3 % (loss percent ia 9 %)

In the style FOM.
Converted power at 4.42 K

8.570 kW X 4.42/(310-4.42) = 124kW

FOM is

32800kW/124kW = 265 kW/kW

(Remarks: This calculation of energy efficiency doesn't include the power of the auxiliary equipments.)

(3) Purification system

As described in 5.8.3, the purification system is planned to purify 10 % of the compressor flow rate.

Capacity	20,000 Nm3/hour (continuously with 2 units)	
Impurities	Air	Water
Inlet	100 ppm	100 ppm
Outlet	1 ppm	1 ppm
Operating time	120 hours/unit	

(4) Liquid nitrogen system

The liquid nitrogen system has a capacity to supply sufficient liquid nitrogen to the

purification system. The average consumption rate of liquid nitrogen in the purification system is 1200 litter/hour. The total consumption is

12,000 litter/hour X 24 hour X 5 days = 144,000 litters

The design capacity of the liquid nitrogen system is estimated 180 m^3 including about 10 % margin.

Furthermore, the liquid nitrogen system need the nitrogen evaporator which is used for regeneration of the purifier.

1,000 Nm^3/hour X 24 hour

5.8.5 Plant Design

(1) System flow

Flow diagram of the cryogenic system for the SSTR is shown in Figure 5.8.4.

(2) Arrangements

The plot plan in the refrigeration area and in the reactor area are shown in Figure 5.8.5, 5.8.6 respectively.

(3) Utilities

The total consumption rate of utilities in the steady state full operation mode (the purification system is not operated) is calculated as followers.

* Electric power : 33,600 kW
* Cooling water : 5,720 m^3/hor
* Liquid nitrogen : 24 litter/hour (only self evaporation)

In case of the steady state mode with operating two cold box units,

* Electric power : 22,400 kW
* Cooling water : 3,820 m^3/hour
* Liquid nitrogen : 24 litter/hour

5.8.6 Subjects for Developments

In this paragraph the main subjects for the technological developments is described.

(1) Helium compressor

In the present technology, the oil injected screw type compressor is adopted because of its high mechanical reliability. The oil injected type screw compressor, however, have following defects.

* A difficulty to make a large capacity because of the its mechanical problem.
* The lower isothermal efficiency.
* The oil contamination problem.

Therefore, for the large capacity compressors for the SSTR, the oil free type centrifugal turbo helium compressor should be developed.

(2) Countermeasure for the contaminations

A problem of the contaminations is not evaluated quantitavely. Simply because the impurities are generated after the long term operation.

Since the SSTR system will be planned to operate for a long term and with a high efficiency, the quantitative evaluation of the impurities and its countermeasure should be investigated.

(3) Expansion turbines

In the refrigeration cycle without the liquid nitrogen as a auxiliary coolant, the expansion turbine be arranged at the position of higher temperature level. Generally speaking, a rotating speed of the turbine should be increased in order to maintain a high efficiency at the high adiabatic heads. To reduce the number of the expansion turbine, a high efficiency turbine with high adiabatic heads should be developed.

In the present technology, the gas flow rate into the turbine is controlled only from changing the inlet pressure by adjusting the inlet valve, because the turbine is made with rigid nozzle. Therefore, the operation region of the turbine with a high efficiency is restricted. Hence, the valuable capacity turbine should be developed for the cryogenic system of the SSTR.

(4) Cryo system

The specifications of the helium compressor is decided form not only the heat loads of the cryostat, deeply dependent on the pressure and temperature conditions of the helium. Therefore, in order to make the SSTR cryogenic system more smart, some case study of the pressure and the temperature condition should be required.

The controllability and the protection concepts should be studied, considering about the unsteady operational consition of the cryostat and the countermeasure for some emergency accidents.

(5) Refrigeration system for NBI

In the NBI system, cryopumps are cooled by helium, the short term regeneration of the cryopump is required. The Handling of a recovering helium gas which is evaporated in

the cryopump at the regeneration should be studied in detail.

(6) Cryogenic pump

In the SSTR system several kinds of the cryogenic pump are installed. The large scale cryogenic pump should be developed And the optimum system configuration should be studied considering about the reliability of the cryogenic pumps.

Table 5.8.1 Required heat loads for SSTR cryogenic system

NO.	Item			Liquid helium line			80K Shield line		remarks
				Steady state	Plasma starting-up	Plasma disruption	Steady state	Plasma starting-up	
1	CS Coil	Refrigeration load (kW)		1.6	6.2	8.0			
		Flow rate (g/s)		720	2,800	2,800			
		Temp. (K)	Entrance	4.5	4.5	4.5			
			Exit	5.1	5.1	(5.2)	80	80	
		Pressure(atm)	Entrance	6.0	6.0	6.0			
			Exit	4.0	4.0	4.0			
		Liquefaction Load(ℓ/h)		1,000	1,000	1,000	—	—	
2	EF Coil	Refrigeration load (kW)		3.2	8.0	8.9			
		Flow rate (g/s)		640	1,600	1,600			
		Temp. (K)	Entrance	4.5	4.5	4.5			
			Exit	5.5	5.5	(5.6)	80	80	
		Pressure(atm)	Entrance	6.0	6.0	6.0			
			Exit	4.0	4.0	4.0			
		Liquefaction Load(ℓ/h)		700	700	700	—	—	
3	TF Coil	Refrigeration load (kW)		7.8	19.5	1.44×10^{4}			
		Flow rate (g/s)		1,960	4,900	4,900			
		Temp. (K)	Entrance	3.8	3.8	3.8			
			Exit	5.3	5.3	—	80	80	
		Pressure(atm)	Entrance	10.0	10.0	10.0			
			Exit	8.0	8.0	8.0			
		Liquefaction Load(ℓ/h)		5,200	5,200	5,200	—	—	
4	FUEL	Refrigeration load (kW)		3.0	3.0	3.0			
		Flow rate (g/s)		—	—	—			
		Temp. (K)	Entrance	4.6	4.6	4.6			
			Exit	4.6	4.6	4.6	80	80	
		Pressure(atm)	Entrance	1.6	1.6	1.6			
			Exit	1.4	1.4	1.4			
		Liquefaction Load(ℓ/h)		—	—	—	—	—	
5	NBI	Refrigeration load (kW)							
		Flow rate (g/s)		—	—	—			
		Temp. (K)	Entrance	3.7	3.7	3.7			
			Exit	3.7	3.7	3.7	80	80	
		Pressure(atm)	Entrance	0.78	0.78	0.78			
			Exit	0.58	0.58	0.58			
		Liquefaction Load(ℓ/h)		—	—	—	—	—	
	Total	Refrigeration Load (kW)		15.6	36.7	—			
		Liquefaction Load(ℓ/h)		6,900	6,900	6,900	—	—	

Attention ; The heat loads for the cryostat is specified to be 1.25 times of this table.

19.5 kW

8,630 ℓ/h (based on the steady state operation mode.)

Table 5.8.2 Thermal design of cryogenic pump system

Loop name		P L	C S	E F	T F	S T R	FUEL	N B I	S H I E L D
Specification of the cryogenic pumps		—	SP: η =70% m=900g/s P=4/6.5atm T=4.5K	SP: η =70% m=800g/s P=4/6.5atm T=4.5K	SP: η =70% m=2,450g/s P=8/10.5atm T=3.8K	SP: η =70% m= P=7/8.5atm T=4.5K	—	LP: η =60% m= P=0.58/0.88atm T=3.7K	LP: η =60% m= P=7/8.5atm T=80K
		—	DP: η =60% m=231g/s P=1.07/1.2atm T=4.3K	DP: η =60% m=322g/s P=1.07/1.2atm T=4.3K	DP: η =60% m=811g/s P=0.52/1.2atm T=3.6K	DP: η =60% m= P=1.07/1.2atm T=4.3K	—	DP: η =60% m= P=0.58/1.2atm T=3.7K	—
Heat loads	Cryostat	8,630 ℓ/s	2.0kW	4.0kW	9.75kW	6.6W/(g/s)	3.75kW	21.8W/(g/s)	183W/(g/s)
	Cryogenic pump	—	SP:2.43kW DP:0.27kW	SP:2.16kW DP:0.37kW	SP:5.75kW DP:7.83kW	SP:(1.53W/(g/s)) DP:(1.16W/(g/s))	—	LP:(0.6W/(g/s)) DP:(8.2W/(g/s))	HP:(57W/(g/s))
	Others	—	—	—	—	—	—	—	—
	Total	8,630 ℓ/s (1.2atm LHe → 1.2atm 250K)	4.7kW	6.5kW	23.3kW		3.75kW		(40K → 80K)

Remarks 1 : LP … Liquid helium pump, SP … Supercritical helium circulation pump, DP … Cold compressor
HP … Low Temp. helium circulation pump, HX … Heat exchanger

Remarks 2 : Heat inleaks from the cryogenic pump structure and from the transfertubes, (Relatively small), are not included into this table.

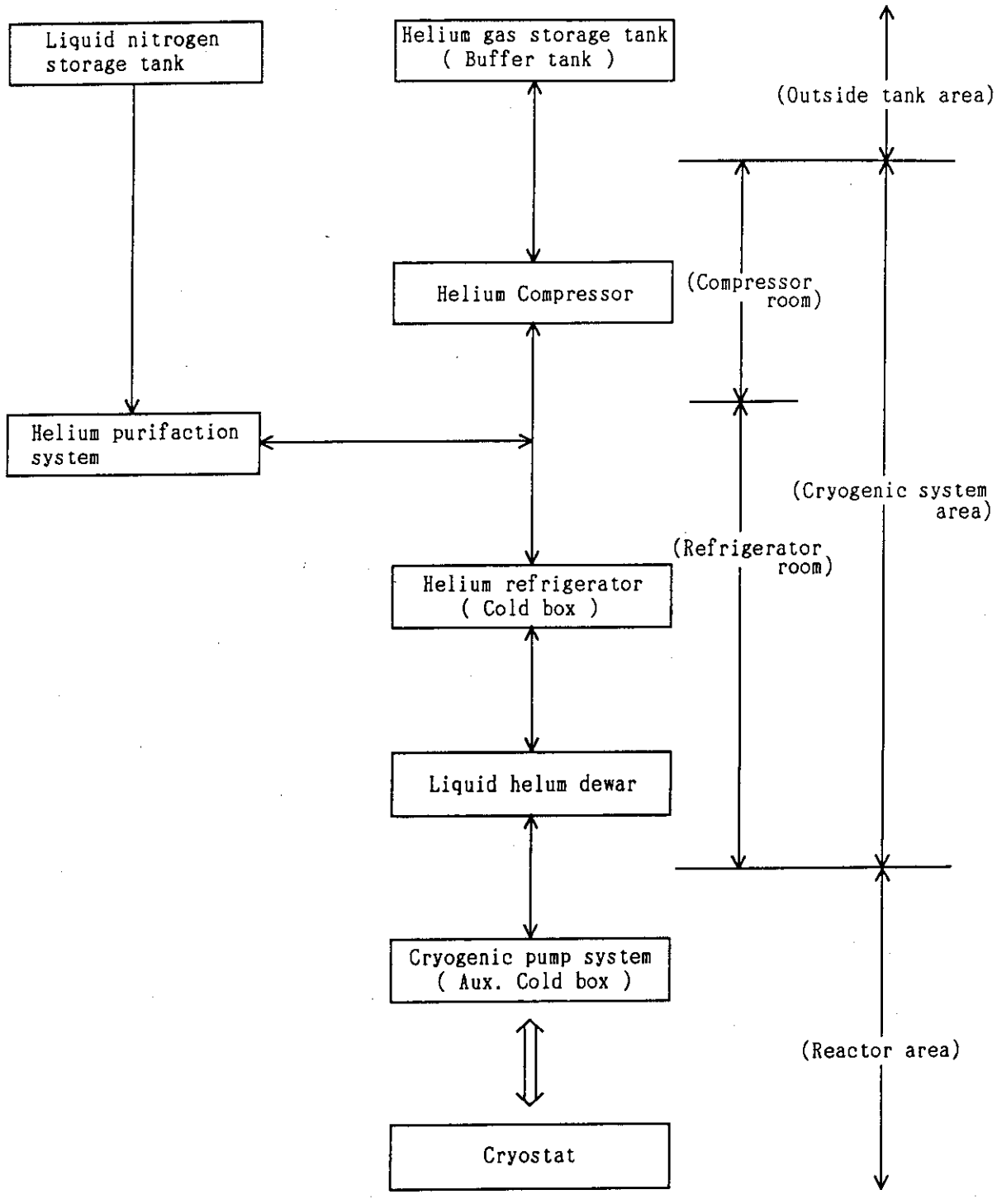

Fig. 5.8.1 Block diagram of cryogenic system for SSTR.

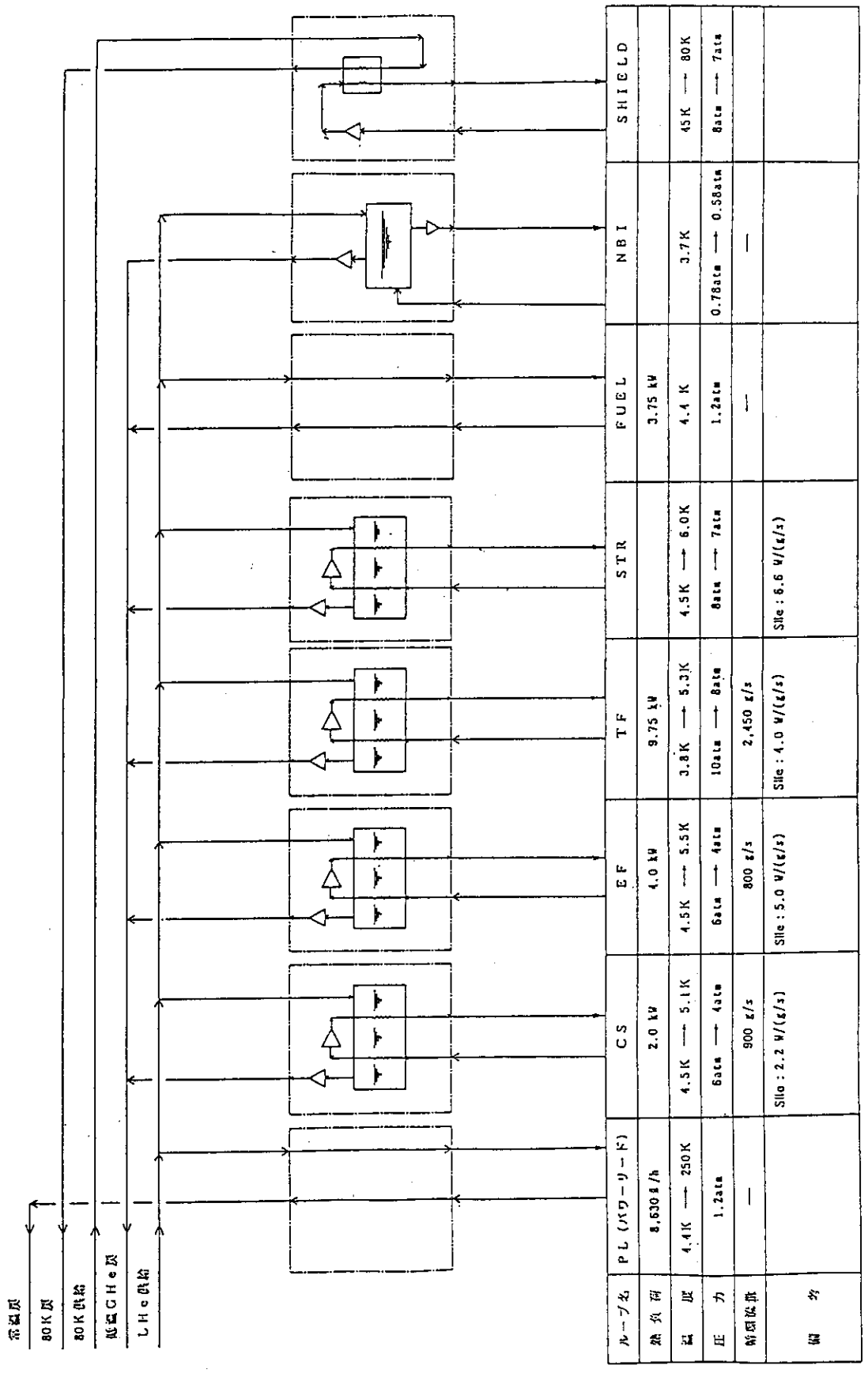

ループ名	PL（パワーリード）	CS	EF	TF	STR	FUEL	NBI	SHIELD
熱負荷	8,630 g/h	2.0 kW	4.0 kW	9.75 kW		3.75 kW		
温　度	4.4K ⟶ 250K	4.5K ⟶ 5.1K	4.5K ⟶ 5.5K	3.8K ⟶ 5.3K	4.5K ⟶ 6.0K	4.4 K	3.7K	45K ⟶ 80K
圧　力	1.2atm	6atm ⟶ 4atm	6atm ⟶ 4atm	10atm ⟶ 8atm	8atm ⟶ 7atm	1.2atm	0.78atm ⟶ 0.58atm	8atm ⟶ 7atm
許容故障	—	900 g/s	800 g/s	2,450 g/s		—	—	
備　考		Silo : 2.2 W/(g/s)	Silo : 5.0 W/(g/s)	Silo : 4.0 W/(g/s)	Silo : 6.6 W/(g/s)			

Fig. 5.8.2 Block diagram of cryogenic pump system.

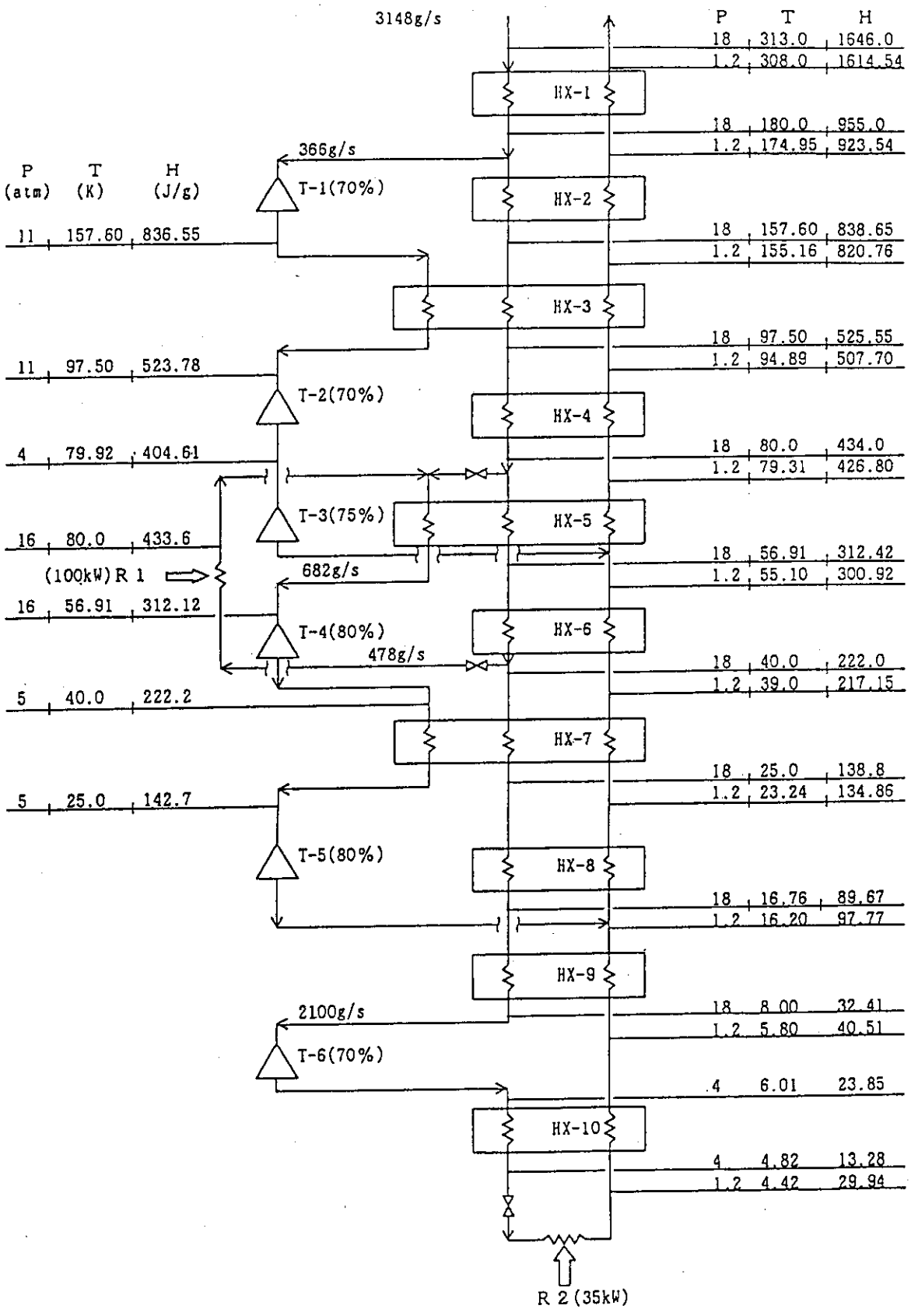

Fig. 5.8.3 Thermal design of cold box (He refrigerator).

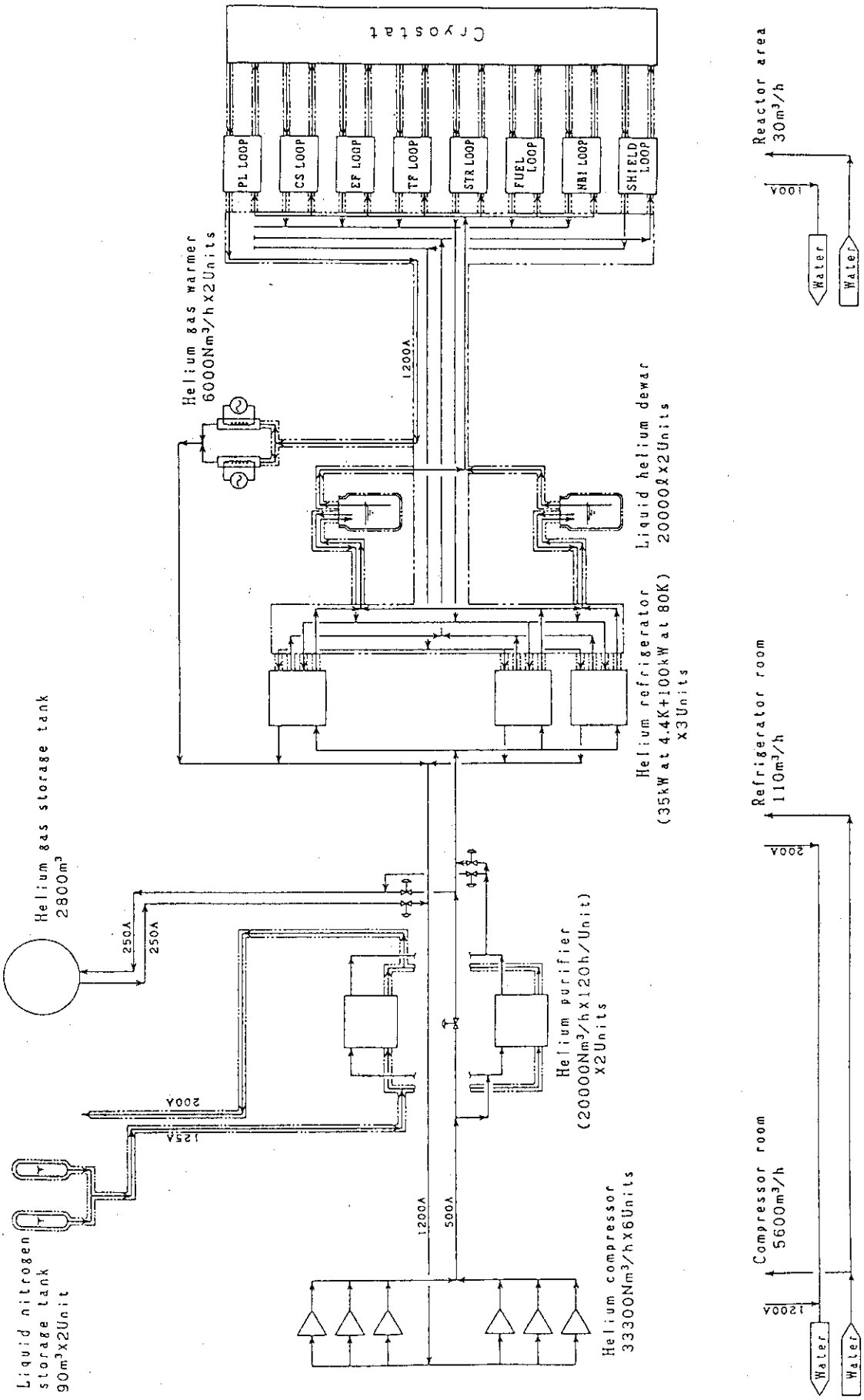

Fig. 5.8.4 Flow diagram of cryogenic system for SSTR.

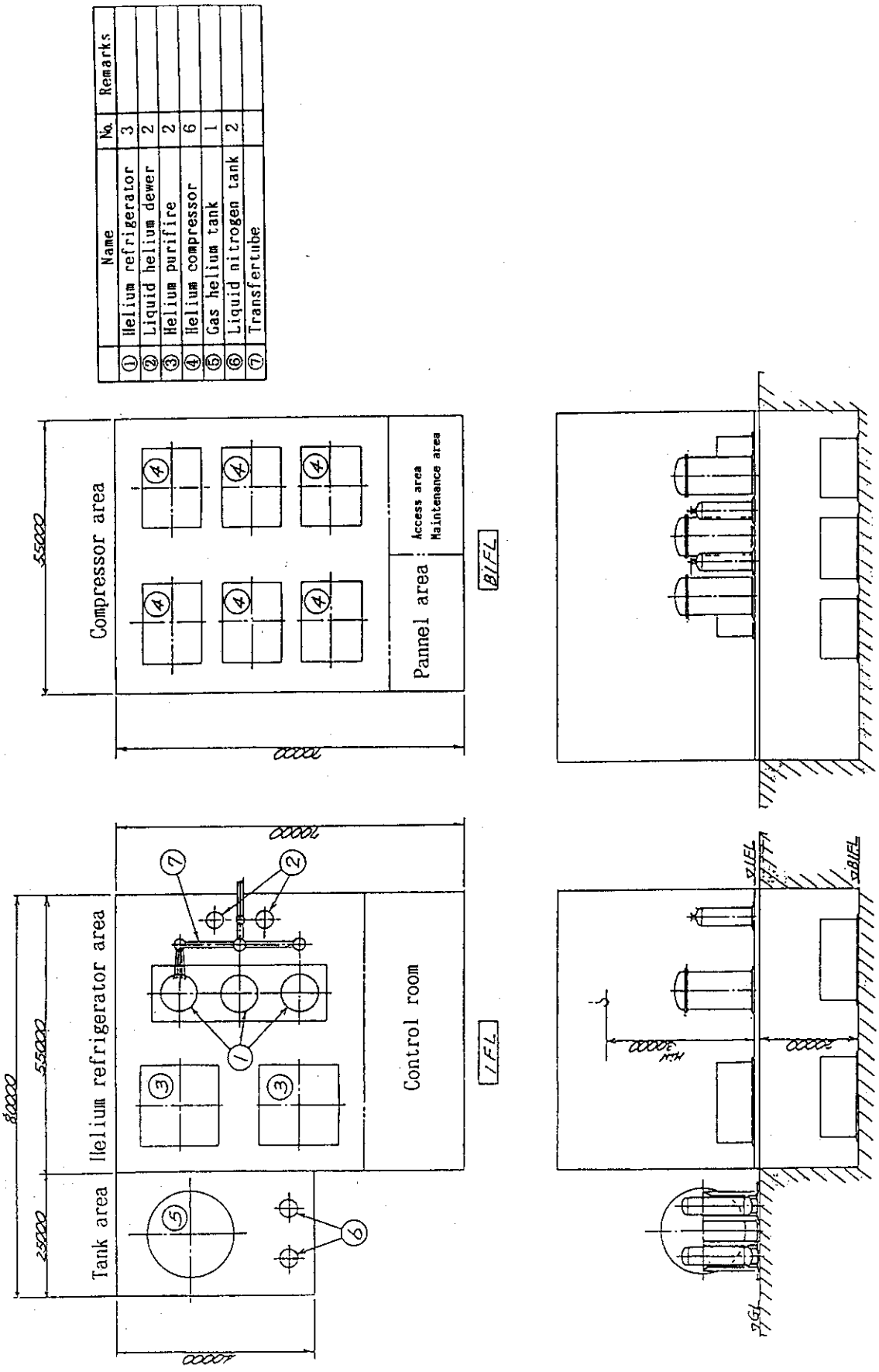

Fig. 5.8.5 Plot plan of cryogenic system for SSTR.

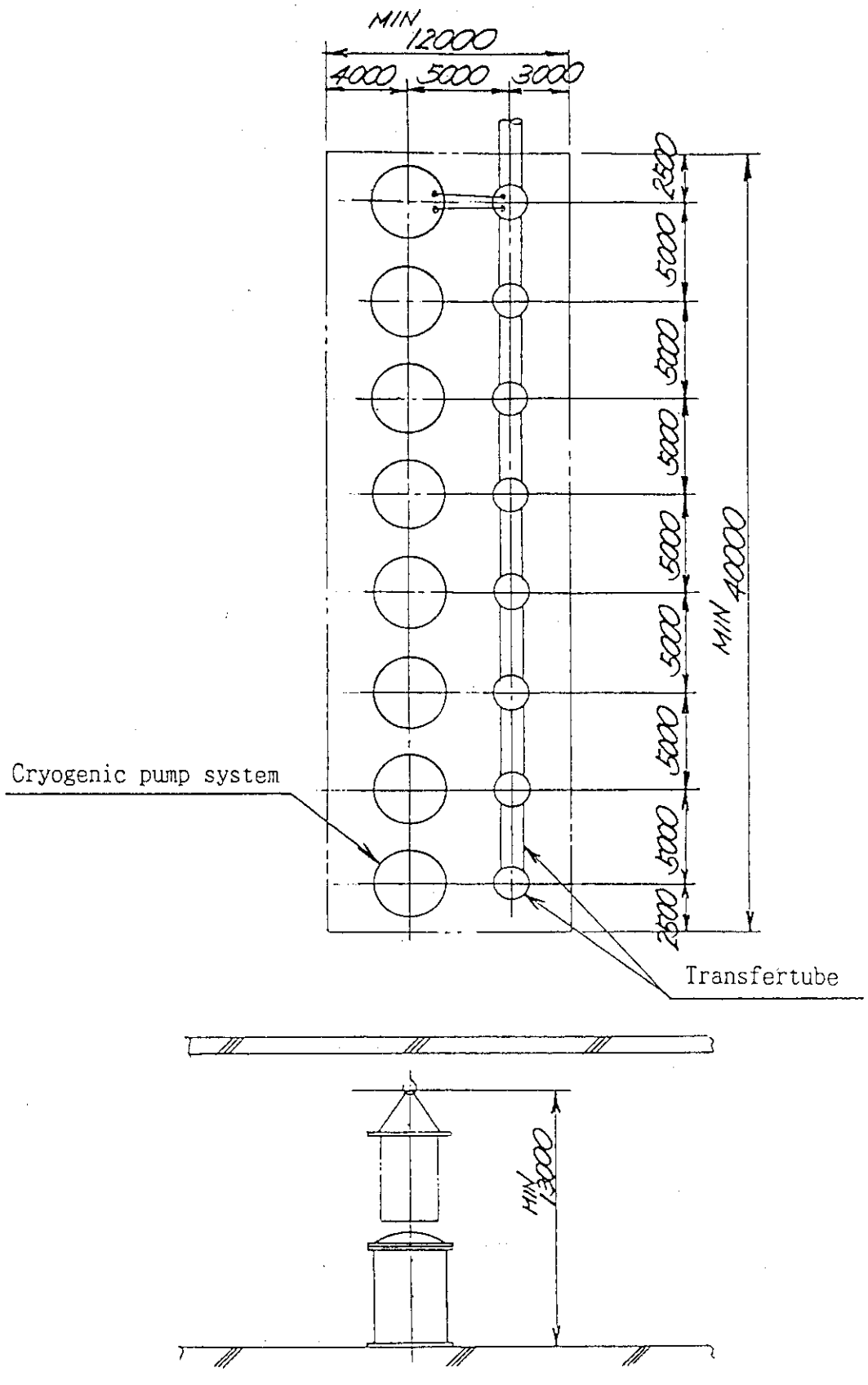

Fig. 5.8.6 Plot plan of supercritical helium circulation system.

5.9 Conclusion

The conceptual design work of the toroidal coil for the SSTR was performed and was demonstrated to be possible with data base obtained so far. However, it is necessary to analysis in detail for mechanical problem such as the centering load support and the amount of strain on the $(NbTi)_3Sn$ conductor. And then the feasibility of the design will be clear by doing R&D for the fabrication using the model coil etc.

6. Poloidal Field coil

6.1 General

The poloidal field coil of the SSTR is required to generate the magnetic flux of 140 Vs. In this report, the design of this coil was performed with the reliability and low cost as based on a present engineering technique. The poloidal coil system consists of a center solenoid coil (CS) and the equilibrium coil (EF). For both coils, a NbTi superconducting material was used. Therefore, the maximum field is below 7 T with supercritical helium coolant of 4.2 K. The maximum changing magnetic fields required in the coil is 0.94 T/s in the coil operation and 0.08 T/s during disruption, respectively. These values are lower than those of ignited machines such as the FER and The ITER. Therefore, it is no difficult to design the SSTR poloidal field coil with a high stability and ac losses. The bore diameters of the poloidal field coils are in the range of 4 - 26 m. The average current density of coil is about 30 A/mm^2. The maximum stress is 620 MPa on the conduit material of conductor to be permitted for JN-1 material with allowable stress of 800 MPa. The total stored-energy is about 7 GJ. The total amper turns is 50 MAT. The weight of coil is about 2,500 tons.

6.2 Conductor

For the poloidal field coil conductor, the cable-in-conduit conductor ws chosen similarly for the toroidal field coil conductor. The cross-section of the conductor is shown in Fig. 6.2.1. The conductor is composed of a circular NbTi/Cu-composite strand cable embedded into the seamless CuNi conduit and two reinforce structures with a semicircular groove, which is a new structual material, JN-1. The surface of the strand is coated with chrome to reduce the coupling losses between strands. Both CS and EF coil conductors have not sub-channel. The poloidal field coil conductors were designed under the condition described in Table 5.2.1 in similar to the toroidal field coil conductors. The parameters of the designed conductors are listed in Table 6.2.1. The characteristics of the conductors are summarized as follows.

1) The unit length of the conductor is below 1 km (the coolant length is below 500 m).
2) The conduit is a CuNi tube with seamless and the reinforcement structures are provided around the conduit.
3) The strand is a NbTi/Cu composite superconductor.
4) The strand is coated with the chrome.
5) To avoid a high pressure drop due to helium gas flow, the EF coil conductors is designed with a larger size strand of 2.2 mm diameter instead of having a sub-channel.

Table 6.2.1 Parameters of the superconductors for the poloidal coil

Item	CS Coil	EF Coil
Size	43 mm x 43 mm	43 mm x 43 mm
Superconducting material	NbTi	NbTi
Strand diameter	0.84 mm	2.2 mm
Filament diameter	10 μm	10 μm
Cu/Non Cu	1.5	7.5
NO. of strands	972	108
Superconducting material area of strands	214 mm^2	48 mm^2
Copper area of strands	324 mm^2	362 mm^2
Total area of strands	538 mm^2	410 mm^2
Helium area	266 mm^2	205 mm^2
First conduit area (CuNi)	104 mm^2	91 mm^2
Secound conduit area (JN-1)	960 mm^2	1148 mm^2
Insulation thickness	0.5 mm	0.5 mm
Void fraction	0.33	0.33
Operating current	40 kA	40 kA
Critical current	300 kA	101 kA
Limiting current	45 kA	47 kA

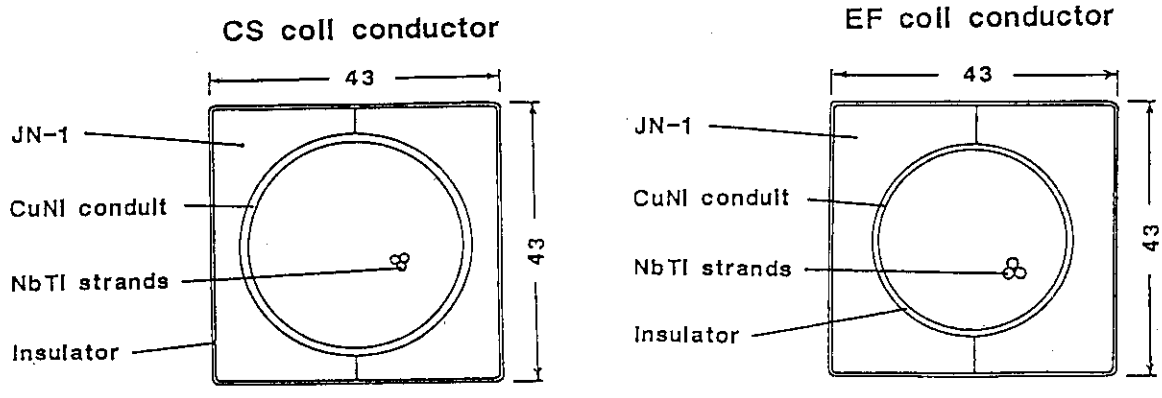

Fig. 6.2.1 Conductors of poloidal coil for the SSTR.

6.3 Poloidal Field Coil Windings

Superconductors with forced-flow cooling are wound into either pancakes or layers during coil fabrication. If the space between the central solenoid coil (CS coil) and the toroidal field coil (TF coil) is greatly restricted, an appropriate coil winding must be selected for the central solenoid coil so as to provide the required volt-seconds for ramp up of the tokamak plasma. In this design, a superconductor pancake winding was selected for the following reasons.

1. Winding packs made up of pancakes have a modular structure and are mechanically rigid.

2. It is difficult to fully understand the structure of winding packs fabricated by layer winding.

3. Coils fabricated by layer winding are difficult to press and can jeopardize the mechanical integrity of the winding pack.

On the other hand, when using layer winding, it is easy to grade the coil winding and make effective use of the space between CS and TF coils. We will therefore conduct a detailed feasibility study of layer winding for use in CS coils.

Cooling channels of support structures are equipped separately from coil windings. The superconductor fills with 4.5-K 6.0-bar supercritical helium under reference operating conditions. Characteristics of poloidal field coils are listed in Table 6.3.1.

6.3.1 Central solenoid coil windings

Each coil has 17 double pancakes with 2 parallel hydraulic flow paths. Each superconductor and pancake are wrapped with insulating tape to thicknesses of 0.5 mm and 2 mm, respectively. All double pancakes are stacked to a coil, wrapped for ground insulation with insulating tape to a thickness of 35 mm, and finally vacuum-impregnated. Vacuum-impregnation of the entire coil produces strong mechanical bonding between the turns and pancakes; it also ensures that the electric strength of the insulation is high.

A GFRP frame is attached to each CS coil as a mechanical back up. The frame also enhances installation accuracy and facilitates coil assembly.

Two typical cooling paths are compared in Table 6.3.2. From the standpoint of stabilizing the cable-in-conduit conductor in high magnetic fields, we selected pancake cooling in which the coolant enters from inside the coil.

Two typical current feeder routes are compared in Table 6.3.3. Both routes have electrical connections between double pancakes on the outer side of the coil. For this design, we selected the outside feeder that does not have electrical connections on the higher magnetic field side.

6.3.2 Equilibrium-field coil windings

The insulation arrangement and thickness of each equilibrium-field coil (EF coil) winding pack are identical to those used in the CS coil. Mechanical reinforcement bands (casings) are used around the winding pack to counteract large bending moments in the radial and axial directions. To slide the coil against hoop forces, a material 50 mm thick is attached between the coil support frame and the reinforcement band.

The cooling paths and the current feeder routes of EF coils are also the same as those in CS coils. 5U and 6L coils have 3 and 7 double pancakes with 2 parallel flow paths, respectively. 7U, 5L, and 6L coils have 7, 11, and 6 double pancakes with 4 parallel flow paths, respectively. Longer cooling paths are used to fabricate two-in-hand winding--an arrangement that helps keep the pressure drop and quench pressure sufficiently low. In the same way, 7L coils have 9 double pancakes with 6 parallel hydraulic flow paths. These coils have the longest cooling paths, and are is fabricated by three-in-hand winding.

Table 6.3.1 Characteristics of PF coils

Coil name & No.	Winding type	No.of co-wound cable	Conductor length (m)	Cooling path length (m)	Prssure drop (bar)	Mass flow rate (g/s)
1. C S	Dbl.Pan.	1	276	138	2.0	10
2. 7 U	Dbl.Pan.	2	830	415	2.0	8
3. 6 U	Dbl.Pan.	1	770	385	2.0	9
4. 5 U	Dbl.Pan.	1	650	325	2.0	9
5. 5 L	Dbl.Pan.	2	724	362	2.0	9
6. 6 L	Dbl.Pan.	2	660	330	2.0	9
7. 7 L	Dbl.Pan.	3	830	415	2.0	8

Table 6.3.2 Comparison of current feeder route

	Method 1 (Inside feeder)	Method 2 (Outside feeder)
Route of current feeder	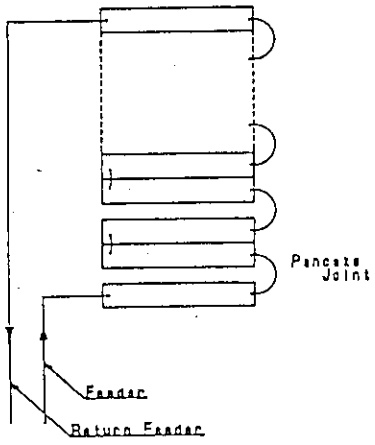 TF coil side	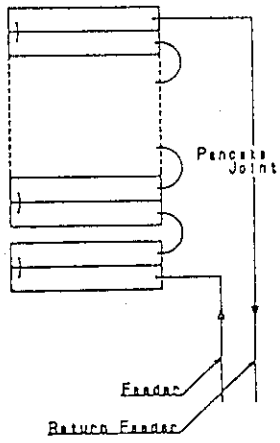 TF coil side
Features	Small space between CS and TF coils. Coil joint in high magnetic field.	Large space between CS and TF coils. Pancake joint in coil outside.

Table 6.3.3 Comparison of cooling path route

	Method 1 (Pancake cooling)	Method 2 (Double pancake cooling)
Route of cooling path	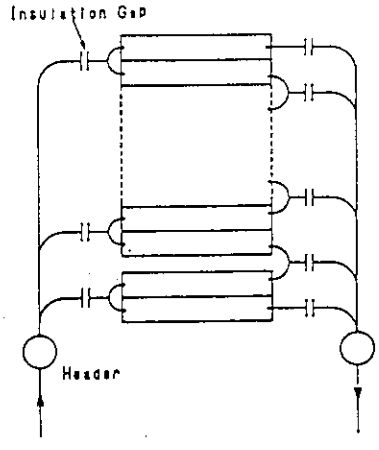 TF coil side	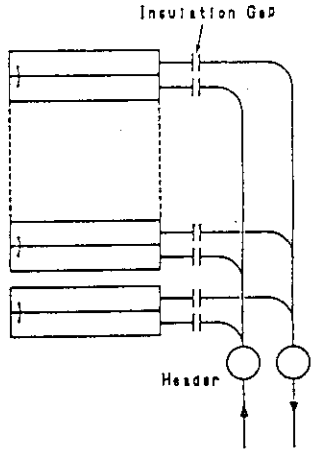 TF coil side
Features	Small space between CS and TF coils. Short path length. Inlet in high magnetic field.	Large space between CS and TF coils. Long path length.

6.4 Electromagnetic Analysis

Basic specifications for the poloidal field coils are shown in Table 6.4.1. The excitation pattern of poloidal field coils is given with reference to the operating conditions described in Chapter 4. The poloidal coil system consists of 14 super-conducting coils that are grouped into CS coils (1U-4U,1L-4L) and EF coils (5U-7U,5L-7L).

The magnetic field and electromagnetic forces were calculated for two typical cases: (1) plasma ramp-up (assuming a period of 100 seconds from initial excitation to plasma ramp-up); and (2) disruption in plasma burning (with a duration of 10 seconds after disruption). We adopted a plasma disruption model in which the plasma current decays linearly at a rate of 12MA/20msec at the fixed position. The current induced in the vacuum vessel upon plasma disruption was evaluated using a circuit analysis in which the vessel was replaced by a number of equivalent loop coils.

6.4.1 Magnetic field analysis

Figure 6.4.1 shows the maximum magnetic field generated in poloidal coils, and Figure 6.4.2 gives the maximum rate of change in these fields. The maximum magnetic field for CS and EF coils is generated during plasma ramp-up. The maximum magnetic flux densities for CS and EF coils are 7.0 T (2U coils at 3 sec) and 5.7 T (5L coils at 80 sec), respectively. In plasma ramp-up, the maximum rates of change in the magnetic fields of CS and EF coils (DB) are 2.4 T / 3 sec and 1.8 T / 3 sec, or 0.8 T / sec and 0.6 T / sec, respectively. The time constant of the decay in the eddy current induced in the vacuum vessel amounts to about one second because of electromagnetic coupling to the poloidal coils.

6.4.2 Electromagnetic force analysis

The maximum values of hoop and vertical forces acting on poloidal coils are shown in Figs. 6.4.3 and 6.4.4. The maximum electromagnetic force amplitudes generated by the ripple of toroidal magnetic field are also given. Figures 6.4.5 and 6.4.6 show arrow-plots of the electromagnetic forces of the poloidal coils upon initial excitation and during plasma burning. Figures 6.4.7 and 6.4.8 show similar arrow-plots at typical times after plasma disruption.

The maximum hoop forces of the CS and EF coils are about 360 MN in 4L coils upon initial excitation and about 410 MN in 7L coils during plasma burning, respectively. In the same way, the maximum vertical forces are about 150 MN in 2L coils during plasma burning and 100 MN in 7L coils during plasma burning, respectively.

Electromagnetic forces induced by ripples in the toroidal magnetic field were rather large in 7U and 7L coils. The vertical amplitudes of these forces in 7U and 7L coils were 110MN/m and 320MN/m, respectively. These values are about equal to or larger than the vertical force acting on poloidal coils.

6.4.3 Electromagnetic parameters

Table 6.4.2 shows the inductance matrix of the poloidal coil system and the plasma which is located at the position in plasma burning. Table 6.4.3 is the list of the magnetic stored energy of poloidal coils in the plasma-ramp-up.

Total magnetic stored energy of all poloidal coils becomes maximum in plasma burning and its value is about 7GJ. Additionally, the stored energy of 2U coil is about 400MJ which is the largest value in CS coils and the stored energy of 7L coil is about 3GJ which is the largest value in EF coils.

Table 6.4.1 PF coil parameters

No.	coil name	R(m)	Z(m)	DR(m)	DZ(m)	pais	turns	total turns
1	7 U	13.2	3.5	0.430	0.632	14	10	140
2	6 U	10.2	7.0	0.258	0.272	6	6	36
3	5 U	3.7	7.5	0.602	0.632	14	14	196
4	4 U	2.18	6.125	0.344	1.530	34	8	272
5	3 U	2.18	4.375	0.344	1.530	34	8	272
6	2 U	2.18	2.625	0.344	1.530	34	8	272
7	1 U	2.18	0.875	0.344	1.530	34	8	272
8	1 L	2.18	-0.875	0.344	1.530	34	8	272
9	2 L	2.18	-2.625	0.344	1.530	34	8	272
10	3 L	2.18	-4.375	0.344	1.530	34	8	272
11	4 L	2.18	-6.125	0.344	1.530	34	8	272
12	5 L	4.8	-7.6	1.032	0.992	22	24	528
13	6 L	10.5	-7.4	0.430	0.542	12	10	120
14	7 L	13.2	-2.5	0.645	0.812	18	15	270

Table 6.4.2 Inductance matrix of PF coil system

	7U	6U	5U	4U	3U	2U	1U	1L	2L	3L	4L	5L	6L	7L	PLASMA
7U	67.970														
6U	15.760	58.128													
5U	1.822	2.780	12.441												
4U	0.676	0.925	2.152	4.734											
3U	0.713	0.845	1.026	1.451	4.734										
2U	0.713	0.716	0.504	0.484	1.451	4.734									
1U	0.676	0.577	0.270	0.204	0.484	1.451	4.734								
1L	0.611	0.452	0.156	0.101	0.204	0.484	1.451	4.734							
2L	0.531	0.349	0.097	0.056	0.101	0.204	0.484	1.451	4.734						
3L	0.449	0.270	0.064	0.034	0.056	0.101	0.204	0.484	1.451	4.734					
4L	0.373	0.210	0.044	0.022	0.034	0.056	0.101	0.204	0.484	1.451	4.734				
5L	1.494	0.785	0.146	0.068	0.097	0.144	0.222	0.361	0.615	1.077	1.773	14.725			
6L	6.224	2.998	0.474	0.203	0.260	0.334	0.429	0.545	0.675	0.800	0.887	4.720	52.217		
7L	16.007	7.081	1.020	0.415	0.495	0.577	0.651	0.701	0.718	0.696	0.641	2.834	13.723	62.726	
PLASMA	7.344	5.166	1.254	0.621	0.892	1.197	1.385	1.304	1.024	0.728	0.500	1.563	4.188	7.344	17.112

Table 6.4.3 Stored energy of PF coil system (Unit: GJ)

	時刻(sec)						
COIL	0.0	3.0	20.0	40.0	50.0	80.0	100.0
7U	0.004	0.019	0.019	0.158	0.087	0.228	1.592
6U	0.060	0.071	0.087	0.008	0.002	0.092	0.007
5U	0.373	0.137	0.345	0.428	0.280	0.315	0.156
4U	0.315	0.111	0.113	0.114	0.074	0.042	0.007
3U	0.337	0.263	0.232	0.134	0.104	0.007	0.009
2U	0.340	0.380	0.274	0.103	0.054	0.052	0.142
1U	0.340	0.366	0.115	0.000	-0.004	0.276	0.284
1L	0.340	0.172	0.071	0.005	-0.004	0.316	0.371
2L	0.339	0.345	0.191	0.016	0.008	0.062	0.225
3L	0.337	0.269	0.205	0.103	0.091	0.034	0.006
4L	0.373	0.177	0.090	0.088	0.096	0.106	0.029
5L	0.218	0.266	0.339	0.489	0.780	1.380	1.095
6L	0.033	0.019	-0.008	0.126	0.208	0.522	0.044
7L	0.016	-0.008	0.000	0.036	0.043	0.626	3.017
TOTAL	3.426	2.585	2.074	1.810	1.820	4.058	6.983

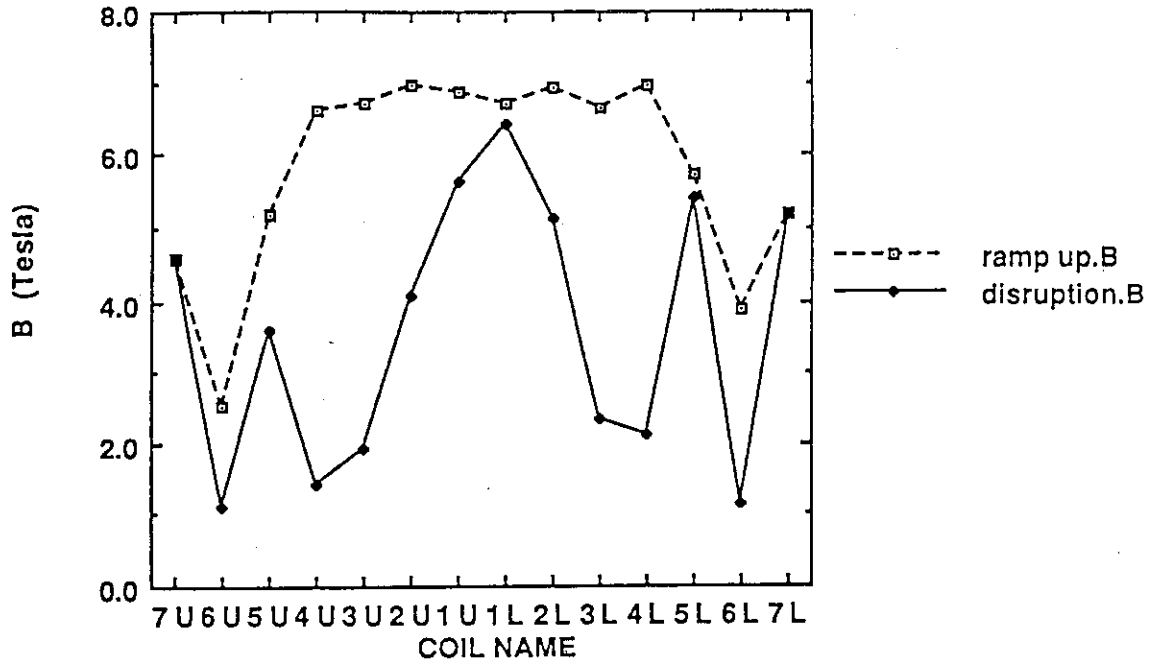

Fig. 6.4.1 Maximum field of PF coils.

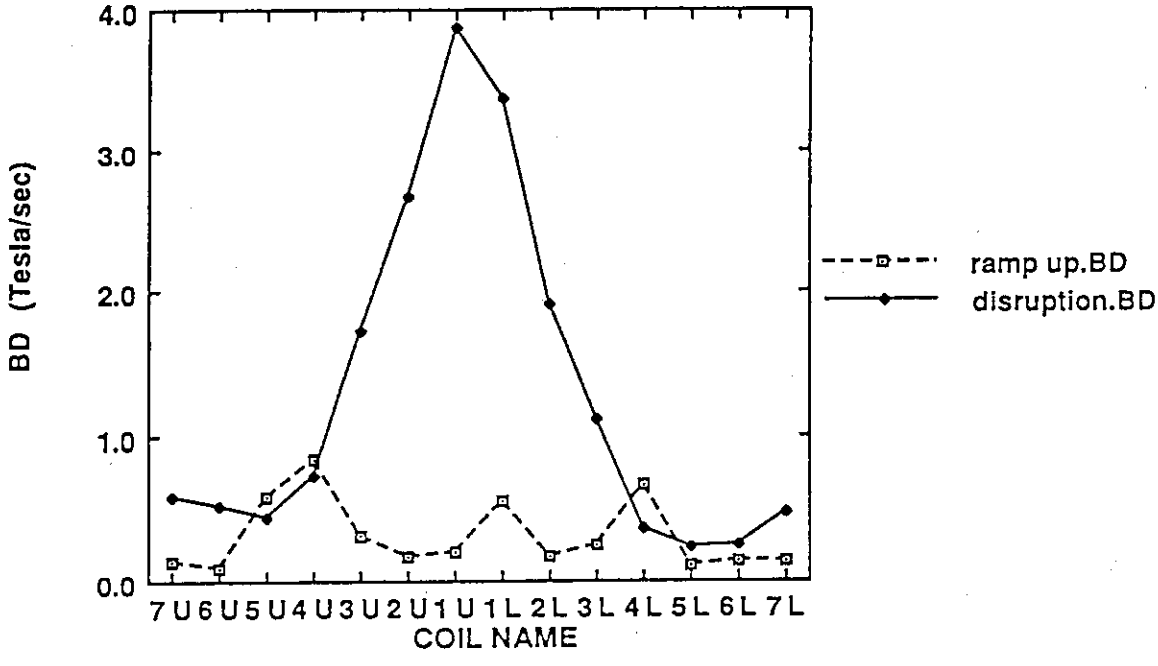

Fig. 6.4.2 Maximum field change rate of PF coils.

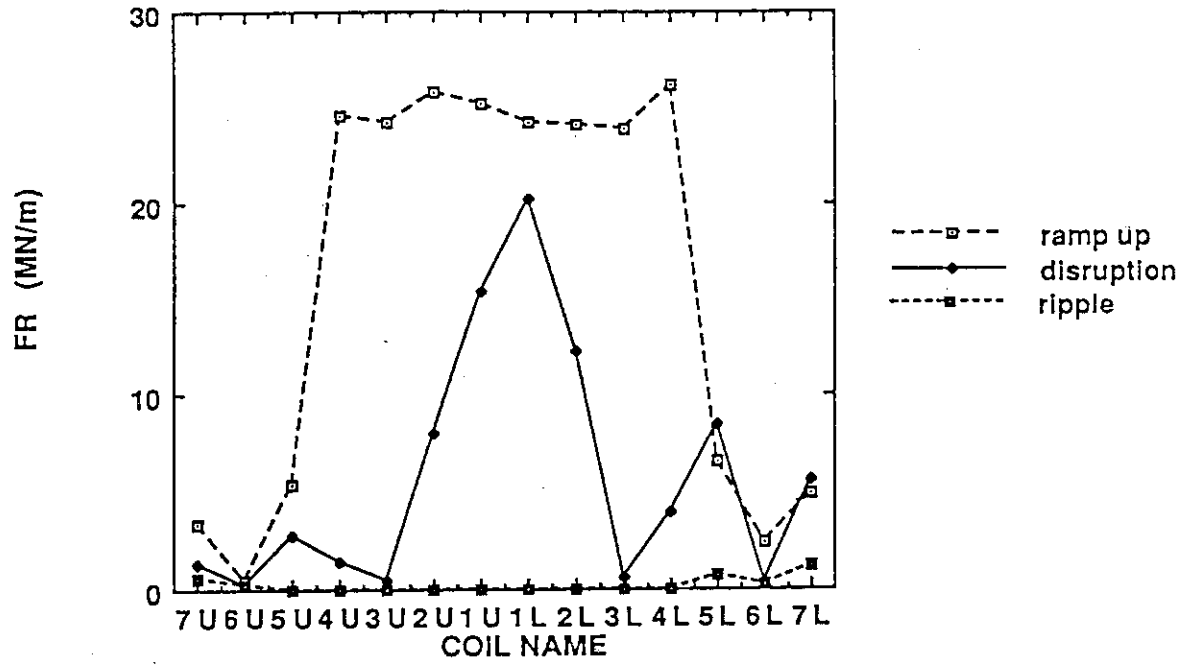

Fig. 6.4.3 Maximum foop forces (MN/m) of PF coils.

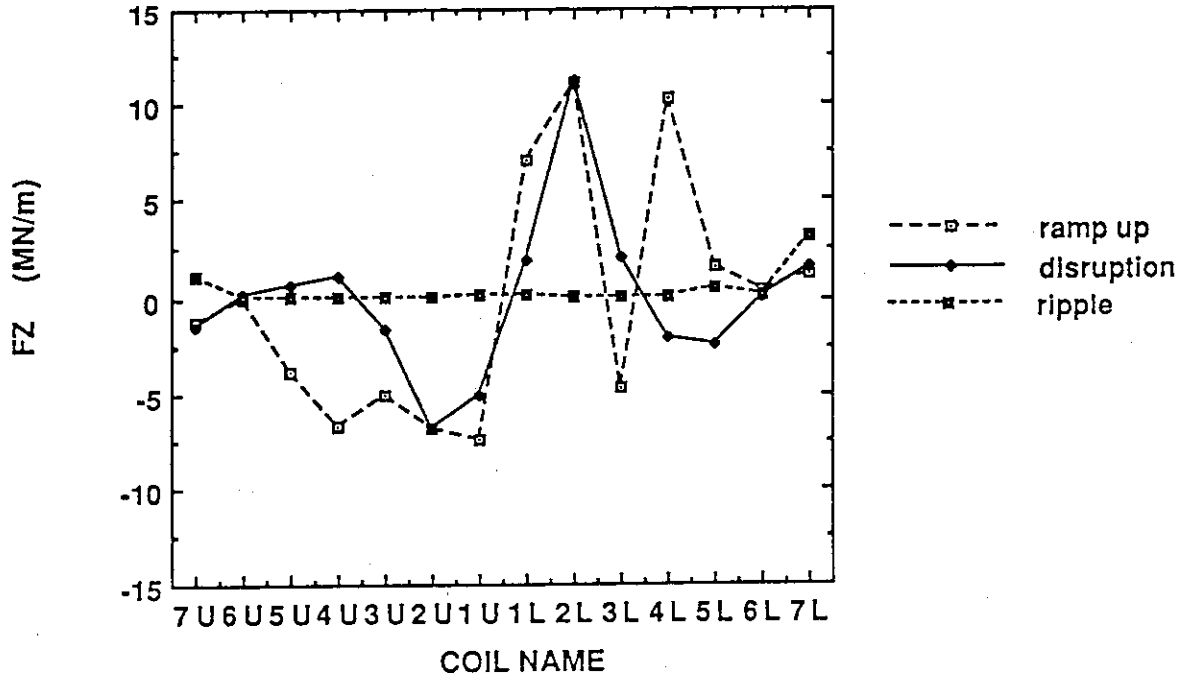

Fig. 6.4.4 Maximum vertical forces (MN/m) of PF coils.

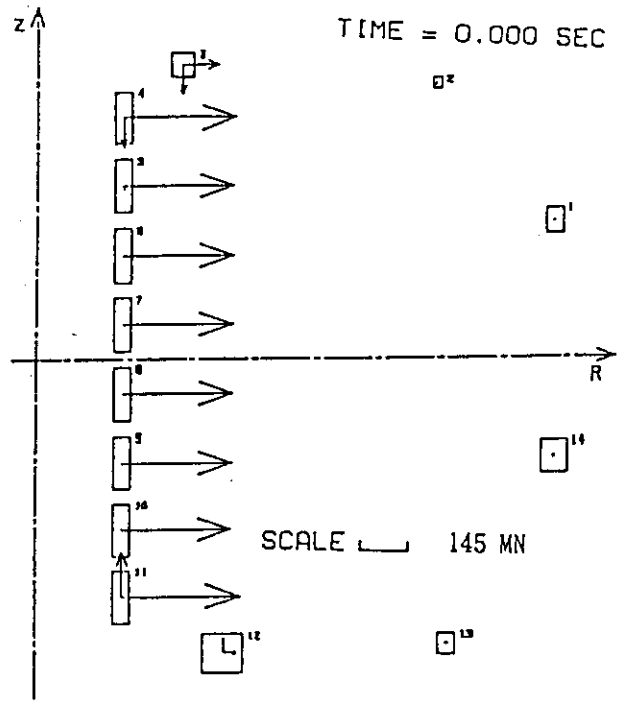

Fig. 6.4.5 Electromagnetic force (at initial magnetization).

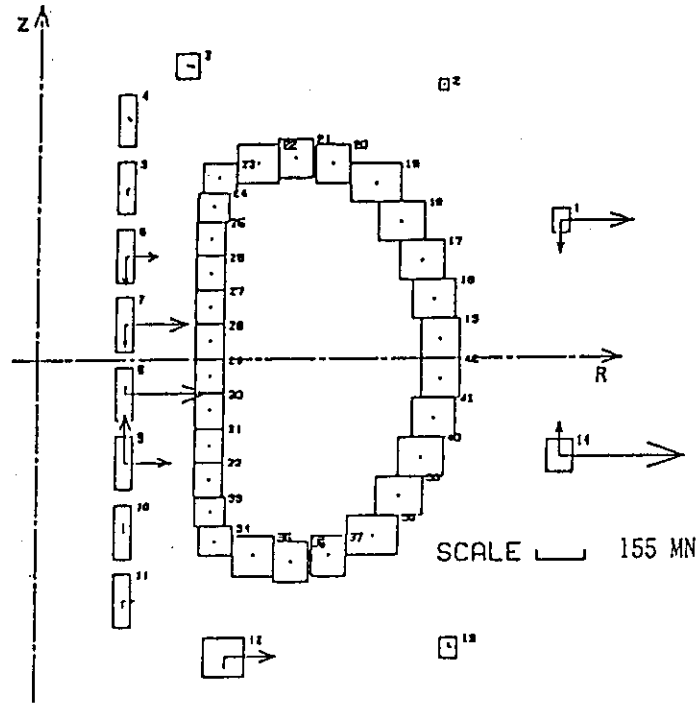

Fig. 6.5.6 Electromagnetic force (at burn phase).

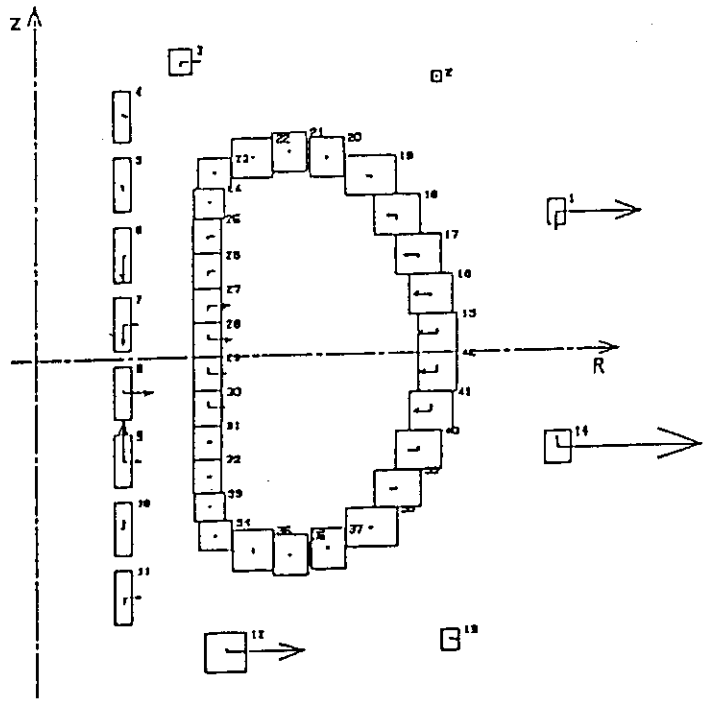

Fig. 6.4.7 Electromagnetic force (at 20msec after disruption).

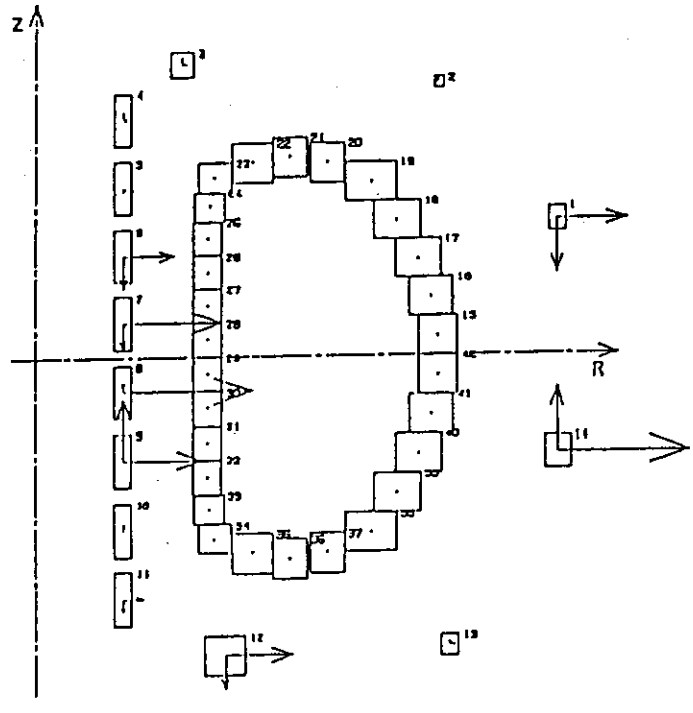

Fig. 6.4.8 Electromagnetic force (at 9.9sec after disruption).

6.5 Stress Analysis

6.5.1 Fundamental view of poloidal coil support

A few fundamental criteria for designing poloidal field coil supports (called the "PF coil supports") are described below:

1. To facilitate periodic inspections of the reactor, it should be easy to maintain, assemble, and disassemble the PF coils supports.

2. To enhance the reliability of the poloidal coils, the support structure should be designed to lessen the accumulation of electromagnetic forces in the coil winding.

3. To guarantee that the support structure has sufficient mechanical strength, the support structure used to install insulation layers and cooling pipes should have as few divisions as possible.

The electromagnetic hoop force is sustained only by the conduit of the conductor.

6.5.2 Support structure for CS coils

The support structure for CS coils is shown in Figs. 6.5.1 and 6.5.2. The structure consists of protruding shelves and a central cylinder that has an insulation breaking induced current. Helium for cooling the CS coils is supplied through pipes laid in inlet gaps in the central cylinder.

The CS coils and support structure are divided into 8 modules in the vertical direction. Each module consists of one CS coil and a corresponding support. The 8 modules are connected together by bolts. Each module's support structure is split in half, and insulation is placed between the two halves. No insulation is placed between modules, however.

Insulations of the support structures for all the modules are aligned when assembling the modules. Adjacent modules are also connected together by several rods set discretely at the fringes of the protruding shelves for the purpose of reinforcement. In these support structures, the vertical force acting on each CS coil is absorbed by the protruding shelves.

6.5.3 Support structure of EF coils

The design concept for the EF coil support structure is shown in Figs. 6.5.3, 6.5.4, and 6.5.5. EF coils are supported mainly by TF coils. The upper and lower diverter coils (5U and 5L coils) may possibly be placed in grooves of the central TF support structure. EF coils that have a large radius (7U and 7L coils) may be combined together to cancel vertical electromagnetic forces. The final selection of EF coil support structures will take easy in assembly and spatial arrangement into account.

EF coils have reinforcement bands. The conductors and reinforcement bands of EF coils bear the bending load caused by vertical and ripple electromagnetic forces. The sliding members are placed between the reinforcement band and the support structure. In this way, EF coils are unrestricted in the radial direction.

6.5.4 Evaluation of mechanical strength

Hoop, vertical, and ripple electromagnetic forces must all be considered when evaluating mechanical strength. The maximum value for each of these forces is given in Figs.6.4.3 and 6.4.4. Sections 6.4 and 6.2 describe the parameters governing poloidal coils and their conductors, respectively.

1. CS coils

(a) Coil windings

CS coils are supported individually by protruding shelves so that the electromagnetic forces acting on any given CS coil is not compounded with forces acting on the other CS coils. Because of this arrangement, we can restrict our analysis to the stress on 4L coils; 4L coils experience the heaviest electromagnetic force. Upon initial excitation (which is when the forces reach a maximum) hoop forces are 360 MN and vertical forces are 140 MN.

The average hoop stress in the outer conduit (material: JN1) and the average compressive stress in the side walls of the outer conduit are as follows:

$$s_R = 250 \text{ MPa} \qquad s_C = 160 \text{ MPa}$$

The peak value of the hoop stress on the outer conduit located inside the coil is obtained by the following equation:

$$s_{R(peak)} = (B_{MAX} * j * R_{IN}/f$$

where

B_{MAX}: maximum magnetic field
j: current density of conductor
R_{IN}: inner radius
f: ratio of outer conduit to conductor

In 4L coils, $s_{R(peak)}$ is 510 MPa.

Finally, the total stress of the outer conduit located inside the 4L coil is as follows:

$$s_{R(peak)} + s_C = 670 \text{ MPa}$$

This is lower than the allowable stress of JN1 (830 MPa).

(b) Support structure

The stress and the displacement in the support structure have been calculated by using NASTRAN. The model is based on a 45° segment of a CS coil and its accompanying support structure. Elements, load conditions, and boundary conditions are described below.

Used elements

central cylinder:	shell element
protruding shelf:	shell element
coil winding:	beam element
connection between winding and shelf:	spring element

Load condition

maximum electromagnetic force in plasma burning

Boundary condition

periodic boundary condition

Figure 6.5.6 shows the mesh geometry. Shape deformation in the support structure is shown in Figure 6.5.7, and the structure's stress distribution is shown in Fig. 6.5.8. The maximum displacement--about 0.7 mm--occurs in the shelf between 3U and 2U coils. The maximum stress in the support structure is 18~19 MPa (equivalent stress of von-Mises).

2. EF coils

(a) Coil windings

Only the outer conduits of EF coil windings are considered to be structural members. The tensile stresses acting on the section of the outer conduits of EF coils subjected to electromagnetic hoop forces are as follows:

5U : s_T = 95 MPa	5L : s_T = 73 MPa
6U : s_T = 139 MPa	6L : s_T = 195 MPa
7U : s_T = 296 MPa	7L : s_T = 261 MPa

The compressive stresses due to vertical electromagnetic forces are as follows:

5U : s_C = 31 MPa	5L : s_C = 15 MPa
6U : s_C = 4 MPa	6L : s_C = 7 MPa
7U : s_C = 44 MPa	7L : s_C = 34 MPa

The outer conduits of EF coils are subjected to a bending action caused by the vertical and ripple electromagnetic forces. Figure 6.5.9 shows the spans between the support structures when EF coils are approximated by linear beams. The span between support structures within the 5U (5L) and 6U (6L) coils is short, and the ripple electromagnetic forces acting on these coils are not so large.

In estimating the bending stresses of 7U and 7L coils, we will assume that there is no bonding between the conductors of these coils. This assumption may cause us to overestimate the bending stress. If the reinforcement band is 50 mm thick, the bending stresses (s_B) in the outer conduits of 7U and 7L coils are as follows:

7U : s_B = 93 MPa	7L : s_B = 91 MPa

Total stresses in the outer conduits of 7U and 7L coils are as follows:

7U : $s_T+s_C+s_B$ = 433 MPa
7L : $s_T+s_C+s_B$ = 386 MPa

These values are lower than the allowable stress of the outer conduit material JN1 (830 MPa) so there is no problem as to the mechanical strength of the coil winding of EF coils.

(b) Support structure

The compressive stresses applied on the sliding members under vertical

electromagnetic forces are roughly as follows:

5U : s_c = 7 MPa	5L : s_c = 4 MPa
6U : s_c = 1 MPa	6L : s_c = 2 MPa
7U : s_c = 9 MPa	7L : s_c = 8 MPa

When each support structure is joined to a TF coil using 10 bolts (diameter: 48 mm), the tensile stresses acting on the bolts are as follows:

5U : s_T = 308 MPa	5L : s_T = 248 MPa
6U : s_T = 17 MPa	6L : s_T = 51 MPa

This analysis demonstrates that the EF coil support structure has sufficient mechanical strength.

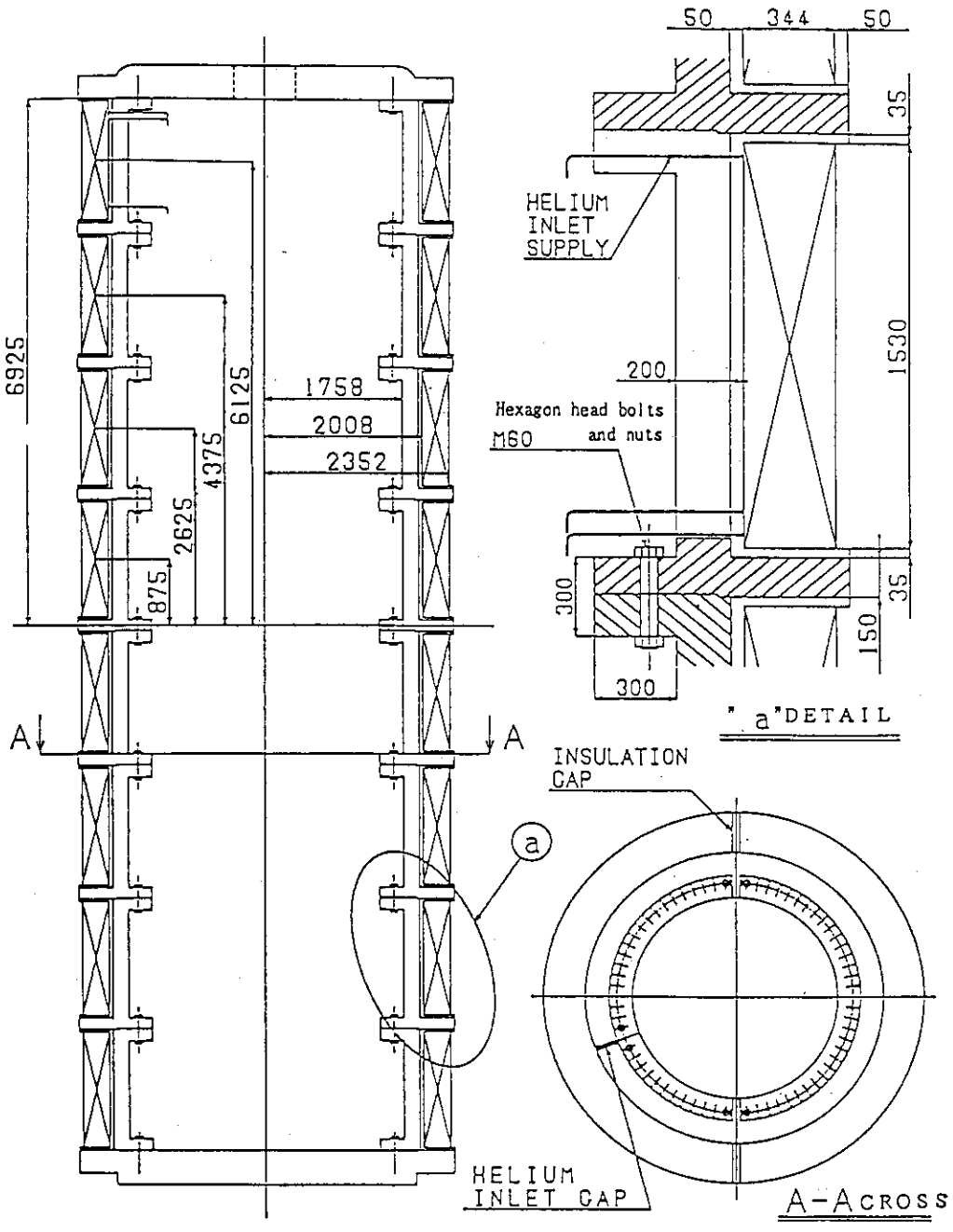

Fig. 6.5.1 Support structure of CS coils I.

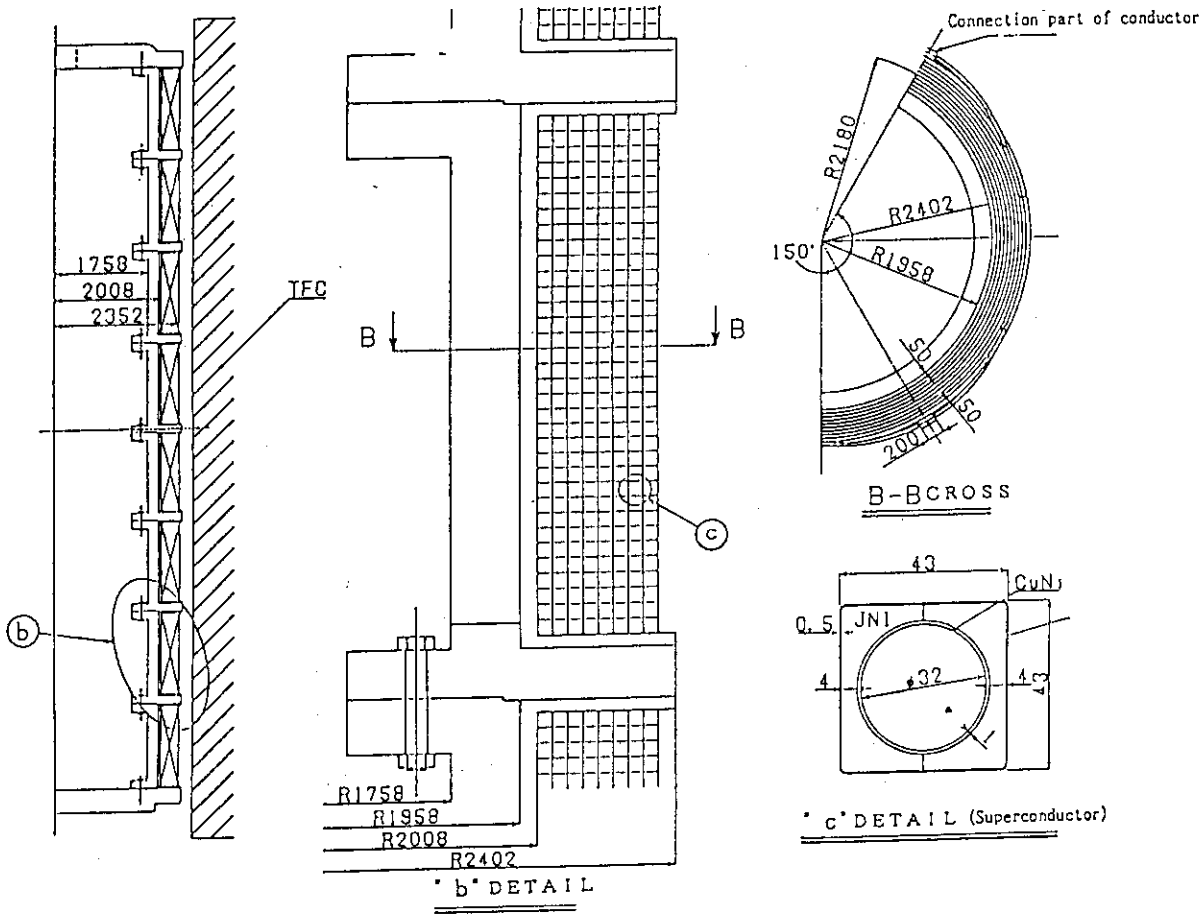

Fig. 6.5.2 Support structure of CS coils II.

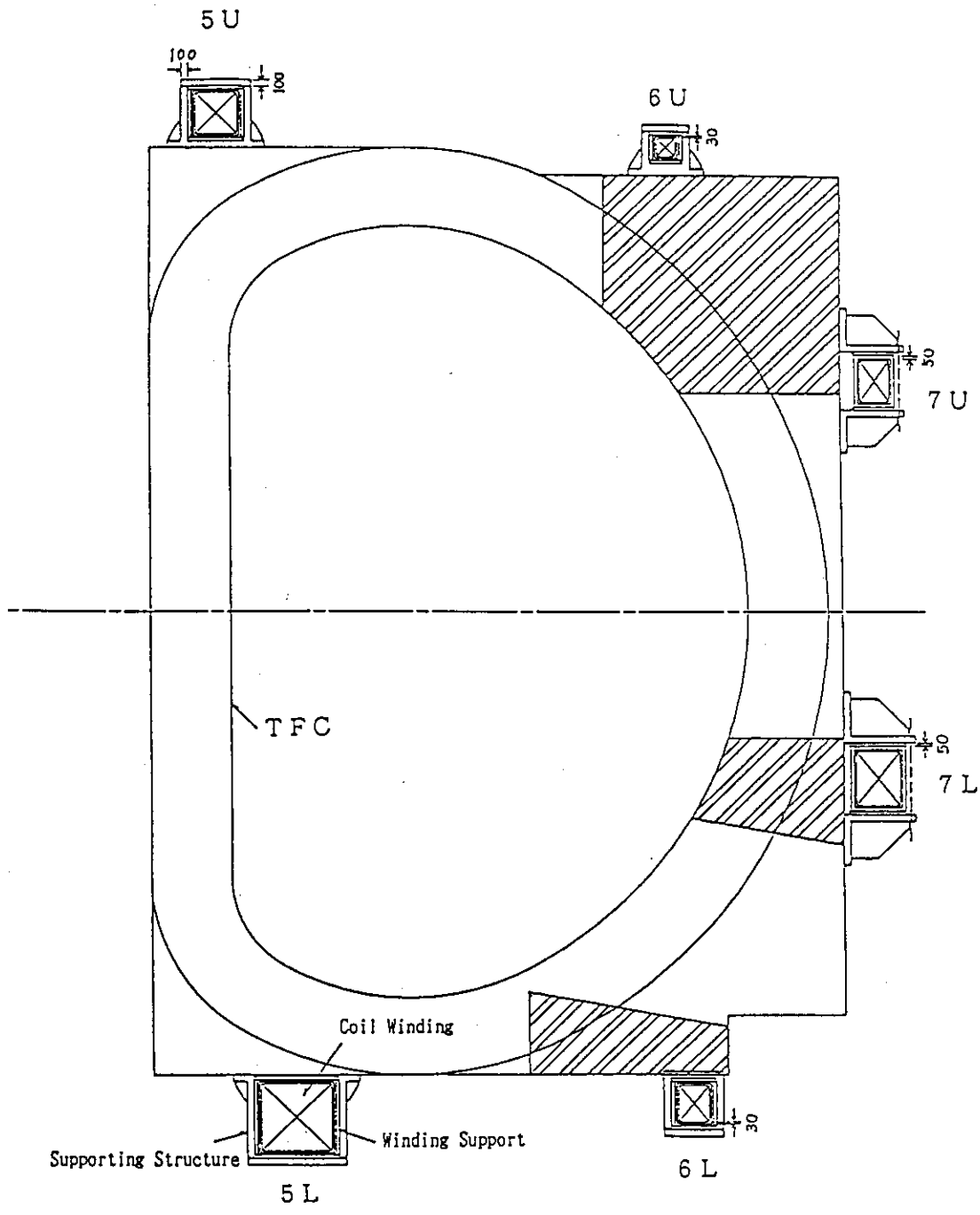

Fig. 6.5.3 Support structure of EF coils (Type A-1).

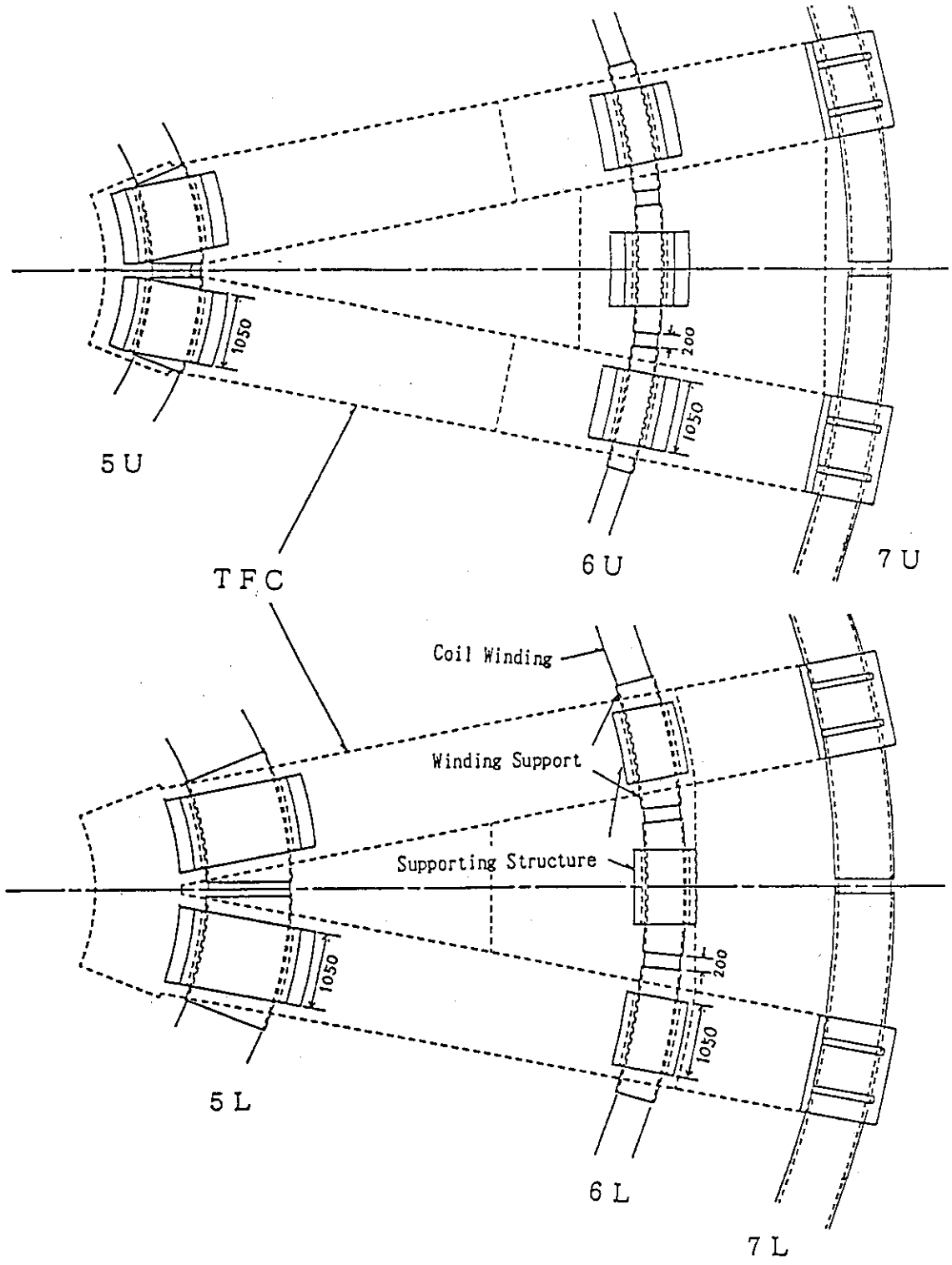

Fig. 6.5.4 Support structure of EF coils (Type A-2).

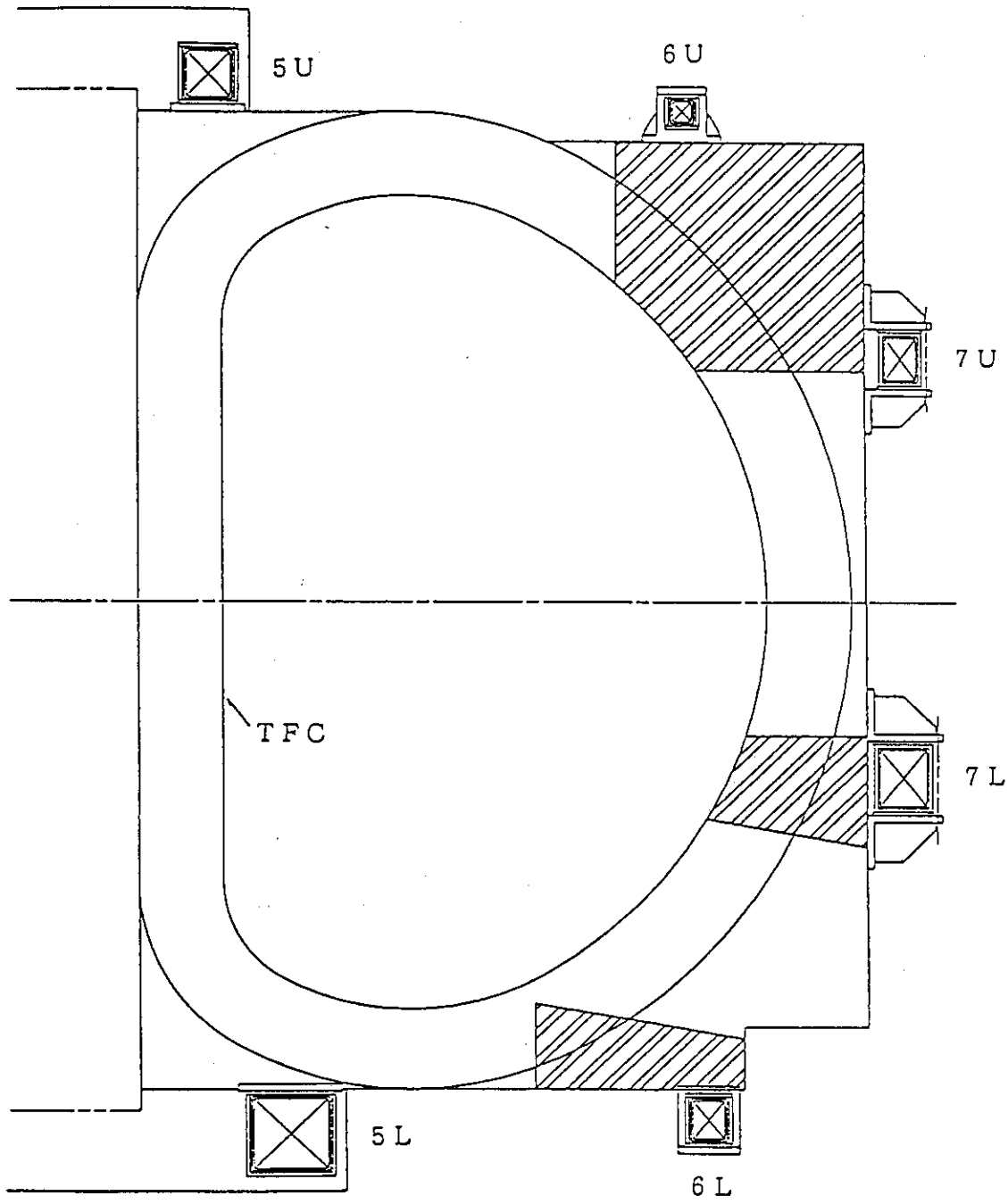

Fig. 6.5.5 Support structure of EF coils (Type B).

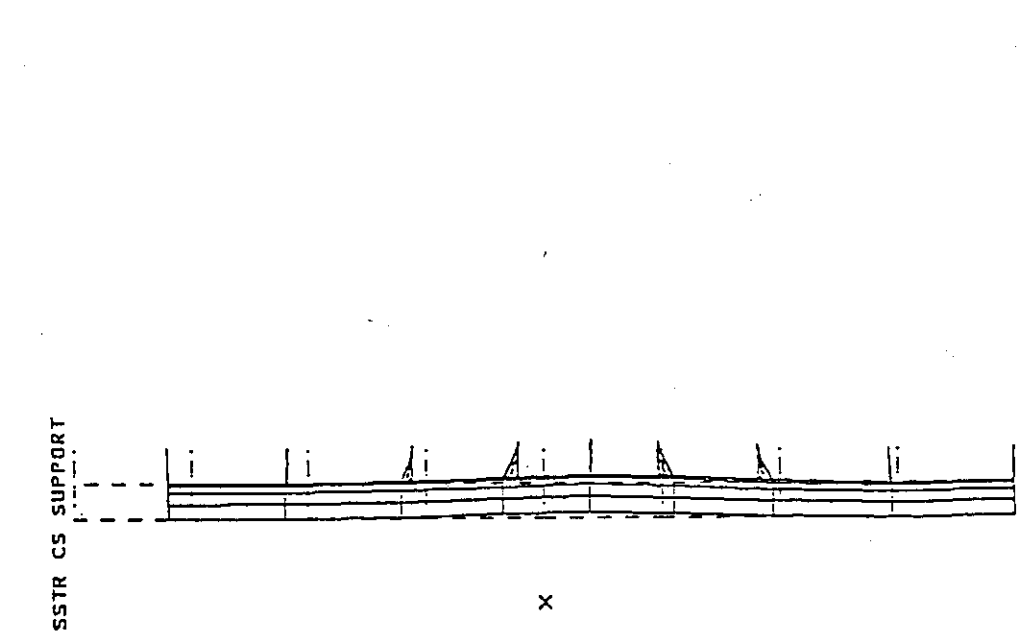

Fig. 6.5.7 Displacement of support structure.

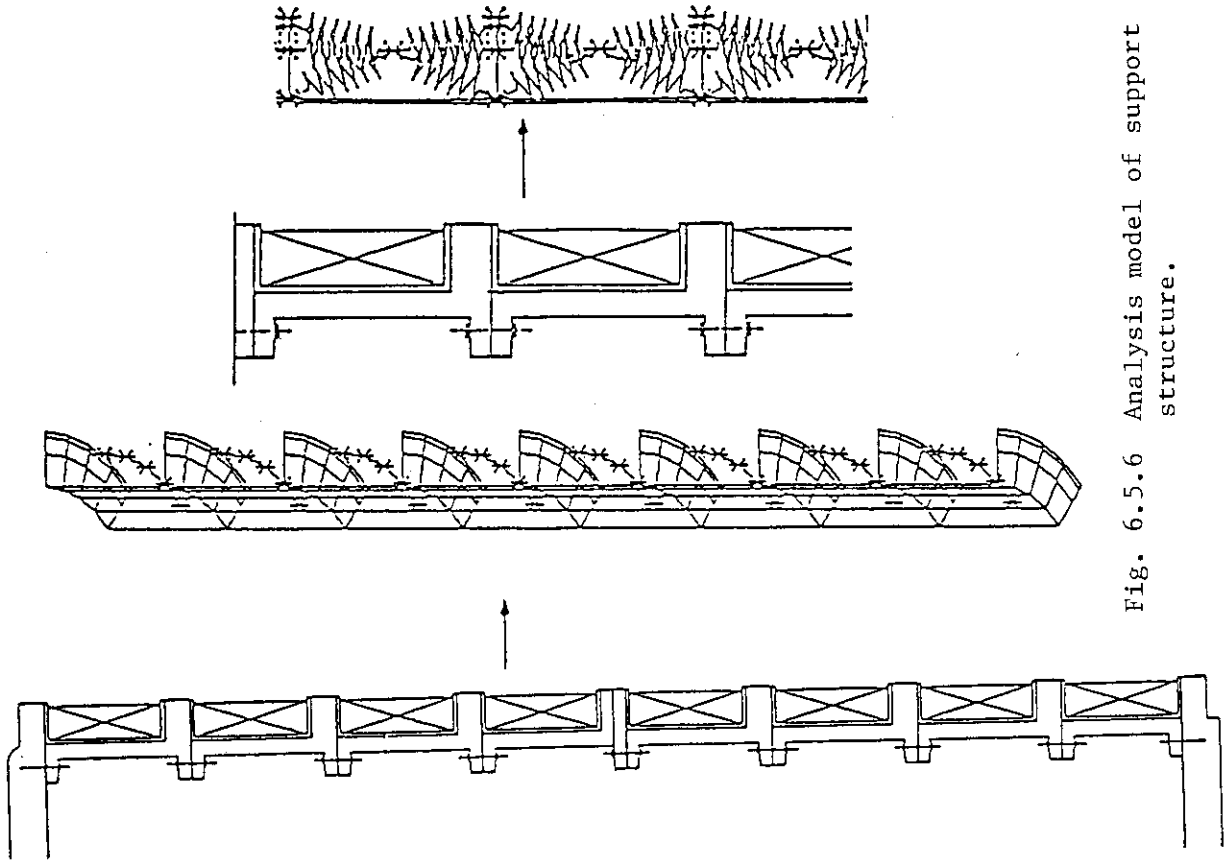

Fig. 6.5.6 Analysis model of support structure.

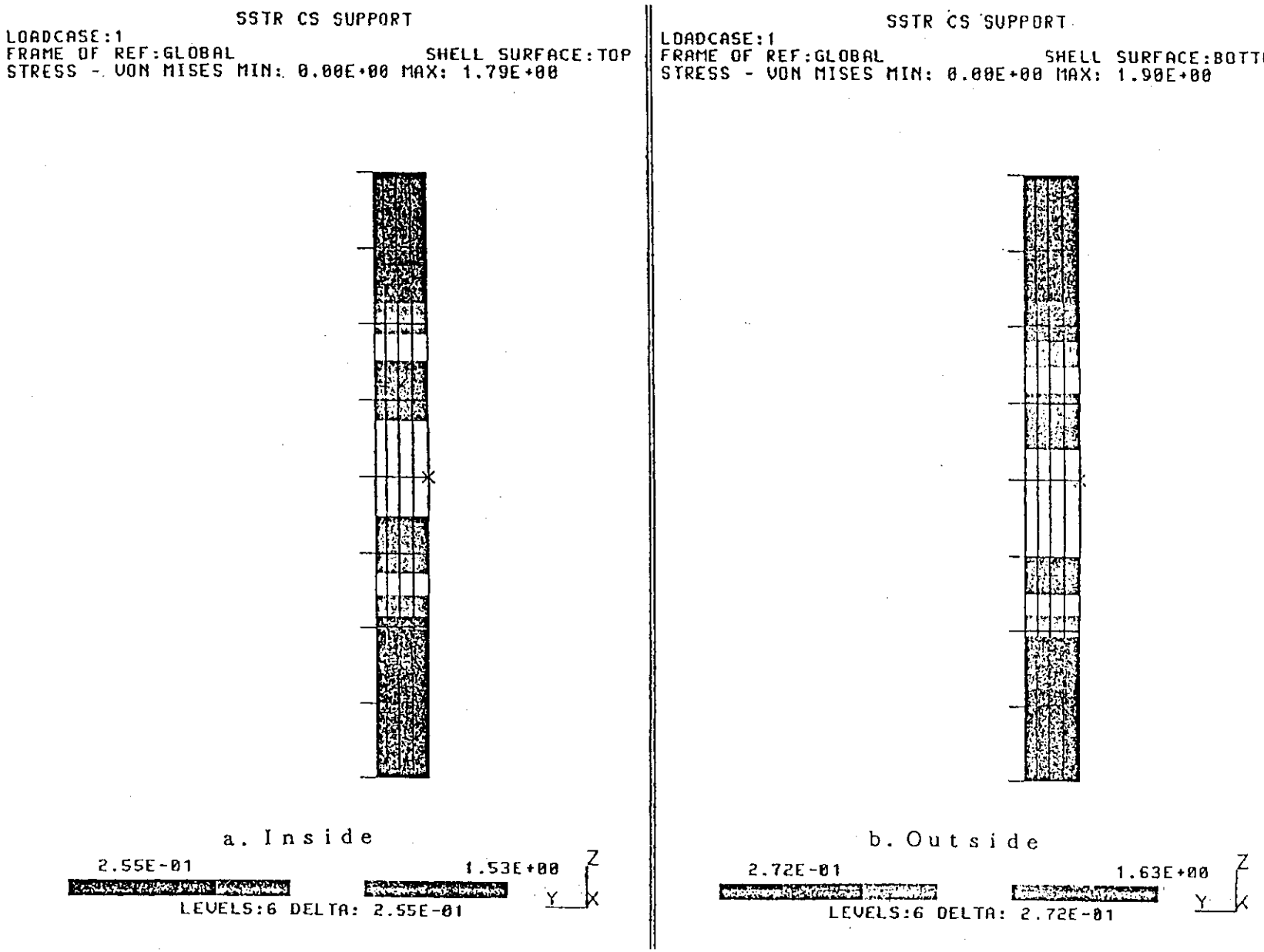

Fig. 6.5.8 Stress of support structure.

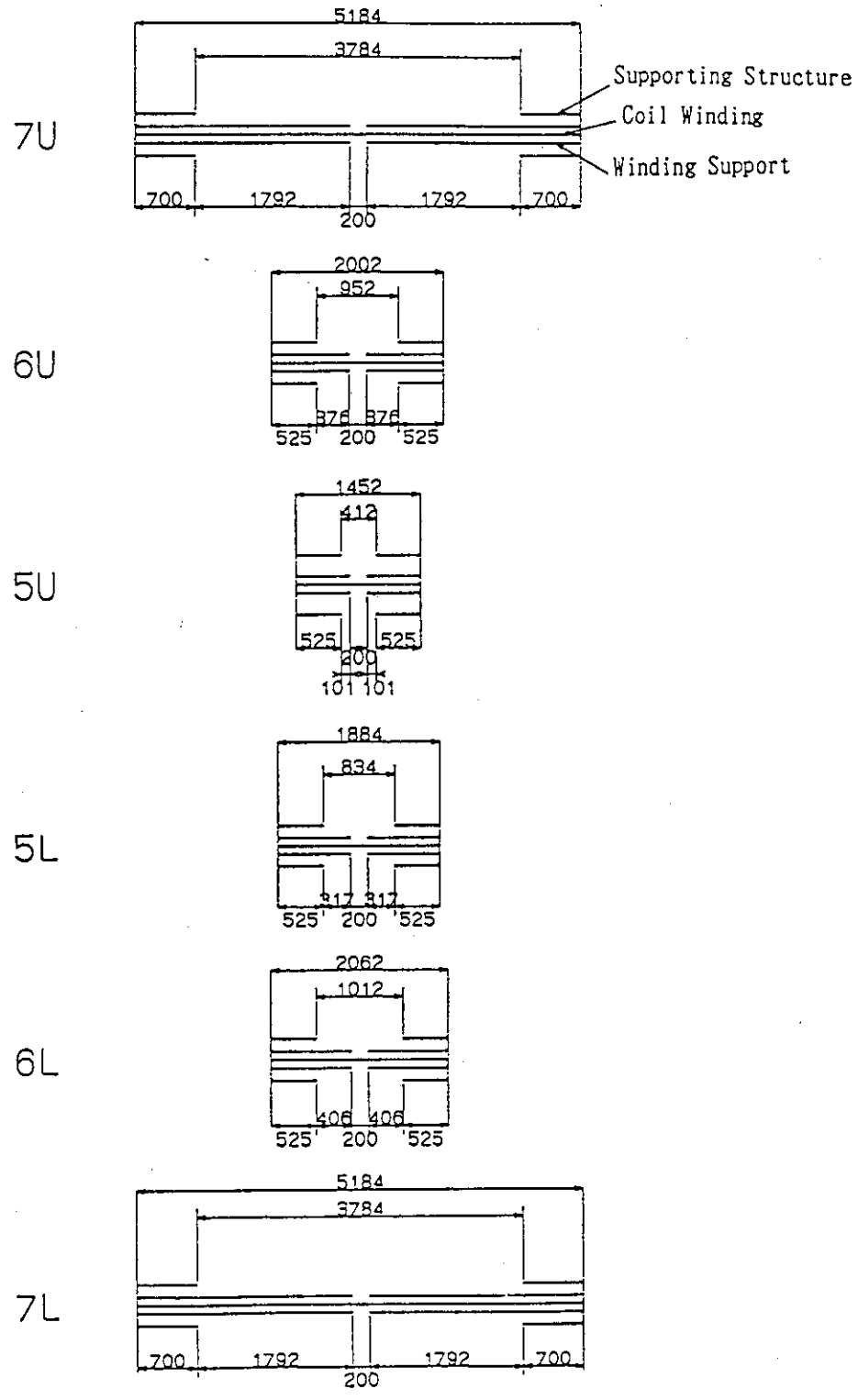

Fig. 6.5.9 Span length of EF coil support.

6.6 Thermal Performance of the Poloidal Field Coil System

6.6.1 AC losses

Time-varying the magnetic field at the coil winding and support structure results in AC losses in the superconductor and in normal metal. These losses arise from several sources: hysteresis losses in the superconducting material, coupling losses between filaments in the composite, coupling losses between strands, and eddy currents in the normal components (e.g., stabilizing copper, conduit, coil casing, and supporting structures).

When estimating AC losses, we have excluded coupling losses between strands because of chromium plating around strand surface. A time constant of more than 1 msec corresponds to the diffusion constant for magnetic flux along the axis in a strand.

The change in the magnetic field during the ramp-up phase and plasma disruption during the burn phase are taken into consideration.

6.6.1.1 Calculation of AC losses in the coil windings

Total AC losses are shown in Table 6.6.1. The first (upper) line in the table corresponds to losses during ramp-up; the second (lower) line corresponds to losses during plasma disruption. The average power loss in the PF coils is about 9 kW for ramp-up and 12 kW for plasma disruption. The total AC loss during the ramp-up phase is 10 times that during plasma disruption. We obtained the coupling time constants of about 12 msec and 40-90 msec for CS and EF coil strands, respectively.

Figure 6.6.1 shows a stack column plot of AC losses in the ramp-up phase. Thirty percent of the total AC loss in PF coils comes from the 7U and 7L coils.

6.6.1.2 Calculation of AC losses in the support structures

Figures 6.6.2 and 6.6.3 give the AC losses due to CS and EF coil support structures for regular time intervals during the ramp-up phase. The average power loss over 100 seconds was 9.3 kW for CS coil support structures and 0.1 kW for EF coil casings and supporting frames.

6.6.2 Stability of superconductors in the ramp-up phase

Table 6.6.2 gives the temperature and stability margins of superconductors inside the PF coils. In each coil, the temperature margin was more than 1.5 K, and the stability margin was more than 270 mJ/cc-strand.

Table 6.6.3 shows the AC loss per unit volume of strand in PF coils. Conduction and radiation losses are estimated based on the measured value of DPC-EX (that is, 15 W per coil). Assuming that the pressure and density of coolant in the cooling path are constant, the outlet temperatures of all PF coils are calculated based on the increase in enthalpy of the coolant (See Table 6.6.4). The outlet temperatures in both the ramp-up and burn phases are less than the current sharing temperatures in all PF coil conductors.

6.6.3 Cool-down time of coils

The cool-down weight of PF coil system is listed in Table 6.6.5. Figures 6.6.4 and 6.6.5 show that the temperature-vs-time relation is a function of the helium mass flow rate of the CS and 7L coil superconductors during cool-down. The calculations were carried out based on the following assumptions.

1. Cooling channels for the support structures are provided separately from those for the coil windings.

2. Because of the way pancakes are cooled, the cool-down time of any given PF coil is the same as that of each pancake stacked on the coil.

3. The weight of a strand is assumed to equal that of a copper wire having the same diameter.

4. The pressure drop of coolant is less than 10 bar during the cool-down.

7L coils that have the maximum weight possible can sustain a superconductivity state for about two weeks with a mass flow rate of 1 g/s. To avoid undue thermal stresses, the temperature differences in each coil and in the elements of the facility as well as between all of these components will be estimated precisely.

Table 6.6.1 Total AC loss of PF coils

(Unit : kJ)

Coil name & No.	Coupling & Eddy loss	Hysteresis loss	Total loss
1. 7U	83.8(54.5)[1]	24.2	108.0(78.7)
	12.2(8.0)[2]	1.9	14.1(9.9)
2. 6U	18.5(12.1)	6.1	24.6(18.2)
	11.6(7.5)	0.8	12.4(8.3)
3. 5U	40.7(26.7)	8.7	49.4(35.4)
	2.2(1.4)	0.5	2.7(1.9)
4. 4U	18.0(4.7)	28.6	46.6(33.3)
	0.4(0.1)	1.3	1.7(1.4)
5. 3U	8.9(2.3)	35.0	43.9(37.3)
	2.1(0.5)	2.8	4.9(3.3)
6. 2U	11.4(2.9)	46.5	57.9(49.4)
	7.6(1.9)	4.1	11.7(6.0)
7. 1U	17.2(4.3)	56.5	73.7(60.8)
	14.8(3.8)	4.9	19.7(8.7)
8. 1L	27.4(6.9)	65.0	92.4(71.9)
	10.9(2.8)	4.1	15.0(6.9)
9. 2L	12.6(3.2)	49.9	62.5(53.1)
	3.8(1.0)	2.9	6.7(3.9)
10. 3L	7.4(1.9)	34.1	41.5(36.0)
	0.8(0.2)	1.9	2.7(2.1)
11. 4L	13.7(3.5)	26.6	40.3(30.1)
	0.2(---)	0.8	1.0(0.8)
12. 5L	30.0(19.6)	19.9	49.9(39.5)
	2.2(1.4)	1.0	3.2(2.4)
13. 6L	53.0(34.6)	18.7	71.1(53.3)
	5.5(3.6)	1.0	6.5(4.6)
14. 7L	131.8(85.9)	42.7	174.5(128.6)
	14.4(9.4)	2.8	17.2(12.2)
Total loss	474.4(263.1)	462.5	936.9(725.6)
	88.7(41.6)	30.8	119.5(72.4)

Remarks 1) 1st line : ramp up phase
2) 2nd line : disruption phase
bracket : mimimum value

Table 6.6.2 Temperature and stability margin for PF coils

Coil name & No.	B_{max} (Tesla)	I OP (kA)	I c (kA)	Δ T (K)	TCS (K)	Δ H (mJ/cc-st)
1. 7U	4.62	45.5	122	1.77	6.27	291
2. 6U	2.52	46.9	170	2.69	7.19	296
3. 5U	5.25	38.7	108	1.64	6.14	276
4. CS	7.0	33.0	300	1.54	6.04	271
5. 5L	5.72	27.3	97	1.68	6.18	286
6. 6L	3.89	39.3	139	2.26	6.76	311
7. 7L	5.21	36.2	108	1.71	6.21	286

Table 6.6.3 AC loss per unit volume of strand in PF coils

(Unit : mJ/cc-st)

Coil name & No.	Coupling & Eddy loss	Hysteresis loss	Total loss
1. 7U	17.6(11.4)[1]	5.1	22.7(16.5)
	2.6(1.7)[2]	0.4	3.0(2.1)
2. 6U	19.5(12.7)	6.4	25.9(19.1)
	12.2(8.0)	0.8	13.0(8.8)
3. 5U	21.8(14.3)	4.6	26.4(18.9)
	1.2(0.8)	0.3	1.5(1.1)
4. 4U	8.1(2.1)	12.8	20.9(14.9)
	0.2(---)	0.6	0.8(0.6)
5. 3U	4.0(1.1)	15.7	19.7(16.8)
	0.9(0.2)	1.2	2.1(1.4)
6. 2U	5.1(1.3)	20.8	27.2(22.1)
	3.4(0.9)	1.9	5.3(2.8)
7. 1U	7.7(1.9)	25.3	25.9(27.2)
	6.6(1.7)	2.2	8.8(3.9)
8. 1L	12.3(3.1)	29.1	41.4(32.2)
	4.9(1.3)	1.8	6.7(3.1)
9. 2L	5.6(1.4)	22.4	29.4(23.8)
	1.7(0.4)	1.3	3.0(1.7)
10. 3L	3.3(0.8)	15.3	28.0(23.7)
	0.4(0.1)	0.8	1.2(0.9)
11. 4L	6.1(1.6)	11.9	18.0(13.5)
	---(---)	0.4	0.4(0.4)
12. 5L	4.6(3.0)	3.0	7.6(6.0)
	0.3(0.2)	0.1	0.4(0.3)
13. 6L	16.3(10.6)	5.7	22.0(16.3)
	1.7(1.1)	0.3	2.0(1.4)
14. 7L	14.3(9.3)	4.6	18.9(13.9)
	1.6(1.0)	0.3	1.9(1.3)

Remarks 1) 1st line : ramp up phase
2) 2nd line : disruption phase
bracket : mimimum value

Table 6.6.4 Outlet temperature of PF coils

Coil name & No.	Heat load[1] (mJ/cc-He)	Heat load[2] (mJ/cc-He)	Outlet temp.[1] (K)	Outlet temp.[2] (K)	Current[3] sharing temp. (K)
1．7U	450	45.5	5.22	5.29	6.27
2．6U	728	51.8	5.60	5.67	7.19
3．5U	260	52.8	4.94	5.03	5.14
4．CS[4]	93	83.7	4.66	4.80	6.04
5．5L	178	15.2	4.80	4.83	6.18
6．6L	336	44.0	5.06	5.13	6.76
7．7L	320	37.8	5.04	5.10	6.21

Remarks 1) conduction and radiation
2) ramp up phase
3) minimum value in ramp up phase
4) 1L coil

Table 6.6.5 Cooldown weight of PF coil system

(Unit:ton)

Coil name	Winding & insulator	Support structure	Total weight
CS coils	415	540	955

Coil name	Winding, insulator & coil case	Support structure & spacer	Total weight
7 U	238	58	296
6 U	53	63	116
5 U	74	58	132
5 L	236	85	321
6 L	160	94	254
7 L	403	68	471
Total weight	1164	426	1590

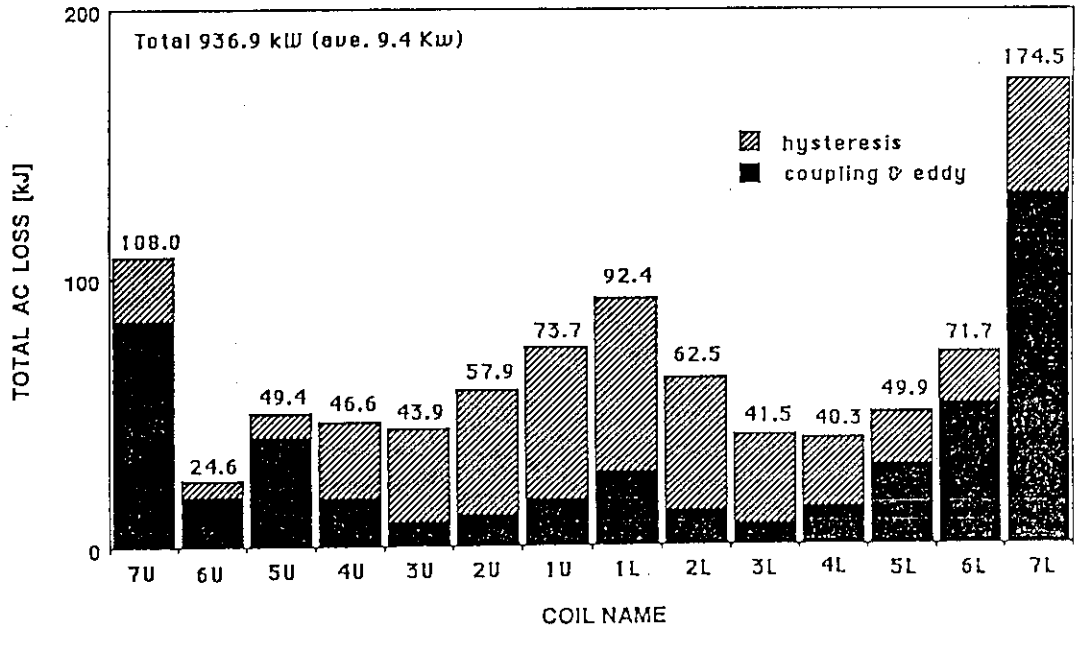

Fig. 6.6.1 AC loss distribution of PF coils in ramp up phase.

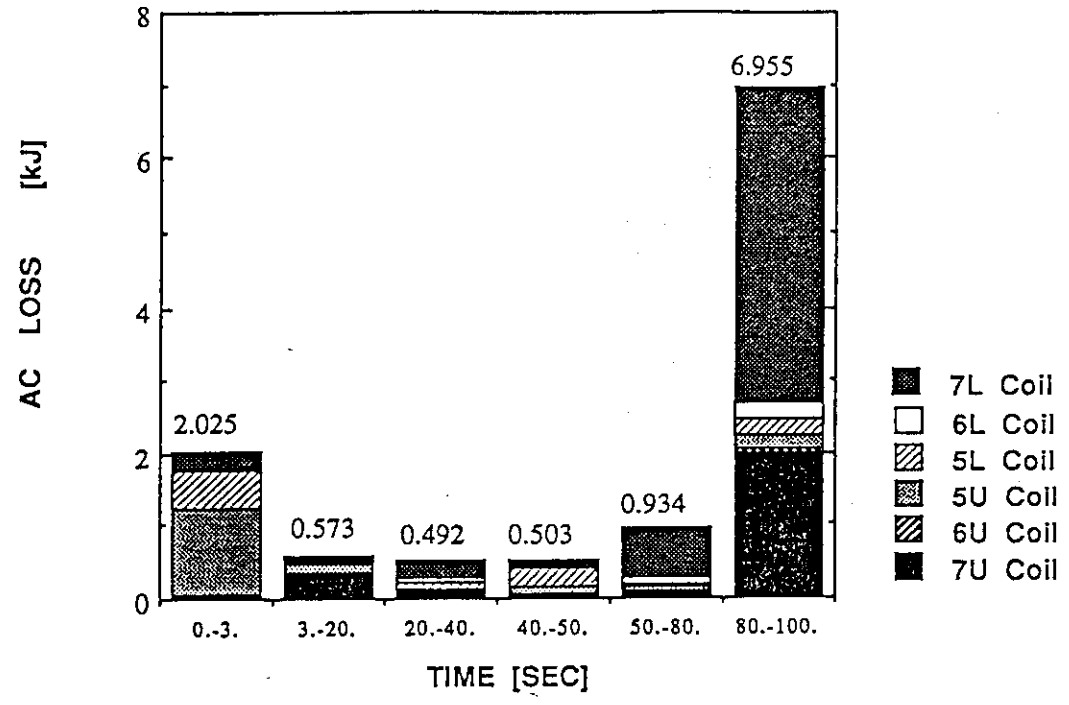

Fig. 6.6.2 AC loss contribution of EF coils support structure in ramp up phase.

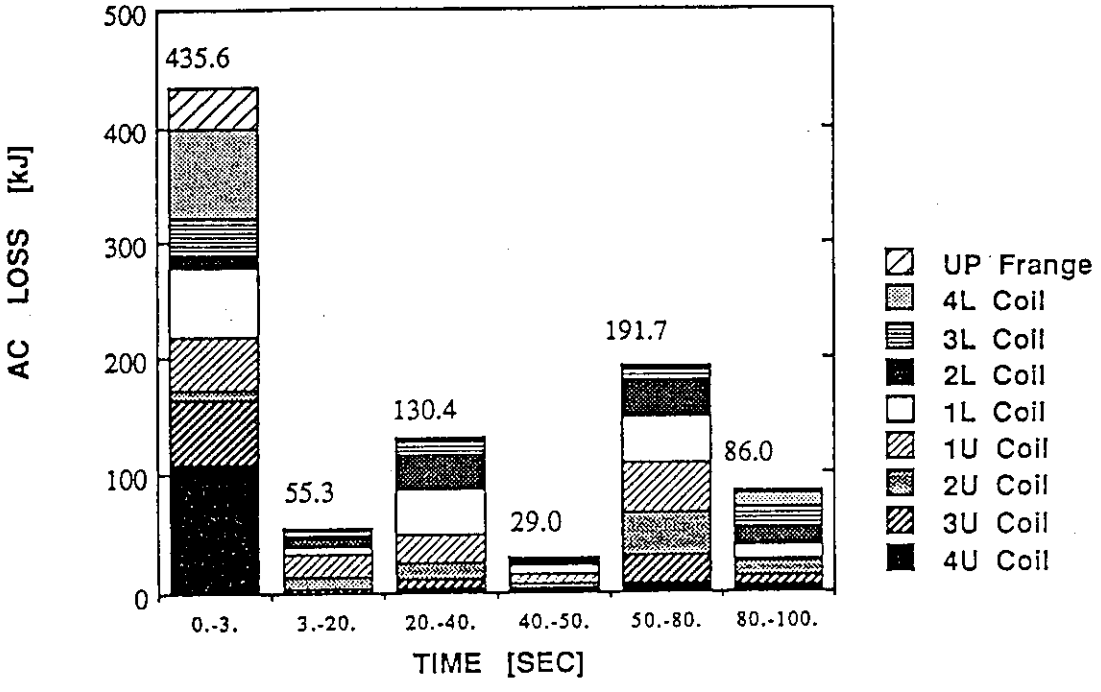

Fig. 6.6.3 AC loss contribution of CS coils support structure in ramp up phase.

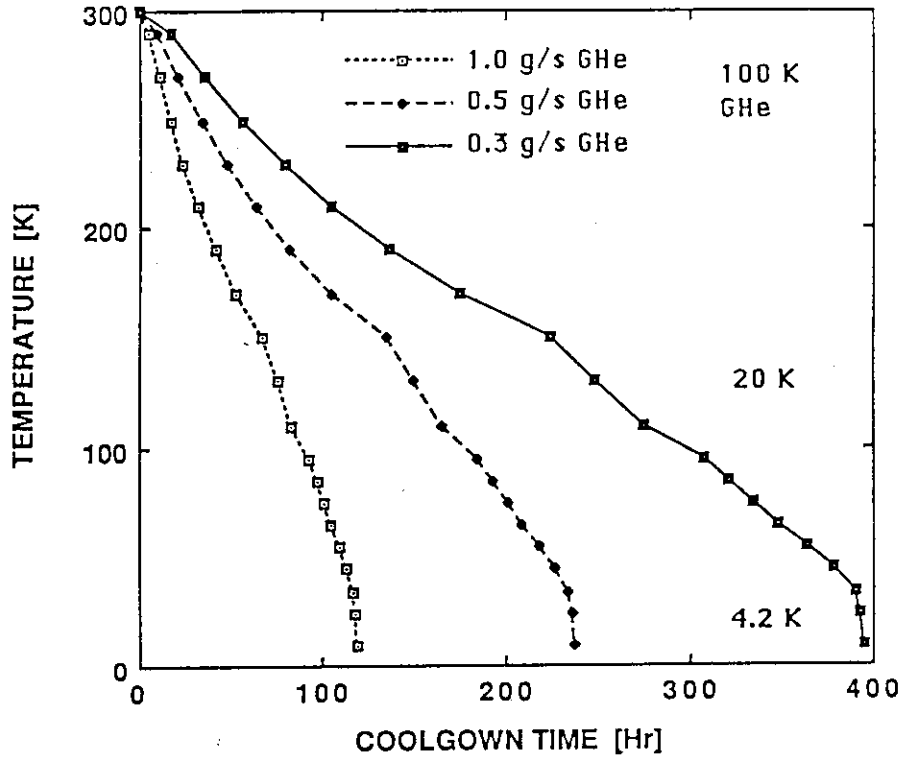

Fig. 6.6.4 Characteristics of cooling-down for CS coil.

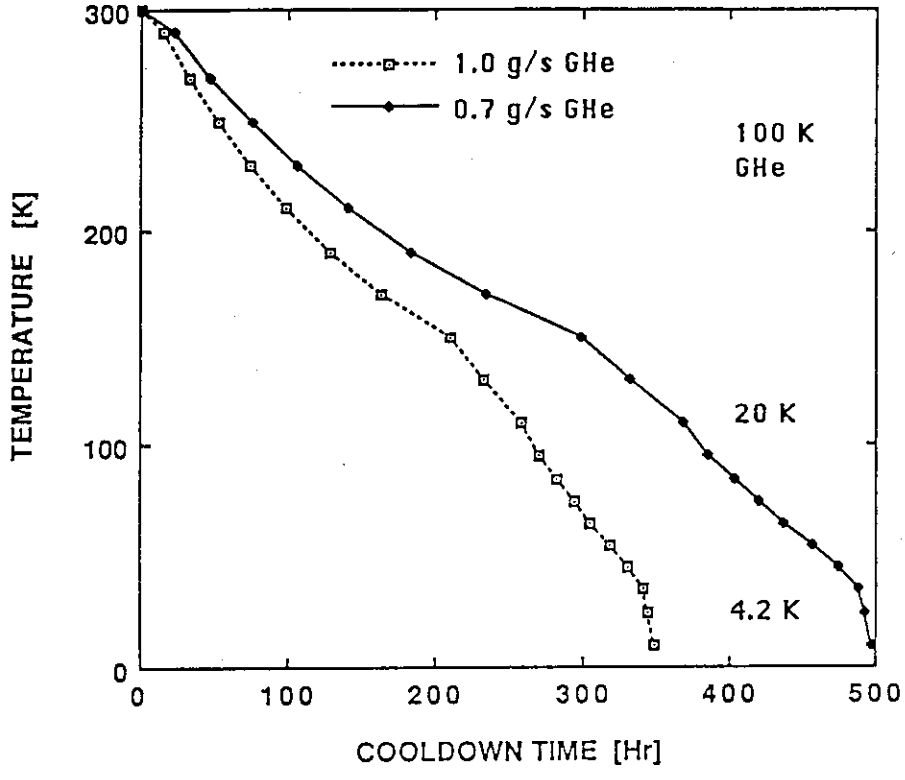

Fig. 6.6.5 Characteristics of cooling-down for 7L coil.

6.7 Coil Protection System and Dump Simulation

When the superconducting coil is quenched as a result of a heat pulse or other disturbance and does not recover its superconducting state, the corresponding coil currents have to be discharged faster so as to prevent coil damage and excessive increases in all other coil currents induced in the electromagnetic coupling. Ideally, the coil protection system should be set up so that the magnetic energy stored in each coil is removed by the external dump resistor in a short period of time. Such an arrangement makes it possible to use a small-capacity power convertor. Moreover, to enhance reliability the coil protection system should be independent from the power system.

In this study, even if only one coil is quenched, all PF coil currents are simultaneously discharged by dump resistors with almost the same current-decay-time constants for the following reasons.

a) It is impossible to prolong plasma preservation using a quench coil. It is not necessary to preserve all the other coil currents. For this reason, the coil system is shut down temporarily.

b) To prevent an initiation of excessive stresses in the coil windings and support structures during the course of the dumps.

c) The kinematic behavior of the tokamak plasma is not clear during an unbalanced discharge into individual PF coils.

6.7.1 Dump resistor values

Taking into account the design specifications of coils and conductors (that is, a maximum dump-voltage of 20 kV and a maximum temperature rise of 150 K, respectively), we selected typical resistance values so that all coil currents are discharged simultaneously. We used an identical time constant of 10 seconds for each operation.

The above resistances Rj are estimated by the time constant t according to the following equation:

$$R_i=(1/t)SM_{ij}\ I_j(0)$$

where

Mij: inductance matrix of PF coil system,

Ij(0): operation current of coil j before discharge.

6.7.2 Dump simulation

Figures 6.7.1 and 6.7.2 show the current and dump-voltage decays of all coils upon initial magnetization and during the burn phase, respectively. The current decays correspond to cases where the time constant is long because the currents in all the coils flow in the same direction; the dump-voltage decays applies to cases where the energy stored in the PF coil system is at a maximum. Table 6.7.1 shows the maximum dump-voltage and temperature rise of all coils during operation. The temperature rise is estimated based on a hot-spot model that includes a superconducting material, a copper stabilizer and helium coolant. The maximum temperature rise of each coil is obtained from the Um-Tm relations in Fig. 6.7.3 together with the following relation:

$$\int Ij(t)dt = Ajcu * Umj(Tm)$$

where

Ij(t):	conductor current of coil j at time t after the dump started,
Ajcu:	cross sectional area of copper stabilizer in coil j,
Umj(Tm):	Um at temperature Tm of coil j.

The maximum dump-voltage and temperature rise of CS coils are about 3 kV and 70 K, respectively. These values are rather small compared to the design specifications. The maximum dump-voltage of 7L coils is about 19 kV. It is possible to reduce the voltage by resetting the dump resistance of 7L coils so as to achieve a maximum temperature rise of about 150 K.

Table 6.7.1 Resistance, maximum terminal voltage and hot-spot temperature during all PF coil dumps in ramp up phase

Coil name & No.	Resistance (mΩ)	Dump voltage (kV)	Maximum hot-spot temperature (K)
1. 7U	181	8.3	~85
2. 6U	171	8.0	~25
3. 5U	73	2.8	~50
4. 4U	90	2.5	~55
5. 3U	90	2.5	~60
6. 2U	90	2.8	~60
7. 1U	90	2.9	~60
8. 1L	90	3.2	~65
9. 2L	90	2.7	~60
10. 3L	90	2.5	~60
11. 4L	90	3.0	~60
12. 5L	341	9.3	~45
13. 6L	80	3.1	~65
14. 7L	527	19.1	~60

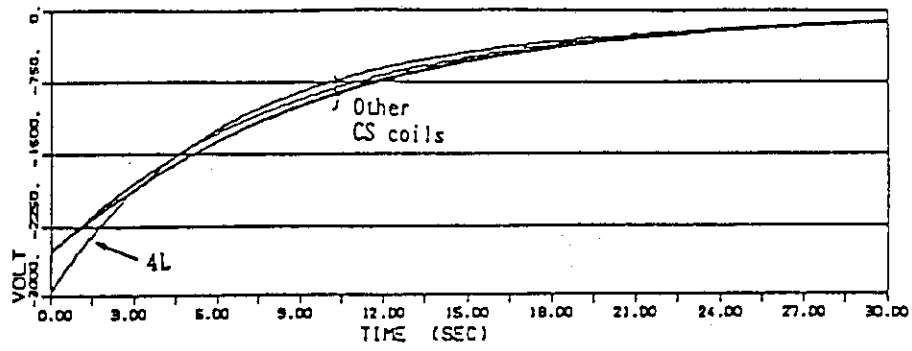

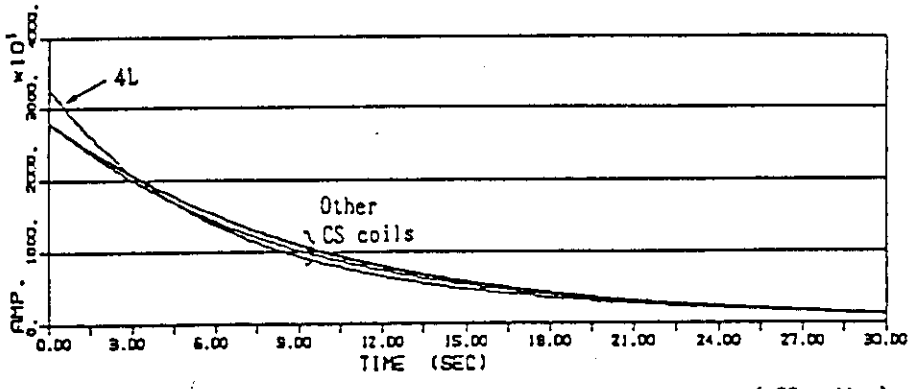

(CS coils)

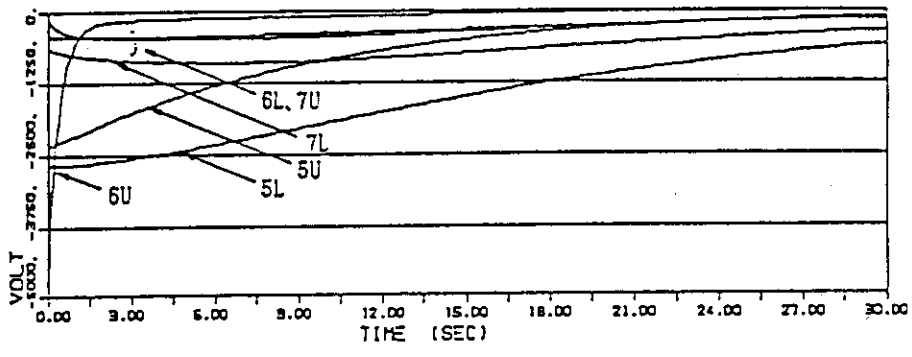

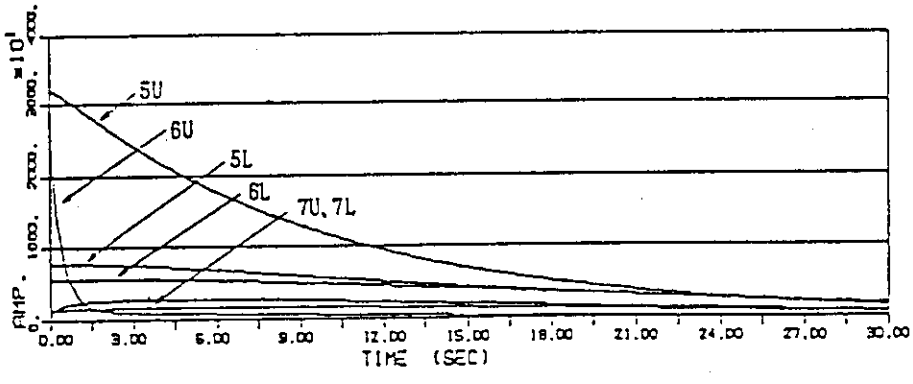

(EF coils)

Fig. 6.7.1 Dump voltage and current in PF coils at initial magnetization.

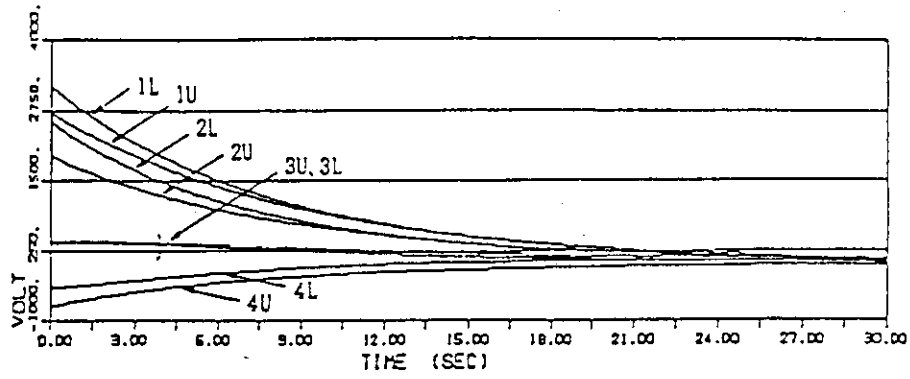

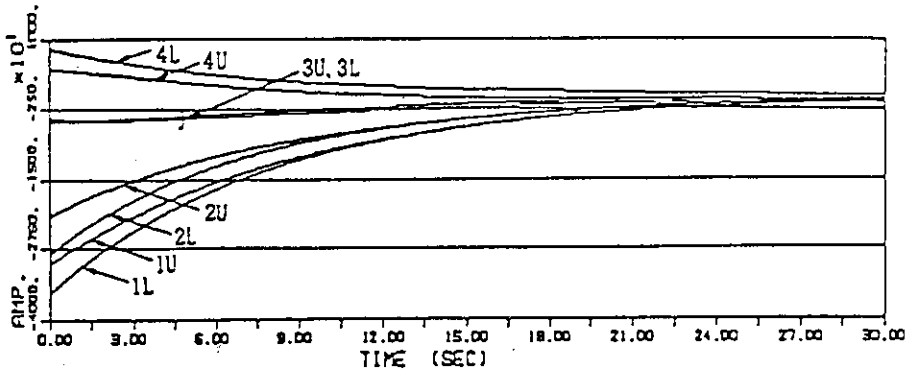

(CS coils)

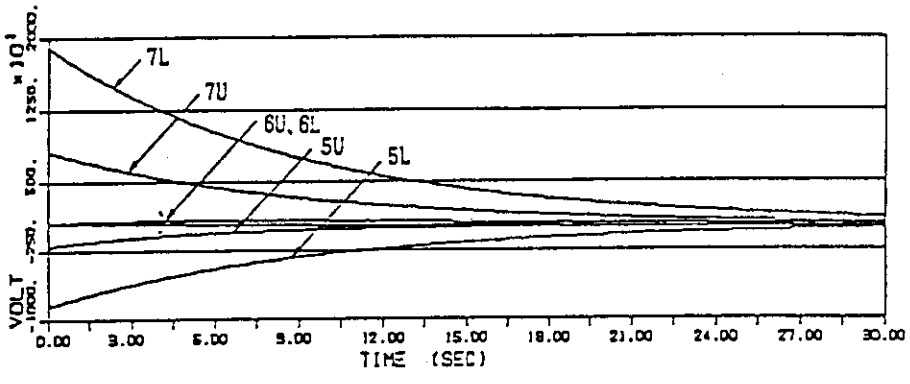

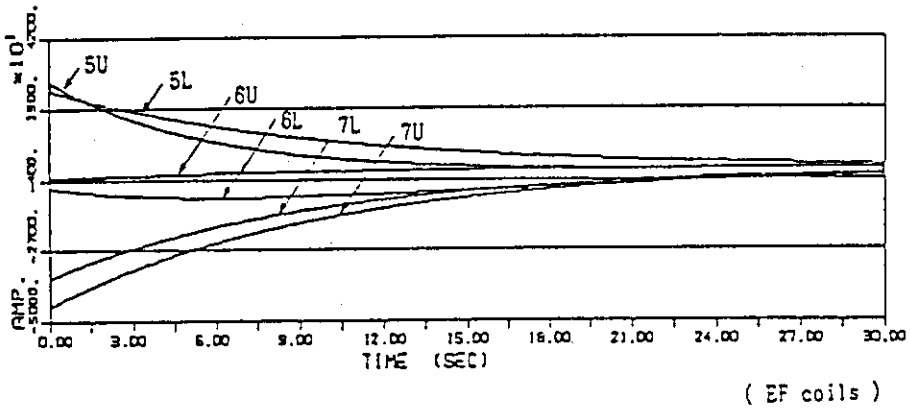

(EF coils)

Fig. 6.7.2 Dump voltage and current in PF coils at burn phase.

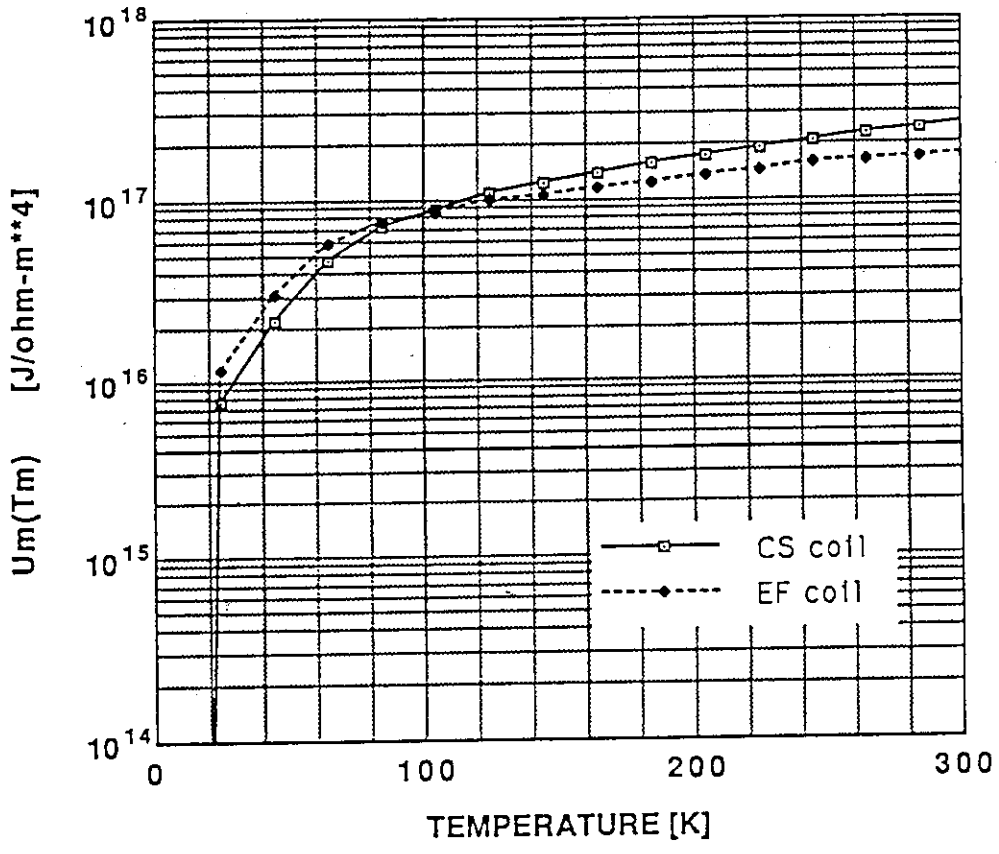

Fig. 6.7.3 Um-Tm relations for CS and EF coils.

6.8 Cryogenic System

The cool-down weight of the PF coil system in SSTR is more than 2500 tons. The total heat load at 4.5 K includes the following: (1) the heat load to coil windings (Table 6.8.1); (2) a heat load of 9.3 kW due to support structures; (3) pumping power losses in the cryogenic pumps; (4) joule heating in electric connections; and (5) conduction and radiation losses in transfer lines associated with valves. A schematic diagram of the cryogenic system for PF and TF coils is shown in chapter 5.8.

6.8.1 Cooling scheme of PF coils

Figures 6.8.1, 6.8.2, and 6.8.3 contain schematics of the current and supercritical helium used in PF coils. Flow control valves, orifice flowmeters, pressure gauges, and other peripheral devices are not shown in the figures. Power leads are cooled by transfer lines at the current terminals. Note that these transfer lines are separate from those used to cool the coil windings.

Table 6.8.1 Main parameters of PF coils for Ref./Liq. system

		Burn phase	Ramp up phase	Disruption
CS[1]	Heat load[2]	1.6 kW	6.2 kW	8.0 kW
	Mass flow rate	2.8 kg/s	2.8 kg/s	2.8 kg/s
	Current lead	1000 l/hr	1000 l/hr	1000 l/hr
	Inlet temp.	4.5 K	4.5 K	4.5 K
	Outlet temp.	4.7 K	4.8 K	4.7 K
	Inlet press.	6.0 bar	6.0 bar	6.0 bar
	Outlet press.	~4.0 bar	~4.0 bar	~4.0 bar

		Burn phase	Ramp up phase	Disruption
EF	Heat load	3.2 kW	8.0 kW	8.9 kW
	Mass flow rate	1.6 kg/s	1.6 kg/s	1.6 kg/s
	Current lead	700 l/hr	700 l/hr	700 l/hr
	Inlet temp.	4.5 K	4.5 K	4.5 K
	Outlet temp.[3]	5.1 K	5.2 K	5.1 K
	Inlet press.	6.01bar	6.0 bar	6.0 bar
	Outlet press.	~4.0 bar	~4.0 bar	~4.0 bar

Remarks 1) 1L coil
2) conduction, radiation and AC loss
3) mean value of all EF coils

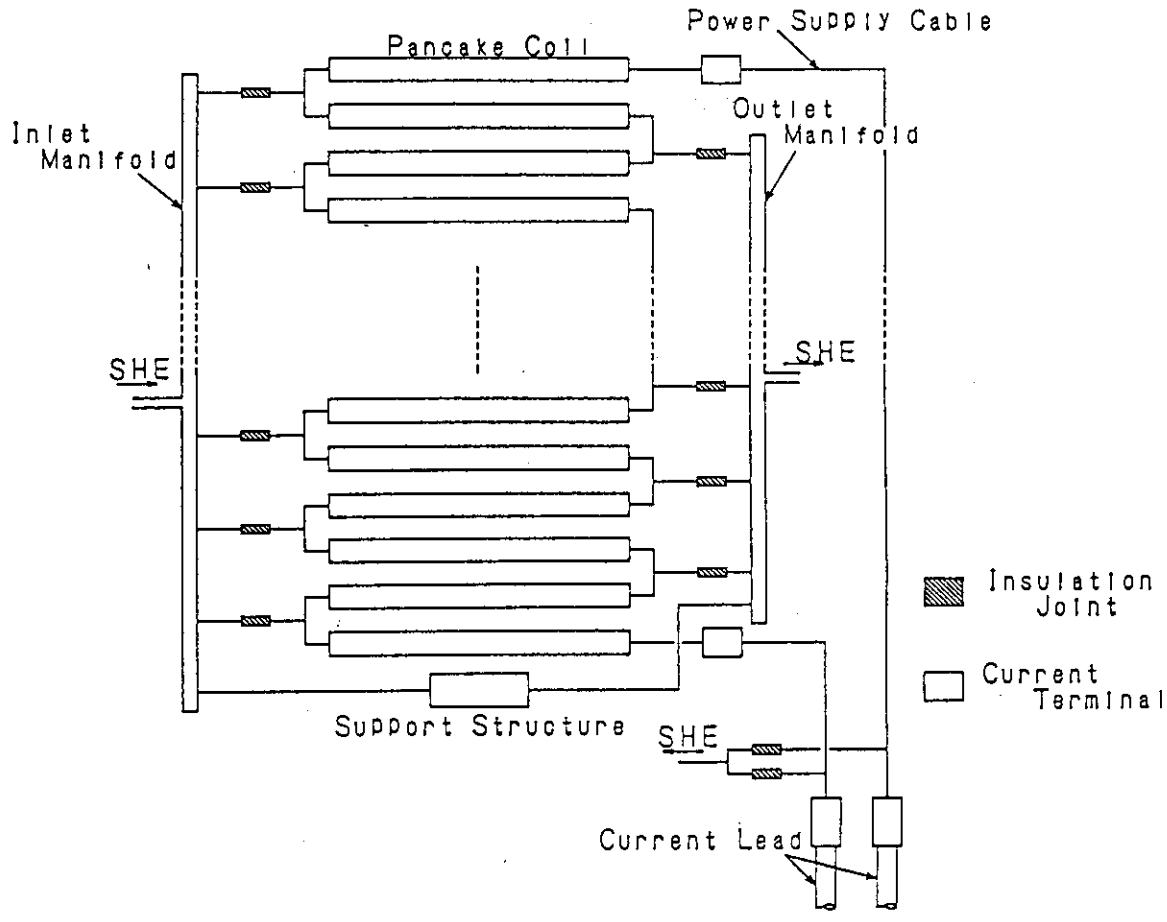

(single winding + double pancake)

	CS	6U	5U
No. of helium paths	30	6	14
helium path length	138m	385m	325m

Fig. 6.8.1 Scheme of current and SHE cooling pass.
(CS Coil, 6U, 5U Coil)

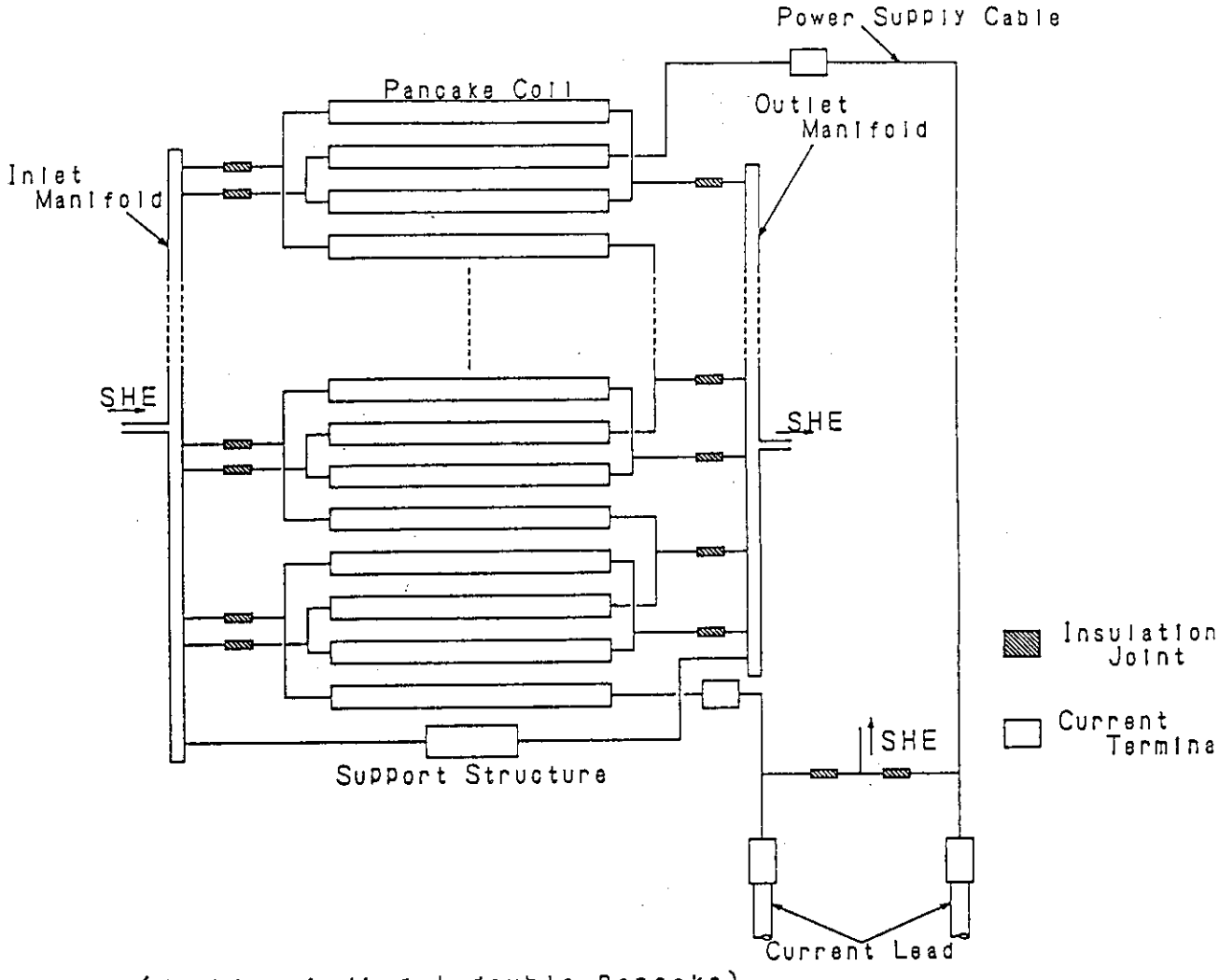

(double winding + double pancake)

	7U	5L	6L
No. of helium paths	28	44	24
helium path length	415m	362m	330m

Fig. 6.8.2 Scheme of current and SHE cooling pass.
(7U, 5L, 6L Coil)

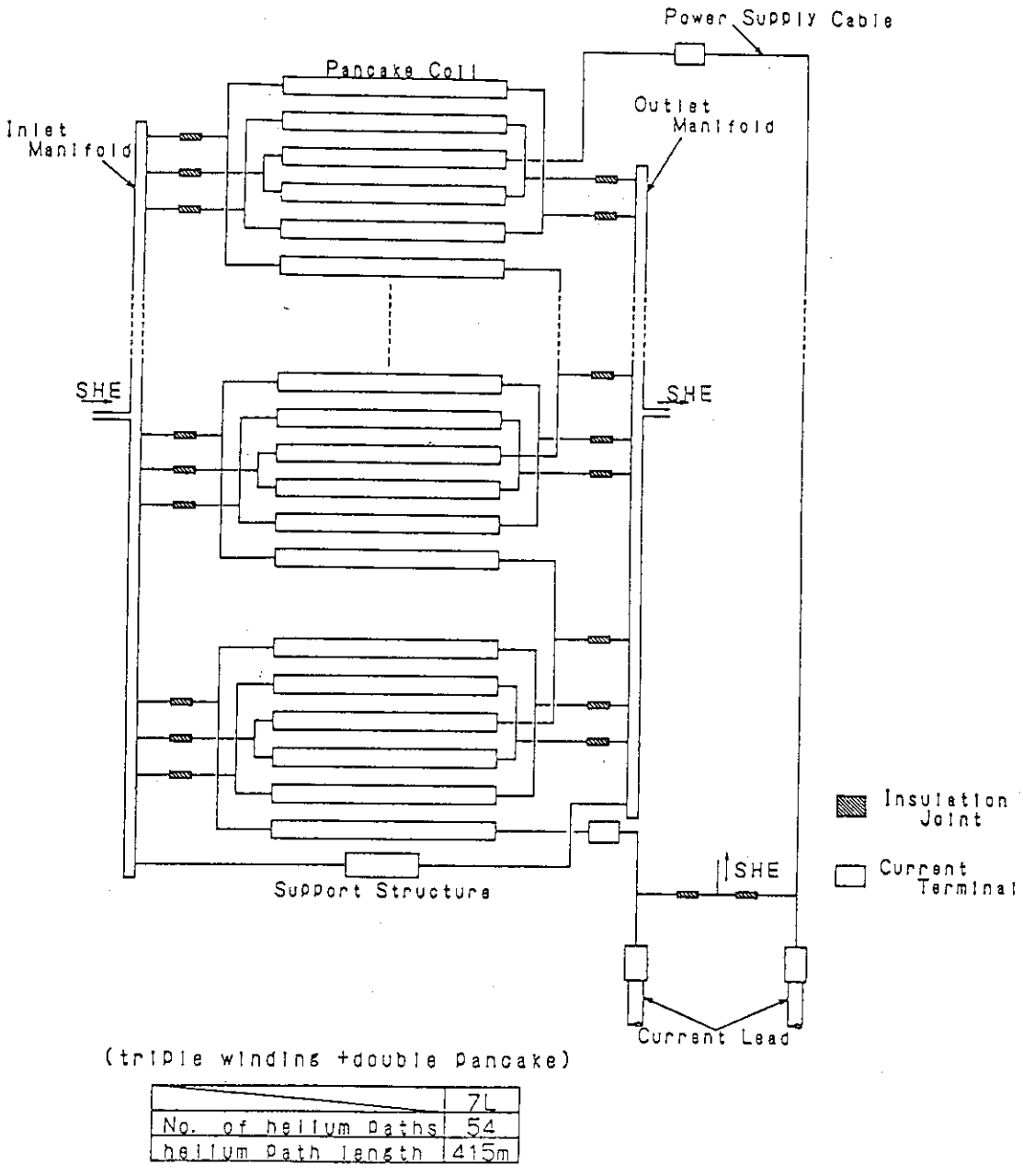

	7L
No. of helium paths	54
helium path length	415m

Fig. 6.8.3 Scheme of current and SHE cooling pass. (7L Coil)

6.9 Conclusion

It was found that the poloidal field coil of the SSTR can be designed with the present data base because of low maximum field and small changing field rate in comparison with that of ignited machines such as the FER and the ITER.

7. Blanket

7.1 Power and particle load conditions

The target of the heat flux control condition in the SSTR is determined from the analyses described in sections 3 and 4 to specify design specifications of the first walls. The design target is defined as radiation from the main plasma 90MW, radiation from peripheral/SOL/divertor plasma 490MW and conduction loss to the divertor plate 80MW. The heat load distribution in the first wall is shown in Fig. 7.1.1.

In the particle balance of the SSTR, fuelling to compensate fuel burn up and the He ash exhaust are particularly important. The D/T fuel burn up rate is $2x10^{21}$/sec for the fusion output power of 3GW. On the other hand, net outflux from the main plasma is $2x10^{23}$/sec which is 100 times the fuel burn up rate. Continuous pellet injection by a centrifugal method is adopted as a fuelling method. On the other hand, strong divertor gas puff of $4.5x10^{23}$/sec D/T molecules is made to form cold and dense divertor plasma. From the two dimensional divertor analysis shown in chapter 4, neutral particle flux to the first wall is ~$1x10^{16}$/cm^2/sec with the average energy of 50eV. Self sputtering with Fe ion is negligibly small because impurity can be condensed near the divertor plate due to strong friction force.

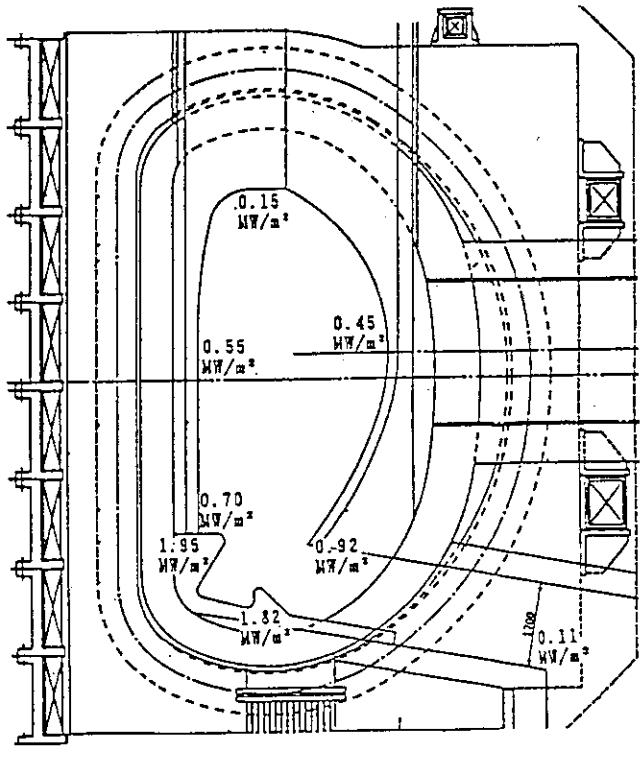

Fig. 7.1.1 Heat load distribution of blanket first wall.

7.2. The blanket structure

7.2.1. The blanket basic design specifications

The basic functions that a commercial reactor breeding blanket is expected to have, are to produce and collect tritium which is fuel of nuclear fusion reaction, and to collect and change the nuclear fusion energy to heat energy for power generation. This blanket is required to have various functions such as functions as the vacuum vessel, because it is a structure which is adjacent to the plasma. Functions required for the commercial reactor breeding blankets are described as follows.

* To have enough tritium breeding performance.
* To keep the tritium inventory in a reactor not to be excessive by continuous tritium recovery.
* To supply recovered heat for power generation, as maintaining breeding materials in the fixed temperature range.
* To prevent the integrity of the breeding region of the solid breeding materials from being ruined by the mass transfer of the breeding materials and damage of the breeding materials by irradiation and thermal stress, etc.
* To prevent the breeding materials from being contaminated when the blankets are manufactured(joint,assembling,inspection test, washing, pressure proof test, etc.).
* To maintain the integrity against heat load and internal pressure, and to have structures which are endurable with intensive surface heat flux and electromagnetic force to be generated at plasma disrupsions.
* To prevent remarkable damage and performance depletion by irradiation.
* To have the structure which is possible to be moved and repaired by remote manipulation.
* To have excellent shielding performance against neutron.
* To keep safety against accidents such as ruptures of tubes.

The breeding blankets must satisfy these various functions equally and have realistic structural concepts in terms of manufacturing and economy. The major factors, by which the blanket structure concept is determined, are the following two.

1. Selection of the shape of the breeding material
2. Selection of the breeding region cooling method

1. The shape of the breeding material

Shape of the solid breeding material, is divided roughly into the following forms : the pebble form, the pellet form, the plate form, and the block form. The pebble-shaped

breeding material is the most appropriate concept according to the point of the reliability of structural simplicity and the pressure boundary maintenance, because the breeding materials cannot help being divided into small pieces from the viewpoint of the integrity maintenance of the breeding region.

2. The breeding material cooling method

There are direct cooling and indirect cooling of the breeding materials by the coolant for heat removal and temperature control of the breeding materials. In the water cooling type commercial reactor, the direct cooling system of the breeding materials is impossible from the point of the breeding material/water reaction and the recovery of generated tritium. The following method is approved as candidate concepts.

- Water cooling commercial reactor : Indirect cooling system
- Helium cooling commercial reactor: Indirect/Direct cooling system

In the indirect cooling system, there are the poloidal flow and the toroidal flow as flow direction of the coolant (i.e. the direction of the installation of the coolant tubes). The poloidal flow pattern is a promising concept in BOT(Breeder-outside-Tube)/CIT(Coolant-inside-Tube) structure to distribute the breeding materials around the coolant tubes, because this pattern is a structurally reliable method according to the fact that this system has a fewer tubes which penetrate through the blanket vessel, compared with the toroidal flow pattern. On the other hand, in the direct cooling system, there considered the blanket of the pressure Tube-in-shell type of BIT (Breeder-inside-Tube) / CIT (Coolant-inside-Tube) structure in which the breeding materials are filled up in the pressure tubes where the coolant gas flows and these pressure tubes are stored in the vessel. The high temperature structural materials are required at the helium cooling, because generally the structural materials are in the high temperature.

It is appropriate for the tritium breeding blanket of the SSTR to basically follow the considerable parts of the blanket design of the nuclear fusion experimental reactor(FER,ITER etc.), because the SSTR is supposed to be the prototype reactor to be constructed after the construction of the experimental reactor. The basic design specifications of the SSTR blanket are summarized in Table 7.2.1. The structural concept is shown in Fig 7.2.1. Ceramics breeding material(lithium oxide, Li_2O as the first candidate) is used as the tritium breeding material and beryllium(Be) is used as the neutron multiplier. Austenitic stainless steel(316SS) is used as the structural material in the experimental reactor, while the ferritic steel(F82H) is used in the SSTR, in consideration of increase of the heat load of the first wall and low activation. The light water(H_2O) was

used as the coolant, and, for the power generation conditions, the inlet/outlet temperature is set at about 285/325 C and the pressure is set at 15 MPa, almost equivalent to the PWR conditions.

The basic structural concept of the selected light water cooling type blanket was described below. This blanket is a TIS (Tube-in-she11) type blanket of BOT (Breeder-outside-Tube) / CIT (Coolant-inside-Tube) structure in which coolant tubes are arranged appropriately in the blanket vessel according to the heating rate of the breeding materials and the breeding material pebbles are filled around them. The first wall is combined with the blanket vessel. The structural material is the above-mentioned ferritic steel and the highest temperature in use during operation is maintained under 500 C. Lithium oxide (Li_2O) is used as the breeding materials, in consideration of the tritium breeding performance and abundance of the database. Spherical pebble are used as for shape, from viewpoint of the integrity of the breeding materials and the easiness of filling. The diameter is one millimeter or less, because it must be reduced as much as possible in order to suppress the decrease of filling rate by the wall effect. Though the permissible running temperature condition of lithium oxide is from 400 C to 1000 C, the nominal temperature range is set set from 450 C from 950 C , in consideration of the margin for the output power variation. The highest temperature of the breeding materials is controlled by an appropriate arrangement of the coolant tubes, and the lowest temperature is controlled by the thermal resistance layer of the solid insulator around the coolant tubes. In the plasma side of the blankets, the beryllium layer about 10cm effective thickness is installed as a neutron multiplier. The coolant is the pressurized light water with the entry pressure about 15.5 MPa, and its inlet temperature is set at 285 C and the outlet temperature is set at 325 C. The flow direction of the coolant is poloidal due to the above-mentioned reason. The net tritium breeding ratio of this blanket is around 1.2.

Tritium generated in the blanket is purged by the helium gas with pressure 0.1 MPa and is continuously recovered. Because the flow rate of the purge gas is small and LiOT is decomposed again in the part of comparatively low temperature in the breeding material region, loss of the quantity of Li_2O is considered not to be a great problem. Tritium inventory in the breeding materials is evaluated to be about 300g(breeding material quantity is about 210 tons) by the analogy from the evaluated value of the ITER design(breeding material quantity is about 90 tons, inventory is about 130g). The one vol.% hydrogen must be added to the helium purge gas for reduction of the inventory. The considerable quantity of the inventory is considered to exist in beryllium. The tritium generation in Be and the quantity of permeation into Be layer and adsorption in Be layer are problems in the future, because the database for the design is not sufficient at the present.

When the design limit value of the atomic displacement of the structural materials is assumed to be 100dpa, the life of the structural materials is under 2FPY (Full Power Year), because the damage in the first wall area is estimated as follows :

3.3 x 10-7 dpa/s/(MW/m^2) x 5 MW/m^2 x 2 year = 117 dpa.

Therefore, when about 70% availability is assumed, the blanket replacement once per 2 or 3 year is required. However, actually only the first wall area reaches irradiation limit and the other parts are almost endurable to use during the lifetime of the reactor.

Ceramics breeding material at the front of the blanket reaches five percent burnup rate for all lithium atoms in about 2-3 years, according to the results of the paragraph 7.3. Therefore, the replacement of the breeding materials is required at that time. However, because burn-up of the almost breeding materials except the front part is very low, it is not reasonable to replace and repair the entire blanket only for the replacement of one part of the breeding materials. In addition, because the life of the structural materials is very short only in the vicinity of the first wall, the concept was that the blanket should be divided into the following two parts, the first wall side(the replaceable blanket) and its rear part(the permanent blanket). At the time of replacement, the blanket structures are taken out from the reactor and its first wall side is demounted, and then the new part is mounted. Re-use of the rear part enables the reduction of the quantity of radioactive waste. The thickness of the replaceable blanket was assumed to be twenty centimeters in consideration of the attenuation of neutron flux (about one order) and self-support as structure.

7.2.2. The blanket structural concept

The vertical cross section of the SSTR core is shown in Fig.7.2.2. The replaceable blanket is installed in the plasma side and the permanent blanket is installed in the rear part. The permanent blanket is divided into several parts in the poloidal direction and each part is fixed to the vacuum vessel. One toroidal sector(22.5 C) of the replaceable blanket of both the inboard and outboard region, is divided into 3 parts, as shown in the horizontal cross section in Fig.7.2.3 (two side module and one center module). The inboard center module is non-breeding blanket used to fix the side modules. The horizontal cross section of the breeding blanket is shown in Fig.7.2.4. The plasma side of the replaceable blanket is the first wall and consists of the coolant tube panels. Beryllium is used for the replaceable blanket as neutron multiplier. Beryllium is divided into small blocks and electric insulation is provided between blocks, in order to decrease the electromagnetic force due to the induced current. Between the first wall and the beryllium layer, the first breeding region is

installed and Li_2O pebbles are filled up for the improvement of tritium breeding ratio. The coolant tubes are installed in the pebble-bed and remove heat in the second breeding region and the permanent blanket. The solid heat insulating material(alumina etc.) are provided around the coolant tubes for the control of the lowest temperature of the breeding material.

In each module of the replaceable blanket, inlet/outlet plenum is installed at the top of the blanket vessel and at the bottom intermediate plenum for turn-up of the coolant is installed , as shown in Fig.7.2.5. Helium sweep gas for the recovery of tritium flows upward from the lower side of the blanket and is taken out from the upper side of the blanket.

The plan for drawing out the coolant pipes from the blanket is shown in Fig.7.2.6 - Fig.7.2.10. The number of the drawing pipes from the header of the outboard replaceable blanket is set to be three (size 5B) respectively for the inlet and the outlet, from the viewpoint of the available space. Three pipes are brought together into one pipe (size10B) respectively for the inlet and the outlet.

The number of the drawing pipes from the header of the inboard replaceable blanket is set to be two (size 5B) respectively for inlet and outlet, from the viewpoint of the available space. Three pipes are brought together into one pipe (size 8B) respectively for inlet and the outlet. The number of the drawing pipes from the header of the center module of the inboard replaceable blanket is set to be one (size 3B) respectively for the inlet and the outlet of each module and then each pipe is drawn out. The number of the drawing pipe from the header of the outboard permanent blanket is set to be one (size 2B) respectively for the inlet and the outlet of three modules. After these pipes and the pipes of the inboard permanent blanket are brought together into the tubes (size 4B) in two systems in the right and the left, these pipes are drawn out from the coolant pipe drawing port for the permanent blanket installed in the side of the port for the replaceable blanket. The number of pipes of the inboard permanent blanket is set to be one respectively for the inlet and the outlet of the two modules. These pipes are brought together with the outboard permanent blanket pipes and are drawn out, as mentioned above.

High resistive part made by the functionally gradient materials is installed in the blanket vessel and the induction current which rounds the vessel is reduced, as shown in Fig.7.2.11, in order to decrease the electromagnetic force which affects the replaceable blanket. Moreover, the reinforcing plate is mounted as shown in Fig.7.2.12 to improve the structural strength of the vessel. The inboard replaceable blanket is fixed by the hydraulic pressure cotter using the flexible tubes installed in the center module, as shown in

Fig.7.2.13. Similarly, the outboard replaceable blanket is fixed by the hydraulic pressure cotter installed in the permanent blanket area.

Table 7.2.1 Basic design parameters of SSTR blanket (1/2)

Structural material	Ferritic steel (F82H)
Maximum temperature	< 500 ℃
Coolant	Water (H_2O)
Inlet／Outlet Temperature	～285／325 ℃
Pressure	15 MPa
Breeding material	Lithium oxide (Li_2O)
Shape	Pebble (1 and 0.2mmφ)
Density	85 % T.D.
Packing fraction	70 %
^6Li enrichment	natural
Temperature range	450 ～ 950 ℃
Neutron multiplier	Berrylium (Be) small blocks
Temperature range	< 400 ℃
Blanket concept	BOT (Tube-in-shell)
First wall concept	Tube-panel
Breeder tempe.control	
Maximum temperature	Cooling tube arrangement
Minimum temperature	Solid insulator around tube
Coolant flow direction	
First wall	Toroidal
Breeding region	Poloidal
Torus segmentation	16 toroidal sectors 3 modules／sector Inboard center replaceable module : Non-reeding blanket to fix side modules
Poloidal segmentation	Replaceable banket
Outboard	1 unit
Inboard	1 unit
	Permanent blanket
Outboard	6 units (side modules) 1 unit (ceter module)
Inboard	1 unit

Table 7.2.1 Basic design parameters of SSTR blanket (2/2)

Maintenanc method	
(Replaceable blanket)	
maintenane unit	module
maintenance port	Vertical port
Blanket thickness	
Outboard	Replaceable blanket 20 cm
	Permanent blanket 30 cm
Inboard	Replaceable blanket 20 cm
	Permanent blanket 30 cm
Blanket weight	
Replaceable blanket	
Structure	～250 MT
Breeder (Li_2O)	～50
Neutron multiplier (Be)	～110
Structre (Vertical port plug)	～470
Permanent blanket	
Structure	～250 MT
Breeder (Li_2O)	～160
Neutron multiplier (Be)	－

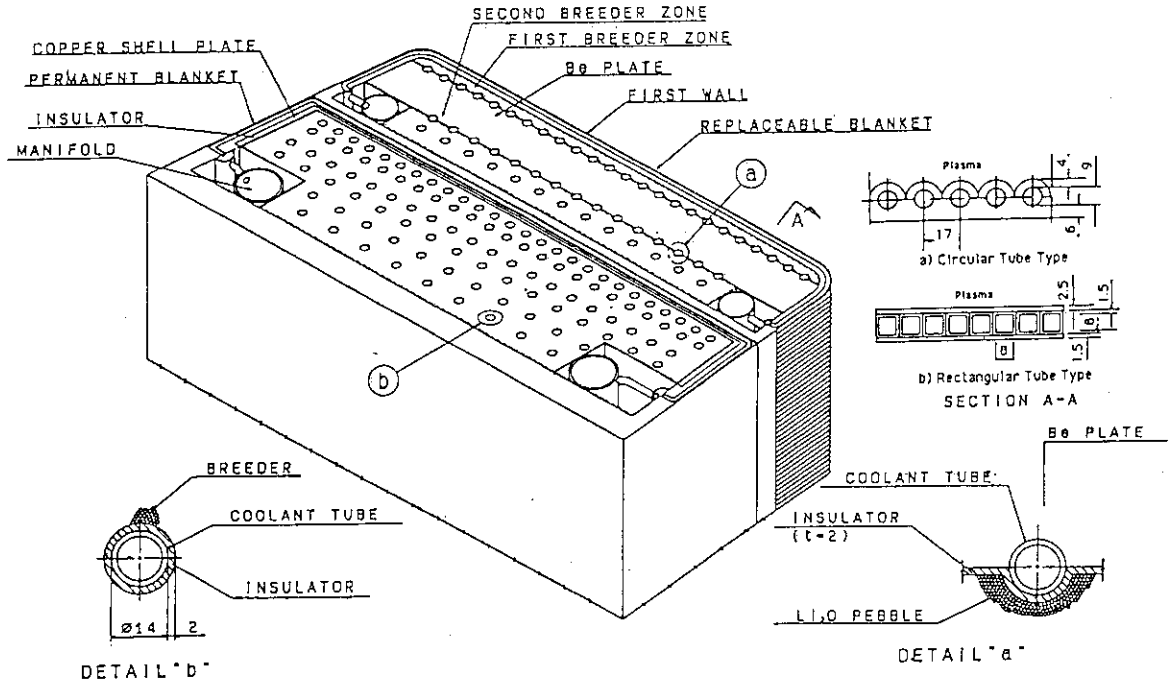

Fig. 7.2.1 Structure concept of SSTR tritium breeding blanket.

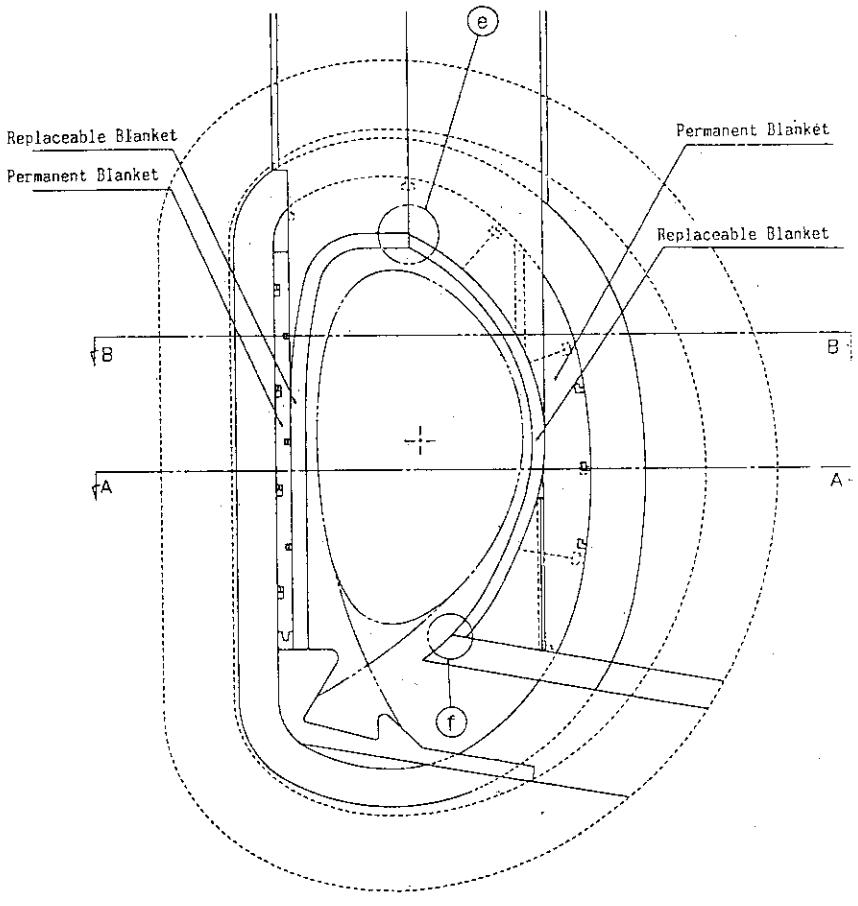

Fig. 7.2.2 Vertical cross section of SSTR in-vessel components.

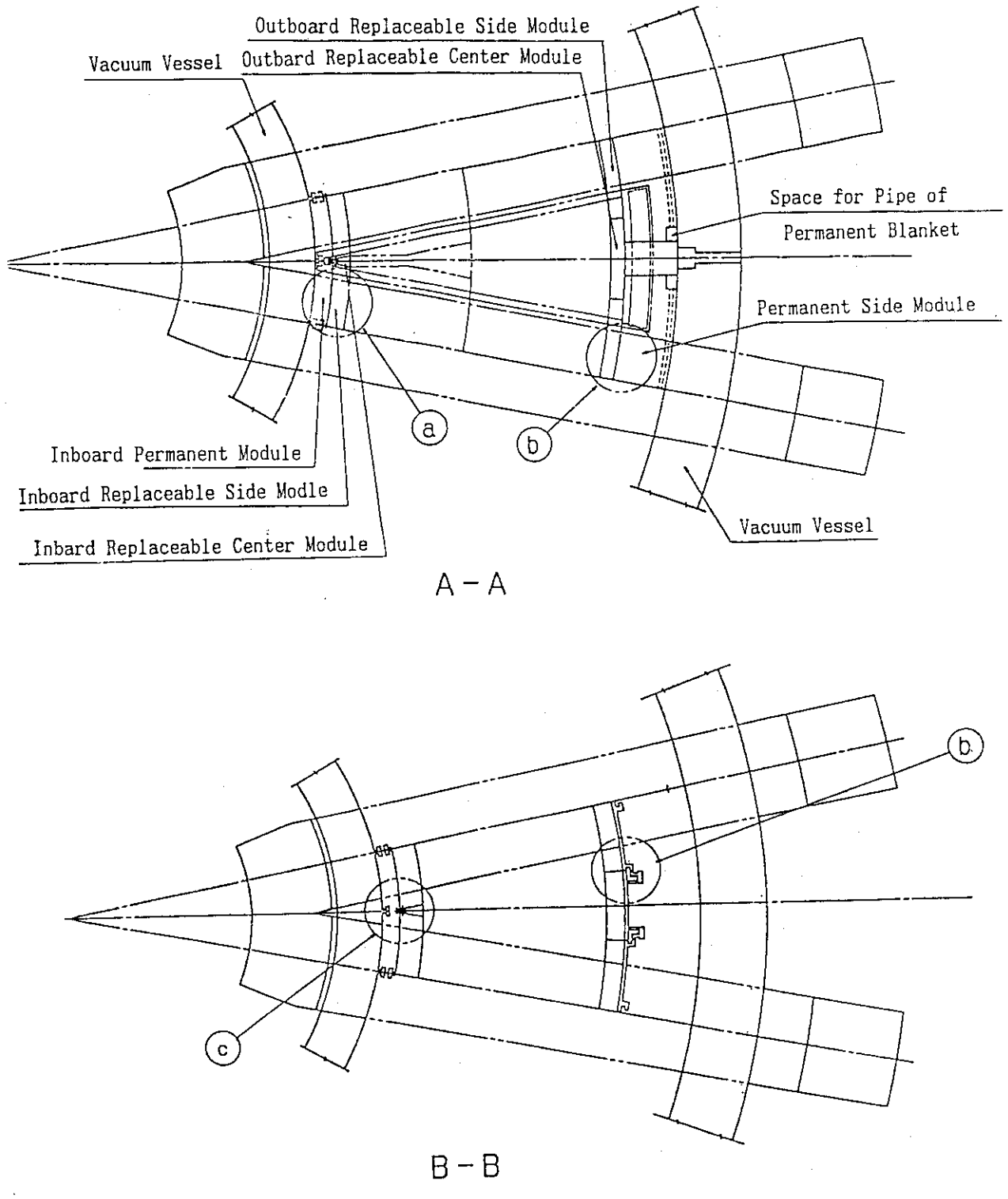

Fig. 7.2.3 Horizontal cross section of SSTR in-vessel components.

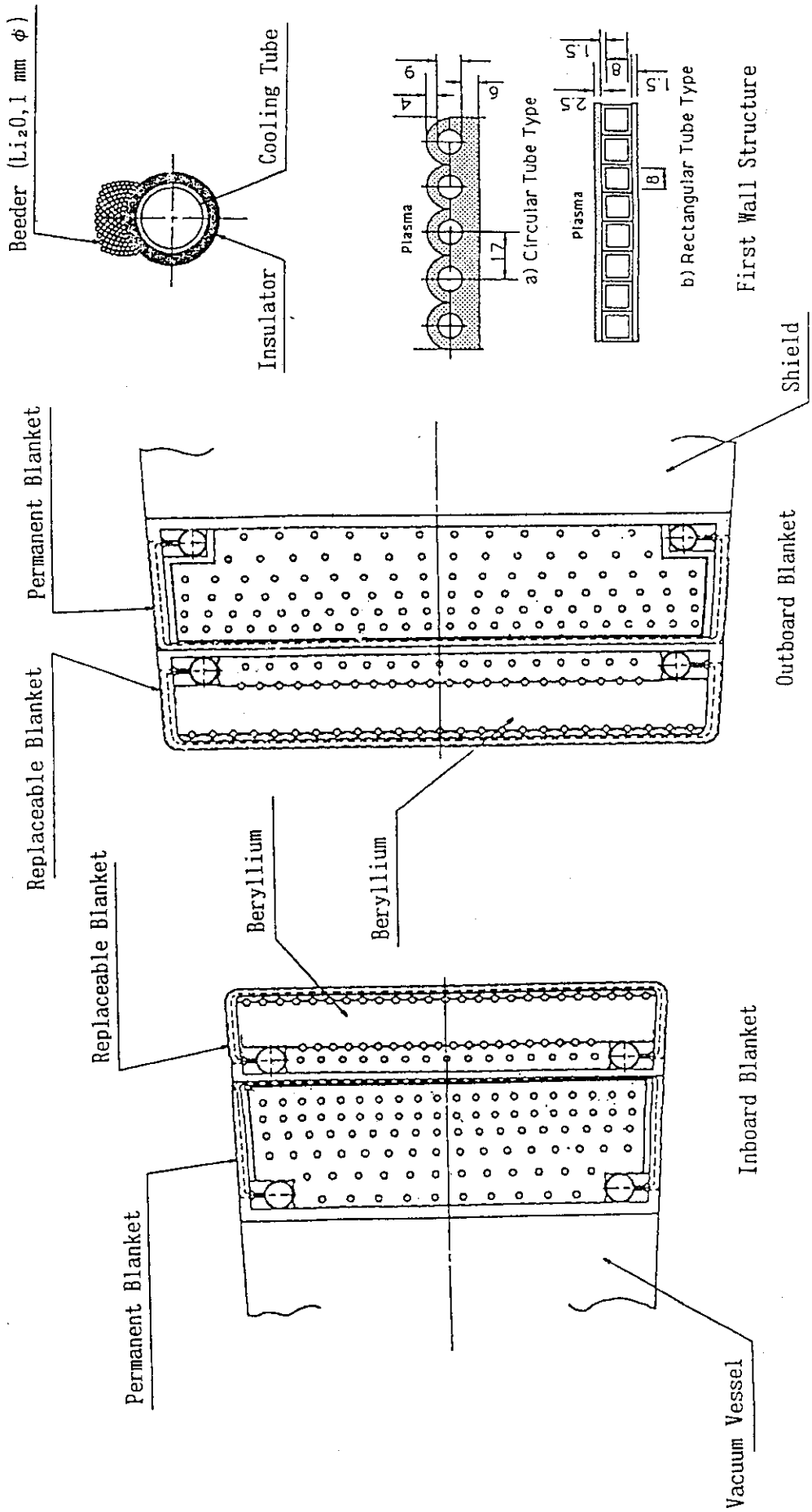

Fig. 7.2.4 Horizontal cross section of SSTR replaceable blanket.

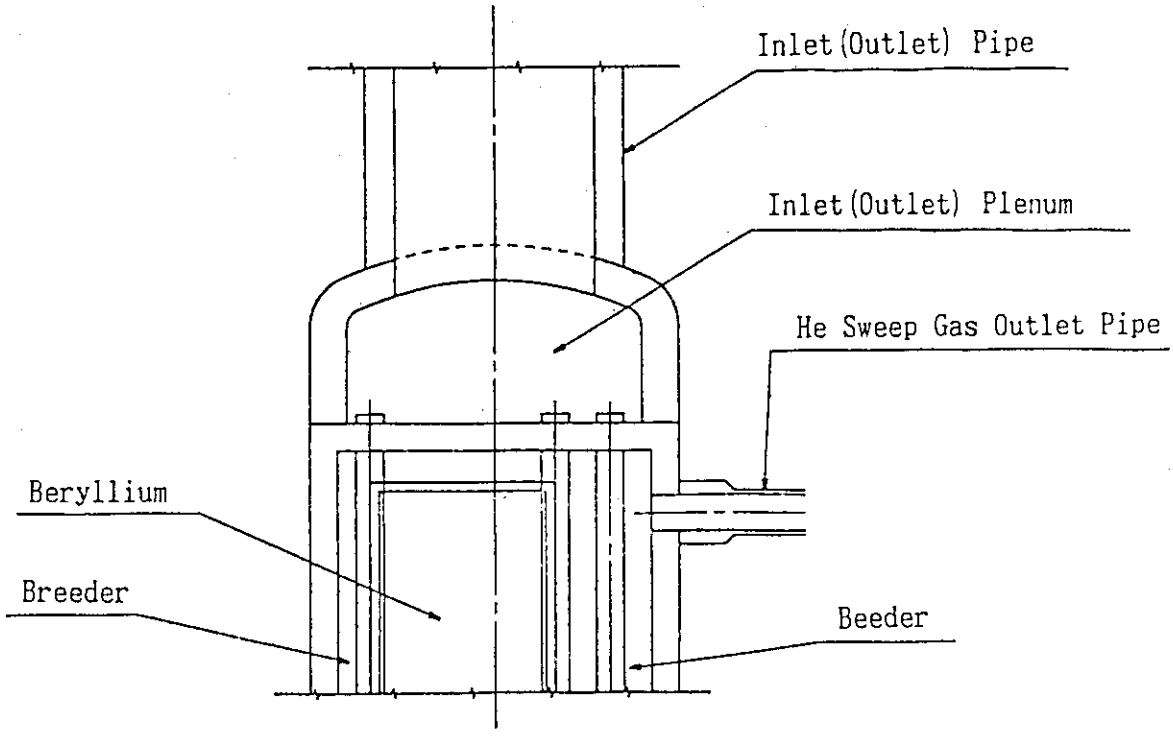

Detail 'e'

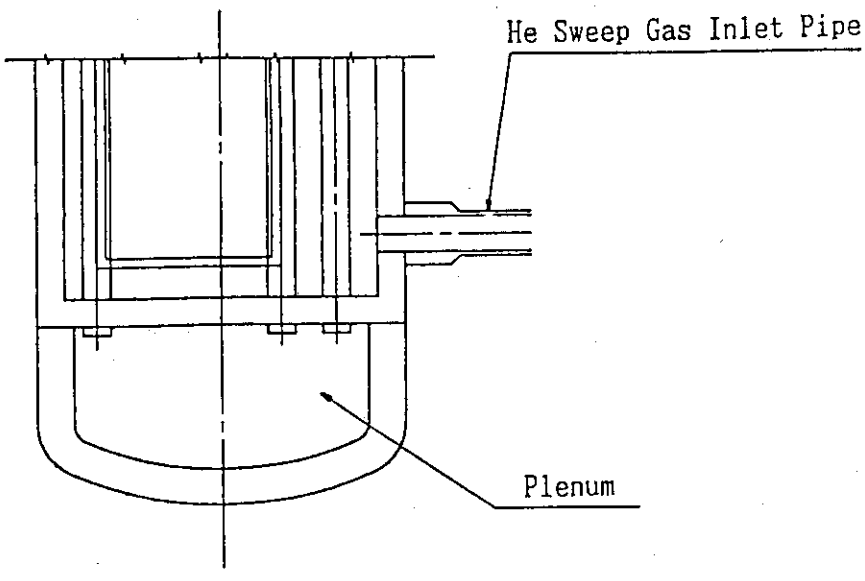

Detail 'f'

Fig. 7.2.5 Structure concept of coolant plenum for replaceable blanket.

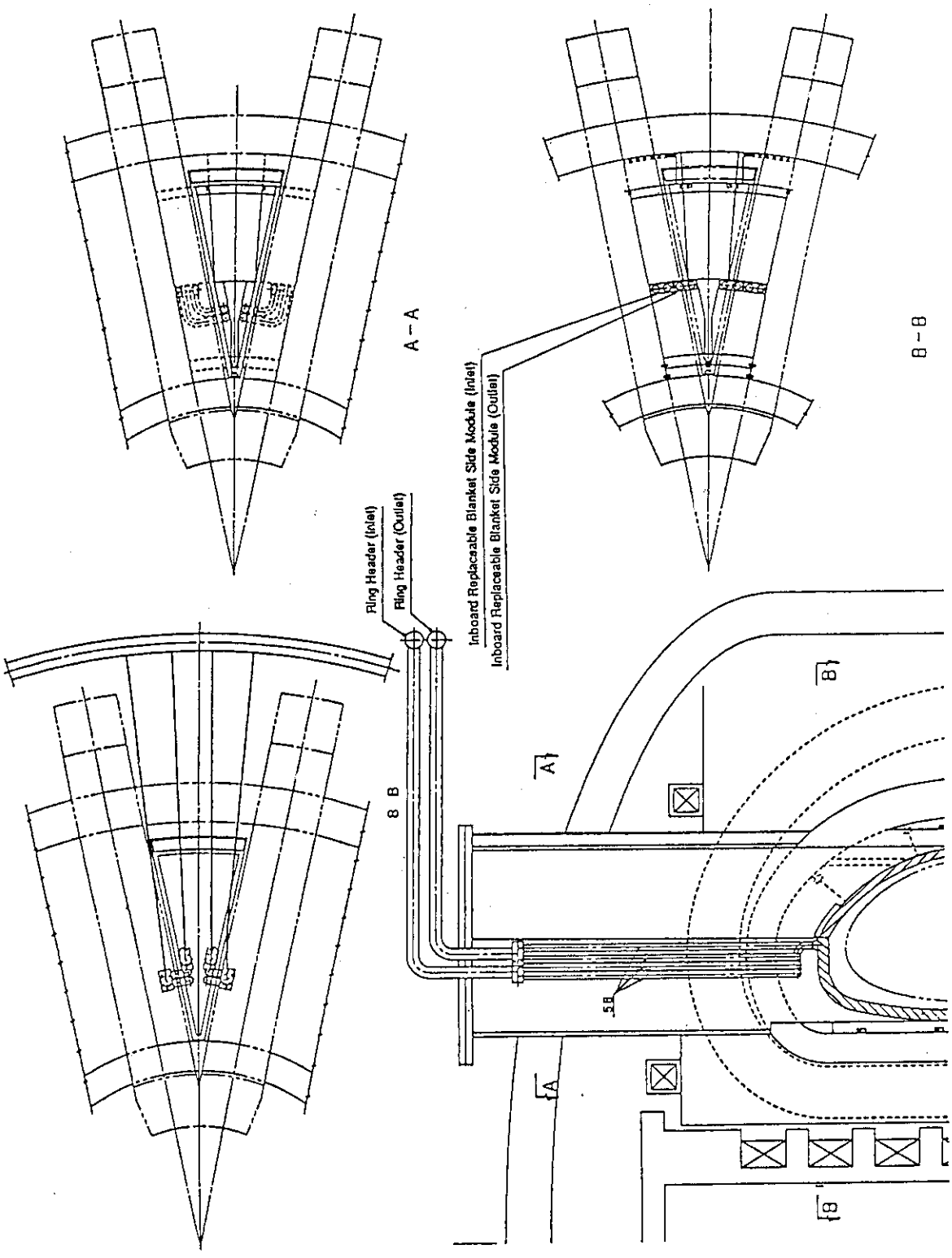

Fig. 7.2.6 Coolant pipe arrangement for inboard replaceable side module.

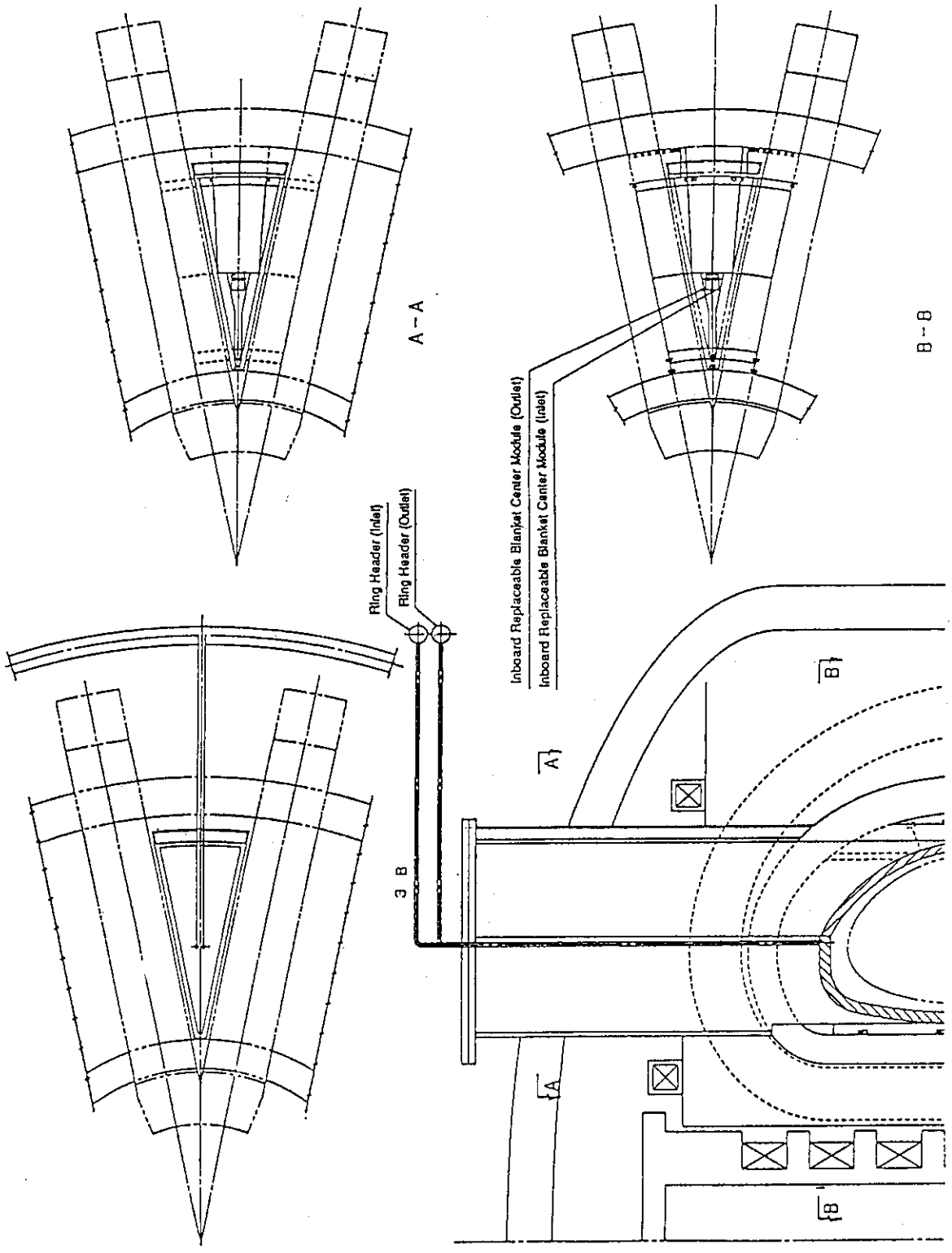

Fig. 7.2.7 Coolant pipe arrangement for inboard replaceable center module.

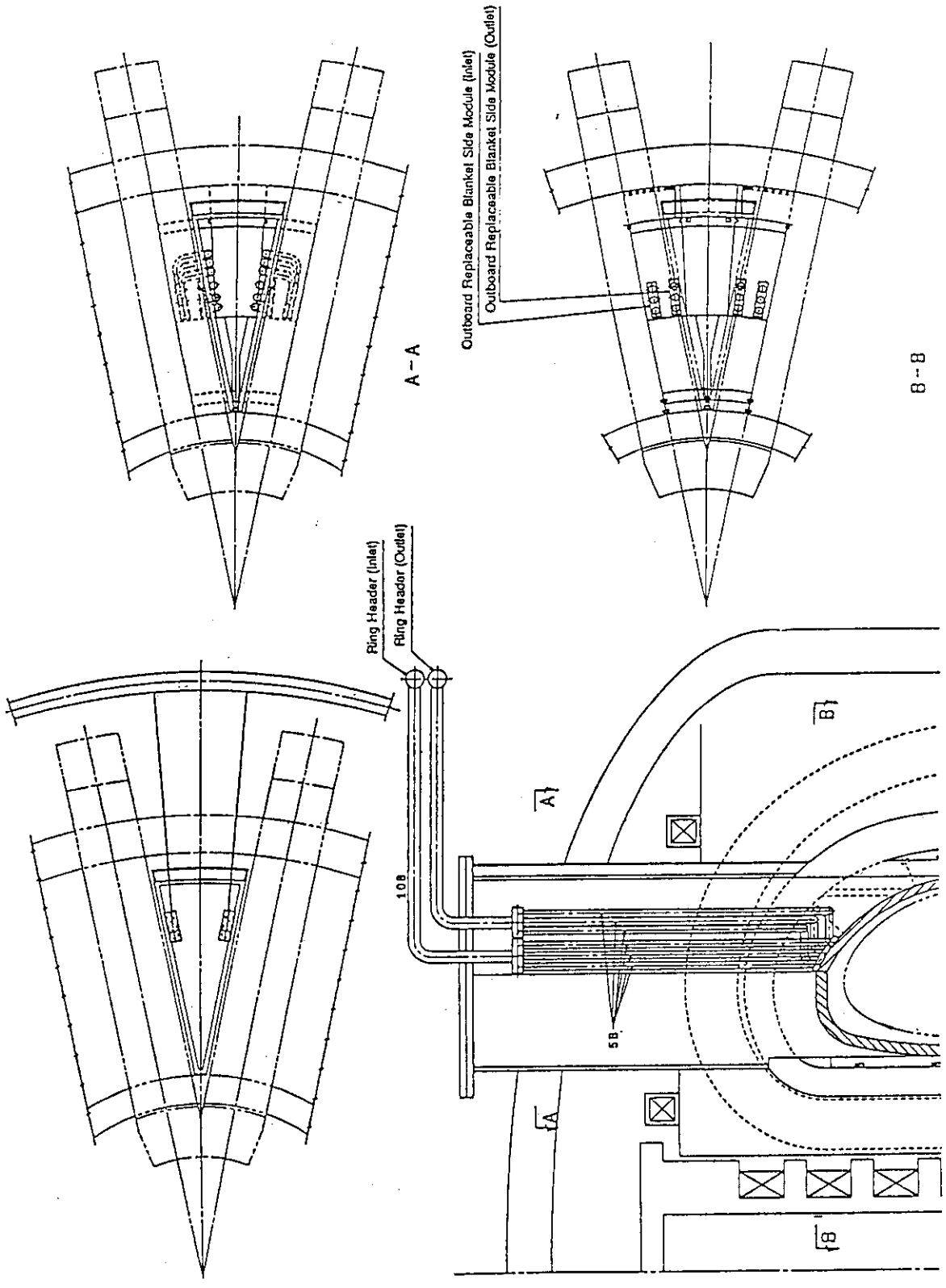

Fig. 7.2.8 Coolant pipe arrangement for outboard replaceable side module.

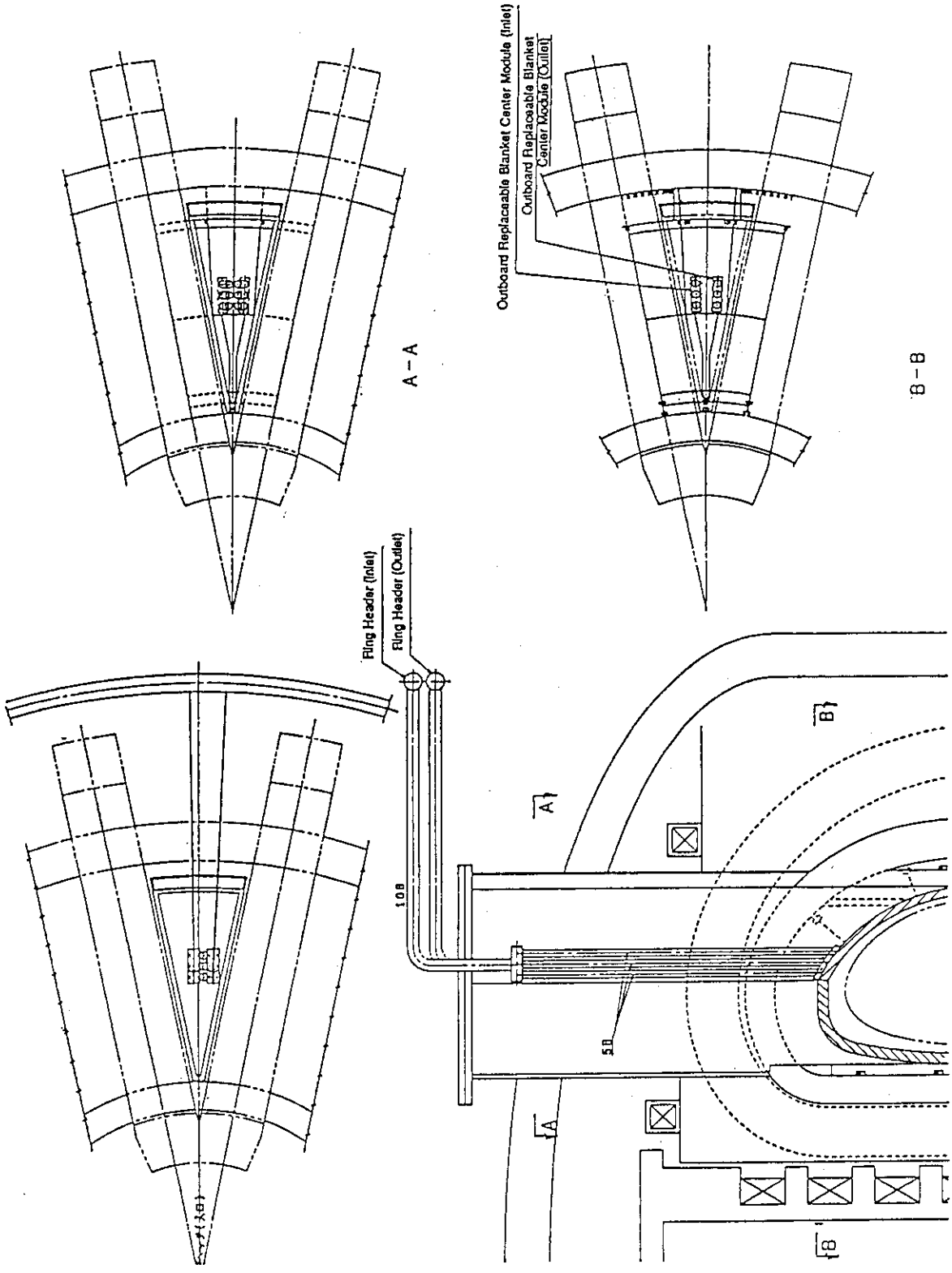

Fig. 7.2.9 Coolant pipe arrangement for outboard replaceable center module.

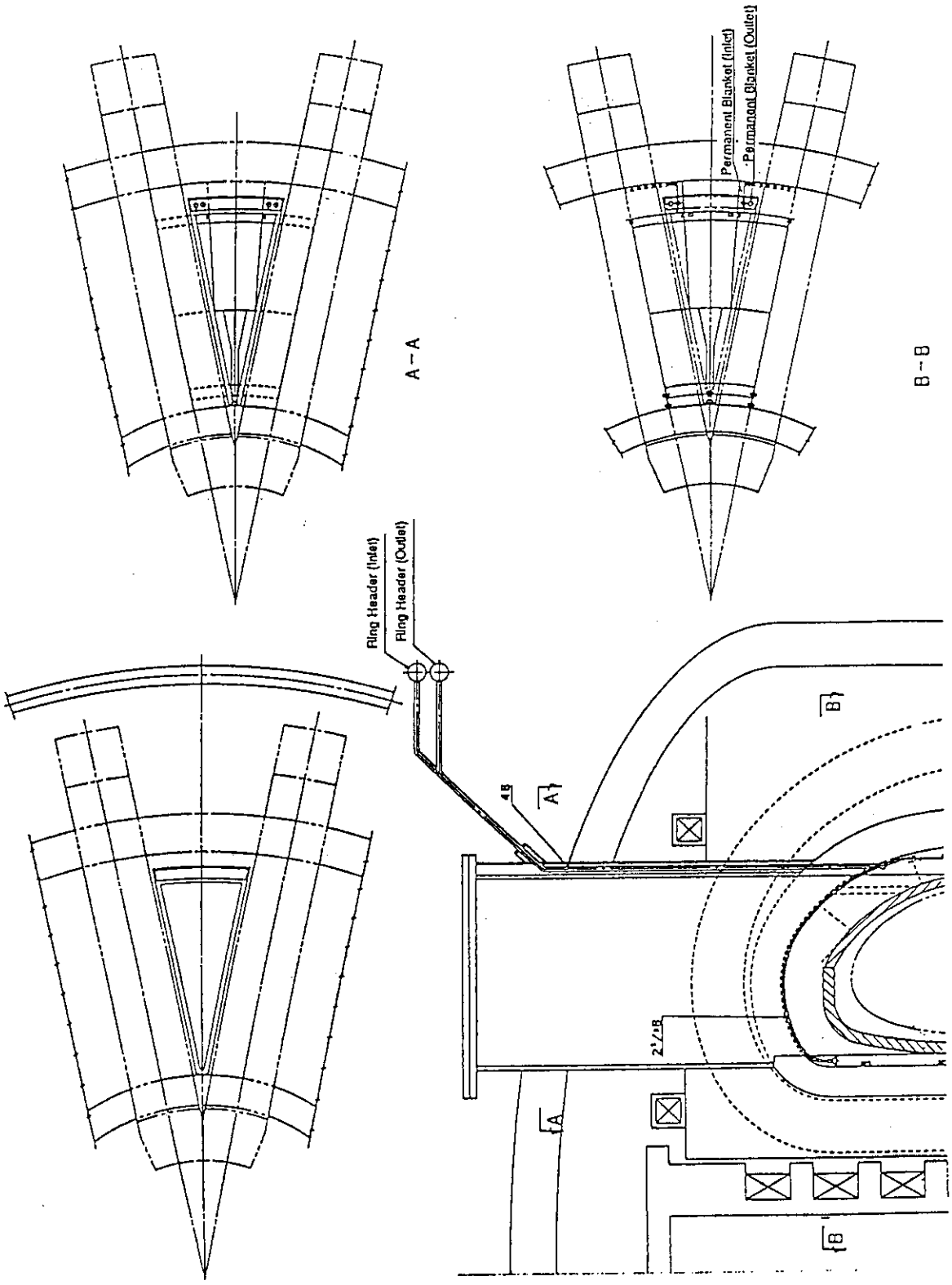

Fig. 7.2.10 Coolant pipe arrangement for permanent blanket.

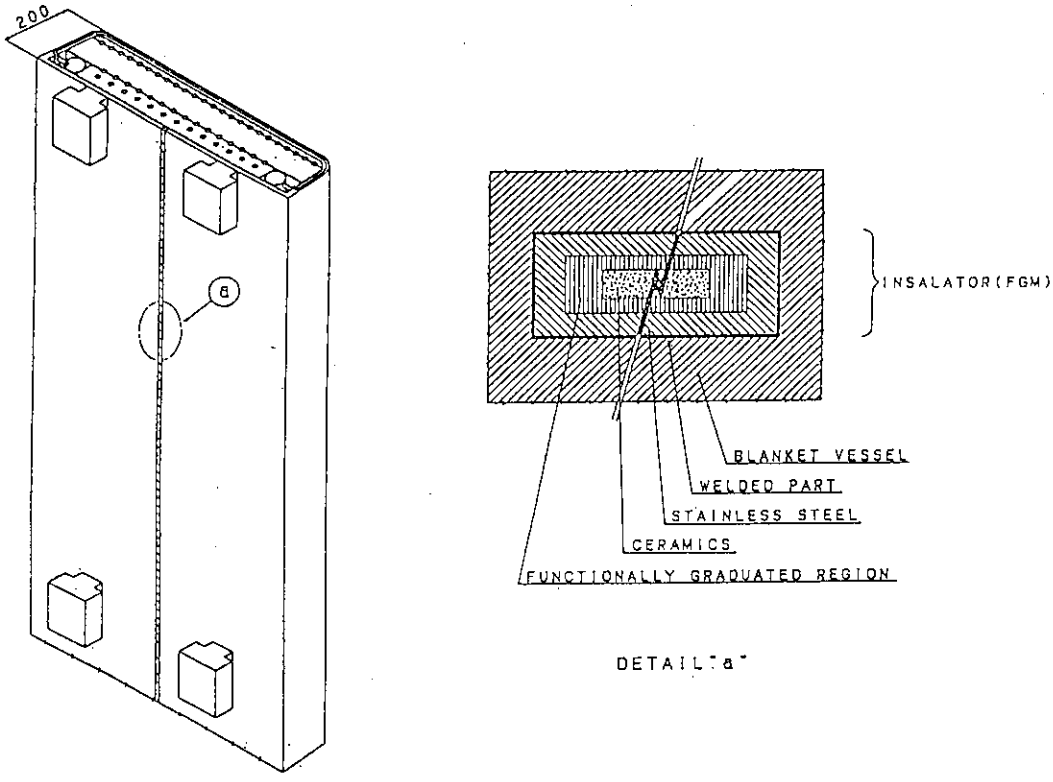

Fig. 7.2.11 Reduction of electromagnetic force by functionally graduated material.

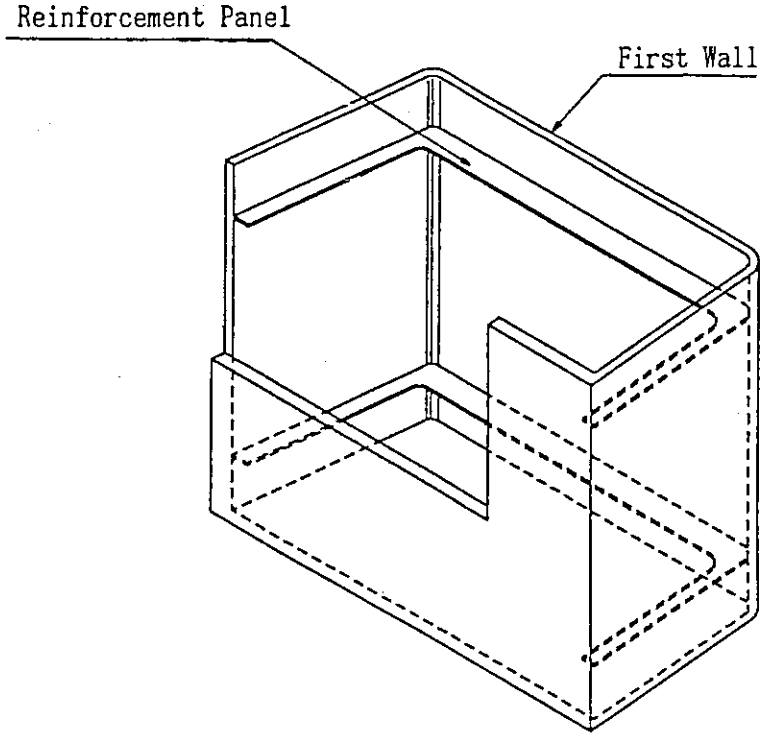

Fig. 7.2.12 Reinforcement structure of blanket vessel.

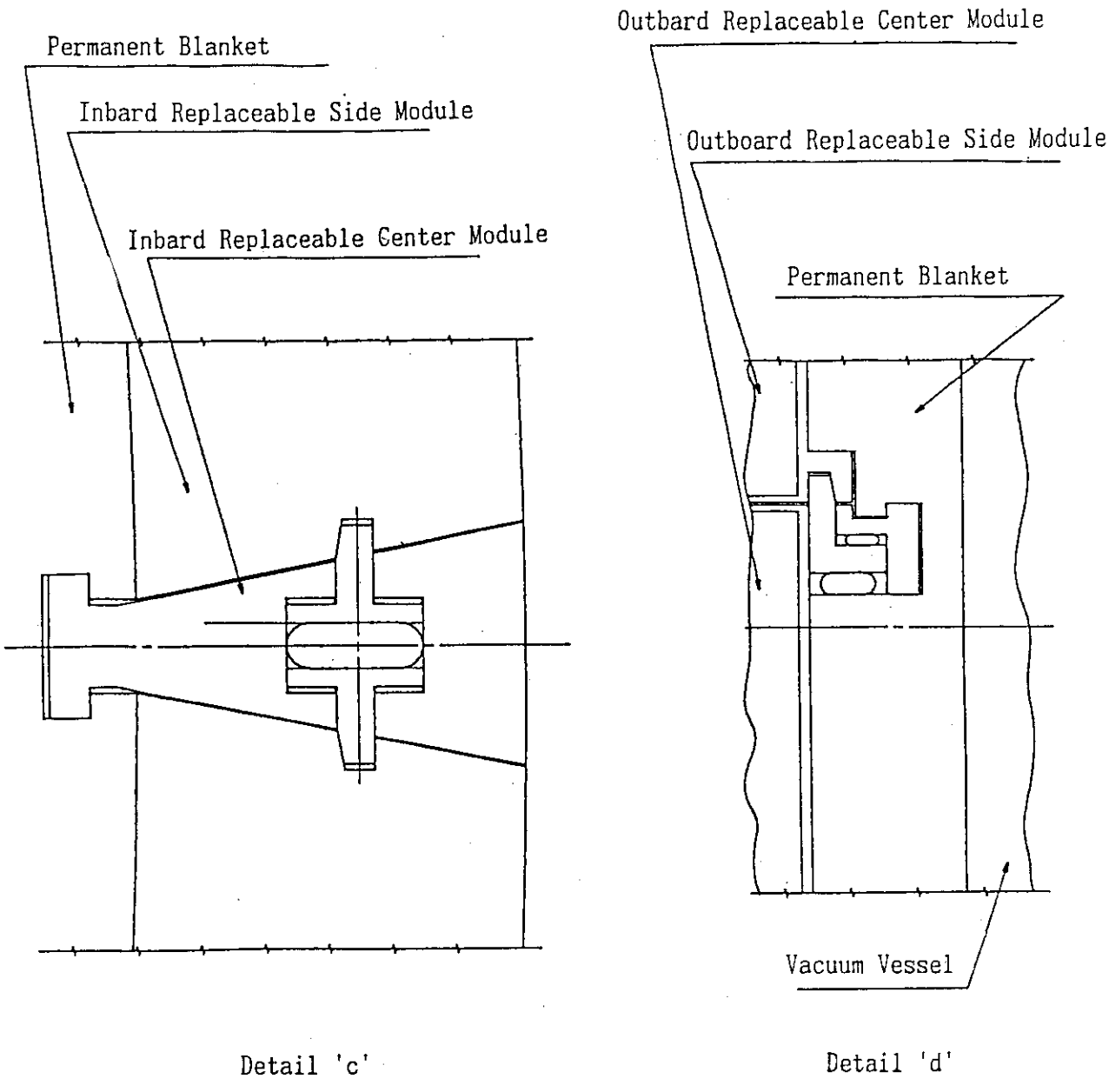

Fig. 7.2.13 Support structure of replaceable blanket by hydraulic cotter.

7.3 Neutronics and thermal design of the blanket

7.3.1 Neutronics design

Tritium breeding ratio was evaluated by one-dimensional neutronics calculation by which the SSTR core geometry was simulated. The poloidal distribution of the neutron wall load was evaluated by three dimensional Monte Carlo calculation. The calculational method of the one-dimensional calculation is as follows.

(1) Calculational cord : ANISN
(2) Nuclear group constant : GICX40 (The atomic composition of the materials used in this calculations is shown in Table 7.3.1.)
(3) Geometry model : one-dimensional toroidal model
(The geometry chart is shown in Fig.7.3.1.)
(4) Source normalization : The neutron generation density was normalized to the average neutron wall load of 3MW/m^2.

$$f_N = \frac{2x3.14x(5.12+8.88)x0.01x3}{14.1x1.602x10^{-19}} = 1.168 \times 10^{18}$$

The evaluation process of tritium breeding ratio is shown in Fig.7.3.2. The neutron wall load in the inboard was estimated to be 2.3 MW/m^2 and in the outboard, 3.4 MW/m^2. It was found that the breeding ratio could reach about 1.2. We roughly evaluated lithium burn-up in the front breeding region of the replaceable blanket by the following method. If atomic number of 6Li is assumed to be N, the variation rate is calculated by the next expression:

$$\frac{dN}{dt} = -\lambda N \qquad (1)$$

where ; $\lambda = \sigma \phi$

σ : Tritium generation cross section by ^{6}Li(barn)

ϕ : Neutron flux.

The expression (1) is rewritten as follows:

$$N = N_0 \exp(-\lambda t) \qquad (2)$$

where;

N_0 : Initial atomic number of ^{6}Li.

The burn-up rate is calculated as follows.

$$\frac{N_0-N}{N_0} = 1- \exp(-\sigma\phi t) \qquad (3)$$

Neutron flux changes as the lapse of time by the burn-up of ^{6}Li, but here the burn-up rate is evaluated by the equation (3) as ϕ = constant in approximation. Tritium generation rate by ^{6}Li can be calculated by ANSIN/APPLE-2 as follows:

$$TPR_{6Li} = N_0 \Sigma \sigma i \, \phi i \qquad (4)$$

where, i : index for energy group

Therefore, effective $\sigma\phi$ is calculated as follows:

$$<\sigma\phi> = \frac{TPR_{6Li}}{N_0} \qquad (5)$$

The burn-up rate of ^{6}Li is calculated by substituting < sf > in the equation (3). The calculated value of burn-up rate of ^{6}Li is shown in Fig.7.3.3. As for natural concentrations, burn-up rate in the foremost part of the breeding region exceeds 10 % within one year's operation(7.5 % of this value for all lithium atoms). If 5 % of all lithium atoms(69 % of ^{6}Li atoms) is assumed to be the limit of the integrity of the breeding materials, it might be necessary to replace the breeding materials once in about three years. The calculational results of the breeding ratio when it is assumed that 30 % of 6Li in the first breeding region had burnt (it corresponds to about 1.4FPY in Fig.7.3.3) are shown in Fig.7.3.2. The breeding ratio decreases by about 2 % from 1.21 to 1.19, but it is considered not to be a great problem in operation of the reactor. Because the neutron wall road has the poloidal distribution as described below and the maximum value was estimated as follows ;

$$5MW/m^2 \times 1.4FPY = 7MWY/m^2$$

(It corresponds to 50 % burn-up of ^{6}Li.)

The local breeding ratio is partially smaller than the above-mentioned value. However, it is considered that the breeding performance as the whole reactor is maintained at the average value mentioned above. Though the irradiation limit will be extended if 6Li is enriched, the nuclear heating rate of the breeding layer increases and the cooling of front breeding region becomes problem.

Next, We describe the poloidal distribution calculation of the neutron wall load. The calculational code in use is the three dimensional Monte Carlo transport code MCNP. We

set the neutron source at the monoenergy of 14.1 Mev and gave the distributed ra source in the plasma. Neutron current to the first wall was evaluated by the surface crossing estimators. The calculational results are shown in Fig.7.3.4. Average neutron wall load is about 2.9MW/m^2, the maximum load is about 5.1MW/m^2, and the minimum load is 1.2MW/m^2. Thus, because the wall load has big poloidal distribution, it is necessary to pay attention to the thermal design and the lifetime of the blanket and the first wall. That is, the first wall and the breeding material in the inboard have the lifetime 1.5 times longer than that in the outboard, from the viewpoint of radiation damage and Li burn-up.

7.3.2 The first wall thermal-hydraulic design

(1) General consideration concerning high heat load

1) Issues in the first wall design

When the first wall of the tokamak nuclear fusion power reactor is designed, it is necessary to pay attention to the following points, in order to remove the steady-state heat load.

i) Maximum temperature of the structural materials

Maximum temperature of the structural materials(T_{max}) is appeared on the surface of the first wall. Tmax must be suppressed under maximum permissible temperature(T_{limit}) defined by the following viewpoints. The most important factors are different according to materials. For instance, it is considered that the maximum permissible temperature is defined by the swelling temperature by the neutron irradiation in the case of austenitic stainless steel, and in ferritic steel, defined by decrease of the strength in the high temperature, and in molybdenum alloy, defined by recrystallization temperature. Because the temperature of the structual materials depends on the magnitude of the surface heat flux directly, this temperature is an important item which defines permissible maximum heat flux.

- Melting $T_{max}<T_{limit}(melt)$
- Decrease of high temperature strength $T_{max}<T_{limit}(strength)$
- Aspect transition $T_{max}<T_{limit}(transition)$
- Radiation damage (swelling etc.) $T_{max}<T_{limit}(irradiation)$
- Recrystallization $T_{max}<T_{limit}(recrystalization)$

ii) Stress

The first wall is required to endure the thermal stresses caused by heat load and the mechanical stresses such as coolant internal pressures, vessel internal pressures, electromagnetic forces, and its own weight etc. and to maintain the integrity. Moreover, it is necessary to have appropriate lifetime as a power reactor, in consideration of creep by the high temperature and neutron irradiation and of fatigue by repetitive heat load. However, because steady-state operation is assumed in the SSTR power reactor, it is considered that heat cycle fatigue can be almost neglected. It is considered that primary stress during normal operation can be sufficiently reduced actually by devising the structure of the first wall so that vessel internal pressure should not be excessive. Therefore, in the first wall of the tokamak nuclear fusion power reactor, it is considered that the limit of the thermal stress(Smax) caused by the surface heat flux might be predominant. The thermal stress is one of the items to define permissible maximum heat flux because it is proportional to the temperature difference in the structural materials, that is, surface heat flux.

- Secondary stress(thermal stress=structural material temperature difference)
  $S_{max} < S_{limit}$ (3Sm; primary + secondary stress)
- Primary stress (vessel internal pressure and coolant pressure) < 1.5Sm
- Creep
- Heat cycle fatigue (can be neglected at normal operation)

iii) Coolant velocity and coolant channel side temperature

It is necessary for the coolant of the fluid like water to pay attention to danger of boiling and causing burn-out as the heat flux is higher. In particular, it is necessary to consider so that heat flux(q") to the coolant channel should not exceed burn-out heat flux(q_{bo}), because the structural material temperature of the first wall rapidly rises and then the first wall is broken when burn-out is caused. The subcool boiling is desirable on the characteristics of the heat removal for the improvement of heat transfer coefficient, but it has high possibility that disuniformity of the distribution of the flow rate is caused in the parallel coolant channel like the first wall. Therefore, it is desirable to suppress coolant channel surface temperature (T_w) lower than boiling beginning temperature (T_{nb}) and to avoid boiling. These points are important problems because the subcool cannot be set higher(that is, the coolant temperature cannot be set lower) in the power reactor.

iv) Pressure drop and circulation power

The coolant channel of the first wall has possibility that its pressure drop might be large because it has large coolant velocity to manage the high heat flux. Therefore, it is necessary for the design of the first wall so that pressure drop should not be excessive.

Because the plant efficiency decreases as the circulation power becomes bigger, the merits as the power reactor for the power generation decreases. It is necessary to design in consideration of the improvement of the thermal efficiency, as well as to note the reduction of pressure drop.

- Pressure drop
- Circulation mobility power

v) Coolant (outlet) temperature

The coolant outlet temperature largely affects the thermal efficiency of the power generation plant. In the first wall, it is desirable that the coolant outlet temperature is as high as possible, in order to obtain the thermal efficiency which is comparable to other plants, and to get the approval as the power reactor.

- Thermal efficiency

vi) Radiation damage

There is a case that the radiation damage of the structural materials due to the neutron might be one of the external factors to define the lifetime. Therefore, it is necessary to design in consideration of the neutron irradiation condition of the first wall.

- Swelling
- Irradiation creep
- Change of physical property

2) Investigation on permissible maximum heat flux

The permissible maximum heat flux is one of the important factors to define the reactor concepts such as the plasma parameters and the reactor sizes, as we mentioned above. Therefore, we examined the permissible maximum heat flux from the viewpoint of maximum temperature of the structural materials and the thermal stress related to the surface heat flux. Moreover, we examined boiling and burn-out because they are important factors to define permissible maximum heat flux in case of the water cooling.

i) Analytical condition

* Candidate coolant --- water
  Core outlet temperature --- about 320 C
  The core outlet temperature of the coolant was set to equivalent to the conditions of the PWR being.
* Candidate structural materials - Austenitic stainless steel
  (316LSS,PCAetc.) : The physical property values of 316 stainless steels were used.
  - Ferritic steel (HT-9 etc.) : The physical properties values of the HT-9 steel were used.

ii) Heat load condition

In this study, we examined the surface heat flux as a parameter in the condition of maximum 10MW/m^2, in order to clarify the permissible maximum heat flux for each candidate material. We treated volume heating (due to nuclear heating by the neutron and gamma rays) as 0, because its effect is small in the power reactor as compared with the surface heat flux.

iii) Analytical results

Maximum temperature of the structural materials was calculated by the following expressions in consideration of heat transfer in the slab and the convective heat transfer in the coolant channel.

$$T_{max} = T_{cool} + \Delta T_f + \Delta T_w \qquad (1)$$

T_{max} : Maximum temperature of structural material (C)
T_{cool} : Coolant temperature (C)
ΔT_f : Film temperature drop (C) = q' / h
ΔT_w : Temperature difference in the first wall structural materials (C) = q" t_w / λ_w
q" : Surface heat flux (W/m^2)
h : Coolant heat transfer coefficient (W/m^2/K)
t_w : Plasma sidewall thickness (m)
λ_w : Wall structural material thermal conductivity (W/m/K)

For two kinds of the candidate structural materials mentioned above, the maximum temperature of each structural material was calculated by changing the surface heat flux and the plasma sidewall thickness of the first wall, based on Eq.(1). The results are shown in Fig.7.3.5 and Fig.7.3.6, respectively. The permissible temperatures of the main items which are considered to be important for each structural material are shown in the figures. It was assumed that water (temperature:320 C and heat transfer coefficient:$10^5 W/m^2K$) was used as a coolant. The following items are clarified from the figure for the combination of structural material and coolant.

a) Austenitic steel-water (Fig.7.3.5)

Melt.--- If the plasma sidewall thickness is assumed to be two millimeters, it reaches melting point (1400C) when the surface heat flux is more than about $9MW/m^2$.

High temperature strength--- From the viewpoint of the high temperature strength, the permissible temperature is considered to be 500-600C and the permissible maximum heat flux is estimated at about $3MW/m^2$.

Irradiation.--- From the viewpoint of swelling(He generation), the limit temperature is about 450 C and it gives the severest limit. That is, the permissible maximum heat flux is about $1MW/m^2$ even if the plasma side wall thickness is set at 1 to 2 millimeters.

b) Ferritic steel-water(Fig.7.3.6)

Melt.--- When the plasma side wall thickness is less than 2 millimeters and the surface heat flux is less than $10MW/m^2$, it does not reach the melting point. That is, the ferritic steel can be designed with enough room concerning the melting point.

High temperature luminous intensity.--- It is clear that the strength of ferritic steel (HT-9) decreases rapidly at more than 550 C. Therefore, from this viewpoint, the permissible maximum heat flux is about $1MW/m^2$ when the thickness of the wall facing to the plasma is 5 millimeters and is about $5MW/m^2$ when the thickness is 1 millimeters.

The thermal stress to be generated in the structural materials was calculated by the following equation, as the thermal stress of the slab completely restrained.

$$S_{max}=\frac{E\beta\Delta T_w}{2(1-\nu)} \qquad (2)$$

where, S_{max} : Generation thermal stress (Mpa)
E : Young's modulus (MPa)
β : Volume expansion rate (1/C)
Tw : Temperature difference in the first wall structural materials (C)
ν : Poisson ratio

For two kinds of the candidate structural materials, the thermal stress (slab) to be generated in the structural materials was calculated by changing the surface heat flux and the plasma side wall thickness by using eq.(2). The results are shown in Fig.7.3.7 and Fig.7.3.8, respectively. The coolant condition and the structural material temperature was set to equal to the study mentioned above. However, as for metallic materials, it was assumed that its primary stress could be reduced enough by the design and the thermal stress to be generated was compared with 3 Sm. The following items are clarified from the figure for each structural material.

a) Austenitic steel-water(Fig.7.3.7)

Even if the plasma side wall thickness is extremely thinned at about 1 millimeter, the permissible maximum heat flux against non-irradiation materials is estimated at about 1 MW/m^2. However, because the strength of the austenitic steel decreases greatly when it suffers the neutron irradiation and 3Sm decreases to 1/2 after operating 100dpa (about $10MWa/m^2$), the permissible maximum heat flux is guessed to be small even at about $0.5MW/m^2$.

b) Ferritic steel-water(Fig.7.3.8)

If the plasma side wall thickness is assumed to be 1-2 millimeters, the permissible maximum heat flux from the viewpoint of the thermal stress is estimated at about 2 to 4 MW/m^2. If it is assumed to be 5 millimeters, the heat flux is estimated at about $1MW/m^2$.

3) Examination concerning boiling and burn-out

Nuclear boiling beginning heat flux q_{nb} is expressed in the following approximate equation according to Bergles-Rohsenow.

$$q_{nb}= 1060\ (p^*)^{1.156}\ [1.8(Tw - Tsat)]^{2.30/P} \qquad (3)$$

where, q_{nb} : boiling beginning heat flux (W/m^2)
P : $p^*0.0234$
p^* : $=10.2p$
p : Coolant pressure (Mpa); 15MPa
T_w : Coolant channel side temperature (C)
T_{sat} : Coolant saturation temperature (C); 342.13C at15MPa

The boiling beginning condition evaluated by Eq.(3) is shown in Fig.7.3.9. Tw(without consideration of the boiling heat transfer) when heat transfer coefficient was assumed to be 56000$W/m^2/K$ or 100000 $W/m^2/K$ is shown in the figure. In the condition of this study, it is considered from the figure that it comes to the subcool boil when Tw reaches about 343C. Tw reaches about 343C when heat transfer coefficient is 56000 $W/m^2/K$ and the heat flux to the coolant channel is about more than 1.3 MW/m^2. The boiling beginning heat flux can be somewhat raised with larger heat transfer coefficient. For instance, if heat transfer coefficient is set at about 100000 $W/m^2/K$, the boiling beginning heat flux might be about 2.3 MW/m^2. However, considering about uncertainties such as shape of the coolant channel and dispersions of the observed data, it is considered that the heat flux to the coolant channel is required to be suppressed under about 1 MW/m^2 and about 2 MW/m^2 for each heat transfer coefficient, when designing with non-boiling condition. It is necessary for higher heat flux to design with the subcool boiling or to enlarge the subcool by reducing the coolant temperature. When the subcool boiling is permitted, it is naturally required to design in consideration of the boiling heat transfer. Moreover, we must consider sufficiently about increase of pressure drop by the boiling and accuracy of the flow rate distribution in the parallel channel. Especially, when the boiling occurs in the hot spot channel, sufficient consideration is necessary for danger that increase of pressure drop causes the decrease of the flow rate and spoils the heat removal performance and then damages the first wall. Because the attractive features as the power reactor will be remarkably decreased, it is undesirable to decrease the coolant temperature.

In the case of the design to permit the subcool boiling, we must take care so as not to cause burn-out in the coolant channel side, as we mentioned above. A lot of empirical formula such as Jens and Lottes and Zenkevich,Griffith,Tong,Janssen and Levy are proposed as expressions of the forced convection burn-out in the coolant. However, there are few experimental results and empirical formula of the burn-out against heat flux from the one side like the first wall. We examined by using the formula of Jens and Lottes and Tong shown as follows in order to obtain the standard of burn-out heat flux. It is necessary in the future to examine based on the more accurate data reflecting the condition of the first wall.

a) Expression of Jens & Lottes

$$q_{bo} = 3.15\ C\ (\ 7344G/106\ )^{m}\ (1.8\ \Delta T_{sub})^{0.22} \qquad (4)$$

where; q_{bo} : Burn-out heat coolant velocity (MW/m^2)
G : Mass velocity ($kg/s/m^2$)
ΔT_{sub} : Outlet subcool (C) ; 22.13 C at 15 MPa

Though C and m are constants defined by the pressure, the value at 13.72 MPa is used here because the scope of eq.(4) is under $140kg/cm^2$(13.72MPa).

$C = 0.445$
$m = 0.500$

b) Expression of Tong

$$q_{nb} = 3.15\ (0.23 + 0.094\ G^*)\ (3.0 + 0.018\ \Delta T_{sub})$$
$$(0.435 + 1.23\ e^{-0.0093\ \lambda/D})\ (1.7 - 1.4\ e^{-a}) \qquad (5)$$
$$G^* = 7.38 \times 10^{-4}\ G$$
$$a = 0.532\ ((I_{l\text{-}s} - I_{l\text{-}in})/L\ )\ (\rho_l/\rho_v)^{1/3} \qquad (6)$$

$I_{l\text{-}s}$: Entropy of saturation temperature (J/kg)
$I_{l\text{-}in}$: Entropy of inlet temperature (J/kg)
L : Vaporization latent heat (J/kg)
ρ_l : Density of saturation water (kg/m^3)
ρ_v : Density of saturated steam (kg/m^3)
λ : Coolant channel length (m); = 1.2m
D : Equivalent diameter (m); $= 9 \times 10^{-3}$m

Burn-out heat flux depends on the shape of the coolant channel and the coolant condition. In this examination, the following condition was assumed.

- Coolant channel diameter	9 millimeters
- Coolant channel length	1.2 m
- Coolant pressure	15MPa
- Coolant velocity	0-10m/s
- Coolant inlet temperature	280-320C
- Coolant outlet temperature	320C

Burn-out heat flux evaluated by using eqs.(3) and (4) to these conditions is shown in Fig.7.3.9 with coolant velocity as abscissa. The range of accuracy evaluated by the proposer of each expression is shown in the figure. The figure shows that there is a tendency that the (4) expression estimates burn-out heat flux smaller than the (3) expression. Moreover, even if coolant velocity is set at 8m/s to10m/s, it is considered that there is possibility that burn-out is caused when heat flux is more than about 3 MW/m2. The surface heat flux must be set at about 1 to 2MW/m^2 in order to cool the first wall by non-boiling according to the above-mentioned investigation. The surface heat flux is limited within 3 to 5MW/m^2 to avoid burn-out even if the subcool boiling cool is allowed. One of the methods to solve this problem is to extend large subcool by lowering the coolant outlet temperature, but this method remarkably decreases the function as the power reactor.

4) Summary of examination results

a) Austenitic steel

Swelling and the thermal stress according to the neutron irradiation are the critical conditions and the permissible maximum heat flux is limited to less than about 1 MW/m^2. The surface heat flux must be set at less than about 1 to 2 MW/m^2 from this viewpoint if the boiling of the coolant is avoided.

b) Ferritic steel

The permissible maximum heat flux is about 3MW/m^2 even if the design to permit the boiling is applied from the viewpoint of the high temperature strength, the thermal stress, and burn-out heat flux from the viewpoint of the structural material maximum temperature . In the case of thickness of about 4mm, the permissible heat load is about 1MW/m^2 and the highest temperature in plasma side might be less than 500 C.

(2) Thermal-hydraulic design

Here we examine the thermal-hydraulics of the first wall structure initially set after the general consideration in the preceding clause.

1) Design conditions

i) Heat load

The surface heat load distribution of SSTR is shown in Fig.7.3.10. The following value is used in the design.

Surface heat flux	: 0.5MW/m^2 (outboard midplane)
Structural material nuclear heating rate	: 65MW/m^3 (corresponds to 5MW/m^2)
Maximum heat flux in coolant channel side	:1.44MW/m^2 (tube diameter 12 mm :0.83MW/m^2)

ii) The first wall concept

The structural concept of the first wall examined in this case is shown in Fig.7.3.11. This is the first wall of the cylindrical tube type combined with the blanket from the viewpoint of tritium breeding performance and the first wall support. The coolant tube of this wall is the tube with inside diameter 9 millimeters and outside diameter 17 millimeters and the coolant flows in the direction of the toroidal. Besides, the value when the outside diameter of the coolant tube is 12mm (thickness 1.5 millimeters) is shown in parenthesis. The selection of the tube diameter is described later.

iii) Structural material

The physical properties values of ferritic steel (HT-9) are used (operating temperature 500C)

iv) Coolant

The coolant condition is assumed to be equivalent to PWR. That is, the pressure is set at about 15MPa, the inlet temperature at 285C, and the outlet temperature at 325C.

v) Coolant channel length

The coolant channel length between headers installed behind the blanket is about 2.2 meters in center unit in consideration of the first wall and the blanket vessel sidewall.

vi) Coolant physical properties values

It is used at the value 15Mpa, 300C.

2) Design calculation

i) Selection of coolant channel shape

In the light water cooled first wall, from the viewpoint of the heat and the fluidity performance, it is necessary to keep the coolant velocity and pressure drop not to be

excessive, and to prevent the subcool boiling in the coolant channel by securing sufficient heat transfer coefficient. However, because these two requirements have a tendency to conflict each other, we must select appropriate coolant diameters. In the case of the cooling without turning-back toward troidal direction, because the coolant diameter becomes extremely small, some problems are caused in respects such as manufacturing and safety. Therefore, if we adopt the concept to turn back the coolants and design so that there should be a lot of coolant channels of each steps in the inlet side and be a fewer channels in the outlet side, heat transfer coefficient in the severe outlet side can be enlarged from the viewpoint of the boiling without excessive pressure drop. In this design, the following coolant channel was selected in consideration of the above mentioned point.

Coolant tube inside diameter	9 mm
Coolant tube outside diameter	17mm[12mm]
Coolant tube pitch	17mm[12mm]
Step numbers (outboard first wall)	four steps (three turn-backs)
	[Three steps(two turn-backs)]
The first step channel number	155 [219]
The second step channel number	124 [219]
The third step channel number	82 [146]
The fourth steps channel number	51

Figures in [ ] are for tubes with 12 mm diameter.

The evaluated results of the heat and flow characteristics in the outboard first wall of this design are shown as follows. Similar characteristics can be obtained concerning the side unit and the inboard first wall.

ii) Coolant velocity

The coolant velocity is calculated by the following expression.

$$U = G_{ch} / (\gamma A)$$

$$G_{ch} = Q_{ch} / (C_p / \Delta T_{cool})$$

where;

G_{ch}	: Mass flow rate for a channel (kg/s)
γ	: Density (725.7kg/m^3)
A	: Coolant channel area (6.36 x 10^{-5}m^2)
Q_{ch}	: Quantity of heat removal per channel (W) (It was assumed that it is about 390MW[350MW] in whole outboard first wall.)
C_p	: Specific heat (5483 J/kgC)
ΔT_{cool}	: Coolant temperature rise (C)

Coolant velocity is calculated from this equation as follows; 5.2m/s in the first step, 6.5 m/s in the second step, 9.7m/s in the third step, 15.6m/s in the fourth steps, [3.3m/s in the first step and the second step, 4.9m/s in the third step]. Judging from the results in the current existing plants, it is considered that these values are in the range which can be technically permitted.

iii) Pressure drop

The friction pressure drop in the coolant channel and the inlet/outlet pressure drop in each steps were considered. That is, pressure drop is calculated by the following expression.

$$\Delta P = \sum_{i=1}^{3} (\Delta P_f + \Delta P_{in} + \Delta P_{out})i$$

where ; ΔP_f : Friction pressure drop
$= f \times (\gamma U^2/2) \times (L/D)$

ΔP_{in} : Inlet pressure drop
$= K_{in} \times \gamma U^2/2$

ΔP_{out} : outlet pressure drop
$= K_{out} \times \gamma U^2/2$

where f : Coefficient of friction (0.03):Roughness of the coolant tube surface is considered.

γ : Density (Kg/m^3)

U : Coolant velocity (m/s)

L : Coolant channel pallet length (m)

D : Equivalent diameter (9 mm)

K_{in} : Inlet pressure drop coefficient (0.5)

K_{out} : outlet pressure drop coefficient (1.0)

i : Steps

The total of pressure drop calculated by this equation is 791.4kpa[147kpa] and exceeds the permissible range of about 200kpa. In case of coolant tube diameter of 12 mm, the value is considered to be in the sufficiently permissible rage. Besides, the change of pressure drop with quantity of the heat removal as a parameter is shown in Fig.7.3.12.

iv) Film temperature drop and coolant channel wall temperature

The coolant channel wall temperature in the coolant outlet side in each step is important concerning the boiling in the coolant channel wall. This is shown by the following equation.

$$T_W = T_{out} + \Delta T_f$$

where, T_{out} : Coolant outlet temperature (325C)
ΔT_f : Film temperature drop

ΔTf is calculated as follows.

$$\Delta T_f = q''' / h$$
$$h = Nu\,\lambda / D$$
$$Nu = 0.023 \times Re^{0.8} \times Pr^{0.4} \quad : \text{Eq.by Dittus Boelter}$$
$$Re = U\,D / \nu$$

where ; q''' : Coolant channel side heat flux 1.44MW/m^2[0.83MW/m^2]
h : Heat transfer coefficient (W/m^{2}C)
Nu : Nuselt number
Re : Reynolds number
Pr : Prantle number (0.866)
D : Equivalent diameter (9mm)
λ : Coolant coefficient of kinematic
ν : viscosity.(1.22 x 10^{-7}m^2/s)

Film temperature drop and the coolant channel wall temperature were calculated by this equation. When the model of one-dimensional slab is used, film temperature drop is calculated as follows; 36.5C in the first step, 30.5C in the second step, 22.1C in the third step, 15.1C in the fourth step [the 30C in the first step, 30C in the second step, and 2C in the third step]. Coolant channel wall temperature in outlet side is estimated as follows; 336.5C in the first step, 342.5C in the second step, 342.1C in the third step, and 340.1C in the fourth step[330C in the first step, 345C in the second step, and 347C in the third step]. The boiling beginning condition at this time was calculated from the following equation of Bergles-Rohsenow.

$$q_i = 1060 \times (10.2 \times P)^{1.156} \times [(T_W - T_{sat}) \times 9/5]^{2.30} / (10.2 \times P)^{0.0234}$$

where ; P : Coolant pressure (15MPa)
T_W : Coolant channel wall temperature (C)
T_{sat} : Saturation temperature (342.1C at 15MPa)

The condition calculated so that qi should be1.44 MW/m^2 [0.83MW/m^2] is about 342.7C(343C). That is, the boiling in the first wall coolant channel is not caused when the tube diameter is 12 millimeters, but it comes to the boil when the coolant diameter is 17 millimeters. Because pressure drop is large when the tube diameter is 17 millimeters,

the adoption of rectangular coolant tube for decrease of the coolant tube pitch is considered in the present condition.(refer to Fig.7.3.11). Because the boiling beginning condition is exceeded when the coolant tube diameter is 12 millimeters, the decrease of the coolant temperature (about 5C) or the increase of coolant velocity is required.

3) Future R&D Issues

The preliminary design at this time clarified following facts.

1. Optimization or trade-off (selection of tube diameter, number of turn-back steps, tube shape, and coolant velocity etc.) are required.

2. In order to enlarge the thickness in the plasma side of the first wall and reduce the coolant tube pitch, the adoption of rectangular coolant tube is desirable, and the thermal-hydraulic design should be executed for it.

3. The thermal design in consideration of three-dimensional distribution of heat load(surface and nuclear) and three-dimensional structure of the first wall is desirable.

7.3.3. Thermal design of the blanket

(1) Thermal design of the front breeding region

1) Design condition

Heat in the front breeding region is removed by the coolants in the first wall and the neutron multiplier layer. The minimum temperature of the breeding materials must be controlled at about 400C. The maximum temperature of the breeding materials is defined by the thickness of the breeding region.

2) Heating rate distribution

One-dimensional heating rate distribution in the replaceable blanket is shown in Fig.7.3.13. (the neutron wall load is normalized to 3.4MW/m^2.) According to the figure, the heating rate in the first wall side is 78MW/m^3 and the heating rate in the neutron multiplier side is 90MW/m^3 (it is renormalized to the neutron wall load 3MW/m^2).

3) Effective thermal conductivity of the breeding region

When packing fraction of pebbles is set at 70 %, the effective thermal conductivity

of the breeding material(Li_2O) pebble which is 1 mm in diameter is 2W/mK without depending on the temperature.

4) The maximum temperature of the breeding materials

The maximum temperature of the breeding material of the front breeding region was calculated by changing the thickness of the breeding area, as a problem of one-dimensional slab thermal conduction of two-sided cooling, provided that the minimum temperature of the breeding materials was assumed to be controlled at 400 C. The maximum temperature of the breeding material when the heating rate is assumed to be constant (78 or 90MW/m^2) is shown in Fig.7.3.14 as a function of the distance from the edge of the breeding region(the first wall or the multipliers). According to these figures, the maximum temperature of the breeding materials reaches 1000C at the distance 5.6 mm from the first wall and 5.3 mm from the multipliers. Therefore, it is considered that the thickness of the front breeding region can be set at about 1 centimeter, but in the design at present, we set the thickness of the front breeding at 5mm in consideration of sufficient margin. When the neutron wall load is assumed to be about 5 MW/m^2 as the peak value because the wall load has the poloidal distribution, it is necessary to examine whether the maximum temperature should be within the permissible temperature or not.

(2) Thermal-hydraulics design of the second breeding region

As for the second breeding region, we examined temperature control of the breeding region and thermal-hydraulic capability of the breeding region.

1) Design condition

We must design according to the following design conditions.

i) Structural material

The ferritic steel (F82H, the physical properties values are those for HT-9.)
(operation temperature < 500C).

ii) Neutron multiplier

The beryllium layer which is 10 cm in thickness is installed in the plasma side of the blanket.

iii) Breeding material

Lithium oxide pebble which is 1 mm in diameter is used as a breeding material. Packing fraction is assumed to be 70 % in the bulk and be 30 % near the tube wall.

iv) Coolant

The coolant condition is equivalent to that of PWR. That is, the pressure is set at 15.5MPa, the inlet temperature is set at 285C, and the outlet temperature is set at 325C.

v) Temperature of the breeding region

Though the permissible operating temperature condition of the breeding material is 400C-1000C, the nominal temperature condition is set at 450C-950C in consideration of some margin for the output power variation. The maximum temperature of the breeding materials is controlled by the appropriate arrangement for the coolant tubes and the minimum temperature of the breeding materials is controlled by thermal resistance layer installed around the coolant tubes.

vi) Heating rate of the breeding material

As the heating rate distribution of the breeding region, the one-dimensional neutronics calculational results mentioned above are used.

vii) Physical property values

The value in 15MPa, 300C is used as a coolant physical properties. As the thermal conductivity of the breeding region, the effective heat conductivity (2W/mK) of the pebble-packed region in consideration of the temperature dependency of lithium oxide and purge helium gas (0.1Mpa) is used.

2) Diameter of the coolant tube

The inside diameter of the coolant tube in the breeding material region must be large to some extent, in order to design so that coolant velocity and coolant pressure drop should not be excessive. To enlarge the coolant tube diameter brings increase of the structural material ratio and decrease of the pebble packing fraction because of the wall effect, and affects tritium breeding ratio negatively. In addition, there is a possibility that it might bring difficulty to the arrangement of the coolant tubes. The coolant tube, which is 1.5 mm in thickness, 12 mm in inside diameter, is used in this design. Because the coolant channel is long in the inboard blankets, it is necessary to set the inside diameter of the coolant tube at more than 20 mm.

3) Temperature control of the breeding material

i) Maximum temperature control

The arrangement of the coolant tubes was done so as to control maximum temperature at less than 950C.

ii) Minimum temperature control

The appropriate thermal resistance layer (solid heat insulating material) was installed around the coolant tubes so as to keep the breeding material temperature at more than permissible minimum temperature(400C) because the coolant temperature in the inlet at 285C and in the outlet at 325C.

iii) Coolant velocity and pressure drop

According to the calculational results, maximum coolant velocity is 3.7m/s and maximum pressure drop is about 112kpa.

4) Summary

The pressure drop of the coolant tube in the blanket was about 115kpa in the design at this time. According to this results, the whole pressure drop to the inlet/outlet manifold in upper side of the core is estimated to be suppressed at about 300kpa in consideration of the factors of another cause of pressure drops.

7.3.4. Induced radioactivity

The one-dimensional neutronics calculation, by which the SSTR core geometry was simulated, was executed and the induced activity was analyzed. The calculational method is shown as follows.

(1) Calculational code : THIDA2 system (ANISN-ACT4)
(2) Group constants : GICX40 and GROUPIN
(3) Geometrical model : One-dimensional toroidal model
(The geometry is shown in Fig.7.3.15 and the atomic number density of the steels is shown in Table 7.3.2.)

(4) Source normalization: The neutron generation density is set so that average neutron wall load should be $3MW/m^2$.

$$f_N = \frac{2x3.14x(5.12+8.88)x0.01x3}{14.1x1.602x10^{-19}} = 1.168 \times 10^{18}$$

(5) Reactor operating mode

1) 1.4 year continuous operating (2 years X 70 % availability)
2) 21 year continuous operating (whole reactor life 30 years X 70 % availability)

(6) Activation calculation materials

1) 316SS (vacuum vessel and shield materials)
2) F82H (blanket materials)
3) CSUS-JN1 (materials for superconducting coil)

The biological dose rate distribution due to decay gamma ray one week after reactor shutdown is shown in Fig.7.3.16 (1.4 years continuous operation) and Fig.7.3.17 (21 years continuous operating). Dose rate is in the order of 10^6 rem/h(10^4Sv/h) in the first wall area as shown in Fig.7.3.16,and is in the order of 1 mrem/h(10^{-2}mSv/h) outside the toroidal magnetic field coil as shown in Fig.7.3.17. It can be sufficiently less than 2.5 mrem/h with the installation of appropriate biological shields (cryostat) even in the area where TFC does not exist. The attenuation tendency of the decay heat in the first wall (the replaceable blanket) after the reactor shutdown is shown in Fig.7.3.18. It is about 0.08W/cm^3 immediately after the shutdown of the reactor and it attenuates to about 0.01W/cm^3 after 1 week from the shutdown. It is about 0.014M/cm^3 in the end wall side of the replaceable blanket vessel immediately after the shutdown.

7.3.5. Evaluation of the thermal power output

The thermal power in the first wall, the blanket, and the divertor was estimated for the input condition of the design of the cooling system. The flow of energy is shown in Fig.7.3.19. The following assumptions were taken :

(1) Neutron distribution to components

Neutron distribution was assumed as follows, referring to the poloidal distribution of the neutron wall load.

Outboard blanket	75 %
Inboard blanket	25 %
Diverter	5 %
Loss to the outside	5 %

(2) Neutron energy multiplication factor

The quantity of nuclear heating in the blanket per one neutron was obtained by the one-dimensional neutronics calculation (the infinite cylindrical model, the poloidal model are shown in Fig.7.3.20) using ANISN. The calculational results are shown in Table7.3.3. The neutron energy multiplication factor (Nuclear heat deposition in the blanket per one DT neutron / 14.1MeV) was evaluated to be1.36.

The surface heat load distribution to the first wall, to which plasma heating power 60MW is added, was estimated based on the evaluation of the paragraph 8.1. Total thermal power to the power generation system is 3710MW, excluding 120MW loss of neutron energy.

7.3.6. Tritium permeation to the primary cooling water

(1) Introduction

Tritium permeates through the first wall and the blanket etc. into the primary cooling water during operation of the fusion reactor. A large amount of tritium permeates into the first wall cooling water by the inplantation of neutral tritium particle. Moreover, in the blanket, tritium generated in the breeding area permeates through the coolant tubes of the blanket into the blanket cooling water.

The tririum permeation rate into the first wall cooling water by the tritium-inplantation in the first wall and that into the blanket cooling water are evaluated in this section. Moreover, the reduction methods of the tritium permeation rate into the primary cooling water is examined.

(2) Tritium permeation rate through the first wall

1) Analytical method

The permeation rate is calculated with the following formula using transport parameter,W given by Doyle and Brice[1].

$$J_2 = \phi\alpha\left[\frac{1+W}{W+\alpha(\gamma^2+1)}\right] \quad (1)$$

$$W = (\phi R/D_1)(k_1/\phi)^{0.5} \quad (2)$$

$$\alpha = \frac{R}{x_o}\frac{x_o/\delta}{\exp(x_o/\delta)-1} \quad (3)$$

$$\gamma = \exp(x_o/x_s)(k_1/k_2)^{0.5} \quad (4)$$

$$1/\delta = 1/X_D + 1/X_S \quad (5)$$

$$x_D = x_o\frac{k_B T_o}{E_D} \quad (6)$$

$$x_s = -x_o \frac{k_B T_o}{Q^*} \quad (7)$$

$$T_0 = T_1 T_2 / (T_1 - T_2) \quad (8)$$

where ;

J	: Flux of the particles
R	: Inplanted range of injected particles
T	: Temperature
X_o	: Thickness of material
k	: Recombination rate constant
k_b	: Boltzmann constant
E_d	: Activation energy of diffusion
Q*	: Heat of transport
	Subscript 1, surface of the plasma side;
	2, surface of the cooling water side

2) Analytical condition

The analytical conditions are shown in Table7.3.4.

3) Analytical results

(a) Effect of materials and temperature

The analytical results are shown in Fig.7.3.21.

Tritium permeation rate: 21.3 g/day from $J_2 / \phi = 1.0 \times 10^{-3}$.

The tritium permeation rate through the austenitic stainless steel was evaluated for comparison.

Material : DIN 1.4914 > SUS304

Temperature : The permeation rate through both DIN 1.4914 and type 304 stainles steel increase with increasing temperature.

(b) Effect of injection particle flux (ϕ)

The calculated results are shown in Fig.7.3.22.

Normalized tritium permeation rate (J_2/ϕ) : $(\phi)^{-1/2}$

Tritium permeation rate (J_2):

(c) Effect of the surface sticking coefficient (σ)

The calculational results are shown in Fig.7.3.23.

Normalized tritium permeation rate (J_2/ϕ): $(\sigma)^{-1/2}$

(d) Effect of trap site binding energy (E_B)

The calculated results are shown in Fig.7.3.24.

As for E_B, the value E_B = 0.2eV is reported for austenitic stainless steel, and as for iron (a), the value E_B = 0.6eV is reported[1]. However, the data of ferritic stainless steel is not yet reported. In 500C, if E_B is 0.2eV, trapped tritium concentration is estimated to be smaller than mobile tritium concentration. However, if E_B=0.6eV, trapped tritium concentration is larger than that of mobile tritium by two order of magnitude.

(e) The time required to reach steady state

The time required to reach steady state ($t_{ss}=x_o^2/6D$) of SUS304 and DIN 1.4914 when the trapping is neglected is shown in Fig.7.3.25.

Because the diffusion constants of DIN 1.4914 is large and its temperature dependency is small, the regular arrival time is less than 1hour at the normal temperature. However, as for SUS304, the regular arrival time is specially long in low temperature and exceeds 1 year at 200C. In SUS304, the time required to reach steady state extends furthermore at the low temperature due to the trapping .

4) Summary

i) The quantity of tritium permeation of the first wall is evaluated at 21.3g/day.

ii) A certain kind of the permeation barrier is required, in order to keep this quantity of tritium permeation under 1g/d.

(3) Reduction method of tritium permeation through the first wall

1) Reduction method

The following methods are thought as a reduction method of the tritium permeation rate through the first wall.

i) Coating of plasma side surface with the materials of high recombination rate constants such as beryllium, silicon, etc. The toughness of coating layer against the injecting particles is considered the R&D item.

ii) Coating of cooling water side surface with material of low tritium diffusion coefficient such as ceramics etc. as diffusion resistant layer of tritium .

2) Effect of diffusion resistant layer

Because oxide layer is generated in the coolant tubes such as SG, the permeation rate is generally reduced less than 1/100 as shown in Fig.7.3.26[4].

1) Calculation formula

Material : HT-9

$$\phi = (4.66 \times 10^{-3}/3) \exp(-11100/RT) \quad (9)$$

ϕ in cc(STP)/cm/s/atm$^{1/2}$

R = 1.987 cal/mol/K

2) Calculation conditions

Material	: HT-9
Coolant tube temperature	: 350C
Coolant tube dimension	: 15mm^{OD} X 1.5mmt X 9000mm^{L}
Number of coolant tubes	: 200 / module
Surface area of coolant tubes	: 4.07 X 10^3 m^2
Number of modules	: 48
T_2 gas partial pressure	: 5 x 10^{-5} atm (5Pa)

3) Calculated results

Tritium permeation = 0.660 cc (STP)/s
= 5.70 x 10^4 cc (STP)/day
= 2.55 mol-T_2/day
= 15.4 g-T/day
= 1.47 x 10^5 Ci/day

4) Summary

i) The quantity of tritium permeation of the blanket is evaluated at 15.4g/day.

ii) A permeation barrier is required in order to reduce tritium permeation rate less than 1g/d.

(5) Measure for the reduction of tritium permeation of the blanket

1) Reduction measure

As the reduction measure of tritium permeation of the blanket cooling tubes, there are the generation of oxide layer as the diffusion resist layer of tritium permeation and the coating of ceramics.

2) Effect of diffusion resist layer

Oxide layer generates in the coolant tube such as SG and the permeation rate is reduced at under1/100, as we mentioned above.

3) Summary

i) The quantity of tritium permeation of the blanket is estimated to be reduced at under 1/100 of 15.4g/day by oxide layer on the surface of the coolant tube.

ii) The maintenance of the integrity of oxide layer is considered as a problem in the future.

[References]

1) B.L.Doyle and D.K.Brice, Radiation Effects 89(1985),21-48

2) K.S.Forcey et al., J.Nucl.Mater. 160(1988),117-124

3) ANL/FPP-84-1, BCSS Final Report (1984)

4) J.T.Bell et al., Conf-800427, p48, (1980)

Table 7.3.1 Atomic number densities or volume fractions of various materials used in neutron transport calculations (1/2)

Material	Element	Number Density (n/cm^3)	Mat. No. in ANISN
Plasma(Void)	He	1.0×10^{13}	253
Ferritic steel (F82H)	W	5.18×10^{20}	295
	Cr	7.09×10^{21}	
	Fe	7.80×10^{22}	
Austenitic steel (316SS)	Mo	1.26×10^{21}	241
	Cr	1.58×10^{22}	
	Ni	9.85×10^{21}	
	Fe	5.91×10^{22}	
Water(H_2O)	H	6.69×10^{22}	247
	O	3.34×10^{22}	
Air	N	4.22×10^{19}	
	O	1.17×10^{19}	
Insulator	H	2.03×10^{22}	313
	C	1.79×10^{22}	
Epoxy(30w%)-glass(70w%)	N	1.95×10^{21}	
ρ =1.8 g/cm³	O	2.55×10^{22}	
(ITER-JL-BL-1-9-1)	Al	2.16×10^{21}	
	Si	6.88×10^{21}	
	Ca	2.30×10^{21}	
B_4C	^{10}B	2.20×10^{22}	259
	^{11}B	8.78×10^{22}	
	C	2.75×10^{22}	
Lead(Pb)	Pb	3.30×10^{22}	301
Beryllium(Be)	Be	1.24×10^{23}	277
Copper(Cu)	Cu	8.46×10^{22}	265
Molybdenum(Mo)	Mo	6.40×10^{22}	283
Titanium(Ti)	Ti	5.66×10^{22}	289

Table 7.3.1 (Continued)

Material	Element	Number Density (n/cm^3)	Mat. No. in ANISN
Lithium oxide (natural)	^6Li	5.12×10^{21}	319
	^7Li	6.39×10^{22}	
	O	3.45×10^{22}	
Liquid helium	He	1.84×10^{22}	307
Superconductor (Nb_3Sn)	Nb	4.09×10^{22}	271
	(Sn	1.36×10^{22})	
Superconducting magnet	316SS	0.552	325
	Nb	0.058	
	Cu	0.118	
	Mo	0.063	
	Ti	0.054	
	Insulator	0.019	
	Liquid helium	0.136	
First wall	F82H	0.63	355
	H_2O	0.37	
Inboard shield, Front wall, Bavk wall	F82H	0.85	331
	H_2O	0.15	
Outboard shield	F82H	0.5	367
	H_2O	0.5	
Support structure	F82H	0.1	361
First breeding zone	Li_2O	0.7	373
Second breeding zone	Li_2O	0.6	343
	F82H	0.05	
	H_2O	0.1	
Permanent breeding zone	Li_2O	0.6	337
	F82H	0.04	
	H_2O	0.09	
Partition wall	F82H	0.15	349
	H_2O	0.25	

Table 7.3.2 Atomic number densities of steels for activation calculation

Unit : (atoms/cm^3)

Element	316SS	F82H	CSUS-JN1	Hi-Mn Steel
B		1.520×10^{19}		
C	2.801×10^{20}	3.730×10^{20}	1.043×10^{20}	9.988×10^{20}
Al		1.790×10^{19}		1.790×10^{19}
Si	2.804×10^{21}	1.540×10^{20}	1.698×10^{21}	3.430×10^{20}
Mn	1.662×10^{21}	4.300×10^{20}	3.683×10^{21}	2.254×10^{22}
P	4.034×10^{19}	7.780×10^{18}	4.044×10^{19}	1.556×10^{19}
S	1.799×10^{19}	1.500×10^{18}	3.005×10^{18}	6.011×10^{18}
Ti		5.030×10^{18}		1.509×10^{20}
V		1.700×10^{20}		
Ni	1.051×10^{22}	8.210×10^{18}	1.210×10^{22}	8.210×10^{18}
Cr	1.538×10^{22}	7.090×10^{21}	2.242×10^{22}	1.257×10^{22}
Mo	1.147×10^{21}	5.020×10^{18}		
Fe	5.635×10^{22}	7.710×10^{22}	4.787×10^{22}	5.181×10^{22}
Co	2.283×10^{20}	4.090×10^{18}	2.628×10^{20}	2.453×10^{18}
N	3.431×10^{19}	6.530×10^{18}	1.169×10^{21}	8.047×10^{19}
Nb		3.630×10^{16}		2.593×10^{18}
Ta		1.010×10^{19}		
W		5.180×10^{20}		

Table 7.3.3 Nuclear heat deposition per DT neutron in blanket

Zone	Heat Deposition (MeV)
First Wall	2.143
Front Breeder	2.440
Partition Wall	2.456
Beryllium	5.173
Partition Wall	1.390
Second Breeder	2.086
End Wall	0.493
Front Wall	0.397
Copper Shell	0.080
Permanent Breeder	2.258
End Wall	0.192
Total	19.108

Table 7.3.4 Analytical conditions for stainless steel

1. Structural Material			
Material			Ferritic Stainless Steel
Surface Area	A(m2)		700
Thickness	x_0(cm)		0.5
2. Temperature			
Maximum / Minimum			773K / 648K
Calculated under following conditions			
Surface Heat Load		(MW/m^2)	0.5
Heat Generation Rate		(MW/m^3)	50
Coolant Temperature		(K)	573
Heat Transfer Coefficient		(W/m^2K)	104
Thermal Conductivity		(W/m K)	25
3. Incident Tritium			
Incident Flux	ϕ'	($1/cm^2s$)	$1x10^{16}$
Incident Energy		(eV)	50
Reflection Coefficient		(-)	0.50
Projected Depth		(cm)	$5x10^{-7}$
4. Tritium Transportation			
Diffusion 2)*	$D = D_0 \exp(-E_D/k_BT)$		
	D_0(cm2/s)		$8.82x10^{-4}$
	E_D(eV)		0.163
Recombination 2)	$k = k_0\sigma\ (500/T) \exp(-E_k/k_BT)$		
(Baskes' formula)			
	k_0(cm4/s)		$9.40x10^{-18}$
	E_k(eV)		0.1184
Sticking Coeff.	σ (-)		1.0
Heat of Transport	Q^*(eV)		-0.065
Hydrogen Solution Sites Density			
	N_S(1/cm3)		$8.5x10^{22}$
Trap Density	N_T/N_S		0.01
Trap Strength	E_B(eV)		0.22

* data for DIN 1.4914 (Fe-11Cr-1Ni-1Mo, Si, V, Mn, Nb, C)

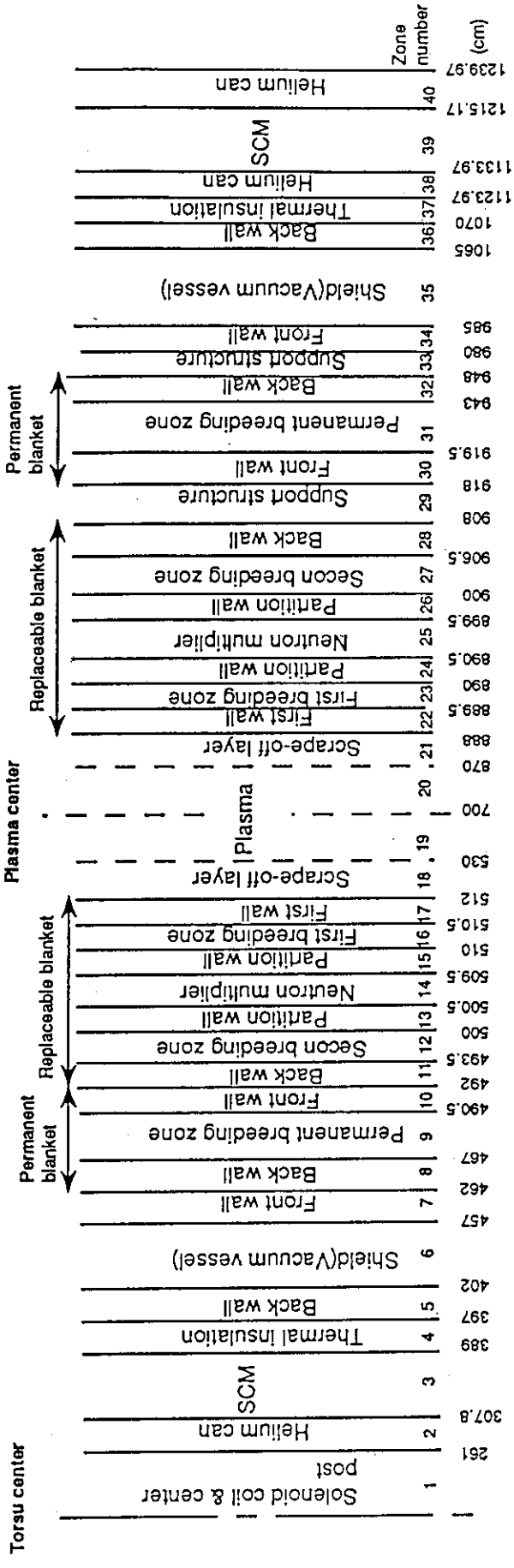

Fig. 7.3.1 1-D toroidal model for neutronics calculation of SSTR.

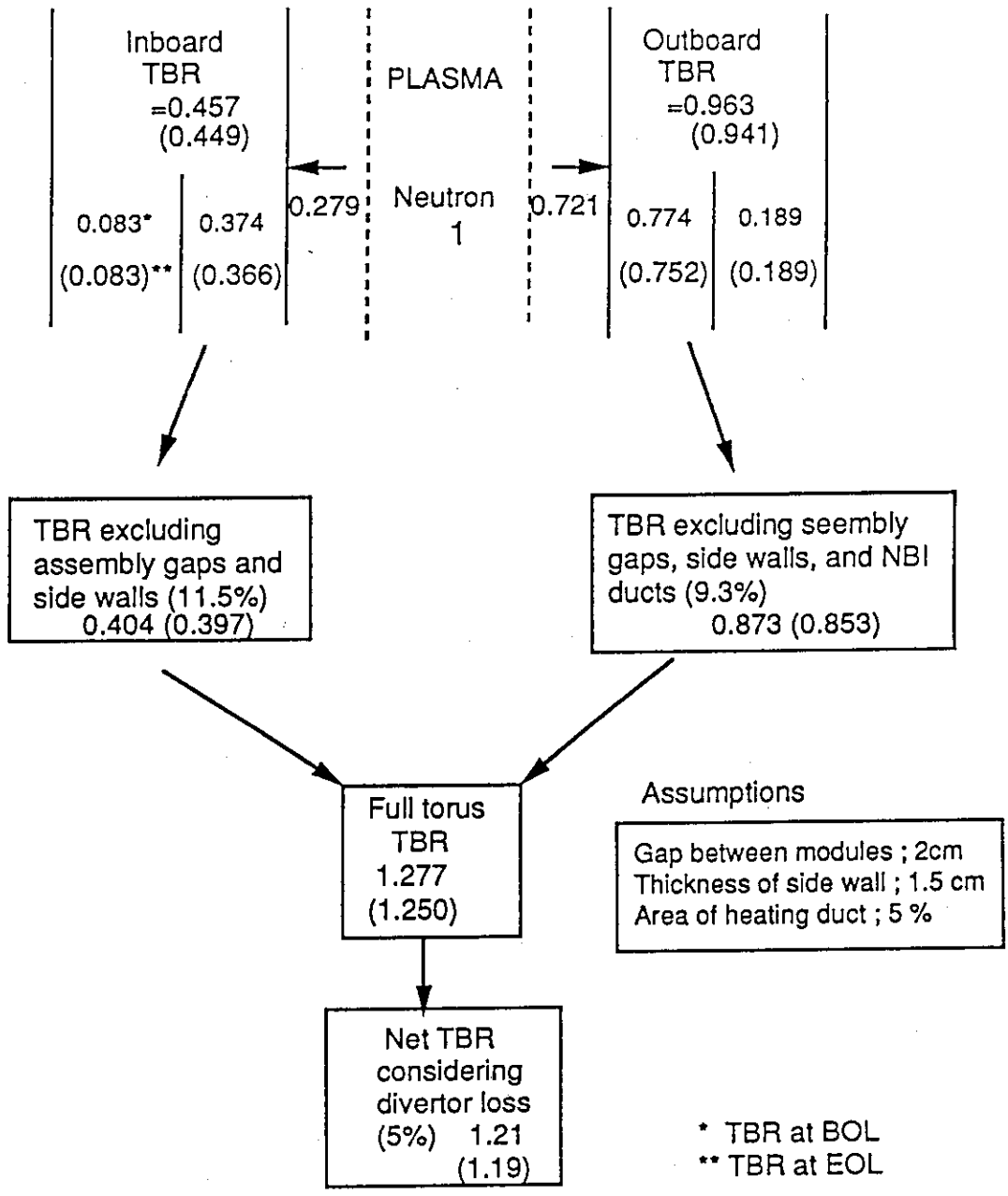

Fig. 7.3.2 Estimation of the net TBR of SSTR blanket. (Values in parentheses are TBR at the end of life of replaceable blanket, 4.2 MWY/m2).

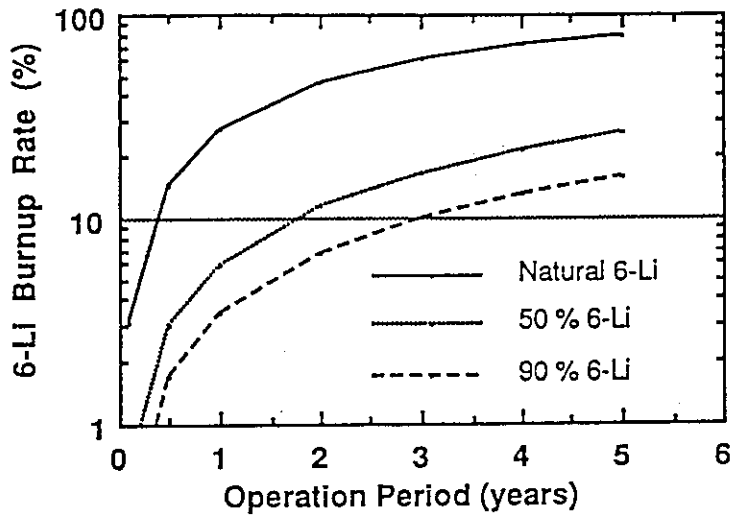

Fig. 7.3.3 Local 6-Li burnup rate in front breeding zone.(Average neutron wall load: 3 MW/m^2)

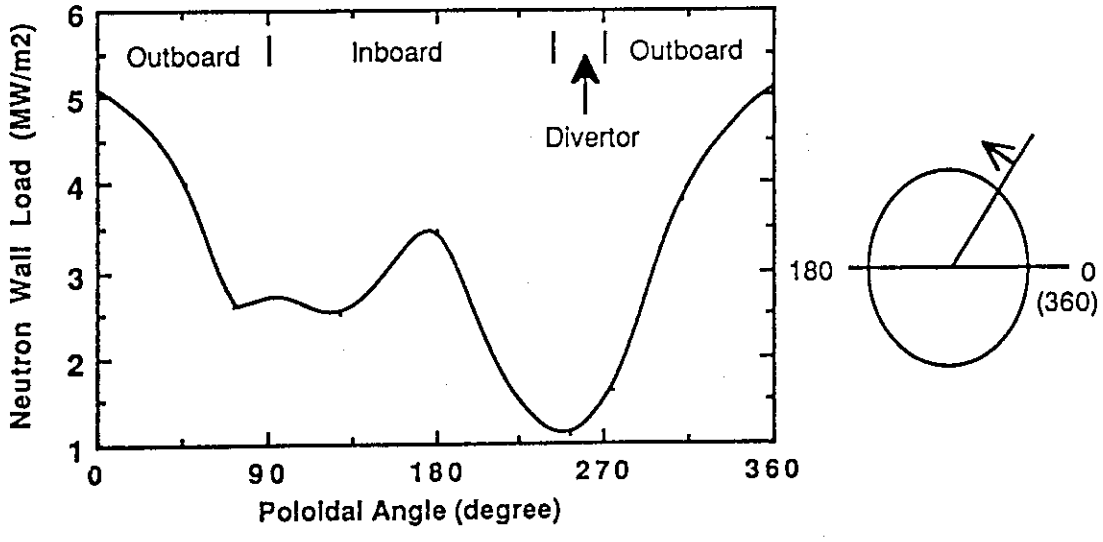

Fig. 7.3.4 Poloidal distribution of neutron wall load of SSTR.

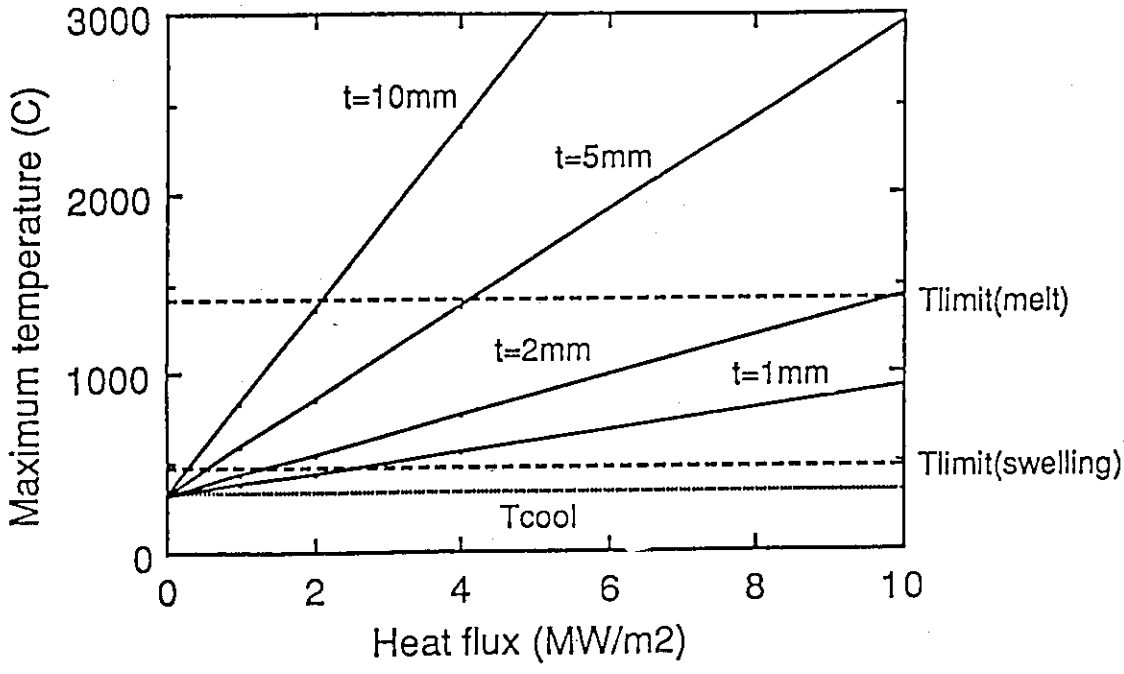

Fig. 7.3.5 Maximum temperature of austenitic stainless steel first wall as a function of wall thickness (t).

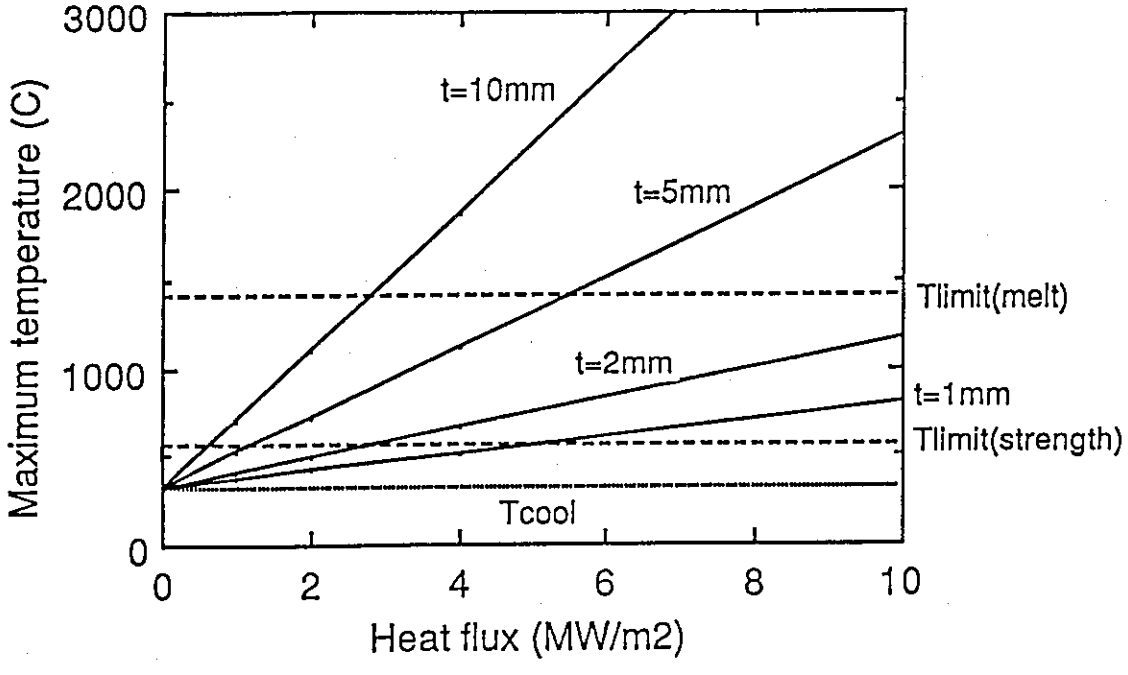

Fig. 7.3.6 Maximum temperature of ferritic stainless steel first wall as a function of wall thickness (t).

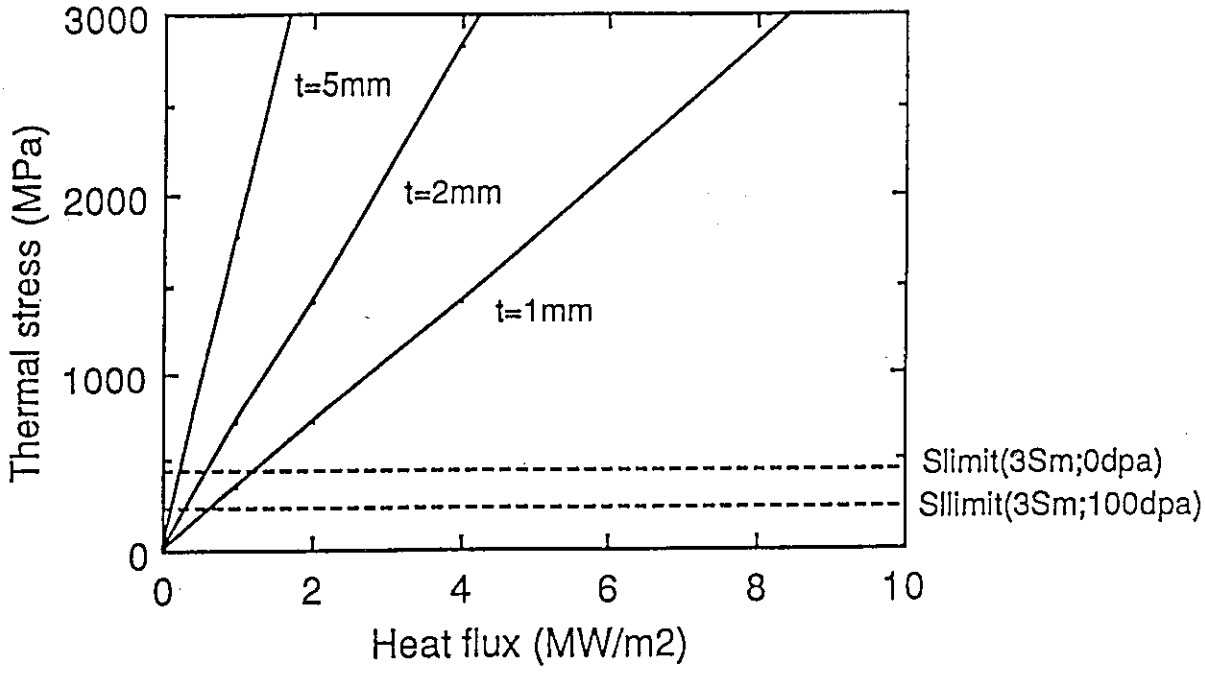

Fig. 7.3.7 Thermal stresses of austenitic stainless steel first wall as a function of wall thickness (t).

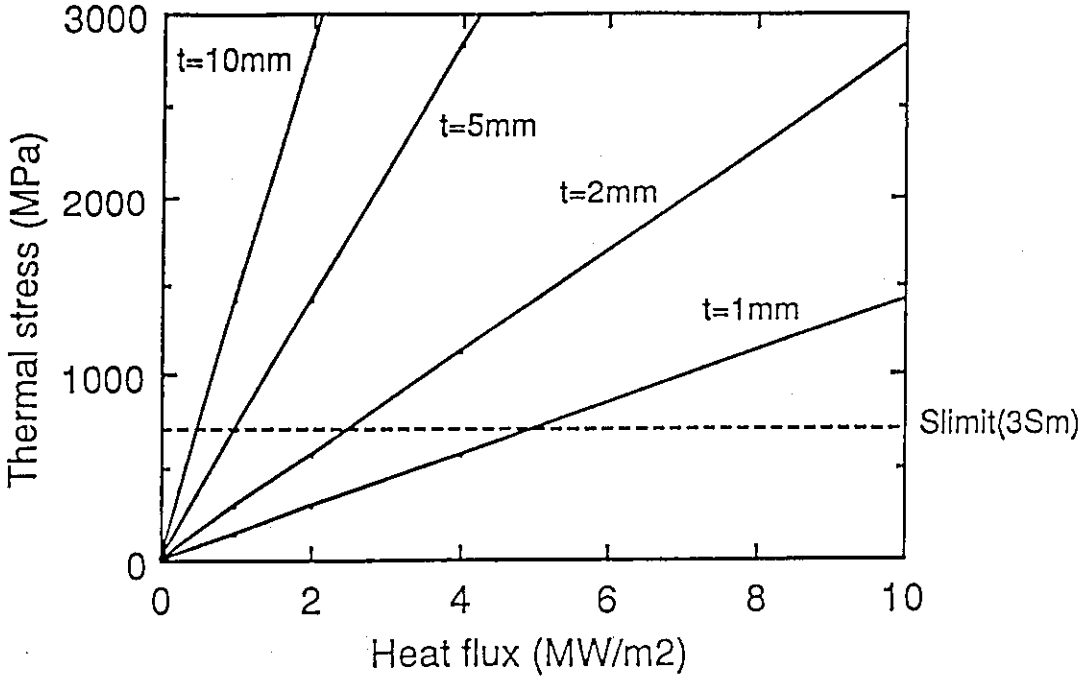

Fig. 7.3.8 Thermal stresses of ferritic stainless steel first wall as a function of wall thickness (t).

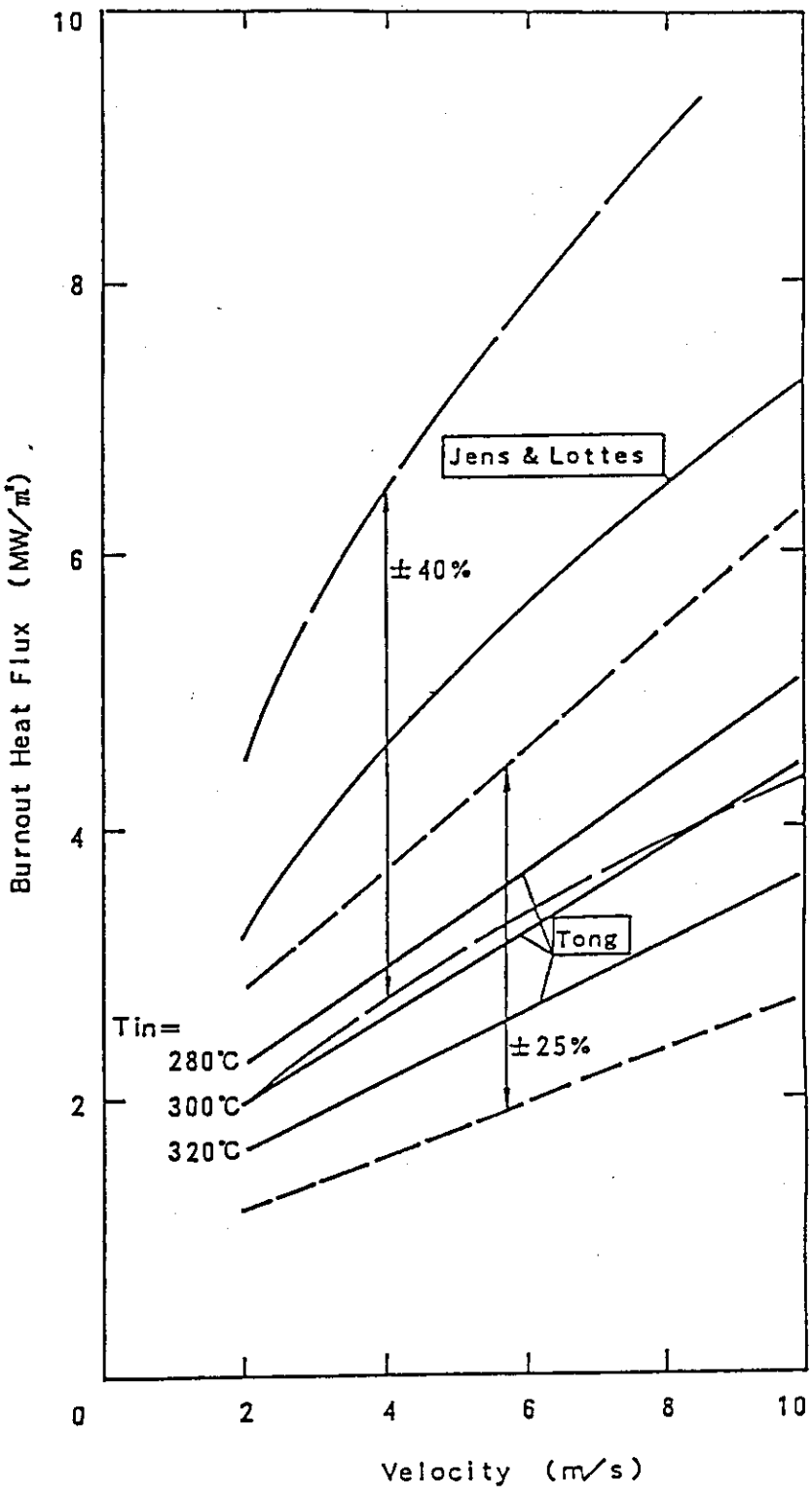

Fig. 7.3.9 Burnout heat flux for first wall.

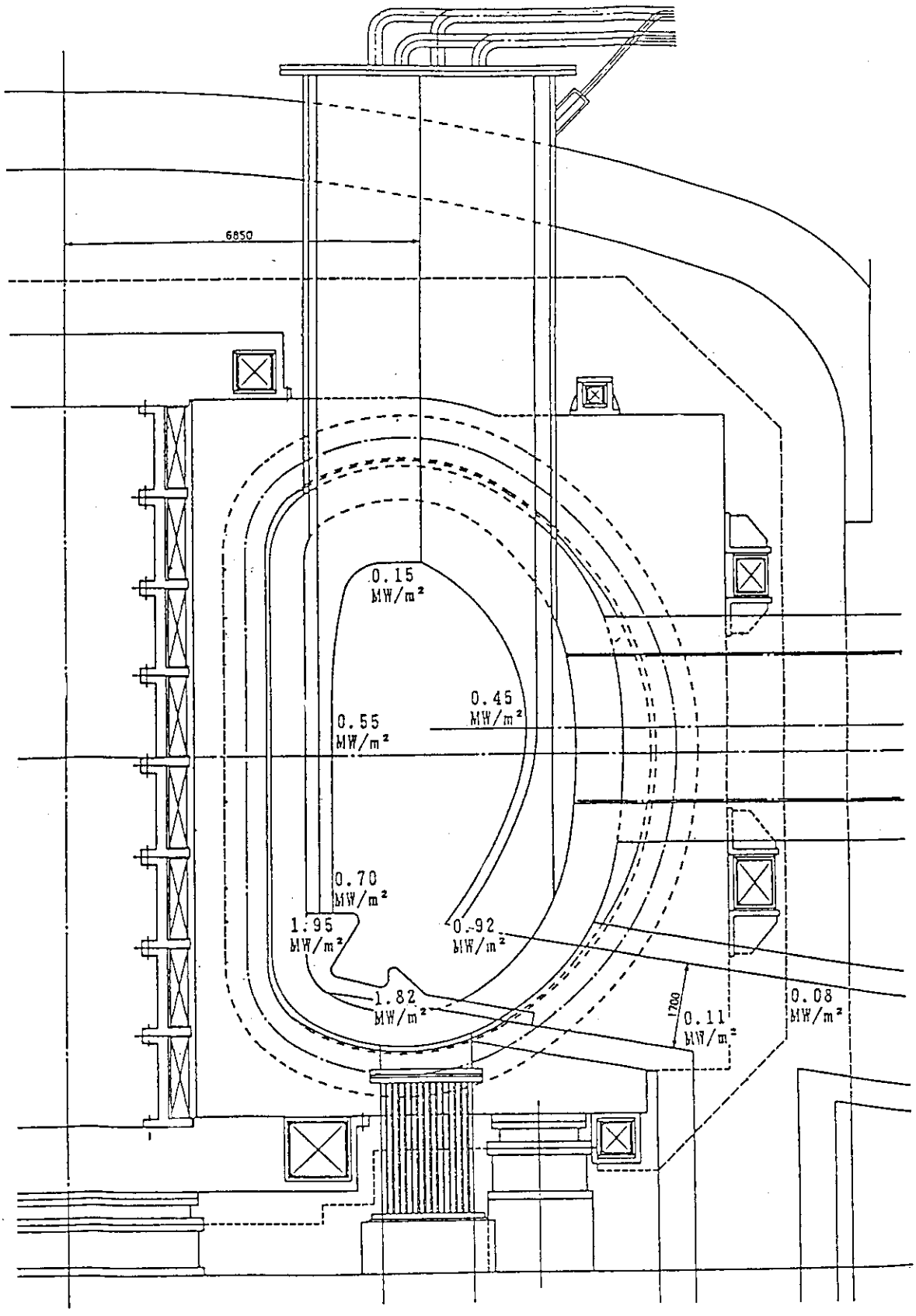

Fig. 7.3.10 Distribution of surface heat flux of SSTR.

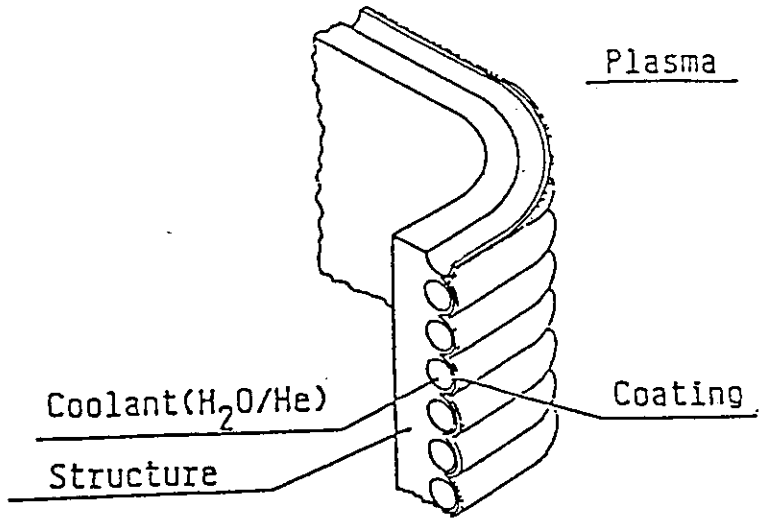

FIRST WALL
TUBE-PLATE TYPE

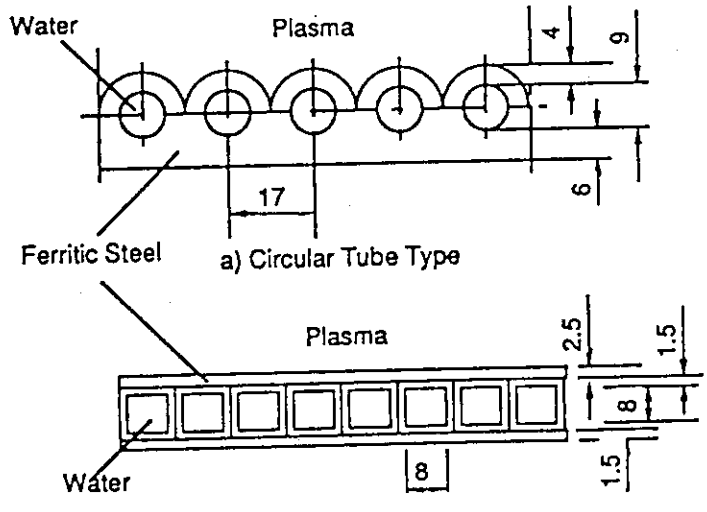

Fig. 7.3.11 Concept of first wall structure.

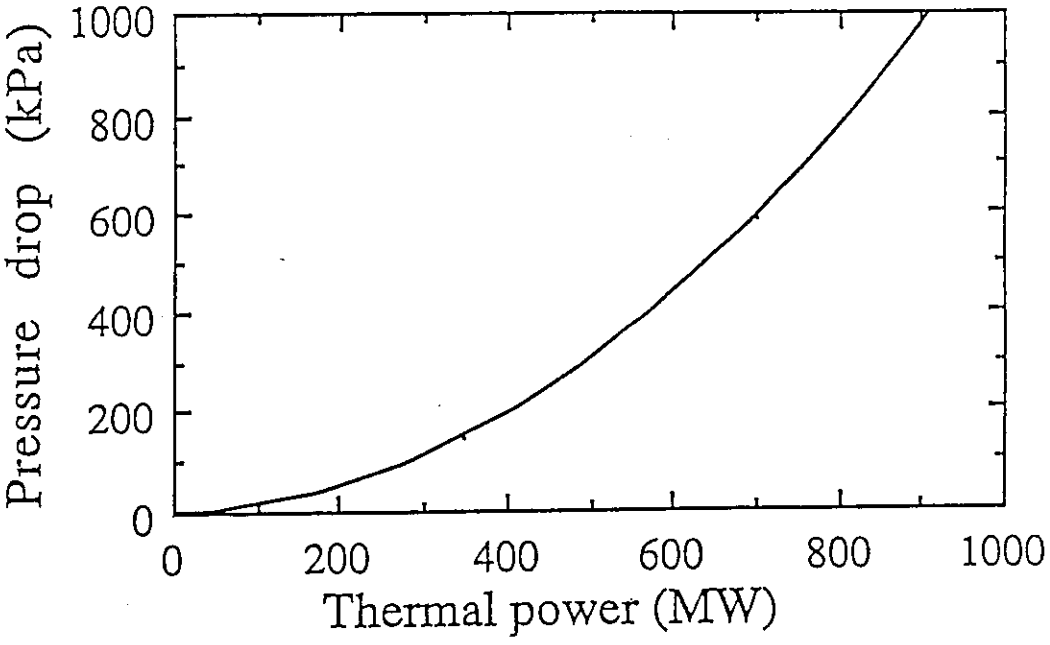

Fig. 7.3.12 Dependence of pressure drop on thermal power.

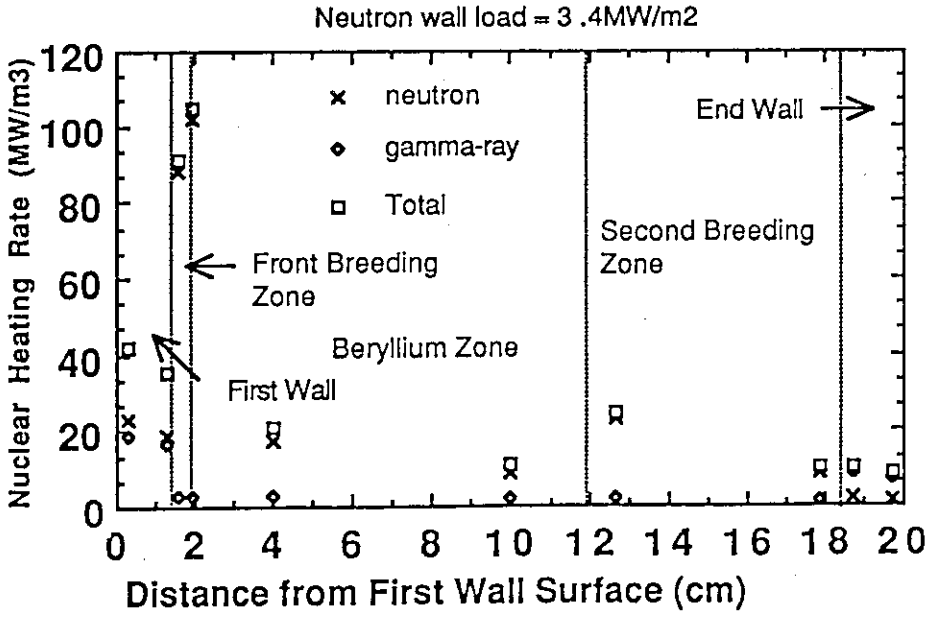

Fig. 7.3.13 Nuclear heating rate profile in replaceable blanket.

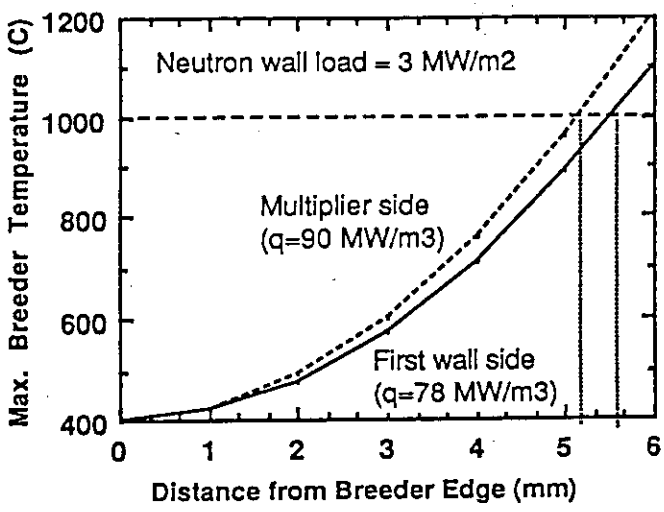

Fig. 7.3.14 Maximum breeder temperature of front breeding zone.

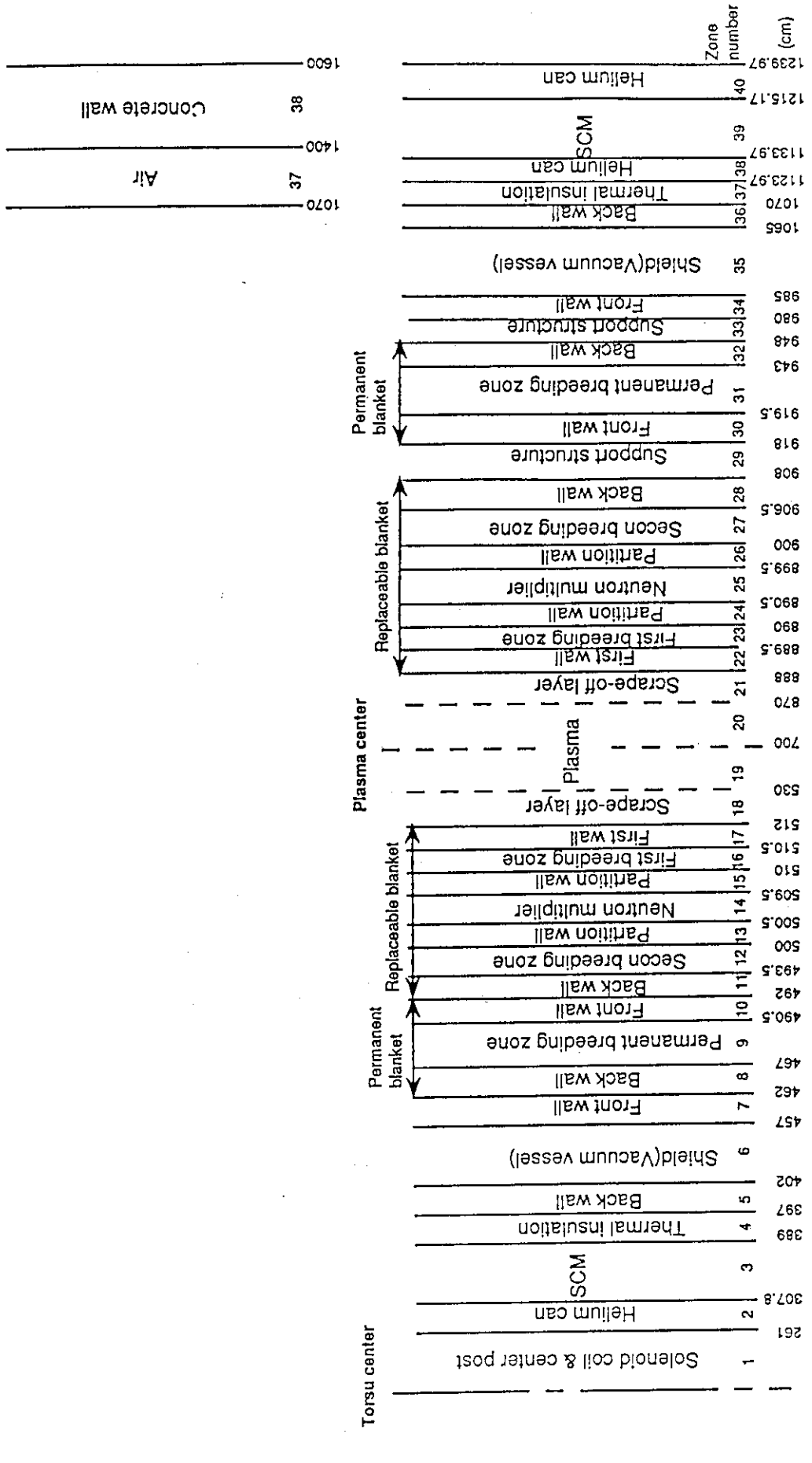

Fig. 7.3.15 1-D toroidal model for neutronics calculation of SSTR.

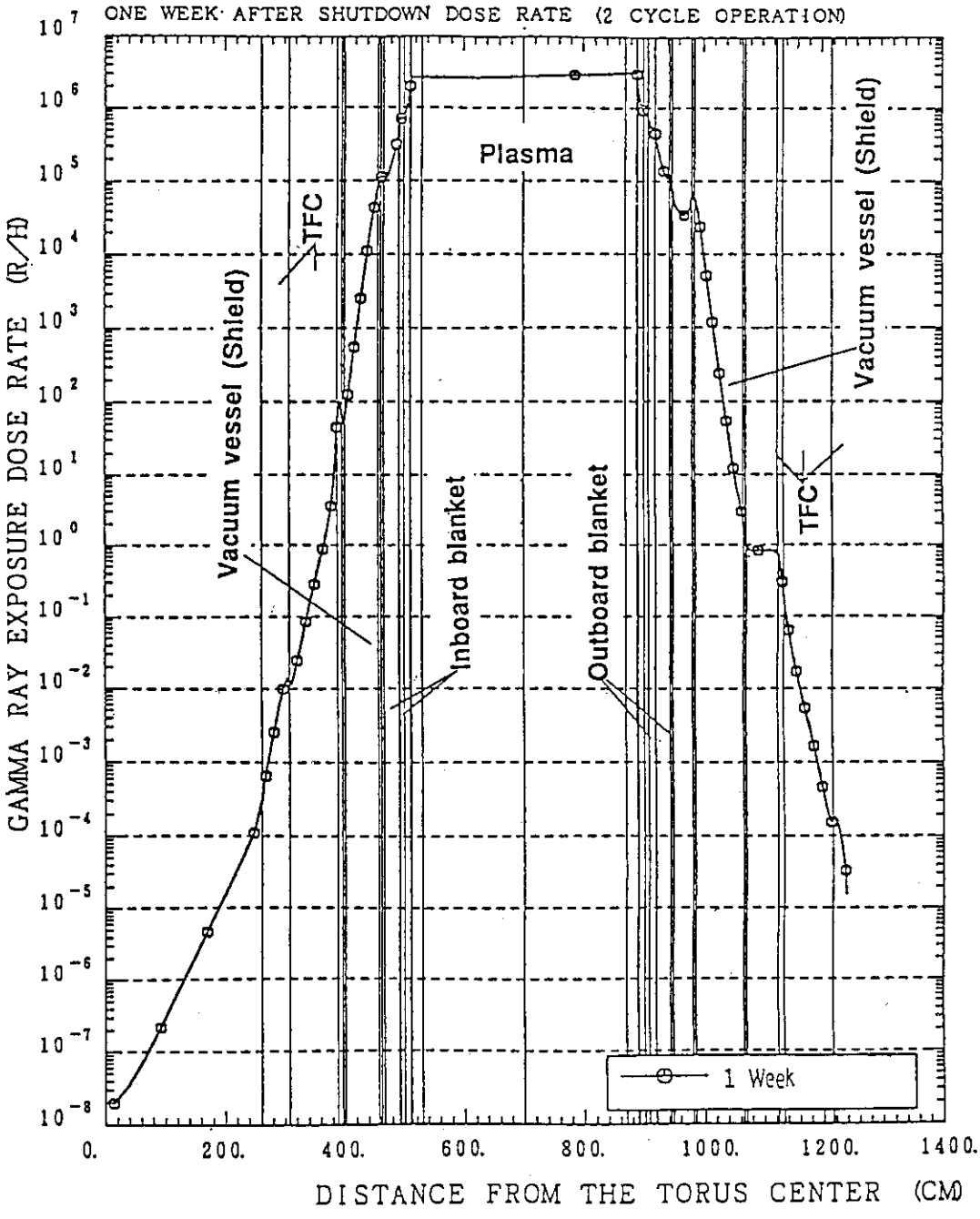

Fig. 7.3.16 Biological dose rate after shutdown (1.4FPY operation).

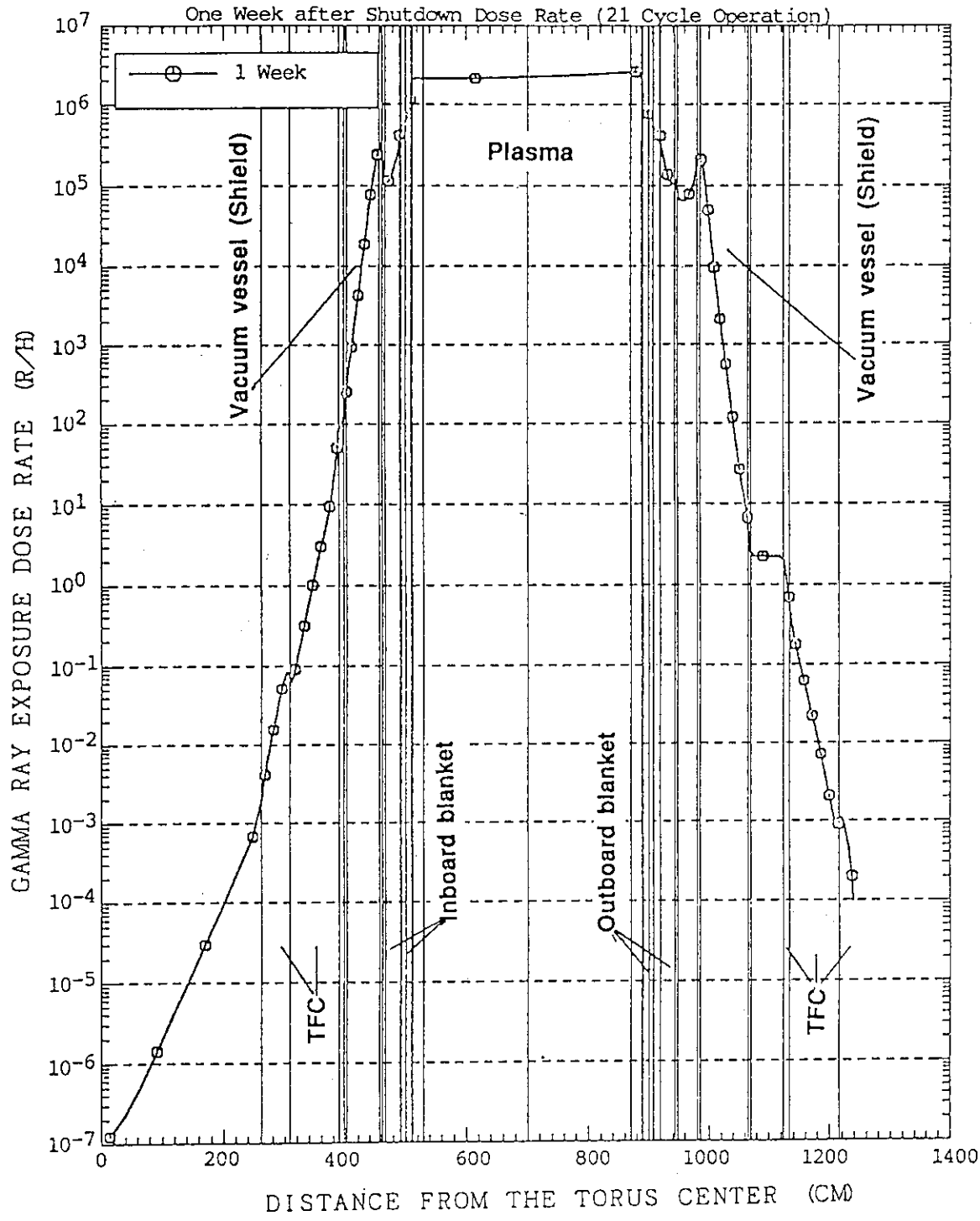

Fig. 7.3.17 Biological dose rate after shutdown (21FPY operation).

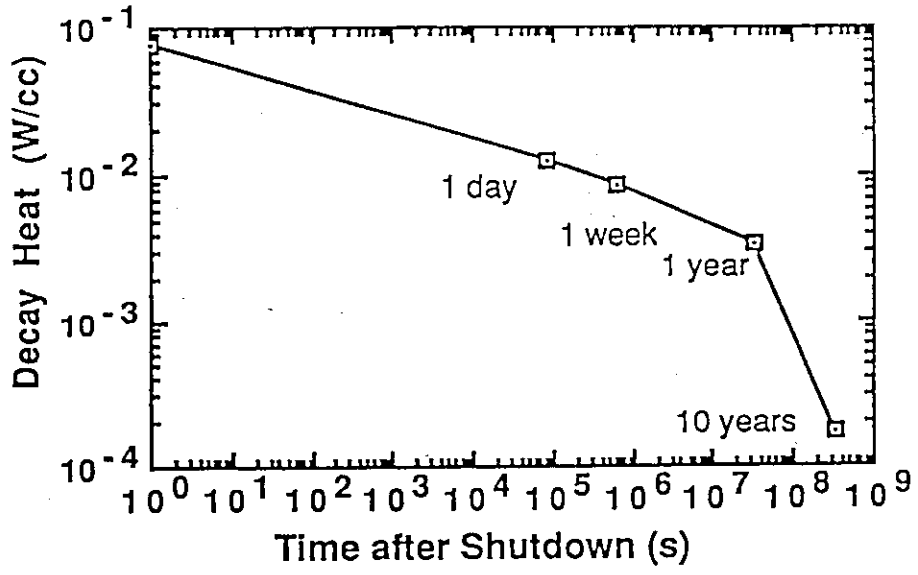

Fig. 7.3.18 Decay heat in first wall after 1.4 FPY.

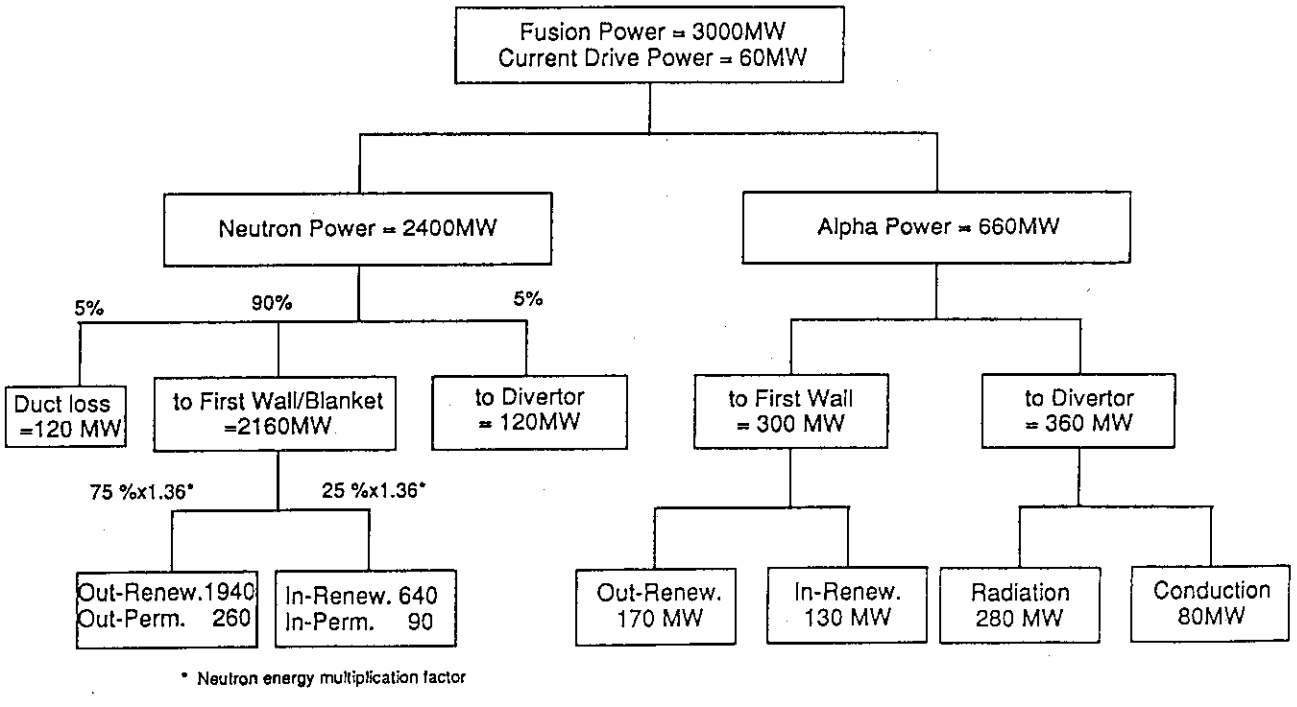

Fig. 7.3.19 Energy flow in SSTR. (Total thermal output for electricity generation=3710 MW)

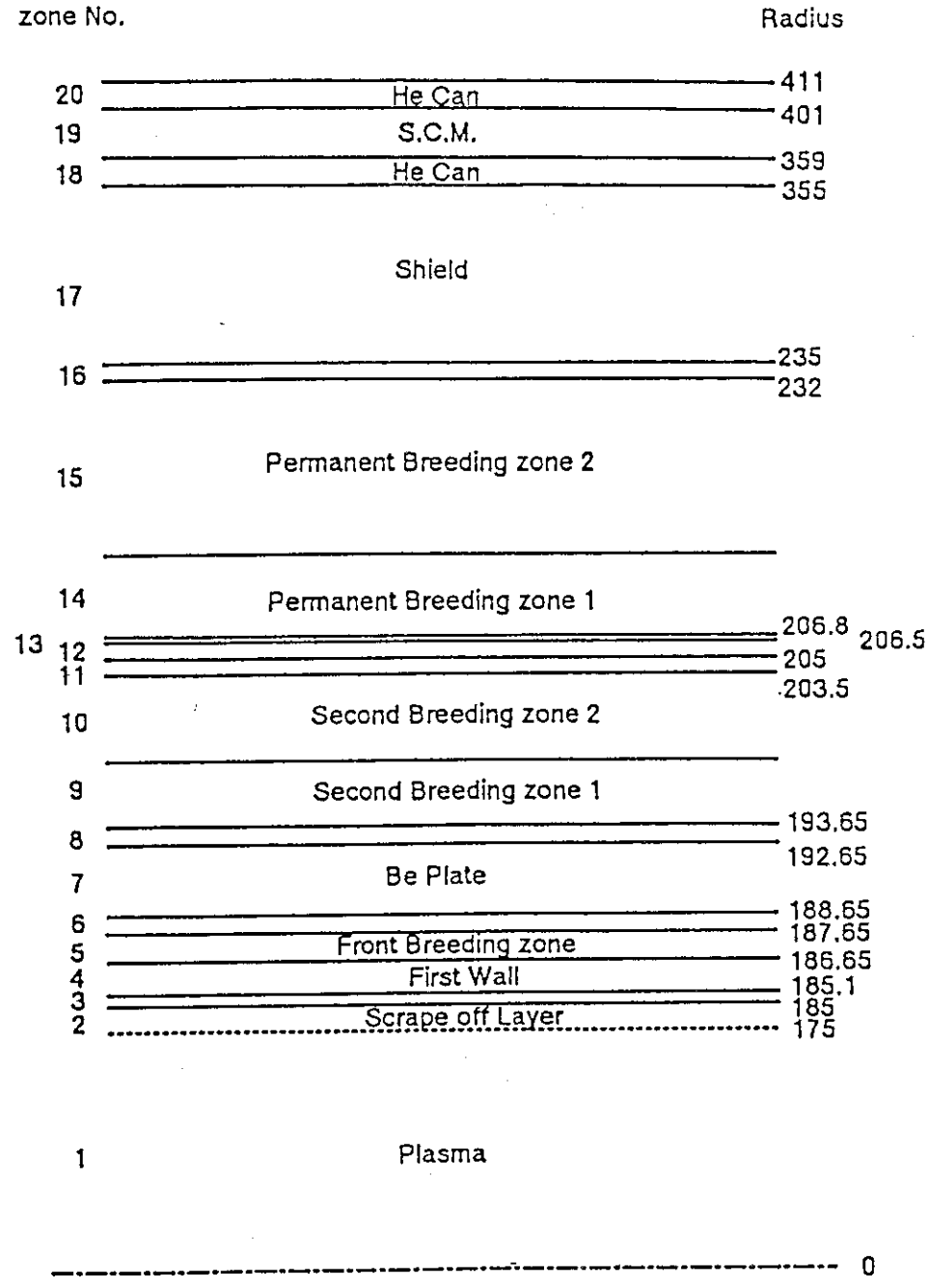

zone 3 Be Armor
zone 6&8 Partition Wall
zone 11 End Wall
zone 12 Second Wall
zone 13 Copper Shell Plate
zone 16 End Wall

Fig. 7.3.20 One-dimensional cylindrical model of SSTR blanket for ANISN. (Poloidal model)

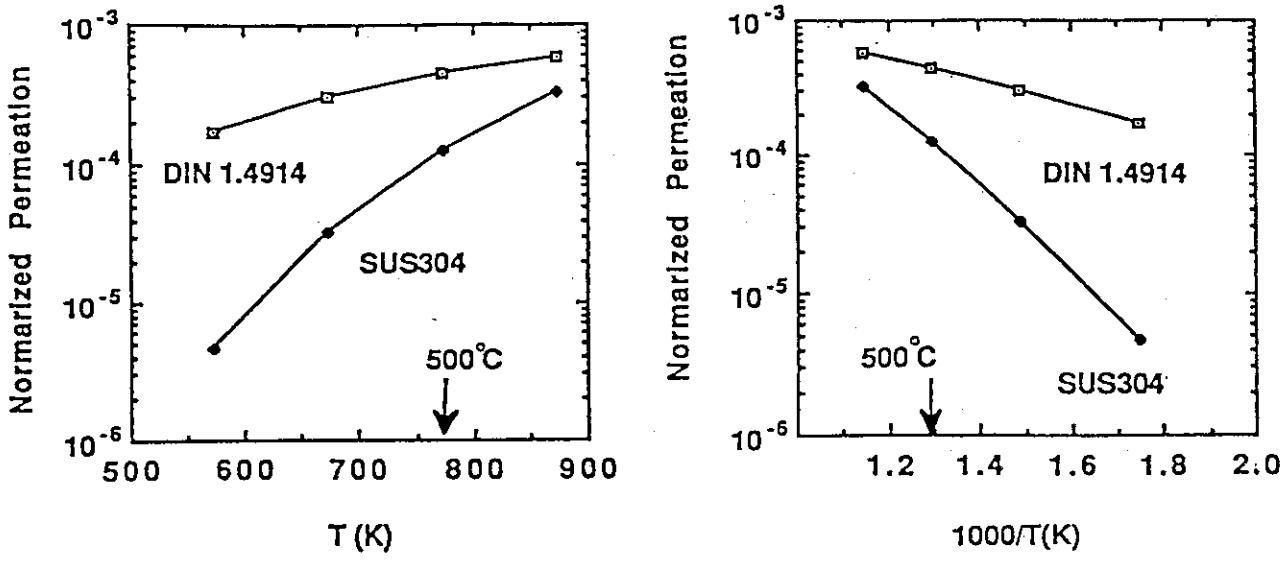

Fig. 7.3.21 Dependence of permeation on type of stainless steels and temperature.

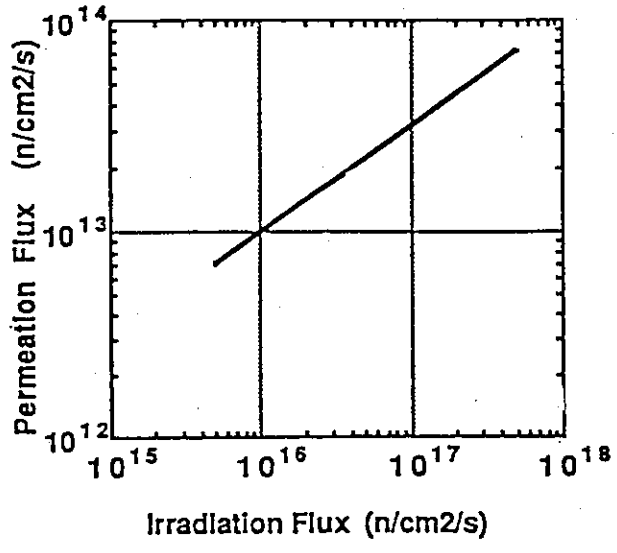

Fig. 7.3.22 Dependence of permeation flux on irradiation flux.

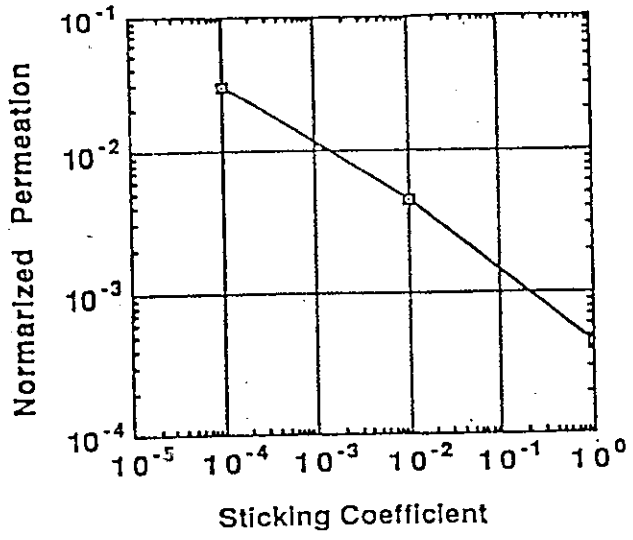

Fig. 7.3.23 Dependence of permeation rate on sticking coefficient.

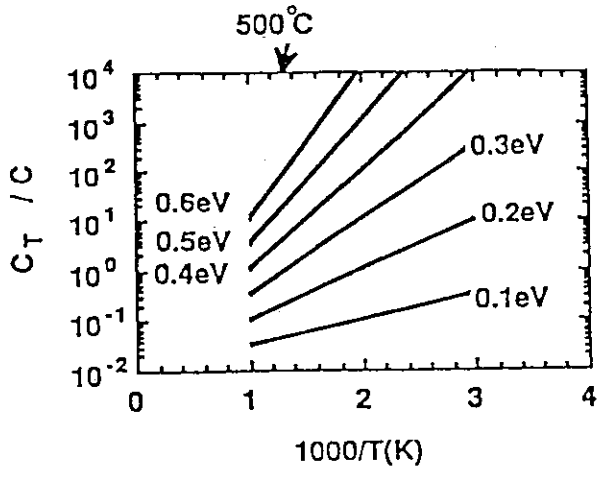

Fig. 7.3.24 Ratio of trapped and mobile concentration as a function of temperature and trap site binding energy.

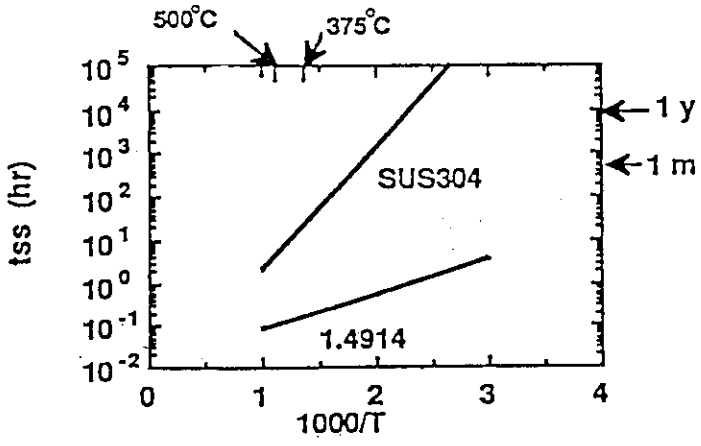

Fig. 7.3.25 Time required to reach steady state. (with neglecting trapping)

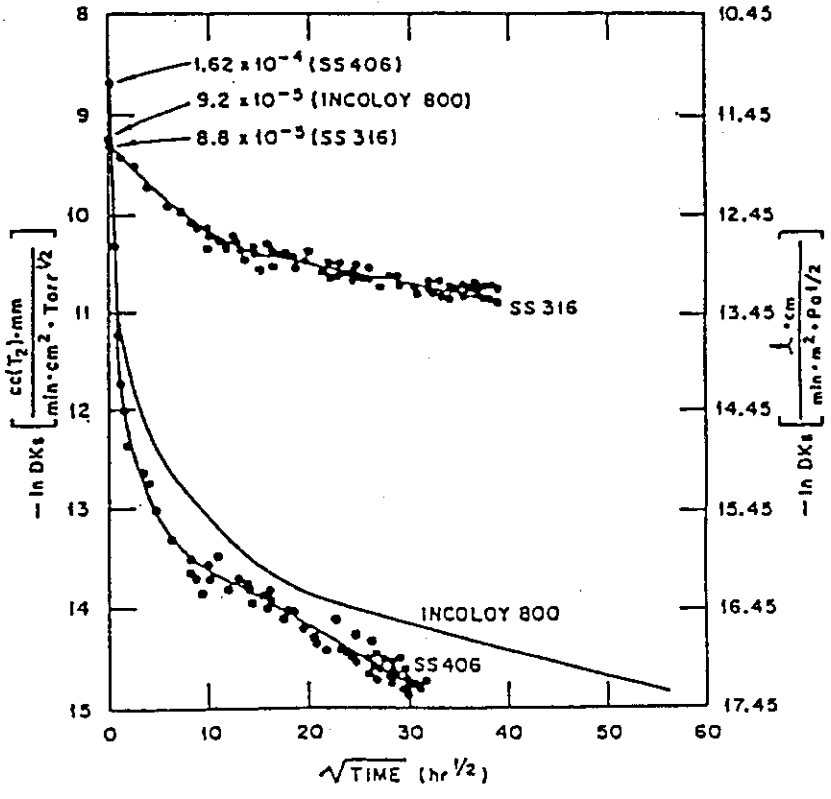

Fig. 7.3.26 Tritium permeabilities of three construction alloys at 660°C as the alloys are oxidized by water at 0.94 atm. (94 kPa)

7.4 Electromagnetic Analysis of the Blanket

To reduce the magnetic force generated on the blanket, a structural idea to install the FGM layers on each surface (except the first wall) of the box-type blanket module is being examined as described in the foregoing section.

In this case, the eddy current generated on the first wall will not be reduced, though there is possibility to reduce the eddy current which flows on the other surface of the blanket during a plasma disruption according to the method of FGM layer installation.

The electromagnetic analysis of the blanket under this condition was then performed to evaluate the eddy current and the magnetic force produced on the first wall. The analysis model is composed by the shell elements with an equivalent thickness of 15 mm accompanied by the vacuum vessel as shown in Fig.7.4.1. It has the electrically insulated boundaries to divide the blanket module into 3 parts per one sector for toroidal direction, and 2 parts for poloidal direction according to the actual separation of the blanket module.

The condition of a plasma disruption is same as that of electromagnetic analysis for the vacuum vessel, as follows:

plasma current : 12 MA
current quench time : 20 ms
plasma motion : downward motion
(the point at which the plasma current decreases to zero is assumed to be the middle point between the magnetic axis of the plasma and the null point.)
plasma motion time : 20 ms

The analysis results are shown in each of the following figures.
eddy current distribution : Fig.7.4.2 ~ Fig.7.4.3
magnetic force distribution : Fig.7.4.4 ~ Fig.7.4.5
And the maximum magnetic force on the blanket is summarized in Table 7.4.1.

From these results, the eddy current produced on the first wall is in a whirl at the 2 or 3 parts per each blanket module. Evaluating the magnetic force per unit length of the first wall, the force takes maximum value at the edge of the wall and the value is 300 ton/m and 400 ton/m for inboard side and outboard side respectively. The direction of the magnetic force is dominant for the mode to twist the first wall toward the minor radius

direction as shown in Fig.7.4.6 and Fig.7.4.7.

As these results are only based on first wall models, in which the electrically insulated layer by FGM cannot be installed, it can be said these forces are minimum values of the blanket. Moreover, as these values are the average on the elements of the model, it can be easily assumed that larger force is actually produced at the edge of the first wall. Thus, safety margins on the design study of the blanket and its support structure require careful consideration.

Table 7.4.1 Maximum magnetic force on blanket (kg/cm^2)

Coupling	Inboard side	Outboard side
Poloidal + self field	0.517	0.791
Toroidal field	17.54	15.27

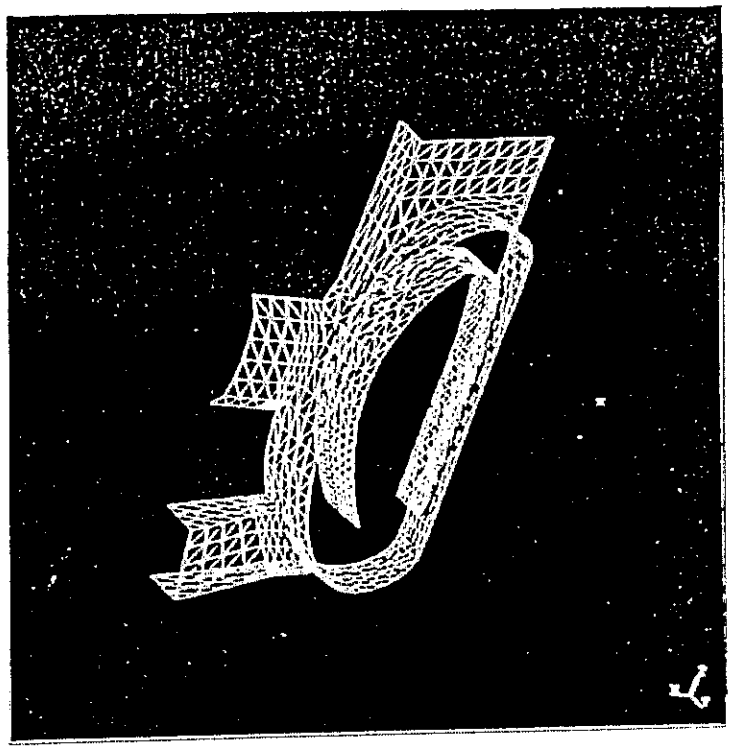

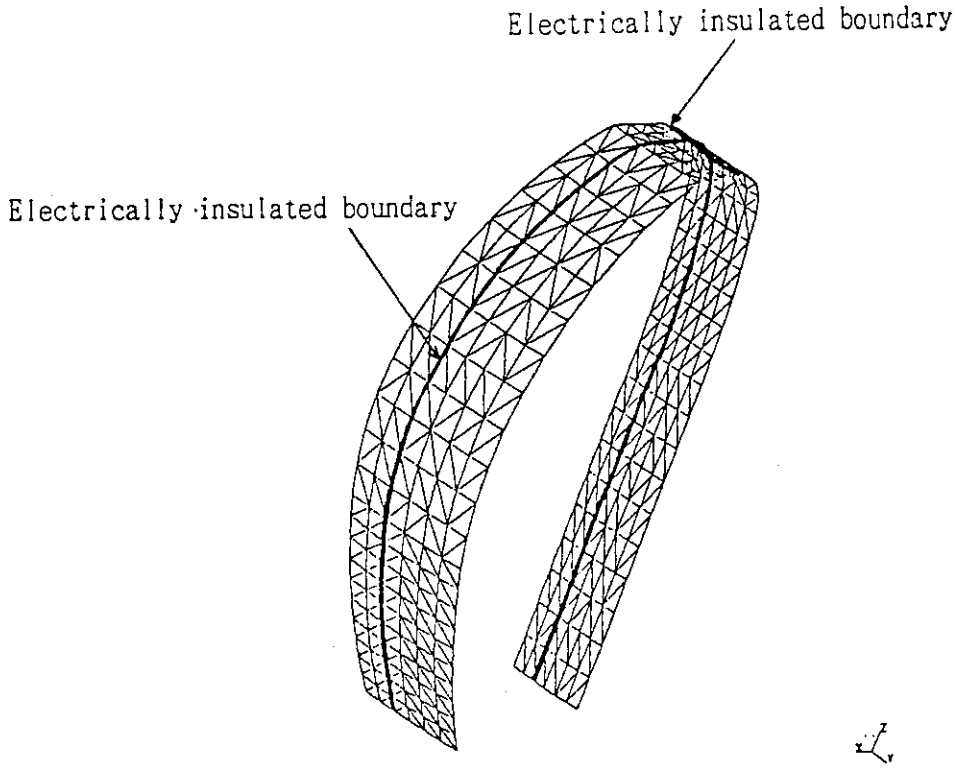

Fig. 7.4.1 Three-dimensional model for electromagnetic analysis of blanket.

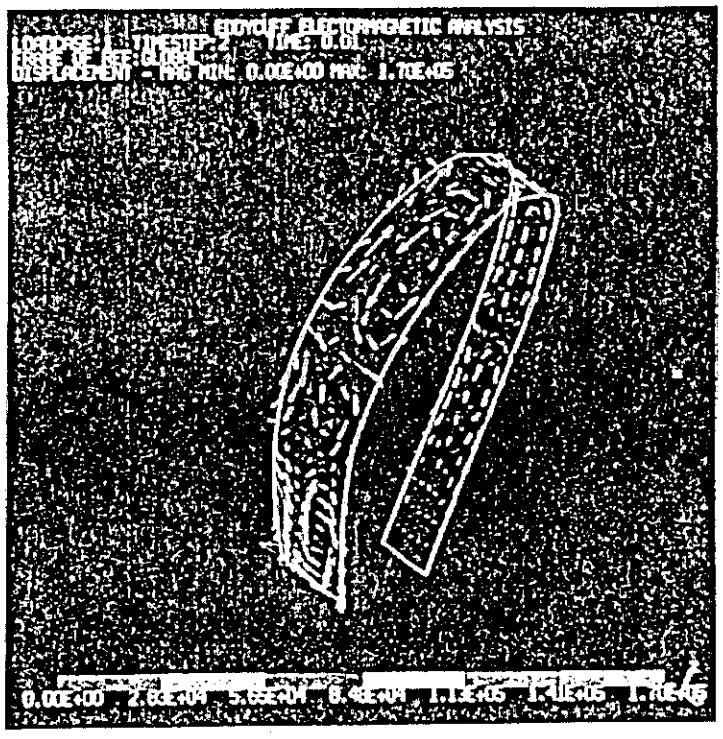

Fig. 7.4.2 Eddy current distribution on the blanket. (t=10ms)

Fig. 7.4.3 Eddy current distribution on the blanket. (t=20ms)

Fig. 7.4.4 Magnetic force distribution on the blanket for poloidal + self field coupling. (t=20ms)

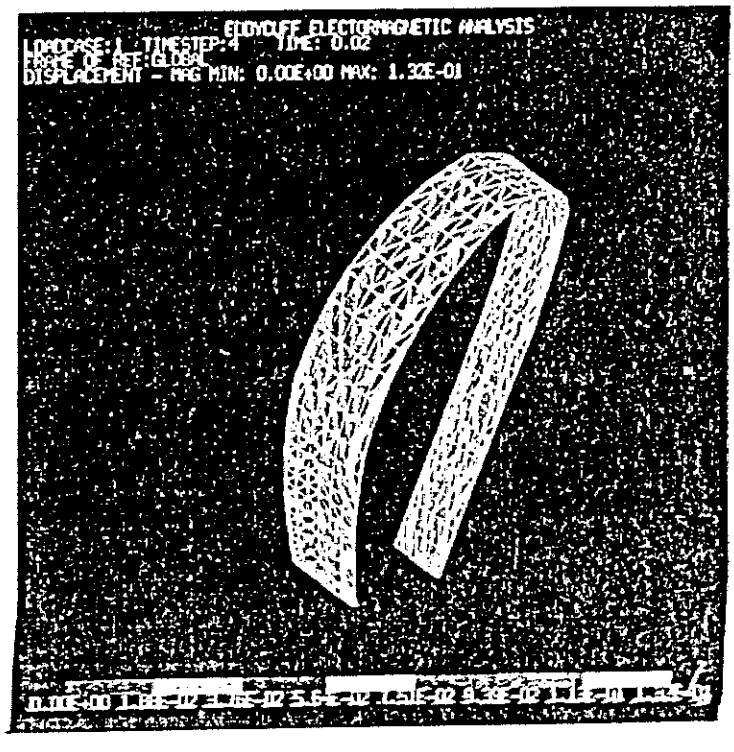

Fig. 7.4.5 Magnetic force distribution on the blanket for toroidal field coupling. (t=20ms)

Fig. 7.4.6 Magnetic force direction on the blanket for poloidal + self field coupling. (t=20ms)

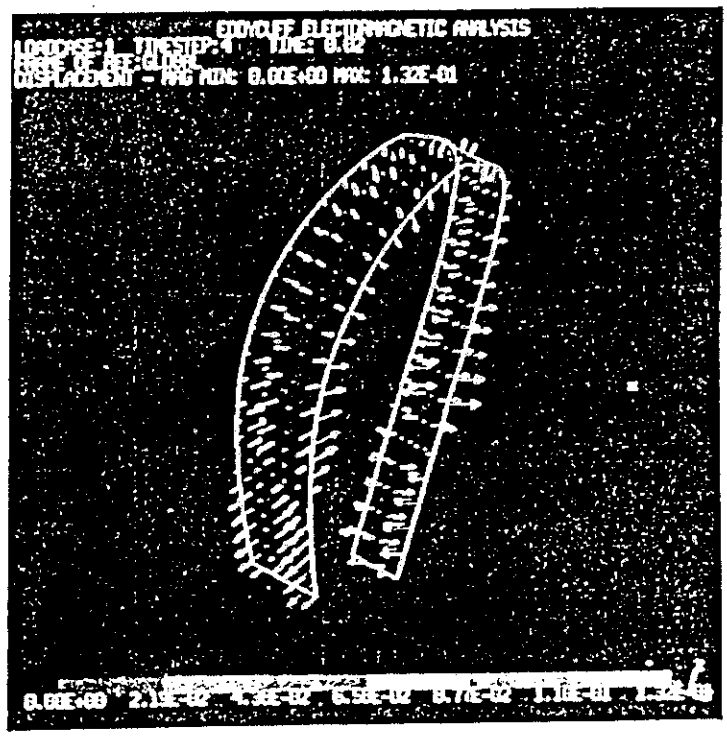

Fig. 7.4.7 Magnetic force direction on the blanket for toroidal field coupling. (t=20ms)

8. Divertor

8.1 Surface heat flux distribution on the divertor plate

In the SSTR, the radiation from the main plasma is 90MW, the radiation loss from the SOL plasma is 480MW, and the conductive heat to the divertor plate is 80MW, as described in the paragraph 3.3.11. The heat flux of the divertor chamber and the first wall, and the surface heat flux distribution on the divertor plate were calculated for this condition.(1) the heat flux distribution with radiation from plasma The calculational results of the heat flux distribution with the radiation from the main plasma and SOL plasma toward the divertor chamber and the first wall were summarized in the Fig. 8.1.1. As for the radiation from the main plasma, the distribution which is equal to that of the neutron wall load shown in the paragraph 7.3.1 was assumed. As for the radiation from the SOL plasma, the distribution shown in Fig. 3.3.13 was used. From the results, though the maximum heat flux due to the radiation from the plasma appeared at the striking points on the surface of the divertor plate, the value was less than 2 MW/m^2. The heat flux was less than 1 MW/m^2 in the divertor chamber and on the surface of the first wall except the divertor plate.(2) the heat flux distribution on the divertor plateThe heat flux distributions on the surface of the outer and inner divertor plates, due to the radiation from the plasma and the injective ions, are shown in Figs. 8.1.2 and Fig. 8.1.3. The followings were found from the results;1. The heat load distribution by conduction is predominant in the heat flux distribution on the divertor plate. The heat flux at the outer and inner striking points are about 7 MW/m^2 and about $5MW/m^2$, respectively. 2. As the surface heat flux exceeds $3MW/m^2$ in the high heat flux area(length of 0.2-0.3 m), There is possibility to cause burn-out near the striking points. It is necessary to use the swirl tube in the high heat flux area and to set coolant velocity highly, in order to avoid burn-out. It is assumed that the swirl tube length in both outer and inner divertor plate should be 0.5 meters in consideration of the safety factor.

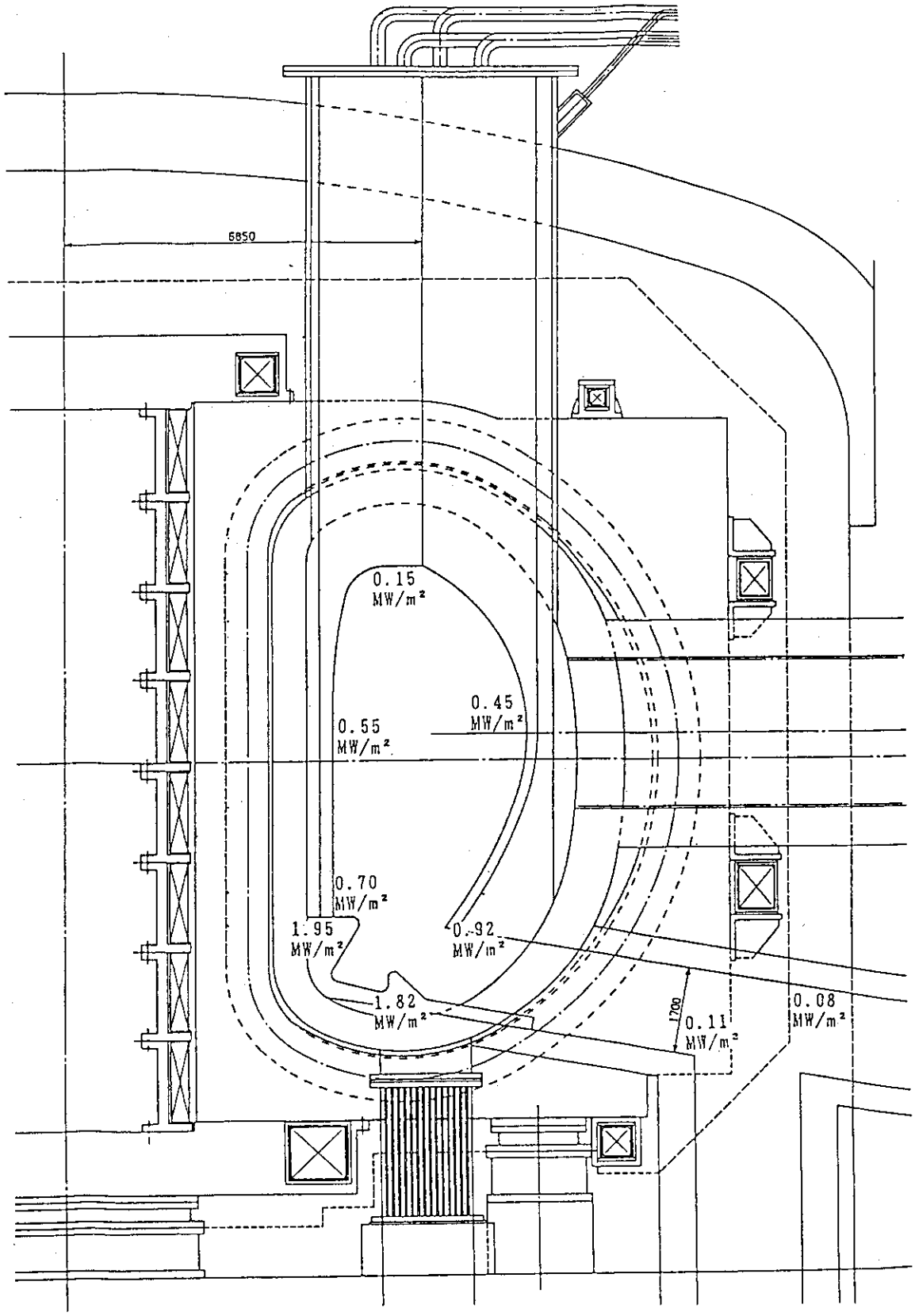

Fig. 8.1.1 Radiative heat flux distribution on divertor and first wall.

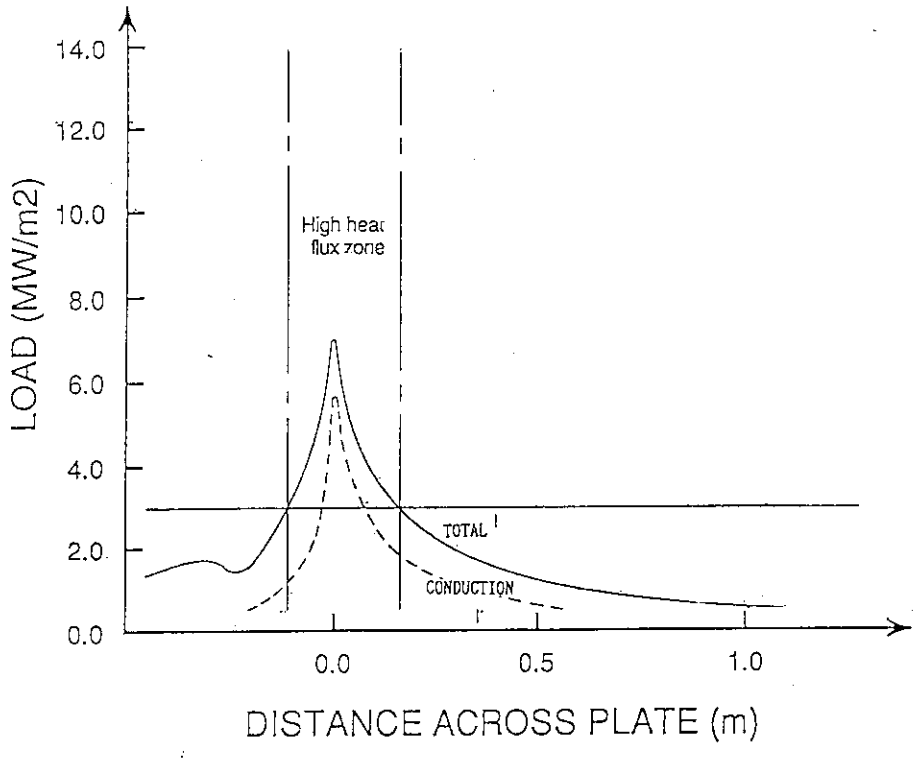

Fig. 8.1.2 Heat flux distribution on divertor plate near outer striking-point considering conduction and radiation from plasma.

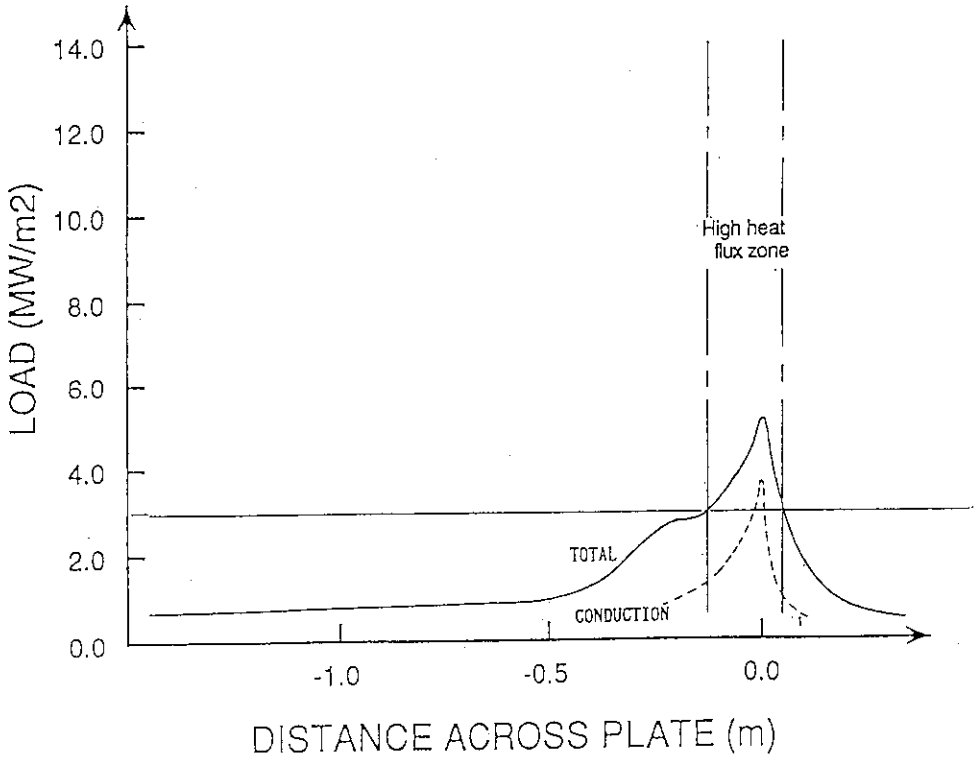

Fig. 8.1.3 Heat flux distribution on divertor plate near inner striking-point considering conduction and radiation from plasma.

8.2 Divertor structure

The following items are desirable to design the divertor plate.

1. To use the heat removed in the divertor plate and the divertor chamber for electricity generation as much as possible (to minimize the quantity of heat which cannot be used for electricity generation).
2. To obtain sufficient performances for heat removal. Especially, to avoid burn-out completely.
3. To reduce the pressure drop and prevent the pumping power from being excessive.
4. Lighten and compact the high frequency exchange part as much as possible.
5. To simplify the structures as much as possible and to enhance reliability by improving manufacturing accuracy etc.
6. To keep the integrity against the thermal stress etc. during operation.
7. To possess sufficient life for sputtering erosion etc.

The divertor was designed from the above-mentioned viewpoints. Especially, it is the most important problem to use a lot of heat for electricity generation as much as possible as avoiding burn-out. In this design, the following two cases were assumed as the divertor plate structure.

CASE1 : All power generation divertor plate

In the case that the surface heat flux of the divertor plate is suppressed at less than about 3MW/m2, to keep the coolant outlet temperature and the coolant temperature rise of the divertor plate at the values for power generation. Simultaneously, burn-out can be avoided, as shown in the paragraph 8.3. When the burn-out heat flux can be improved by the adoption of the swirl tube etc. , the heat removed in the divertor plate can be entirely used for the electricity generation for higher heat flux.

CASE2 : Low temperature (separated) divertor plate

When the peak heat flux near the separatrix is more than 3MW/m2 and the burn-out heat flux cannot be improved sufficiently even if the swirl tubes are applied, the design of the divertor plate which aims to avoid burn-out is required. Therefore, the divertor plate is divided into the low temperature divertor plate (for high heat flux zone) to cool by the water with comparatively high velocity and low temperature and the high temperature divertor plate for power generation. At this time, the heat removed in the low temperature divertor plate is used for the feed water heating system.

8.2.1 All power generation divertor plate

The structure of the all power generation divertor is shown in Fig. 8.2.1 and the main design parameters are shown in Table 8.2.1. In SSTR, the peak surface heat flux toward the divertor plate was reduced by using gas-puffing with Fe addition, as shown in the paragraph 4.5. However, the peak heat flux near the striking point was about 7MW/m^2 in the outboard and about 5MW/m^2 in the inboard, as described in 8.1. In each area of about 200 mm, the heat flux exceeded 3MW/m^2 and there was possibility to cause burn-out. Therefore, we decided to apply the swirl tubes with twist ratio of about 3 in this area, to improve the burn-out heat flux. It is necessary to confirm the results by R&D in the future, because few researches about burn-out heat flux with the swirl tube for the low subcooled(high temperature) cooling water have been performed at present. Here, it was assumed that the burn-out heat flux was able to be improved to be doubled according to the results of the experiment results for the high subcooled(low temperature) cooling water shown in the paragraph 8.3.

In order to keep necessary temperature rise of the coolant as preventing pressure drop in all divertor plate systems from being excessive, we designed the structure to flow the coolants at first into the modules(No.1&No.3) in the area where the heat flux is comparatively high and then to flow the coolants again into the modules(No.2&No.4) in the area where the heat flux is comparatively low. That is, the pressure drop per unit length in the swirl tube increases by about one order, but the pressure drop in all systems is suppressed at about 300 kPa because the length with swirl tube is short.

In the design of this divertor plate, the divertor plate was divided into four modules in the poloidal direction, in consideration of manufacturing of the curved part, difference of the structural materials, partial application of the swirl tubes, thermal expansion difference, and reduction of radioactive waste. It was divided equally into three parts in the toroidal direction in each sector. As for the material of the coolant tube, the molybdenum alloy is used in the high temperature load area in consideration of the high temperature strength, and the ferritic steel is used in the low heat load area. The divertor plate are installed with some angle by the unit, in order to prevent increase of the heat flux because of the offset.

In this design, the burn-out is avoided by using the swirl tube near the striking point. However, it is necessary to confirm the data of the burn-out with the swirl tube for the high temperature cooling water by R&D in the future, because very few data exist at present. When the sufficient effect of the swirl tube cannot be expected for the high temperature cooling water, it is necessary to adopt the low temperature divertor or make an

effort in the plasma side to decrease the peak heat flux further(3MW/m^2 or less).

8.2.2 Low temperature divertor plate

When the burn-out heat flux is not improved sufficiently even if the swirl tube is used, or when the heat flux reduction for the divertor plate described in the paragraph 4.5 is not sufficient, it is necessary to avoid the burn-out by reducing the coolant temperature as shown in 8.3. However, in this design, in the area of comparatively low heat flux, the heat was also used for the power generation in this case. The heat in the low temperature divertor is used for the feed water heating system, in order to improve the plant efficiency. The structure of the divertor in this case is shown in Fig. 8.2.2 and the main design parameters are shown in Table 8.2.2.

In this design, the low temperature divertor with the coolant in the condition of high subcool and high velocity in the high heat flux area(about higher than 3MW/m^2) near the striking point to avoid the burn-out . At this time, the coolant inlet temperature was set at 185C, the outlet temperature was set at 200C, and the coolant velocity in the plasma side was set at about 10 m/s. In this condition, the burn-out heat flux can be improved at about 20MW/m^2 as shown in the paragraph 8.3.

The coolant velocity has been decreased by enlarging the coolant channel area in the rear side to prevent pressure drop from being excessive . Therefore, the pressure drop in the low temperature divertor plate can be suppressed at about 200 kPa. The heat removed in the low temperature divertor was used for the feed water heating system. To maintain the integrity of the coolant in the high temperature, molybdenum alloy(Mo-Re), which has high temperature strength and comparatively high thermal conductivity, was used in the low temperature divertor plate.

On the other hand, in the low heat flux area(about 3MW/m^2 or less), the inlet temperature was set at 285C and the outlet temperature was set at 325C in consideration of using heat for the power generation. As for the structural materials of the divertor for the power generation, the ferritic steel was used as well as in case of the first wall. Maximum coolant velocity in the plasma side of the coolant is about 2 m/s. The coolant channel area in the rear side was set larger than the plasma sides as well as the low temperature divertor, in order to reduce pressure drop as much as possible. The low and high temperature divertors were divided into the poloidal direction, in consideration of the difference of materials and temperature condition, the thermal expansion, the manufacturing accuracy, and the reduction of radioactive waste. Each divertor was divided into two modules in the

inside and the outside. It is divided equally into three parts in the toroidal direction in each sector.

Table 8.2.1 Design parameters of power generation divertor plate

	modules No.1 & No.3	modules No.2 & No.4
Configuration	Plate with swirl tubes (twist ratio : 3)	Plate with rectangular coolant tubes
Maximum heat flux	7 MW/m²	3 MW/m²
Total heat load	490 MW	
Coolant tube		
material	molybdenum alloy	ferritic steel
plasma side wall thickness	2.5 mm	1.5 mm
channel size(plasma-side)	ϕ 10 mm	^{w} 15 mm x ^{d} 15 mm
channel size(rear-side)	^{w} 15 mm x ^{d} 15 mm	^{w} 15 mm x ^{d} 15 mm
pitch	18 mm	
maximum temperature	600 ℃	550 ℃
Swirl tape	Inconel	−
Coolant	pressurized water	
inlet pressure	15 MPa	
total pressure loss	ab. 300 kPa	
inlet temperature	285 ℃	300 ℃
outlet temperature	300 ℃	325 ℃
maximum velocity	10 m/s	3 m/s
Electric insulator	ceramics	
Support plate	ferritic steel	

Table 8.2.2 Design parameters of low temperature divertor plate

	low temperaure modules	power generation modules
Configuration	Plate with rectangular coolant tubes	Plate with rectangular coolant tubes
Maximum heat flux	20 MW/m²	3 MW/m²
Total heat load	163 MW	327 MW
Coolant tube		
material	molybdenum alloy	ferritic steel
plasma-side wall thickness	1.5 mm	
channel size (plasma-side)	^{w} 15 mm x ^{d} 8 mm	^{w} 15 mm x ^{d} 8 mm
channel size (rear-side)	^{w} 15 mm x ^{d} 15 mm	^{w} 15 mm x ^{d} 15 mm
pitch	18 mm	
maximum temperature	750 ℃	550 ℃
Coolant	pressurized water	
inlet pressure	15 MPa	
total pressure loss	ab. 200 kPa	
inlet temperature	185 ℃	285 ℃
outlet temperature	200 ℃	325 ℃
maximum velocity	10 m/s	2 m/s
Electric insulator	ceramics	
Support plate	ferritic steel	

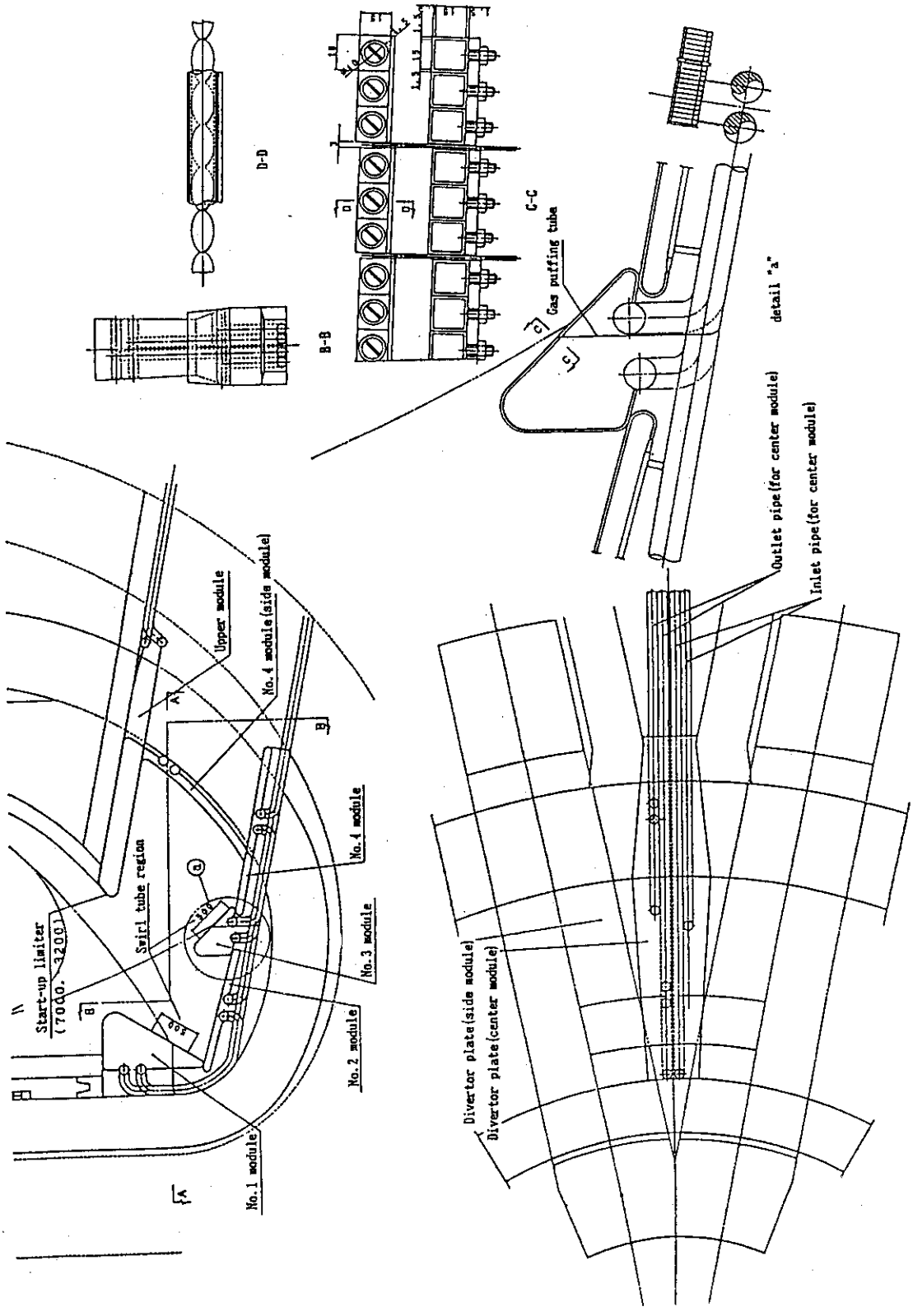

Fig. 8.2.1 Configuration of power generation divertor plate system.

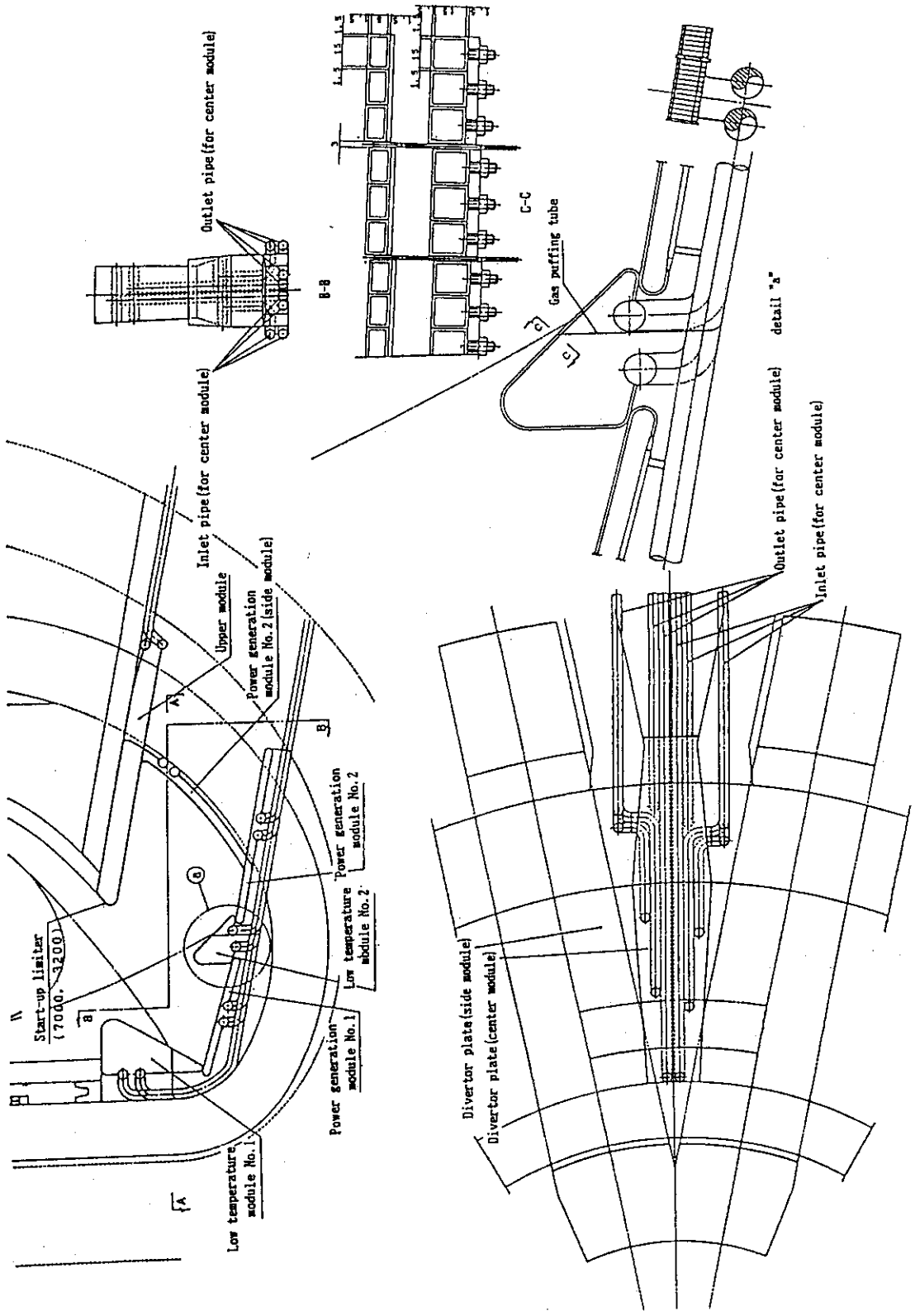

Fig. 8.2.2 Configuration of low temperature divertor plate system.

8.3 Cooling water condition and allowable heat flux

In the divertor plate, it is desirable to remove the high heat flux and to obtain the coolant outlet temperature for the power generation. A preliminary examination has been performed to evaluate the thermal-hydraulic characteristics which might be the problem to design the divertor plate. The allowable design window of heat flux and coolant condition was also investigated.

(1) Important thermal-hydraulic characteristics for the design

The important thermal-hydraulic characteristics for the design are as follows.

1. Burn-out heat flux

As the divertor plate can be suffered to a high heat flux (about higher than 10 MW/m^2), the coolant channel may be damaged by the burn-out. It is necessary to set the design condition that can certainly avoid the burn-out.

2. Heat transfer coefficient and the temperature at the coolant channel surface (the structural materials)

It is necessary to keep the temperature at the coolant channel surface (structural material) within the permissible range, by securing sufficiently large heat transfer coefficient so as to correspond to the high surface heat flux (about 10MW/m2). In the divertor plate, especially it is necessary to evaluate the heat transfer by forced convection with subcool boiling.

3. Pressure drop and pumping power

It is necessary to enlarge the coolant velocity and to prevent the pumping power from being excessive, to obtain the high burn-out heat flux and heat transfer coefficient .

4. Coolant temperature rise between inlet and outlet

It is necessary to obtain the appropriate temperature rise between inlet and outlet, for the realistic design of the power generation system. Therefore, it is necessary to reduce the coolant velocity or to increase the coolant channel length. It will bring the problem the low allowable heat flux and high pressure drop. Because the heat load to the divertor plate has large spatial distribution, it is necessary to devise such as putting the coolants(the inlet temperature 285C) into the high heat flux zone with high velocity at first, and then raising the temperature to the outlet temperature (325C) necessary for the power generation by cooling the low heat flux zone with low velocity.

5. Corrosion/erosion etc.

Additionally, the coolant velocity and the temperature are limited by the limit of the corrosion and the erosion etc. of the coolant tubes. It is not considered in this examination because that depends largely on the structural materials or surface treatment. The problems such as vibrations of the coolant tubes must be considered when coolant velocity is high enough.

(2) Thermal-hydraulic characteristics

(a) Conditions

The investigation of thermal-hydraulic characteristics was performed in the following condition. The investigation was mainly carried out for the divertor plate with the smooth tubes, however, the divertor with the swirl tubes was also investigated.

Coolant	light water
Coolant pressure	15 MPa
Coolant temperature	100C, 200C, 100C
Coolant tube inside diameter (equivalent diameter)	5 mm, 10 mm, 15 mm
Coolant velocity	< 20 m/S

(b) Burn-out heat flux

The burn-out heat flux q was evaluated for the smooth tube with the expression of modifyed Tong [1]. The results are shown in Fig. 8.3.1. Experimental data concerning effect of the burn-out heat flux improvement using the swirl tube, is shown in Fig. 8.3.2 [2]. Figure 8.3.2 shows the results at the coolant temperature of 50C and the coolant pressure of 3.5 MPa. The following items were found from these results.

1. Burn-out heat flux strongly depends on the coolant temperature (subcooling). In the condition that the coolant velocity is about 10 m/s, each burn-out heat flux at Tb=100C, 200C, and 300C is about 40MW/m^2, 20MW/m^2, and 10MW/m^2, respectively. It is hardly affected by the coolant tube diameter. The burn-out heat flux increases with the coolant velocity, but its dependency becomes smaller as the coolant temperature is higher.

2. It was considered that the safety factor must be more than 2 for design, because the burn-out heat flux expression has large uncertainty. From this viewpoint, we must set the heat flux at less than about 3MW/m2, so that the coolant temperature should correspond to the power generation condition (the inlet temperature 285C

and the outlet temperature 325C) with avoiding burn-out in the smooth tube.

3. The burn-out heat flux in the swirl tube is expected to be improved at about two times better than in the smooth tube. That is, if the burn-out heat flux in the inlet temperature condition(285C) can be improved at about 15-20MW/m2 by using the swirl tube, it is considered that the quantity of heat of the divertor can be used to generate electricity by regarding the high temperature load area as the inlet side. However, because the data of the swirl tube for the high temperature cooling water does not exist, we must execute R&D to confirm the approval.

4. When the sufficient improvement of the burn-out heat flux is not obtained even if the swirl tube is used, we must set the coolant temperature of the high heat flux zone at about 200C(the low temperature divertor).

(c) Heat transfer coefficient and temperature at coolant channel surface(structural material)

The heat transfer coefficient of non-boiling forced convection was evaluated by expression of Dittus-Boelter[3]. The results are shown in Fig. 8.3.3. The coolant channel wall temperature according to the heat flux of the subcool boiling forced convection was evaluated by the expression of Thom et al[4]. The results are shown in Fig. 8.3.4 with the wall temperature evaluated by non-boiling forced convection (50000 $W/m^2/K$ and 100000 $W/m^2/K$). The followings were found from these figures.

1. The heat transfer coefficient of non-boiling forced convection increases as coolant velocity is increased. At the coolant velocity about 10 m/s, it is about 50000W/m2/K, and at the coolant velocity about 20 m/s, it is about 100000 W/m2/K. The effect of the coolant temperature and the coolant tube diameter on the heat transfer coefficient of non-boiling forced convection is small. There is possibility that the heat transfer coefficient is improved at twice by using the swirl tube, but the sufficient data does not exist for the high temperature cooling water.

2. The coolant channel wall temperature with subcool boiling is about 350-360C. It is considered that the use of the copper/copper alloy is difficult from the viewpoint of corrosion etc. It is necessary to examine the usableness of the metal such as Mo-Re alloy, which has high thermal conductivity and can be expected to have the high temperature strength.

3. Boiling must be considered, when the heat flux is about higher than 3-5MW/m^2 at the coolant temperature 300C, and when the heat flux is higher than about

10MW/m^2 at the coolant temperature 200C.

(d) Pressure drop and pumping power

Pressure drop in the divertor coolant channel (unit length) was calculated by changing the coolant velocity, temperature, and channel diameter. The results were summarized in Fig. 8.3.5. The friction coefficient was evaluated by expression of Colebrook [5]. It is necessary to design to keep the total pressure loss about 500 kPa in the system, to achieve the realistic pumping power. In the divertor plate, the pressure drop will increase in about one order by the application of the swirl tube near the striking point and the local boiling. However, the design is possible if the swirl tubes are installed because this area is short such as 500 mm shown in paragraph 8.1.

In this design, the burn-out are avoided and the heat transfer are improved by combining the divertor module in the high and low heat flux zones. In the inlet side , which is high heat flux zone, the coolant channel area is set small to obtain high coolant velocity(about 10 m/s). On the other hand, in the outlet side, that is low heat flux zone, the coolant channel area must be larger to reduce the pressure drop in the entire system, with lower coolant velocity (about 3 m/s).

(e) Coolant temperature rise

The coolant temperature rise in unit channel was calculated changing the coolant tube diameter and the coolant velocity. The results are shown in Fig. 8.3.6. In the figure the heat removal per divertor unit is also indicated. It was assumed that the divertor is divided into two modules(outer and inner), the heat load into 1 module x torus are 180 MW, and the number of coolant channel(1 module x torus) is 1600 to evaluate the heat removal.

The followings are found from the figure.

1. When the coolant tube inside diameter is set at 5 mm, sufficient coolant temperature rise can be obtained but the pressure drop might be excessive.

2. When the coolant tube inside diameter is 10 mm and the coolant velocity is more than 10 m/s, it is necessary to decrease the number of the channel so that the coolant outlet/inlet temperature difference should be 40C.

3. Because it is estimated that the coolant temperature rises only about 10C, when the coolant tube inside diameter is 15 mm, the measure such as coolant re-entrant is required from the viewpoint of the use of the heat.

4. In this design, necessary outlet temperature can be obtained by suppressing the pressure drop in the whole system at appropriate value by re-entrant the water which cools the module in the high heat flux zone into the module in the low heat flux zone again.

(3) Allowable design window

The allowable design window of the coolant velocity and the coolant temperature of the divertor plate, which was calculated from the viewpoint of the burn-out heat flux and the pressure drop is summarized in Fig. 8.3.7. From the results, the followings were found about the design window of the divertor plate of SSTR.

(a) In the case of all power generation divertor(inlet temperature 285C and outlet temperature 325C)

1. The maximum heat flux is suppressed in the divertor area at lower than 3MW/m^2, to keep the coolant outlet temperature 325C and to secure two times of safety factor of the burn-out heat flux.
2. Because the peak heat flux is about 7MW/m^2 in the SSTR design as shown in the paragraph 8.1, it is necessary to improve the burn-out heat flux at about two times by adoption of the swirl tubes. In this case, it is necessary to shorten installation length of the swirl tube as much as possible so that the pressure drop should not be excessive.

3.It is necessary to make the coolant cooled in the high heat flux zone re-enter to the low heat flux zone, to obtain sufficient coolant temperature rise without excessive pressure loss. In the high heat flux zone at inlet side, the coolant channel area is small for taking the coolant velocity high (about 10 m/s), to avoid burn-out and take high heat transfer coefficient. The coolant temperature rise up in the low heat flux zone at the outlet side, in which the coolant channel area is larger and the coolant velocity is lower(about 3 m/s), to obtain realistic pressure loss in divertor system.

4. Because few burn-out data for the swirl tube with high temperature water exist, R&D efforts in the future is very important. When the sufficient improvement of the burn-out heat flux is not obtained even if the swirl tube is used, we must set the coolant temperature of the high heat flux zone at about 200C(the low temperature divertor), or make further efforts to reduce the peak heat flux with a improved plasma design.

(b) In the case of the low temperature divertor (inlet temperature:185C and outlet temperature:200C)

1. The method to apply the low temperature divertor near the striking point is promising, when the effect of the swirl tube of the high temperature cooling water is not sufficient or the surface heat flux is higher than the prediction in the plasma side. That is, the burn-out heat flux can be more than 20MW/m^2 and the pressure drop can be suppressed at the appropriate value, if the coolant velocity is set in the smooth tube at about 10 m/s, the inlet temperature is set at 185C, and the outlet temperature at 200C.

2. In the low temperature divertor method, the power generation divertor is applied in the area where the heat flux is about less than 3 MW/m2 for the plant efficiency improvement. The heat removed in the low temperature divertor is used for the feed water heating system.

References

[1] Tong L.S., A phenomenological study of critical heat flux, ASME paper No.75-HT-68, ASME (1968).
[2] Kuroda T. and Vieider G. et al., ITER PLASMA FACING COMPONENTS, IAEA/ITER/DS/No.30 (1991), to be published.
[3] JSME Data Book: Heat Transfer (4th ed.), JSME (1986), 56 (in Japanese).
[4] Thom J.R.S. et al., Proc. Inst. Mech. Engr., Part C 180 (1966), 226.
[5] Flow resistance in pipes and ducts, JSME (1979), 26 (in Japanese).

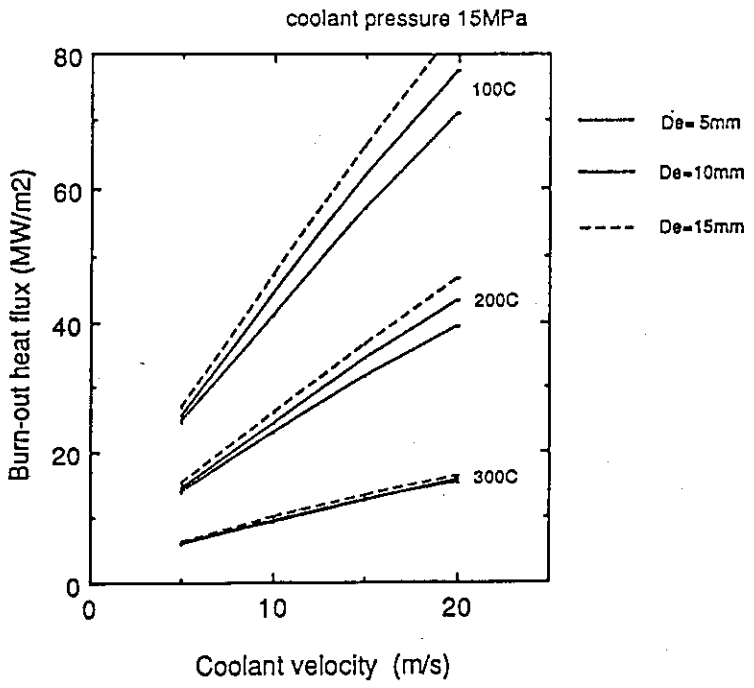

Fig. 8.3.1 Burn-out heat flux of water coolant as functions of coolant velocity, temperature and channel diameter.

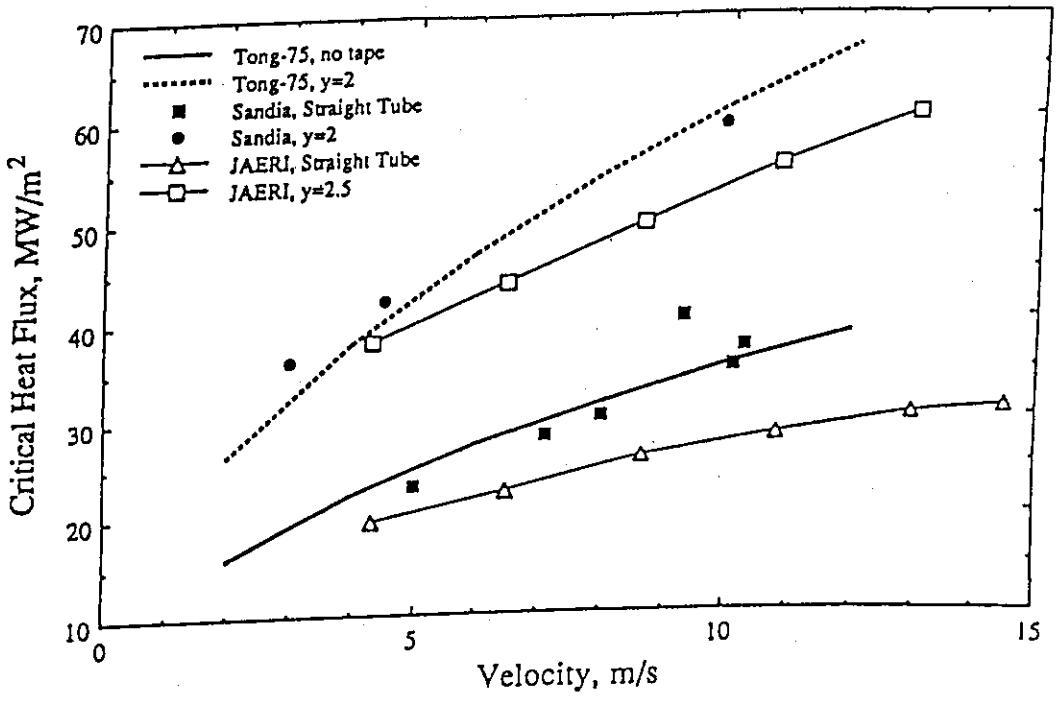

Fig. 8.3.2 Critical heat flux data comparison. (based on peak flux at water interface)

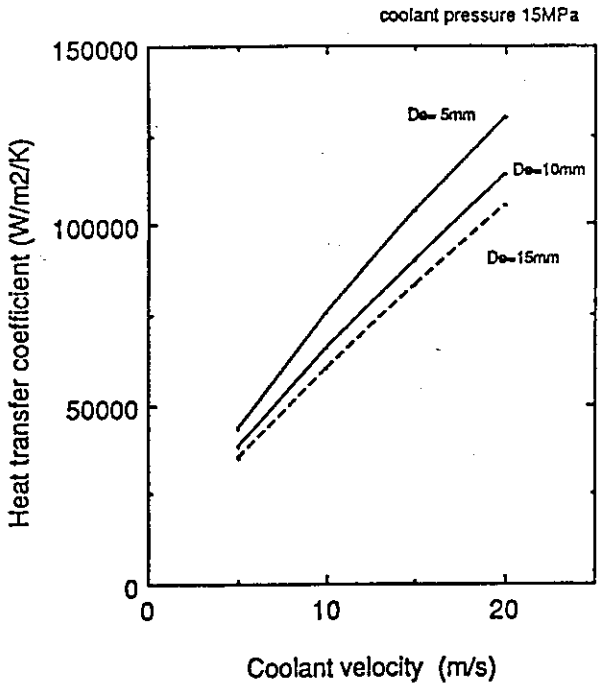

Fig. 8.3.3 Heat ransfer coefficient of divertor coolant tube with non-boiling forced convection.

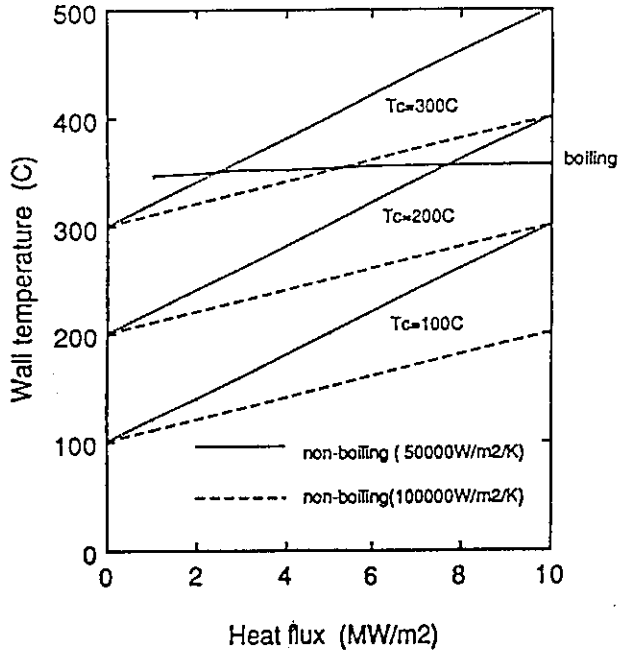

Fig. 8.3.4 Wall temperatures of divertor coolant tubes with and without boiling.

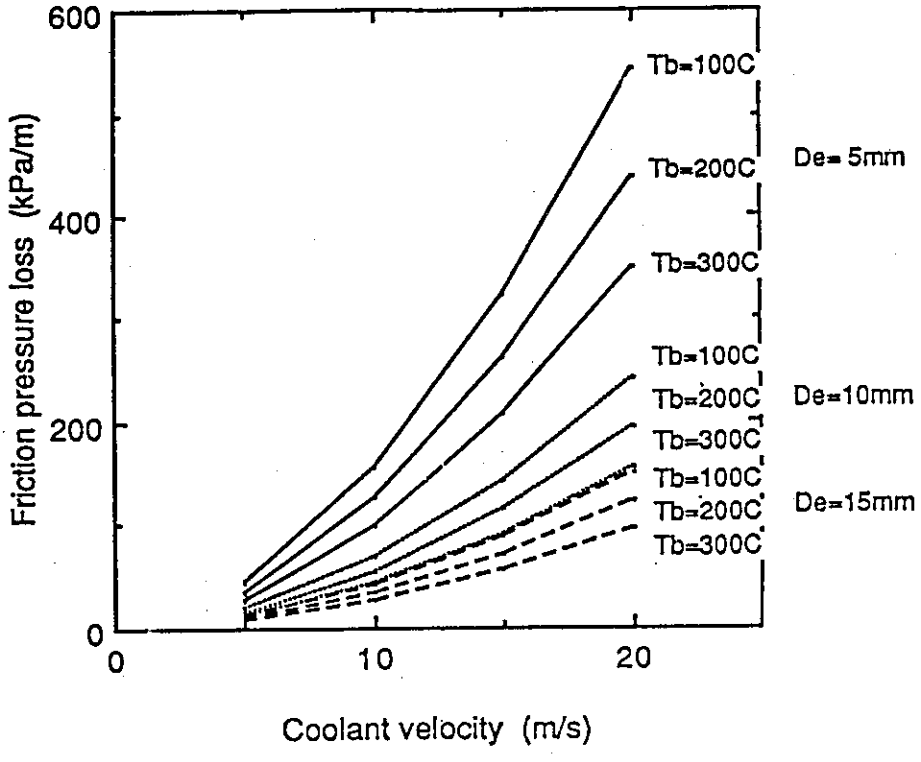

Fig. 8.3.5 Friction pressure loss of water coolant as functions of coolant temperature and velocity. (De=15mm)

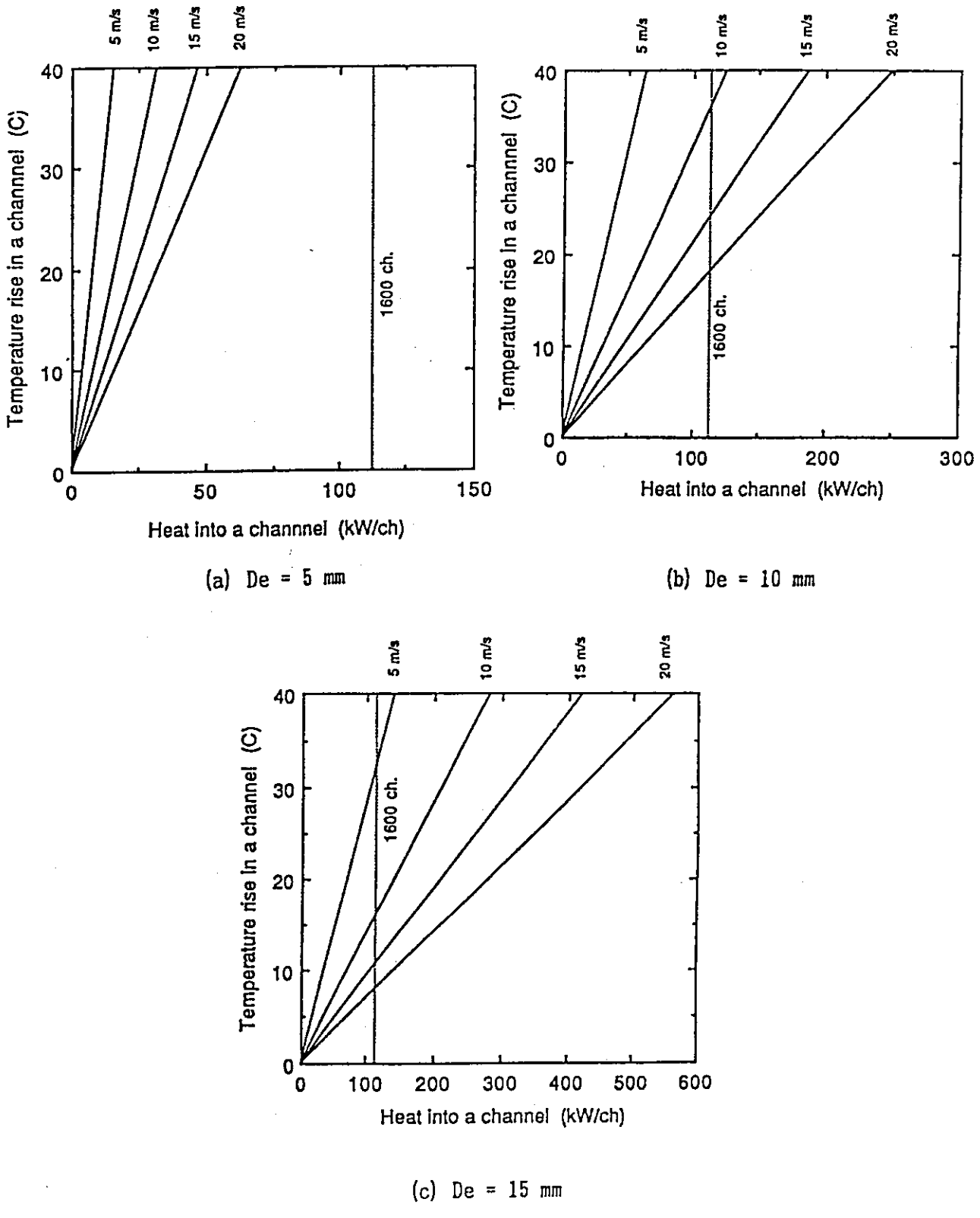

Fig. 8.3.6 Heat into divertor channel and temperature rise.

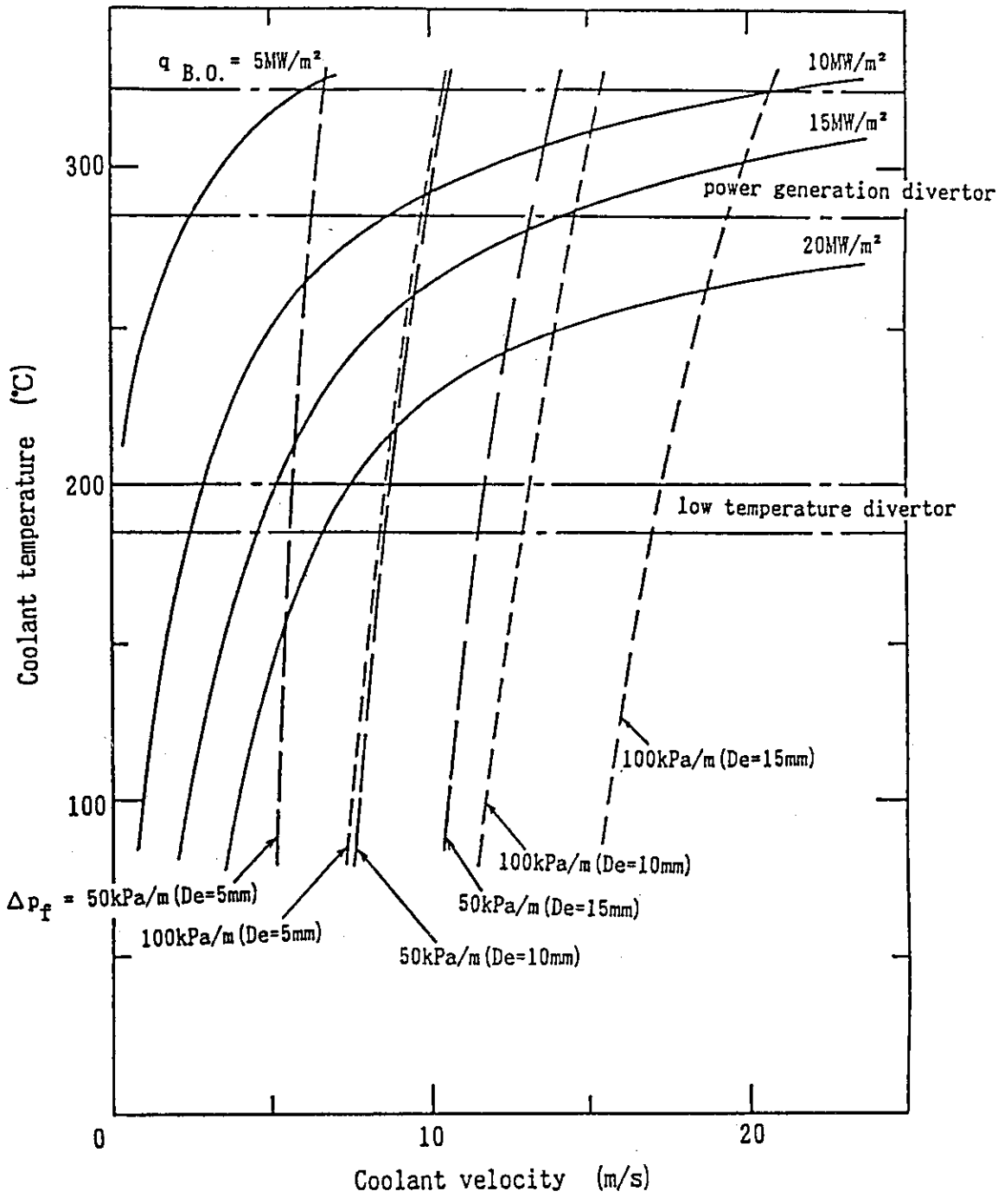

Fig. 8.3.7 Design window of coolant velocity and temperature for divertor plate. (without swirl tube).

8.4 Pumping speed of the divertor

The exhaust duct conductance from the diverter chamber, the effective pumping speed, and the neutral particle pressure in the diverter chamber were evaluated.

(1) Pumping speed of neutral particles

atom	pumping speed	molecular	pumping speed
D	1×10^{23} n/s	DT	1×10^{23} n/s
T	1×10^{23} n/s		
He	1×10^{21} n/s	He	1×10^{21} n/s
total	2×10^{23} n/s		1×10^{23} n/s

The pumping speed of fuel gas is equivalent to 1×10^{23} n/s (= 410 Pa m^3/s at 300K).

(2) Evaluation of the exhaust duct conductance

1) Analytical model

The analytical model is shown in Fig. 8.4.1.

Because the conductance in the diverter chamber was much larger than the one in the exhaust duct, the conductance in the diverter chamber was neglected and the conductance from the exhaust duct entrance to the gate valve at exhaust system was used in the evaluation.

2) Flow mode

A molecular flow was assumed as the flow mode.

3) Calculational conditions and results

Molecular weight : M=5 (DT fuel gas)

Temperature : T=300K

The calculational conditions, equations, and the results are summarized in Table 8.4.1

The conductance in the exhaust duct was evaluated to be 7.4 x 10 m^3/sec.

(3) Evaluation of the effective pumping speed in the diverter room

1) equations

$$1 / S_{eff} = 1 / S_p + 1/C$$

Here, S_{eff}(m^3/s) : Effective pumping speed in the diverter chamber

Sp (m^3/s) : Pumping speed of the exhaust pump

2) Effective pumping speed per one port

The effective pumping speed per one port is shown in Table 8.4.2, by regarding the pumping speed of the exhaust pump per one port as a parameter (50-200 m^3/s).

When the pumping speed of the exhaust pump is 100 m^3/s (25 m^3/s/unit x 4 unit), the effective pumping speed per one port is 45 m^3/s.

(4) Pressure in the diverter chamber

The effective pumping speed and the pressure in the diverter chamber, regarding the exhaust pumping speed per one port as a parameter, are shown in Table 8.4.2.

When the pumping speed of the vacuum exhaust pump is 100 m^3/s (25 m^3/s/unit x 4 unit), the pressure in the divertor chamber might be 0.57 Pa at 300 K (1.4 x 10^{20} DT-molecules/m^3).

(5) Summary

It was evaluated that the conductance per one exhaust duct in the diverter chamber is 74 m^3/s and the effective pumping speed is 45 m^3/s, when the exhaust pumping speed is 100 m^3/s. According to the results, the pressure in the diverter chamber might be 0.57 Pa at 300K.

Table 8.4.1 Exhaust duct conductance

Position	Condition	Formula m^3/sec	Conductance Ci, m^3/sec
Duct Entrance	$A = 1.22\times10^{4}cm^2$ (Aperture) $A_o = 3.3\times10^{4}cm^2$ (80cmx410cm)	$3.64\times10^{-3}(T/M)^{1/2}\dfrac{A}{1-(A/A_o)}$	5.44×10^{2}
Tapered Duct	$a = 170$ cm $b_1 = 71.5$ cm $b_2 = 200$ cm $L = 400$ cm	$\dfrac{1.94\times10^{-2}(T/M)^{1/2}}{\int_0^L (B/A^2K)\,dL}$ $A = ab,\ B = 2(a+B)$	3.07×10^{2}
Duct of Rectangular Cross Section Horizontal + Vertical + Horizontal	$a = 200$ cm $b = 200$ cm $L_1 = 100$ cm $L_2 = 900$ cm $L_3 = 500$ cm $L_e' = 118$ cm $L_e'' = 133$ cm $K = 1.108$	$9.70\times10^{-3}(T/M)^{1/2}\dfrac{a^2b^2}{(a+b)L}K$ $L = L_1+L_e'+L_2+L_e''+L_3$	1.90×10^{2}
Gate Valve Opening	$A = 1.77\times10^{4}cm^2$ (150 cmϕ)	$3.64\ (T/M)^{1/2}A$	4.99×10^{2}
Summary		$\dfrac{1}{C} = \dfrac{1}{C_1}+\dfrac{1}{C_2}+\dfrac{1}{C_3}+\dfrac{1}{C_4}$	8.09 x 10

C (1/sec) : Conductance
T (K) : Temperature
M (amu) : Molecular Weight

a (cm) : Large Side of Rectangle
b (cm) : Small Side of Rectangle
A (cm^2) : Area
L (cm) : Length

K : Correction Factor

b/a	K
1	1.108
0.667	1.126
0.5	1.151
0.333	1.198
0.2	1.297

Table 8.4.2 Effective pumping speed and pressure of divertor room

Pumping Speed of Pump (per port)	S_p (m³/s)	50	100	150	200
Effective Pumping Speed (per port)	S_{eff} (m³/s)	31	45	53	58
Effective Pumping Speed (total)	S_{eff}^{TOTAL} (m³/s)	490	720	840	920
Pressure of Divertor Room	P(Pa) at 300K	0.84	0.57	0.49	0.44
	n_{DT} (m⁻³)	2.0×10^{20}	1.4×10^{20}	1.2×10^{20}	1.1×10^{20}

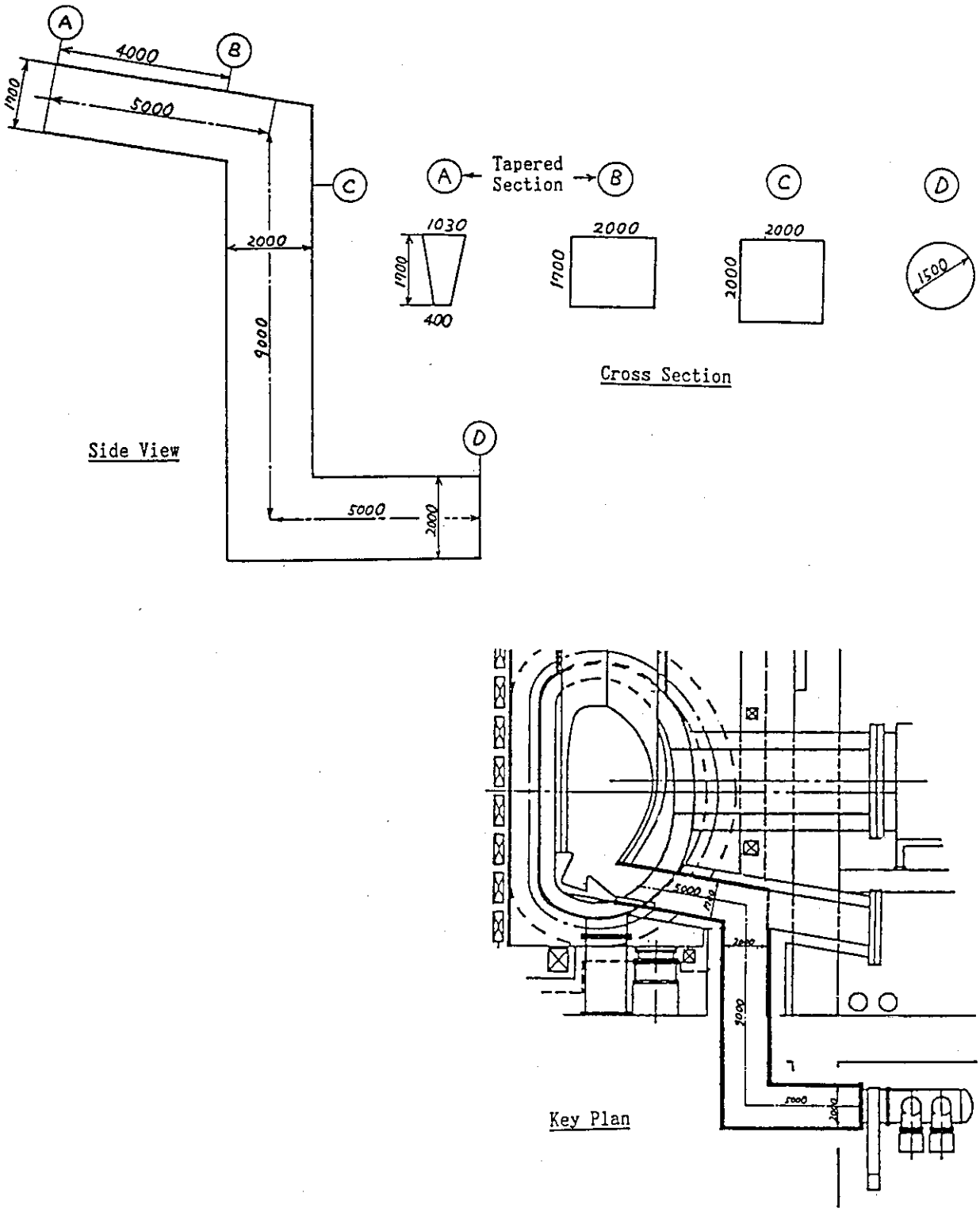

Fig. 8.4.1 Calculation model for exhaust duct conductance.

8.5 Concept of divertor remote maintenance, and the structure of the divertor duct

(1) Basic idea of remote maintenance

The basic idea of remote maintenance of the divertor module was summarized as follows.

1. The cassette maintenance is applied as the remote maintenance concept of the divertor module. The divertor plate is pulled out into the divertor maintenance room (in the reactor hall), with the support structures, the cooling water tubes, the movable duct shields, and the shield plugs etc.

2. A part of the cooling tubes are cut off when pulled out, and they are welded when installed, in order to reduce spaces of the divertor maintenance room.

3. The cutting of the cooling tubes when pulled out and the welding when installed are performed at the outside of the shield plug installed on the cryostat.

4. The repair and exchange of the divertor plate are not executed in the reactor hall, but in the repair room(outside the reactor hall) after transporting it with the movable duct shield etc., due to the following reasons.

* A lot of equipments are required in the maintenance room, when the repair is done there.
* As the operation is difficult during repairing divertor plate, the availability decreases.
* There is high possibility to contaminate radioactively in the maintenance room during repair.

(2) The division of divertor module

Because the space between toroidal coils is restricted, the width of the divertor module which can be pulled out from the duct is limited. That is, the width of the duct permissible to be installed is about 2000 millimeters, according to the interference of the toroidal coils. On the other hand, the duct shield thickness of about 600 millimeters is required from the viewpoint of shielding performance for toroidal coils. Then, the width of pulling out space is limited to be about 800 millimeters. As a result, it is difficult to pull out the divertor which is divided into three same size modules in a sector. The following measures are considered to solve this problem.

1. to divide the divertor into 5 same size modules (Fig. 8.5.1).
2. to pull out a part of the duct shield with the divertor plate as movable duct shields (Fig. 8.5.2).

If the divertor is divided into 5 modules, there are some problems as follows; the width of the divertor module might be unstable because of small width of each module, the space for cooling tubes might be extraordinarily small, and the remote maintenance procedure is complicated. Therefore, we decided to apply the movable duct shield concept in this design. However, because the width of the duct has some room outside of the toroidal coil, we designed so as to lose the movable duct by expanding the width of the exhaust duct (Fig. 8.5.3).

(3) Structure of the divertor duct

Because the width of the divertor duct is restricted between toroidal coils, it comes to be very difficult to pull the divertor module out and install the cooling water tubes. We suggest the structure of the duct which enables to pull the divertor module out and install the cooling water tubes around. This study indicates the followings results.

1. It is necessary to design the cross section of the duct as a trapezoid shape which becomes narrower in the bottom.
2. The cooling tubes for center and side modules are installed in different vertical position.
3. It is necessary to set the thickness of the movable duct shield at 500 millimeters in the area where the duct is narrowest.

As the results of the above study, the feasibility of this divertor ducts was indicated. However, it is necessary to advance optimization further because there was possibility that the problem such as the lack of the shield thickness toward TFC will be caused.

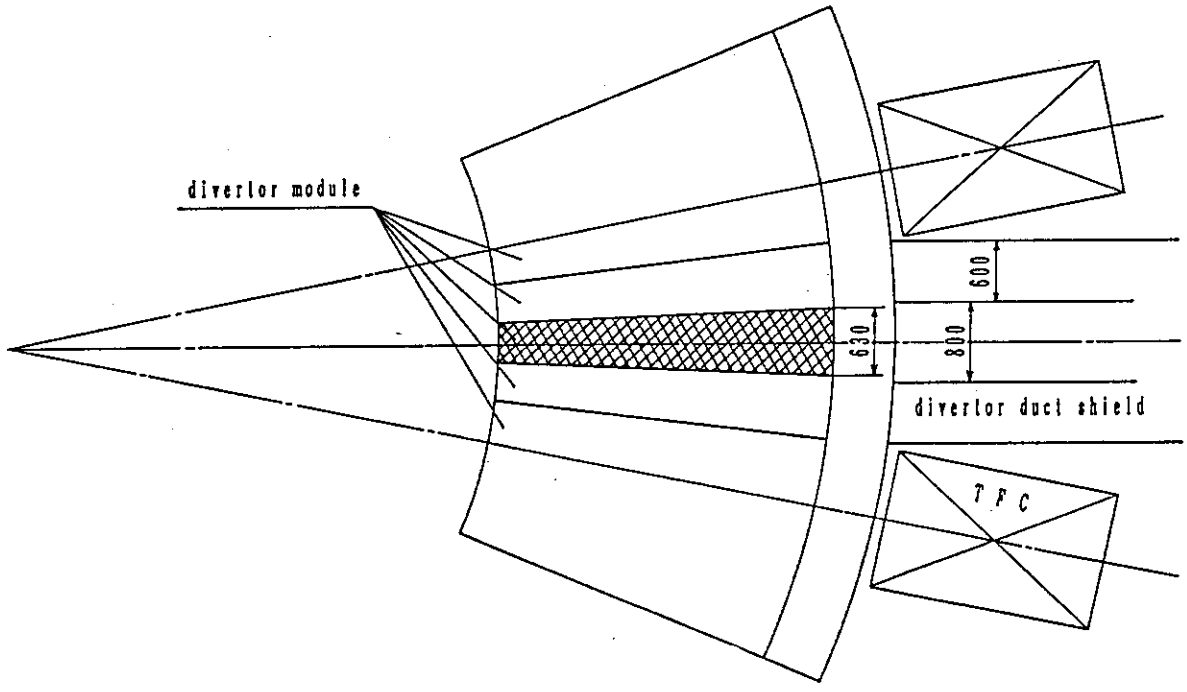

Fig. 8.5.1 Divertor module divided in five sub-modules.

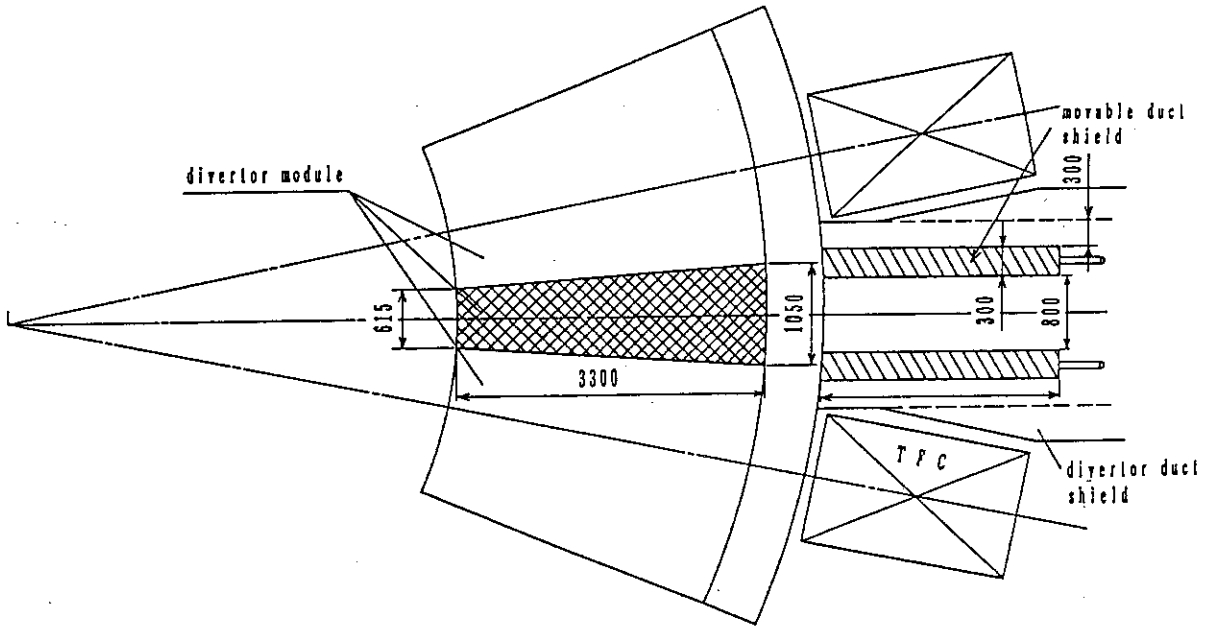

Fig. 8.5.2 Divertor module divided in three sub-modules with movable duct shield.

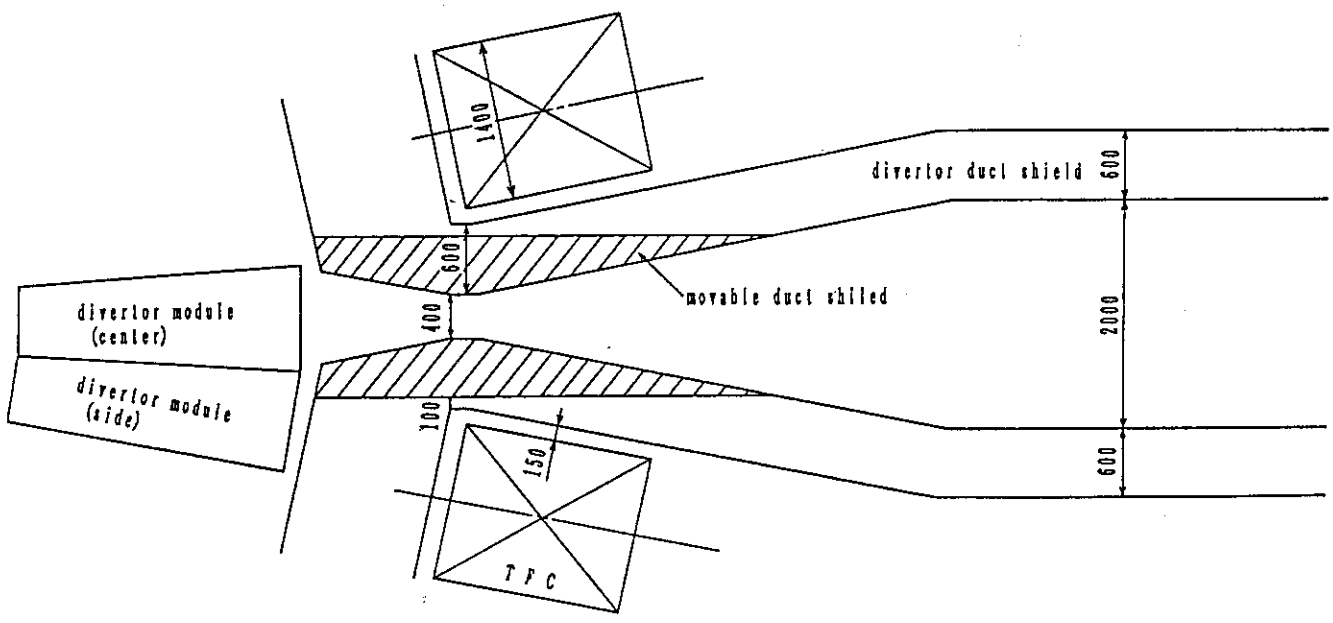

Fig. 8.5.3 Cross sectional plan view of divertor module and divertor duct at the bottom of divertor duct.

8.6 Thermal and stress analyses of the divertor plate

The thermal and stress analyses was performed for the following two divertor plates, and their integrity was evaluated; the divertor plate for the power generation which receives the heat flux of 3 MW/m^2 or 6 MW/m^2, and the low temperature divertor plate which receives the heat flux of 20MW/m^2, near the striking point.

8.6.1 Analysis of the divertor plate for power generation

In the divertor plate for power generation, the thermal analysis in the following two cases was performed and the temperature distribution and the maximum temperature were calculated. One is the case that the heat flux from the plasma is controlled so as to be the heat flux that burn-out can be avoided without avoiding the swirl tube(3MW/m^2), and the other is the case that the swirl tube is adopted for avoiding the burn-out(6MW/m^2) .

The analytical model and the condition of the coolant tubes in the plasma side were shown in Fig. 8.6.1. In this analysis, the coolant temperature was 325C and the heat transfer coefficient was 80000W/m^2/K. However, because the local boiling is caused on the coolant channel surface in the plasma side, the coolant channel surface temperature was assumed to be 360C(constant). The ferritic steel was assumed as a structural material, and the thermal conductivity of 26.6W/m/K was used in the analysis. The effect of the swirl tubes is not considered.

The results when the heat flux is 3MW/m^2 are shown in Fig. 8.6.2 and those when the heat flux is 6MW/m^2 are in Fig. 8.6.3. The maximum temperatures of structural material for each case were 596C and 834C, respectively. From the results, the followings were found.

1. When the ferritic steel is used as a coolant tube structural material of the divertor, the maximum temperature of the structural material exceeds the permissible maximum temperature (550C) defined from the viewpoint of the high temperature strength of the ferritic steel, for the surface heat flux of more than 3MW/m^2. Therefore, it is necessary to apply Mo alloy as a structural material when the surface heat flux exceeds 3 MW/m^2, even if burn-out can be avoided.

2. According to the results of the stress analysis of the low temperature divertor shown in the paragraph 8.6.2, it is considered that the thermal stresses can be suppressed within the range of the permissible limit.

8.6.2 Analysis of the low temperature divertor plate

Even when the conductive heat from the plasma is large and high heat flux is received near the striking points, the divertor plate can be approved by setting the coolant temperature lower.The thermal and stress analyses for the surface heat flux of 20 MW/m2 were performed and show the applicability of the low temperature divertor plate.

(1) Analytical conditions

(a) Analytical model

The analytical models and condition s of of the coolant tube in the plasma side and the rear wall side, are shown in Fig. 8.6.4. In this analysis, the coolant temperature was assumed 200 C and the heat transfer coefficient was 80000W/m^2/K. However, because the boiling is caused in the coolant channel surface in the plasma side, the coolant channel surface temperature was set at 360 C(constant) as well as 8.6.1.

(b) Analytical method and code

1. Thermal analysis

Two-dimensional steady state thermal analysis with the computer code of HEAT-K.

2. Stress analysis

Two-dimensional elastic stress analysis with the computer code of PLANE-K.

(c) Thermophysical and mechanical properties

The properties of the Mo alloy used in this analysis are summarized in Table 8.6.1.

(2) Analytical results

(a) Temperatures

Temperature distributions in the plasma side and rear side coolant tubes are shown in Figs. 8.6.5 and 6, respectively. From the results, maximum temperatures in each side are 747C and 201C, respectively.

(b) Stresses

The primary stress distributions in plasma side and rear side coolant tubes are shown in Figs. 8.6.7 and 8, and the stress intensity distributions are shown in Figs. 8.6.9 and 10. The maximum stresses are summarized in Table 8.6.2 and the positions of the maximum point and the values are shown in Fig. 8.6.11. From the results, the compressive stress is predominant among the stresses generated in the coolant tubes, and the maximum stress intensities in the plasma and wall sides are 827 MPa and 667 MPa, respectively.

(4) Discussions

The followings were found from the results of this analyses.

1. The maximum temperature of the coolant tube made of molybdenum alloy can be maintained at less than 750 C for the heat flux of 20 MW/m^2. Because the thermal stress generated in the tube is smaller than the yield stress(870 MPa), the integrity of the divertor plate can be maintained by applying the low temperature divertor concept in the high heat flux zone by using molybdenum alloy.

2. The structural material temperature of the coolant tube in the rear wall side is sufficiently low. And if a rectangular tube is used, the stress by the coolant internal pressure and the nuclear heating are small.

Table 8.6.1 Properties of molybdenum alloy for divertor plate.

thermal conductivity	105 W/m/K
heat capacity	0.287 J /m³/K
Young's modulus	300 KN/mm²
Poisson's ratio	0.29
thermal expansion coefficient	5.5 × 10^{-6} 1/ K

Table 8.6.2 Maximum tensile and compressive stresses and stress intensity

	maximum stress (tensile)	minimum stress (compressive)	maximum stress intensity
plasma side	580 MPa	761 MPa	827 MPa
rear side	120 MPa	340 MPa	667 MPa

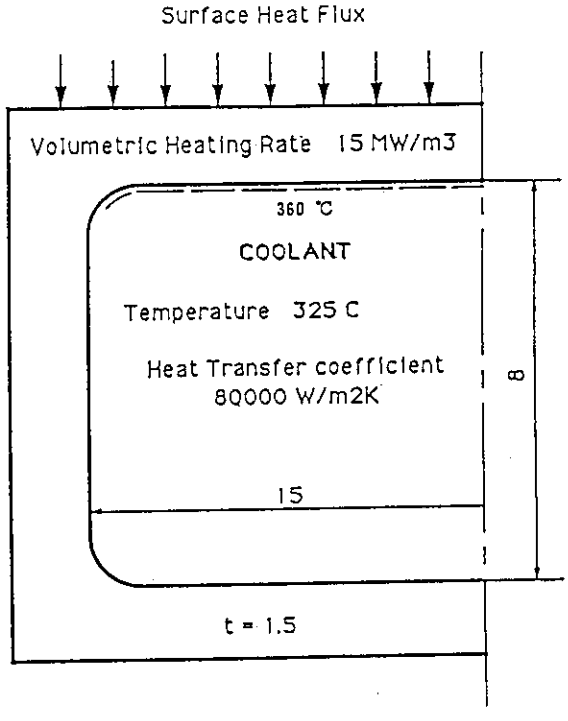

Fig. 8.6.1 Analytical models of divertor plate for power generation in thermal analysis.

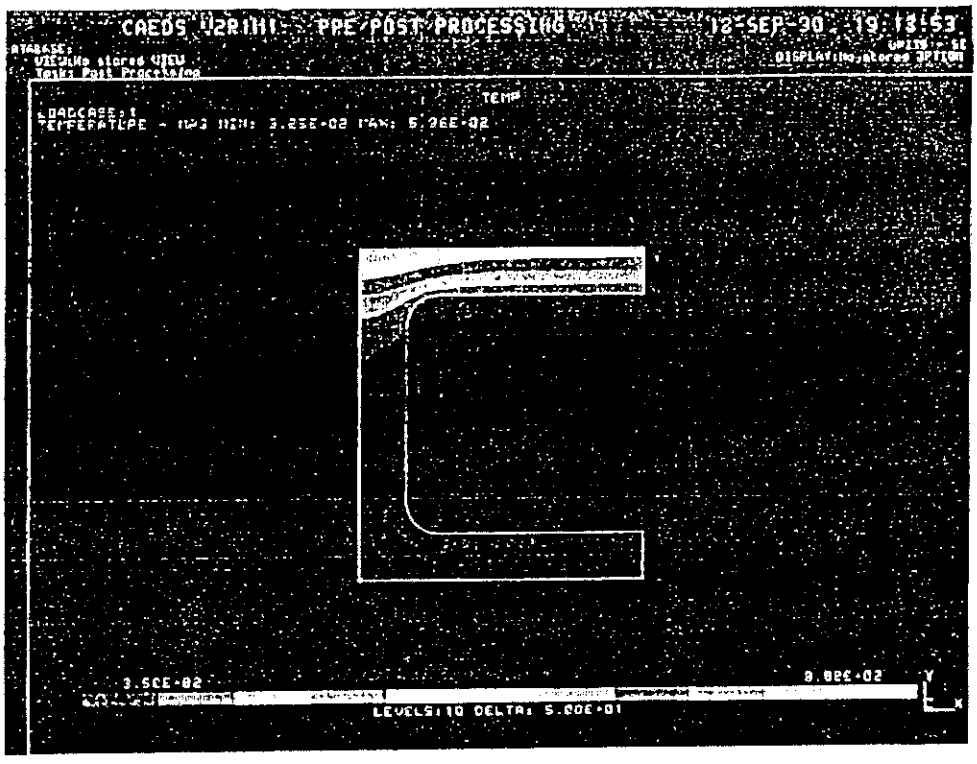

Fig. 8.6.2 Temperature distribution of plasma side tube. (surface heat flux: 3 MW/m^2)

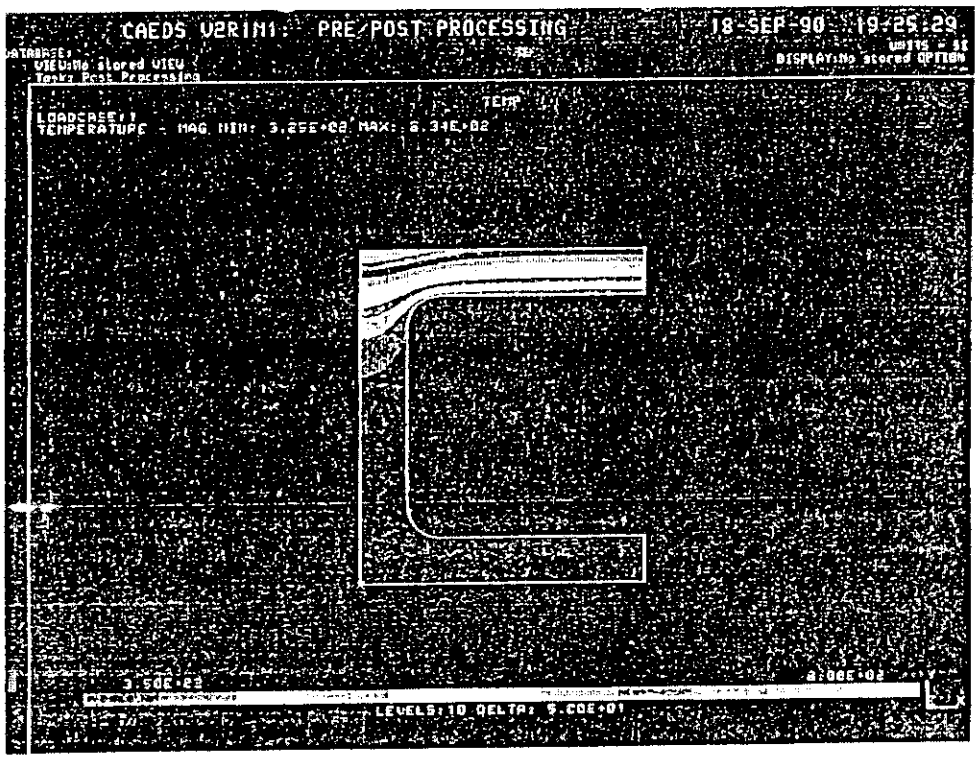

Fig. 8.6.3 Temperature distribution of plasma side tube. (surface heat flux: 6 MW/m^2)

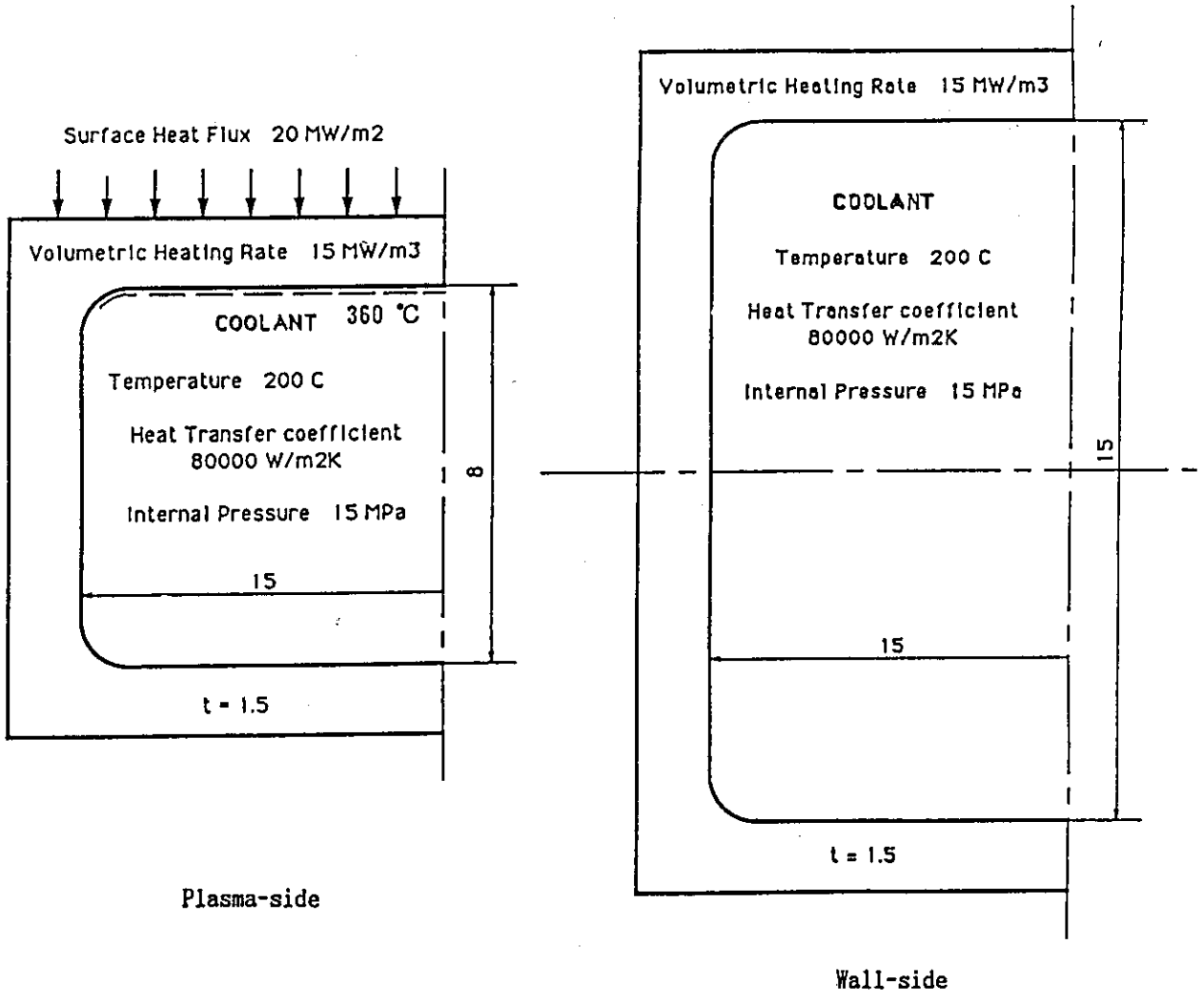

Fig. 8.6.4 Analytical models of low temperature divertor plate in thermal-stress analyses.

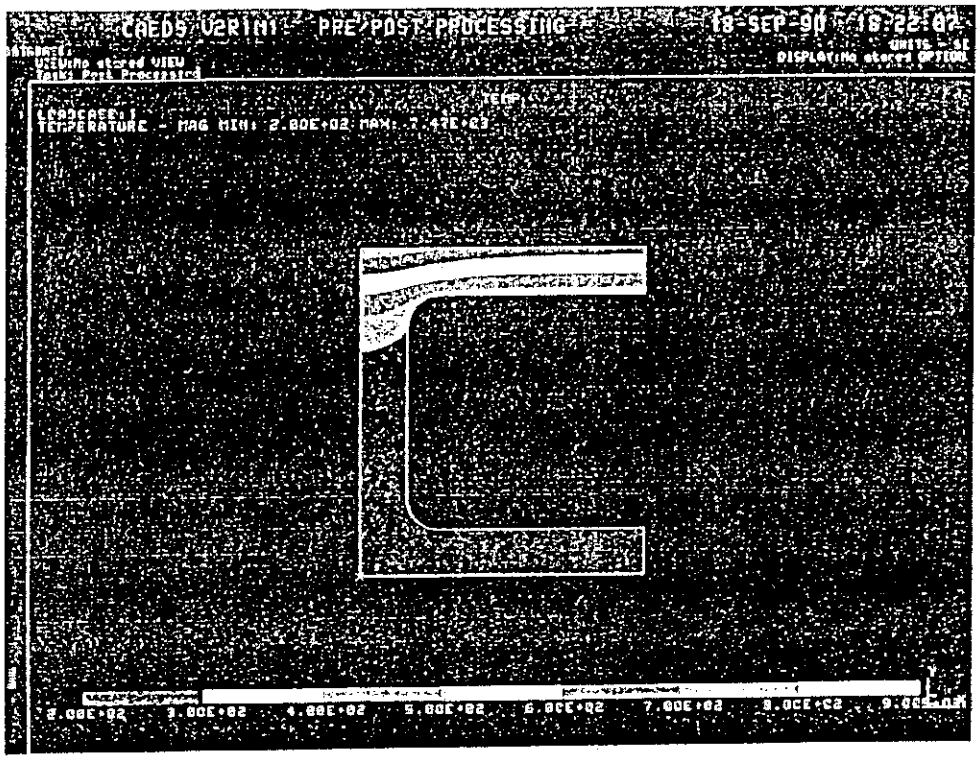

Fig. 8.6.5 Temperature distribution of plasma side tube.

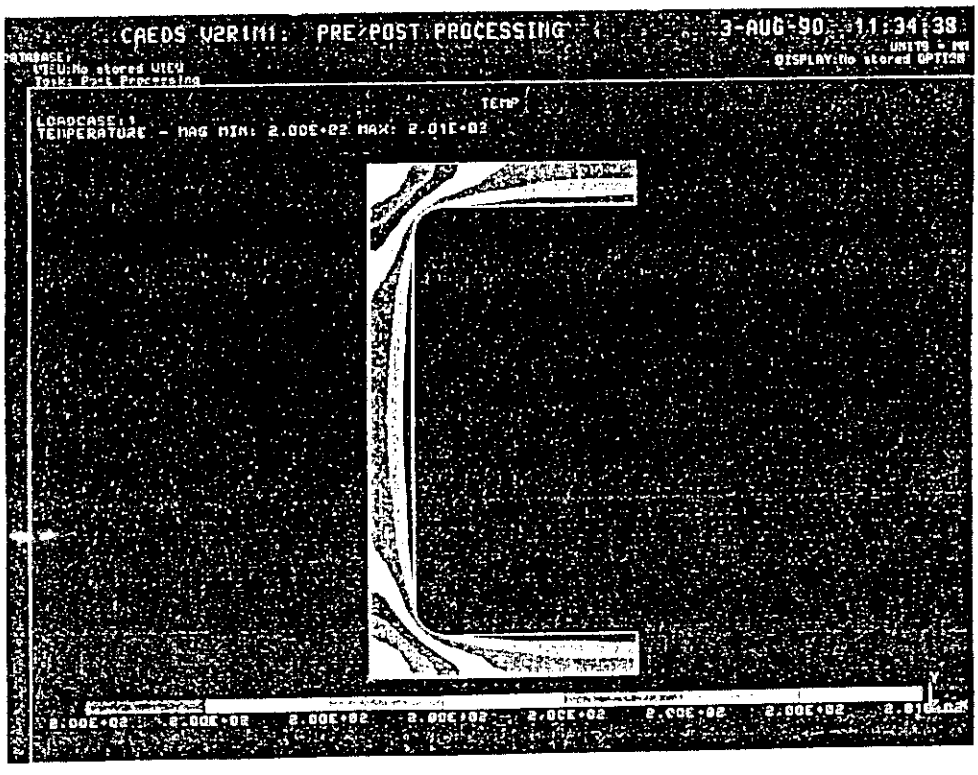

Fig. 8.6.6 Temperature distribution of wall side tube.

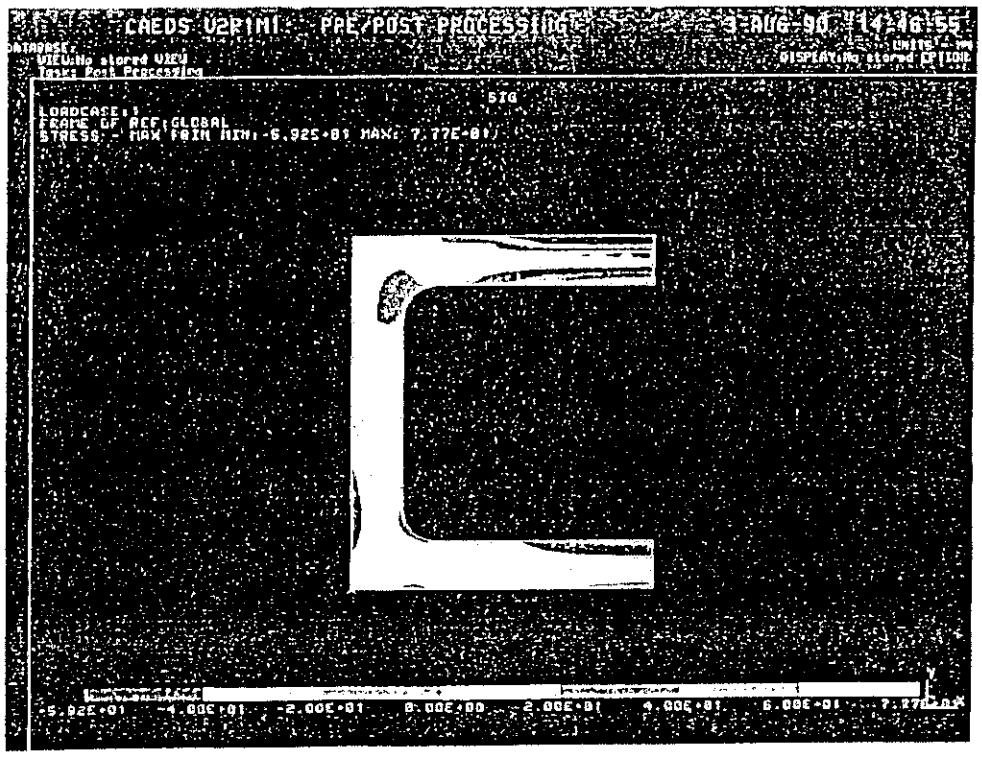

Fig. 8.6.7 Stress distribution of plasma side tube.

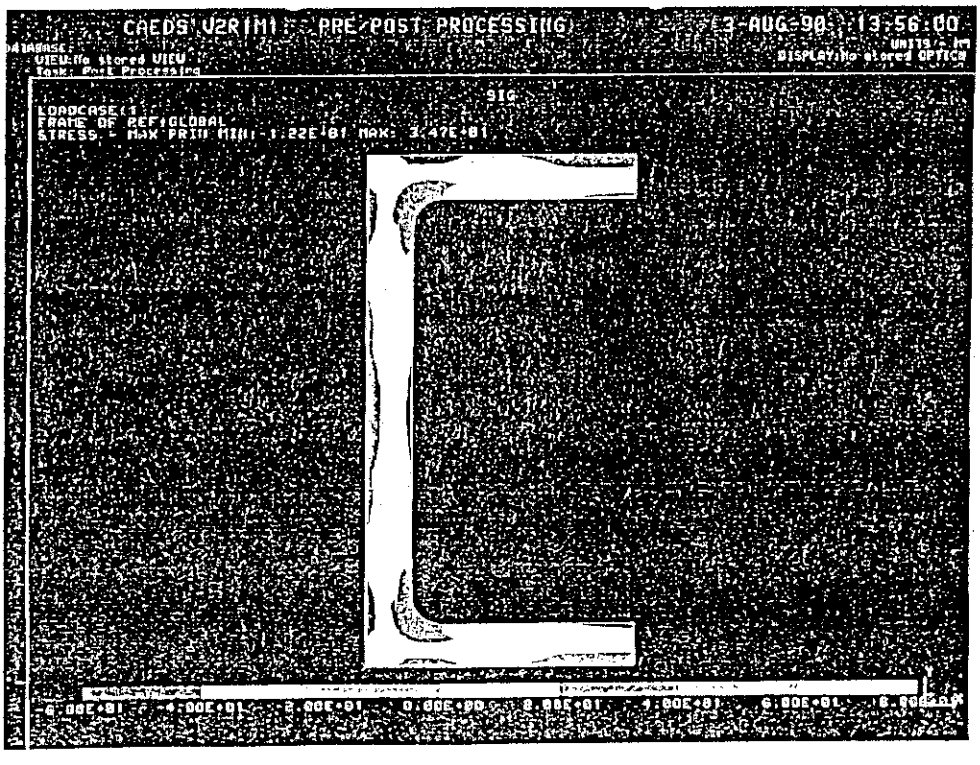

Fig. 8.6.8 Stress distribution of wall side tube.

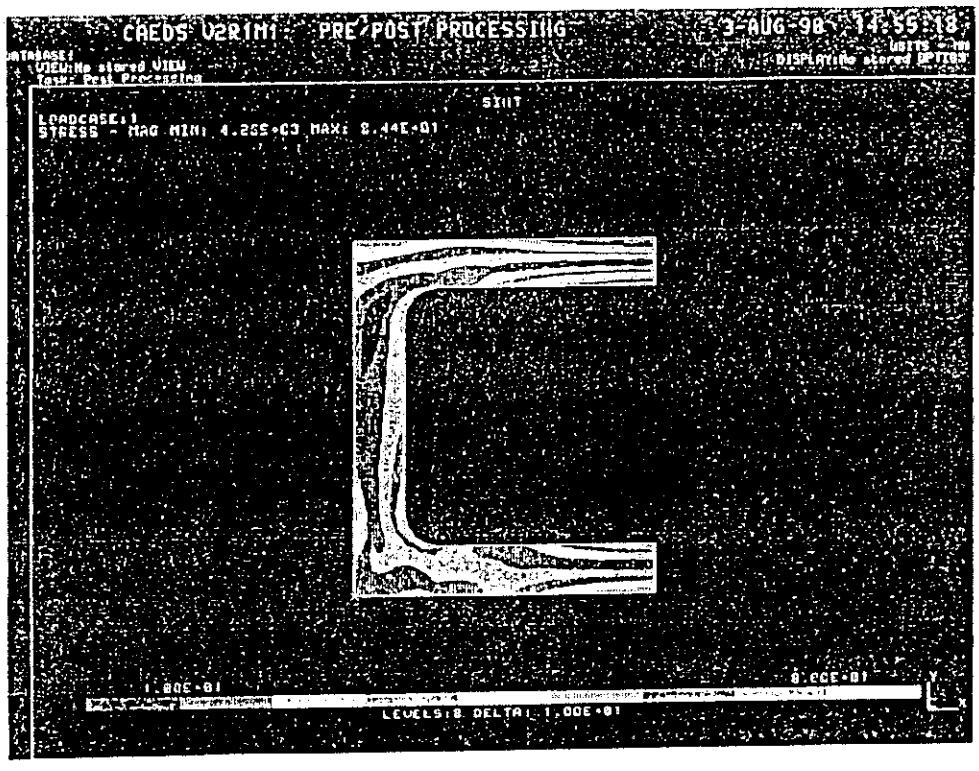

Fig. 8.6.9 Stress intensity distribution of plasma side tube.

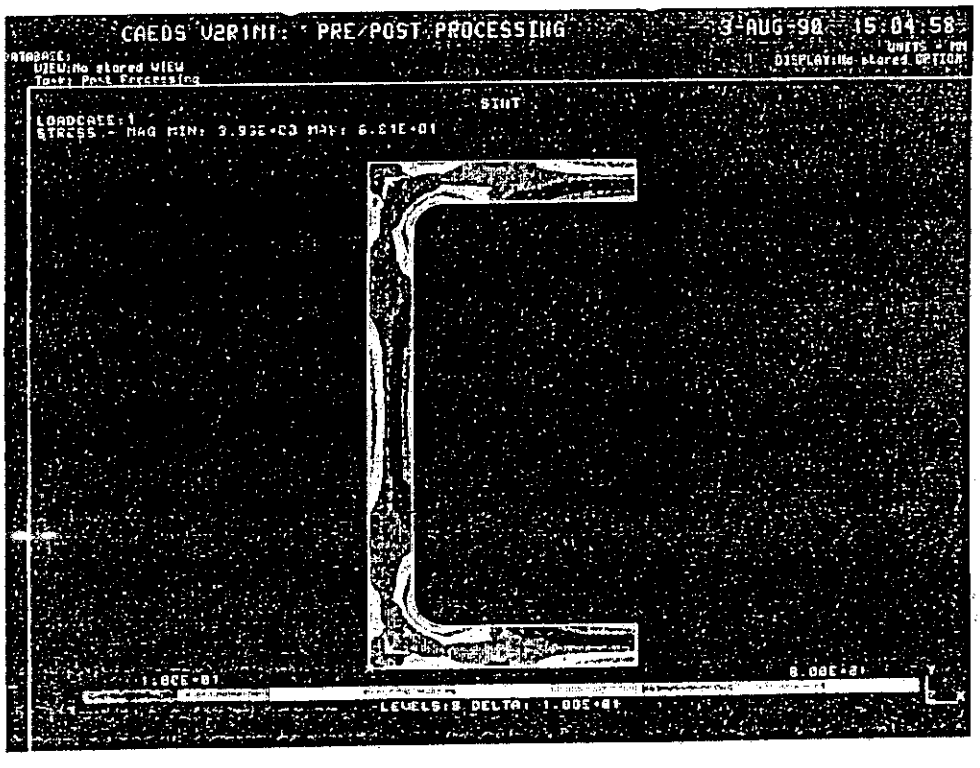

Fig. 8.6.10 Stress intensity distribution of wall side tube.

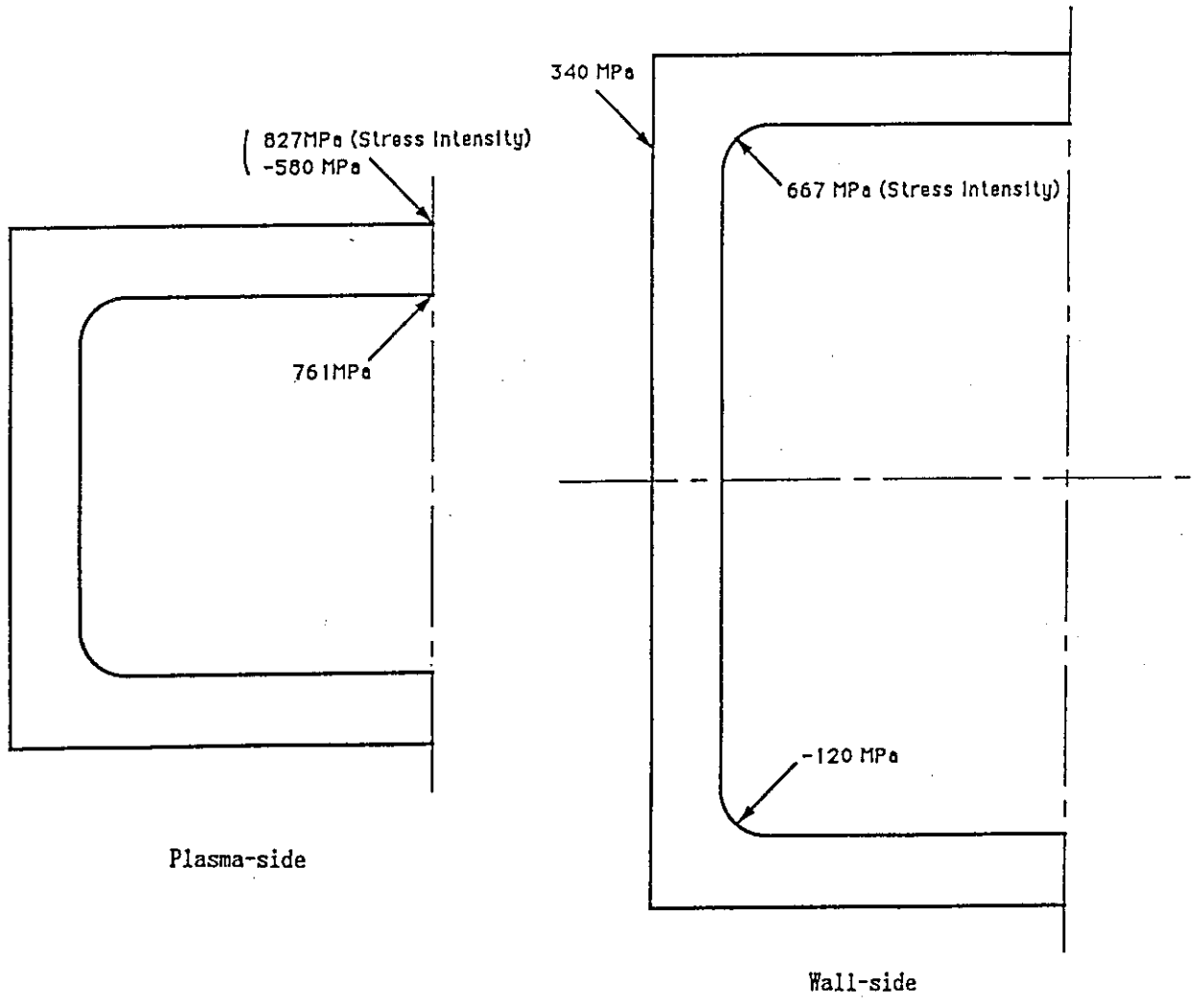

Fig. 8.6.11 Maximum and minimum stresses and maximum stress intensity of low temperature divertor plate.

8.7 Sputtering erosion of divertor plate

The physical sputtering erosion of the divertor plate was evaluated by changing the surface material and the divertor-plasma temperature

(1) Conditions

1. Particle flux — All: 2.0×10^{23} n/s; Outboard: 1.3×10^{23} n/s
2. Particle flux multiplication factor : 60
3. Particle component — D : 0.50; T : 0.50; He : 0.005; Fe : 0.008
4. Divertor plasma temperature: 5 eV - 300 eV

(Sheath acceleration of the incident particles was considered in the evaluation.)

5. Scrape-off layer thicknesses — Outboard: 4 cm; Inboard: 8 cm

(Uniform particle distribution in the scrape-off layer was assumed)

6. Divertor plate inclination degrees — Outboard: 15 deg; Inboard: 30 deg
7. Position of the striking points — Outboard: 7.0 m; Inboard: 5.5 m
8. Divertor plate surface materials: Be, C, Fe, Ti, Mo, V
9. The evaluation expression: expression of Matsunami et al.[1]. (2)

(2) Results

The sputtering yields and the erosion thicknesses per 1FPY(full power year) of each particle component for various wall surface materials were summarized in Tables 8.7.1 and 8.7.2. The divertor plasma temperatures were 10 eV and 300 eV, respectively. As the erosion thicknesses in the outboard were about 1.5 times larger than in the inboard,we evaluated it in the outboard.

The erosion thicknesses per 1FPY were calculated with various divertor plasma temperatures and surface materials of Fe, Mo, W. The results are summarized in Table 8.7.3.

(3) Summary

As the results of the evaluation, the followings are indicated.

1. When Be is used as the surface material, the erosion thickness is very large (more than 2 m/FPY) even if the divertor plasma temperature is 10 eV. Then, it is difficult to be approved Be for SSTR divertor plate. When the carbon material is used, its erosion thickness might be about 30 mm/FPY at the case of 10 eV of divertor plasma temperature. It indicates it is also difficult to be approved.

2. When the surface material is Fe and Ti, the erosion thickness for the divertor plasma temperature of 10 eV is 4 - 5 mm/FPY, and several times repair in a year is necessary. It is possible to be approved by reducing the particle flux multiplication factor smaller or decreasing the divertor plasma temperature lower furthermore(for example, less than 5 eV).

3. If Mo or W can be used as the surface material, when the divertor plasma temperature is 10 eV, the sputtering erosion can be almost 0.

4. In case that the divertor plasma temperature is not reduced sufficiently and might be about 300 eV, because the erosion thickness might be extraordinarily large (more than 3 m/FPY) for all candidate surface materials. Especially, Fe has possibility to cause the destructive damage because its self-sputtering yield comes large.

5. In order to suppress the sputtering erosion to be sufficiently small even when the divertor plasma temperature rises near the separatrix, it is necessary to suppress the temperature at less than about 20 eV for Mo, and less than about 40 eV for W.

6. As a result, the SSTR divertor plate(high heat flux zone) can be approved, by using Mo or W as the surface material, or by using Fe or Ti after decreasing its particle flux multiplication factor or the divertor plasma temperature. The most simplest approval concept is the structure to expose the coolant tube made of Mo alloy in the surface of the plasma side. However, there is possibility that the tungsten coating is required when the rise of the plasma temperature near separatrix must be considered.

reference

[1] Matsunami N. et al., IPPJ-AM-52 (1987)

Table 8.7.1 (a) Physical sputtering erosion thickness of divertor plate.

surface material : Be　　electron energy : 10 eV *1

density : 1850 kg/m³　　atomic weight : 9.012

incident particle	fraction	sputtering yield (n/part.)	erosion thickness*2 (mm/FPY)
D	0.500	0.00848	
T	0.500	0.00919	
He	0.005	0.02854	
self	0.008	0.01053	
total		0.00906	2652.

*1 : Sheath potential acceleration was considered to evaluate incident energy of ions.

*2 : Outerleg

Table 8.7.1 (b) Physical sputtering erosion thickness of divertor plate.

surface material : C　　electron energy : 10 eV *1

density : 1800 kg/m³　　atomic weight : 12.01

incident particle	fraction	sputtering yield (n/part.)	erosion thickness*2 (mm/FPY)
D	0.500	0.00000	
T	0.500	0.00004	
He	0.005	0.00218	
self	0.008	0.00518	
total		0.000072	28.9

*1 : Sheath potential acceleration was considered to evaluate incident energy of ions.

*2 : Outerleg

Table 8.7.1 (c) Physical sputtering erosion thickness of divertor plate.

suraface material : Fe　　electron energy : 10 eV *1

density : 7900 kg/m³　　atomic weight : 55.85

incident particle	fraction	sputtering yield (n/part.)	erosion thickness*2 (mm/FPY)
D	0.500	0.00000	
T	0.500	0.00000	
He	0.005	0.00237	
self	0.008	0.00000	
total		0.000012	5.1

*1 : Sheath potential acceleration was considered to evaluate incident energy of ions.

*2 : Outerleg

Table 8.7.1 (d) Physical sputtering erosion thickness of divertor plate.

surface material : Ti　　electron energy : 10 eV *1

density : 4500 kg/m³　　atomic weight : 47.90

incident particle	fraction	sputtering yield (n/part.)	erosion thickness*2 (mm/FPY)
D	0.500	0.00000	
T	0.500	0.00000	
He	0.005	0.00111	
self	0.008	0.00000	
total		0.0000056	3.6

*1 : Sheath potential acceleration was considered to evaluate incident energy of ions.

*2 : Outerleg

Table 8.7.1 (e) Physical sputtering erosion thickness of divertor plate.

surface material : Mo　　electron energy : 10 eV *1

density : 10200 kg/m³　　atomic weight : 95.94

incident particle	fraction	sputtering yield (n/part.)	erosion thickness*2 (mm/FPY)
D	0.500	0.00000	
T	0.500	0.00000	
He	0.005	0.00000	
self	0.008	0.00000	
total		0.00000	0.0

*1 : Sheath potential acceleration was considered to evaluate incident energy of ions.

*2 : Outerleg

Table 8.7.1 (f) Physical sputtering erosion thickness of divertor plate.

surface material : W　　electron energy : 10 eV *1

density : 19250 kg/m³　　atomic weight : 183.85

incident particle	fraction	sputtering yield (n/part.)	erosion thickness*2 (mm/FPY)
D	0.500	0.00000	
T	0.500	0.00000	
He	0.005	0.00000	
self	0.008	0.00000	
total		0.00000	0.0

*1 : Sheath potential acceleration was considered to evaluate incident energy of ions.

*2 : Outerleg

Table 8.7.2 (a) Physical sputtering erosion thickness of divertor plate.

surface material : Be electron energy : 300 eV *1

density : 1850 kg/m³ atomic weight : 9.012

incident particle	fraction	sputtering yield (n/part.)	erosion thickness*2 (mm/FPY)
D	0.500	0.05510	
T	0.500	0.07156	
He	0.005	0.18475	
self	0.008	0.46419	
total		0.06797	19893.

*1 : Sheath potential acceleration was considered to evaluate incident energy of ions.

*2 : Outerleg

Table 8.7.2 (b) Physical sputtering erosion thickness of divertor plate.

surface material : C electron energy : 300 eV *1

density : 1800 kg/m³ atomic weight : 12.01

incident particle	fraction	sputtering yield (n/part.)	erosion thickness*2 (mm/FPY)
D	0.500	0.03035	
T	0.500	0.04450	
He	0.005	0.11917	
self	0.008	0.49643	
total		0.04199	16833.

*1 : Sheath potential acceleration was considered to evaluate incident energy of ions.

*2 : Outerleg

Table 8.7.2 (c) Physical sputtering erosion thickness of divertor plate.

surface material : Fe electron energy : 300 eV *1

density : 7900 kg/m³ atomic weight : 55.85

incident particle	fraction	sputtering yield (n/part.)	erosion thickness*2 (mm/FPY)
D	0.500	0.03951	
T	0.500	0.06418	
He	0.005	0.16227	
self	0.008	0.96582	
total		0.06038	25646.

*1 : Sheath potential acceleration was considered to evaluate incident energy of ions.

*2 : Outerleg

Table 8.7.2 (d) Physical sputtering erosion thickness of divertor plate.

surface material : Ti electron energy : 300 eV *1

density : 4500 kg/m³ atomic weight : 47.90

incident particle	fraction	sputtering yield (n/part.)	erosion thickness*2 (mm/FPY)
D	0.500	0.01961	
T	0.500	0.03214	
He	0.005	0.08239	
self	0.008	0.44944	
total		0.02988	19109.

*1 : Sheath potential acceleration was considered to evaluate incident energy of ions.

*2 : Outerleg

Table 8.7.2 (e) Physical sputtering erosion thickness of divertor plate.

surface material : Mo　　electron energy : 300 eV *1

density : 10200 kg/m³　　atomic weight : 95.94

incident particle	fraction	sputtering yield (n/part.)	erosion thickness*2 (mm/FPY)
D	0.500	0.00645	
T	0.500	0.01352	
He	0.005	0.04016	
self	0.008	0.43003	
total		0.01363	7703.

*1 : Sheath potential acceleration was considered to evaluate incident energy of ions.

*2 : Outerleg

Table 8.7.2 (f) Physical sputtering erosion thickness of divertor plate.

surface material : W　　electron energy : 300 eV *1

density : 19250 kg/m³　　atomic weight : 183.85

incident particle	fraction	sputtering yield (n/part.)	erosion thickness*2 (mm/FPY)
D	0.500	0.00101	
T	0.500	0.00332	
He	0.005	0.01368	
self	0.008	0.36996	
total		0.00519	2978.

*1 : Sheath potential acceleration was considered to evaluate incident energy of ions.

*2 : Outerleg

Table 8.7.3(a) Physical sputtering erosion thickness of divertor plate.

surface material	divertor plasma temperature (eV)	total sputtering yield (n/part.)	erosion thickness at outerleg (mm/FPY)
Fe	5	0.00000	
	10	0.000012	5.1
	20	0.00177	752.3
	40	0.01206	5130.
	60	0.02188	9299.
	80	0.02981	12669.
	100	0.03603	15312.
	300	0.06038	25662.

Table 8.7.3(b) Physical sputtering erosion thickness of divertor plate.

surface material	divertor plasma temperature (eV)	total sputtering yield (n/part.)	erosion thickness at outerleg (mm/FPY)
Mo	10	0.00000	0.0
	20	0.0000005	0.28
	40	0.00014	79.1
	60	0.00109	616.0
	80	0.00254	1435.
	100	0.00406	2294.
	300	0.01363	7703.

Table 8.7.3(c) Physical sputtering erosion thickness of divertor plate.

surface material	divertor plasma temperature (eV)	total sputtering yield (n/part.)	erosion thickness at outerleg (mm/FPY)
W	10	0.00000	0.0
	20	0.00000	0.0
	40	0.00000	0.0
	60	0.000037	21.2
	80	0.00017	97.6
	100	0.00043	246.7
	300	0.00519	2978.

8.8 Tritium permeation into the primary cooling water

A large amount of tritium permeates into the primary cooling water from the divertor plasma by implantation of tritium neutral particles. The quantity of tritium, which permeates into the primary cooling water, was evaluated here.

(1) Equation

The permeation rate was evaluated same as in 7.3.6, using the equation with the transport parameter W introduced by Doyle and Brice[1].

(2) Analytical conditions

Analytical conditions are summarized in Table 8.8.1.

The evaluation has been performed at the inner and outer striking points receiving the highest heat and particle fluxes. Molybdenum alloy was assumed as the surface material of divertor plate. The incident particle energy of the divertor plate is lower than that of the first wall studied in 7.3.6., but the particle flux is much higher. The incident particle energy of 10 eV was evaluated in consideration of sheath potential acceleration. The incident particle flux was assumed as same as in 8.4. Reflection rate and implanted range of the incident particles were calculated with the incident angle of 60 degree from the perpendicular to the divertor plate.

(3) Results

Tritium permeation rate normalized by the incident particle flux is evaluated as follows.

$$J2 / \phi = 1.57 \times 10\text{-}6$$

This is equivalent to the following value as tritium permeation flux.

$$J2 = 7.87 \times 1012 \ (T/cm^2 \ s)$$

As the evaluated divertor surface area is 10 m^2, the quantity of tritium permeation into the divertor cooling water is evaluated as follows.

$$6.80 \times 10^{22} \ T/day = 0.34 \ g/day$$

(4) Summary

1. The quantity of tritium permeation into the primary cooling water of the divertor in the high heat flux zone is evaluated at 0.34 g/day. This value is less than 1 g/day which is the guideline of the quantity of tritium permeation into the primary cooling water. It is considered that this value is permissible from the viewpoint of tritium safety, without any measures of tritium permeation.

2. As for the measure of tritium permeation, it is difficult to coat beryllium etc. on the surface of the plasma side, from the viewpoint of the sputtering erosion as evaluated in 8.4 . Therefore, it is considered that the measure to coat with ceramics etc. which works the permeation barrier on the cooling side is highly reliable. In this case, the permeation can be reduced by two orders of magnitude from the analogy of the oxide layer data. The integrity retention of the coating layer might be a problem.

3. Because the incident particle conditions of the divertor in the low heat flux zone were not clarified, the quantity of tritium permeation of that zone must be evaluated in the future.

4. Tritium permeation rate into the divertor coolant normalized by the incident particle flux is smaller than that into the first wall. The reason is that molybdenum is higher in tritium recombination rate on the surface of the plasma side than the ferritic steel, and the surface area of the divertor plate is smaller than that of the first wall. Then, the quantity of total permeation is smaller than that of the first wall in spite of higher particle flux.

5. The time required to reach steady state is evaluated at about 13 days. It indicates that the tritium permeation into the coolant reaches steady state during one year's operation.

6. In this evaluation, the divertor plasma temperature is assumed to be low. However, it is considered that the evaluation including the particle distribution profile should be performed in the future, because it strongly affect to the quantity of tritium permeation.

reference

[1] Doyle B.L. and Brice, D.K., Radiation Effects 89 (1985), 21-48.

Table 8.8.1 Analytical conditions

1. Structural Material			
Material			Mo-alloy
Calculated as Molybdenum			
Surface Area	$A(m^2)$		10
Equivalent to Area of Total High Heat Flux Zone			
Thickness	x_0(cm)		0.15
2. Temperature			
Maximum / Minimum			803K / 633K
Calculated under following conditions			
Surface Heat Load		(MW/m²)	3.0
Heat Generation Rate		(MW/m³)	15
Coolant Side Temperature		(K)	633
Thermal Conductivity		(W/m K)	105
3. Incident Tritium			
Incident Flux	ϕ'	(1/cm²s)	0.5×10^{20}
Incident Energy		(eV)	10
Angle of Incidence		(deg)	60
Reflection Coefficient		(-)	0.90
Projected Depth		(cm)	2.9×10^{-8}
4. Tritium Transportation [1]			
Diffusion	$D = D_0 \exp(-E_D/k_BT)$		
	D_0(cm²/s)		4.8×10^{-3}
	E_D(eV)		0.39
Recombination	$k = k_0\sigma\sqrt{(500/T)}\exp(-E_k/k_BT)$		
(Baskes' formula)			
	k_0(cm⁴/s)		3.1×10^{-17}
	E_k(eV)		-0.15
Sticking Coeff.	σ (-)		1.0
Heat of Transport	Q^*(eV)		—
Hydrogen Solution Sites Density			
	N_S(1/cm³)		6.4×10^{22}
Trap Density	N_T/N_S		0.05
Trap Strength	E_B(eV)		0.8

8.9 Review for critical heat flux

In next generation fusion reactor, water is the promising candidate as the coolant for plasma facing components. At first, critical heat flux is reviewed from measured CHF data based on forced convection cooling. CHF depends mainly on any parameters. Influences of major parameters on CHF are summarized as follows;

(1) Effects of flow

(1-1)Subcooling:

The CHF value increases with subcooling of the coolant.

(1-2)Flow velocity:

In high subcooling flow, the CHF value generally increases with flow velocity. For low-quality annulation flow, the CHF value decreases with increasing mass flow velocity.

(1-3)Outlet pressure:

CHF has maximum value, when an equivalent pressure that is defined as the ratio of pressure to the critical pressure reaches around 0.75.

(2) Effects of shape of cooling line

(2-1) Heated length:

The CHF value increases with decreasing heated length at a constant deposited power.

(2-2) Inner diameter:

With decreasing inner diameter of the cooling line, the CHF value increases.

(3) Effect of heat flux distribution

(3-1) Heat flux distribution in flow direction:

At constant deposited power and heated length, CHF in uniform heating is larger than that in nonuniform heating such as a cosine distribution. CHF has maximum value in case of nonuniform heat flux distribution, when heat flux has maximum value at the water entrance region and then gradually decreases along the flow direction.

(3-2) Heat flux distribution in circumferential direction:

In the vertical flow, there are no influences of heat flux distribution on CHF. In the horizontal flow concentration, CHF under nonuniform heating condition is higher than that under uniform heating.

(4) CHF enhancement effect

(4-1) Internal fin:

Because of enlargement of heat transfer area by applying internal fins, apparent CHF of tubes with internal fins is higher than that of tubes without them.

(4-2) Rough surface:

In general, the CHF value in rough surface is large compared with that in smooth surface.

(4-3) Vortex flow:

CHF value of tubes applied to vortex flow is improved compared with that to normal flow.

Figure 8.9.1 shows CHF data obtained by Araki[1]. It is found that relatively high CHF values in tubes with a swirl tape or internal fins are obtained. Existing high heat flux components in fusion facilities are summarized in Table 8.9.1. Especially, high CHF values can be obtained at the limited heating condition. It is possible to remove high heat flux under the high subcooling and vortex flow conditions, if the coolant is used for heat removal of plasma facing components without recovery of fusion power. Since it is very important to recover the fusion power produced in the commercial fusion power reactor, high outlet temperature of the cooling water is required to efficiently produce electric power. For this reason, limited subcooling value and flow velocity are available in the plasma facing components. To handle high heat load in the divertor for the commercial fusion reactors, peak heat flux must be modified to be uniform, or CHF value at the high heat flux region will locally be enhanced. Many way, it will be difficult to get high critical heat flux applying to present heat removal technologies based on fission reactors, especially, PWR.

An achievement of nuclear fusion reactor will be next generation. When the nuclear fusion reactor is applied to the heat source, cooling technology which can handle the coolant under the condition of high outlet water temperature and high heat flux environment. Though aggressive R&Ds on high heat removal are done intensively, long term R&Ds will be required. At the same time, it is very important not only to obtain high critical heat flux but also to develop high performance heat removal components considering materials properties, geometric structures and overall cooling system for the nuclear fusion reactor.

References

(1) M. Araki, et al., Burnout experiments on the externally-finned swirl tube for steady-state and high-heat flux beam stops, Fusion Engineering and Design 9(1989) 231

(2) K. Miya, M. Seki and M. Araki, Present Status of High Heat Flux Experiments in Relation to Fusion Reactors, Journal of the Atomic Energy Society of Japan, Vol. 29, No. 10 (1987) 855 (in Japanese)

(3) Toda, The Japan Society of Plasma Science and Nuclear Fusion Research, Vol. 65 (1991) 5 (in Japanese)

Table 8.9.1 Existing high heat flux components in fusion facilities

		HYPER-VAPOTRON [1] (JET)	Beam dump for [2] NBETF-NBI (LBL)	(DESIGN) Steady-state [3] beam dump for TFTR-NBI (PPPL)	Beam target for [4] METF-NBI (ORNL)	Beam dump for [5] MFSTF-NBI (LLNL)	Rotating target
Max. heat flux (kW/cm²)		1.2 - 1.6 (1.0 - 2.0)	- 1.6 (1.0)	1.0 - 2.0	- 5.4 (3MW-30s)	- 1.33 (8.0)	(20.0)
Material		1% Cr + Cu	0.2% Zr + Cu	Zr + OFHC or INCONEL	OFHC (tape : INCONEL)	Mo	
Size	width	112	215	OD : 19.1	OD : 9.5	OD : 5.0	
	height	30	-	t : 1.6	t : 1.6	t : 0.25	
	length	940 (540)	200	Int. finned tubes	Swirl-tubes	Int. finned tubes	
Cooling water	Inlet	-	-16.5	-	16.0	-	
	Press. outlet	-	6.5	-	4.0	-	
	operat	7.0	-	22.0	-	54.0	
	Flow rate (l/min/tube)	166	220	29 (average) (max. 60)	20	5.4 (total : 2700)	
	Press. drop (kg/cm²)	- 0.5	- 7.2	-	- 11.0	-	
Pulse length (sec)		> 10 (10)	30 (30)	>30	30 (30)	- 0.4 (30)	
Life time (cycle)		(100000)	(> 25000)	-	30000 1000 (LP)	(300000)	
Structure of surface		Beam V - shape	V - shape	Bowl - shape	V - shape	V - shape	
Remarks		ION SOURCE 75keV, 10MW, D-BEAM (TOMSON CSF)	ION SOURCE 120keV, 50A, 30s, D (170keV, 65A, 30s) (MDAC)	ION SOURCE 120 keV, D-BEAM	ION SOURCE 75 keV, 40A, 30s (UNITED TECH.)	(UNITED TECH.)	

		JT-60 NBI (JAERI)			Active diagnostics for JT-60 (JAERI) [7]		(DESIGN) [8] Beam dump for FER NBI (JAERI)
		Beam dump [6]	Water jacket	Calorimeter	Beam dump	Calorimeter	
Max. heat flux (kW/cm²)		0.5 (0.5)	0.4 - 0.5 (0.45)	- 1.0 (1.0)	- 7.5 (9.0)	3.7 (4.0)	(4.0) (17MW)
Material		0.2% Ag + OFHC	0.2% Ag + OFHC	0.2% Ag + OFHC	W/ OFHC	0.2% Ag + OFHC	0.2% Ag + OFHC (tape : INCONEL) (or NI)
Size	width	OD : 14.0	16 x 16	30	49	140	(OD : 10.0)
	height	t : 2.0		36	50	260	(t : 1.5)
	length	Ext. finned tubes		30	49	20	Ext. finned swirl-tubes
Cooling water	Inlet	10.0	9.0	9.0	8.0	8.0	(20.0)
	Press. outlet	9.0	5.0	5.0	-	-	-
	operat	11.5	-	-	-	-	-
	Flow rate (l/min/tube)	22.6 (max 27) (total : 2400)	16.1 (average) (total : 1000)	9.3 (average) (total : 250)	4.5 - 11.0 (series)	1.6 - 2.0 (series)	(20.0 - 30.0)
	Press. drop (kg/cm²)	0.5 - 1.0	0.5 - 1.0	0.5 - 2.0	-	-	(10.0 - 15.0)
Pulse length (sec)		10 (10)	10 (10)	0.5 - 1.0 (0.5)	- 0.1 (0.1)	- 0.1 (0.1)	Continuous
Life time (cycle)		(10^6)	(10^6)	(10^6)			-
Structure of surface		Bowl - shape	Flat	V - shape	W OFHC Flat	V - shape	Flat
Remarks		ION SOURCE 100 keV, 70A, 10s H-BEAM			ION SOURCE 200keV, 3.5A, 0.1s He-BEAM		ION SOURCE 500keV, 100A, Cont D - BEAM

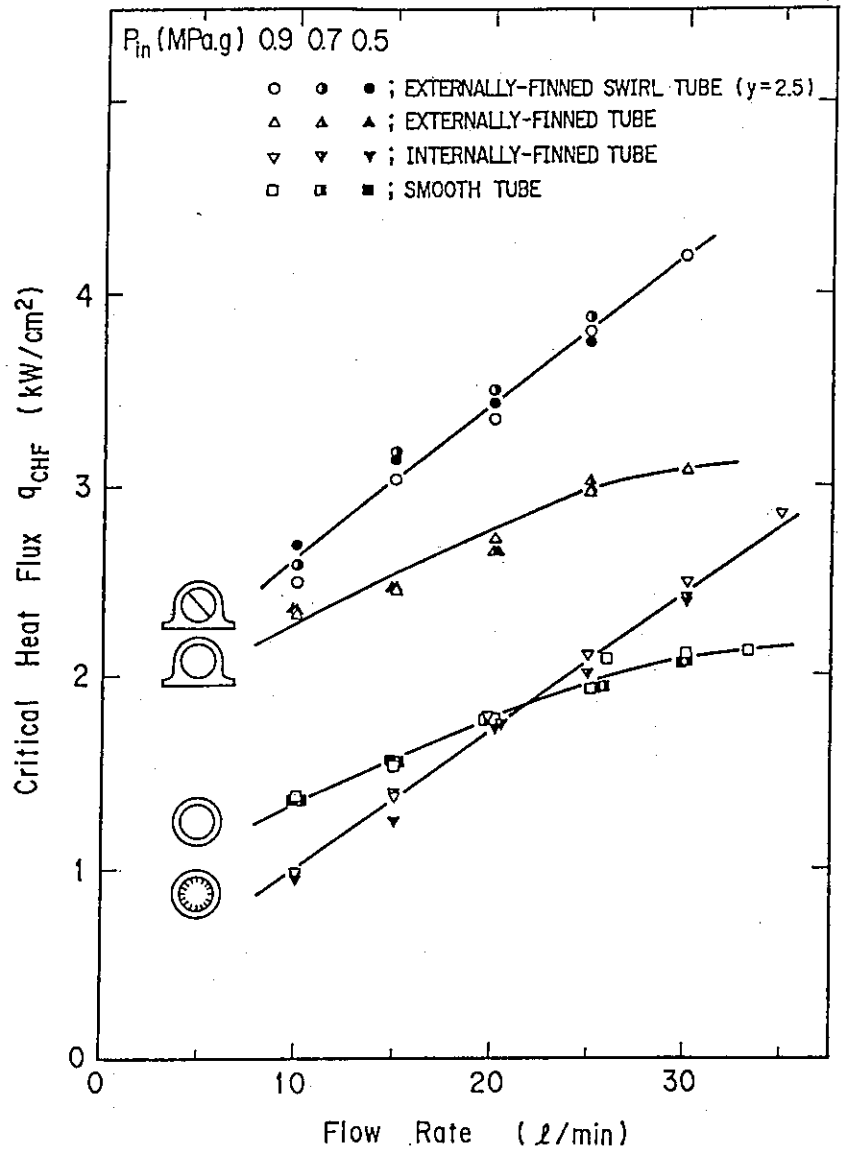

Fig. 8.9.1 Burnout heat flux for various tubes.

9. Vacuum Vessel and Shield

9.1 Low resistance vacuum vessel

Basic structure of the vacuum vessel in a fusion reactor is influenced very much by the required break down voltage to form the plasma current. Design values of the applied voltage and the one turn resistance are 300V and 1.3mΩ in the original JT-60, respectively. Similar values are adopted in TFTR and JET. On the other hand, simple and uniform vacuum vessels with the one turn resistance of 0.2mΩ are adopted in DIII-D and JT-60U taking account of the large tokamak experiences. Maximum applied voltage of JT-60U is 36V. Preionization experiments with the electron cyclotron heating (ECH) made a significant progresses with the development of ECH power source. In JFT-2, the break down voltage is reduced from 23V to 12V with 100kW ECH injection. Recent DIII-D experiment shows a reduction of the break down voltage from 10V without ECH to 2V with ECH. Break down voltage for well preionized plasma will be governed by the electron energy confinement characteristics. The energy balance during the current lamp up phase is expressed by the Neo-Alcator scaling as follows,

$$\frac{3n_eT_eV}{P_{ECH}} = cR^2an_eq \qquad (9.1.1)$$

This relation leads to $T\sim(R/a)P_{ECH}$. With this relation, resistive one turn voltage for the SSTR is estimated as $\sim 0.1V_L$(DIII-D)=0.2V for the ECH power of 5MW. The applied surface voltage is calculated by,

$$V_{sur} = \frac{d(L_pI_p)}{dt} + \Omega_pI_p \qquad (9.1.2)$$

The shield effect of the vacuum vessel reduces the applied voltage and the surface voltage is expressed as follows,

$$V_{sur} = V_{app} - L_v\frac{dI_v}{dt} = V_{app}(1-e^{-t/\tau}) \qquad (9.1.3)$$

The self inductance of the vacuum vessel is ~4μH and $0.63V_{app}$ penetrates into the vacuum vessel within 1 second for the one turn resistance of 4μΩ. The applied voltage of 4V is enough for the current ramp up rate of $dI_p/dt\sim 0.1$MA/sec even including the resistive voltage of 1V. The induced current in the vacuum vessel is less than 1MA which produces ~200G vertical field. So there is no serious issue for the plasma current initiation by cancelling this field with the pre vias field. This significant reduction of the one turn resistance to 4μΩ simplifies the vessel structure. Moreover, this low resistance vacuum vessel can shield the time variation of the magnetic field during plasma disruption which simplifies the design for the AC loss. This vessel is also effective in stabilizing the vertical instability to low frequency regime and in reducing the capacity of the power supply .

9.2 Selection of the Type of the Vacuum Vessel for SSTR

The main functions required by the vacuum vessel and the shield structure are the formation of vacuum boundary as a plasma confinement vessel, neutron shielding, one-turn resistance to toroidal direction, and structural strength.

Until recently, in order to satisfy these requirements, the structure of the vacuum vessel has been adopted either by a resistive element type which installs resistive elements in the toroidal direction, or by a uniform resistive type which separates the shield structure from the vacuum vessel, which is composed by double walls, both electrically and structurally.

Resistive element type vacuum vessel; the reference design of ITER vacuum vessel is shown in Fig.9.2.1 as one example of this structural concept. The structure of the vacuum vessel consists of a shield structure with the necessary thickness to shield the neutron, some resistive elements and electrical insulations to keep the one-turn resistance of the vacuum vessel, and the protection shields to suppress the nuclear heating in the resistive elements.

Joule heating is generated in the resistive elements by the eddy current induced on the vacuum vessel during a plasma disruption. Therefore, sufficient heat capacity is required in the resistive elements to accept the joule heating, and sufficient strength and a reliable support mechanism are necessary to endure the magnetic force.

Uniform resistive type vacuum vessel; the reference design of FER vacuum vessel is shown in Fig.9.2.2. Because the shield structure is separated from the vacuum vessel both electrically and structurally, the structural strength and the one-turn resistance (except the shielding efficiency) are required on the vacuum vessel. For example, the vacuum vessel keeps the one-turn resistance without any resistive element and bellows by adopting a double-thin-wall structure, and holds the structural strength by suitable arrangements of square pipes between the double walls. However, in this structure, a certain support mechanism between the vacuum vessel and the shield structure is required to support each other. The requirements of enduring the magnetic force during a plasma disruption, of keeping the electrical insulation between the vacuum vessel and the shield structure, and of absorbing the thermal expansion between these components conflicting with the previous two items, must be satisfied at the same time in this support mechanism. Therefore, a support concept with reliability and feasibility, at the connecting structure between the vacuum vessel and the shield structure, is required for the uniform resistive type vacuum vessel.

As described in the foregoing section, due to recent progress of the plasma technology, such as decrease of the loop-voltage for plasma ignition by ECH, it has been possible to reduce the one-turn resistance of the vacuum vessel up to several μΩ. For example, when the vacuum vessel of SSTR is composed of stainless steel and water, a wall thickness of about 100 cm will be necessary for neutron shielding and an effective thickness less than 15 cm will be required for several μΩ one-turn resistance, on the contrary, in a conventional design of the vacuum vessel.

Then, the uniform resistive type vacuum vessel based on the new concept which satisfies one-turn resistance, shielding efficiency, structural strength, and structural simplicity at the same time is introduced in SSTR by means of integrating the shield structure with the vacuum vessel without electrical connection. The structure of the vacuum vessel for SSTR is shown in Fig.9.2.3. The vacuum vessel is composed of a double-thin-wall (consisting of an inner skin and an outer skin), the reinforcement plates welded between these skins in both toroidal and poloidal directions, and the shielding units installed in each chamber with electrical insulation from these skins and plates. As a result, holding necessary shielding thickness and keeping several μΩ one-turn resistance can be realized at the same time. However, it is necessary in this concept to insulate the vacuum vessel electrically from the in-core structure (such as the blanket) from the viewpoint of keeping one-turn resistance of the vacuum vessel.

The characteristics of this new type vacuum vessel are summarized as follows.

• Necessary shielding thickness and several μΩ one-turn resistance are achieved at the same time, in spite of adopting the uniform resistive type vacuum vessel.

• Because of the simple structure of the vacuum vessel, it has much flexibility in the structural design. For example, it is possible to sectionally reinforce the vacuum vessel by suitable arrangements of the reinforcement plates.

• The in-core structure can be simplified by adopting this simple concept of installing the shielding units into each chamber without any support mechanism.

• The reliability of the vacuum vessel will be improved and a cost reduction will be expected because of the simplification of the in-core structure and the improvement of quality for manufacturing of the vacuum vessel.

When the characteristics of this concept are compared with the conventional structural concept from the viewpoint of the design of tokamak machine, they will be described as follows.

(1) Effect on the poloidal coils

From the viewpoint of plasma ignition, it is required to increase the one-turn resistance of the vacuum vessel. On the other hand, decrease of the one-turn resistance is required for the protection of the power supply system and the coil system during a plasma disruption. Especially, the selection of the value of the one-turn resistance can greatly affect the design of the poloidal coil system.

In both uniform resistive type and resistive element type, the one-turn resistance of the vacuum vessel can be set optionally (several μΩ ~ several scores μΩ). The vacuum vessel of FER, uniform resistive type, and ITER, resistive element type, are designed on the one-turn resistance of about 20 μΩ. Because the one-turn resistance of SSTR vacuum vessel is several μΩ by adopting the uniform resistive and built-in shield structure type considered in recent progress of plasma ignition technology, the protection of the poloidal coil system is very effective.

There is another type vacuum vessel concept which is called break type. When adopting this type, an excessive voltage will be generated on the power supply system and the coil system during a plasma disruption. Therefore, the shunt-resistances are installed at the electrical insulated parts of the break type vacuum vessel in order to protect the damage of the poloidal coil system. If the break type vacuum vessel is adopted for SSTR, extremely large shunt-resistance will be required in consideration of the joule heating generated on the resistance during a plasma disruption. Moreover, if the quality for manufacturing and the maintenance for damage or repair of the shunt-resistance are considered, the feasibility of the break type vacuum vessel as the steady state rector can be judged to be extremely small.

(2) Quality for manufacturing of the vacuum vessel

When the resistive element type vacuum vessel with several scores μΩ one-turn resistance is adopted, the structure of the resistive part becomes extremely complex as shown in the example of ITER design, Fig.9.2.1.

Because sufficient heat capacity is required in the resistive elements to accept the joule heating during a plasma disruption, a wide space is necessary to install the several scores μΩ resistive elements as shown in Fig.9.2.1. In addition, to suppress the nuclear

heating of the resistive elements, the protection shields are installed internally in the vacuum vessel. Moreover, a generation of large thermal stress is expected in these elements and it is necessary to develop the support structure considering the thermal expansion of the elements.

Though the coolant channels are required in the vessel wall according to the shielding condition, it is difficult to flow the cooling water into such a complex divided structure.

In the case of several μΩ one-turn resistance of this type vacuum vessel, the resistive elements can be thick and short to be installed within a narrow area where shielding performance will not be affected so much, and can be a simpler structure.

Because SSTR vacuum vessel takes the simple structure, only installing the shielding units into each chamber of the uniform resistive type vacuum vessel, the support mechanism of the shield structure is not necessary. Therefore, the structure of the vacuum vessel can be further simplified, and the reliability and the quality for manufacturing can be improved.

(3) Efficiency of the twin-loop shell

The shell performance is required on in-core structure to stabilize the vertical plasma position. Some methods to form a saddle-loop shell on the wall of the blanket, in-core structure that is closest to the plasma, or to compose a twin-loop shell by coupling the currents induced on both vacuum vessel and shell element (which is installed on the blanket like a headband) are considered for the shell structure.

The saddle-loop shell method is a method to connect the induced currents flowing to the opposite direction on the upper and the lower shell by using the side wall of the blanket. Therefore, the distance flowing the induced current is long in the poloidal direction and the response for the vertical plasma positioning is not so well. Moreover, it is necessary to consider the interference of the saddle-loop path with each port in the port layout design.

On the other side, the twin-loop shell method is considered to be technologically better than the saddle-loop shell method, because of the good response for the vertical plasma positioning by the shorter current path in the blanket and the flexibility for the in-core structure design such as the port layout design.

Because the uniform resistive type vacuum vessel is adopted in SSTR, the walls of the vessel and the blanket can form the twin-loop shell by itself. In addition, because the one-turn resistance of the vacuum vessel is as small as several μΩ, the induced current will flow more easily in the vessel wall and the efficiency of the twin-loop shell will be more effective.

In the resistive element type vacuum vessel, the efficiency of the twin-loop shell decreases compared to that of the uniform resistive type vacuum vessel due to the complex current loop in the resistive element.

(4) Electromagnetic force

The electromagnetic force produced on the vacuum vessel and the shield structure has the following characteristics according to the type of the vacuum vessel.

In the case of the resistive element type vacuum vessel; because the poloidal component of the induced currents is generated at both ends of the resistive element parts, the electromagnetic force increases at those areas relatively.

In the case of the uniform resistive type vacuum vessel; because the induced current on the general part of the vacuum vessel is generated in the toroidal direction fundamentally, the electromagnetic force becomes smaller than the previous type vacuum vessel. However, the poloidal component of the currents on the vessel wall is produced by the eddy currents flowing around the ports and the large electromagnetic force is generated by the coupling of the currents with the toroidal magnetic field.

Because of the simple structure of SSTR vacuum vessel, the structural flexibility is large and it is easily possible to sectionally reinforce the vacuum vessel at the areas of high magnetic force by suitable arrangements of the reinforcement plates.

(5) Port layout design

In the case of the resistive element type vacuum vessel, a careful design is required, not to interfere with the resistive parts of the vacuum vessel, for the port layout design. Especially, careful consideration is required in the layout design of the tangential port such as NBI port.

Such problems will not occur in the uniform resistive type vacuum vessel.

(6) Support structure of the vacuum vessel

In the case of the resistive element type vacuum vessel; because the vessel is required to have the shielding performance by itself and composed of thick wall, a direct support system is generally adopted.

In the case of the uniform resistive type vacuum vessel with several scores μΩ one-turn resistance; because the vessel is required to be a separate type composed of a double-thin-wall structure, in order to keep the one-turn resistance, a direct support system from the thin wall can not be adopted. Therefore, the indirect support system, which directly supports the stiff shield structure and holds the vacuum vessel through the shield structure, is generally adopted.

For the sake of high flexibility of SSTR vacuum vessel, the direct support system can be adopted by suitable arrangements of the reinforcement plates near the areas of support points.

The result of above comparison is summarized in Table 9.2.1.

Table 9.2.1 Comparison of the type of vacuum vessel

Item	Uniform resistive type vacuum vessel (built-in shield structure type : SSTR type)	Uniform resistive type vacuum vessel (separate shield structure type : FER type)	Resistive element type vacuum vessel (ITER type)	Remarks
Effects on the poloidal coils	Very good for low resistive type vacuum vessel ($\sim 4\mu\Omega$).	Good for $\sim 20\mu\Omega$ resistant vacuum vessel.	ditto	Break type vacuum vessel concept would not be avail -able because of its lack of feasibility and relia -bility for steady state commercial reactor.
Quality for manufacturing	Very good because of simple structure without support mech -anism for shield structure.	Good, but support mechanism between shield structure and vacuum vessel is necessary.	Not so good. Because of the complicated design for vacuum vessel.	
Efficiency of twin-loop shell	Very good for low resistive type vacuum vessel ($\sim 4\mu\Omega$).	Good for $\sim 20\mu\Omega$ resistant vacuum vessel.	Not so good. Because of the complicated current loop at the part of resistive element.	———
Electromagnetic force	Very good because of the high flexibility for structural design.	Good, but high stress would be produced by eddy current arround the ports.	Not so good. High stress would be produced at the resistive parts of the vessel.	———
Port layout design	Good.	Good.	Not so good. Careful design is required not to interfere with the resistive parts.	———
Support structure	Good because of the high flexibility for structural design.	Not so good. Because of the indirect support system through the shield structure.	Very good. Rigid and direct support system is available.	———

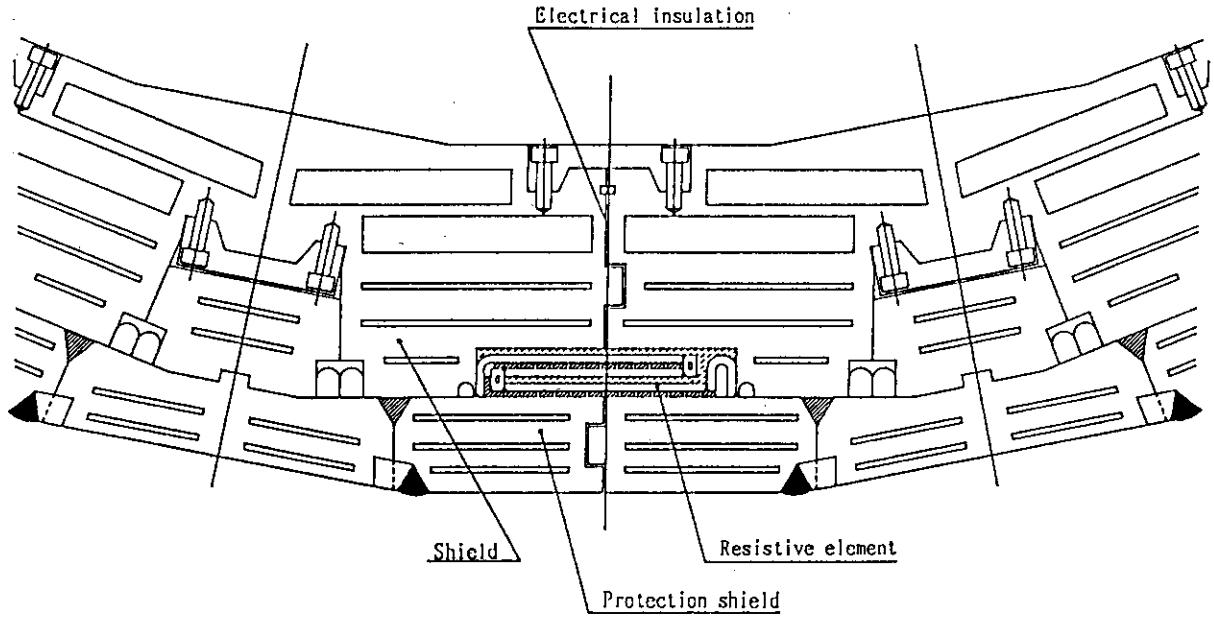

Fig. 9.2.1 Reference vacuum vessel design for ITER.

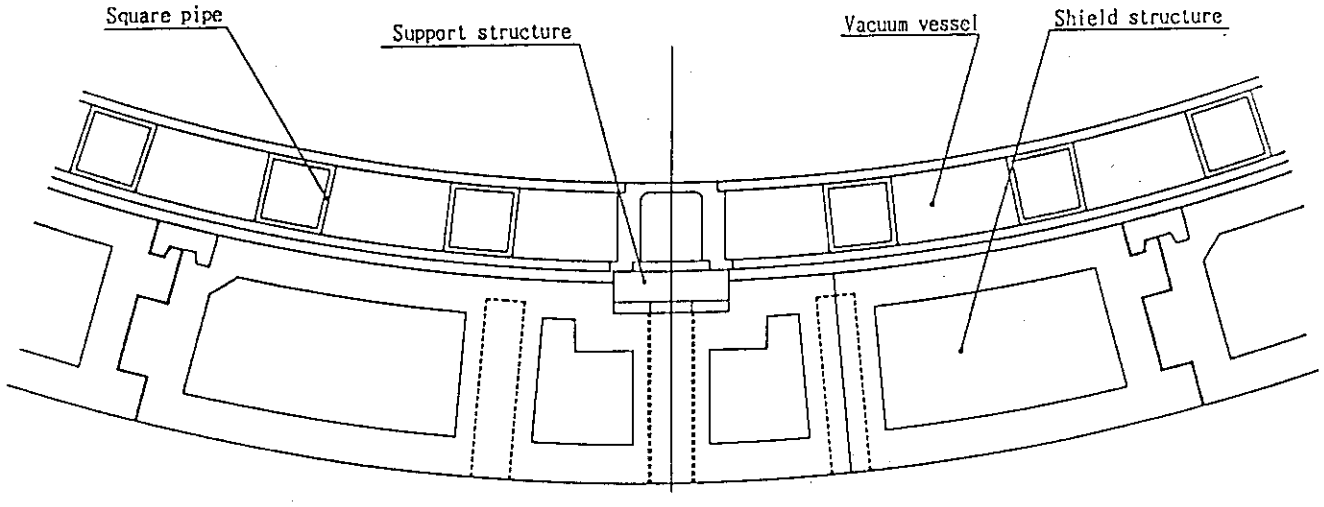

Fig. 9.2.2 Thin-wall vacuum vessel design with separate shield structure for FER.

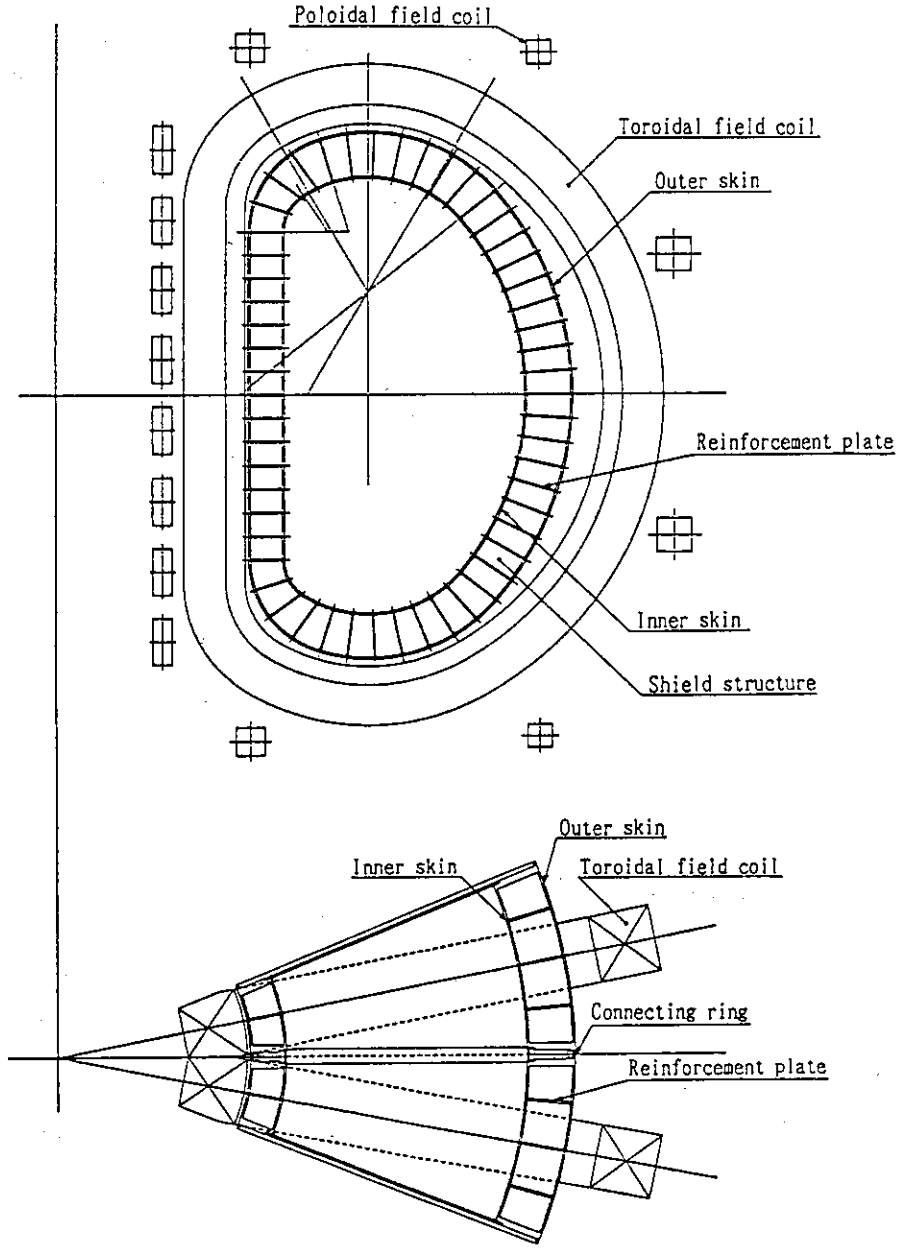

Fig. 9.2.3 Plan view of SSTR vacuum vessel.

9.3 Structural Design of the Vacuum Vessel

9.3.1 Detail Dimension of Vacuum Vessel and Layout Study of In-core Structure

The main items to decide the basic shape of the vacuum vessel are summarized as follows :

- radial-build and vertical-build
- the shape of the toroidal coil
- required space between the vacuum vessel and the toroidal coil
- required thickness for neutron shielding
- the shape of plasma including the width of the scrape-off layer
- required thickness of the blanket including the space for the support structure
- required space for the divertor region

Based on the radial-build which defines the relative location of in-core structure on the mid-plane, the shape of the poloidal cross section of the vacuum vessel should be determined as follows.

The elevation view of SSTR in-core structure layout is shown in Fig.9.3.1. The distance between the double walls is determined 650 mm / 900 mm on the inboard side / outboard side mid-plane respectively from the requirements for shielding design. The shapes of the inner skin and the outer skin at the poloidal cross section consist of several circular arcs gradually increasing the distance between the two skins, in consideration of the shielding effect, the interference with the in-core structure, and following items.

The gap between the vacuum vessel and the shield structure should be determined by considering the structure of the thermal insulation for large thermal difference between the normal temperature of the vacuum vessel and the liquid-He temperature of the toroidal field coil, the thermal expansion or contraction of those structure, the space required for assembling and constructing main components, and other factors. Therefore, this gap is determined 80 mm at the inboard side and more than 100 mm at the other areas of the vacuum vessel. However, more detail researches concerning the structure of the thermal insulation and the manufacturing accuracy will be required in the future for maintaining these severe spaces.

On the other hand, the shape of the inner skin of the vacuum vessel is determined from the layout of the in-core structure based on the plasma configuration. That is, the

inner surface of the blanket takes the shape along the plasma considering the installation of the plasma stabilization shell, and the thickness of the blanket is enlarged to maximum extent to keep sufficient tritium breeding ratio. In addition, the shape of the divertor is determined so as to keep the distance of 1.2 m between the striking point and the null point of the plasma on the outboard side and consider the maintenance and the accessibility from the divertor port.

Though the shape of the plasma is unsymmetrical between the upper and lower halves because of the single-null configuration, the shape of the vacuum vessel should be symmetrized, considering the space for the divertor region, the quality for manufacturing, and other factors. The detail dimension of the vacuum vessel based on the above result is shown in Fig.9.3.2.

9.3.2 Basic Structure of the Vacuum Vessel

(1) Structure of the vacuum vessel

As described in the section 9.2, SSTR vacuum vessel has double-thin-wall structure with the inner skin and the outer skin, and the structural strength of the vacuum vessel is held by both skins and the reinforcement plates welded in both toroidal and poloidal direction between these skins. These skins and plates are made of stainless steel with 50 mm thickness. In addition, the shielding units are installed in each chamber of the vacuum vessel in order to shield the neutron. These shielding units are not considered as the strength members. The reference design of SSTR vacuum vessel is shown in Fig.9.3.3.

The vacuum vessel has the vertical ports for the extraction of the removable blanket; the horizontal ports for N-NBI, ECH, pellet injection, and maintenance; and the lower-diagonal ports for the vacuum exhaust and the extraction of the divertor.

The vertical port has to occupy large bore for the extraction of the removable blanket. Therefore, the vertical port is composed of a single plate with 100 mm thickness by installation of the shielding plug in it. The horizontal port and the lower-diagonal port are composed of the double-twin-wall structure, with the shielding units in each chamber, as well as the structure of the vacuum vessel. The standard interfaces with the vacuum vessel for each port are shown as follows.

- Elevation view of SSTR vacuum vessel and port layout : Fig.9.3.4
- Standard interface for N-NBI port : Fig.9.3.5

- Standard interface for the divertor port : Fig.9.3.6
- Standard interface for the vertical port : Fig.9.3.7

(2) Structure of the shielding unit

The structure of the shielding unit is shown in Fig.9.3.8. The shielding unit is composed of several shield plates coupling each other with the connecting rods and the spacers, which locate the plates according to the shielding condition. Each space between these shield plates is filled with cooling water circulating through the vacuum vessel to perform the shielding effect. The cooling water flows in and out from the manifold installed on the vacuum vessel, as shown in Fig.9.3.9, and circulates through the coolant channel bored in the reinforcement plates. Moreover, in order to keep the one-turn resistance of the vacuum vessel, it is necessary to insulate the shielding units from the vacuum vessel electrically by means of surface treatment such as ceramic coating (e.g. alumina spraying) on the surface that is in contact with the vacuum vessel.

(3) Support structure of the vacuum vessel

The function required for the support structure of the vacuum vessel is to hold the forces such as dead weight of the vacuum vessel, electromagnetic force, seismic load, and so forth. Moreover, it is necessary to release the thermal expansion of the vacuum vessel under baking condition because the vacuum vessel is a rigid structure in itself. In addition, the support structure has to be designed in consideration of the electrical insulation between the vacuum vessel and the base, the quality for manufacturing, the space for setting, and so forth.

There are some support mechanisms as follows.

- low-rigid support mechanism

The advantages of this method enable minimized setting space and well-balanced release of thermal expansion of the vacuum vessel. In contrary, the disadvantages are the low stiffness of the support structure for a horizontal load such as seismic loads and generation of bending moments at the support point of the vacuum vessel.

- slide type support mechanism

The advantage of this method is having no unexpected vibration and no excessive deformation because of the well-balanced system in itself. The disadvantages are the necessity of considerably large setting space and the shortage of reliability for the slide mechanism.

• rod-pin support mechanism

Though wide setting space is not required, it is structurally difficult to support a horizontal load by itself.

When the vacuum vessel has the form of torus, such as the tokamak device, the stiffness for a horizontal load can be maintained because some support points are rigid for arbitrary direction load by its radial layout, even if the low-rigid support mechanism is adopted. In result of the above comparison, the spring plate support mechanism is adopted for SSTR support system as shown in Fig.9.3.10 because this method enables reduction of setting space and well-balanced release of thermal expansion of the vacuum vessel. The spring plate support mechanism is also considered as the reference support system for ITER and FER. In addition, to confirm the structural feasibility of this mechanism for SSTR, a simple stress evaluation is held as summarized in Table 9.3.1.

Moreover, the estimation of the weight of each part of the vacuum vessel is also held based on the above basic structure. The volume ratio of stainless steel to water is assumed to be 85 % to 15 % for inboard side to improve the neutron shielding, and 50 % to 50 % for outboard side to reduce the weight and the cost of the vacuum vessel. The result of estimation is summarized in Table 9.3.2.

In the near future, the main items for the research and development on design study of SSTR vacuum vessel are considered as follows :

• Development of a low radioactive material

In order to reduce radioactive wastes at a plant shutdown, it is necessary to develop a low radioactive material for the vacuum vessel.

• Development of technology on electrical insulate treatment like ceramic coating

This new concept of SSTR vacuum vessel can be basically realized to separate the vacuum vessel electrically from the in-core structure such as shield structure, blanket, and so forth. Therefore, it is necessary to develop a technology on electrical insulate treatment which can guarantee the reliability during plant operation. At present, research and development is actively being held at JAERI with successful results.

Table 9.3.1 Result of stress calculation of support structure

	Allowable stress (kg/mm^2)	Calculated stress (kg/mm^2)
Spring plate		
compression stress	7.3	1.3
bending stress	16.1	6.2
Anchor bolt		
tensile stress	30.0	22.4
shear stress	23.0	3.4
Baseplate		
bending stress	46.1	22.0

Note

1) The allowable stress is based on the technical guide of the structure for nuclear power plant (the notification 501 of MITI in Japan).

2) The material is assumed as stainless steel (SUS316 ; JIS-G4304) for spring plate and heat-resisting steel (SUH660 ; JIS-G4311,4312) for anchor bolt and baseplate.

Table 9.3.2 Weight of each part of the vacuum vessel

	Volume (m^3)	Volume percent of s.s. (%)	weight (ton)
Vacuum vessel			
inboard side	257.7	85	1752.4
outboard side	682.8	50	2731.2
total	940.5		4483.6
Port			
vertical port	8.2 X 16	100	1049.6
exhaust duct	59.1 X 16	20	1513.0
horizontal port	54.1 [1] X 6	85	2207.3 [1]
divertor port [2]	47.9 X 16	20	1226.2
total	2167.8		5996.1
Support structure	3.9 X 16	100	499.2
Sum total	3170.7		10978.9

Note

1) This value is the weight per 10 m port length. The horizontal ports include the following 6 ports ;

NBI port	2 sets
Pellet injection port	1 set
ECH port	1 set
Maintenance port	2 sets

2) The weight of removable shield in divertor port is not included.

3) The specific gravity of s.s. is assumed to be 8 ton/m^3.

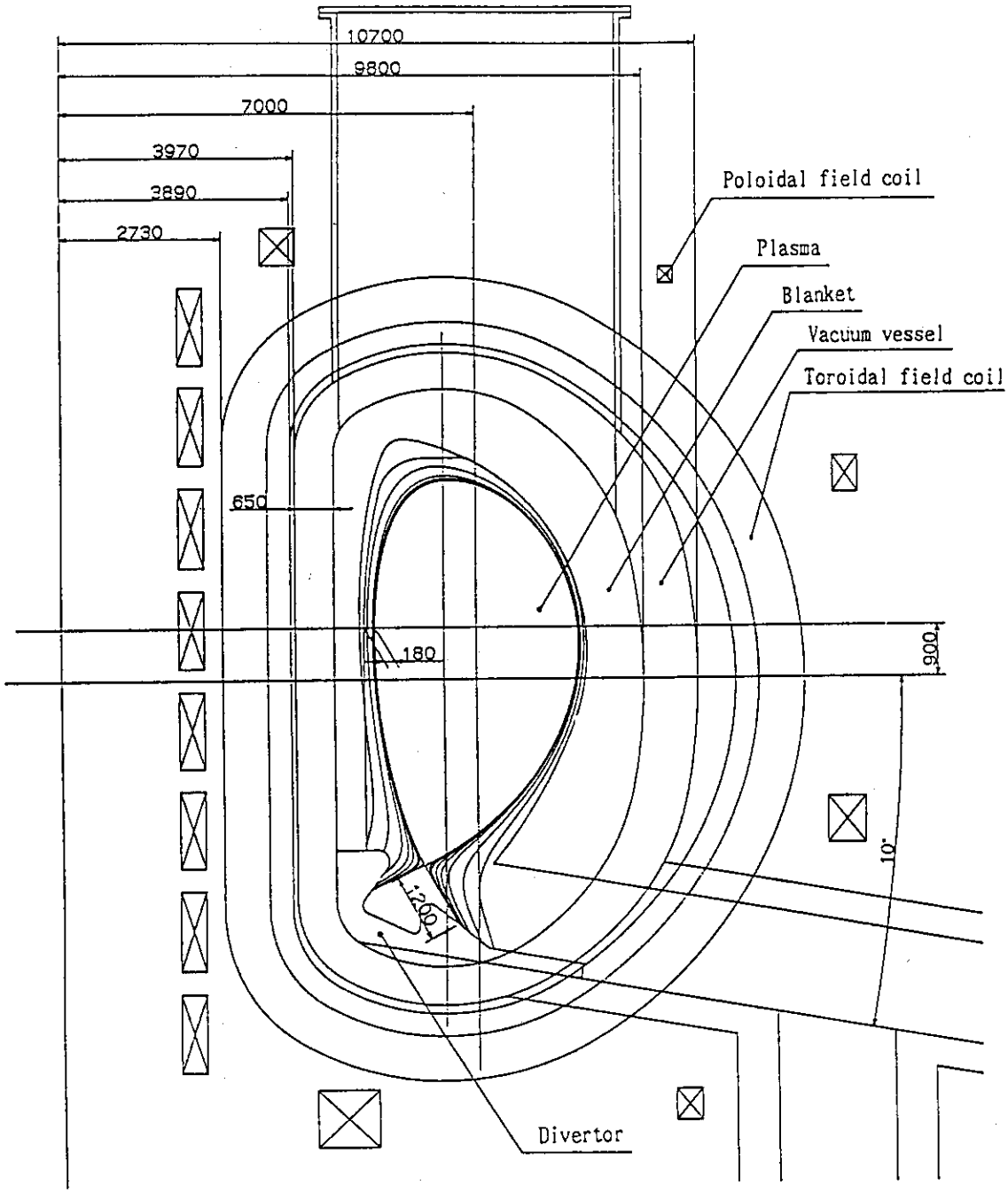

Fig. 9.3.1 Elevation view of SSTR in-core structure layout.

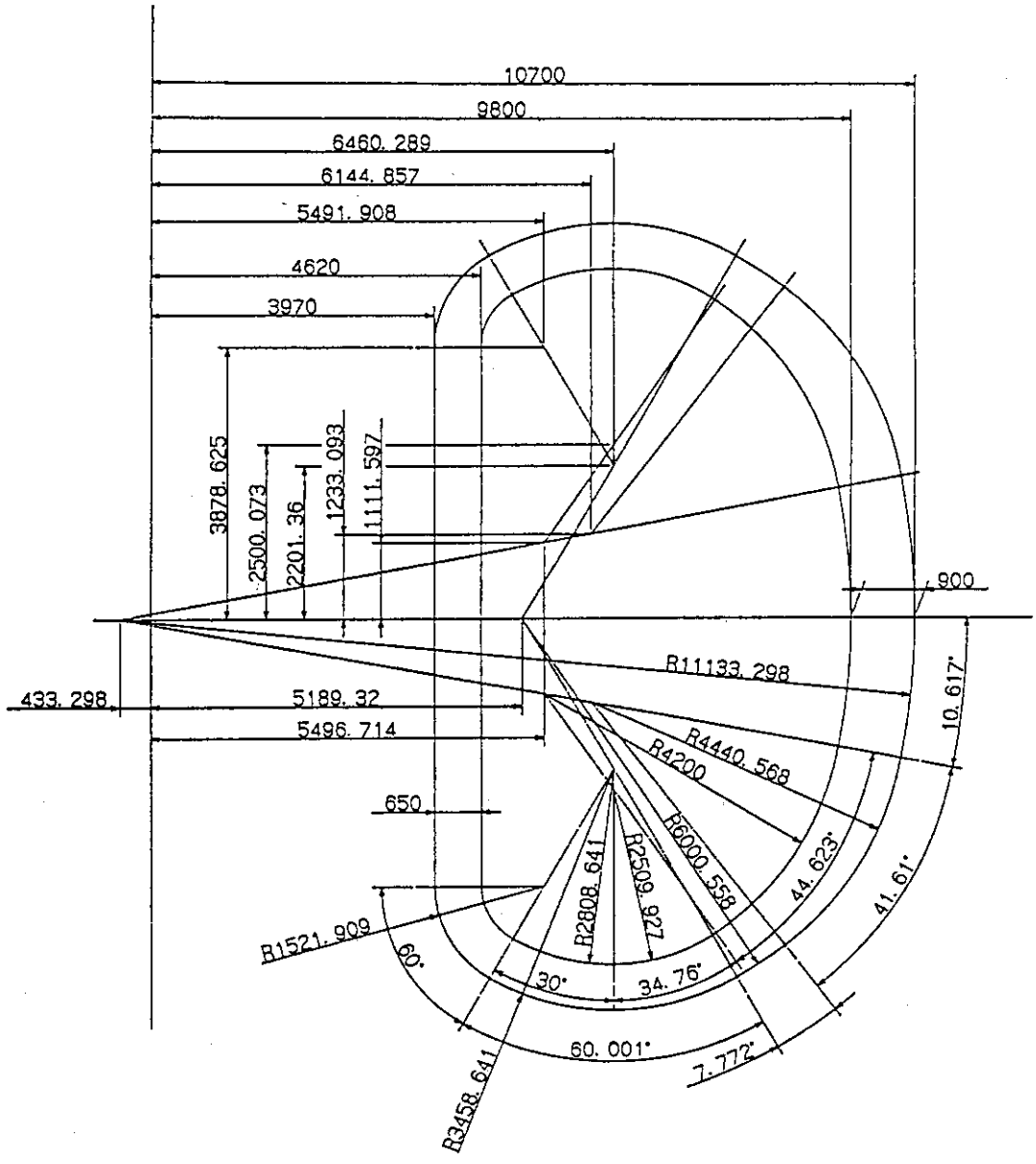

Fig. 9.3.2 Detail dimension of SSTR vacuum vessel.

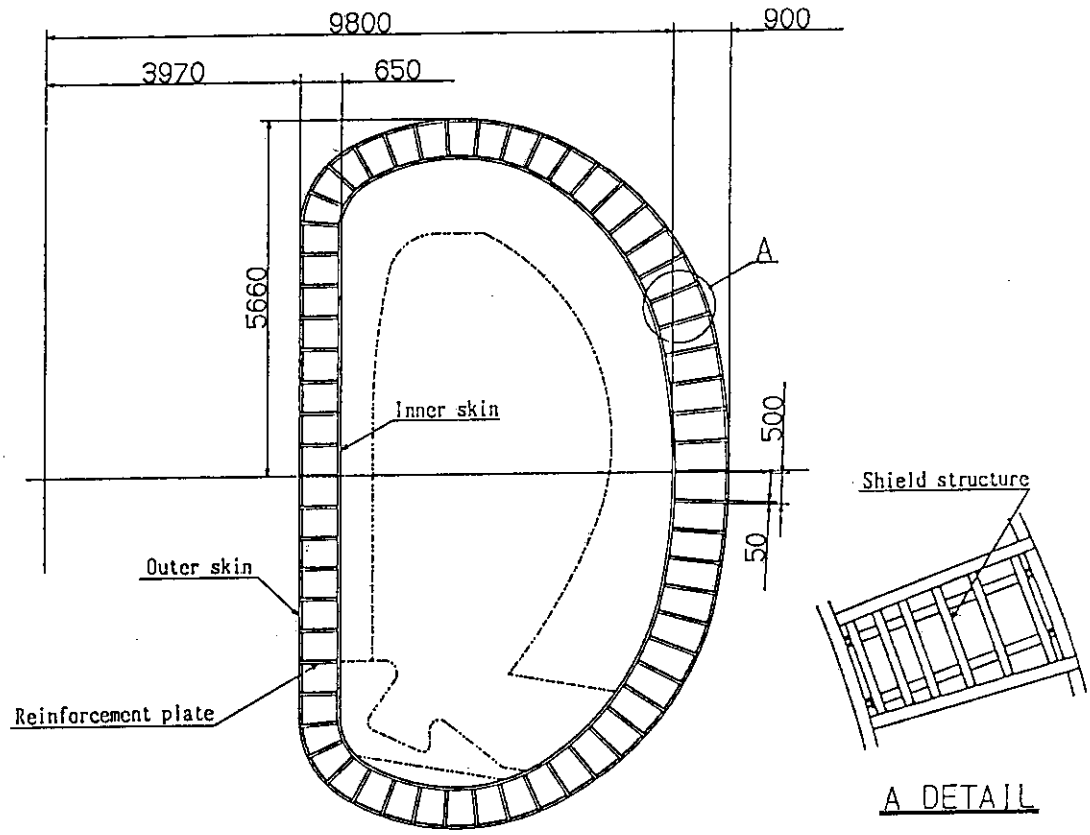

Fig. 9.3.3 Reference design of SSTR vacuum vessel.

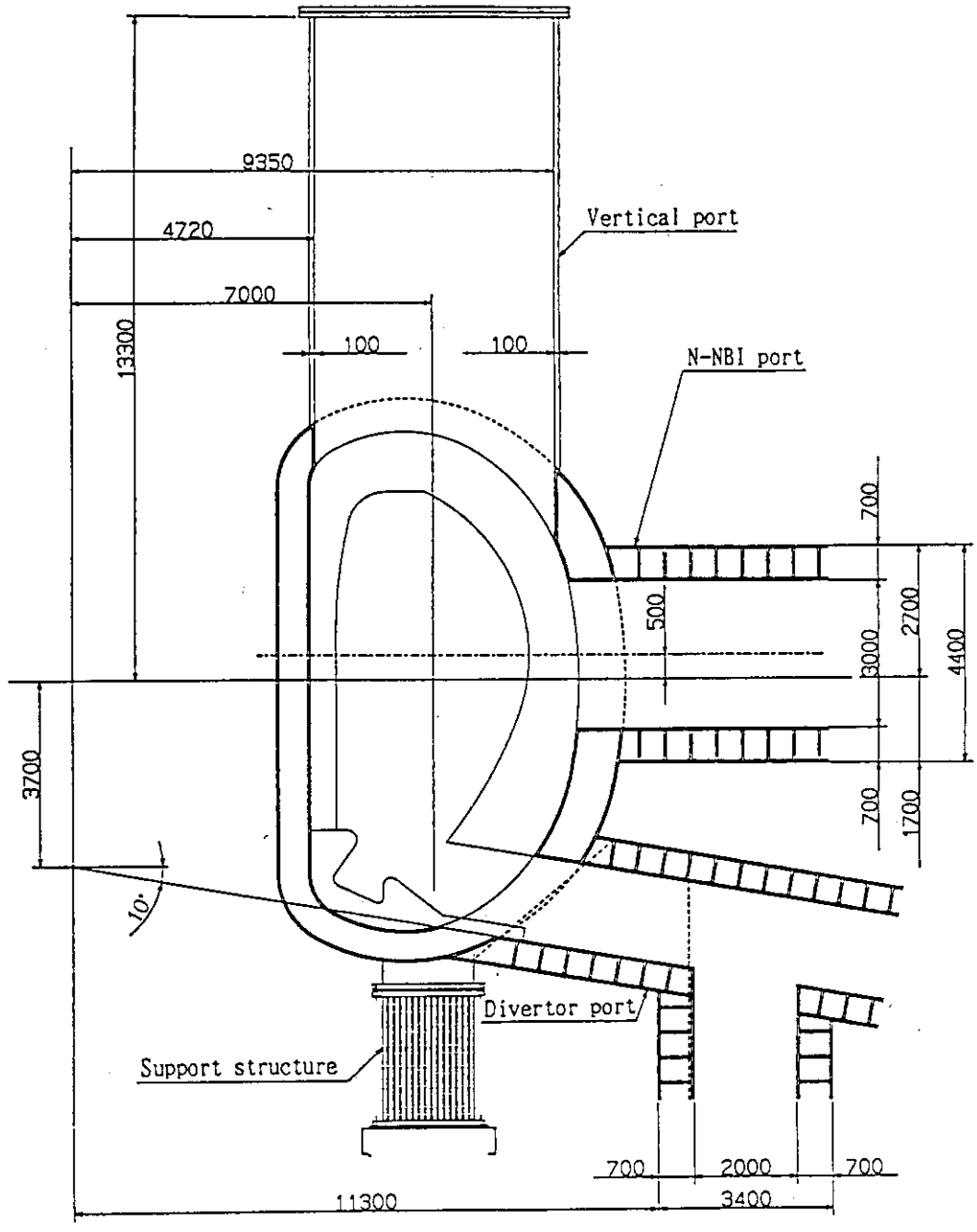

Fig. 9.3.4 Elevation view of SSTR vacuum vessel and port layout.

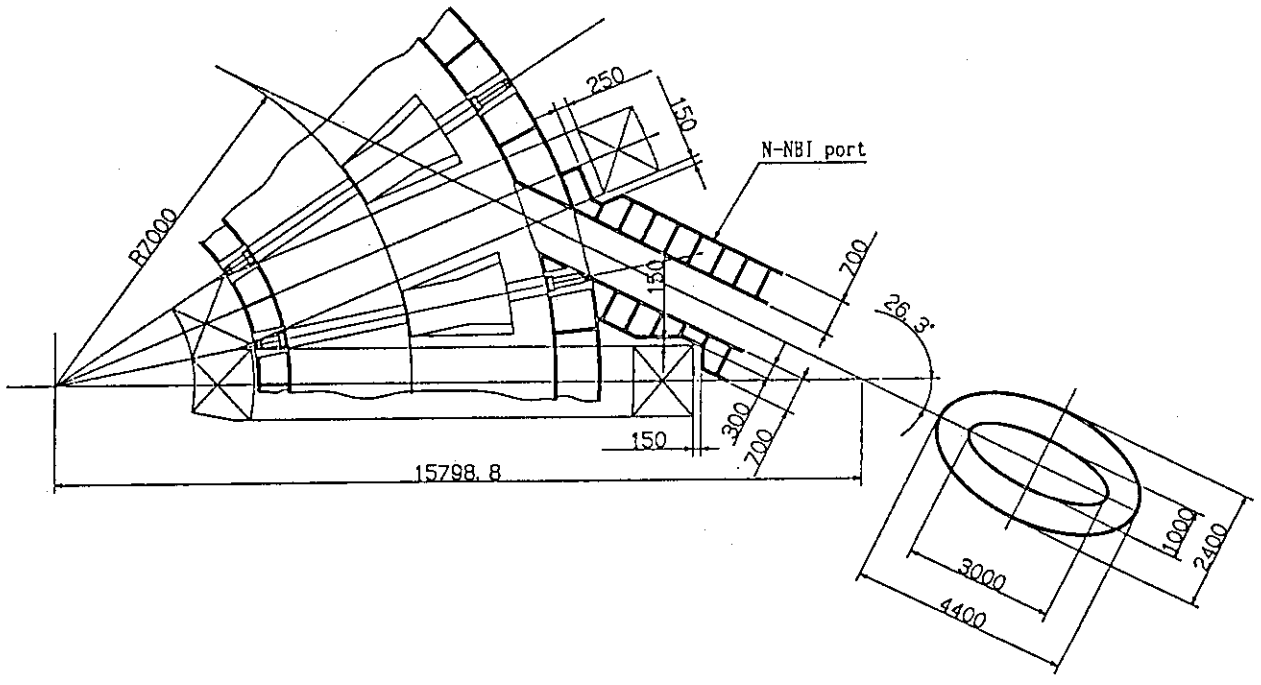

Fig. 9.3.5 Standard interface for N-NBI port.

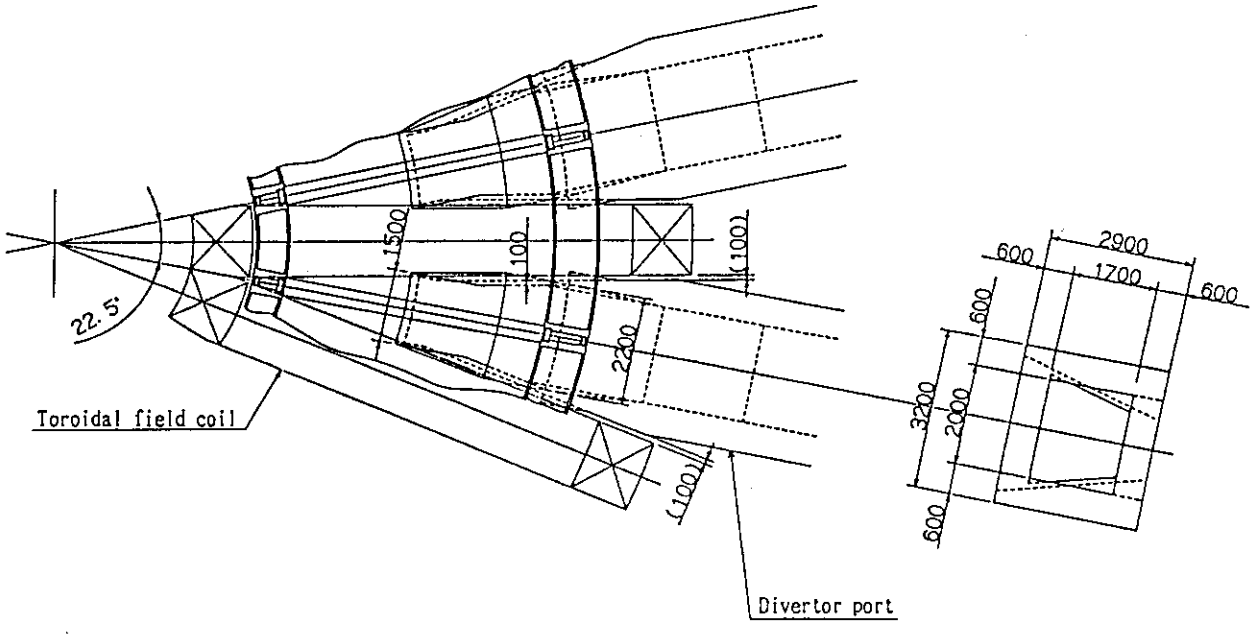

Fig. 9.3.6 Standard interface for the divertor port.

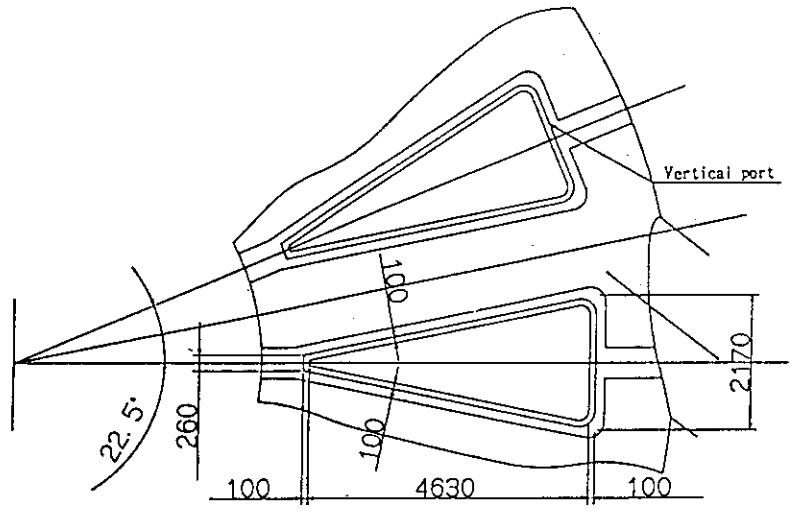

Fig. 9.3.7 Standard interface for the vertical port.

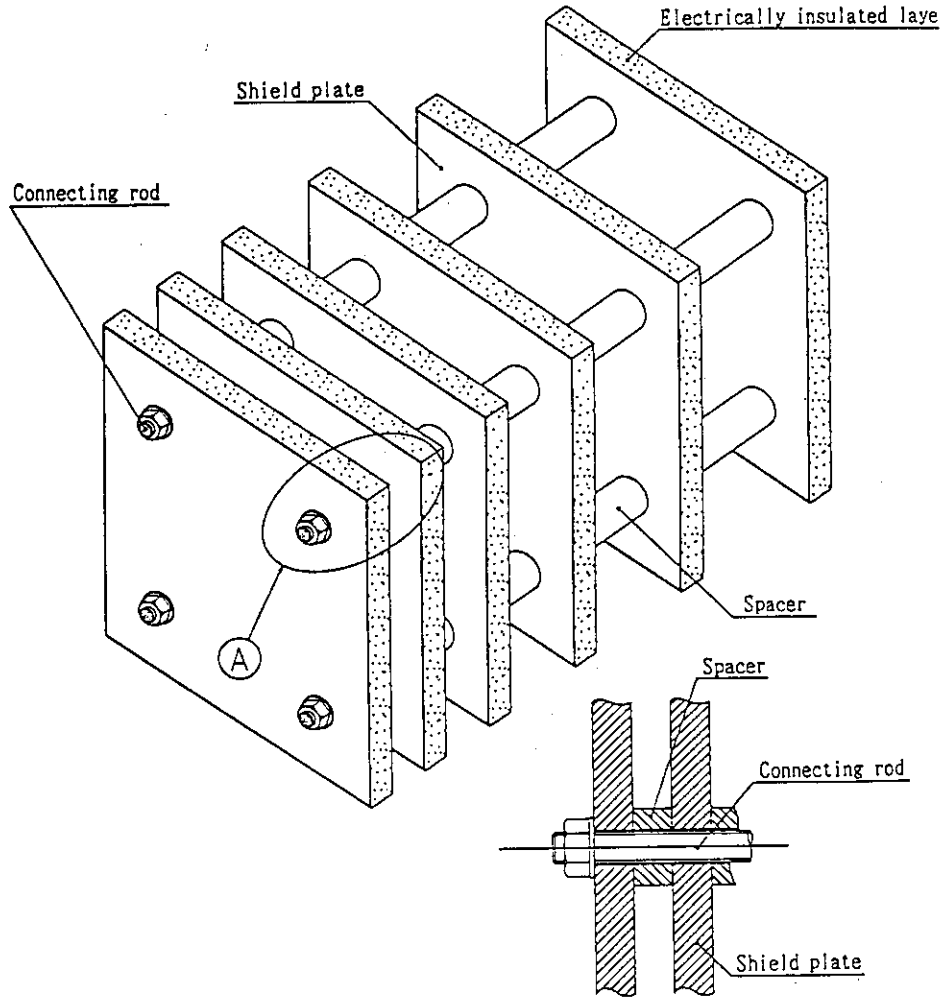

Fig. 9.3.8 Schematic view of the shield structure.

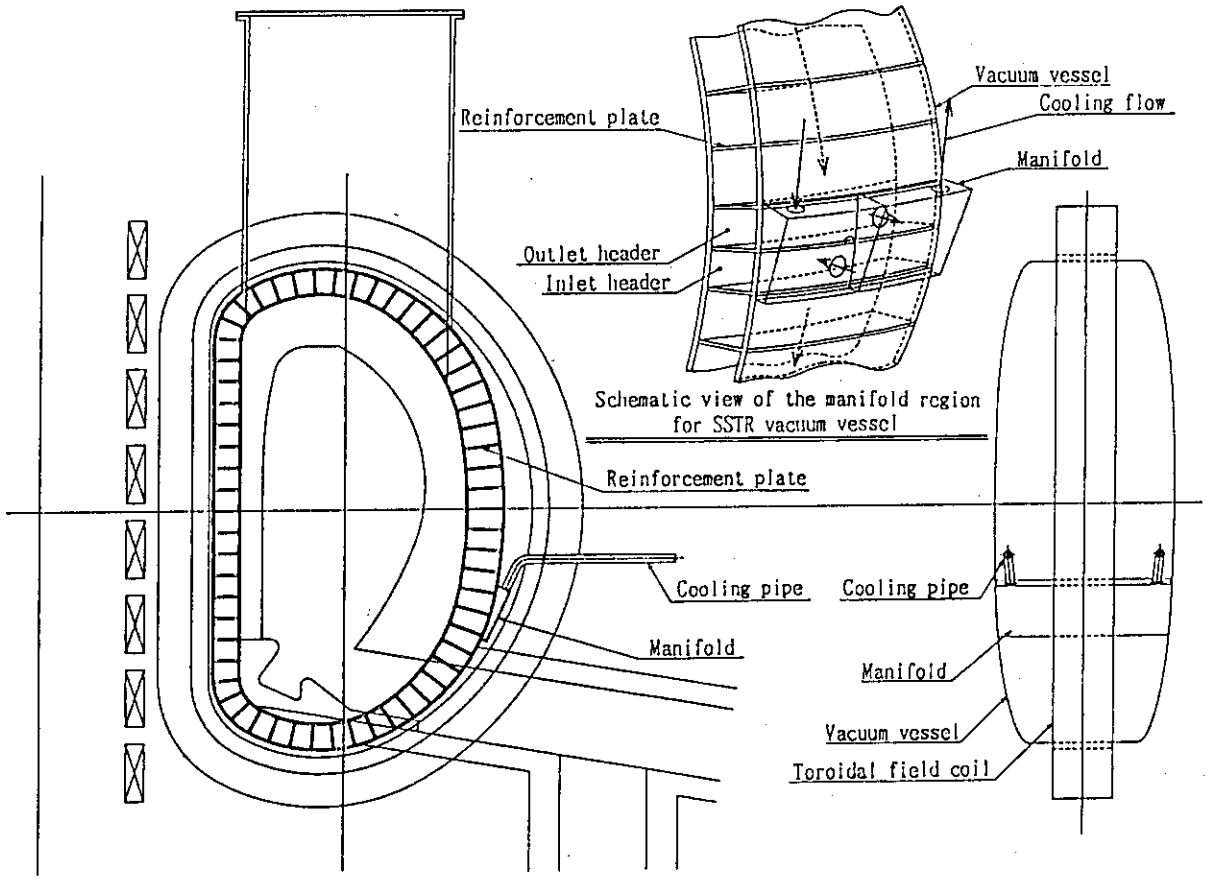

Fig. 9.3.9 Basic concept of cooling pass for SSTR vacuum vessel.

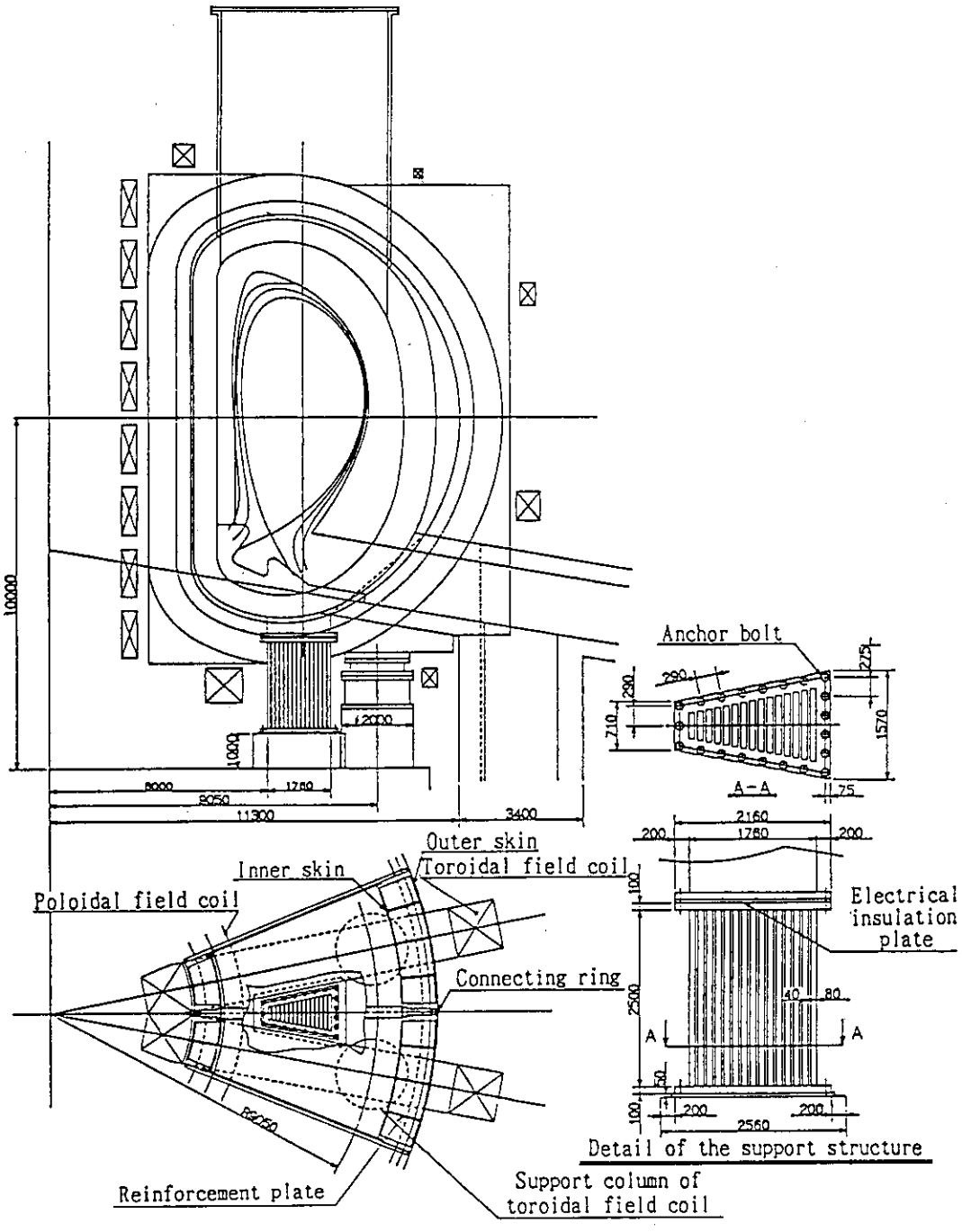

Fig. 9.3.10 Basic concept of the support structure.

9.4 Electromagnetic and Structural Analysis of the Vacuum Vessel

The electromagnetic and structural analysis during a plasma disruption has been performed to study the feasibility of SSTR vacuum vessel concept as described in previous sections. The condition of the plasma disruption is as follows.

- plasma current : 12 MA
- current quench time : 20 ms
- plasma motion : downward motion

(the point at which the plasma current decreases to zero is assumed to be the middle point between the magnetic axis of the plasma and the null point.)

- plasma motion time : 20 ms

Though the eddy current is induced on the vacuum vessel during a plasma disruption, the plasma current is transferred to the inner skin of the vacuum vessel at first, and then, gradually transferred to the outer skin. Therefore, in evaluating the eddy current and the magnetic force produced on the vacuum vessel by the electromagnetic analysis, the estimation is considered to be safe using only inner skin model of double-thin-wall structure. Then, the analysis model is formed of a half sector of the inner skin (11.25 degrees in the toroidal direction) as shown in Fig.9.4.1 in consideration of the toroidal symmetry.

The results of analysis are summarized in Table 9.4.1 and Table 9.4.2. In addition, the distributions of the eddy current and the magnetic force on the vacuum vessel are shown in following figures.

- distribution of eddy current
  - t = 10 msec : Fig.9.4.2
  - t = 20 msec : Fig.9.4.3
  - t = 30 msec : Fig.9.4.4
- distribution of magnetic force (coupling with poloidal + self field)
  - t = 10 msec : Fig.9.4.5
  - t = 20 msec : Fig.9.4.6
  - t = 30 msec : Fig.9.4.7
- distribution of magnetic force (coupling with toroidal field)
  - t = 10 msec : Fig.9.4.8
  - t = 20 msec : Fig.9.4.9
  - t = 30 msec : Fig.9.4.10

Time evolutions of the toroidal one-turn current and the total magnetic force on the vacuum vessel are shown in Fig.9.4.11 and Fig.9.4.12.

For comparison, the electromagnetic analysis without plasma motion has also been performed and the results of analysis are shown in following figures.

- distribution of eddy current
  t = 20 msec : Fig.9.4.13
- distribution of magnetic force (coupling with poloidal + self field)
  t = 20 msec : Fig.9.4.14
- distribution of magnetic force (coupling with toroidal field)
  t = 20 msec : Fig.9.4.15

In result, about 95 % of plasma current is transferred to the inner skin of the vacuum vessel at 20 msec, and intensive eddy current is induced on the inboard side of the vessel and the area among the ports, especially between the horizontal and the vertical port. Therefore, the magnetic force has a maximum at the horizontal and the vertical port walls near the vessel for toroidal coupling and at the area between these ports for poloidal coupling. The results during the disruption without plasma motion are almost similar to those with plasma motion.

The stress analysis of the vacuum vessel has been performed based on the results obtained through the electromagnetic analysis. Three-dimensional model for the stress analysis is formed of one sector (22.5 degrees) of the vessel extended the electromagnetic analysis model as shown in Fig.9.4.16, considering the symmetry of the eddy current components coupled with toroidal and poloidal magnetic field. The double-thin-wall structure in the vacuum vessel and the ports is modeled as a single wall with equivalent stiffness. The conditions for analysis are as follows.

- load condition : magnetic force (moving disruption : t = 20 msec)
- boundary condition : degrees of freedom, except translation in major radius direction, are fixed at the node point within support structure.
- material property : equivalent to stainless steel (SUS316 ; JIS-G4304) with the equivalent stiffness
- analysis code : MSC/NASTRAN

The result of the stress analysis is summarized in Table 9.4.3. In addition, the deformation and the stress distribution on the vacuum vessel are shown in following figures.

- deformation of vacuum vessel : Fig.9.4.17
- stress distribution on vacuum vessel
  - maximum principal stress (top of elements) : Fig.9.4.18
  - maximum principal stress (bottom of elements) : Fig.9.4.19
  - minimum principal stress (top of elements) : Fig.9.4.20
  - minimum principal stress (bottom of elements) : Fig.9.4.21
  - maximum shear stress (top of elements) : Fig.9.4.22
  - maximum shear stress (bottom of elements) : Fig.9.4.23

In result, the stress on the vacuum vessel is almost within the allowable stress. Though the stress produced by toroidal coupling at the partial region near the port joint is intensive, to some extent, it can be reduced to a suitable level by suitable arrangements of the reinforcement plates between the double walls. Therefore, the characteristics of this new type vacuum vessel, such as the flexibility of structural design of the reinforcement plates according to the stress distribution, the feasibility to simplify the in-core structure, and so forth, are confirmed by this design study.

Table 9.4.1 Maximum magnetic force on vacuum vessel (kg/cm^2)

Coupling	Downward motion	Without motion
Poloidal + self field	10.0	8.22
Toroidal field	52.0	58.4

Table 9.4.2 Total magnetic force on vacuum vessel (ton)

Component	Downward motion	Without motion
Fr	20111	20446
Fz	1466	1318

Table 9.4.3 Summary of stress analysis for vacuum vessel

port	Vacuum vessel (general part)	Vacuum vessel (around the ports)	Vertical (port wall)
Displacement(mm)	0.82	5.27	7.57
Stress (kg/mm^2)	1.78	21.6	13.5

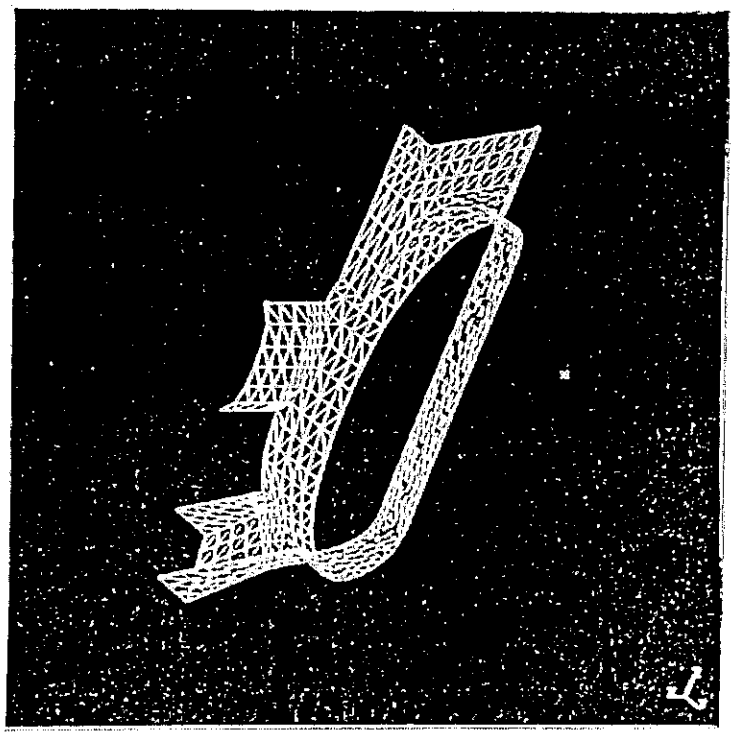

Fig. 9.4.1 Three-dimensional model for electromagnetic analysis.

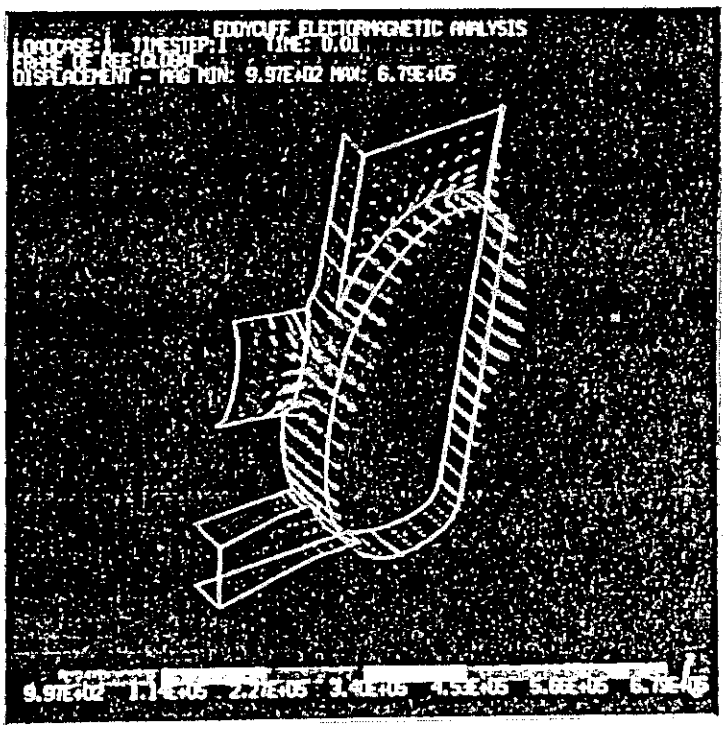

Fig. 9.4.2 Eddy current distribution on the vacuum vessel. (t=10ms)

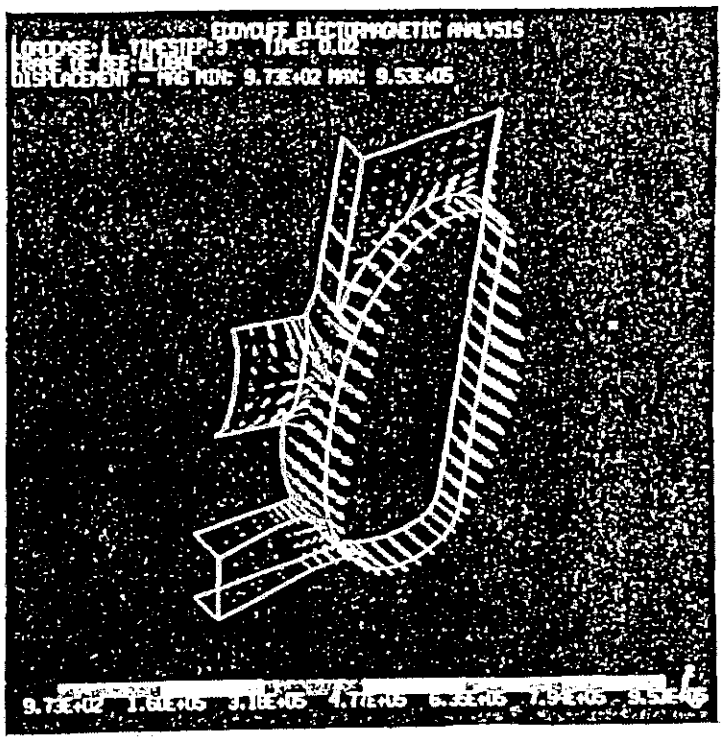

Fig. 9.4.3 Eddy current distribution on the vacuum vessel. (t=20ms)

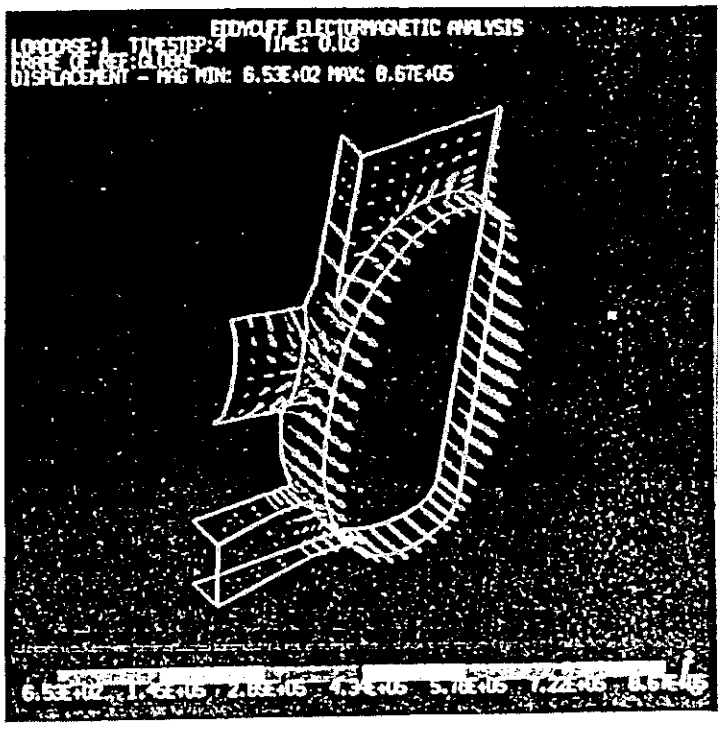

Fig. 9.4.4 Eddy current distribution on the vacuum vessel. (t=30ms)

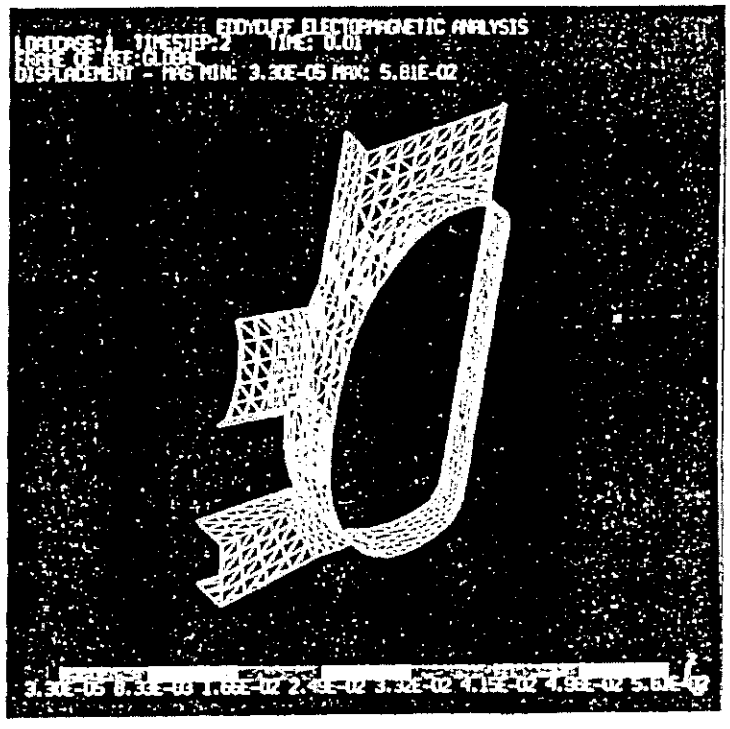

Fig. 9.4.5 Magnetic force distribution on the vacuum vessel for poloidal + self field coupling. (t=10ms)

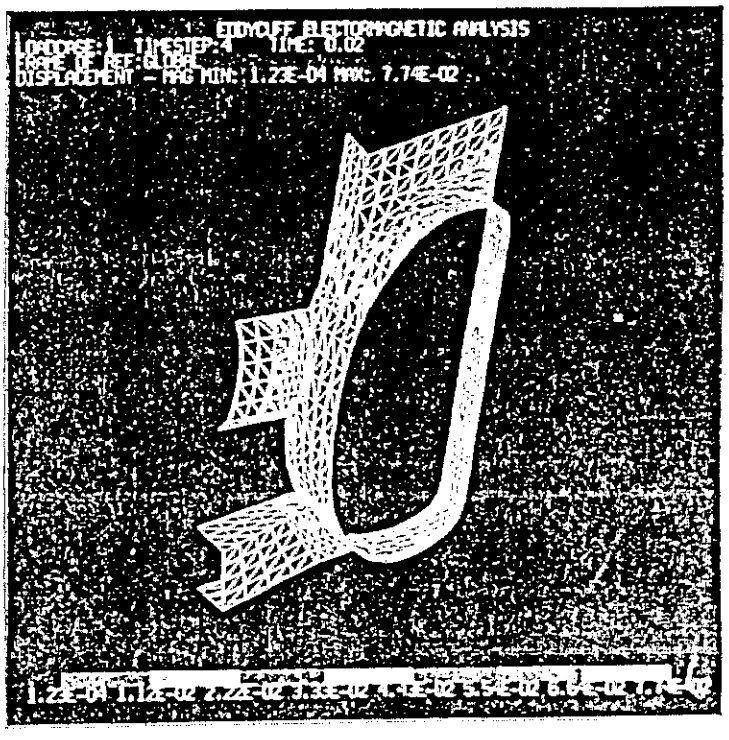

Fig. 9.4.6 Magnetic force distribution on the vacuum vessel for poloidal + self field coupling. (t=20ms)

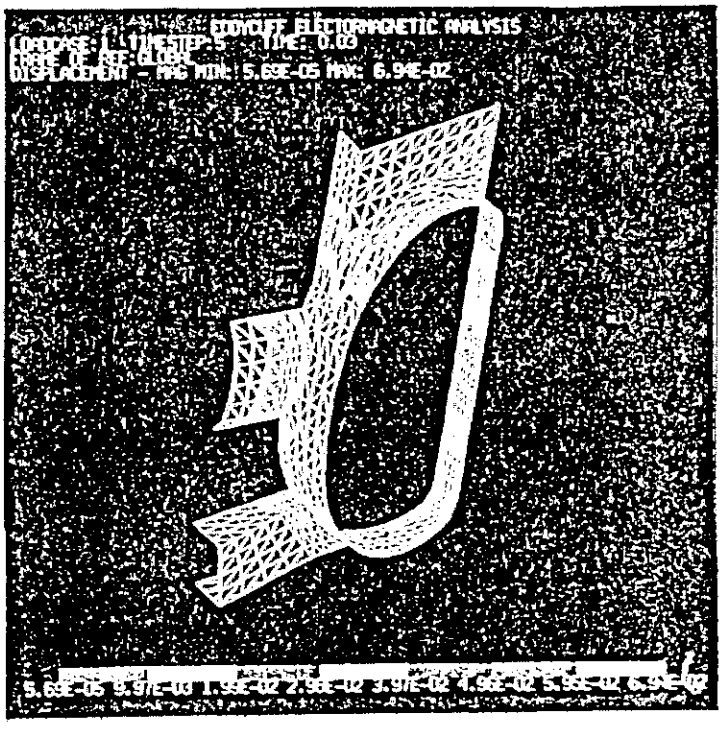

Fig. 9.4.7 Magnetic force distribution on the vacuum vessel for poloidal + self field coupling. (t=30ms)

Fig. 9.4.8 Magnetic force distribution on the vacuum vessel for toroidal field coupling. (t=10ms)

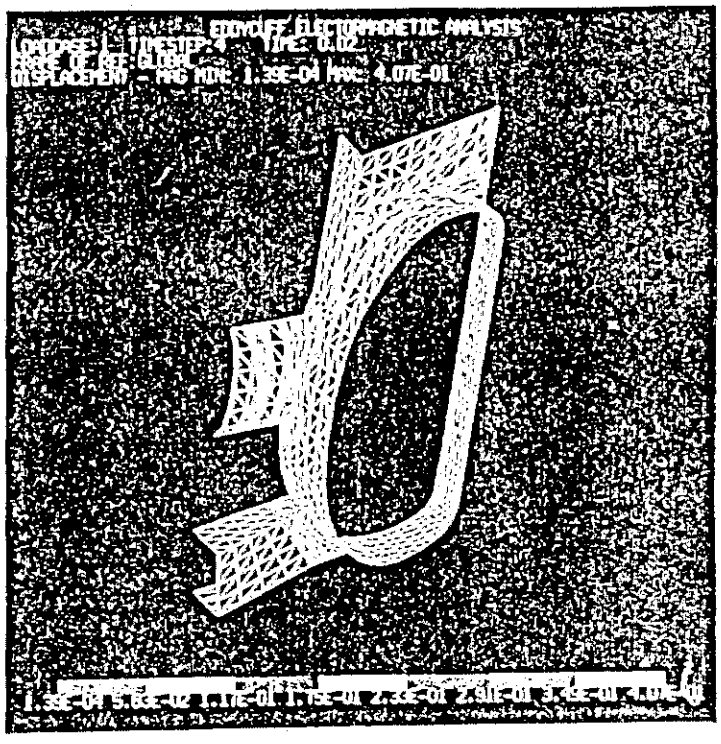

Fig. 9.4.9 Magnetic force distribution on the vacuum vessel for toroidal field coupling. (t=20ms)

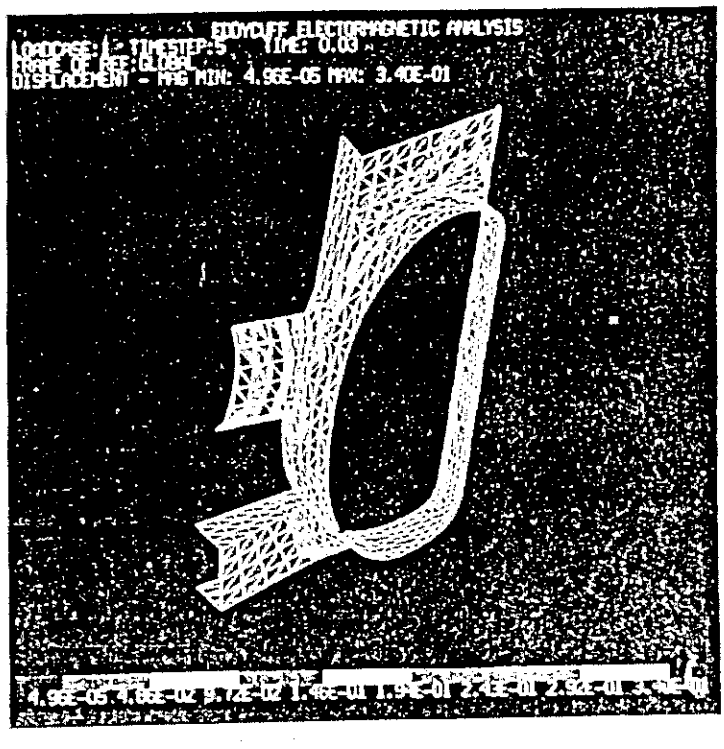

Fig. 9.4.10 Magnetic force distribution on the vacuum vessel for toroidal field coupling. (t=30ms)

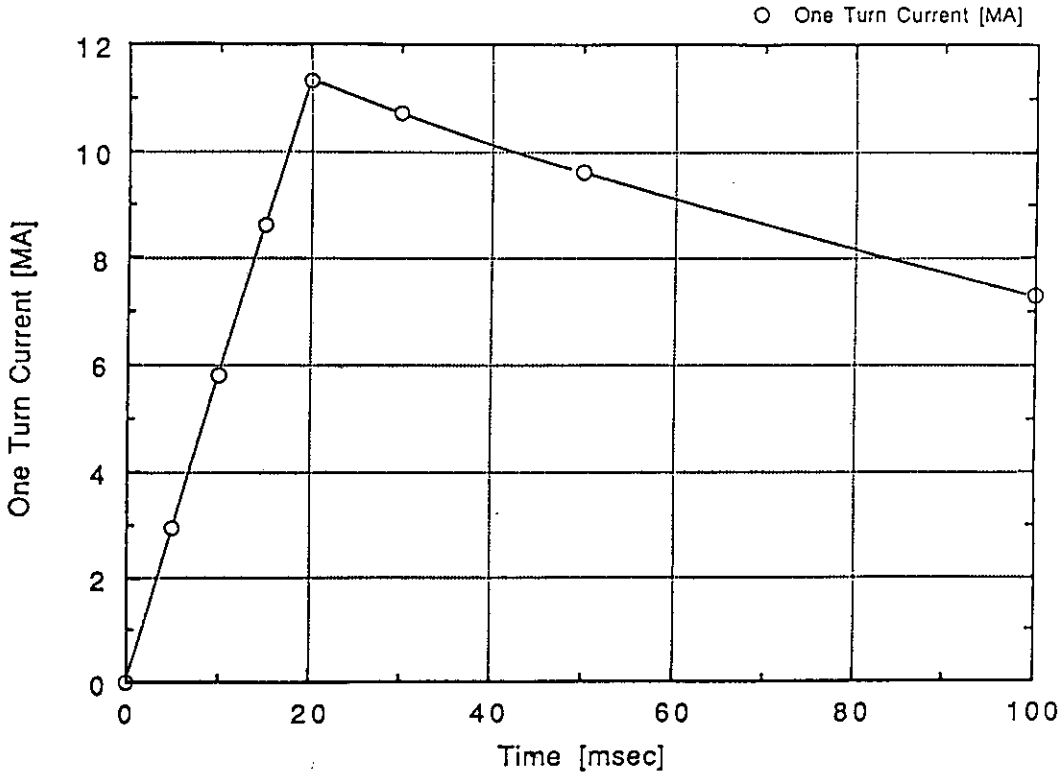

Fig. 9.4.11 Time evolution of toroidally induced current.

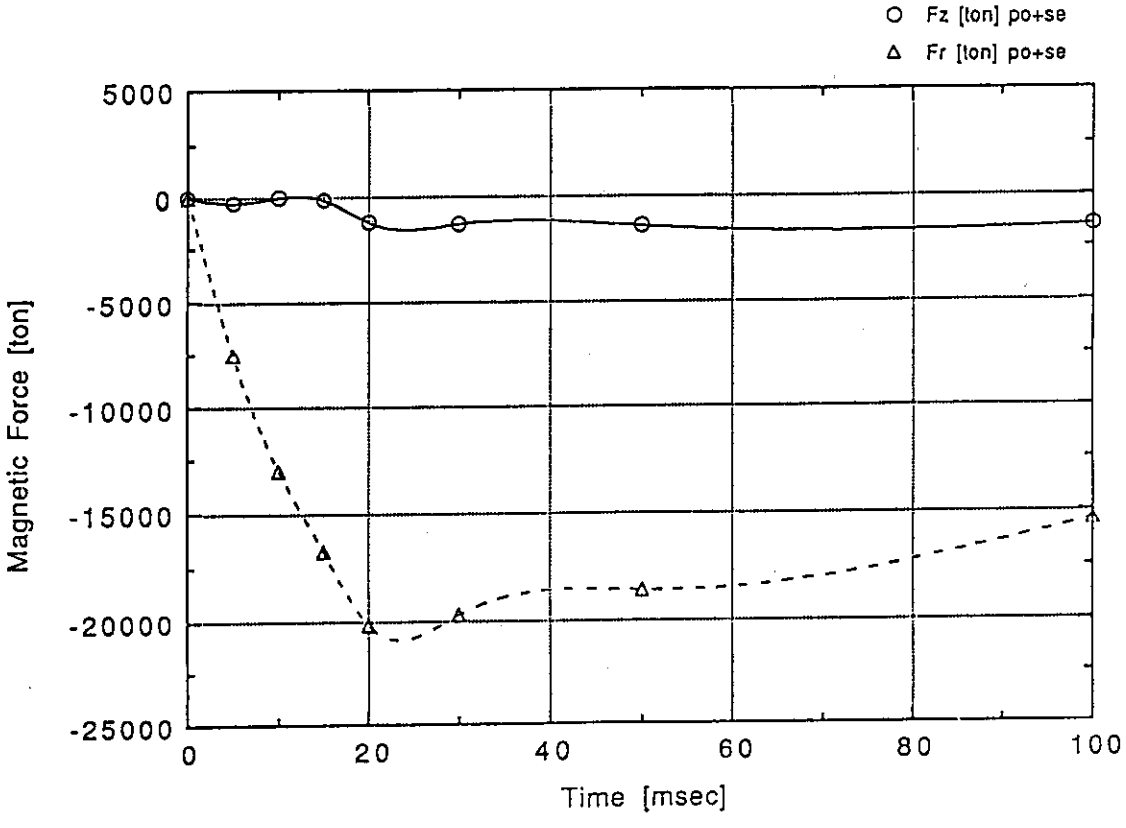

Fig. 9.4.12 Time evolution of total magnetic force.
(F_z and F_r are the vertical and centering magnetic force)

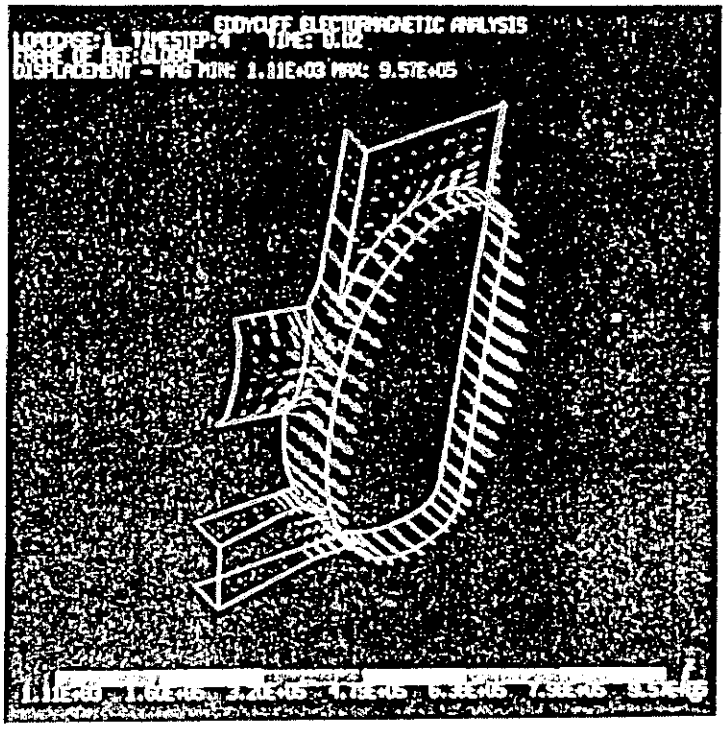

Fig. 9.4.13 Eddy current distribution on the vacuum vessel.
(disruption without motion: t=20ms)

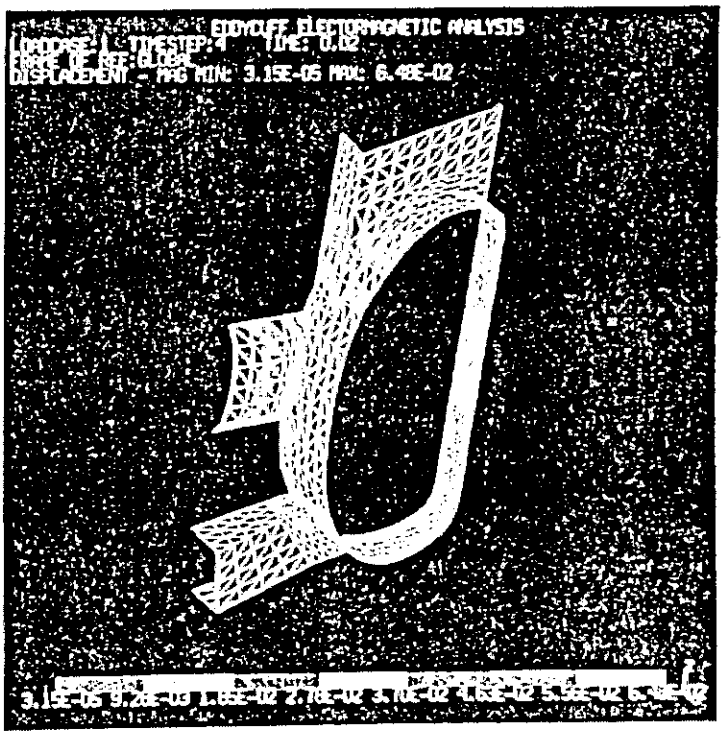

Fig. 9.4.14 Magnetic force distribution on the vacuum vessel
for poloidal + self field coupling.
(disruption without motion: t=20ms)

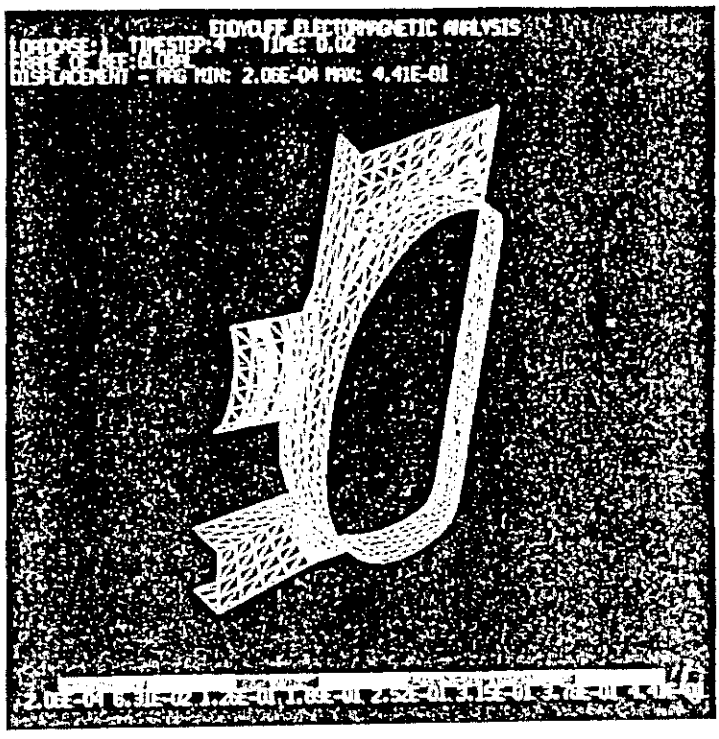

Fig. 9.4.15 Magnetic force distribution on the vacuum vessel for toroidal field coupling.
(disruption without motion: t=20ms)

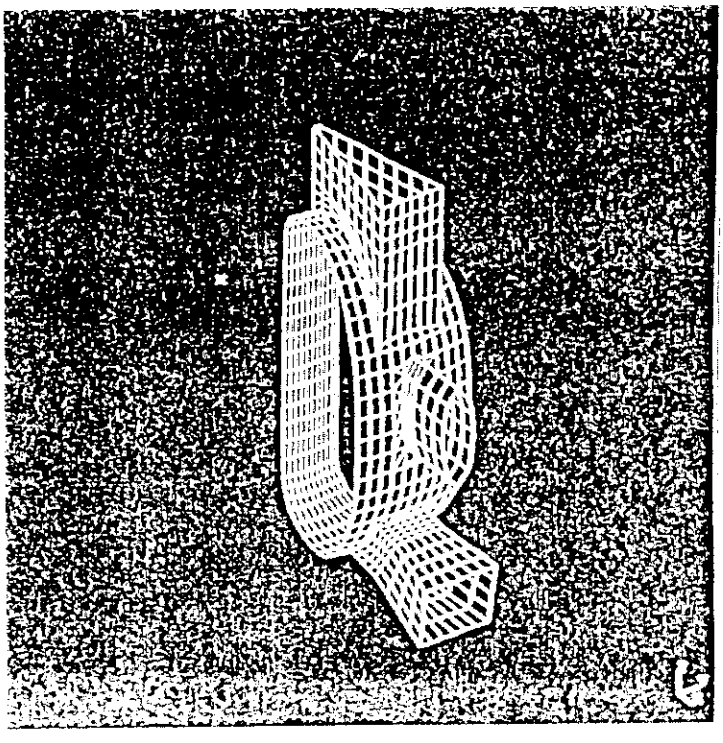

Fig. 9.4.16 Three-dimensional model for structural analysis.

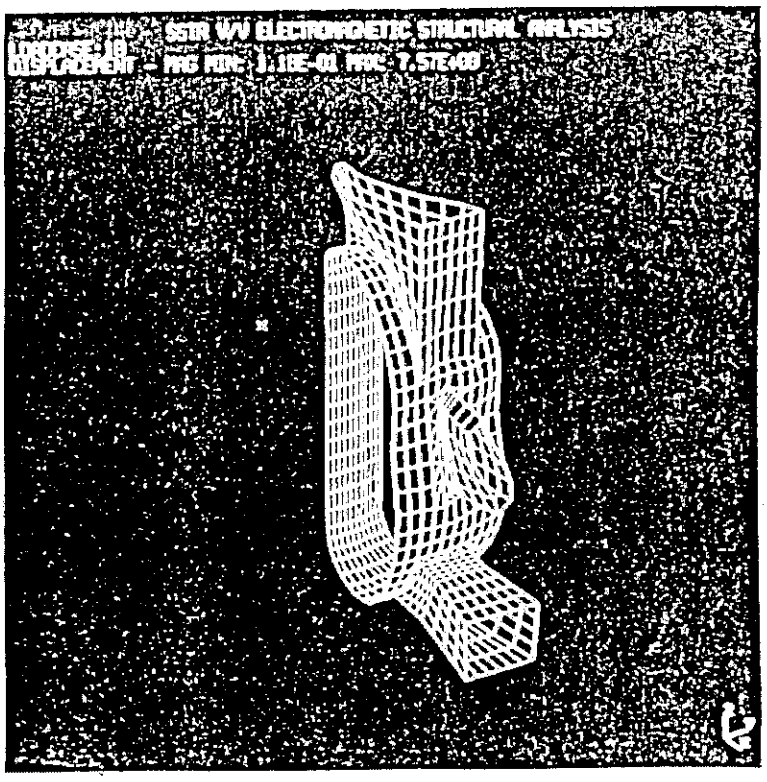

Fig. 9.4.17 Deformation of vacuum vessel at disruption.

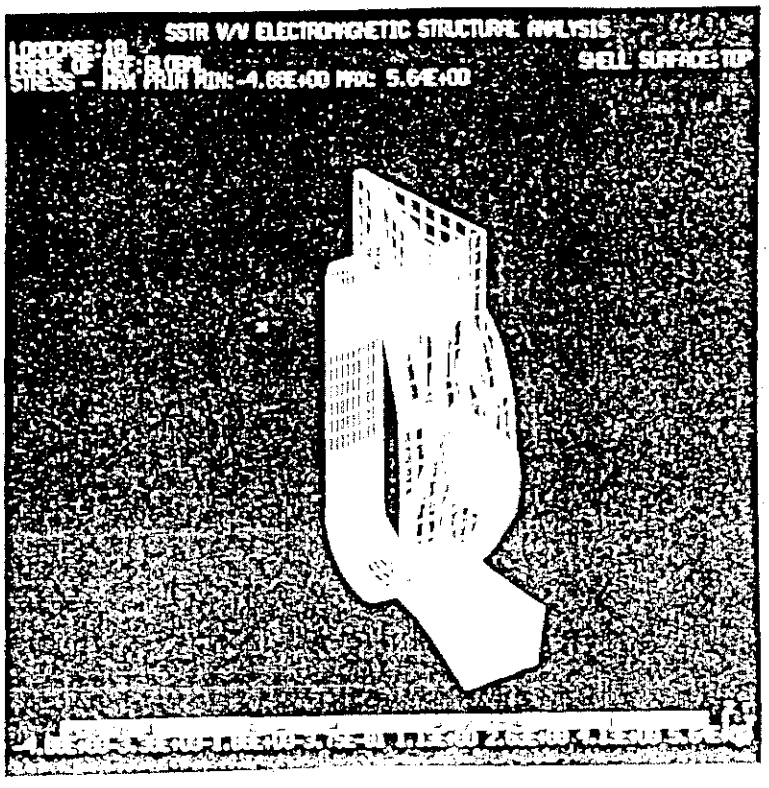

Fig. 9.4.18 Stress distribution at disruption.
(σ_1 for outside of shell)

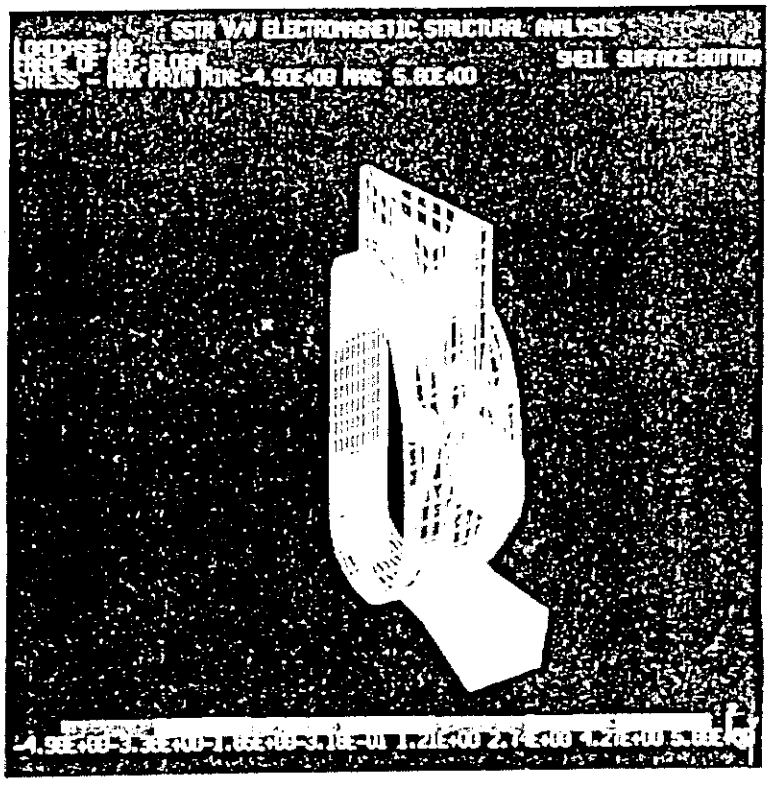

Fig. 9.4.19 Stress distribution at disruption.
(σ_1 for inside of shell)

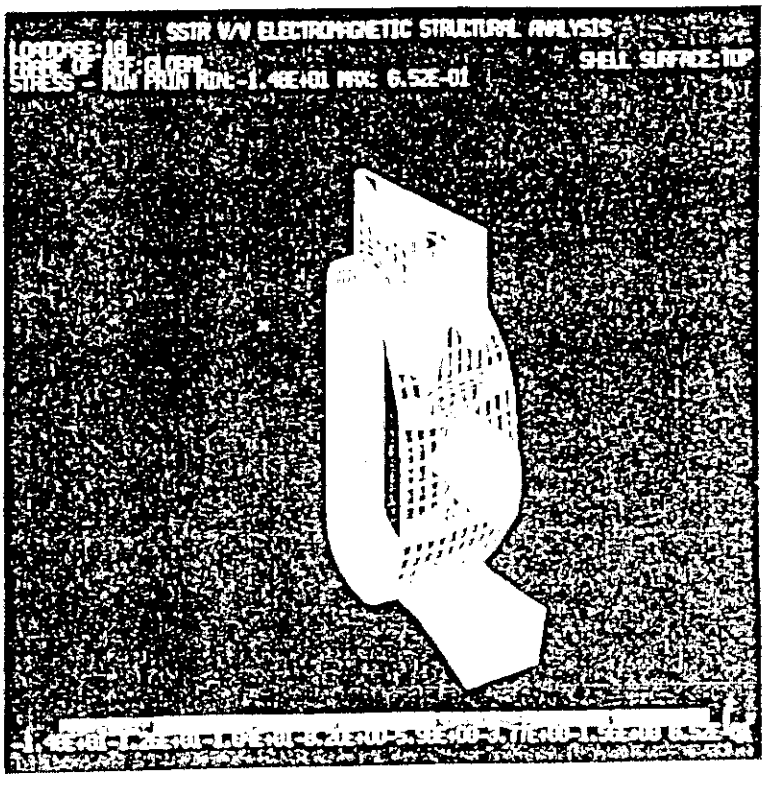

Fig. 9.4.20 Stress distribution at disruption.
(σ_2 for outside of shell)

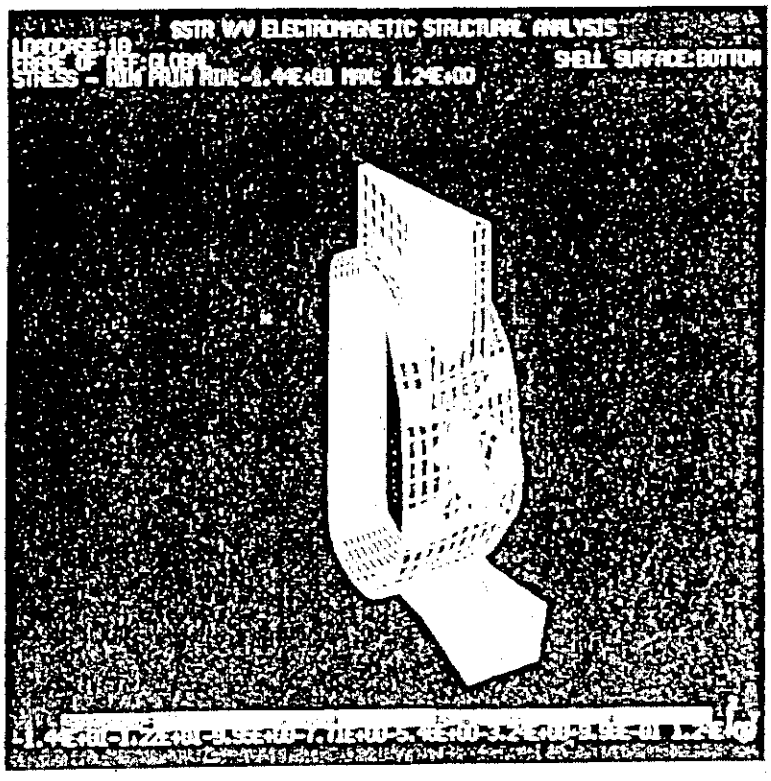

Fig. 9.4.21 Stress distribution at disruption. (σ_2 for inside of shell)

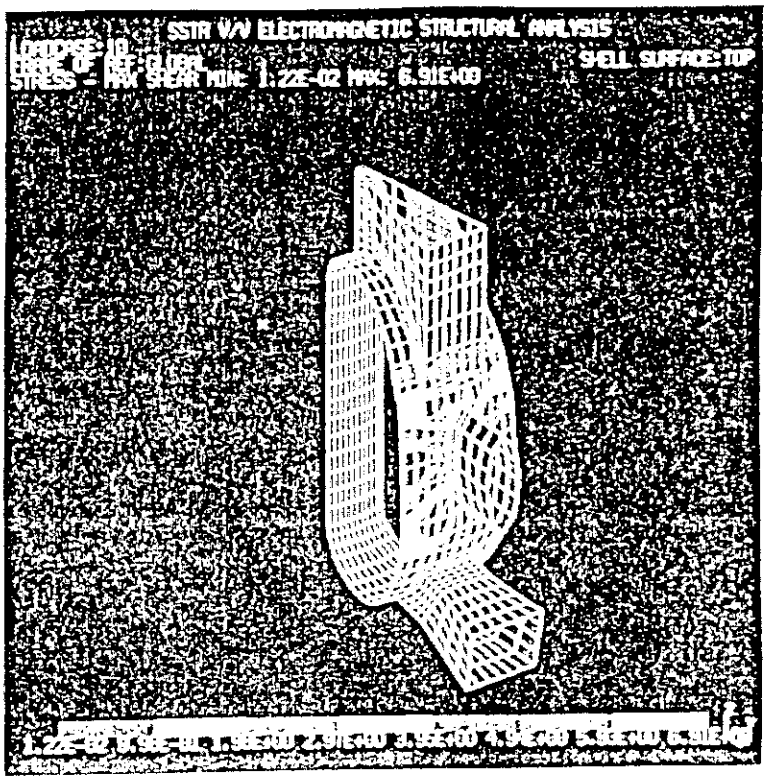

Fig. 9.4.22 Stress distribution at disruption. (τ_{max} for outside of shell)

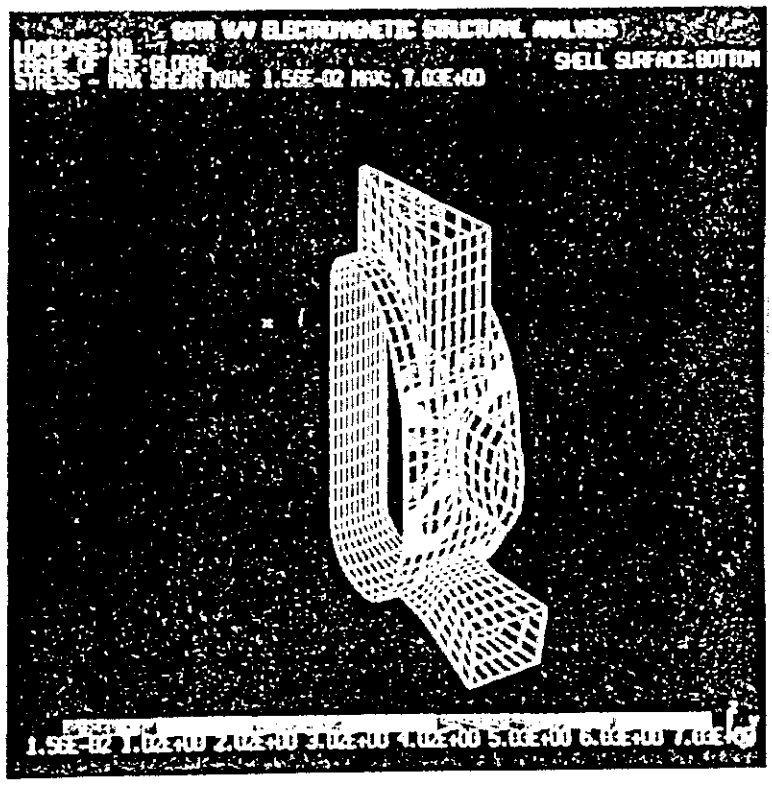

Fig. 9.4.23 Stress distribution at disruption.
(τ_{max} for inside of shell)

9.5 Shield calculation

The one-dimensional transportation calculation, by which the SSTR core geometry was simulated, was executed and the TFC shield performance was evaluated. The calculational method is as follows.

(1) Calculational code : ANISN
(2) Group constants : GICX40
(3) Geometry model : One-dimensional toroidal model
(The geometry chart is shown in Fig.9.5.1)
(4) source normalization: The neutron generation density was set so that the average neutron wall load should be $3MW/m^2$.

$$f_N = \frac{2x3.14x(5.12+8.88)x0.01x3}{14.1x1.602x10^{-19}} = 1.168 \times 10^{18}$$

According to the calculational results, the neutron to be injected into the inboard first wall is 0.279 in number per one DT neutron, and the neutron to be injected into the outboard first wall is 0.721(refer to Fig.7.3.2). If the neutron wall load is converted from this value, the load might be $2.3MW/m^2$ in the inboard and $3.4MW/m^2$ in the outboard. The space distribution of the neutron flux and the gamma-ray flux during operating the reactor was shown in Fig.9.5.2. Moreover, the shield characteristics of the inboard toroidal coil was shown in Table9.5.1. However, as we mentioned above, while the inboard wall load is 2.3 MW/m^2 according to the one-dimensional calculation, it is 3.4 MW/m^2 according to the three-dimensional calculation(refer to clause 7.3.1). Therefore, the value caluculated by the one-dimensional calculation was multiplied by the factor of 3.4(MW/m^2) / 2.3(MW/m^2). Because the attenuation of the fast neutron is somewhat insufficient among the shield characteristics, the improvement of the shield(to increase the steel component) is required. Moreover, because the atomic displacement of the copper stabilizer is about three times as large as the standard value, it is necessary to improve the shield(to increase the steel component) or to annealing the superconducting coil about two times during the life of the reactor. The gross heat deposition in TFC is as considerably small as about 2 kilowatts, when only the inboard straight lines(800cm) are considered.

The evaluation of the biological dose rate after the reactor shutdown is shown in the clause 7.3.4. The installation of the cryostat/the biological shield in the TFC outboard can suppress the radiation dose rate during one week after shutdown at less than 2.5mrem/h.

Table 9.5.1 Inboard shielding properties of SSTR (Inboard neutron wall load: 3.4MW/m^2, 21 full power year operation)

Items	Criteria	Calculation results
Fast Neutron Fluence (n/cm2)	2×10^{18}	3.09×10^{18}
Copper Stabilizer Atomic Displacement (dpa)	4×10^{-4}	1.88×10^{-3}
Insulator Absorbed Dose (rad)	3×10^{9}	2.12×10^{9}
MaximeumNuclear Heating Rate (W/cm3)	1×10^{-3}	9.80×10^{-5}
Total Nuclear Heating in SCM (kW)	-	1.98 *

* Inboard leg of TFC is assumed to be 800 cm.

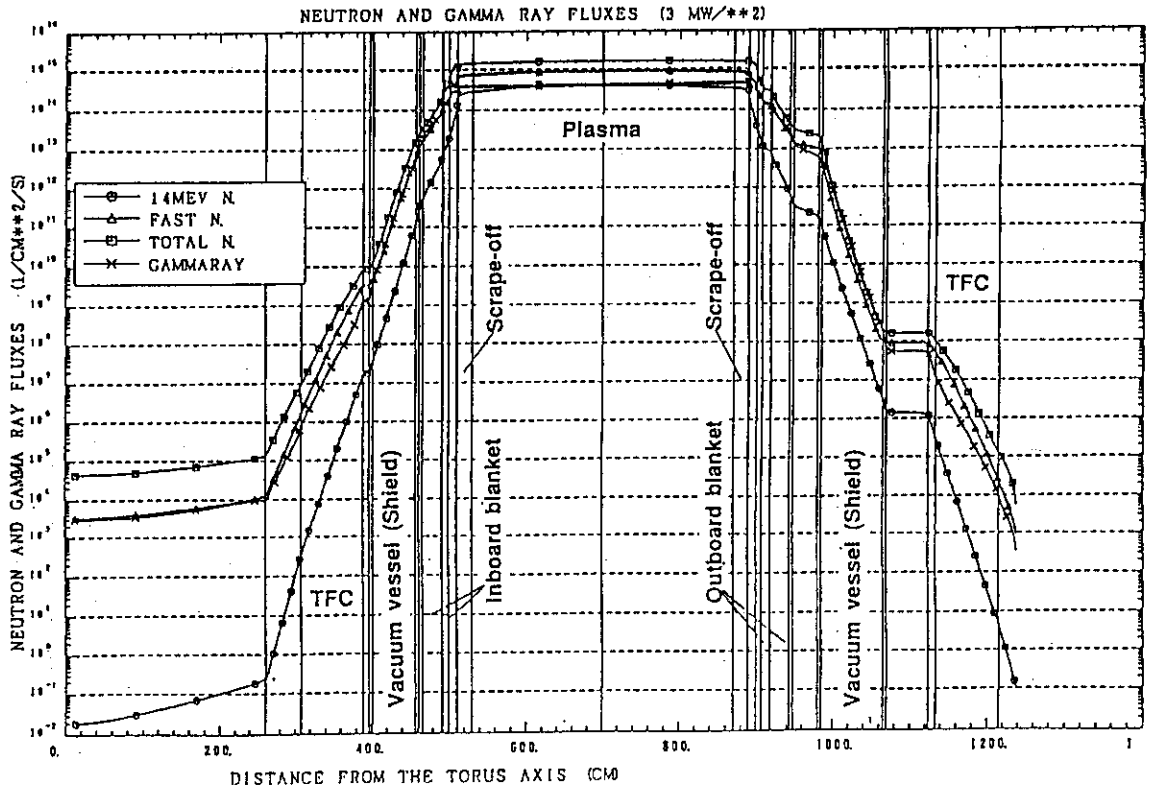

Fig. 9.5.2 Spatial distribution of neutron and gamma-ray flux in SSTR

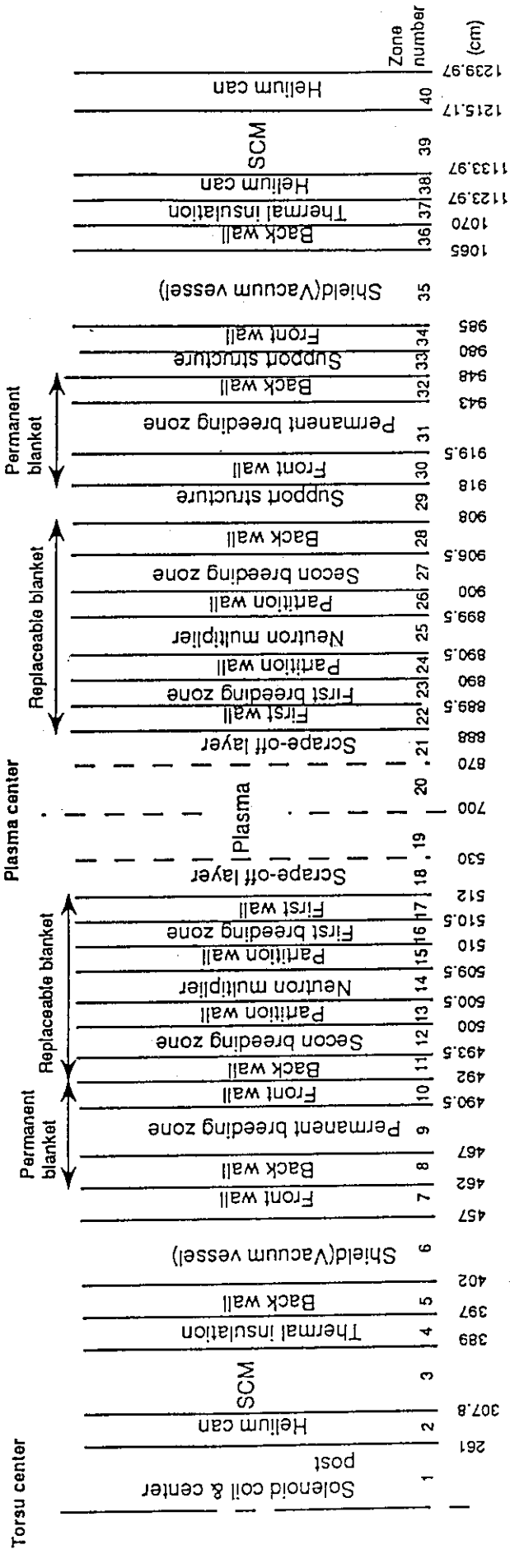

Fig. 9.5.1 1-D toroidal model for shielding calculation of SSTR.

10. Maintenance

10.1 Conceptual Design of SSTR Core Structure

Realization of fusion power reactor largely depends on the development of key technologies such as vacuum vessel, magnet system and so on. Reliabilities of these components must be improved in time of fusion reactor constructions, to be admired as reliable energy source for future generation. In the design of SSTR core structure, therefore, it is assumed that the vacuum vessel, shielding structure, toroidal and poloidal magnets are highly reliable and not replaced throughout reactor lifetime. Only in-vessel components, namely first wall armour, tritium breeding blankets and divertor components are required a regulating maintenance during the lifetime. Based on these assumptions, the SSTR is designed, aiming to simplifying the core structure and maintenance scheme. Fig.10.1.1 shows the cross section view of and Fig.10.1.2 shows the plane view of SSTR.

Characteristics of SSTR are the followings. The configuration of burning plasma is the D-shaped, of which elongation is 1.85, and lower single-null divertor. The first wall configuration is designed to be smoothly along the plasma separatrix. However, to reduce an effect of interaction between plasma particles and first wall, the thickness of the outer and inner scrape-off layers are designed to 13cm and 18cm at midplane, respectively. The maximum gap of the upper scrape-off layer is given to 30cm. The poloidal cross sectional shape of the first wall configuration is shown in Fig.10.1.3. The detail design of the first wall structure has been described in the previous section. For divertor configuration, the distance between null point and striking point at the outer divertor plate is 1.2m and the angle of the separatrix line to the divertor plate is 15 degree to reduce peak heat load.

The total thickness of the tritium breeding blanket at midplane is 50cm for the inner and 60cm for the outer. The blanket structure is designed to divide two regions, namely movable and fixed blanket. The thickness of the movable blanket is 25cm at inboard and 20cm at outboard. The poloidal cross sectional view of the movable blanket is also shown in Fig.10.1.3. The thickness of the fixed blanket at midplane is therefore 25cm and 40cm for the inboard and outboard, respectively. All of the fixed blankets is firmly fixed to the vacuum vessel, but they are disconnected to the vacuum vessel electrically. Each fixed blanket side by side is also disconnected electrically. Only the movable blankets are replaced regularly and the fixed blankets are not removed except an abnormal condition The movable blankets are divided to 48 modules at outboard and another 48 at inboard.

The thickness of the vacuum vessel at the midplane including shield blocks is 65 cm and 90cm at the inboard and outboard, respectively. The detail structure of the vacuum vessel is described at the previous section. There are sixteen upper maintenance ports, sixteen divertor maintenance ports, two neutral beam injection ports, pellet injection port, ECH port and two horizontal maintenance ports. A exhaust duct is connected to each divertor maintenance port. The arrangement of these ports is shown in Fig.10.1.4. Four steam generator systems occupy almost a half of sixteen port sections.

Toroidal coil is designed to become closely constant tension mode. It is designed that the centering force is supported by the wedge and the overturning force is supported by the shear panel. The vertical bore is 11.6m and the horizontal bore at midplane is 7.4m. The bore of central solenoid coils is 2m.

The thickness of the cryostat is 2m and mostly made of concrete. The thickness of the bell-jar is 1.5m. The reactor core size can be said that the diameter of the cryostat is 34m ant its hight is 23m. The most of reactor core is located under the level of grand.

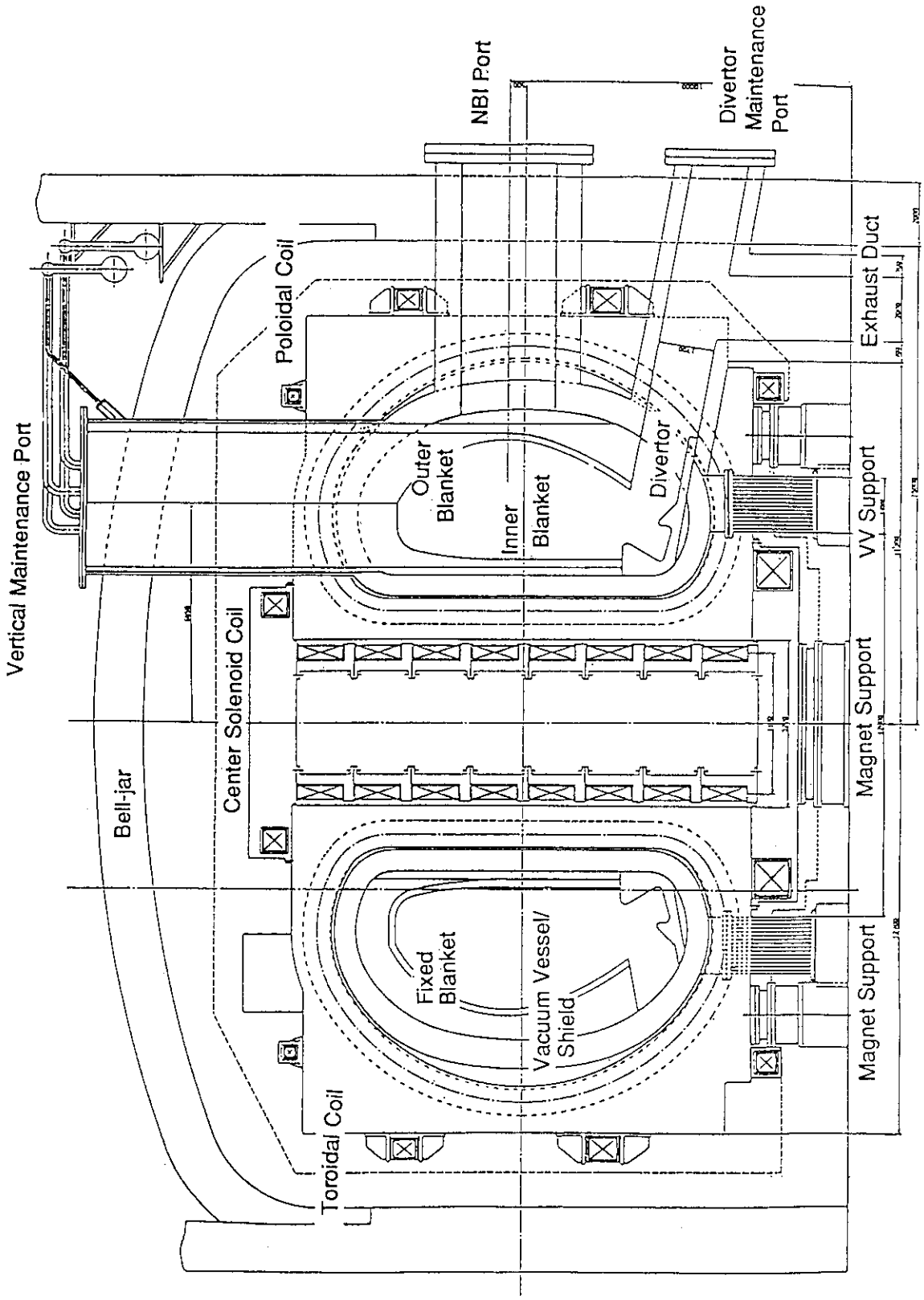

Fig. 10.1.1 Cross section view of SSTR.

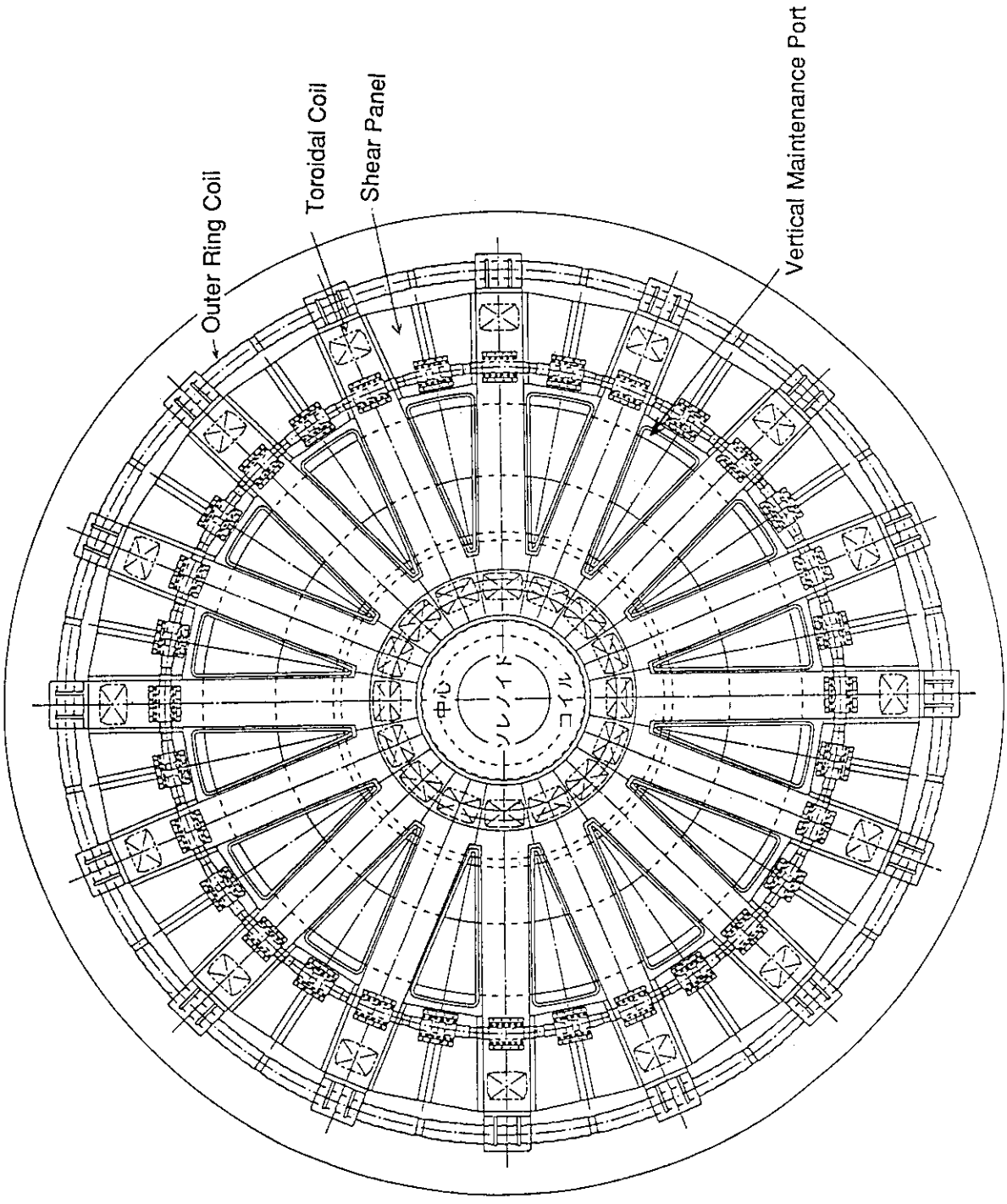

Fig. 10.1.2 Plane view of SSTR.

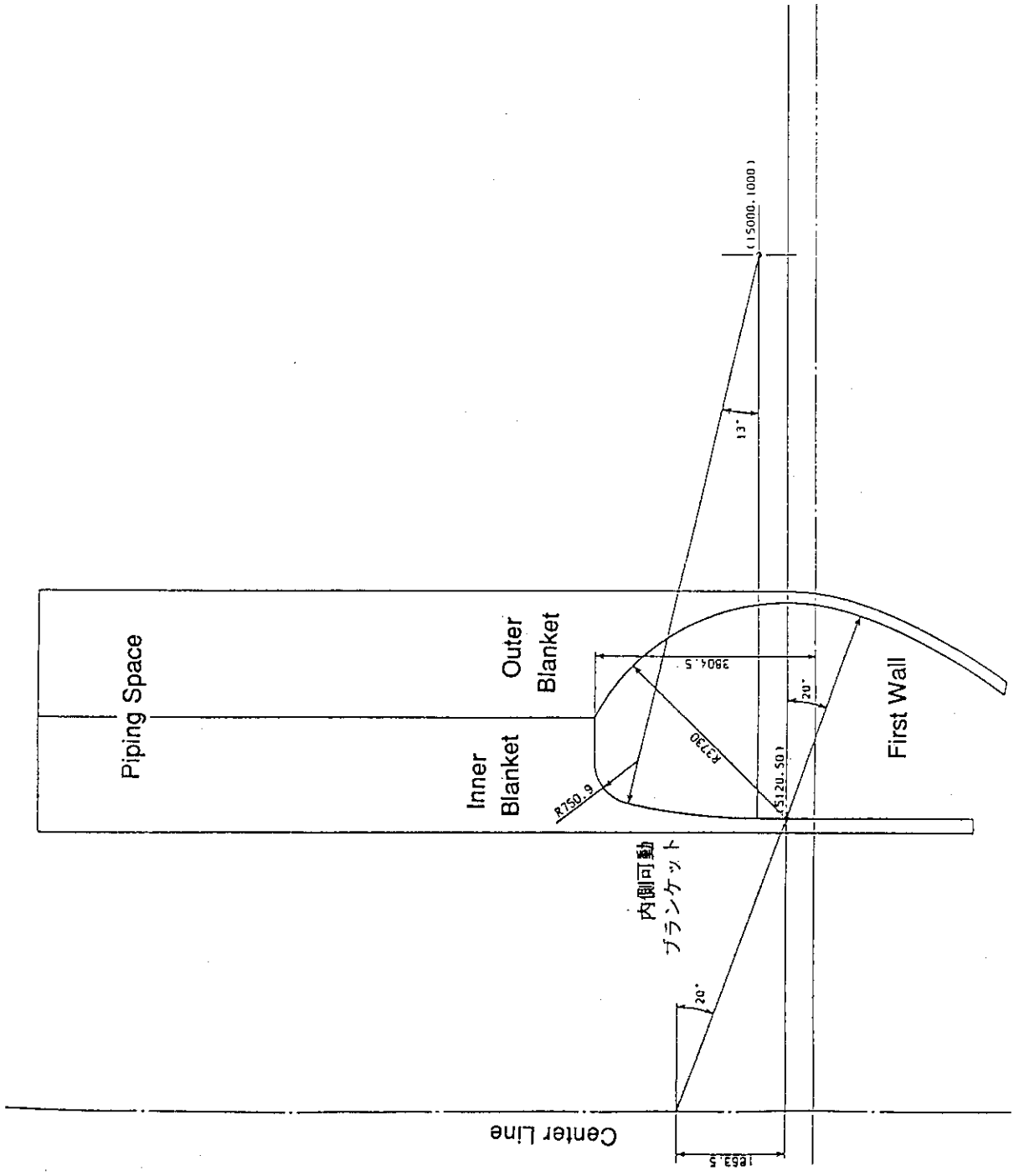

Fig. 10.1.3 Dimension of first wall and movable blankets.

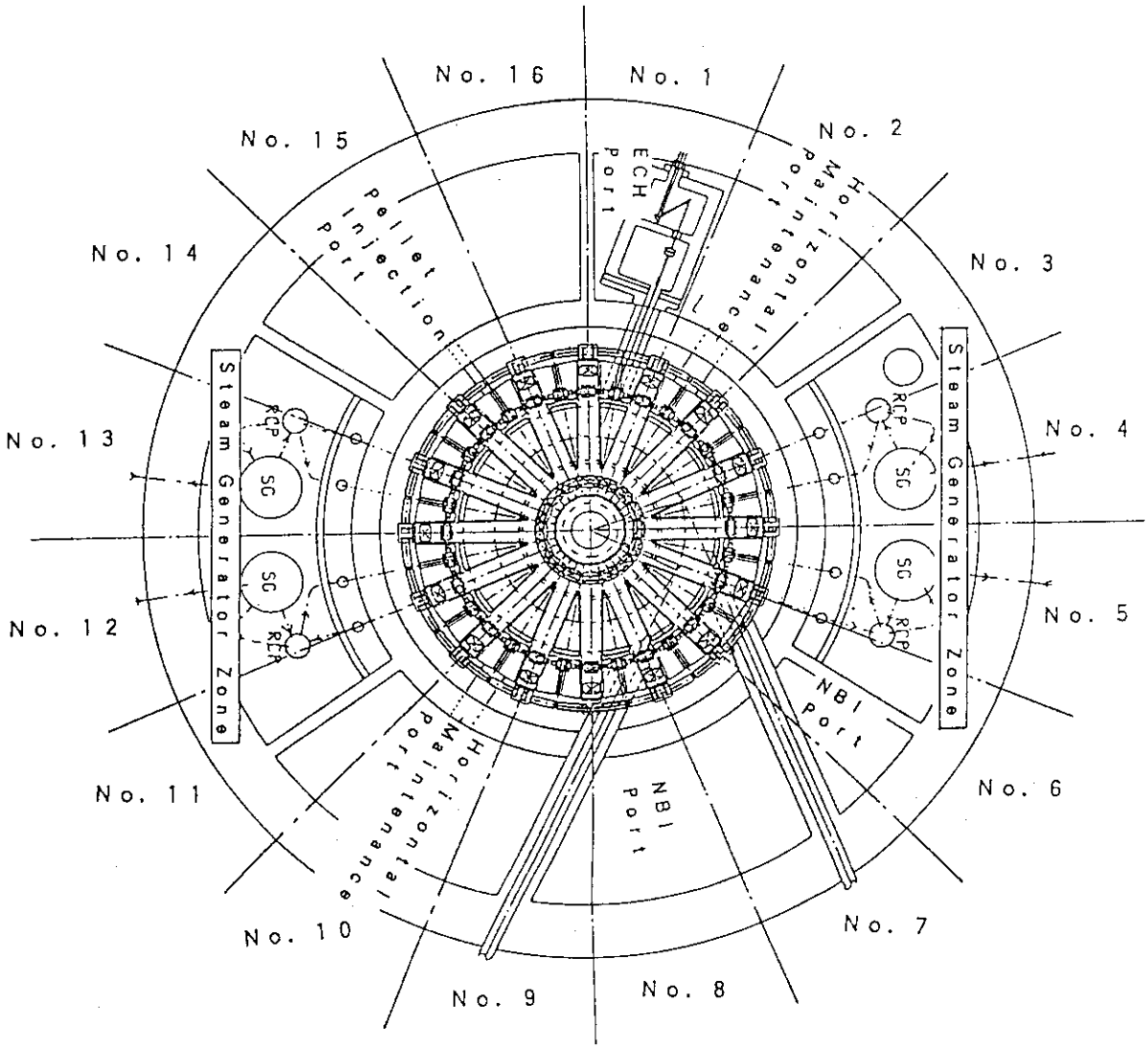

Fig. 10.1.4 Planning of horizontal ports usage.

10.2 Blanket Segmentation and its Maintenance

In-vessel components such as movable blankets are removed and reassembled through 16 upper vertical maintenance ports. Fig. 10.2.1 shows the dimension of one maintenance port located at between two toroidal magnets. A gap between toroidal coil and side wall of the port is just 80mm and thermal shield structure is put in it. The side wall thickness of the port is 100mm.

There are 16 toroidal field coils. The maintenance port is set to two adjacent toroidal field coils. Thus the in-vessel components are divided to 16 sectors. Furthermore, the inner and outer blankets are divided to three modules, respectively, in one sector. Fig 10.2.2 shows the plane view of the segmentation of the blanket modules in one sector. The center module of the outer blanket is removed or reassembled with one simple vertical motion. The side modules of the outer blanket are removed or reassembled with two motions, namely one horizontal motion in toroidal direction along a guide mechanism and one vertical motion. The inner center module is removed or reassembled with also two motions. It is shifted outward once and lift up when it is removed. For the side modules of the inner blankets, three motions are required.

In this segmentation, the center module of the outer blanket is removed or installed without any interference to another modules. Each side module of the outer blankets is removed or installed in the situation of no center module. However, all of inner modules of the inner blankets can not be removed or installed without removing all of the outer modules.

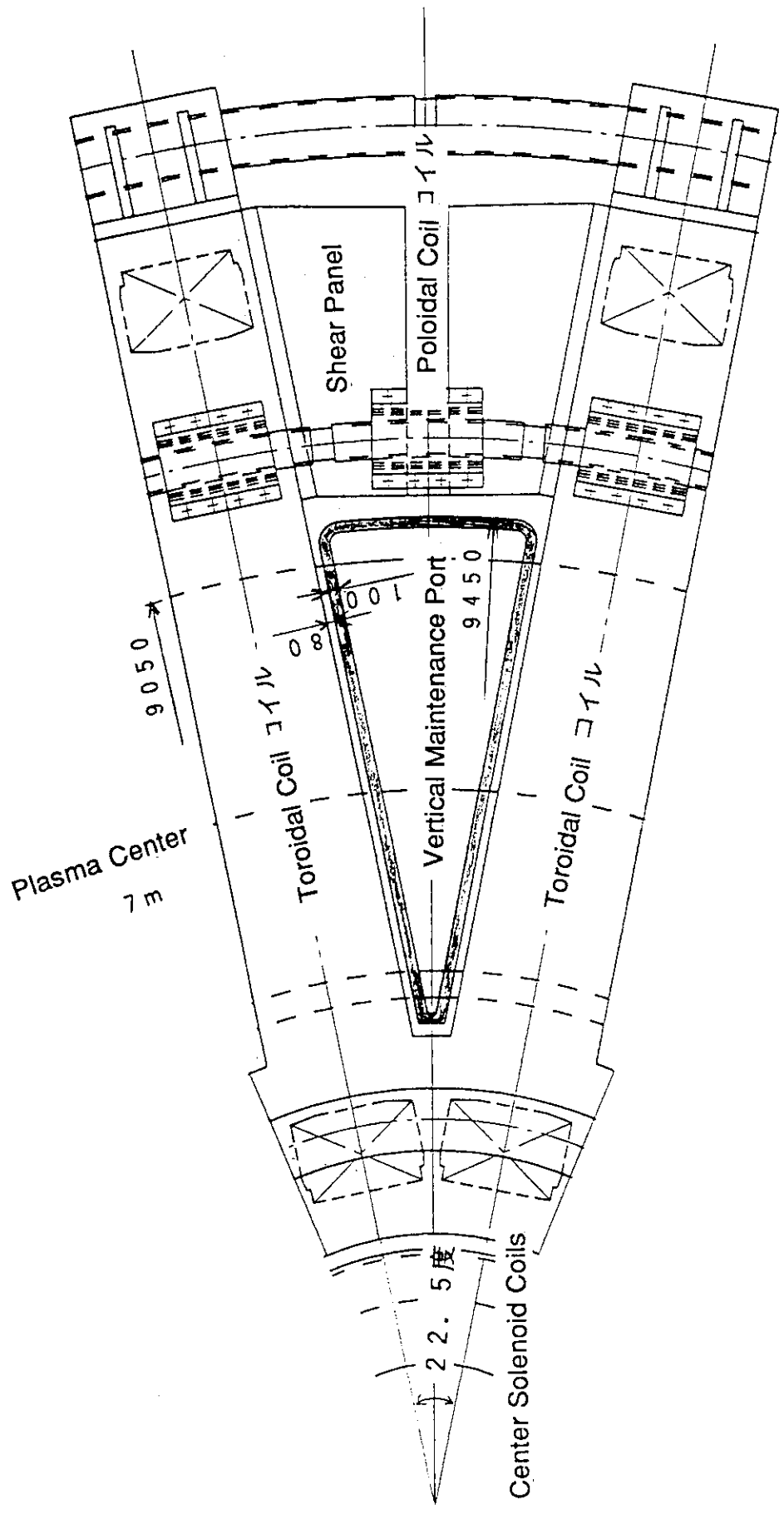

Fig. 10.2.1 Dimension of vertical maintenance port.

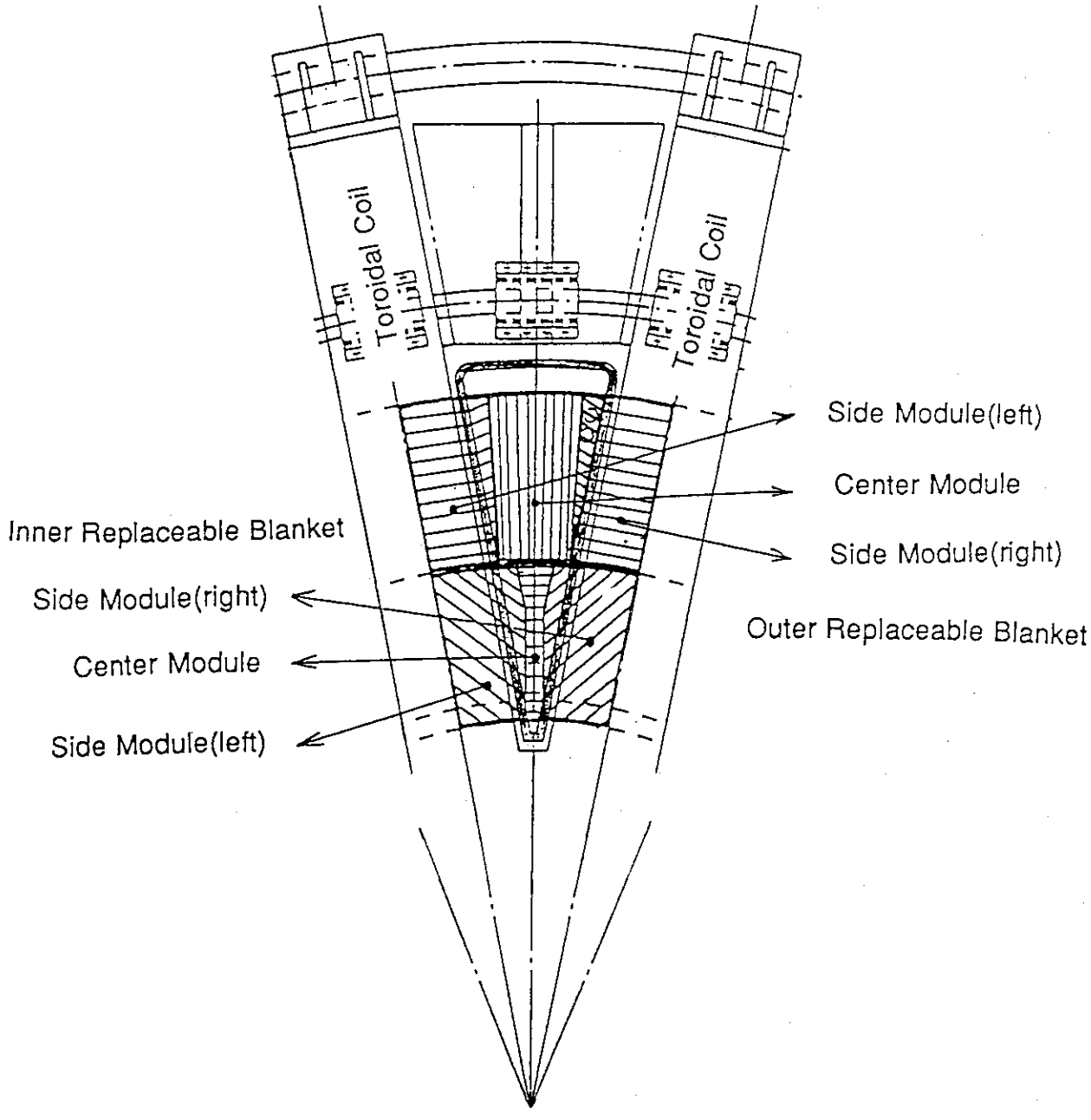

Fig. 10.2.2 Concept of movable blanket separation regarding to maintenance consideration.

10.3 Divertor Segmentation and its maintenance

SSTR has only lower divertor system. Maintenance of divertor is carried out through lower divertor ports located at between two adjacent toroidal field coils. Divertor target with piping and support structure is removed or installed together as an unified component. Fig.10.3.1 shows the cross sectional view of the divertor maintenance port. As shown in A-A cross section in Fig.10.3.1, the divertor port is very narrow so that the divertor plate should be divided at least to three modules in one sector. The segmentation of the divertor in one sector is described in Fig.10.3.2 as an plane view. To maintain the shielding effect for the toroidal magnets, the shield block must be installed in the divertor port. Considering the maintainability of the divertor, these shield blocks should be unified to divertor modules and removed or installed together. Divertor port is extended to the cryostat and the cooling piping system is also extended to the outside through the cryostat wall. Total length of the divertor modules including the shield block and cooling pipe is about 15m Divertor maintenance room next of cryostat wall has only 10m depth. Thus, the cooling pipes should be cut and joint at the middle at least once. There are 16 divertor maintenance rooms. These rooms are connected each other through tunnel and each four rooms has an elevators to reach the reactor hall. During maintenance procedure, the tunnel are opened and the divertor modules are moved out through the tunnel and elevator.

It is not good idea to unify the divertor system to reduce radio active materials. It will be resolved, however, if only divertor target is throw away and the base structure and shield blocks are reused .In addition, the erosion of the divertor target is localized to the hitting point at where the huge heat and particle flux bombard. It may be enough to replace this part of target instead of replacing whole divertor target.

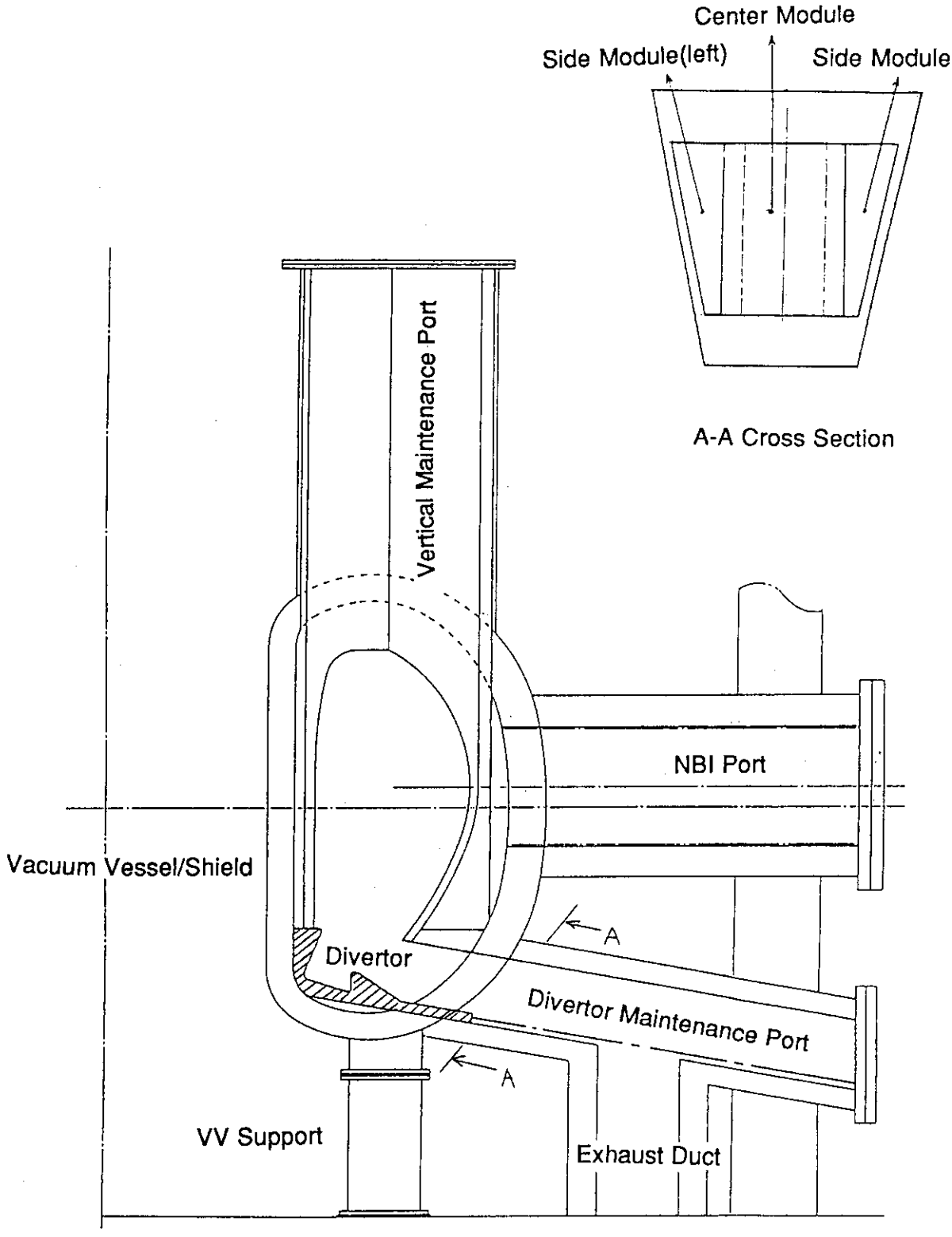

Fig. 10.3.1 Dimension of divertor maintenance port and exhaust duct.

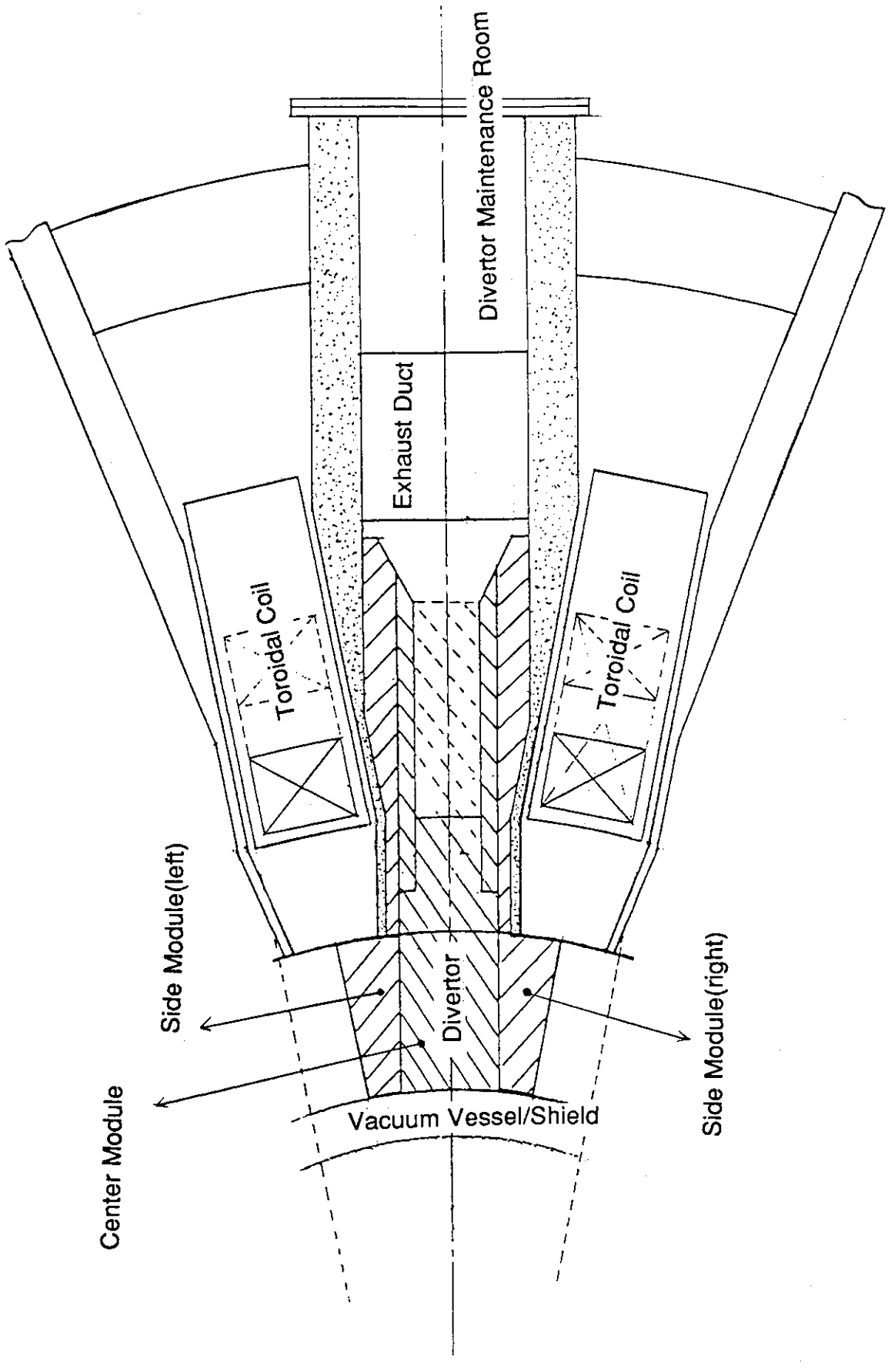

Fig. 10.3.2 Concept of divertor separation regarding to maintenance consideration.

10.4 Operation and Maintenance Scenario

For a commercial reactor, availability of more than 70% is a basic specification. Similar to conventional nuclear power reactor, we assume a basic operation scenario such as nine month operation and three month regular shutdown in a year.

Movable blanket and divertor are main components to replace regularly during shutdown.The first wall material is ferritic stainless steel. Considering irradiation damage due to high energy neutron, it had better replace the movable blankets before total neutron fluence exceed 10MWy/m2(about 100dpa) at which the strength of the ferritic stainless steel will reduce. The peak neutron wall load at the outer movable blankets is about 6MW/m2. On the other hand, it of the inner movable blankets is about 3MW/m2. Giving the availability of 70%, the outer movable blankets should be replaced each other year and the inner movable blankets must be replaced once in four years. Therefore, the maintenance scenario of the movable blankets is the following;

(1) During regular shutdown of first year, a half of the outer blankets are replaced and one forth of the inner blankets are replaced.

(2) At second year, the other half of the outer blankets are replaced and another one forth of the inner blanket are replaced.

(3) At third year, the first half of the outer blankets are replaced again to new one and another one forth of the inner blankets are replaced.

(4) At forth year, the second half of the outer blankets are replaced again and the last one half of the inner blankets will be replaced.

These procedure will be repeated afterwards.

In one maintenance period, the number of removed blanket modules is 36 in total and another 36 new modules has to installed. Since the regular shutdown time is three months, it is simply estimated that four modules have to be removed and new four modules to be installed in a week, including cut and re-joint of many cooling pipes and tritium reprocessing pipes. Improving a maintainability, two sets of remote maintenance system are used in parallel operation.

All of divertor modules have to be replaced every year because of not irradiation problem but erosion of divertor target. As noted before, it is necessary to re-use most of base structure and shield block and to throw away only locally eroded target plate. The eroded target is replaced to new target at hot-cell. Six divertor modules have to be replaced, at least, in one week. Two or three sets of divertor remote maintenance systems will be used at same time to improve maintainability.

10.5 Reactor Dome

It is studied the size of reactor dome for 1000MW class of fusion reactor. During normal operation, the reactor dome is in nitrogen gas circumstances. In the reactor dome, there are a reactor core, four steam generators and primary cooling pumps, one pressurizer, primary piping system, pellet injection system, exhaust system, ECR heating system and so on.

Fig.10.5.1 shows the cross sectional view of the reactor dome and Fig.10.5.2 shows the plane view. The diameter of the reactor dome is 64m. It is almost 1.5 time the diameter of
a conventional 1000MW class of PWR. The hight of the reactor dome is 94m which is similar to the conventional PWR. Although a beam dump system of neutral beam injection system can install inside the reactor dome, it sets to NBI room outside the reactor dome. It is because the vacuum system for the NBI is located around the beam dump and a maintainability of these vacuum system has to be concerned. The hight of removable blanket is about 20m. The hight of blanket maintenance equipment will be about 24m. The hight of the polar crane is designed to 27m to lift it.

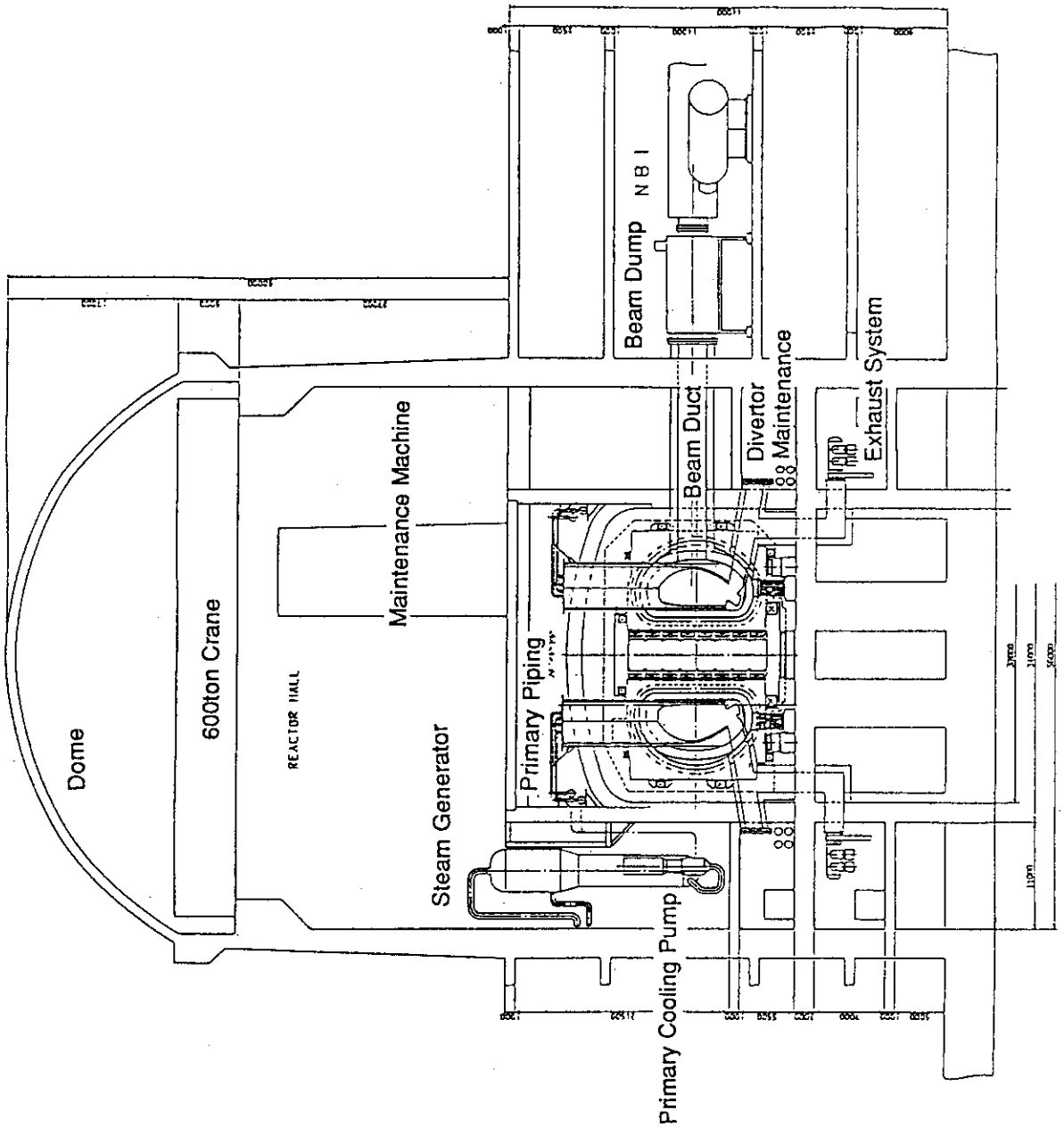

Fig. 10.5.1 Cross sectional view of the core of reactor building.

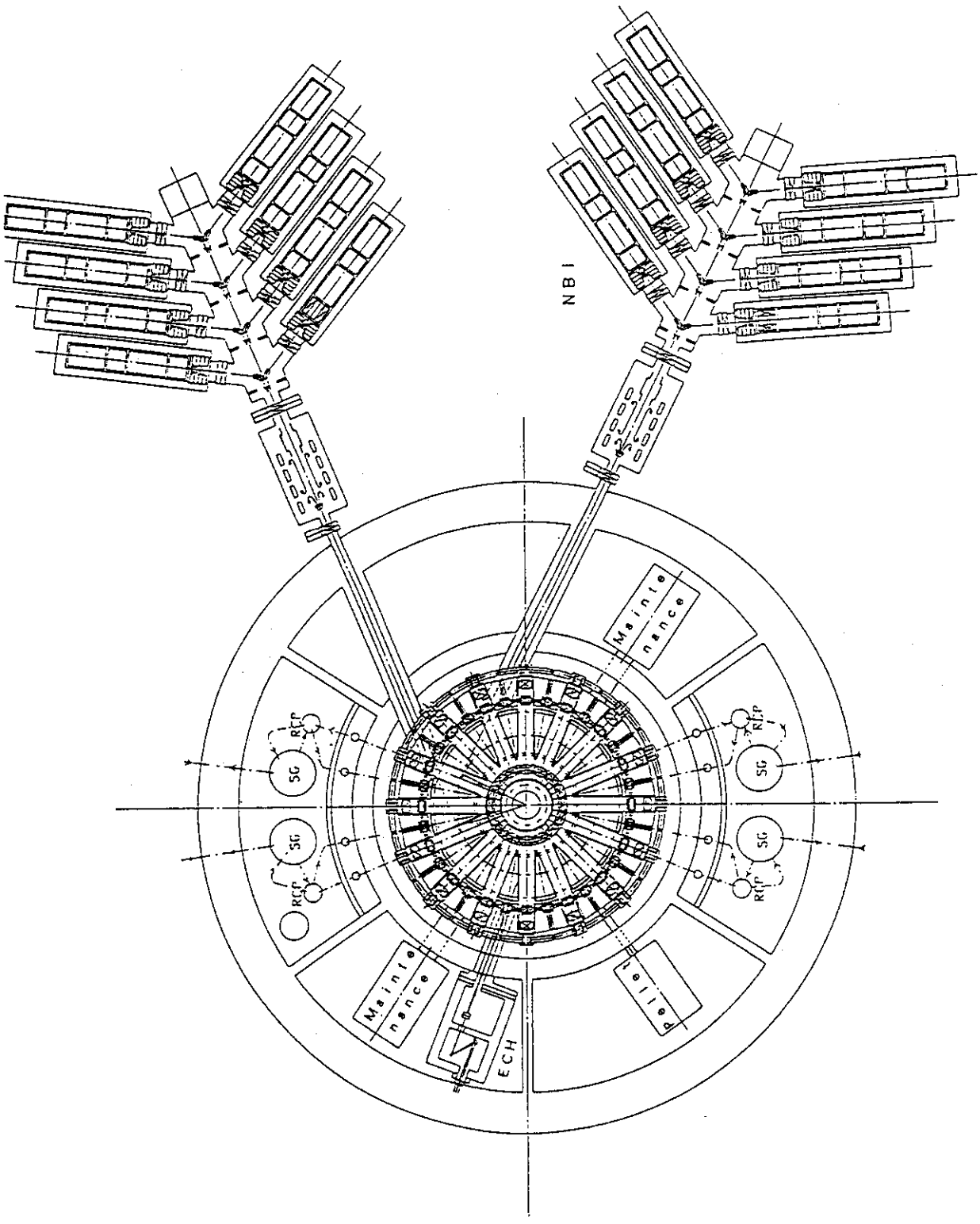

Fig. 10.5.2 Plane view of the core of reactor building.

10.6 Initial Assembly

Initial assembly is briefly studied. We consider that most of reactor components including vacuum vessel, toroidal and poloidal magnet systems, steam generators and so on, are installed by using external crane. Fig.10.6.1 shows the case of using a mobile crawler crane to install a toroidal coil. Heaviest component will be a toroidal coil of which weight is about 550 tons. The capability of the crawler crane is up to 840 tons and its working radius is 30m. For a lifting weight of 600 tons, the working radius will be about 60m. The advantage of this method is that an assembly room in the reactor dome is not required. Most of large size components are assembled at a site factory or other place. It may result in the reduction of assembly period. Another advantage of this method is that large components such as outer poloidal ring, of which diameter is 26m, can easily install through the open ceiling. Disadvantage of this method is, however, that emvailoment inside the reactor dome can not control during the open ceiling. Working condition have to be controlled at least inside the cryostat. To avoid such a situation, temporally dome will be covered over the reactor core. It will be opened when a necessary component is installed in the cryostat and then closed during the assembly period. After finishing the reactor core assembly, the temporally dome is removed and the bell-jar of the cryostat cover the reactor core.

Fig.10.6.2.(1) to Fig.10.6.2.(10) show the scheme of reactor core assembly.

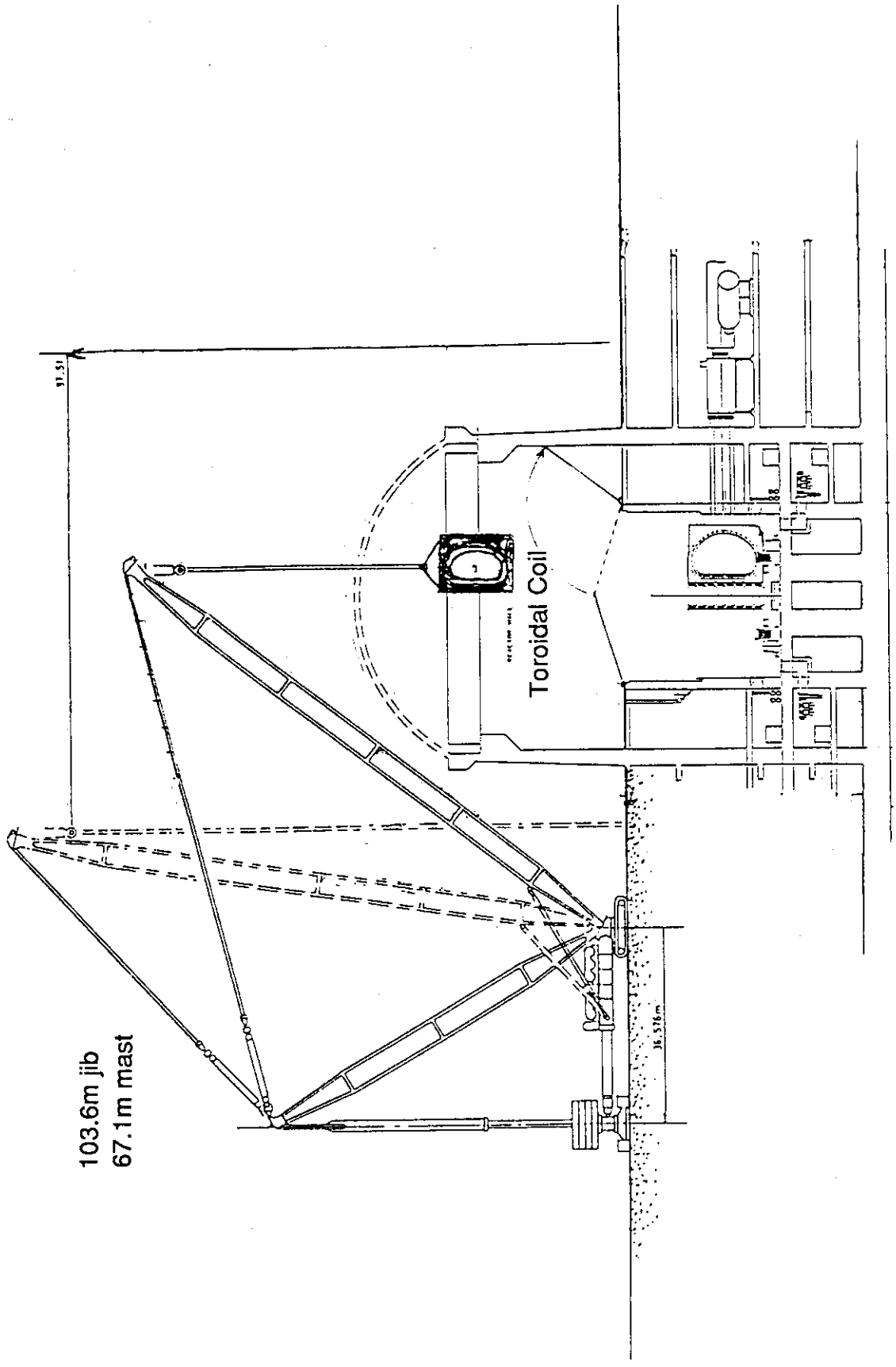

Fig. 10.6.1 Initial assembly of TF coil using mobile crawler crane.

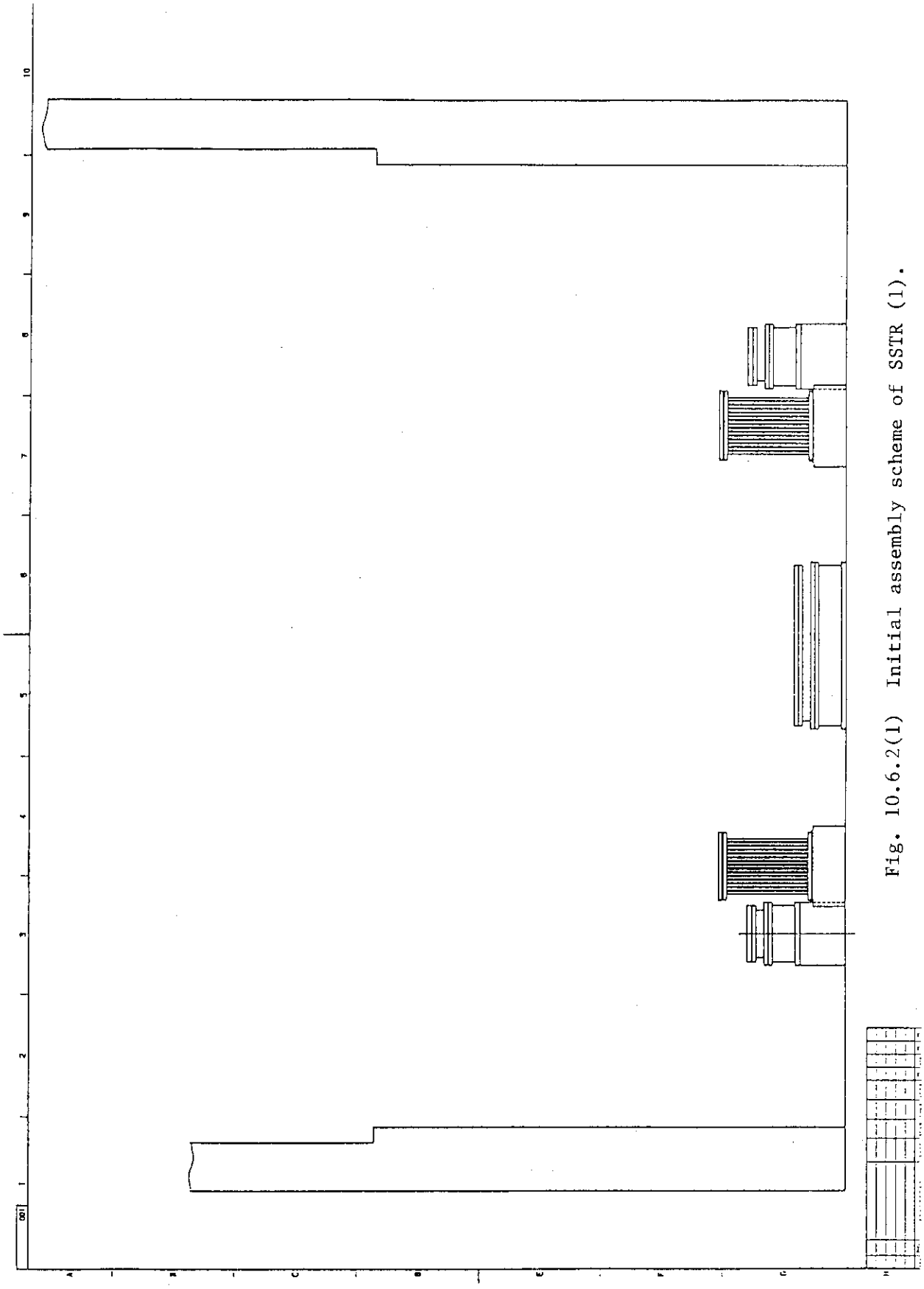

Fig. 10.6.2(1) Initial assembly scheme of SSTR (1).

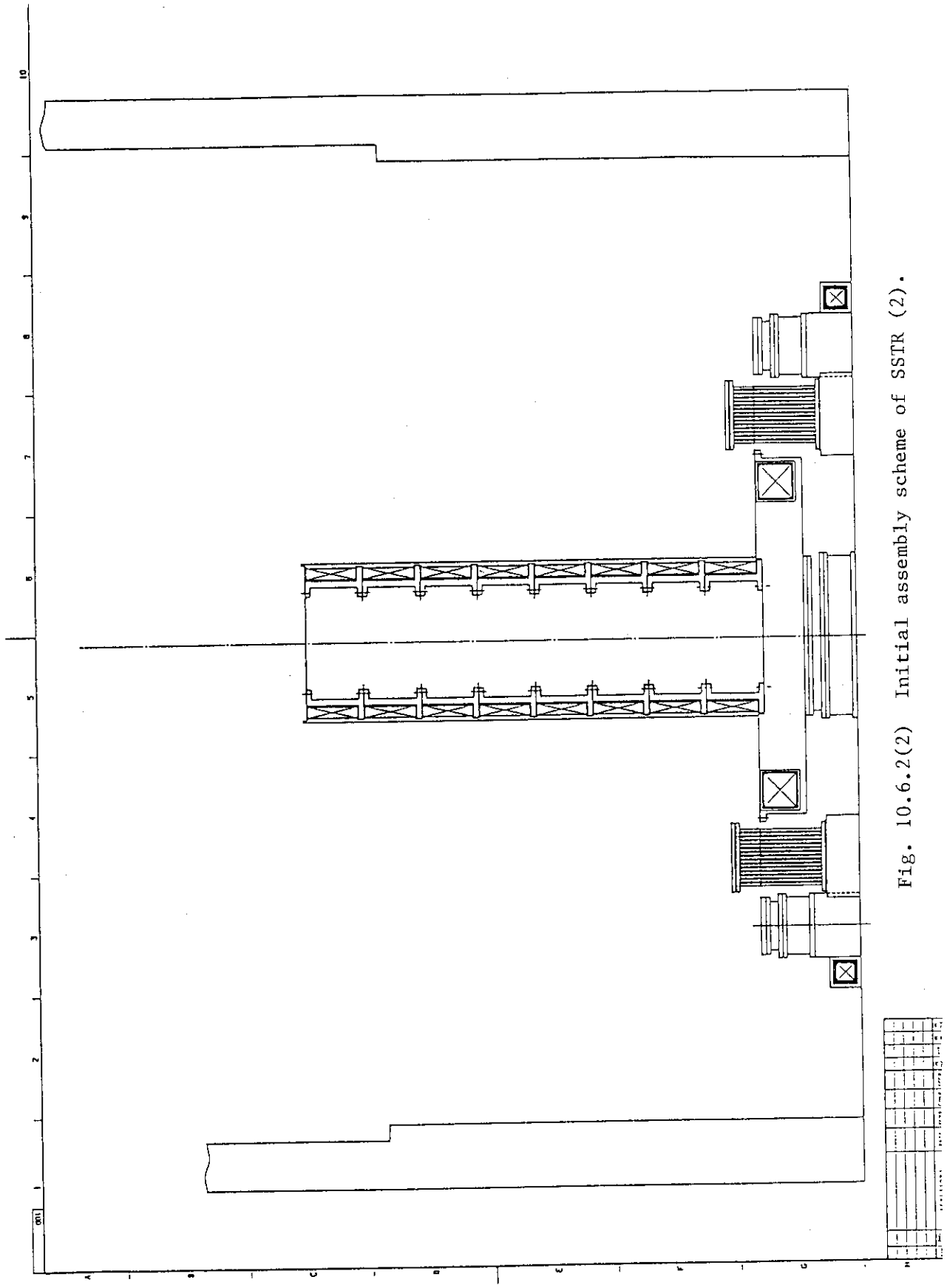

Fig. 10.6.2(2) Initial assembly scheme of SSTR (2).

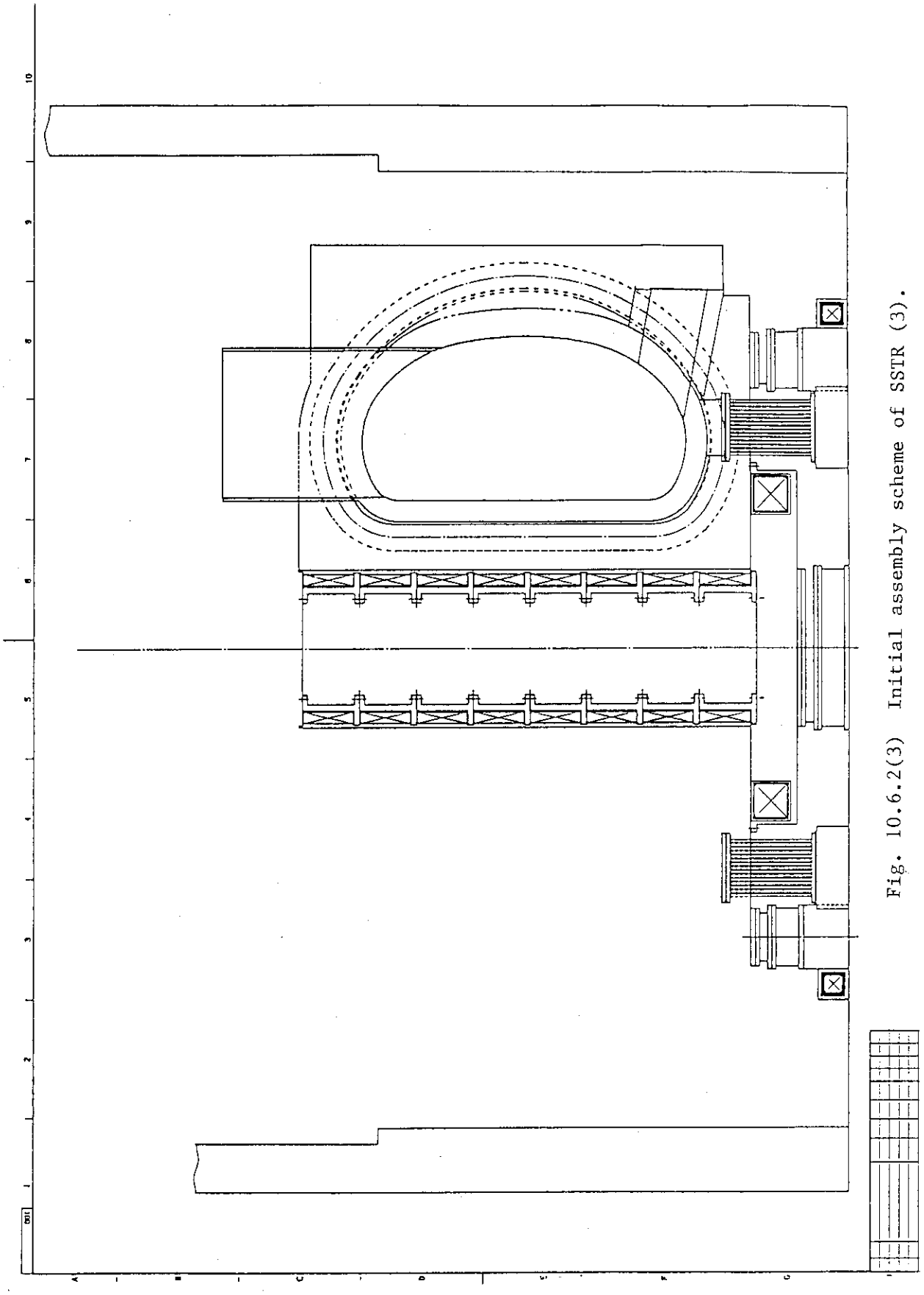

Fig. 10.6.2(3) Initial assembly scheme of SSTR (3).

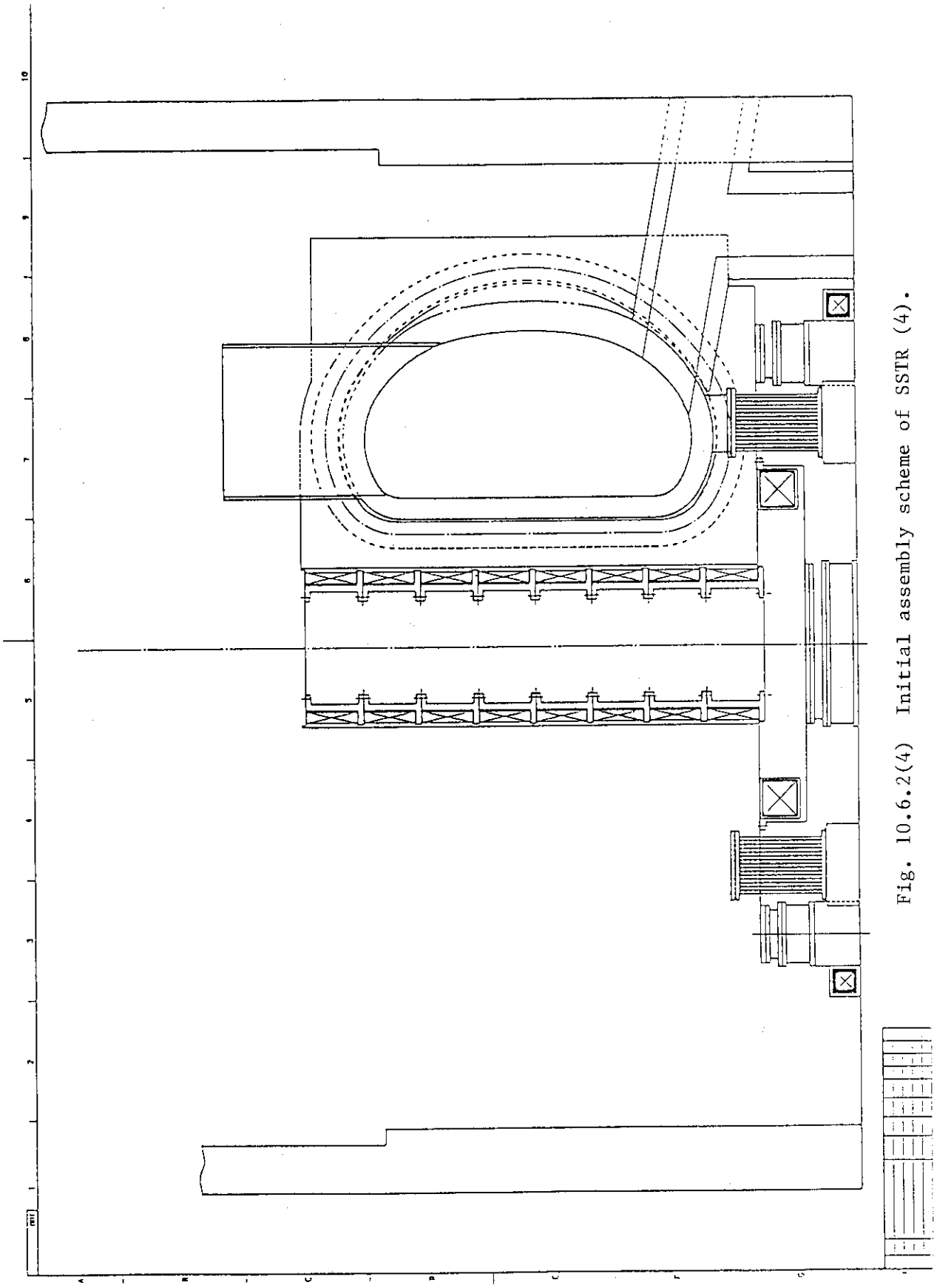

Fig. 10.6.2(4) Initial assembly scheme of SSTR (4).

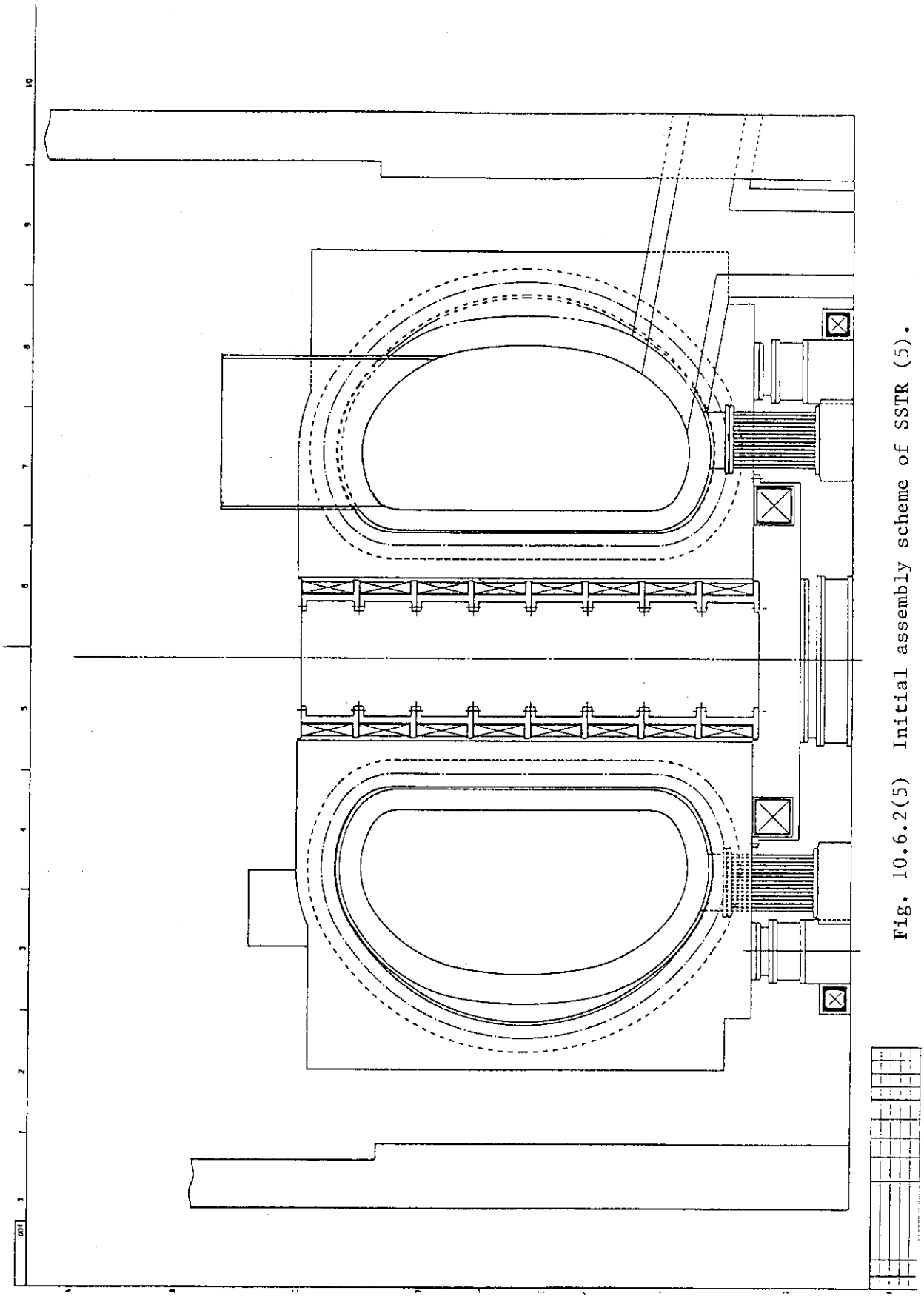

Fig. 10.6.2(5) Initial assembly scheme of SSTR (5).

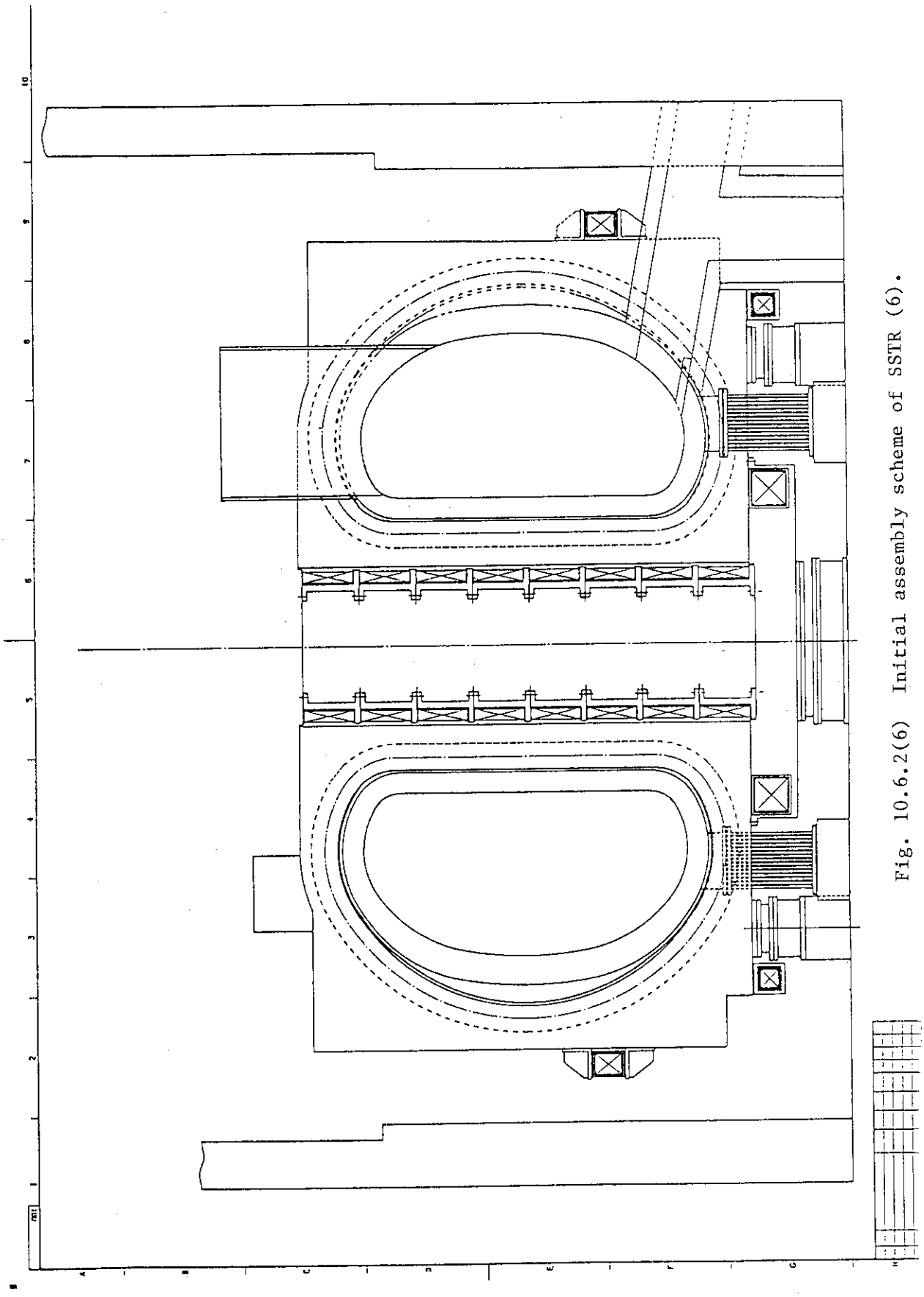

Fig. 10.6.2(6) Initial assembly scheme of SSTR (6).

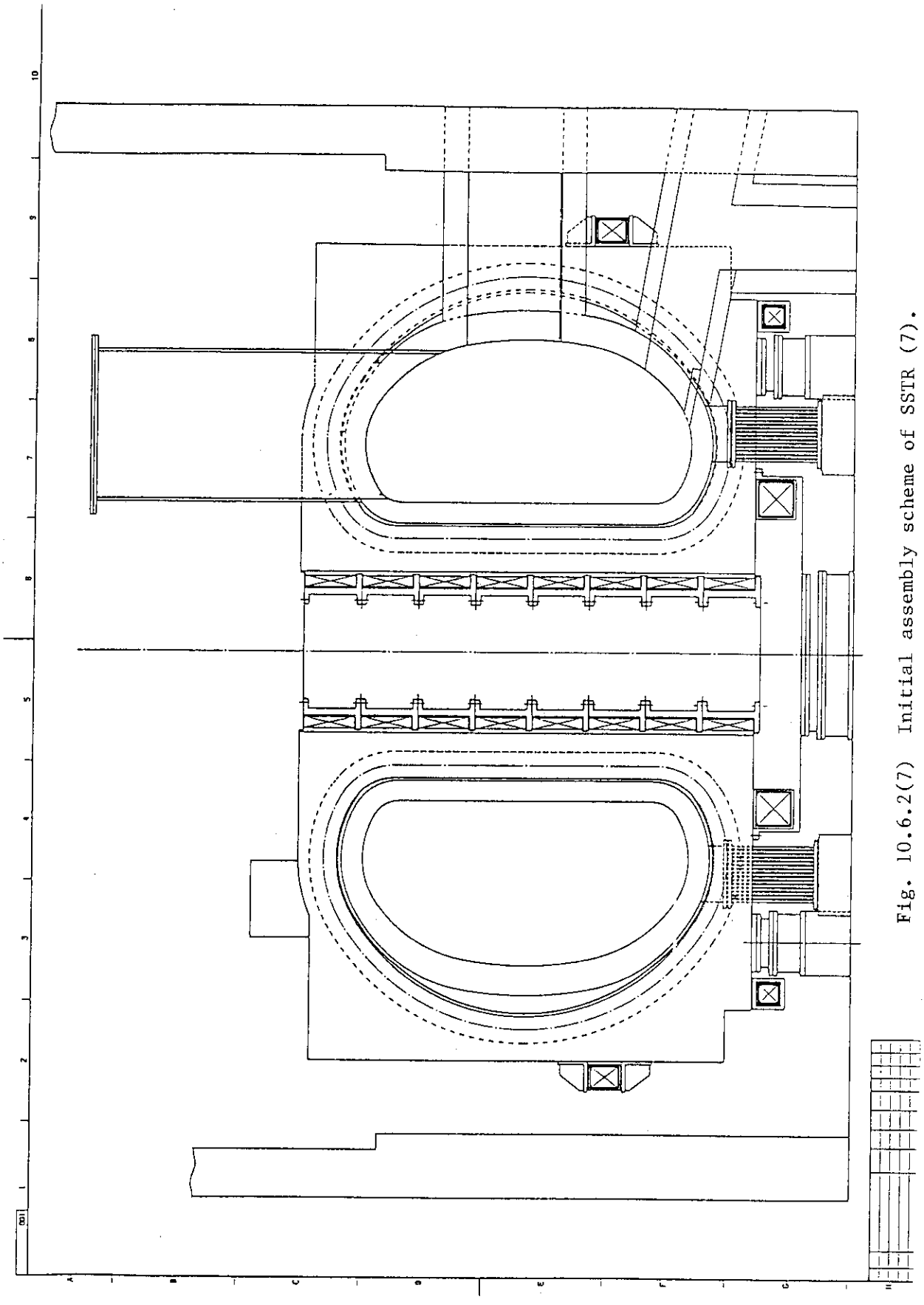

Fig. 10.6.2(7) Initial assembly scheme of SSTR (7).

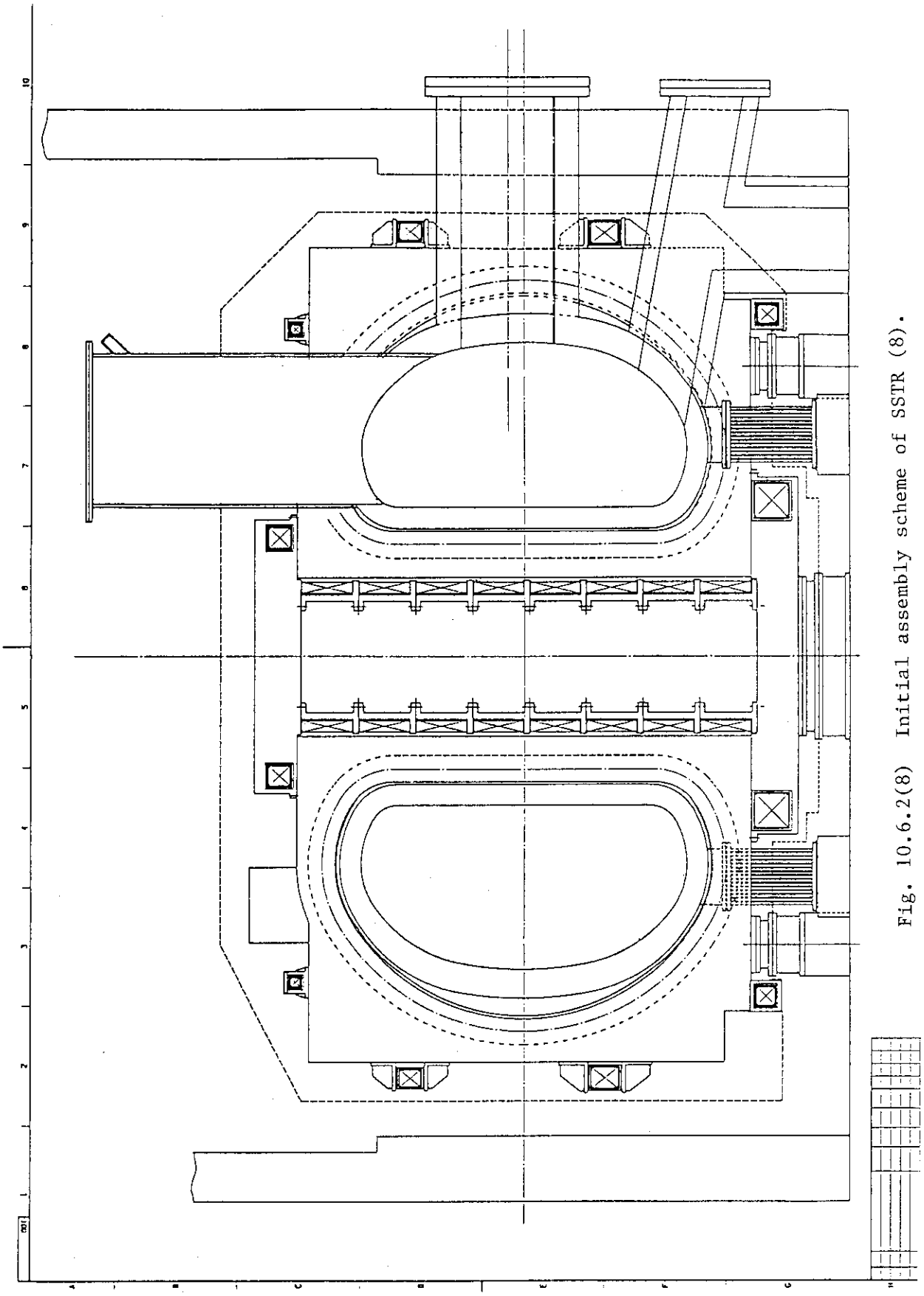

Fig. 10.6.2(8) Initial assembly scheme of SSTR (8).

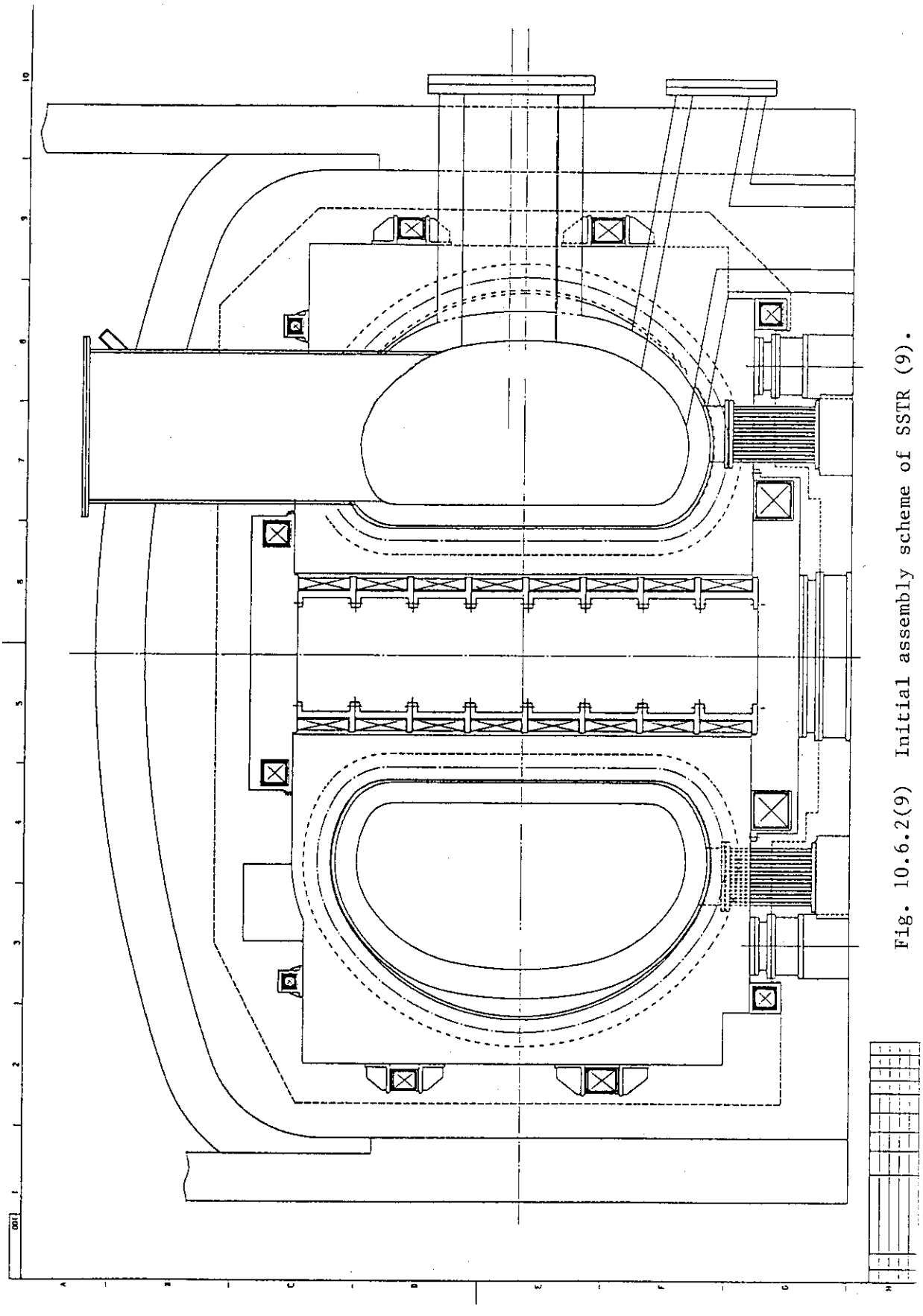

Fig. 10.6.2(9) Initial assembly scheme of SSTR (9).

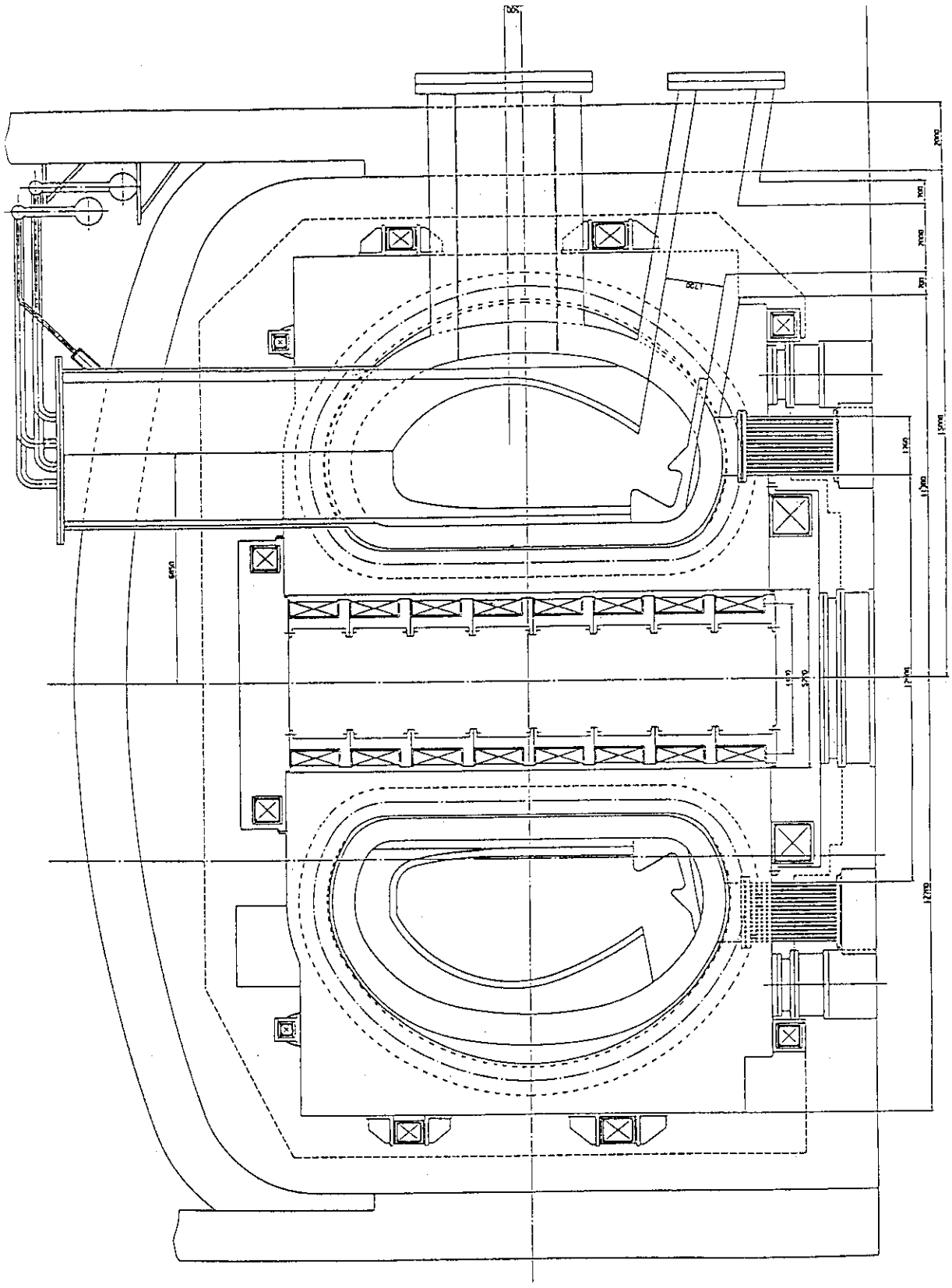

Fig. 10.6.2(10) Initial assembly schme of SSTR (10).

11. Neutral Beam Injection System

11.1 Introduction

The neutral beam injection system(NBI) for the fusion power reactor SSTR is required to deliver a 2MeV, 60MW neutral deuterium beam to the reactor plasma. The most important point in designing the NBI systems for the fusion power reactor is to attain a system efficiency higher than 50 %, preferably higher than 60 %. Since the NBI system for the fusion experimental reactor has a system efficiency lower than 40%, this system can not be applied for the fusion power reactor only by doubling the beam energy. In order to improve the system efficiency appreciably, a plasma neutralizer or a laser neutralizer which gives high neutralization efficiency higher than 80 - 90 %, or an energy recovery system must be utilized. With respect to the design of a 2MeV class NBI system, two systems have been proposed so far. The LBL group proposed a 2.1MeV, 110MW NBI system which utilizes an electrostatic quadrupole accelerator(ESQ) and a laser neutralizer.(1) On the other hand, the ORNL group proposed a 2MeV, 80MW NBI system which utilizes a radio-frequency quadrupole accelerator(RFQ) and a plasma neutralizer.(2) Though these designs are attractive, there is no sufficient data base to design the laser neutralizer and an efficient RFQ.

Unlike these design, the present proposal utilizes an electrostatic accelerator and the plasma neutralizer. Concerning the beam acceleration, the acceleration voltage is 2MV which is about twice the voltage for the fusion experimental reactor. The voltage holding characteristics at MV level is not so clear; in particular, high beam current and radiation from the reactor plasma may have a big influence on the voltage holding. Therefore, in order to improve the possibility to produce a high current 2MeV beam stably, the ion beam current per source was determined to be a modest value and the beamline layout was determined so that the accelerator should not be exposed directly to the strong radiation from the reactor. Additionally, decrease of ion beam output per source makes it possible to use a cockcroft type DC high voltage power supply as an acceleration power supply, and hence to eliminate the high voltage transmission line. Due to these considerations, we could propose a more realistic design concept of the 2 MeV NBI system.

The present design was conducted so that it would be realized using the technology for the NBI system of the fusion experimental reactor and technologies to be obtained by the additional 5 - 6 years' R&D.

11.2 System Overview

The NBI system was designed according to the basic performance characteristics shown in Table 11.2.1. A deuterium neutral particle beam of 60MW is injected nominally through two tangential ports (80MW at maximum). On each port is mounted one beamline which has eight ion sources. The front view and the plan view of the beamline are shown in Fig.11.2.1 and Fig.11.2.2, respectively. Four ion sources are mounted symmetrically on both side of the beamline axis. The ion beam extracted from the source is deflected by 60 degrees with an ion beam bending system, and injected in the plasma neutralizer cell. The gas pressure in the downstream region of the accelerator and the ion beam bending system is kept to be 0.007Pa to suppress the negative ion loss by the collisions with gas particles below 10% of the negative ions. In such a low gas pressure, it is thought that the space charge blow-up does not occur. In particular, xenon gas from the plasma cell enhance the effect of space-charge neutralization. Since the four ion sources on each side are arranged with some vertical shift, the ion beams from each source does not interfere with each other. Eight(8) beams, 2 rows by 4 lines, are injected in the plasma cell. Since each ion source is shifted sideways with respect to the beamline axis, the source is not exposed directly to the strong radiation from the reactor plasma. This arrangement makes many advantages: the ion source radioactivation is mitigated so that the maintenance becomes easy, voltage holding characteristics of the accelerator is not disturbed by the radiation, and the neutron shield of the source is easy so that the weight can be reduced. Additionally, the remote maintenance of the source is simple because the beamline components including the ion source are arranged on the same floor.

In the plasma cell, a high density Xe plasma is produced efficiently by the RF discharge, and the negative ions lose their electrons by collisions with the plasma to be neutralized. About 85% of the negative ion beam is neutralized, while the residual ions of 15% are deflected by a couple of coils placed at the exit of the neutralizer and handled by the beam dump. The pressure in the beam dump region and the torus port region is kept to be 0.002Pa to suppress the electron stripping loss of the neutral beam below 5%.

The beamline vacuum vessel and the ion source high pressure SF_6 gas vessel serves as a magnetic shield and a neutron shield. In the gas evacuating system, large turbo molecular pumps are adopted instead of a cryopump, and hence this makes it possible to simplify the evacuating system.

Thus the beamline is designed to deliver a maximum neutral beam power of 5MW per ion source, and 40MW per port. Since the output of the acceleration power supply of each source is about 10MW and relatively small compared to the design for the fusion experimental reactor, a cockcroft type DC high voltage power supply was adopted. The output power is still one order of magnitude higher than that of the power supply

commercially available, though it will be reasonable technologically to develop this power supply. By utilizing this power supply, the high voltage components can be arranged in the ion source region, and the high voltage transmission line, which makes the system complicated, can be eliminated. The design concept of this NBI system is shown in Fig.11.2.3 schematically. The power flow and the mass flow in the beamline are shown in Fig.11.2.4.

Table 11.2.1 Basic design parameters for SSTR

Beam Energy	: 2 MeV
Neutral beam power	: 60 MW (Max. 80 MW)
Pulse Duration	: CW
Beam Species	: D
Injection Port	: 2
Port Size	: 0.8 m x 2.8 m elliptic
Total System Efficiency	: > 50 %

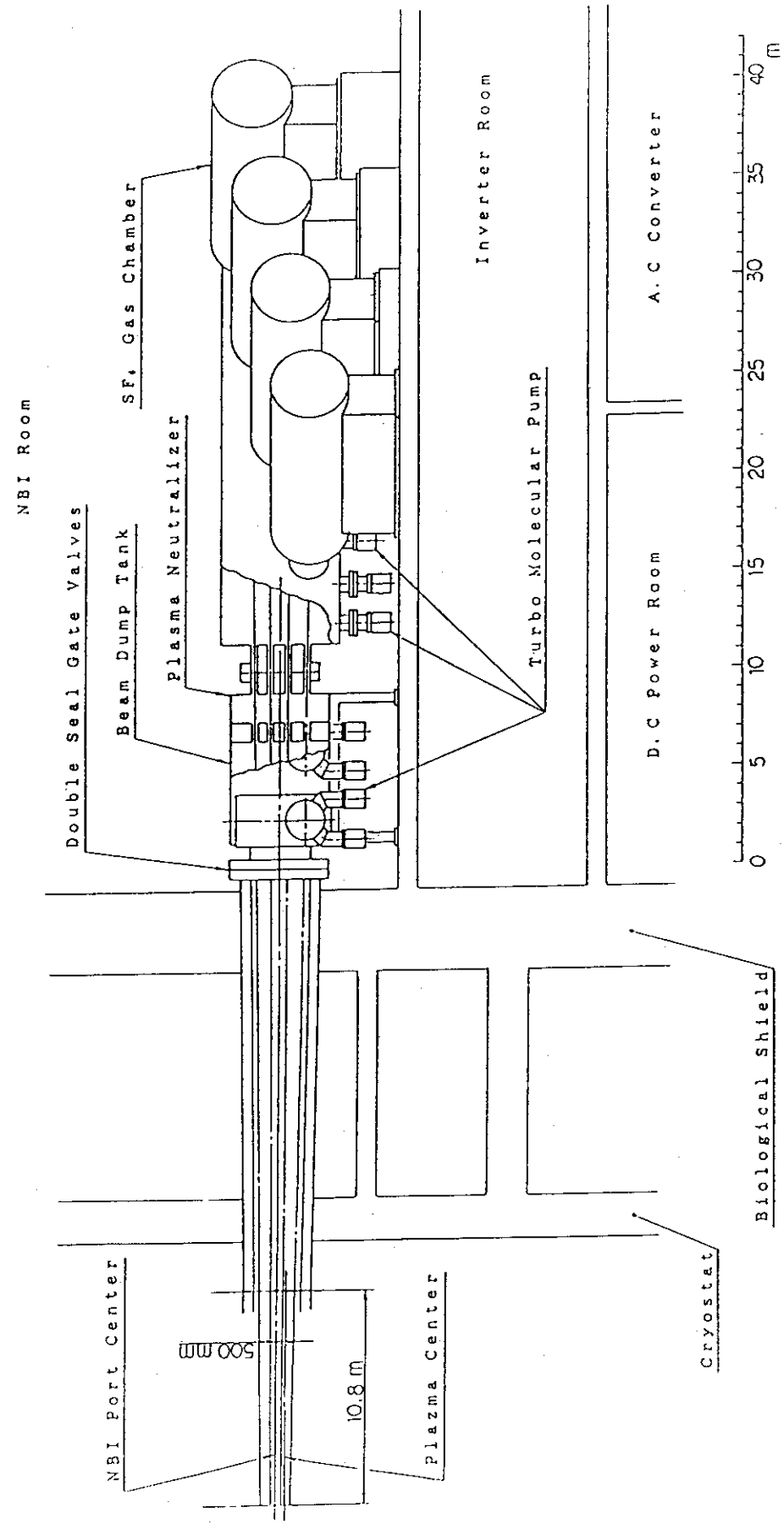

Fig. 11.2.1 Side view of the NBI beamline module layout.

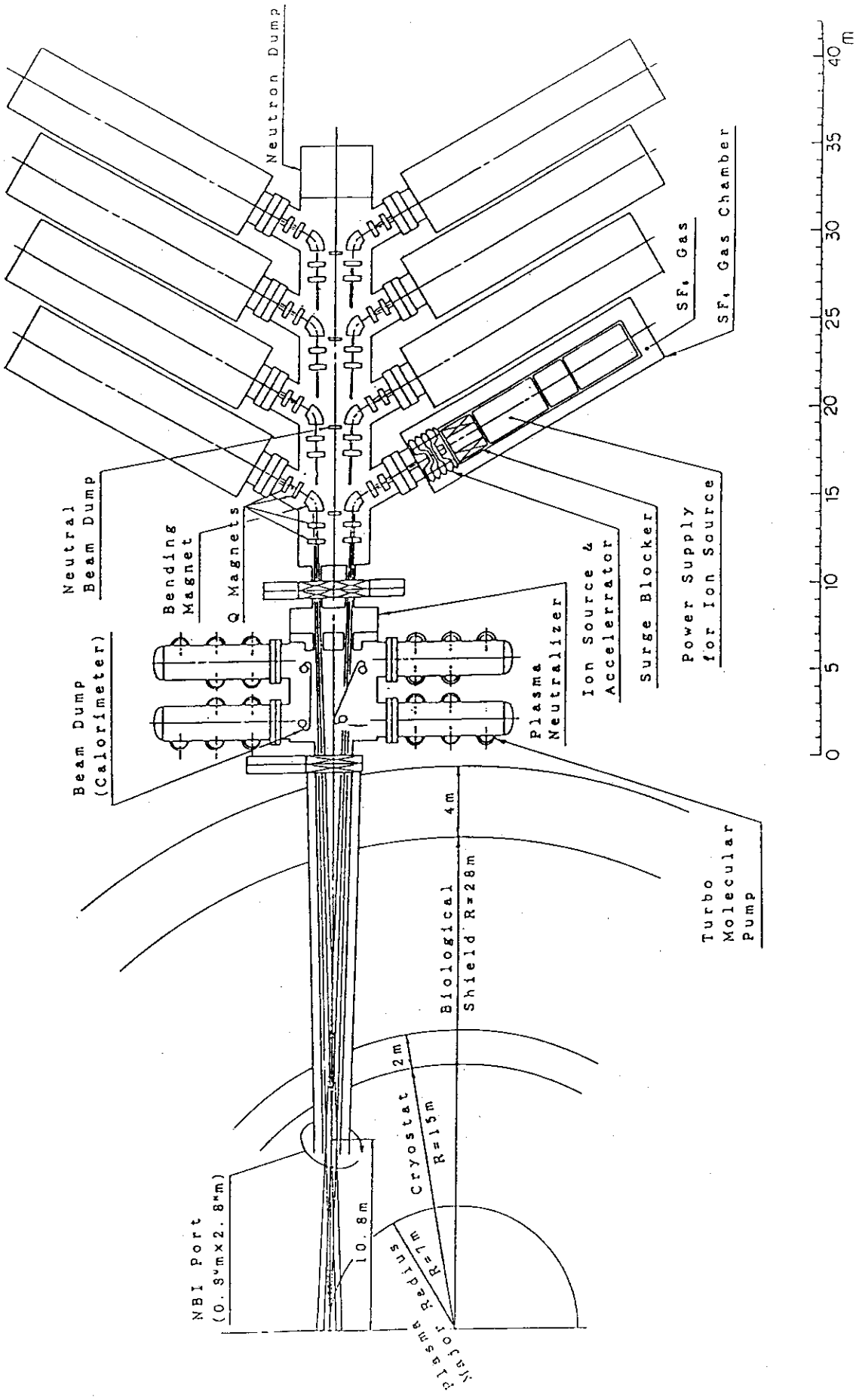

Fig. 11.2.2 Top view of the NBI beamline module layout.

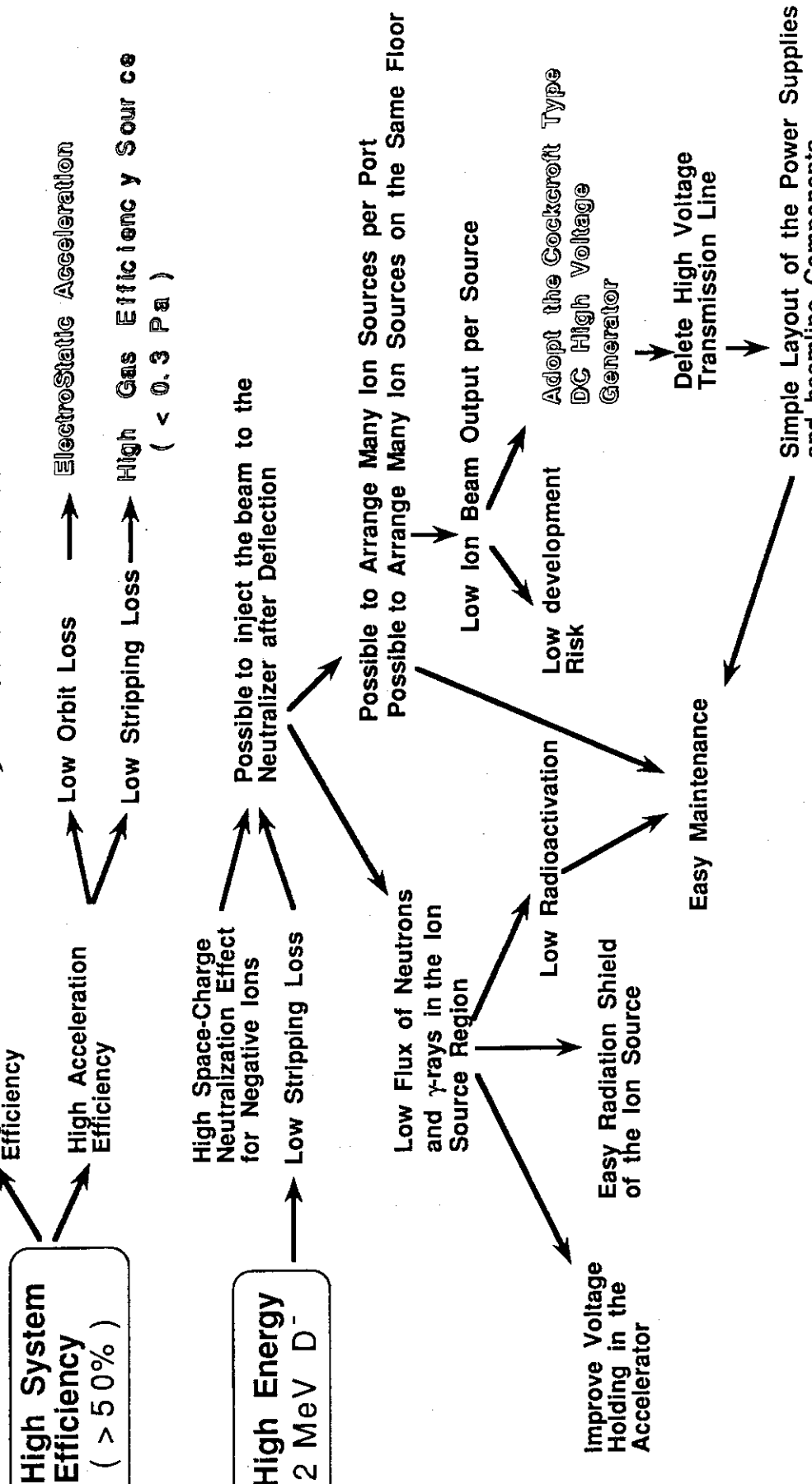

Fig. 11.2.3 Design concept of the SSTR-NBI.

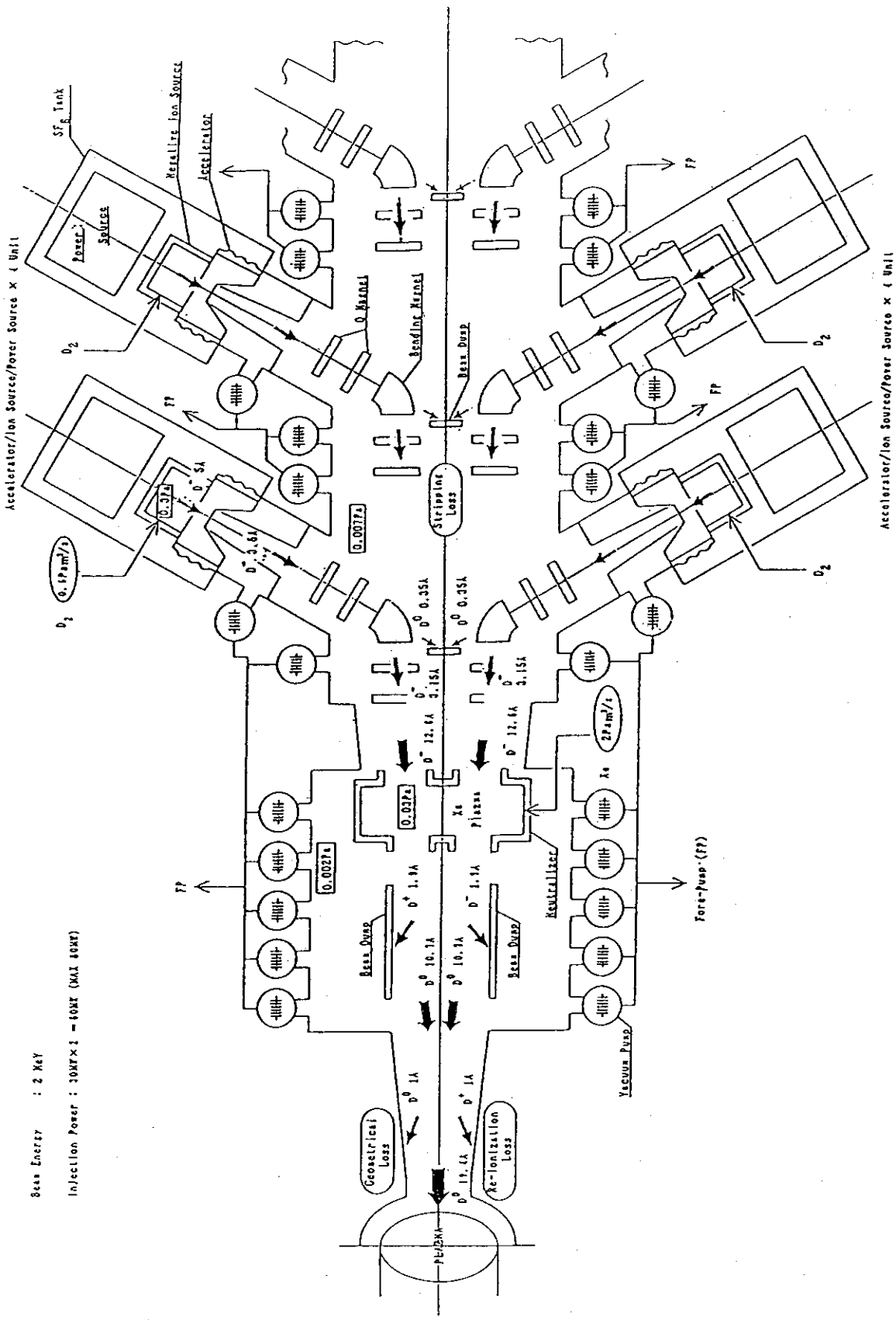

Fig. 11.2.4 Power and mass flow diagram in the beamline.

11.3 Beamline

11.3.1 Ion Source

The ion source specifications required are shown in Table 11.3.1. The ion source, which is composed of a negative ion generator and an accelerator, is shown in Fig.11.3.1. The type of negative ion source will be determined depending on the future R&D results. The most important point to develop the source is to obtain a higher negative ion current density at the source operating pressure as low as possible. Even if a high negative ion current density should be attained, most of the ions will be lost with collisions of gas particles when the operating pressure is high. So far, a cesium-seeded volume type negative ion source has produced a negative ion current density of 16mA/cm^2 at the pressure of 0.3Pa. It will be reasonable to expect to attain the design value of 40mA/cm^2 at 0.3Pa from the recent rapid progress on the source development.

With respect to the negative ion acceleration, high frequency acceleration such as RFQ can not be utilized because of its poor acceleration efficiency. On the other hand, electrostatic acceleration gives a high acceleration efficiency and high power supply efficiency, though it is not clear yet whether or not an ampere class high current ion beam can be accelerated to 2MeV stably. If we can develop an effective method to suppress the production of high energy electrons, stable acceleration of a high current beam will be possible. This electrostatic acceleration method has several types such as a multi-aperture and multi-stage acceleration or an electrostatic quadrupole acceleration. The best type will be determined depending on the results of future R&Ds. The design value of beam output at 2MeV is still two orders of magnitude higher than the achieved value. Stable acceleration of a high current beam is a critical R&D issues in realizing this NBI system.

11.3.2 Ion beam bending system

(1) Deuterium beam condition

The condition of the deuterium beam entering the ion beam bending system from the accelerator is as follows.

- Accelerating particle : D^-
- Beam energy : 2 MeV
- Beam size : 30 cm wide x 12 cm high
- Beam current : 3.5 A (up to 10 mA cm^2)
- Beam divergence : 3 mrad
- Energy spread : ±1%

(2) Structure of ion beam bending system

The configuration of the ion beam bending system is shown in Fig. 11.3.2. In order to avoid damage by neutrons directly from the core plasma, the ion source and accelerator are at an angle of 60 degrees with respect to the NBI port. The deuterium negative ion beam from the ion source is accelerated to 2 MeV in the accelerator, and bent by 60 degrees by the ion beam bending system, and enters the plasma neutralizer.

There is one unit of ion beam bending system for one ion source, and eight units are installed in one beam line. One ion beam bending system is composed of four quadrupole magnets and one bending magnet.

The deuterium beam leaving the accelerator has a rectangular cross section 30 cm in width and 12 cm height, and runs forward while gradually spreading at a divergence of 3 milliradians. The deuterium beam is reduced in the horizontal direction by the quadrupole magnet Q1 and in the vertical direction by Q2, and enters the bending magnet B1. By reducing the sectional size of the deuterium beam entering B1, the size of B1 is kept small.

The deuterium beam entering the B1 is bent by 60 degrees. To bend the deuterium beam of 2 MeV by a radius of 1 m, a magnetic field with an intensity of 3 kG is required. The deuterium neutralized from the exit of the accelerator up to bending magnet B1 runs straight forward, and enters the neutral beam dump.

Of the deuterium beams of 7 MW leaving the accelerator, ten percent or 0.7 MW are estimated to be neutralized. Since the spreading of the beam when entering the bending magnet B1 is suppressed, the thermal load of the neutral beam dump is as much as 4 kW/cm^2 on average per beam spot, and some countermeasures are necessary.

The deuterium beam passing through the bending magnet B1 is adjusted by the quadrupole magnets Q3, Q4 so that the size may be minimized near the neutralizer cell in the vertical direction, and that it may be narrowest in the NBI port near the toroidal magnet in the horizontal direction. The direction of incidence is fine-adjusted by the fine-adjusting bending magnet so as to enter the opening part of the neutralizer cell exactly.

(3) Beam transport calculation

Fig. 11.3.3 shows the result of calculation of the beam transport together with the configuration of the ion beam bending system in the fourth stage, the remotest one from the

core plasma. In the calculation, the "TRANSPORT" code developed by SLAC was used. Since the beam come out from the rectangular porous plate electrode, it is approximated by an ellipse here.

From the accelerator outlet to the plasma center, the beam track is 67 m. The beam leaving the accelerator is reduced by the quadrupole magnets Q1, Q2, and is formed into a section of 18 mm x 18 mm at the exit of the bending magnet B1. After passing through the quadrupole magnets Q3, Q4, it advances while spreading at a certain divergence. At the plasma neutralizer entrance, it becomes 376 x 259 mm, and then it has a section of 542 x 626 mm at the narrowest part of the NBI port.

Fig. 11.3.4 shows the configuration of eight beams at the narrowest part of the NBI port. The lower the beam, the closer becomes the distance from the ion source and core plasma, and the smaller is the beam spread.

(4) Coil design

The shape and specification of quadrupole magnets Q1, Q2, bending magnet B1, and quadrupole magnets Q3, Q4 are shown in Figs. 11.3.5, 11.3.6, 11.3.7, respectively. These are ordinary conductive coils, and designing is easy. The biggest one, B1, is 1.14 m high, and the ion beam bending system can be installed at a step difference of 1 m in the form of a staircase.

Since the coil is directly exposed to fast neutrons from the core, it seems necessary to shield it. Besides, since it is in a vacuum, Joule's heat cannot be dissipated, and water cooling may be required.

11.3.3 Plasma Neutralizer Cell

(1) Efficiency and Optimum Line Density

Negative ion beams injected into the plasma neutralizer cell are neutralized by the collisions with the plasma particles. The main process is the electron stripping collision with multiply charged xenon ions;

$$D^- + Xe^{q+} \text{ --- } D^0 \text{ ..... } \sigma_{-0}$$

The following two processes, the double electron stripping process and the ionization of neutrals, occurs simultaneously;

$$D^- + Xe^{q+} \text{ --- } D^+ \text{ ..... } \sigma_{-+}$$

$$D^0 + Xe^{q+} \text{ --- } D^+ \text{ ..... } \sigma_{0+}$$

Since the beam energy is high and the ion charge number is large, reactions with electrons such as the electron capture reaction is negligible. Hence the maximum neutralization efficiency η_N and the optimum ion line density which gives the maximum value π_{opt} are expressed as follows;

$$\eta_N = \left(\frac{\sigma_{-0}}{\sigma_{-0} + \sigma_{-+}}\right)\left(\frac{\sigma_{0+}}{\sigma_{-0} + \sigma_{-+}}\right)^{\gamma} \qquad (1)$$

$$\gamma = \frac{\sigma_{0+}}{\sigma_{-0} + \sigma_{-+} - \sigma_{0+}}$$

$$\pi_{opt} = \frac{1}{\sigma_{-0} + \sigma_{-+} - \sigma_{0+}} \ln\left(\frac{\sigma_{-0} + \sigma_{-1}}{\sigma_{0+}}\right) \qquad (2)$$

There is no sufficient data base on the cross section of the reaction between the negative deuterium ions and multiply charged xenon ions with a charge number of q. In the present estimation, therefore, σ_{-0} was assumed to be proportional to q^2 and the cross section data on argon in reference (3) was used. Additionally, the charge number q was assumed to be 3.6 which was an average charge number obtained at JAERI in the xenon plasma production experiment using microwave.[4] Namely, substituting the cross section data at q = 3.6 and E = 2 MeV;

$$\sigma_{-0} = 5.9 \times 10^{-15} \text{ cm}^{-2}$$

$$\sigma_{-+} = 2.3 \times 10^{-16} \text{ cm}^{-2}$$

$$\sigma_{0+} = 1.9 \times 10^{-16} \text{ cm}^{-2}$$

in the equations (1) and (2), the neutralization efficiency and the optimum line density are obtained as follows;

$$\eta_N = 0.86$$

$$\pi_{opt} = 4.8 \times 10^{14} \text{ ions / cm}^2.$$

Though the present design uses these values, they may be changed depending on the accumulation of the data base. For example, the optimum line density must be doubled according to the experimental result that σ_{-0} is proportional to $q^{1.3}$. [5]

(2) Structure

Figure 11.3.8 shows the structure of the plasma neutralization cell. The cell is a rectangular discharge chamber with the length of 2 m, whose wall surfaces are enclosed with line cusp magnetic field produced by the permanent magnets. In the discharge chamber, xenon gas is introduced and microwave is injected to make electron cyclotron resonance on the line cusp and a highly ionized plasma is produced by the fast electrons. Though the strong magnetic line cusp field serves as the resonant field and the plasma confinement, the line cusp field is arranged symmetrically so as not to produce a residual magnetic field in the beam path.

The plasma cell has eight (8) slots at both ends, 2 rows by 4 lines, corresponding to the eight beams from the eight sources. The dimensions of each slot are 400mm wide by 300mm high.

The basic parameters of the plasma neutralization cell are as follows;

Gas Species	: Xe
Effective Length	: 200 cm
Plasma Density	: 2.4 x 10^{12} cm^{-3}
Ion Line Density	: 4.8 x 10^{14} ions / cm^2
Average Ion Charge Density	: 3.6
Ionization Ratio	: 25 %
Xenon Gas Pressure	: 0.03 Pa.

11.3.4 Beam dump

In the beam dump, 15% of the total beam not neutralized in the plasma neutralizer are bent, and enter the beam dump to be gasified. The beam dump input for each ion source is 0.24 A, 475 kW as for both D^- and D^+. When the beams are arranged properly so that the positions where they enter the beam dump are not be concentrated, the heat receiving density of the beam dump is about 0.4 kW/cm^2 in average per beam spot, and when the peak is 2 or 3 times, it seems enough to be handled by the conventional swirl tube system.

In contrast, the calorimeter has a thermal load of about 4 kW/cm^2 per beam spot, and a cooling method must be considered. The structure of beam dump tank is shown in Figs. 11.3.9, 11.3.10. The calorimeter is arranged within the beam dump in order to shorten the overall length of the beam dump tank, and is driven vertically.

The beam inlet and outlet are opened at every eight beams for suppressing the inflow of gas and invasion of neutrons from the core plasma. The inlet is 50 cm wide by 30 cm high, and the outlet is 50 cm width by 50 cm high. The vacuum pumping system comprises an pumping duct and manifold provided at the lower part of the beam dump, a configuration with greater efficiency. The main vacuum pump is for 20 turbo molecular pumps.

The specification of the bending coil is as follows.

· Magnetic field on track	: 1 (kG)
· Bending radius	: 3 (m)
· Magnetomotive force	: 295 (kAT)
· Distance between magnetic poles	: 4 (m)
· Coil length	: 1.5 (m)

11.3.5 Exhaust system

A block diagram of the exhaust system of neutral beam injection system is shown in Fig. 11.3.11. The pumping system is assumed to be a combination of a turbo molecular pump and scroll pump, the same as in the vacuum pumping system of the main vacuum vessel.

(1) Ion source and accelerator

Deuterium gas flows into the ion bending system from the ion source through the accelerator. To suppress it, a pumping port is provided at the accelerator, for differential pumping. As a result, 90% of the deuterium is released differentially, and gas of 0.07 Pa·m^3/s per unit flows into the ion bending system.

(2) Ion bending system

The pumping conditions of the ion bending system are as follows.

1) Vacuum pressure: 0.007 Pa

2) Pumping volume

· Deuterium gas - 0.59 Pa·m^3/s

· From ion source - 0.56

· Stripping loss - 0.03

· Xenon gas flowing in from the plasma neutralizer: 0.35 Pa·m^3/s

(3) Beam dump tank

The pumping conditions of the beam dump tank are as follows.

1) Vacuum pressure: 0.002 Pa

2) Pumping volume

- Deuterium, DT gas - 0.2 Pa·m^3/s
  From beam dump - 0.04
  From plasma - 0.16
- Xenon gas flowing in from the plasma neutralizer: 0.35 Pa·m^3/s

Meanwhile, the xenon gas flow diffusing into the core plasma from the beam dump tank is 0.03 Pa.m^3/s. The pump composition is 35 turbo molecular pumps per beam line, and 2 fore pumps.

(4) Subjects for future research and development

- Development of large-capacity magnetic levitation turbo molecular pump.

  At present, the development of a magnetic levitation turbo molecular pump with the large capacity of 25 m^3/s is in progress, and it is expected to be put to practical use shortly.

- Development of large-aperture gate valve

  In the vacuum pumping system, since the conductance must be increased, a large-aperture gate valve of over 2 m will be required.

Table 11.3.1 Specifications of the ion source

(1) Negative Ion Generator

Type	: Volume - Surface
Extracted Current	: 5 A
Current Density (at Plasma Boundary)	: 40 mA/cm2
Extraction Voltage	: 50 kV
Extraction Area	: 12 cm x 30 cm = 360 cm2
Aperture	: 12.4 mm ID x 100 = 125 cm2
Transparency	: 35 %
Filling Pressure	: 0.3 Pa
Gas Flow Rate	: 0.6 Pa.m3 / s
Stripping loss in the extractor	: ~ 10 %

(2) Negative Ion Accelerator

Type	: Electrostatic
Accel. Energy	: 2 MeV
Beam Current	: 3.6 A
Current / channel	: 36 mA
Ripple of Energy	: < ± 1 %
Beam Divergence 1 / 2 x 1 / e	: 3 mrad
Stripping Loss in the accelerator	: ~ 20 %
Number of Stages	: 10
Electric Field Grad.	: ~ 3 kV / mm
Insulator	: ~ 2.5 m OD Aluminum

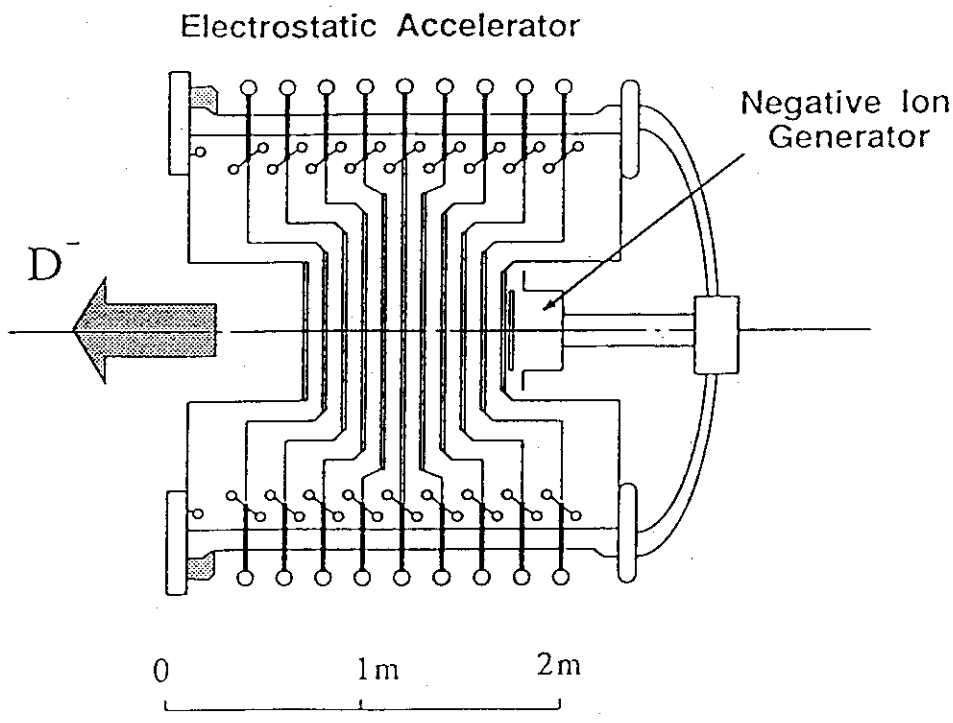

Fig. 11.3.1 Schematic view of the 2 MeV, 3.5 A deuterium negative ion source.

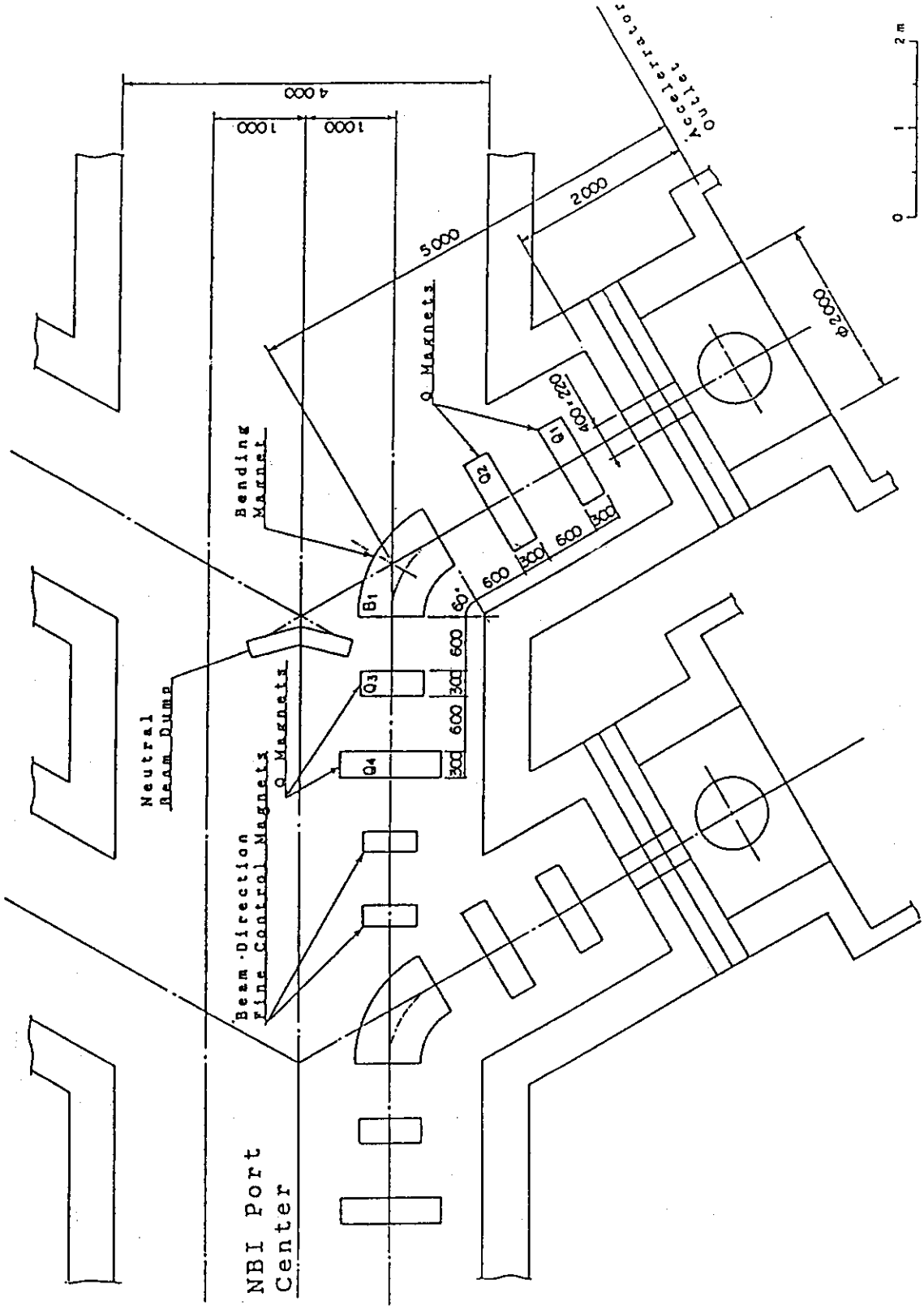

Fig. 11.3.2 Ion beam bending system. (top view)

Drift or Magnet	Distance (m) or Bending Angle (°)	Magnetic Field (kG)	Magnetic Field Gradient (kG/m)	Beam Size (mm)		Divergence (mrad)	
				Horizontal	Vertical	Horizontal	Vertical
Accelerrtor Outlet	0			300	120	3.	3.
Drift	2.62			300	121		
Q-Magnet Q1	0.3		6.4	270	134	13.5	6.7
Drift	0.6			154	184		
Q-Magnet Q2	0.3		-10.7	120	178	23.3	62.1
Drift	0.6			94	104		
Bending Magnet B1	60° (ρ=1a)	3.		18	18	53.4	58.3
Drift	0.6			61	87		
Q-Magnet Q3	0.3		-16.6	112	97	124.9	25.9
Drift	0.6			262	67		
Q-Magnet Q4	0.3		8.2	301	60	3.4	6.2
Bending Tank Outlet	17.42			371	240		
Neutralizer Inlet	1.0			376	259		
Neutralizer Outlet	1.5			383	270		
Neutralizer Duct Outlet	1.0			388	282		
Beam Dump Tank Outlet	6.5			422	362		
Biological Shield Inlet	1.0			427	374		
Biological Shield Outlet	4.1			449	425		
Cryostat Inlet	11.6			515	568		
Cryostat Outlet	2.2			527	595		
The Smallest Cross Section	2.5			542	626		
Plasma Center	10.8			607	760		

Fig. 11.3.3 Transport calculation result of the beam made in the most far ion source from plasma.

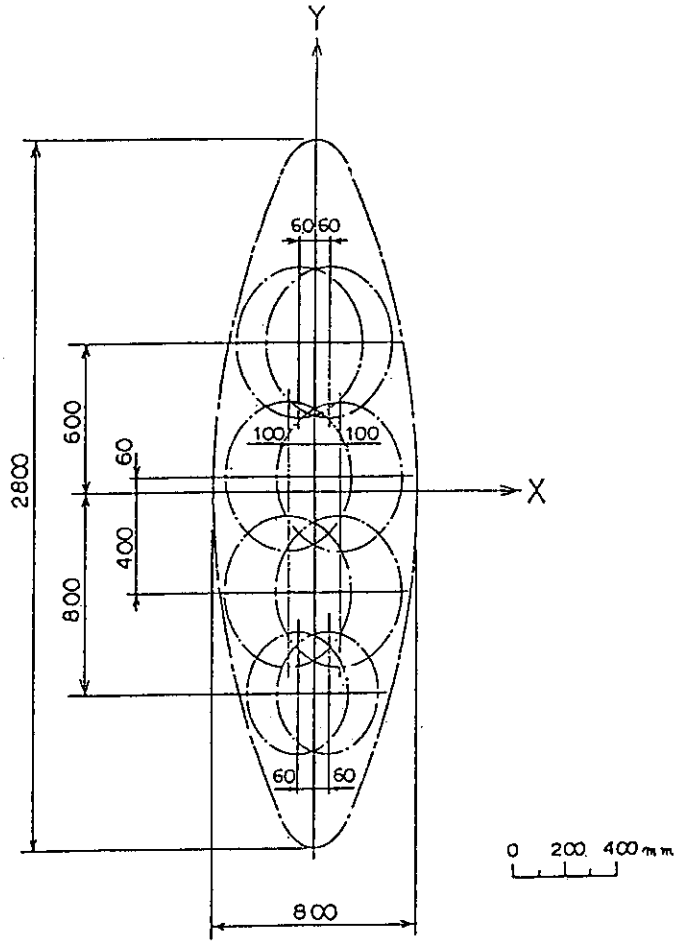

Fig. 11.3.4 Beam layout at the smallest cross section.

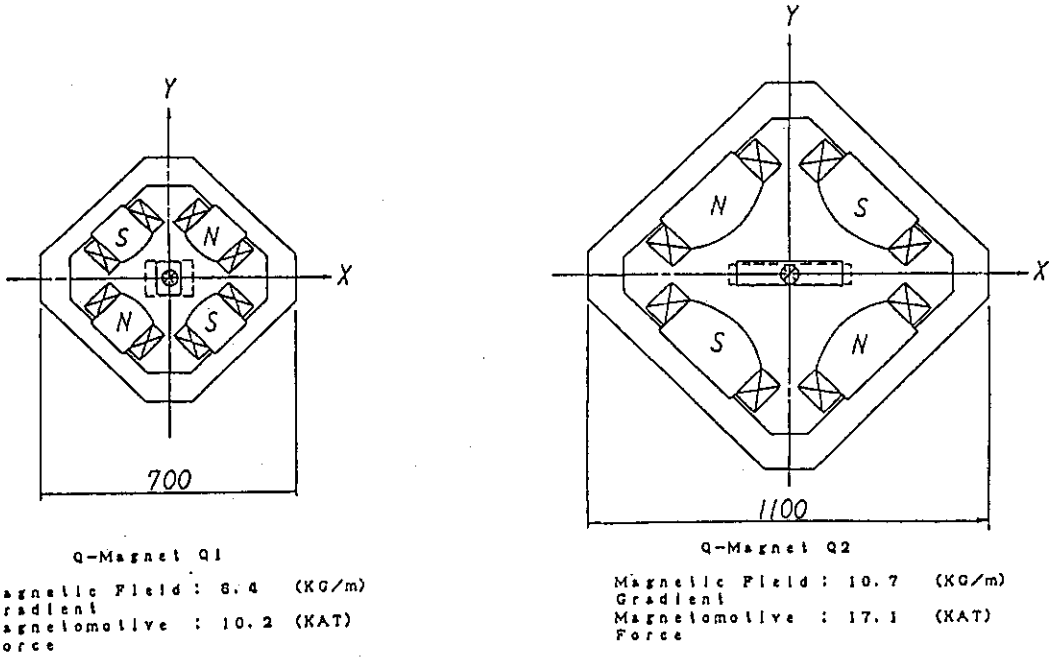

Fig. 11.3.5 Q-magnets Q1, Q2 of beam bending system.

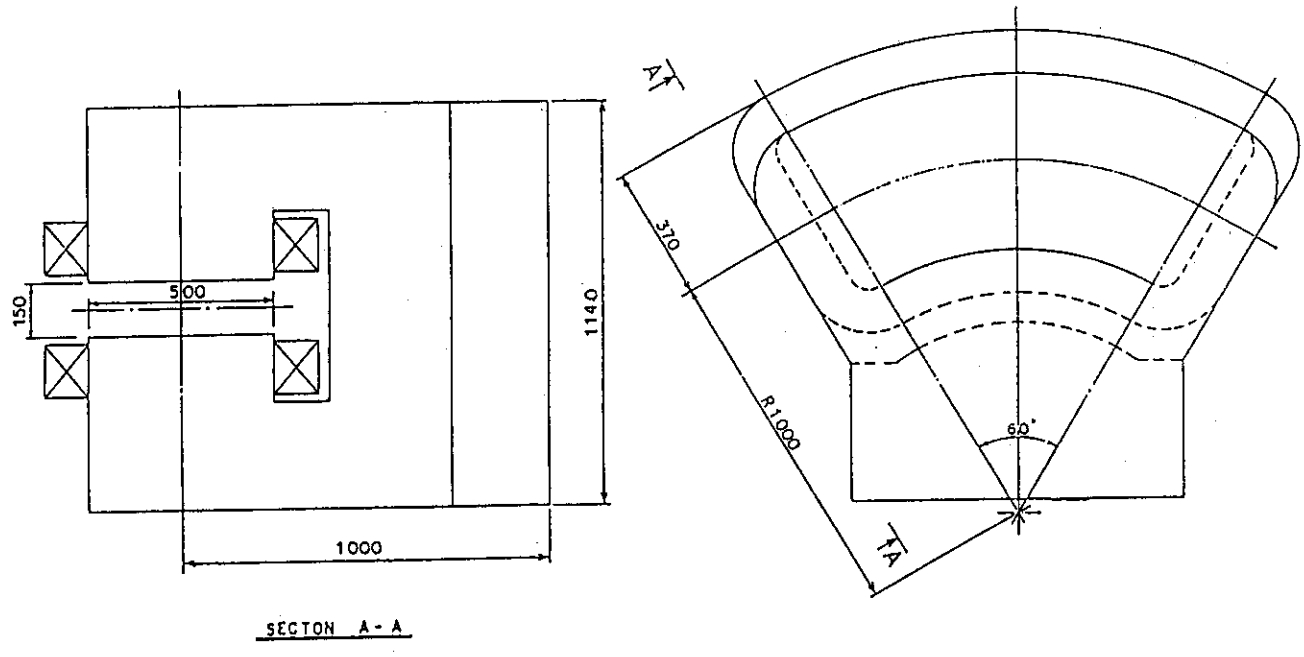

Fig. 11.3.6 Bending magnets of beam bending system.

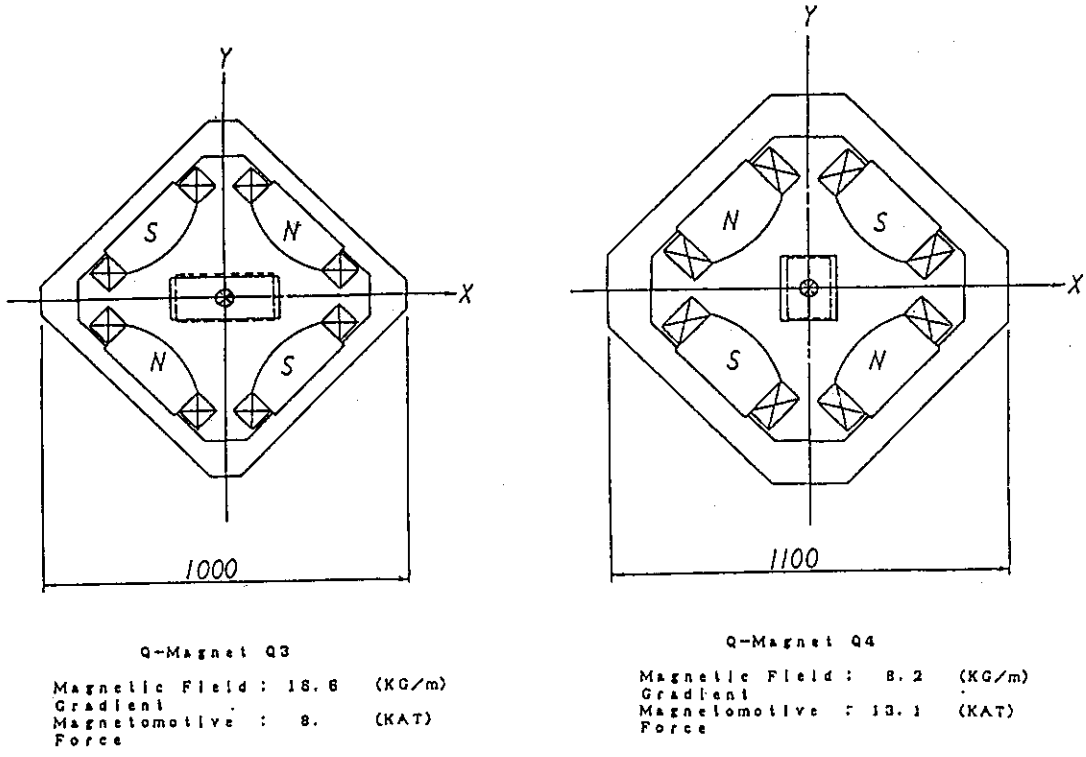

Fig. 11.3.7 Q-magnets Q3, Q4 of beam bending system.

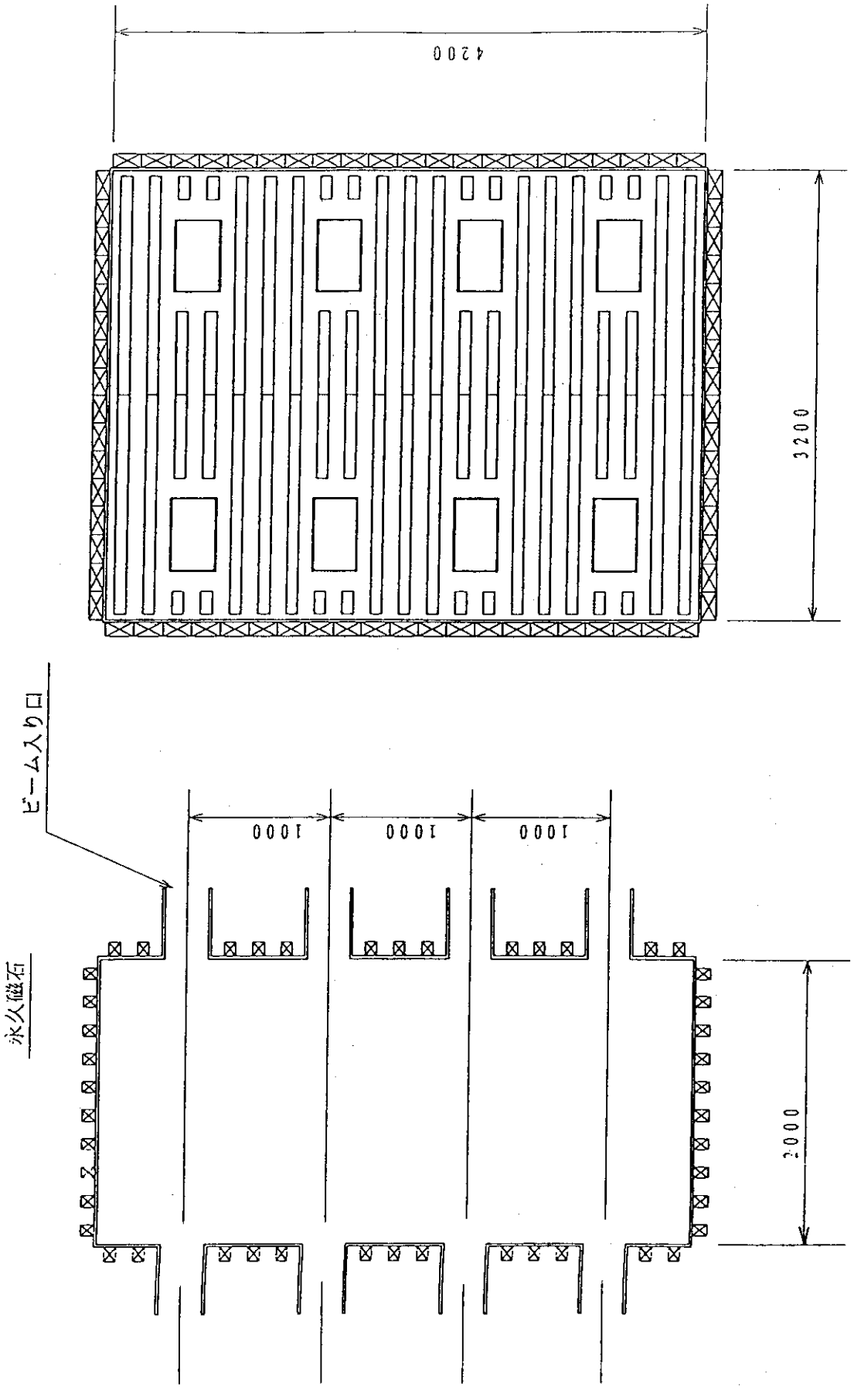

Fig. 11.3.8 Plasma neutralizer.

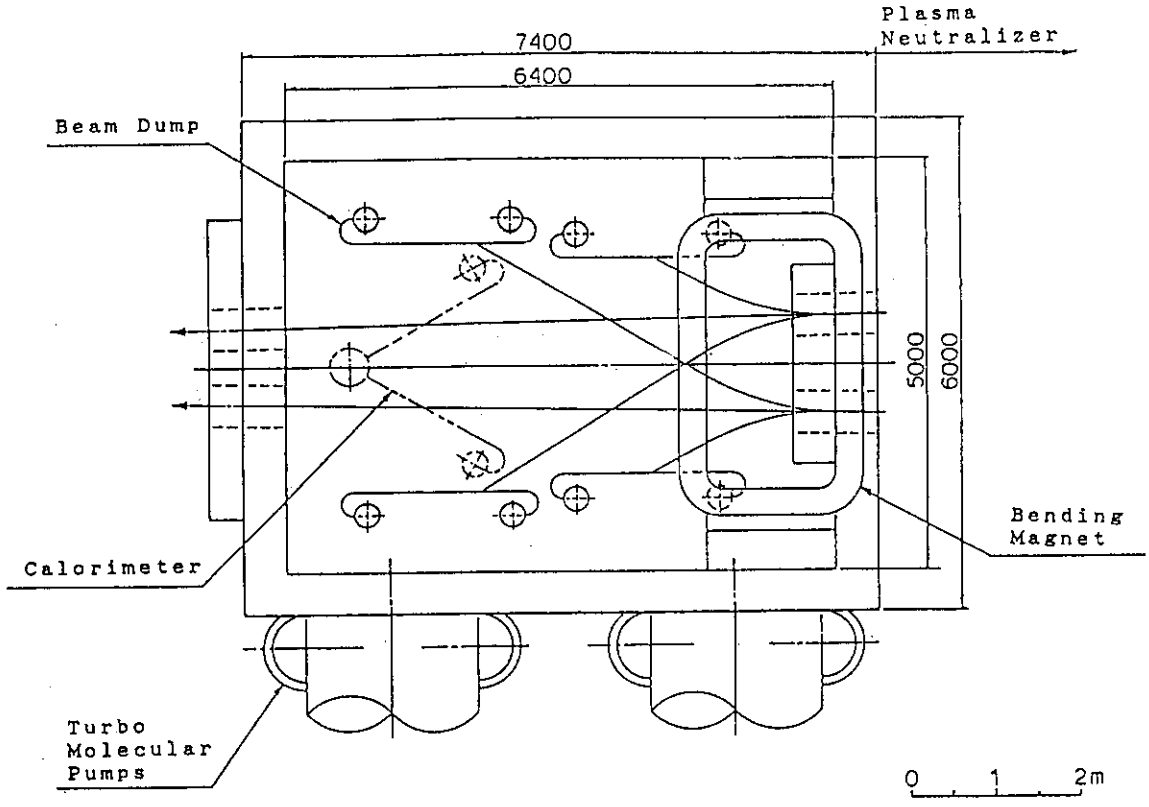

Fig. 11.3.9 Beam dump tank. (top view)

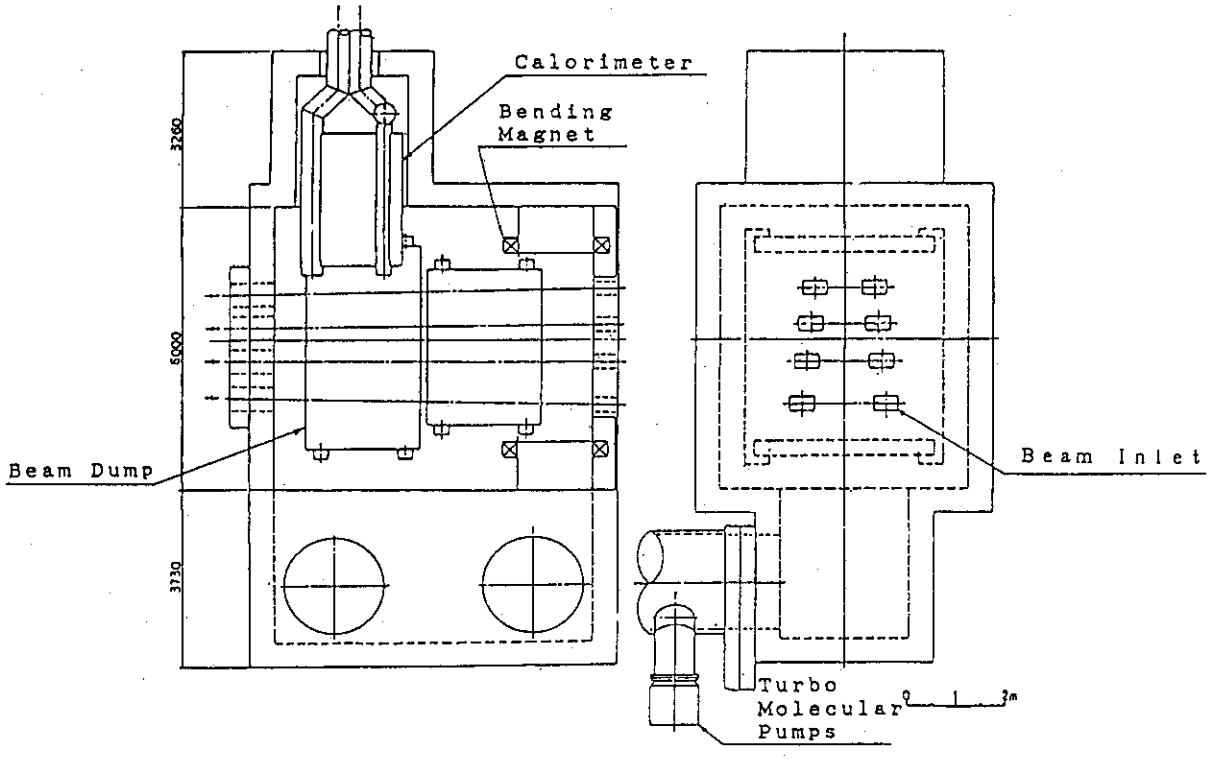

Fig. 11.3.10 Beam dump tank. (side view)

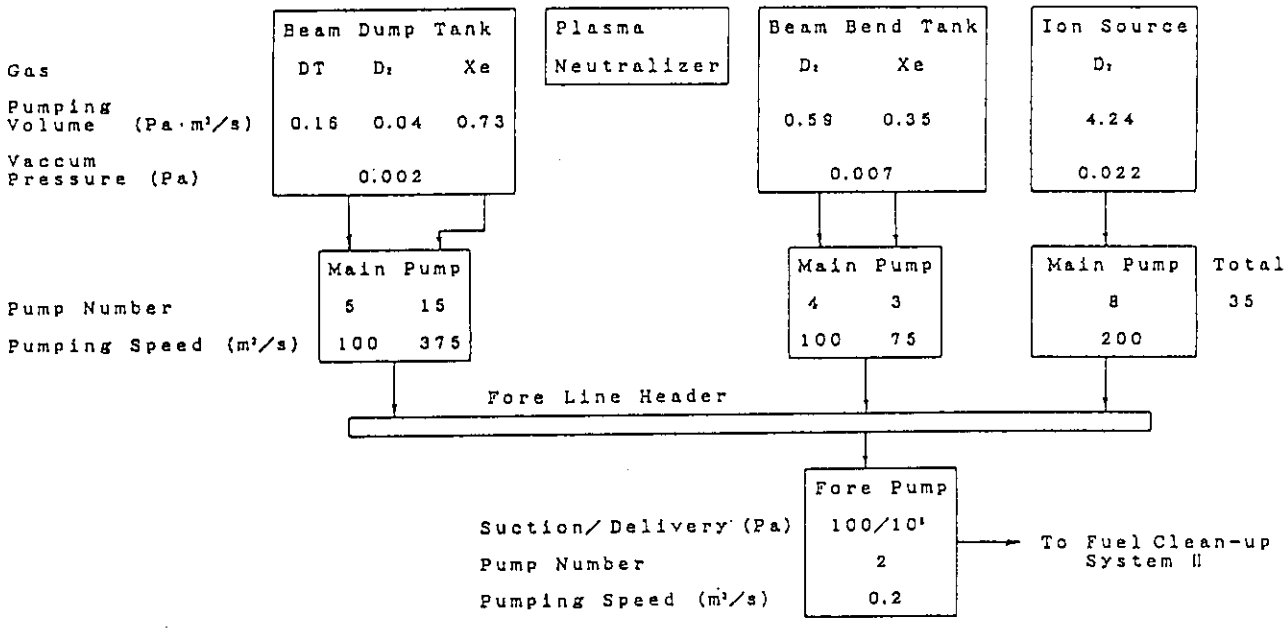

Fig. 11.3.11 NBI vacuum pumping system of 1 beam line.

11.4 Power supply

11.4.1 Acceleration power supply

11.4.1.1 Cockcroft & Walton type DC generator

The most usual method to obtain a DC high voltage is to combine a high voltage transformer and a rectifier. As examples of a method to obtain a DC high voltage that is n times the secondary voltage of the high voltage transformer, a Schenkel circuit which is a multi-stage cascade rectifier circuit, and a Cockcroft & Walton circuit can be used. Considering the specification of the acceleration power supply, this paragraph is to review the design of DC high voltage generator of a symmetric multi-stage cascade rectifier circuit which can improve the voltage drop and the ripple of a Cockcroft & Walton circuit.

(1) Acceleration power suply specification (design conditions)

1) Output voltage (V)	: 2 [MV]
2) Output current (I)	: 5 [A]
3) Voltage drop (ΔV)	: 10 [%] or less (200 kV or less)
4) Ripple (δV)	: 1 [%] or less (20 kV or less)
5) Number of stages (n)	: 10
6) Power supply frequency (f)	: 10 [kHz]
7) Voltage step up	: Symmetrical

(2) Attached drawings

Fig. 11.4.1 CIRCUIT DIAGRAM OF ACCELERATION POWER SUPPLY
Fig. 11.4.2 TOP VIEW OF ACCELERATION POWER SUPPLY
Fig. 11.4.3 SIDE VIEW OF ACCELERATION POWER SUPPLY
Fig. 11.4.4 SCHEMATIC CONSTRUCTION OF NBI POWER SYSTEM

(3) Design of constituent elements

1) Capacitor: C

1. C_m: Capacitance

The voltage drop ΔV of a symmetrical circuit is expressed as follows:

$$\Delta V = \frac{I}{fC_m}\left(\frac{n^3}{6} + \frac{n^2}{4} + \frac{n}{3}\right)$$

where,

f : frequency --- 10 [kHz]

C_m : Capacitance

n : Number of stages --- 10

I : Output current --- 5 [A]

Therefore it follows that

$$C_m = \frac{I}{f\Delta V}\left(\frac{n^3}{6} + \frac{n^2}{4} + \frac{n}{3}\right)$$

and supposing ΔV to be 10% of 2 MV (that is, 200 kV), we obtain

$$C_m = \frac{5}{10\times10^3\times2\times10^5}\left(\frac{10^3}{6} + \frac{10^2}{4} + \frac{10}{3}\right) = 0.5\mu F$$

At this time, the ripple (voltage) δV is expressed as

$$\delta V = \frac{I}{fC_m}\frac{n}{2}$$

$$\delta V = \frac{5}{10\times10^3\times0.5\times10^{-6}}\frac{10}{2} \approx 5kV$$

and it satisfies the specified value of 1% (20 kV).

2. V_C: Capacitor voltage (voltage per stage)

The voltage efficiency is expresses as $\eta = \frac{a}{n}\tanh(\frac{a}{n})$

Supposing the stray capacitance between columns to be C_S, it follows that

$$a = \left(\frac{C_m}{C_s}\right)^{0.5}, \text{hence } a = 100$$

Therefore, we obtain $\eta = \frac{100}{10}\tanh(\frac{10}{100}) = 0.997 = 99.7\%$.

The capacitor voltage V_C is expressed as $V_c = \frac{V}{\eta} \times \frac{1}{n} \times \varepsilon$.

where,

V : Output voltage [V] ---------- 2 [MV]

ε : Voltage distribution coefficient --- 1.05

The generation of rated output voltage V [V] and output current I [A] yields

$$V_c = \frac{V(2MV)+\Delta V(195kV)}{0.997} \times \frac{1}{10} \times 1.05 = 231[kV]$$

Meanwhile, supposing 110% (2.2MV) of the rated output voltage is to be generated as a test voltage, it becomes

$$V_{ct} = \frac{2.2MV}{0.997} \times \frac{1}{10} \times 1.05 = 232[kV]$$

2) Power transformer: T

1. Vs: Power transformer output voltage

$$V_s = \frac{V_c}{2} \times \frac{1}{\sqrt{2}}$$

and when the rated voltage and rated current are generated,

$$V_s = \frac{231kV}{2} \times \frac{1}{\sqrt{2}} = 82kV$$

or when the test voltage is generated,

$$V_s = \frac{232kV}{2} \times \frac{1}{\sqrt{2}} = 82kV$$

2. Q_T: Power transformer capacity

The charging current I_D (DC component) per unit is

$$I_D = \frac{1}{2} I \times n \times \tau$$

where,

I_D	: Charging current (DC component) [A]	
I	: Output current	[A] (I=5[A])
n	: Number of stages	(n=10)
τ	: Waveform factor	(τ=3)

Therefore, it follows that

$$I_D = \frac{1}{2} \times 5 \times 10 \times 3 = 75 \text{ [A]}$$

Hence the capacity Q_W of the DC component is

$$Q_W = V_{SI} \times I_D$$
$$= 82 \text{ [kV]} \times 75 \text{ [A]} = 6150 \text{ [kVA]}$$

The capacity Qs of the AC component (for stray capacitance between columns and the trans-former is)

$$Q_s = V_{SI}^2 \times 2pf \times C_0$$
$$= (82 \times 10^3)^2 \times 2 \times p \times 10^4 \times 5 \times 10^{-9} = 2110 \text{ [kVA]}$$

The total capaity Q_T is

$$Q_T = (Q_W^2 + Q_S^2)^{1/2}, \text{ that is}$$
$$Q_T = 6500 \text{ [kVA]}$$

3. Is: Power transformer secondary current

From $Is = Q_T/V_{sl}$, we obtain 80 [A].

3) Rectifier: D

In the case of symmetrical type, the current flowing in the rectifier is 1/2 of the output current. Therefore, assuming the waveform factor to be 2.0, the current flowing in the rectifier at the output current of I = 5A is as follows.

$$I_{REC} = \frac{1}{2} \times I \times 2.0 = 5A$$

The reverse withstand voltage V_1 applied per rectifier is the voltage (V_C) per step of the capacitor, therefore V_1 = 232 [kV]. Supposing three times the applied voltage to be the reverse withstand voltage V_{REC} of the rectifier,

$$V_{REC} = 232\ kV \times 3 = 696\ [kV]$$

4) Protective resistor: R1, R2

1. R1: Capacitor protective resistor

The condition of becoming non-oscilating discharge at the time of capacitor discharge is,

$$R = 2\sqrt{\frac{L}{C}}\ [\Omega]$$

supposing L to be 10 μH, the resistance is,

$$R1 = 2\sqrt{\frac{10\mu H}{0.5\mu F}} = 9\ [\Omega]$$

The capacity is the largest in the bottom resistor, that is,

$$W_{RI} = I_D^2 \times R1 = 75^2 \times 9 = 50.6\ [kW]$$

2. R2: Rectifier protective resistor

Supposing the rectifier forward surge current I_{FSM} = 100A, the resistance is $R_2 = V_C/I_{FSM} = 82kV/100A = 820\ \Omega$.

The capacity is $W_{R3} = I_{REC}^2 \times R2 = 5^2 \times 820 = 20.5$ [kW]

5) Compensating reactor

This is to compensate for leading phase capacity of the stray capacitance of the power transformer, and it is 2500 to 3000 kVA from the above calculation.

(4) Future subjects for research and development

After research and development of constituent elements, they must be combined to make up a trial unit to study and investigate structural problems, stray capacitance and other characteristics.

1) Capacitor:

It is possible to design and manufacture at the present technical level, but further research and development of the dielectrics should be required for reducing size.

2) Power transformer, compensating reactor

· Development of iron core material
(Thin sheet silicon steel, large amorphous sheet)
· Review of winding structure
To lower the stray loss, leakage impedance, etc.

3) Rectifier

1. Study on stray capacitance and voltage distribution
(checking in the state as close to the mounting state as possible).

2. Study on cooling method for large current of 5A(structure, overall dimensions), and parallel connection method.

3. Measurement of voltage and current waveforms in mounted state and calculation of reverse recovery loss from the measured values.

4. Study on cooling method of reverse recovery loss (structure, overall dimensions).

5. Summing up 1 to 4, measurement of temperature rise of each diode parts in the state as close to the mounted state as possible.

4) Protective resistor

Protection by a resistor alone may involve problems such as thermal capacity, and it is necessary to develop a new protective method, including detailed circuit analysis.

11.4.1.2 Converter/inverter power supply

(1) Power supply equipment

Converter/inverter power supply provides AC source power to Cockcroft circuit which is the high voltage generator of acceleration power supply. Generally, Cockcroft circuit becomes compact as frequency of AC source is higher. Therefore, the power source consists of inverter which generates high frequency AC voltage and thyristor converter which supplies DC power to the inverter.

Key component in realizing high frequency inverter is switching device. Stress applied on the switching device depends on circuit configuration and structure. For example, circuit configuration is classified into two groups from the commutation method as follows:

a) Commutation by the device
   Commutation by turn-off capability of the device such as GTO, IGBT and transistor.
b) Resonant commutation
   Commutation by turn-off at current zero point which is produced by resonant circuit (L and C in general) provided in the inverter.

Using resonant commutation, for example, circuit for induction heating power supply is as shown in Fig.11.4.5. With this configuration, characteristics of inverter using various switching devices are summarized in Table 11.4.1. To use this method, impedance of the load has to satisfy the resonant condition and inductance of the circuit has to be very low in the case of large capacity power supply. Matching with Cockcroft circuit would be a problem.

In the case of commutation by the device, operation frequency is limited mainly by switching loss in the device. However, surge voltage caused by stray inductance in the circuit and current imbalance among the devices connected in parallel become significant at higher operation frequency and larger capacity.

Comparison of commutation method in high frequency converter are shown in Table 11.4.2. Both methods has many difficulties in applying to inverters of large capacity. In this design, commutation by the device is adopted considering control of the inverter and matching with the load (Cockcroft circuit). Operating frequency of the inverter is chosen to be 10kHz which is realistic upper limit in the case of commutation by the device. Although capacity of unit inverter with this frequency is less than 100kW at present, it is chosen to be

500kW expecting improvement in device and inverter technology. In this case, 30 units inverter have to be operated in parallel as requirement from the Cockcroft circuit is 15MVA for acceleration power of 10MW.

One common thyristor converter is used to provide DC voltage for 30 unit inverters which are operated in parallel. Out•put voltage of the Cockcroft circuit is controlled by the thyristor converter which regulates DC in•put voltage for inverters through delay angle control. Capacity of the thyristor converter is 16MW admitting 5% loss for total inverter out put of 15MW. Voltage rating of the converter is 600V considering high power transistor such as IGBT is used for the switching device of the inverter.

Specifications of converter/inverter power supply are summarized in Table 11.4.3. Configuration of the power supply is shown in Fig.11.4.6.

(2) R&D requirements

High frequency inverter for acceleration power supply is far beyond present state of technology and requires R&D including the followings:

1) High power high frequency switching device

High speed turn-off device of high current capacity, high withstand voltage and small switching loss is required in order to increase capacity of unit inverter and to simplify the configuration of the system.

2) Structure of inverter circuit

Performance of inverter is affected not only by performance of the switching device but by stray inductance and/or stray capacitance of the circuit at higher operation frequency and larger capacity. Structure of inverter circuit which enables to make the best use of performance of the switching device has to be developed.

3) Parallel operation of inverters

Considering a power supply of 10MW range, parallel operation of inverters is indispensable even if capacity of unit inverter is increased. Current balance and control/protection method in parallel operation has to be investigated.

11.4.2 Ion source power supply

Ion source power supply consists of filament, arc, bias power supply, which are used to produce source plasma by arc discharge, extraction, electron suppression, PG filter and EG filter power supply, which are used to extract negative ions from source plasma. These power supplies are located at high voltage potential produced by acceleration power supply.

Specifications of ion source power supply are listed in Table.11.4.4. Total in put power for these power supplies is about 600MVA and this power is supplied by a motor-generator which is driven with insulated shaft. Configuration of ion source power supply is shown in Fig.11.4.7.

Table 11.4.1 Characteristics of resonant inverter with various switching device

Switching device	FET	SIT	Transistor	Thyristor	SITH
Switching frequency	～1MHz	～100kHz	～10kHz	～1kHz	～60kHz
Capacity range	～5kW	～200kW	～200kW	～2000kW	～200kW
Operating voltage	DC 300V	DC 600V	DC 600V	DC 1000V	DC 600V
Dead time	0.1μS	1μS	7μS	30μS	7μS

SIT : Static Induction Transistor
SITH : Static Induction Thyristor

Table 11.4.2 Comparison of commutation method of high frequency inverter

Item	Device turn off	Resonant commutation
Switching loss	large	small
Operating frequency	several kHz	several 10kHz
Output control	easy	difficult
Applicability	common	special

Table 11.4.3 Specifications of converter/inverter power supply for acceleration power supply

Thyristor converter	16MW - 600V - 26.7kA
High frequency inverter	500kW - 600V - 833A -10kHz x 30 unit

Note:These values are for 1 ion source

Table 11.4.4 Specifications of ion source power supply

Filament P.S.	15V - 1500A
Arc P.S.	100V - 750A
Bias P.S.	10V - 75A
PG filter P.S.	2V - 4000A
Extraction P.S.	10kV - 15A
Electron suppression P.s.	5kV - 3A
EG filter P.S.	2V - 2000A

Note:These values are for 1 ion source

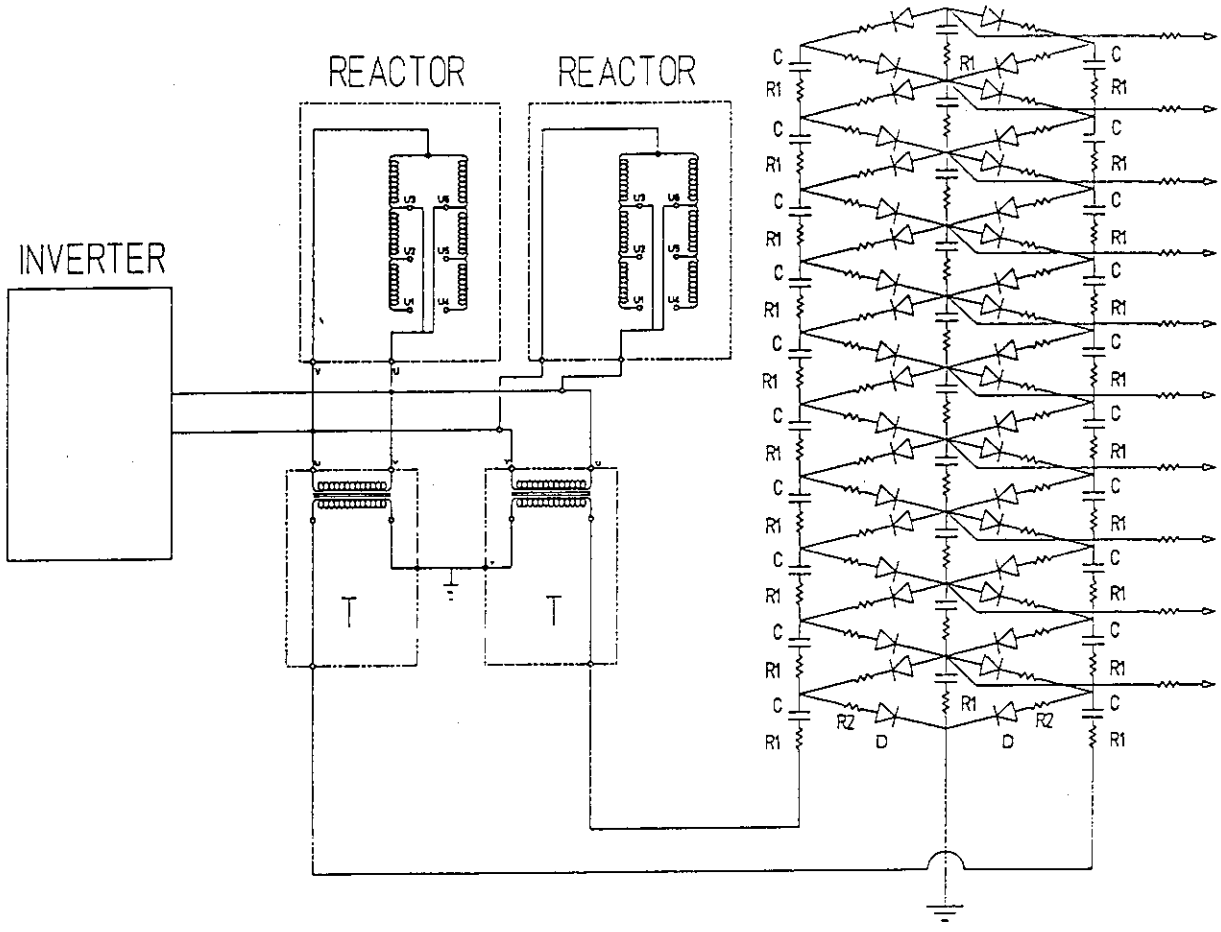

Fig. 11.4.1 Circuit diagram of acceleration power supply.

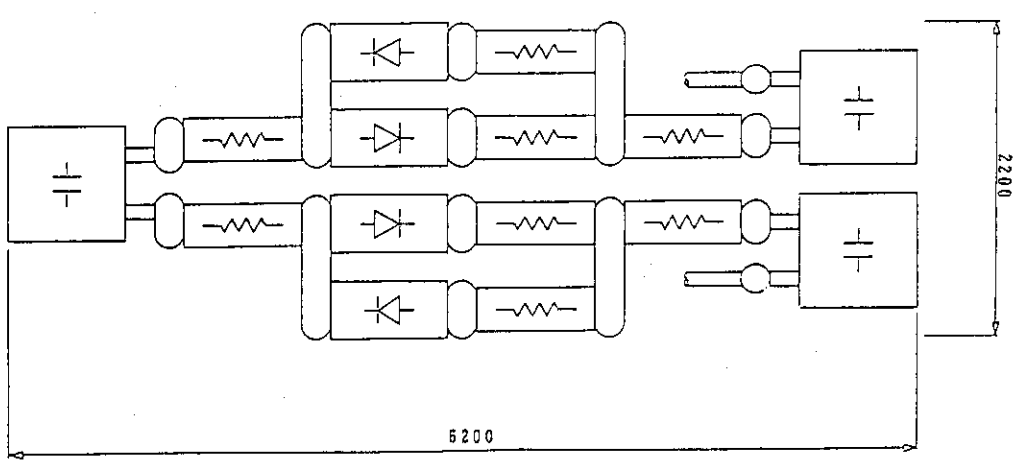

Fig. 11.4.2 Top view of acceleration power supply.

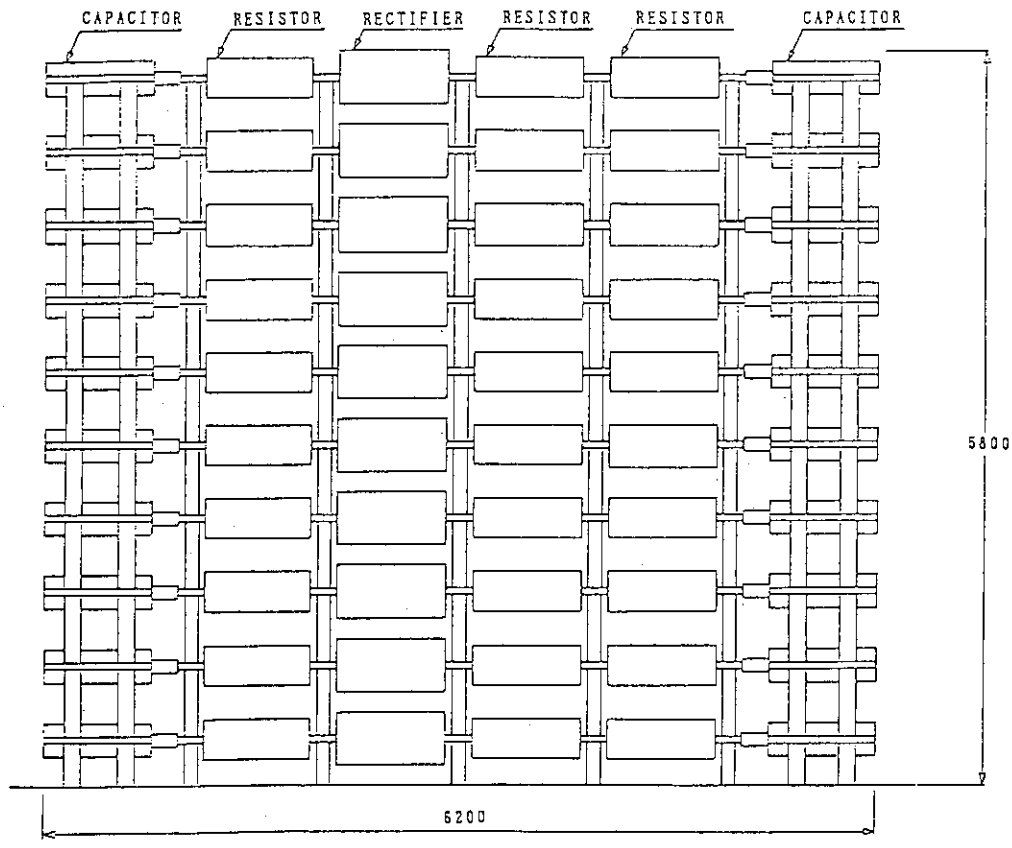

Fig. 11.4.3 Side view of acceleration power supply.

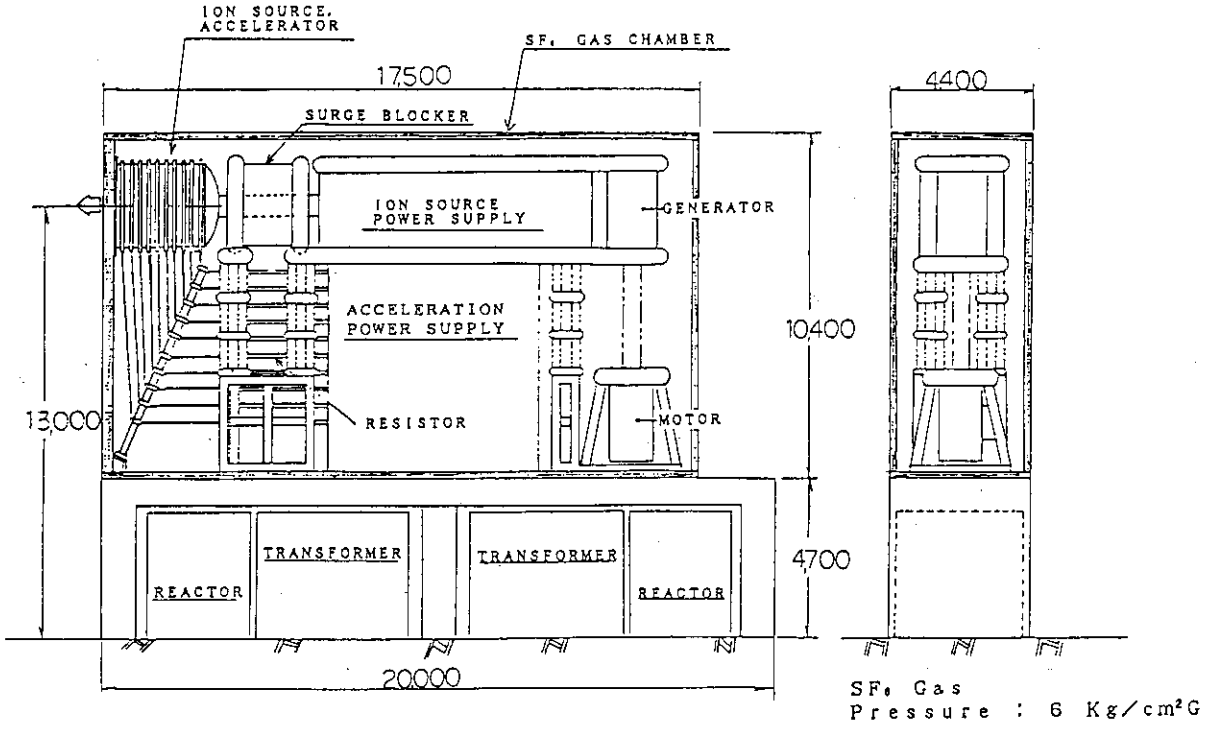

Fig. 11.4.4 Schematic construction of NBI power supply.

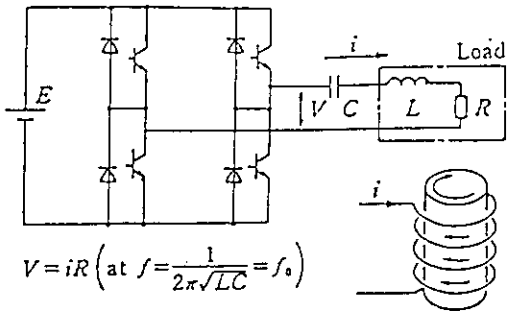

Fig. 11.4.5 Example configuration of resonant inverter.

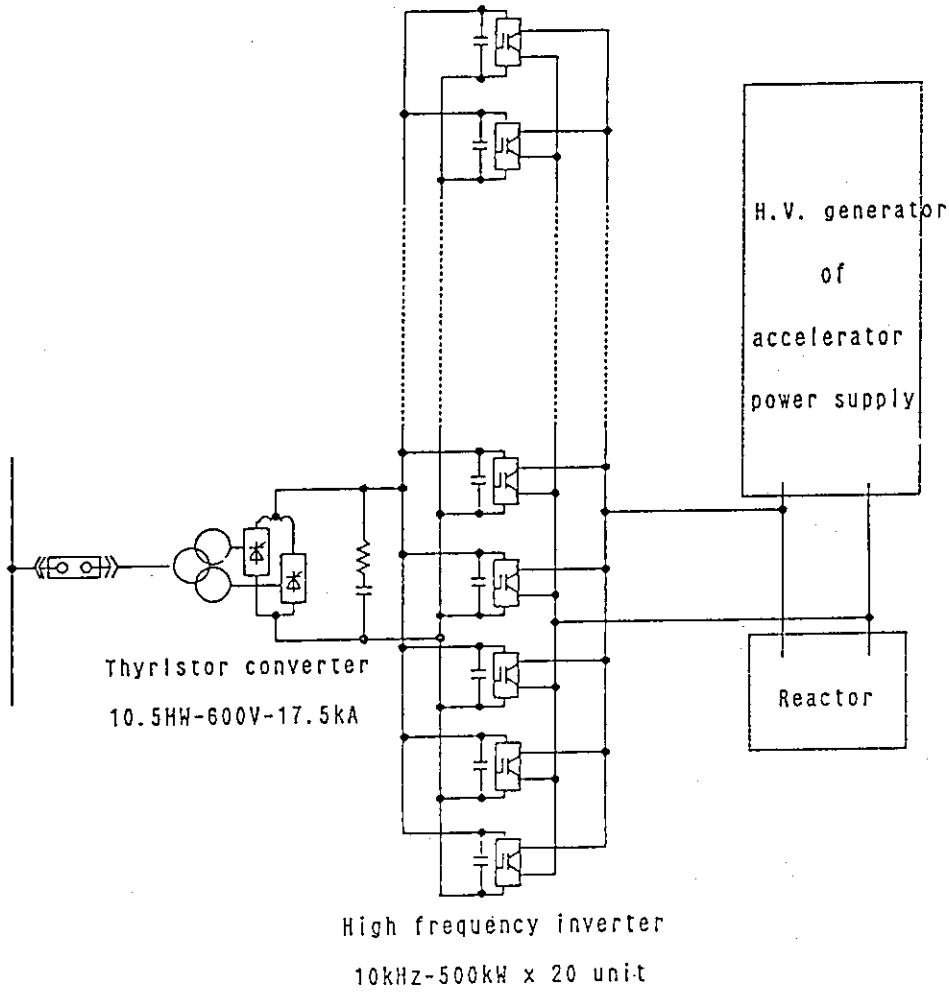

Fig. 11.4.6 Configuration of converter/inverter system for accelerator power supply.

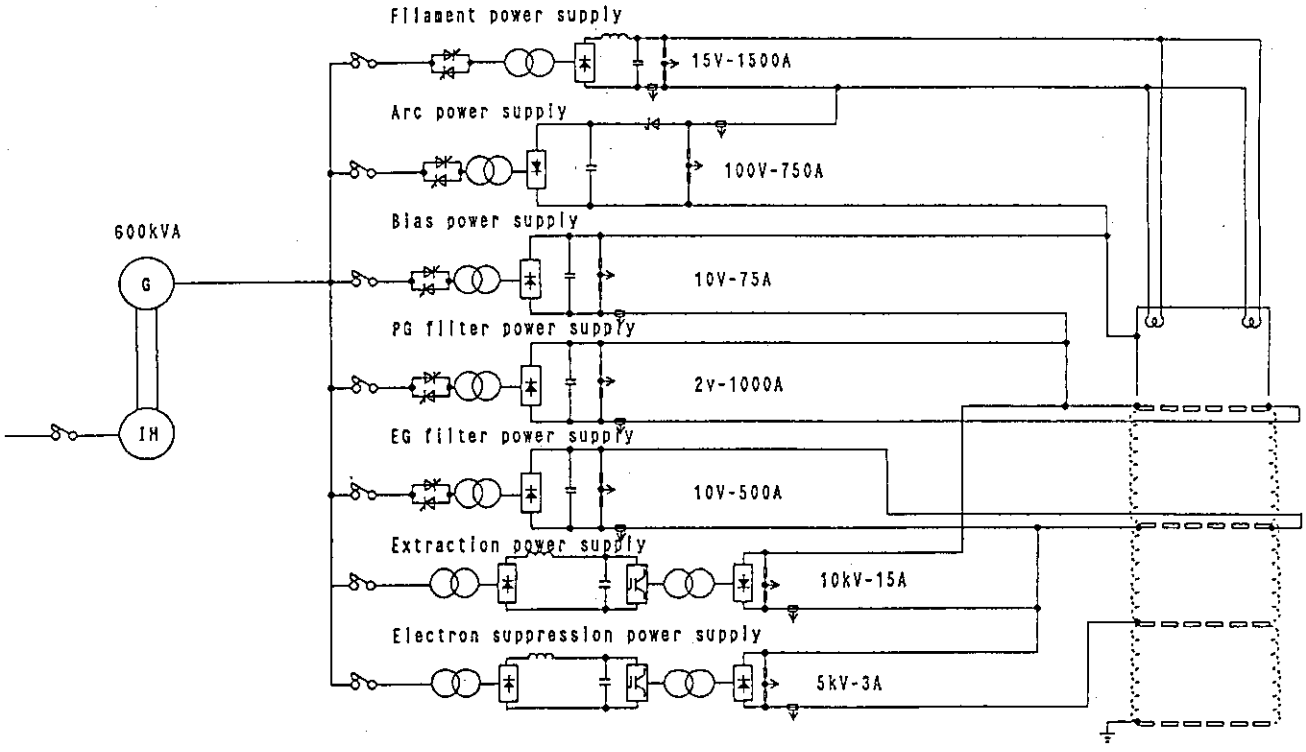

Fig. 11.4.7 Configuration of ion source power supply.

11.5 Neutron shielding

11.5.1 Neutron condition

In the SSTR core, 6 mol of tritium atoms are consumed per hour. Therefore, the number of fast neutrons of 14 MeV generated in unit time, N_T, is as follows.

$$N_T = 6 \text{ mol/hr} \times \text{Avogadro's number} = 1 \times 10^{21} \text{ (persecond)}$$

Supposing the plasma has a circular cross section of minor radius r = 2 m, major radius R = 7 m, the plasma surface area Sp is as follows.

$$S_P = 4p^2Rr = 5.5 \times 10^6 \text{ (cm}^2\text{)}$$

Ignoring all of scatter, neutron growth by blanket etc. the number of neutrons n_N entering the NBI port is as follows.

$$n_N = N_T/S_P = 1.8 \times 10^{14} \text{ (n/cm}^2\text{)}$$

11.5.2 Concept of neutron shielding

In the neutral beam injection system it is difficult to employ an effective shielding method, such as bending of the duct due to the characteristic of the system for injecting the neutral beams. It is, therefore necessary to expect the effect of duct streaming by minimizing the opening and extending the duct.

The allowable duct dimensions estimated from the configuration and beam transport calculation are as follows.

1) Between NBI port and beam dump tank 50 cm x 50 cm x 2 m x 8 ducts x 1 location

2) Between beam dump tank and plasma neutralizer 50 cm x 30 cm x 1 m x 8 ducts x 1 location

3) Between plasma neutralizer and ion bending system 50 cm x 30 cm x 2 m x 8 ducts x 1 location

4) Between ion bending system and SF6 gas tank (accelerator, ion source) 42 cm x 22 cm x 70 cm x 1 duct x 8 locations

When first considering the beam dump tank, it seems reasonable to consider that the effect of duct streaming is small and that the condition is same as in the main vacuum vessel. Then, in order for the personnel to enter the NBI room during operation, shielding with the same thickness as the port wall 50 cm (iron) plus biological shield 5 m (concrete) should be required. This is practically difficult in structure, and the admission of personnel into the NBI room during operation is prohibited, and the shielding wall is provided so that the residual radioactivity level may be lowered to allow the personnel to enter 2 to 4 weeks after stopping operation.

The ion beam bending system is basically in the same condition as the beam dump tank. The SF_6 gas tank has the effect of long-duct streaming from the main vacuum vessel and one scattering, and it is expected that the thickness of the shielding wall may be reduced considerably. Depending on the amount of radioactivity, personnel may enter the SF_6 gas tank.

11.5.3 Subjects for future research and development

1) Summing up the allowable doses of the machines, instruments and electrical parts, the allowable dose inside and outside the system is determind.

2) By modeling the equipment and shielding calculation, effective shielding materials are selected and the thickness is determined. By assessing the radioactivity in the SF_6 gas tank, the damping period is evaluated.

11.6 Maintenance

All machines and electric appliances in the NBI room of the neutral beam injection system should be monitored by remote control. In particular, the following items must always be monitored.

1. Ion source
2. Vacuum pumping system turbo molecular pump
3. MG bearing unit

Items which it may be possible to replace include, aside from the three above, the calorimeter. They are most frequently used during trial running and are heavily loaded, and they must be considered to be replaced once before starting commercial operation. Parts requiring periodic maintenance and checking at the time of annual inspection include the ion source and MG bearing. In particular, the ion source must be overhauled, and it must be considered to be taken out of the SF_6 gas tank.

A hatch is provided on the top of the SF_6 gas tank, and a cask is connected at the time of periodic inspection to lift and store the ion source. A maintenance room, exclusively for the NBI, is installed in the NBI room. It is not advantageous, in control or economically, to install a maintenance room on each top of SF6 gas tank without using a cask. The state of the ion source stored in the cask is shown in Fig. 11.6.1.

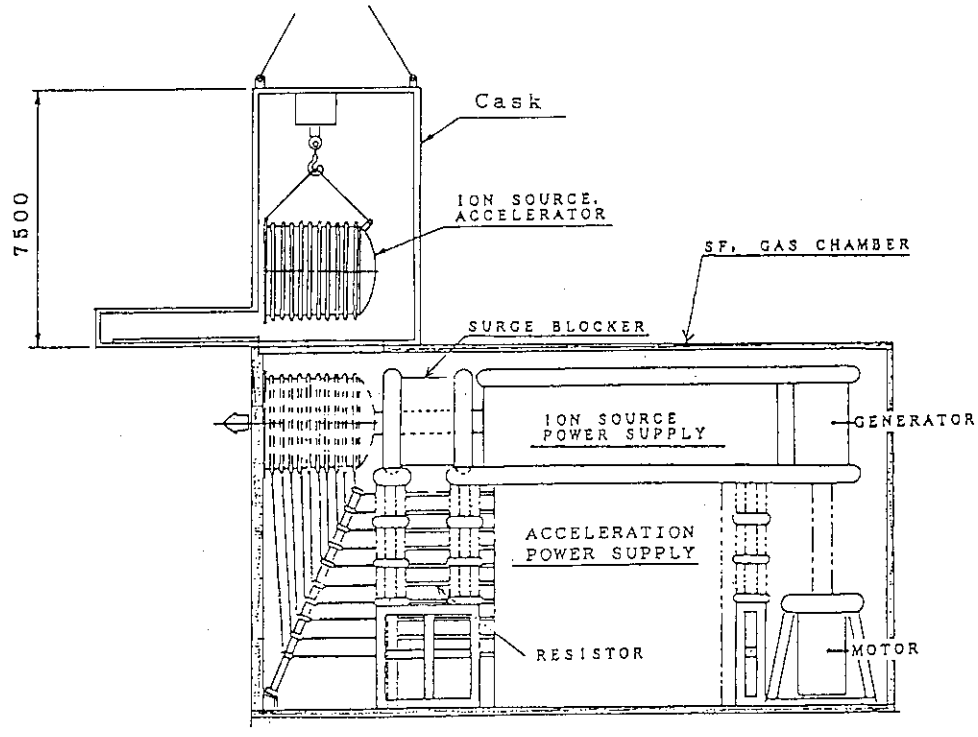

Fig. 11.6.1 Maintenance of ion source.

11.7 Total System Efficiency

The total power efficiency of the present NBI system was estimated assuming various efficiencies and losses. The acceleration current I_{acc} defined by the beam current at the entrance of the main accelerator can be estimated using the following equation;

$$Iacc = \frac{P_{inj}}{N \times V_{acc} \times (1 - \eta_{RI}) \times \eta_G \times \eta_N \times (1 - \eta_{st}) \times \eta_{acc}}$$

where

P_{inj} : Total Injection Power
V_{acc} : Beam Acceleration Voltage
N : Total Ion Source Number
η_{RI} : Reionization Loss
η_G : Geometric Efficiency
η_N : Neutralization Efficiency
η_{st} : Electron Stripping Loss
η_{acc} : Acceleration Efficiency.

Since P_{inj} = 80MW, V_{acc} = 2MeV, N = 16, η_{RI} = 5%, η_G = 95%, η_N = 85%, η_{st} = 10%, and η_{acc} = 90%, the required acceleration current per unit I_{acc} = 4.0 A. Since the electron stripping loss in the extractor is about 20%, the negative ion current extracted from the plasma is 5 A. The required outputs of each power supplies for the ion source are shown as follows;

Cathode Power Supply	:	15 V x 1200 A
Arc Power Supply	:	70 V x 600 A
Bias Power supply	:	2 V x 60 A
PG Filter Power Supply	:	2 V x 4 kA
Extraction Power Supply	:	10 kV x 5 A
Electron Suppression Power Supply	:	5 kV x 1 A
EG Filter Power Supply	:	2 V x 2 kA
Main Acceleration Power Supply	:	1990 kV x 3.8 A.

When the efficiency of each power supply is assumed as follows,

Cathode, Bias, PG Filter, and EG Filter Power Supplies	: 40 %
Arc Power Supply	: 60 %
Extraction and Electron Suppression Power Supply	: 90 %
Main Acceleration Power Supply	: 85 %,

the input powers of the main acceleration power supply and other power supplies becomes 8896 kW and 206 kW, respectively. Since the power supplies except the main

acceleration power supply are fed by a motor generator(M-G), the driving power of M-G becomes 258 kW with an assumption of the M-G efficiency of 80 %. Therefore, the total electric power P_{ps} for ion production and acceleration is 9154 kW. Additionally, auxiliary power for the plasma neutralizer (1MW / beamline) and for the beamline utilities (8MW / system) are taken into account, total input power per unit is calculated as follows;

$$P_{total} = 9154 + \frac{1000}{8} + \frac{8000}{16} = 9779 \text{ (kW)}.$$

Therefore, total system efficiency η_{total} becomes as follows finally;

$$\eta_{total} = \frac{P_{inj}}{P_{total} \times 16} = \frac{80000}{9779 \times 16} = \underline{\mathbf{0.511}}.$$

11.8 Concluding Remarks

Performance characteristics of the major components in the NBI system are shown in Table 11.8.1. A layout of the NBI system in the SSTR building is shown in Fig.11.8.1. In designing the present NBI system, particular attension was paid to make the system as simple and as compact as possible by utilizing the aggressive technologies and experiences in the design work of the 1 MeV NBI system for the fusion experimental reactor. Though there are still many issues to be studied further, we think we were able to propose an attractive NBI system for the fusion power reactor. If the following R&D items are carried out intensively, it will be possible to realize this NBI system.

1. Negative Ion Production : 40mA/cm^2 at 0.3Pa
2. Negative Ion Acceleration : 2 MeV, 3.5 A, D^-
3. Efficient Plasma Neutralizer : Neutralization Efficiency > 85 %
4. High Power Cockcroft Type DC Generator : 2 MV, 10 MW

References

(1) W.S. Cooper : Lawrence Berkeley Laboratory Report LBID-1593 (1989).

(2) W.L. Stirling, W.R. Becraft, J.H. Whealton, and H.H. Haselton : Proc. 13th Symp. on Fusion Engineering, Knoxville, Oct. 2-6, 1989, pp. 1448-1454.

(3) A.S. Schlachter et al.: Proc. 4th Int. Symp. on the Production and Neutralization of Negative Hydrogen Ions and Beams, edited by J.G. Alessi, AIP Conf. Proc. No. 158 (1987) pp.631-642.

(4) Y. Matsuda et al.: Proc. 12th Symp. on Ion Source and Ion-Assisted Technology, Tokyo (1989) pp.107-110.

(5) F. Melchertt, et al.: Europhysics Letters 9 (5), (1989) pp. 433-439.

Table 11.8.1 NBI system design specifications

Beam Energy	2 MeV	Accelerator	Electrostatic
Beam Power	60 MW (Max. 80 MW)	Beam Current	3.5 A / module
		Acceleration Stages	10
Beam Species	D	Beam Divergence	3 mrad
Beamlines	2		
Source Modules	8 / beamline	Beam Deflector	60 Bending Magnet + Q - Magnets
System Efficiency	50 %		
Acceleration	90 %	Neutralizer	Plasma Cell
Stripping Loss	10 %	Gas Species	Xe or Ar
Neutralization	85 %	Ionization	50 %
Geometric Loss	5 %	Pressure	0.03 Pa
Reionization Loss	5 %		
Power Supply, etc.	80 %	Beam Dump	Externally-finned Swirl Tube
Ion Source Type	Volume - Surface		
Extraction Current	5 A	Pumping	25 m3 / s TMP x 38 x 2
Current Density	40 mA / cm2		
Extraction Grid	12 cm x 30 cm	Power Supply	Cockcroft-Walton
Apertures	12.4 mm ID x 100	Ripple	< ± 1 %
Filling Pressure	0.3 Pa	Frequency	10 kHz
Gas Flow Rate	0.6 Pa.m3 / s		

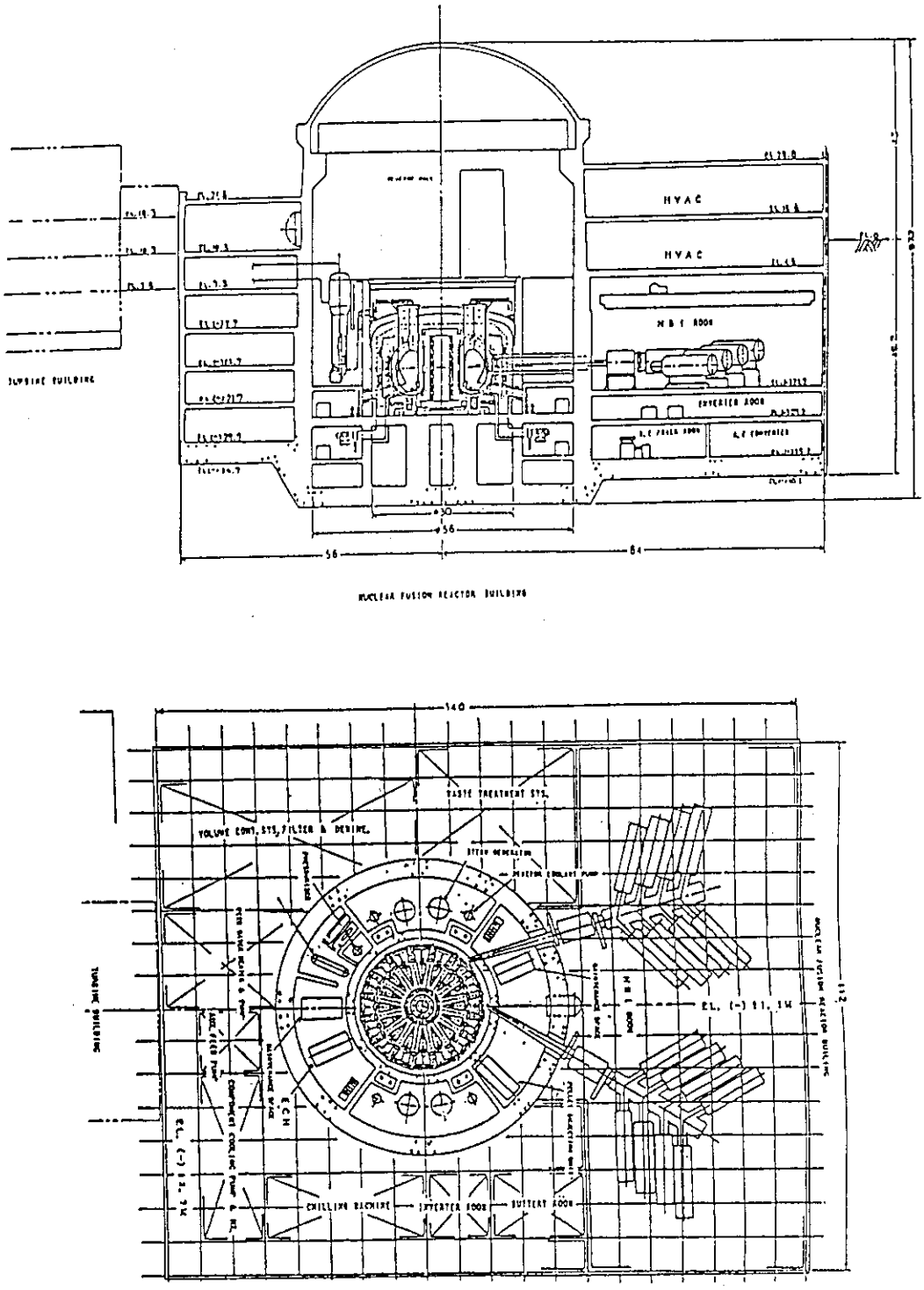

Fig. 11.8.1 Layout of the NBI system in the SSTR building.

12. Power Plant

12.1 Conditions

The following conditions are examined.

(1) Nuclear fusion reactor heat output (MWt) ; 3,710

Items:		
	Outer replacement blanket	2,110
	Inner replacement blanket	770
	Permanent blanket	350
	Diverter	480

(2) Coolant temperature, pressure and flow rate (at full output under high temperatures)

	Temperature (°C) (Outlet/Inlet)	Pressure (MPa)	Flow rate* (kg/s)	
Outer replaceable blanket	325/285	15.7	(9,620)	
Inner replaceable blanket	325/285	15.7	(3,510)	High-temperature header coolant
Permanent blanket	325/285	15.7	(15,960)	
Diverter	325/285	15.7	(2,189)	

* The flow rate necessary to remove heat, taking the reactor core heat output and coolant temperature to be positive.

(3) Pressure loss at the reactor core

at the reactor core.
300 kPa

(4) Inventory of high-temperature coolant for power generation 120 m³ (provisional)

(5) The primary cooling system of the nuclear steam supply system (NSSS) will be interfaced with a pair of high-temperature ring headers on the reactor side on the basis of the four loops in the existing PWR plant

12.2 Primary cooling system

12.2.1 Outline

The facilities of the primary cooling system function to produce steam for the turbine by transferring heat, which are generated when neutrons generated due to nuclear fusion reaction lose their energy in the blanket , to the secondary system (the turbine plant).

As shown in Fig. 12.2.1, the primary cooling system consist of four heat transfer loops, each of which is equipped with a primary coolant pump and steam generator. In addition, each of the loops connects to heat transfer pipes in the blanket through a common header (the primary coolant ring header).

The primary coolant is heated in the blanket and enters the steam generator through the primary coolant ring header to produce steam by heating water in the secondary system. The water from the steam generator enters the primary coolant pump and returns to the primary coolant ring header.

The pressure in the primary cooling system is controlled by a pressurizer in which the liquid and the vapor phases are kept in equilibrium by heating and spraying. Pressure variations due to the expansion and contraction of primary coolant are accommodated by condensing steam using the pressurizer spray or producing steam using a pressurizer heater. With the safety valve and air-actuated relief valve attached to the pressurizer, steam is discharged into the pressurizer relief tank when the pressure in the pressurizer becomes too high. In the pressurizer relief tank, the steam is mixed with water to be condensed and cooled.

Auxiliary systems such as the chemical and volume control system, residual heat removal system, safety injection system, and waste disposal system are connected to the primary cooling system. A facility to recover tritium in the primary coolant is also provided.

12.2.2 Steam generator

The steam generator is a vertical shell and U-tube heat exchanger provided with a moisture separator on the secondary side.

The primary coolant enters the inlet of the water chamber (located in the lower part of the steam generator) and is discharged from the outlet of the water chamber through tubes. The inlet- and outlet-sides of the semi-spherical water chamber are separated by a partition. Each water chamber is provided with an operation man-hole.

Steam is produced when the water on the secondary side is heated by the primary coolant, and is discharged from the outlet nozzle of the upper part of the steam generator after removing moisture with the moisture separator.

Figure 12.2.2 shows the structure of the steam generator.

12.2.3 Primary coolant pump

The primary coolant pump is a vertical single-stage mixed-flow pump that is driven by an air-cooled three phase induction motor installed on the pump. The pump has a flywheel to increase the pump's inertia and relieve the flow rate coast down of the primary coolant. The pump's inlet is located at the bottom, and the outlet is on the side.

Leak from the coolant pump is controlled so that the primary coolant does not leak into the containment vessel. Shaft sealing is accomplished in three stages arranged in series.

High-pressure sealed water, which is fed into the underside of the first-stage seal from the chemical and volume control system, prevents primary coolant from entering the shaft seal. The sealed water flows out in two directions separately: the one returns to the chemical and volume control system through the shaft seal, and the other flows into the primary cooling system through the thermal barrier.

All the parts of the pump that contact the primary coolant, except the seals, bearings, and other special parts, are made of stainless steel.

12.2.4 Piping

The primary coolant main pipes and fittings are made of stainless steel. Small pipes, including the pressurizer surge line, pressurizer spray line, pressurizer relief line, loop drain, and interfacing line with the other systems, are also made of stainless steel.

All the fittings and connections are welded together with the exception of the pressurizer safety valve, which is fitted with a flange.

12.2.5 Pressurizer

The pressurizer is installed as a part of the primary cooling system facilities to keep the liquid- and vapor-phases in equilibrium under saturated conditions and to control the pressure.

Electric heaters are inserted from under the container. A spray nozzle, relief valve, and safety valve are furnished on the upper part of the container.

The pressurizer is designed to be able to accommodate variations in the primary coolant volume that result from load variations. The pressurizer is welded to the high-temperature side of the coolant loop through the surge line attached to the lower part of the pressurizer. During surging, steam in the pressurizer is condensed with the spray system fed from the low-temperature side of the two coolant loops suppressing the pressure in the pressurizer to below the set pressure of the relief valve. The air-actuated pressurizer spray valve may operate also manually from the main control room.

Figure 12.2.3 shows the structure of the pressurizer.

12.2.6 Pressurizer relief tank

With the pressurizer relief tank, the discharged steam from the pressurizer safety valve and pressurizer relief valve is condensed and cooled.

The discharge lines from the other relief valves also connect to the pressurizer relief tank which is filled with water and nitrogen gas.

Steam is discharged from the sparger pipe under the surface of the water and cooled to ambient temperature after being condensed. The inner spray and drain furnished in the tank cool the tank as steam is discharged.

12.2.7 Facility specification of the primary cooling system

(1) General items

Nuclear fusion reactor heat output (provided for power generation)	3710 MWt
SG heat output (provided for power generation)	3724 MWt
Number of loops	4
Primary coolant conditions	
Total flow rate	approximately 59×10^6 kg/h
Cooling water header outlet temperature (full output)	325°C
Cooling water header inlet temperature (full output)	285°C
Normal running pressure	approximately 157 kg/cm²
SG secondary side conditions	
Steam generator outlet pressure (full output)	59.2.kg/cm² a
Steam generator outlet temperature (full output)	Saturation temperature

(2) Steam generator

Type	Vertical U-tube
Number of generators	4
Heat transfer rate	approximately 801×10^6 kcal/h

Primary side:

Highest working pressure	175 kg/cm²
Highest working temperature	343°C
Primary coolant inlet temperature	325°C
Primary coolant outlet temperature	285°C
Primary coolant flow rate	approximately 14.7×10^6 kg/h

Secondary side:

Highest working pressure	83.3 kg/cm²
Highest working temperature	298°C
Steam pressure (Steam generator outlet, full output)	59.2 kg/cm² a
Steam temperature (Steam generator outlet, full output)	Saturation temperature
Feedwater temperature	226.7°C
Steam wetness	less than 0.25%
Steam flow rate	approximately 1.85×10^6 kg/h

(3) Primary coolant pump

Type	Vertical,Single-stage, Mixed-flow type
Number of pumps	4
Highest working pressure (Casing)	175 kg/cm²
Highest working temperature (Casing)	343°C
Design head	94.8 m
Design flow rate	approximately 20000 m³/h

(4) Pressurizer

Type	Vertical cylindrical container with semi-spherical heads at the upper and lower ends.
Number of pressurizers	1
Highest working temperature	360°C

Highest working pressure	175 kg/cm²
Capacity	51 m³
Heater capacity (Total)	1800 kW

(5) Pressurizer relief tank

Type	Vertical cylinder
Number of tanks	1
Highest working temperature	170°C
Highest working pressure:	
Internal pressure	7 kg/cm²
External pressure	1 kg/cm²
Capacity	51 m³

(6) Primary coolant pipe

Highest working pressure	175 kg/cm²
Highest working temperature	343°C
Pipe I.D.	
Low-temperature side	approximately 700 mm
High-temperature side	approximately 740 mm
Between the steam generator and pump	approximately 790 mm
Pipe thickness	
Low-temperature side	approximately 69 mm
High-temperature side	approximately 73 mm
Between the steam generator and pump	approximately 78 mm

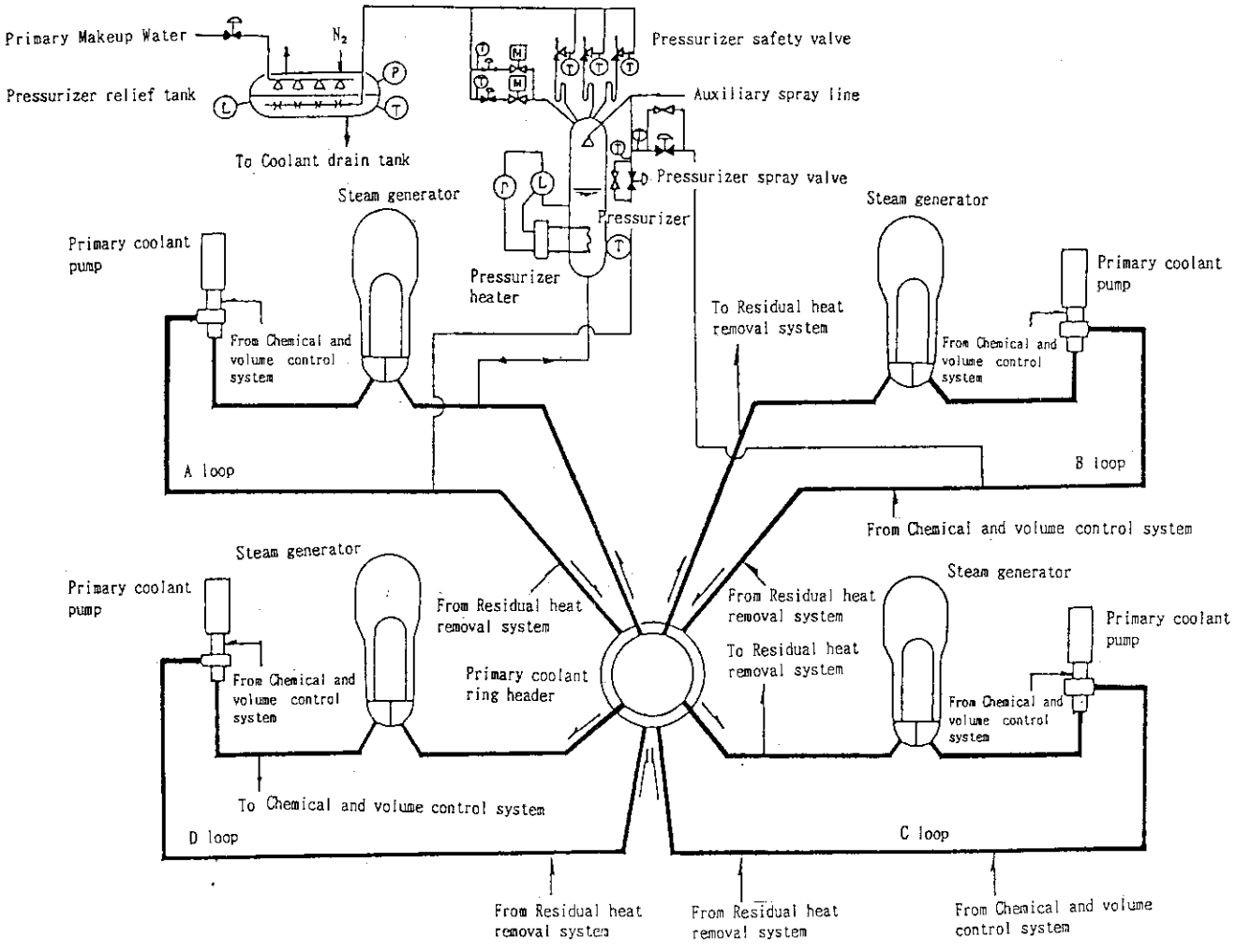

Fig. 12.2.1 SSTR primary cooling system.

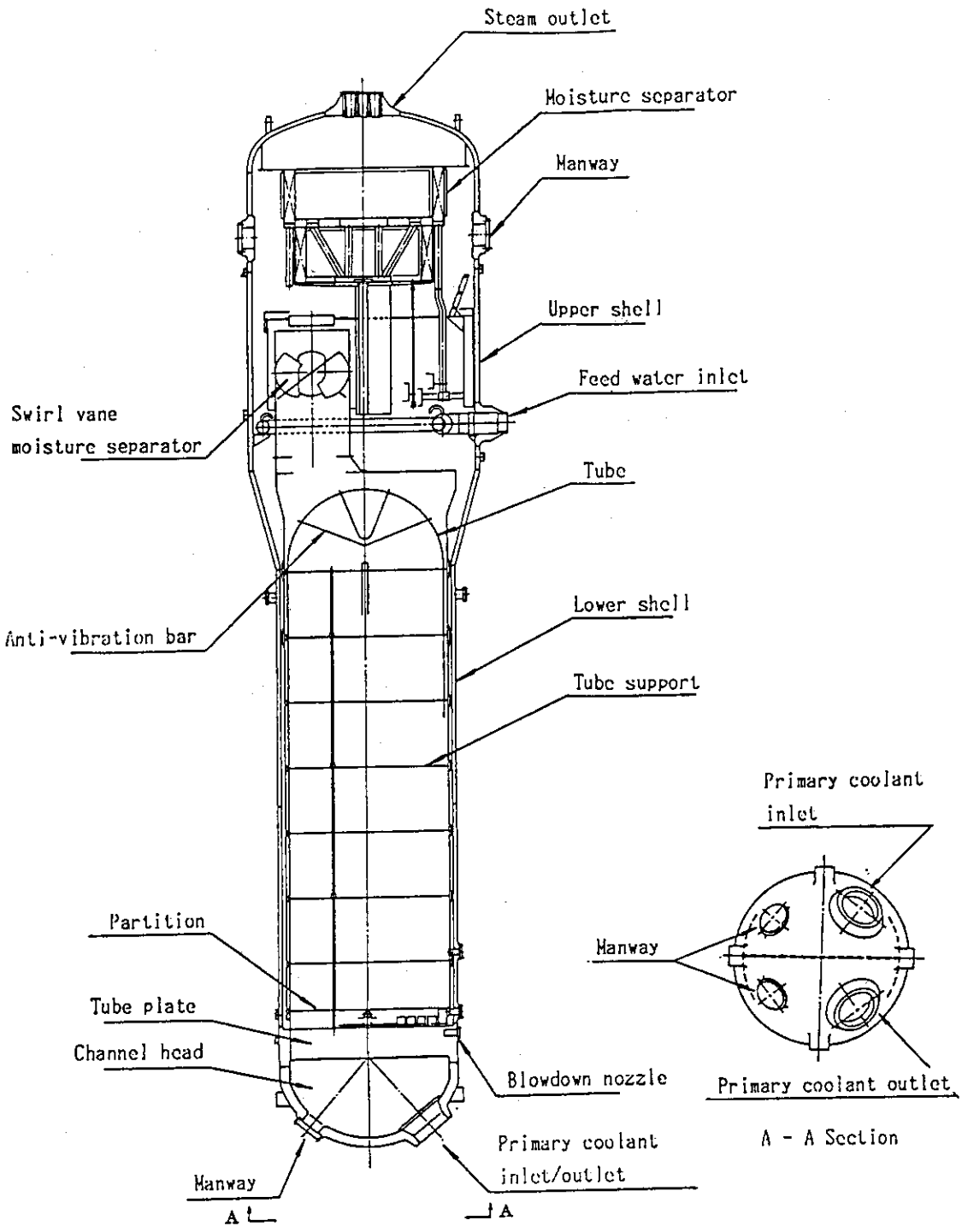

Fig. 12.2.2 Steam generator.

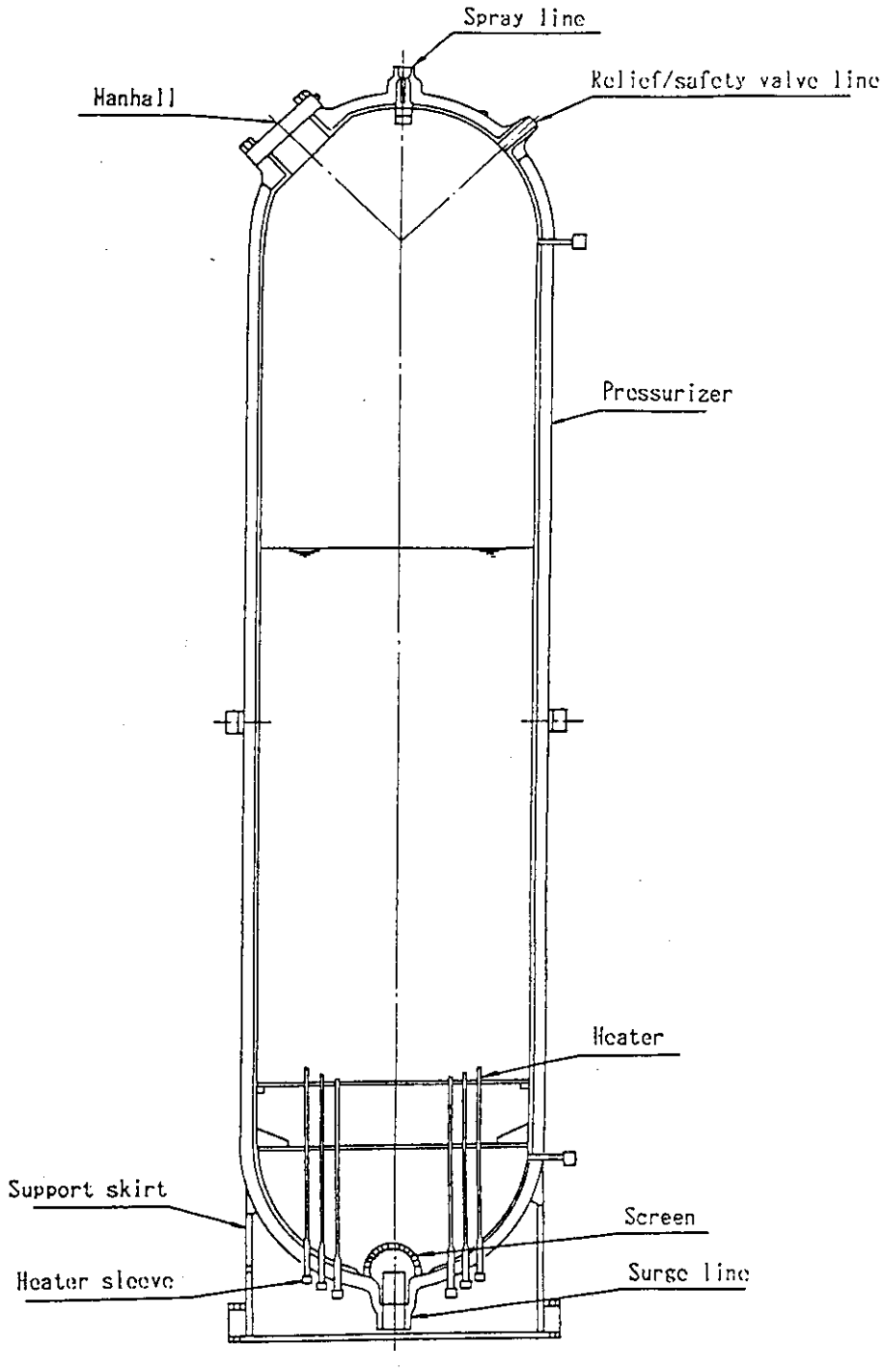

Fig. 12.2.3 Pressurizer.

12.3 Secondary cooling system - Turbine plant

12.3.1 Outline

The turbine plant removes effective electric energy from the electric generator by converting the energy in steam generated from the steam generator to rotational energy. To increase efficiency, a reheat cycle, which is heated with main steam or high-pressure steam extracted from the turbine stage (at the outlet of the high-pressure turbine), and a regenerative cycle, which heats the feedwater sent to the steam generator with the turbine extract steam, are adopted.

In general, the heat generated by the fusion reaction is converted to steam to be sent to the turbine with the steam generator. In the present plan, the turbine plant may be designed according to the conventional technique, because both of the pressure and temperature are nearly the same as that used in the light-water reactor, and because the amount of steam increases only 5% comparing with the PWR 4loop plant.

The turbine plant consists of a main steam system, a feedwater and condensate system, and a circulating water system. However, this document deals only with specifications for the main turbine and the feedwater and condensate system directly relating to the primary cooling system. The condenser and circulating water pump are omitted here because their specifications may vary with such factors as topography and weather.

12.3.2 Turbine body

The nuclear turbine is made large so that the blades will have a long length, because the turbine runs under a large amount of a saturation steam at a pressure of 5 to 7 MPa. Its rotation speed is therefore limited to 1500 rpm (for 50 Hz) or 1800 rpm (for 60 Hz) for the stress to the materials to remain under maximum limits.

The type of nuclear turbine is chosen based on a combination of the last blade length and the number of exhaust branches (number of low-pressure casings) corresponding to the output ranges as shown in Fig. 12.3.1. Considering the present steam conditions at the turbine inlet, a 1300 MW class plant is expected. TC6F52, which is applicable to more than 1200 MW, was selected. In addition, a moisture separator and reheater was installed between high- and low-pressure turbines to increase efficiency. Figure 12.3.2 shows the whole outline of the turbine generator.

12.3.3 Plant output

Heat input to the turbine plant is used for power generation by transferring steam sent from the steam generator to the turbine directly, as is the case with the conventional PWR plant. Figure 12.3.3 shows the main systems included in the turbine plant.

To determine plant output, it is necessary to decide on the turbine outlet conditions, including the design condition of the condenser. Common valves are selected on the basis of conditions in existing power plants because the site conditions of the present power plant are not yet known.

The design conditions of the turbine power generator output are as follows;

Turbine inlet	steam pressure	56.4 kg/cm²
	steam temperature	Saturation temperature
	steam wetness	less than 0.43%
Turbine exhaust vacuum		705 mm Hg
SG blow amount		1.0%
Number of extraction stages		5
Number of feedwater heating stages		6
Number of reheating stages		2
Feedwater pump driving system		Turbine driven

Given the conditions stated above, the output of the turbine generator will be 1270 MW assuming that the SG heat output is 3724 MWt, the plant efficiency being 34.1%.

The non-utility power for the power generation plant will be 4% to 5% of the generator output assuming that it is equivalent to that of conventional PWR. The main equipment driven in the plant are as follows:

Primary coolant pump
Auxiliary equipment cooling pump
Condensate pump
Circulating water pump
Condensate booster pump
Feedwater booster pump
Others

12.3.4 Feed water and condensate system

Of a series of the systems to feed the secondary coolant, the system from the condenser to the deaerator is referred to a condensate system, and the system from the deaerator storage tank to the steam generator, a feed water system.

The feed water system feeds water from the deaerator to the steam generator using a turbine driven feedwater pump, just as in a conventional PWR. As part of the system, a feedwater heater is installed to heat the water with high-pressure steam extracted from the turbine.

12.3.5 Facility specifications

(1) Turbine body

Type	TC6F52
Rated output	1270 MW
Number of feedwater heater extraction stages	6
Primary steam stop valve	4 plug valves
Steam control valve	4 plug valves
Reheat primary steam stop valve	4 butterfly valves
Intercept valve	4 butterfly valves

(2) Moisture separating heater

Type	2-stage reheat of moisture separation
Number of heaters	1/6 capacity x 6
Moisture separator	Corrugated sheet
Heater	Finned U-tube

(3) Power generator

Type	Rotor hydrogen cooling Stator-water cooling
Rated capacity	1410 MVA
Rated power factor	0.9
Exciter type	Brushless

(4) Condensation facility

Condenser	Surface cooling with 3 shells
Circulating water pump	50% capacity x 2
Condenser air ejector	2
Condensation pump	Vertical centrifugal type 50% capacity x 3 (one of the pumps is a spare)

(5) Feedwater facility

Low-pressure feedwater heater	Horizontal U-tube
Number	4 stages x 3 systems
Deaerator	Spray tray
High-pressure feedwater heater	Horizontal U-tube
Number	1 stage x 2 systems

(6) Feedwater pump facility

Type of main feedwater pump	Horizontal centrifugal type
Number of main feedwater pumps	50% capacity x 3 (two turbine-driven, one spare driven electrically)
Pump driving turbine	7300 kW

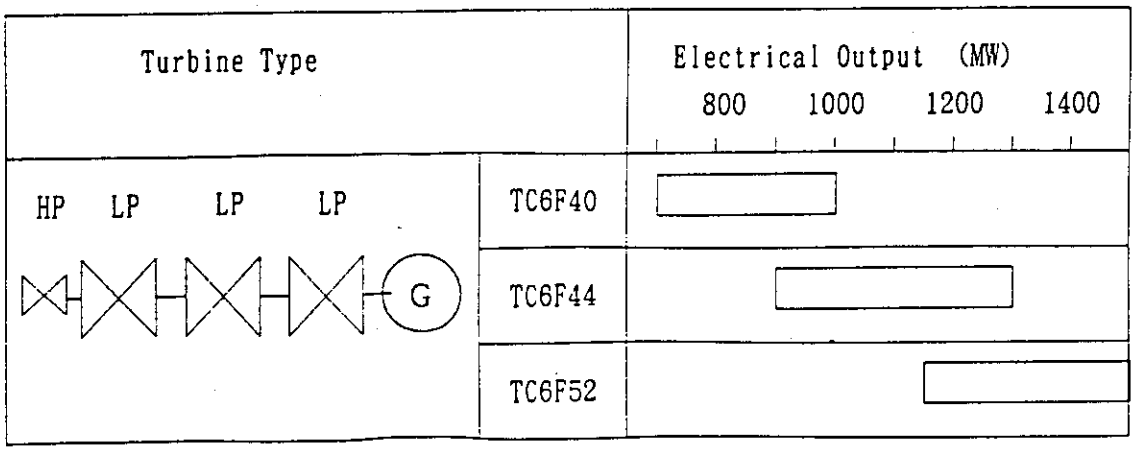

Fig. 12.3.1 Turbine type vs electrical output.

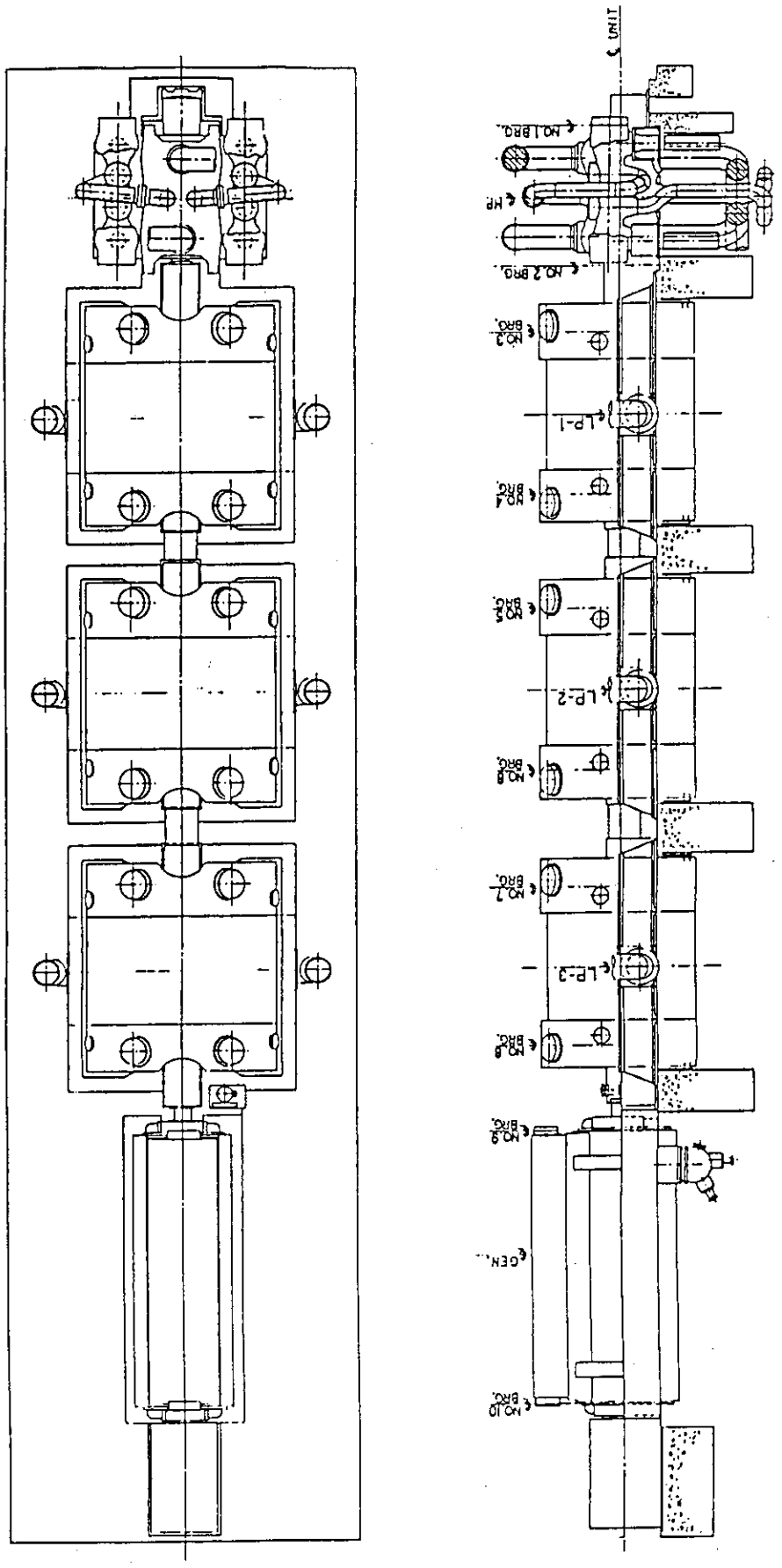

Fig. 12.3.2 Turbine-generator outline.

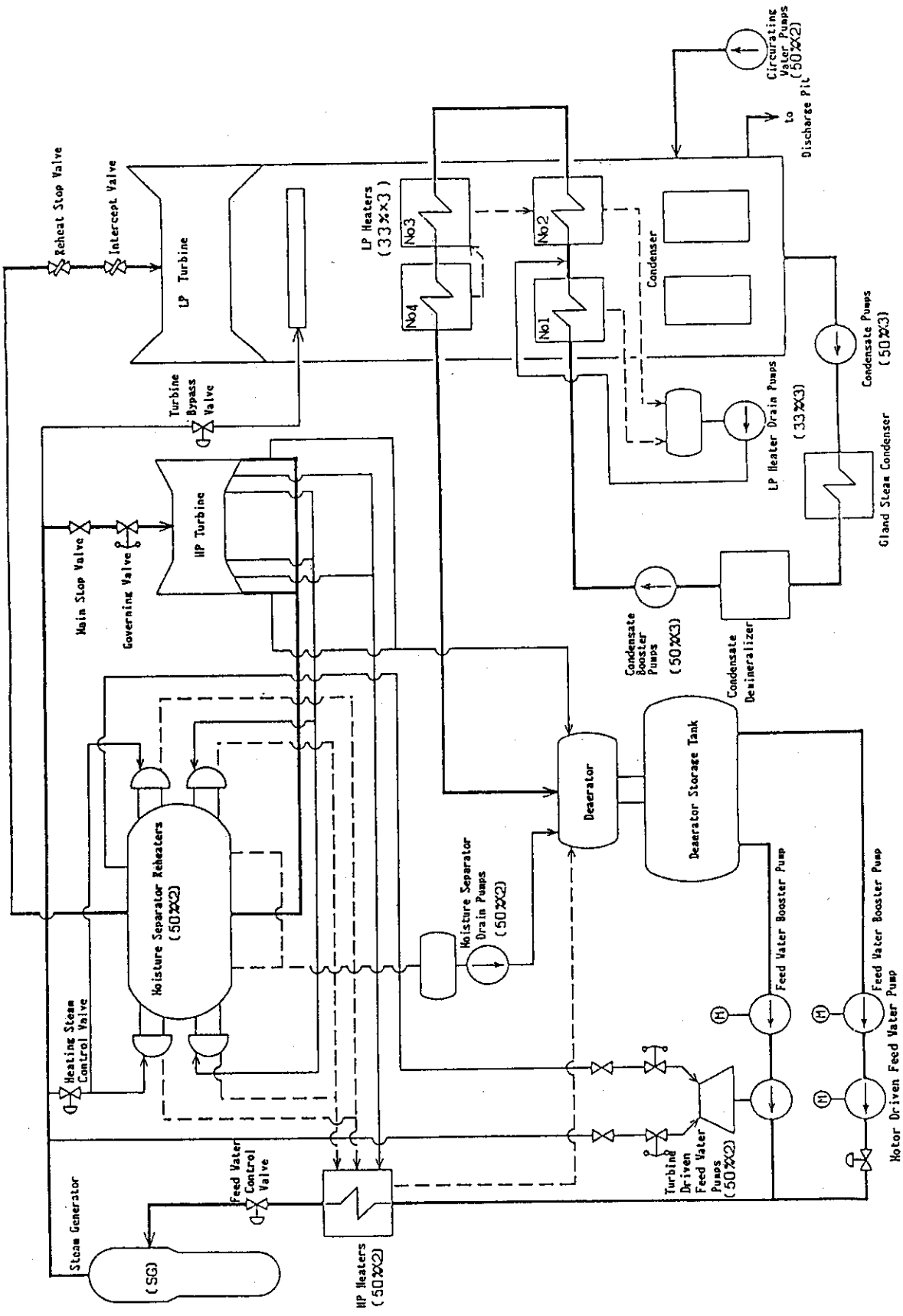

Fig. 12.3.3 Flow diagram. (turbine island)

12.4 Low-temperature diverter

When the diverter plate is unable to cool down using only high-temperature pressurized water, hot loaded portions may be cooled by a low temperature water. We call this as a low-temperature diverter.

If this system is selected, heat of the cooling water from the low-temperature diverter having temperatures on the order of 200/185°C (outlet/inlet) cannot be used in the primary cooling system. Replacing part of the feedwater heaters based on turbine extraction, with the low-temperature diverter heater in the secondary cooling system, will make it possible to efficiently use the heat of the cooling water at the low-temperature diverter. The efficiency of the power plant, however, is reduced.

If a low-temperature diverter is used, the following equipment should be installed.

Low-temperature diverter cooling water pump
Low-temperature diverter cooling water pressurizer
Low-temperature diverter heater

Figure 12.3.4 shows the main turbine plant system according to the system stated above.

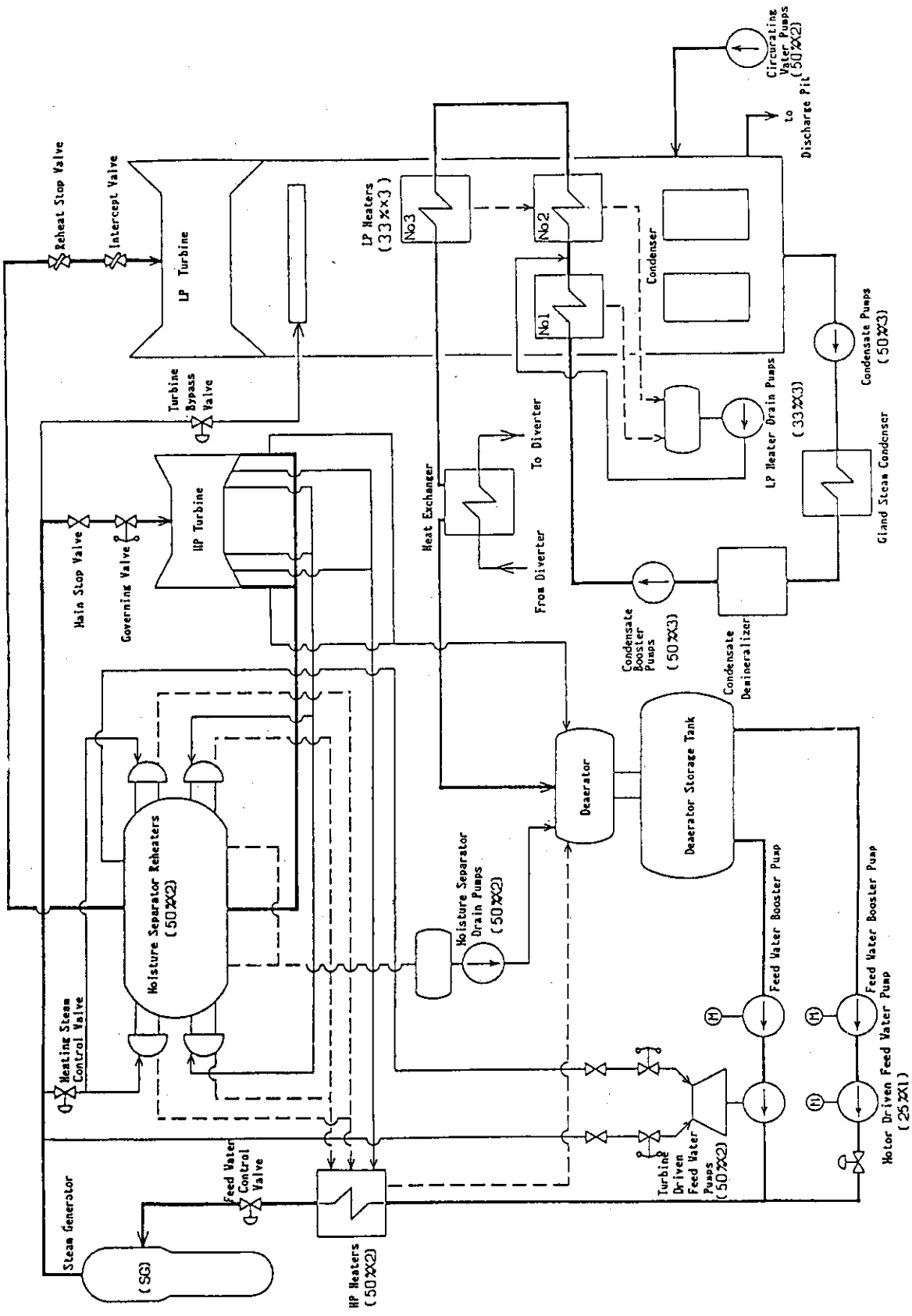

Fig. 12.4.1 Flow diagram (turbine island) - low temperature divertor.

12.5 Lacking facilities in SSTR plants among those of the PWR plant

This paper describes an SSTR power plant based on a PWR power plant. Of the main facilities installed at the PWR plant, the following are not used for SSTR plants.

* Reactor vessel and reactor internals
* Control rods and control rod drive system
* Neutron source
* Accumulating tank
* Boric acid tank, boric acid pump, etc.
* Spent fuel pit purification & cooling facility
* Fuel handling and storage system
* Reactor instrumention system(External nuclear instruments, Internal nuclear instruments, Internal thermocouple instruments, Shutdown margin monitoring facility)
* Reactor control system (Control rod control system, Boric acid concentration control system)
* Power source for the control-rod drive mechanism

In addition, further examination is required on how to arrange safety facilities.

12.6 Items to be researched in the future

This report describes the outline of the power plant, and roughly outlines the primary cooling system, the secondary cooling system and the turbine plant as main facilities. On the systems and facilities for the whole of the power generation plant, design and research in a harmonious manner are required. In the future, consideration should be given to the following issues.

(1)Interface of the core cooling system with the primary cooling system
(2)Examination of auxiliary systems to be connected to the primary cooling system.

13. Tritium system

13.1 Review of fuel balance in nuclear fusion reactor

(1) Exhaust gas by nuclear combusion of SSTR

(a) He output

1×10^{21} ions/s

(b) Diverter chamber condition

(assuming He ratio in main plasma: 5%, He enrichment factor of diverter: 0.1)

Total exhaust ion quantity: 2×10^{23} ions/s

When converted to molecules:

D, T, 1×10^{23}/s = 370 Pa·m^3/s = 0.167 mol/s

He 1×10^{21}/s = 3.7 Pa·m^3/s = 1.7×10^{-3} mol/s

(c) Summary of type and quantity of exhaust gas

	Mol ratio	Gas quantity	
D.,T	98.0%	0.167 mol/s	600 mol/h
He	1.0%	1.7×10^{-3} mol/s	6 mol/h
H	0.5%	8.5×10^{-4} mol/s	3 mol/h
Impurities	0.5%	8.5×10^{-4} mol/s	3 mol/h

The mol ratios of H and impurities are based on ITER values. Contents of impurities also conform to ITER. The gas composition of hydrogen isotopes refers to the values determined with the equilibrium constant as 4 (see Table 13.1.1).

Gas composition of hydrogen isotopes:

T_2 : 24.5% HT : 1%

DT : 49.0% HD : 1%

D2 : 24.5%

(2) Diverter plate cooling gas

To cool the diverter plate, gas is steadily blown on the diverter plate from the gas injection unit.

Cooling gas flow : 2,700 mol/h

Gas composition : Mixed gas of He and hydrogen isotopes removing impurities in the fuel clean-up system.

(3) Gas balance of NBI

(a) Feed gas quantity to ion source D_2

0.6 Pa·m^3/s x 8 x 2 = 9.6 Pa·m^3/s = 14.6 mol/h

The design value of the fuel system side should be as follows considering a margin for safety. 14.6 mol/h x 2 = 29.2 mol/h = 30 mol/h

(b) Feed gas quantity to plasma D_2

20 A x 2 = 40 A = 0.75 mol/h = 1 mol/h

(c) Feed gas quantity to plasma neutralizer Xe

The fuel system side should be designed with the following condition.

Beam dump side:	Plasma neutralizer	Accelerator	electrode side
0.02 Pa	0.03 Pa		0.007 Pa
0.84 Pa·m^3/s ←	Xe	→	1.012 Pa·m^3/s
C = 30 m^3/s	↑		C = 44 m^3/s

(0.84 + 1.012) x 2 = 3.7 Pa·m^3/s = 6 mol/h

(d) Diffusion gas quantity between plasma and beam dump

The drift pipe shape and gas pressure are assumed as shown in Fig. 13.1.1.

Total conductance:

DT C_T = 80 m^3/s Xe C_T = 16 m^3/s

Ignoring the diffusion suppression effect due to intermolecular collisions in the drift pipe, the design condition of the fuel system is as follows.

DT diffusion from plasma to beam dump tank

0.002 x 80 x 2 = 0.32 Pa·m^3/s = 0.52 mol/h = 0.6 mol/h

Xe diffusion from beam dump tank to plasma

0.002 x 16 x 2 = 0.064 Pa·m^3/s = 0.1 mol/h

(4) Fuel supply from pellet injection system

When compared with the necessary fuel feed to the core plasma, the supply of deuterium by NBI can be ignored, and all of fuel gas is assumed to be supplied by the pellet injection system.

(a) Fuel feed from pellet injection system to core plasma

From the type and quantity of exhaust gas mentioned above:

D,T unconsumed content	: 600 mol/h
D,T consumption	: 6 mol/h
Total	: 606 mol/h

(b) Feed gas from the fuel circulation system to the pellet injection system

Considering pellet breakage during acceleration, aboutg 1.5 times of the required gas should be supplied to the pellet injection system.

Feed : 600 x 1.5 = 900 mol/h

The balance from the required amount should be differentially pumped out and returned to the fuel system.

Exhaust: 900 - 600 = 300 mol/h

Composition of feed gas, exhaust gas

Feed gas : Ratio of D, T 50%, 50%

Exhaust gas : Principal ingredients should be the same as in the feed gas.

(5) Fuel supply from gas injection system

Supply of gas from the gas injection system is not necessary in the stationary state, and is required only when starting up the plasma, and the guideline of the feed amount is for the portion consumed in 100 seconds.

Feed gas for plasma start-up: D, T 20 mol/each time

As the fuel circulation system, without any extra treating capacity for supplying gas to the gas injection system, only the tank for temporarily storing the gas required for initial

start-up should be provided.

Gas feed tank capacity : Amount required for initial start-up x 1.5 times.

(6) Recovery of tritium from blanket

In the feed gas from the blanket-tritium recovery system to the fuel circulation system, all components except for hydrogen isotopes (H, D, T) are removed, and the chemical form is assummed to be hydrogen gas.

The amount of tritium recovered should be equivalent to the amount of tritium consumed, that is, 3 mol/h.

(7) Recovery of tritium from primary cooling water

The tritium passing into the primary cooling water is totally recovered in the tritium recovery system, and enriched, and transformed into a chemical form of hydrogen gas, and sent to the fuel system to be recycled as fuel gas.

Table 13.1.1 Equilibirum constants* for hydrogen and water exchange

T(°K)/Equilibrium	0	273.1	298.1	400	500	600	Classical limit
$[HD]^2/[H_2][D_2]$	0	3.18	3.25	3.48	3.62	3.72	4.0
$[HDO]^2/[H_2O][D_2O]$	0	3.94	3.96	4.00	4.02	4.03	4.0
$[HDO][H_2]/[H_2O][HD]$	∞	4.29	3.70	2.46	1.94	1.66	1.0
$[D_2O][HD]/[HDO][D_2]$	∞	3.46	3.05	2.14	1.75	1.53	1.0
$[HT]^2/[H_2][T_2]$	0	2.42	2.56	2.97	3.24	3.44	4.0
$[HTO]^2/[H_2O][T_2O]$	0	3.34	3.42	3.63	3.74	3.80	4.0
$[HTO][H_2]/[H_2O][HT]$	∞	7.64	6.19	3.46	2.47	1.99	1.0
$[T_2O][HT]/[HTO][T_2]$	∞	5.54	4.63	2.84	2.15	1.80	1.0
$[DT]^2/[D_2][T_2]$	0	3.79	3.82	3.88	3.92	3.94	4.0
$[DTO]^2/[D_2O][T_2O]$	0	3.55	3.59	3.70	3.76	3.80	4.0
$[DTO][D_2]/[D_2O][DT]$	∞	1.63	1.55	1.34	1.23	1.16	1.0
$[T_2O][DT]/[DTO][T_2]$	∞	1.75	1.65	1.40	1.28	1.21	1.0

* Most of the data in this Table are Urey's calculated values for the gas phase reactions.

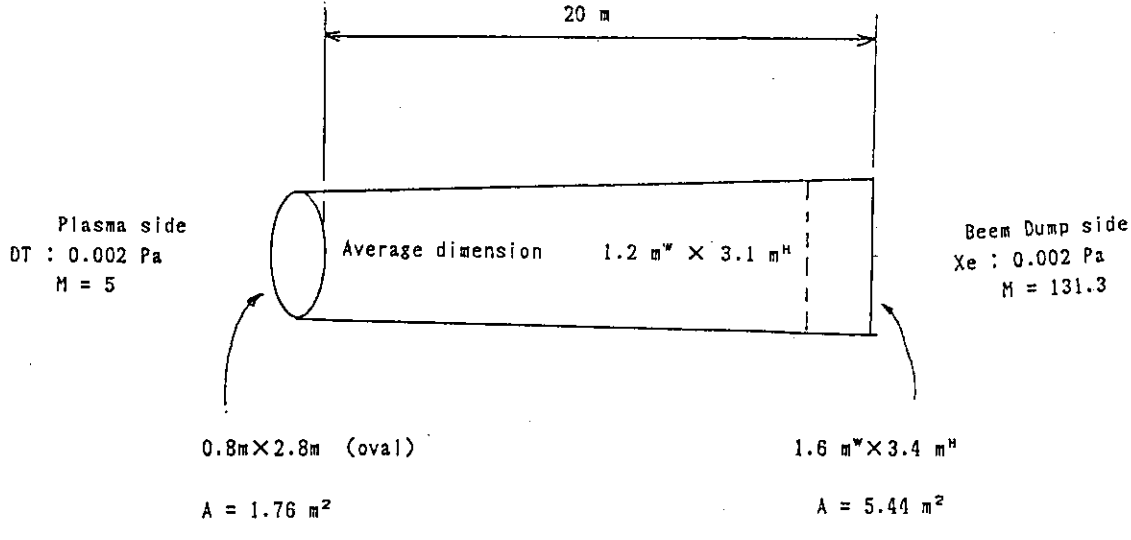

Fig. 13.1.1 Dimension of drift tube.

13.2 Design condition of fuel circulation system

(1) Basic function

This equipment is designed to pump out plasma combustion gas from the SSTR, purify hydrogen isotope gas from it, and feed tritium (T) and deuterium (D) as combustion gas to the fuel pellet injection system and neutral beam injection system (NBI). It also has functions for recovering tritium from the blanket recovery system and also recovering tritium from the primary cooling water.

(2) Design condition

The received, feed gas conditions of this equipment are shown below, together with the conditions of tritium recovery from the primary cooling water.

(a) Around the torus

(i) Plasma exhaust gas

D, T	: 3,273.0 mol/h
He	: 24.0 mol/h
Others (H, impurities)	: 15.1 mol/h

(ii) Exhaust gas from pellet injection unit and NBI

Pellet injection unit	: D, T	300.0 mol/h
NBI	: D	29.3 mol/h
	T	0.3 mol/h
	Xe	5.0 mol/h

(iii) Feed gas

Pellet injection system	: D,T 906 mol/h
	(from fuel storage & supply system)
NBI:	: D_2 30 mol/h
	(from fuel storage & supply system)
	Xe 5 mol/h
	(from fuel clean-up system II)

Gas injection system: He and hydrogen isotope gas 2,700 mol/h
(from fuel clean-up system I)

At the time of initial start-up only, 20 mol of D, T should be supplied from the gas injection system.

(b) Blanket recovery system

(i) Lead-in gas from blanket recovery system

H: 346.5 mol/h

T: 3.5 mol/h

(ii) Feed gas to blanket recovery system

H: 346.5 mol/h (from isotope separation system)

T: 0.5 mol/h (from isotope separation system)

(c) Tritium recovery conditions from primary cooling water

Amount of tritium entering primary cooling water : 2 g/day

Allowable tritium concentration in primary cooling water : 1 Ci/liter

(3) Composition of the equipments

Equipment composition

This equipment is composed of various types of facilities with different purposes, and the basic specification is given below. The material balance among facilities and among other equipments is shown in Fig. 13.2.1

(a) Plasma exhaust system

This system is to pump out helium which is nuclear fusion reaction product, and tritium and deuterium which are unburnt fuel components, from the core plasma, and supply them into the fuel clean-up system.

Main exhaust pump: Turbo molecular pump

(b) Fuel clean-up systems I, II

These are intended to remove impurities from the exhaust gas from the core plasma, pellet injection system, and neutron injection system, and supply the purified hydrogen iotopes into the isotope separation system.

Impurity removal process : Cryogenic adsorption method.

Tritium recovery process : Electrolytic method (ceramic electrolysis cell)

(c) Isotope separation system

This is to separate tritium and H_2 from the mixed hydrogen isotope gas discharged from the fuel clean-up system, blanket recovery system, and primary cooling water tritium removal system, and supply them to the fuel storage and

supply system.

Separation process : Cryogenic distillation method

(d) Fuel storage and supply system

This is to recover and store the D, T separated and purified in the isotope separation system, and supply the fuel gas to the pellet injection system and NBI at a specified flow rate. The storage capacity should be designed to store the whole amount of fuel gases.

Storage and supply method : Tank storage + getter method.

(e) Fuel gas injection system

This system is to feed cooling gas for the diverter plate, and supply fuel gas necessary when starting up the plasma, and it has only the supply line and the temporary storage tank for the gas necessary for initial start-up.

Gas feed tank capacity : 30 mol (necessary amount for initial start- up x 1.5 times)

(f) Tritium recovery system for primary cooling water

This is to separate and recover the tritium entering the primary cooling water, and supply it into the isotope separation system to be used as fuel gas, and also control the tritium concentration in the primary cooling water to be under the allowable level.

Recovery process: Water distillation method

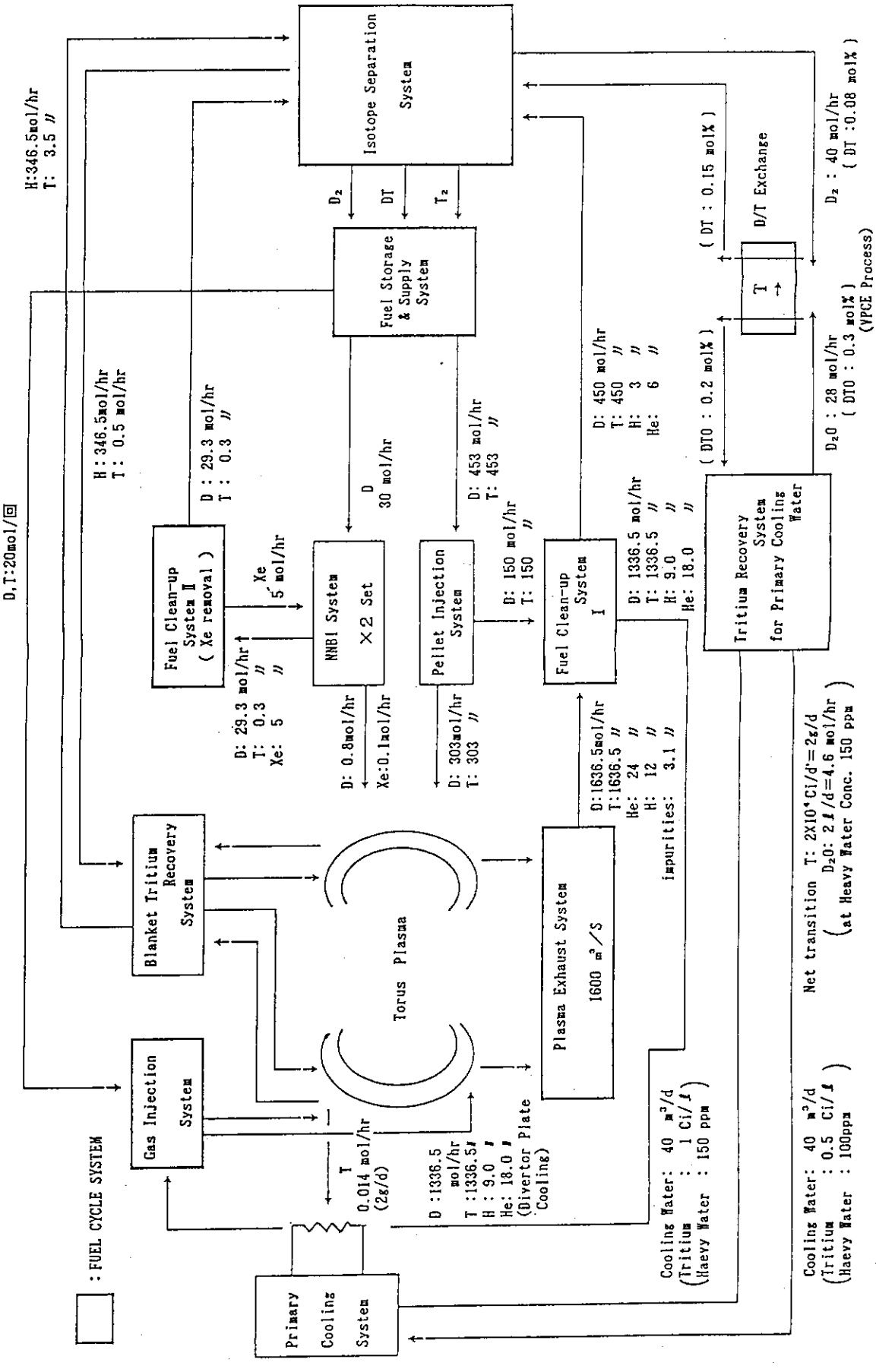

Fig. 13.2.1 SSTR fuel cycle.

13.3 Composition of fuel circulation systems

(1) Plasma exhaust system

(a) System composition

The main exhaust pump is a turbo molecular pump of 25 m^3/s. The pump composition of this system is shown in Table 13.3.1, and a system flow diagram is given in Fig. 13.3.1.

(b) Review of exhaust capacity

(Conditions)

Exhaust gas quantity Q : 3312 mol/h = 2044 $Pa \cdot m^3/s$

Exhaust port : 2,000 mm square section duct

(No. of exhaust ports: 16)

(Exhaust port pressure)

S_{p1} : Main exhaust pump pumping speed (4units/port) (m^3/s)

C_1 : Exhaust port conductance (m^3/s)

S_{e1} : Effective pumping speed at exhaust port (m^3/s)

P_1 : Pressure at exhaust port (Pa)

The calculation formulae are as follows:

$$S_{e1} = 1/(1/S_{p1} + 1/C_1)$$

$$C_1 = 97.4 \cdot K \cdot (T/M) \cdot a^2 \cdot b^2/(a + b)/l$$

where,

T = 300 K M = 5 (DT) a,b: Section shape If a=b, then K=1.115

l: Duct length (m) $P_1 = (Q/16)/S_{e1}$

Using these expressions, the values are obtained from a=b=2 m, and the results are as follows.

Main exhaust pump piping speed	S_{p1}	(m3/s)	100
Exhaust port conductance	C_1	(m3/s)	210
Effective pumping speed	S_{e1}	(m3/s)	67.7
Exhaust port pressure	P_1	(Pa)	1.9

(2) Fuel clean-up system

(a) Conditions

The lead-in gas conditions are as follows.

From plasma exhaust system	From pellet injection system
D : 1636.5 mol/h T : 1636.5 mol/h H : 24.0 mol/h He: 12.0 mol/h Impurities: 3.1 mol/h	D: 150 mol/h T: 150 mol/h
Total 3312.1 mol/h	Total 300 mol/h

Composition of impurities

Ar : 0.375 mol/h
N_2 : 0.75 mol/h
NQ_3 : 0.375 mol/h
Q_2 : 0.75 mol/h
Q_2O : 0.75 mol/h
Xe : 0.1 mol/h

(b) System composition

The system is composed of the following main units.

Impurity adsorber (I): To adsorb and remove water (Q_20) from the lead-in gas.
Impurity adsorber (II): To adsorb and remove impurity components other than water from the lead-in gas at low temperature (-193°C).
Heat exchanger :To exchange heat between the inlet and outlet gas of impurity adsorber (II) ;a plate type heat exchanger.
Regeneration unit(I):To regenerate impurity adsorber I. To electrolyze regeneration gas by a ceramic electrolysis cell to recover tritium in the form of gas.
Regeneration unit (II); To regenerate impurity adsorber (II). To recover tritium in the form of gas from regeneration gas by metal catalyst + ceramic electrolysis cell.

The system configuration is shown in Fig. 13.3.2.

(3) Fuel clean-up system (II)

(a) Conditions

The lead-in gas conditions are as follows.

D : 29.3 mol/h

T : 0.3 mol/h

Xe : 5.0 mol/h

(b) System composition

This system mainly comprises three Xe adsorber and regeneration unit (Xe recovery unit). The system configuration is shown in Fig. 13.3.3.

(4) Isotope separation system

(a) Condition

Since the composition is significantly different between the gas sent in from the blanket-tritium recovery system and the gas sent in from the fuel clean-up system, they should be treated in independent lines in this equipment.

Also, in order to minimize the tritium inventory of the system, the gas sent in from the fuel clean-up system (I) is once sent into the condenser to liquefy D, T components, and its off-gas is separated and enriched in the cryogenic distillation process.

(b) System composition

The line for treating the gas supplied from the fuel clean-up system is shown in Fig. 13.3.4, and the line for treating the gas supplied from the blanket-tritium recovery system in Fig. 13.3.5.

(5) Fuel storage & supply system and gas injection system

The configuration, mainly composed of storage tank, storage getter, and gas supply tank, is shown in Fig. 13.3.6.

(6) Tritium recovery system from primary cooling water

(a) System composition

This is composed of two main lines.

Tritium recovery system 1 (tritium removal system):

To remove tritium from primary cooling water.

Tritium recovery system 2 (high concentration system):

To enrich the removed tritium with high concentration, and finally recover tritium in the form of gas.

System configurations are shown in Figs. 13.3.7, 13.3.8. The design condition of this system is shown in Table 13.3.2.

(b) Outline of specifications

The outline of the specification of the tritium removal system is shown in Table 13.3.3, and its rectifying column specification is given in Table 13.3.4. The specification of the high concentration system is shown in Table 13.3.5, and its rectifying column specification in Table 13.3.6.

Table 13.3.1 Pump of plasma exhaust system

Name of Pump	No.	Type OF Pump
Main Exhaust Pump	64 (4/1Port)	Turbo Molecular Pump
Fore Pump (I)	16	Booster Pump
Fore Pump (II)	5	Scroll Vacume Pump

Table 13.3.2 Design condition for tritum recovery system

Net Transition of Tritium (to Cooling Water)	Ci/day	2.0×10^4
Permissible Tritium Conc. (of Cooling Water)	Ci/l	1.0
Method of Detritiation		Water Distillation
System of Tritium Removal		Closed Cycle
Decontamination Factor(DF)	－	2
Consentration Factor(CF)	－	100
Distillated Water		to Primary Cooling System
Waste Water		to VPCE Process
Flow Rate of Feed Water	l/h	1.7×10^3
Flow Rate of Waste Water	mol/h	4.8

Table 13.3.3 Tritium recovery system I
(Tritium removal system)

Flow Rate of Feed Water	l/h (kmol/h)	1.7×10^{3} (9.44×10^{1})
Tritium Conc. of Feed Water	Ci/l (Ci/kmol)	1.0 (1.8×10^{1})
Flow Rate of Distillated Water	l/h (kmol/h)	1.699×10^{3} (9.439×10^{1})
Trutium Conc. of Distillated Water	Ci/l (Ci/kmol)	5.0×10^{-1} (9.0)
Flow Rate of Waste Water	l/h (kmol/h)	9.4 (5.25×10^{-1})
Trutium Conc. of Waste Water	Ci/l (Ci/kmol)	100 (1800)
Press. at the Top of Column	Torr (MPa)	60 (8.0×10^{-3})
Temp. at the Top of Column	℃	41.5
Press. at the Bottom of Column	Torr (MPa)	112 (1.49×10^{-2})
Temp. at the Bottom of Column	℃	53.9
Reflux Ratio		9.6

Table 13.3.4 Column of tritium recovery system I
(Tritium removal system)

		No.1 Column	No.2 Column
Number	－	1	1
Type	－	Regular Packing Column	
Packing	－	Sumitomo-Suluzer Packing BX Type	
Inside Dia. of Column	m	3.4	1.9
Height of Filling-up	m	6.5	13.5
Volume of Packing	m^3	59.0	38.3
Height of Column	m	20.0	25.0

Table 13.3.5 Tritium recovery system 2
(High concentration system)

Flow Rate of Feed Water	l/h (kmol/h)	9.4 (5.25×10^{-1})
Tritium Conc. of Feed Water	Ci/l (Ci/kmol)	100 (1.8×10^{3})
Flow Rate of Distillated Water	l/h (kmol/h)	9.45 (5.25×10^{-1})
Trutium Conc. of Distillated Water	Ci/l (Ci/kmol)	10 (1.8×10^{2})
Flow Rate of Waste Water	l/h (kmol/h)	0.096 (4.8×10^{-3})
Trutium Conc. of Waste Water	Ci/l (Ci/kmol)	10000 (1.8×10^{5})
Press. at the Top of Column	Torr (MPa)	60 (8.0×10^{-3})
Temp. at the Top of Column	℃	41.5
Press. at the Bottom of Column	Torr (MPa)	141 (1.88×10^{-2})
Temp. at the Bottom of Column	℃	58.7
Reflux Ratio		20.2

Table 13.3.6 Column of tritium recovery system 2
(High concentration system)

		No.1 Column	No.2 Column
Number	－	1	1
Type	－	Regular Packing Column	
Packing	－	Sumitomo-Suluzer Packing CY Type	
Inside Dia. of Column	m	0.4	0.15
Height of Filling-up	m	10.0	12.8
Volume of Packing	m^3	1.3	0.23
Height of Column	m	20.0	20.0

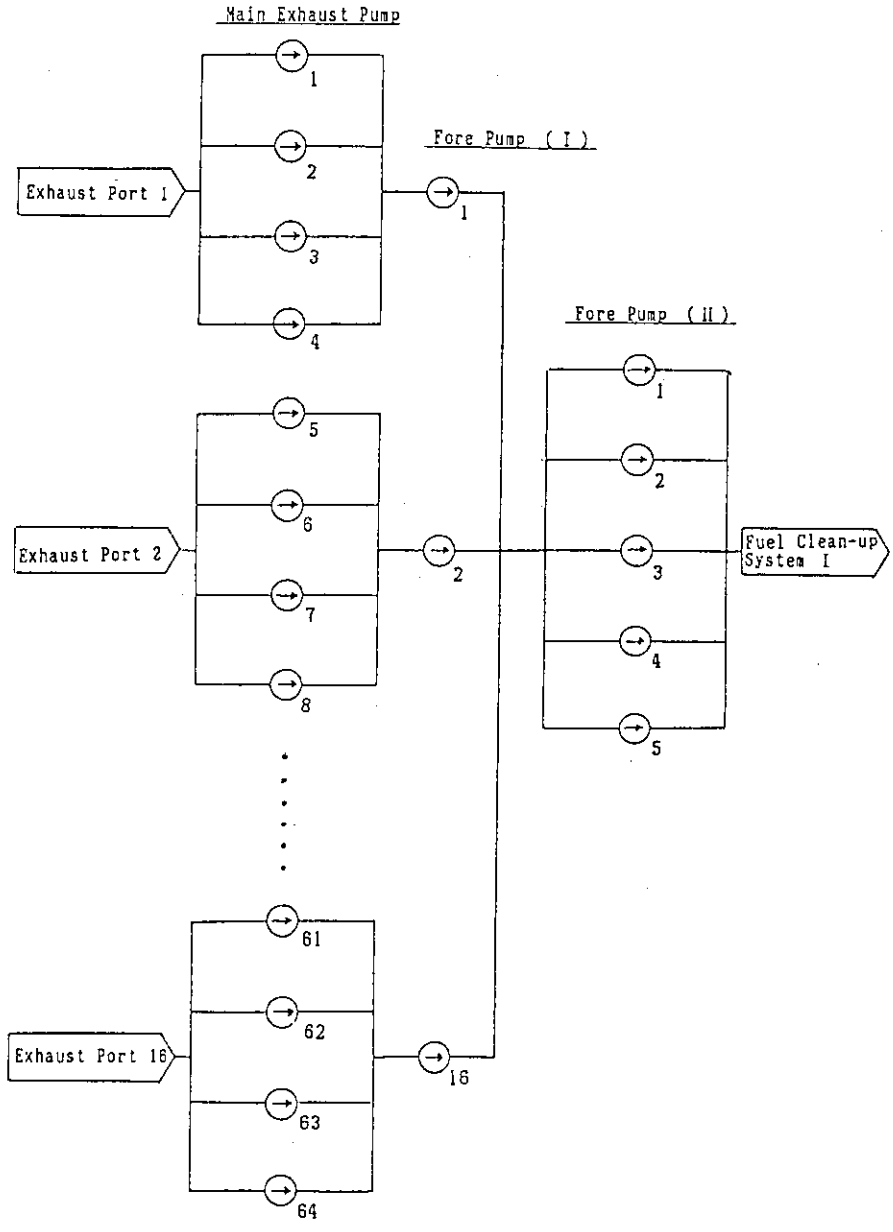

Fig. 13.3.1 Plasma exhaust system flow diagram.

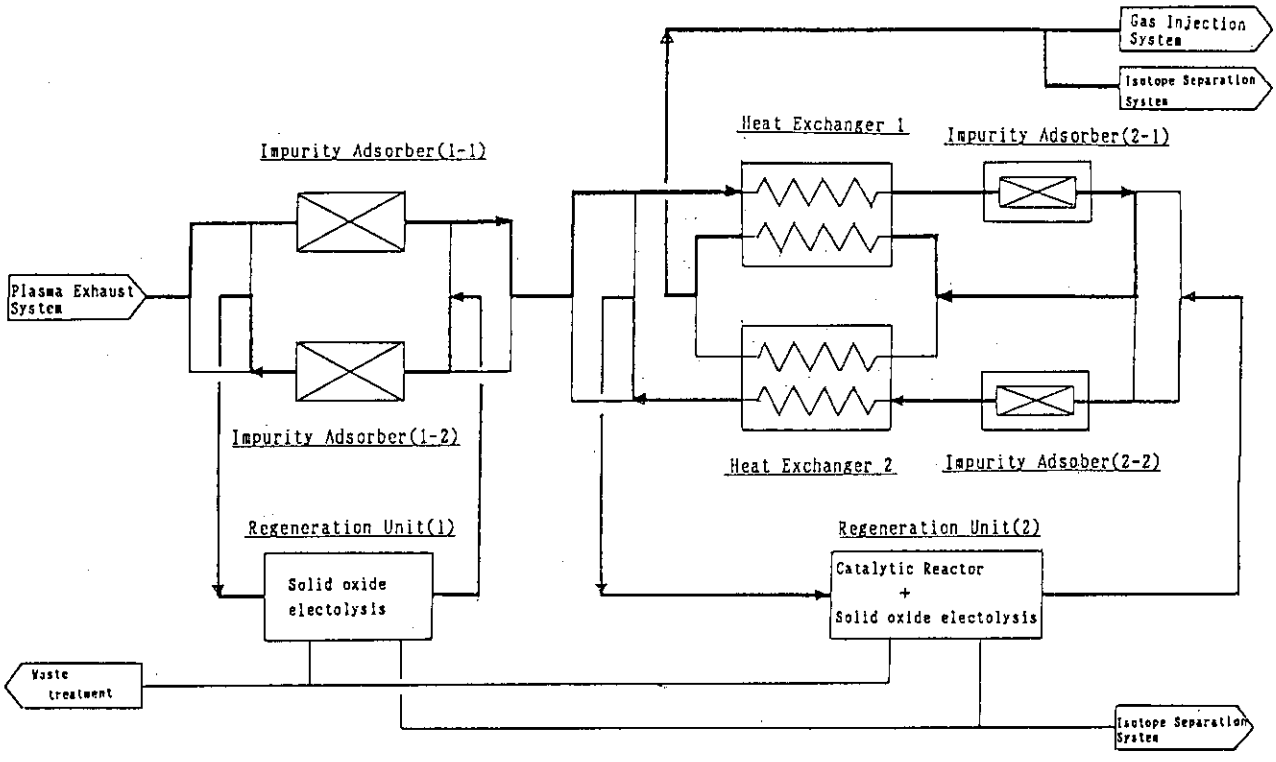

Fig. 13.3.2 Fuel clean-up system flow diagram.

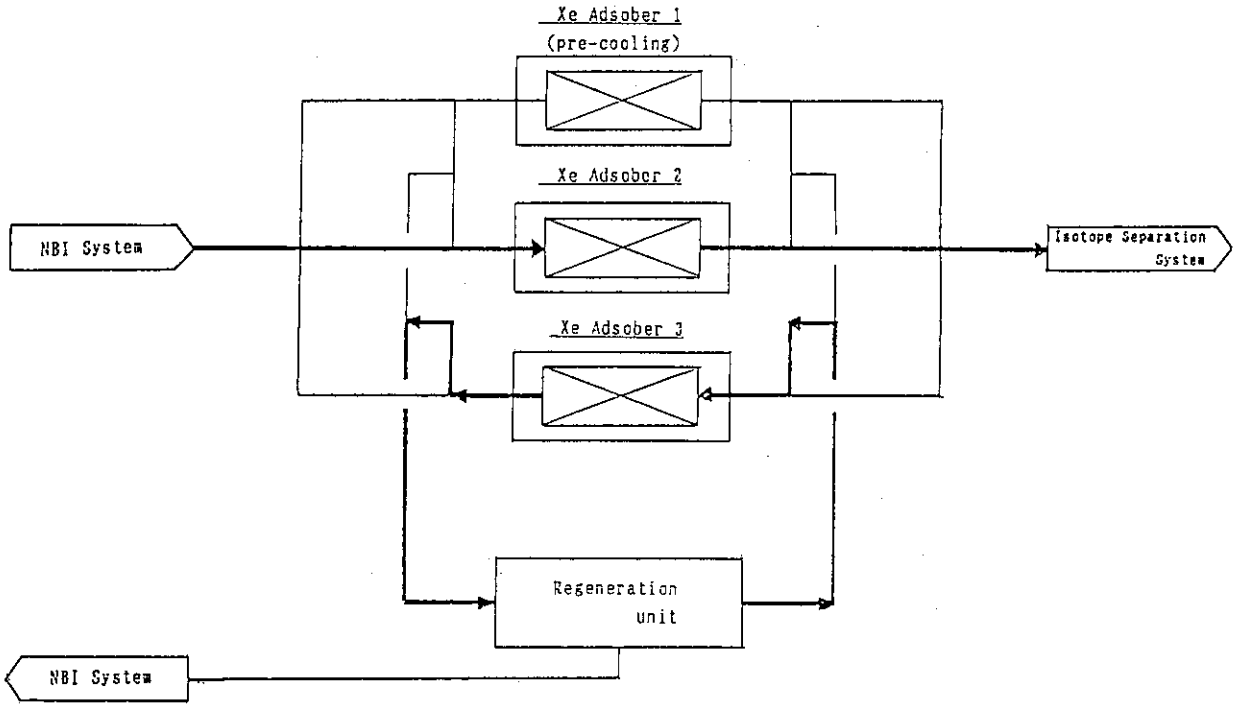

Fig. 13.3.3 Fuel clean-up system II flow diagram.

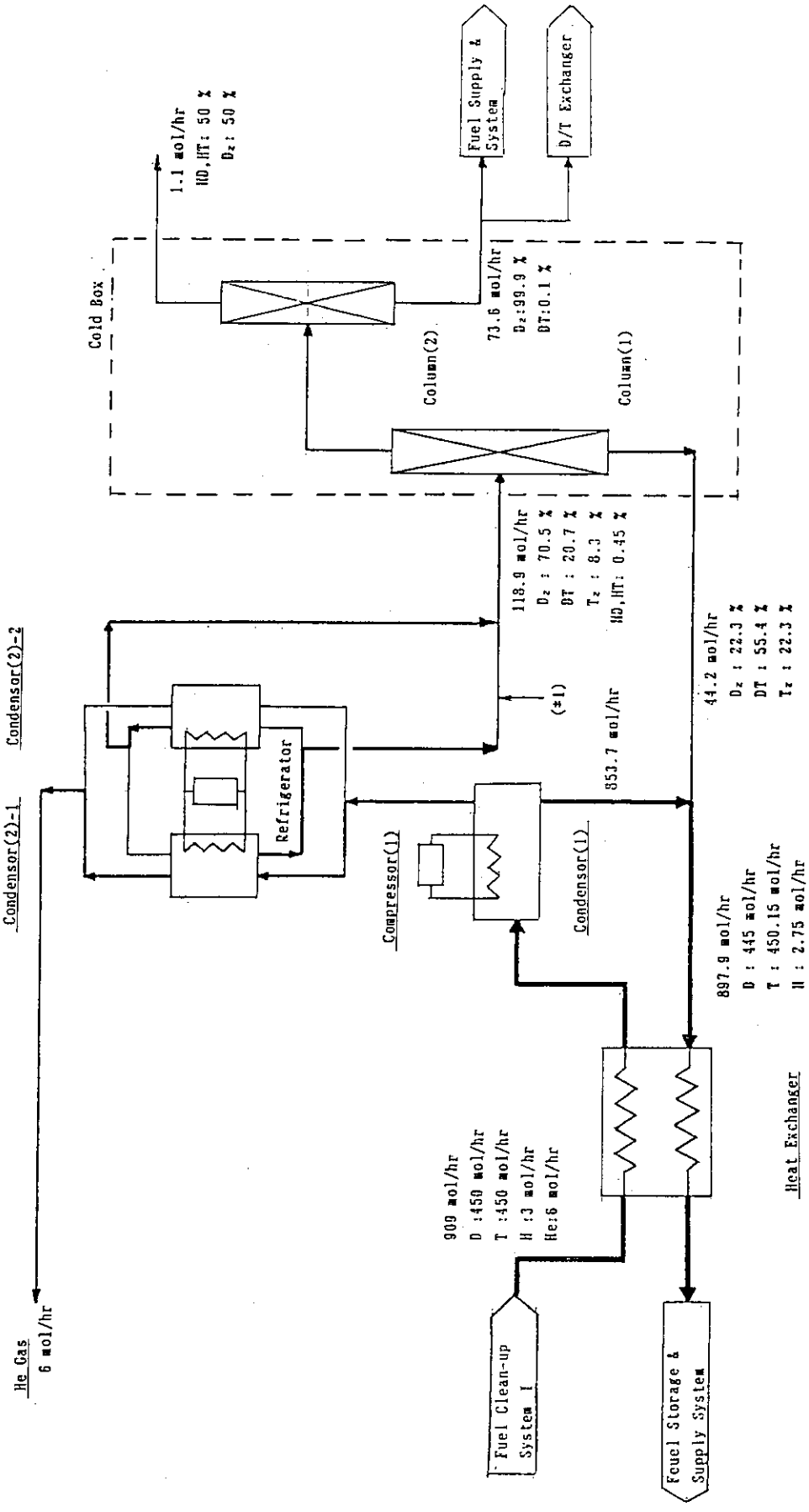

Fig. 13.3.4 Isotope separation system (1).

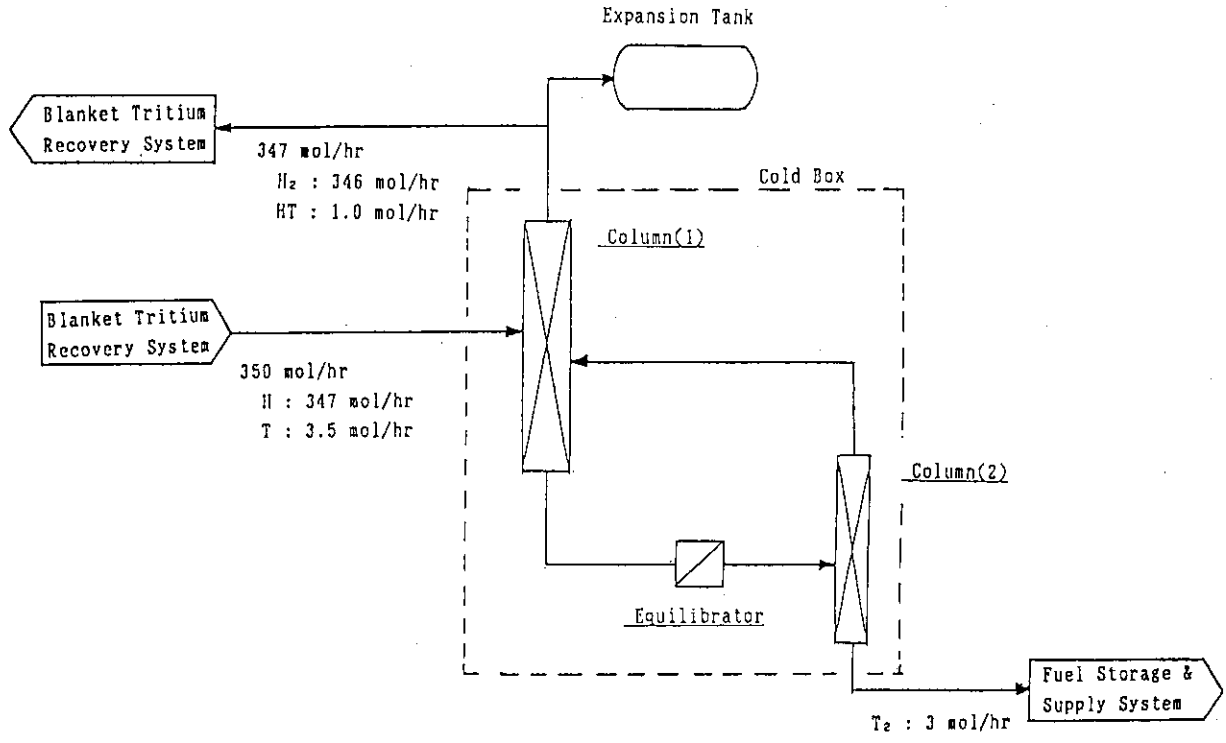

Fig. 13.3.5 Isotope separation system (2).

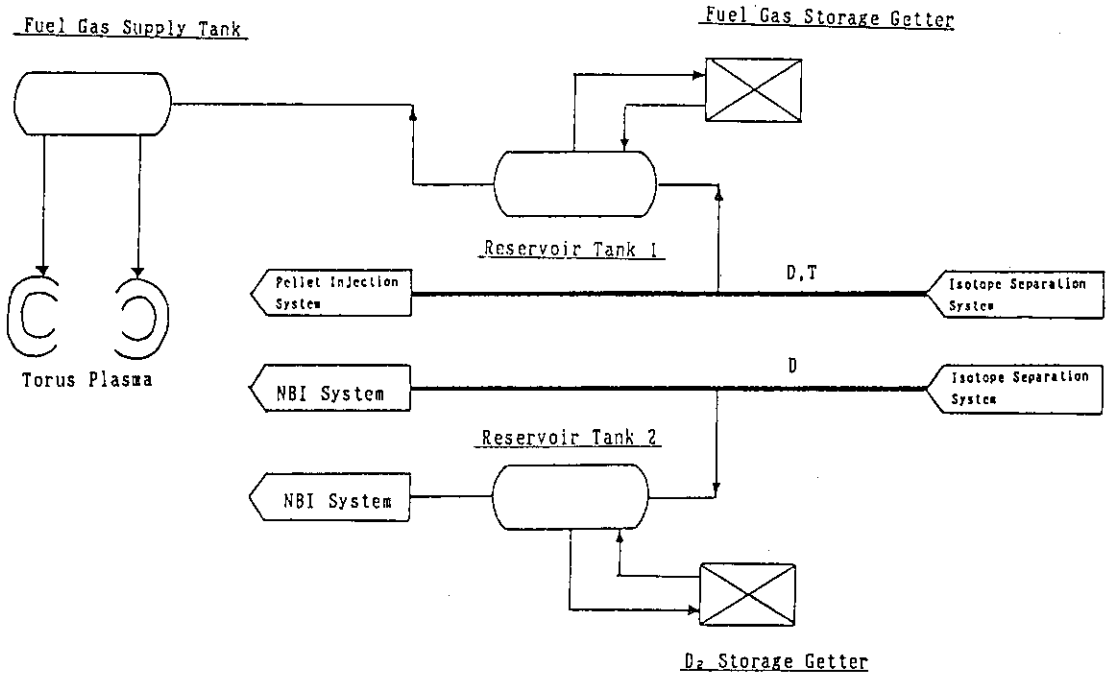

Fig. 13.3.6 Gas injection, fuel storage & supply system flow diagram.

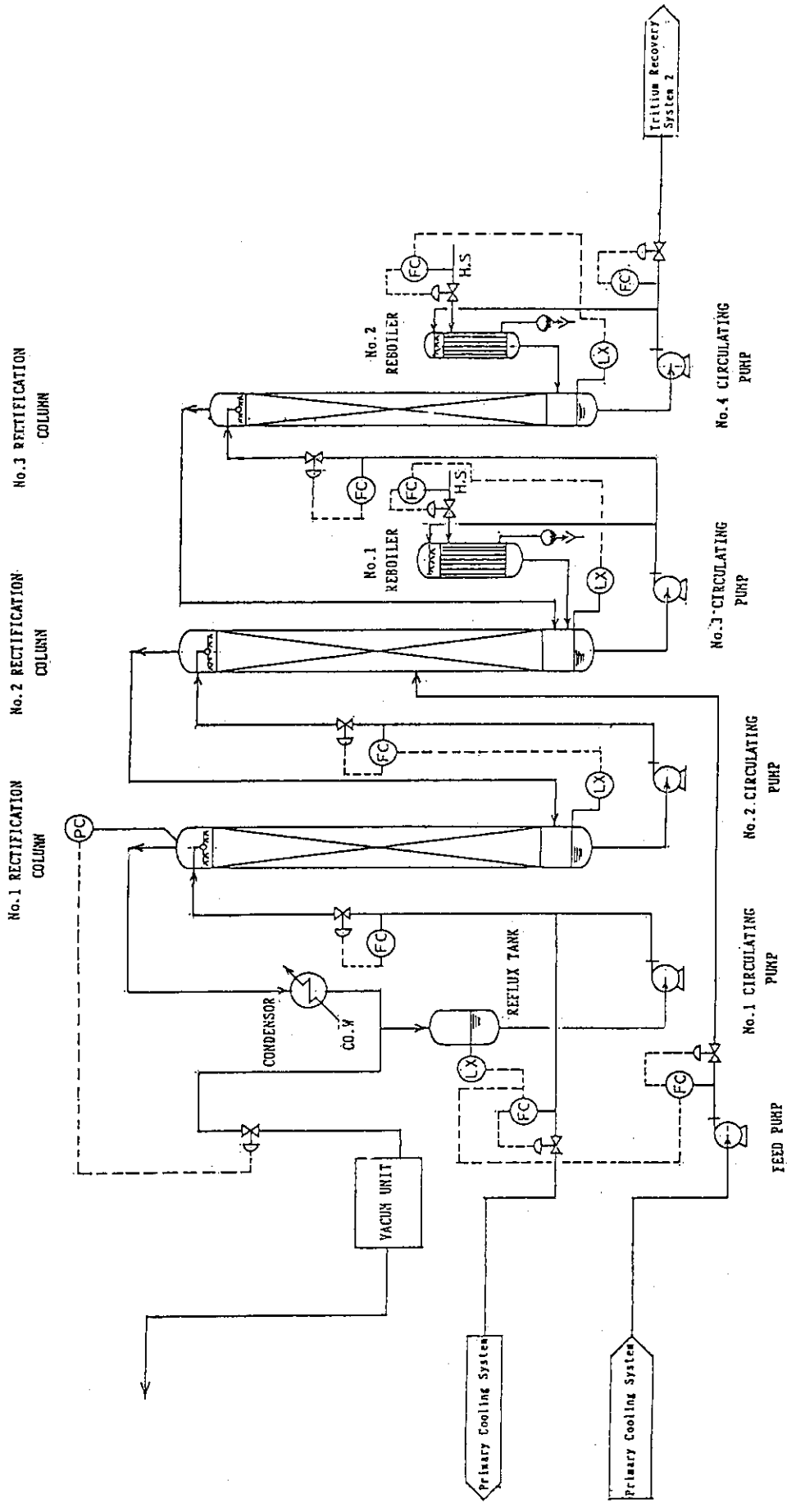

Fig. 13.3.7 Tritium recovery system flow diagram.
(Tritium removal from primary cooling water)

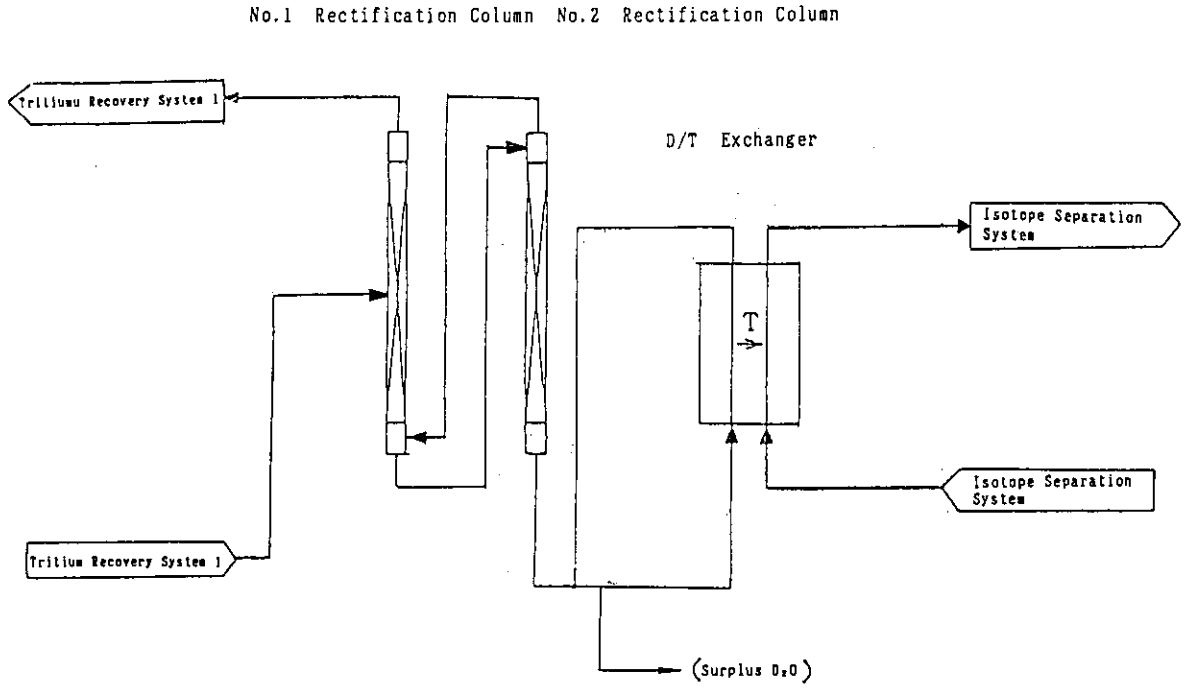

Fig. 13.3.8 Tritium recovery system 2 flow diagram.
(High concentration for tritium)

13.4 Review of tritium inventory

(1) Tritium inventory of fuel circulation system

In the fuel circulation system mentioned in 13.3, the tritium inventory was approximately reviewed. As a result, the total tritium inventory was found to be 1.5 kg as shown in Table 13.4.1.

Only principal parts of total inventory are mentioned here, and the devices and piping discussed in this section are the isotope separation system, the piping from plasma exhaust system to the pellet injection unit, and the piping for diverter cooling gas. The tritium inventory in the piping is shown in Table 13.4.2.

(2) Tritium inventory when treating diverter cooling gas in isotope separation system

The total material balance of the fuel circulation system in this case is shown in Fig. 13.4.1. The devices and piping discussed here are the isotope separation system, and the piping from the plasma exhaust system to the pellet injection system.

(a) Tritium inventory of isotope separation system

Considering the system composition of the isotope separation system in this condition, it may be as shown in Figs. 13.4.2, 13.4.3.

Case 1: Deuterium, tritium atomic ratio (T/D) of product gas to be 70%.
Case 2: D/T of product gas to be 50%.

In each case, the tritium inventory in the rectifying column is:

Case 1:10 kg
Case 2: 6 kg

(b) Tritium inventory in piping

The tritium inventory in the piping in this case is 78 g. Meanwhile, the tritium distribution in the piping in this condition is shown in Table 13.4.3.

Table 13.4.1 Tritium inventory of fuel cycle

Name of System	Tritium Inventory	Ref.
Isotope Separation System	1200 g	
Piping	300 g	Table 13.4.2
Total	1500 g	

Table 13.4.2 Tritium inventory (piping)

	Amount of Flowing	Piping Dia.	Piping Length	Tritium Conc. (mol.R)	Tritium Inventory
1. Plasma Exhaust Sys.～ Fuel Clean-up Sys.(I)	3312 mol/hr	φ55 mm	400 m	0.494	21 mol
2. Fuel Clean-up Sys.(I)～ Isotope Separation Sys.	909 mol/hr	φ30 mm	180 m	0.495	2.8 mol
3. Isotope Separation Sys.～ Pellet Injection Sys.	906 mol/hr	φ30 mm	400 m	0.5	6.3 mol
4. Fuel Clean-up Sys(I)～ Gas Injection Sys.	2700 mol/hr	φ50 mm	400 m	0.495	17.4 mol

Total Tritium Inventory (Piping) = 50 × 6 = 300g　　合計　47.5≒50 mol

Table 13.4.3 Tritium inventory (piping)

	Amount of Flowing	Piping Dia.	Piping Length	Tritium Conc. (mol.R)	Tritium Inventory
1. Plasma Exhaust Sys.～ Fuel Clean-up Sys.(I)	3312 mol/hr	φ55 mm	400 m	0.091	4 mol
2. Fuel Clean-up Sys.(I)～ Isotope Separation Sys.	3609 mol/hr	φ55 mm	180 m	0.125	2.4 mol
3. Isotope Separation Sys.～ Pellet Injection Sys.	906 mol/hr	φ30 mm	400 m	0.5	6.3 mol

Total Tritium Inventory (Piping) = 13 × 6 = 78 g　　合計　12.7≒13 mol

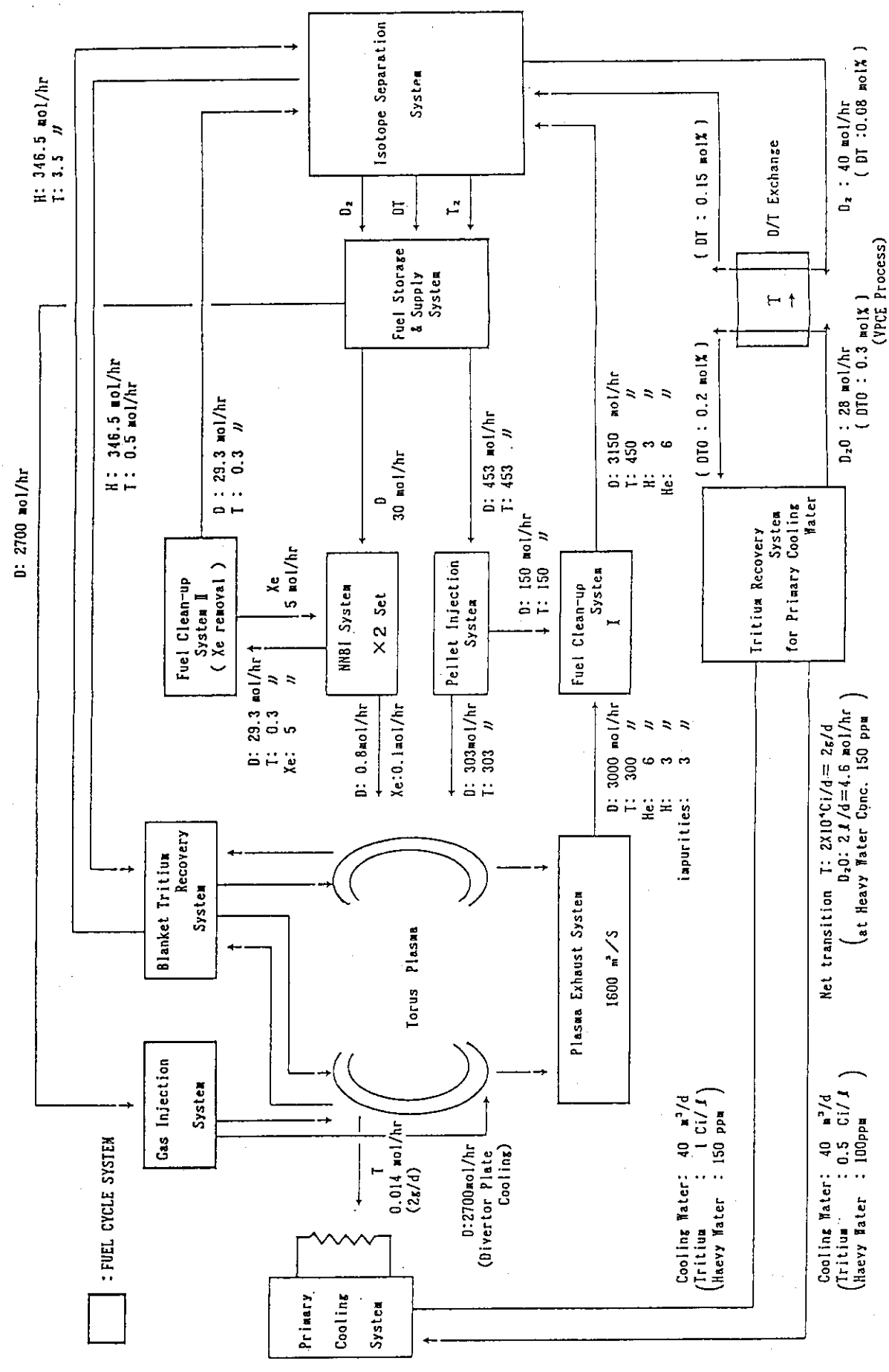

Fig. 13.4.1 SSTR fuel cycle.

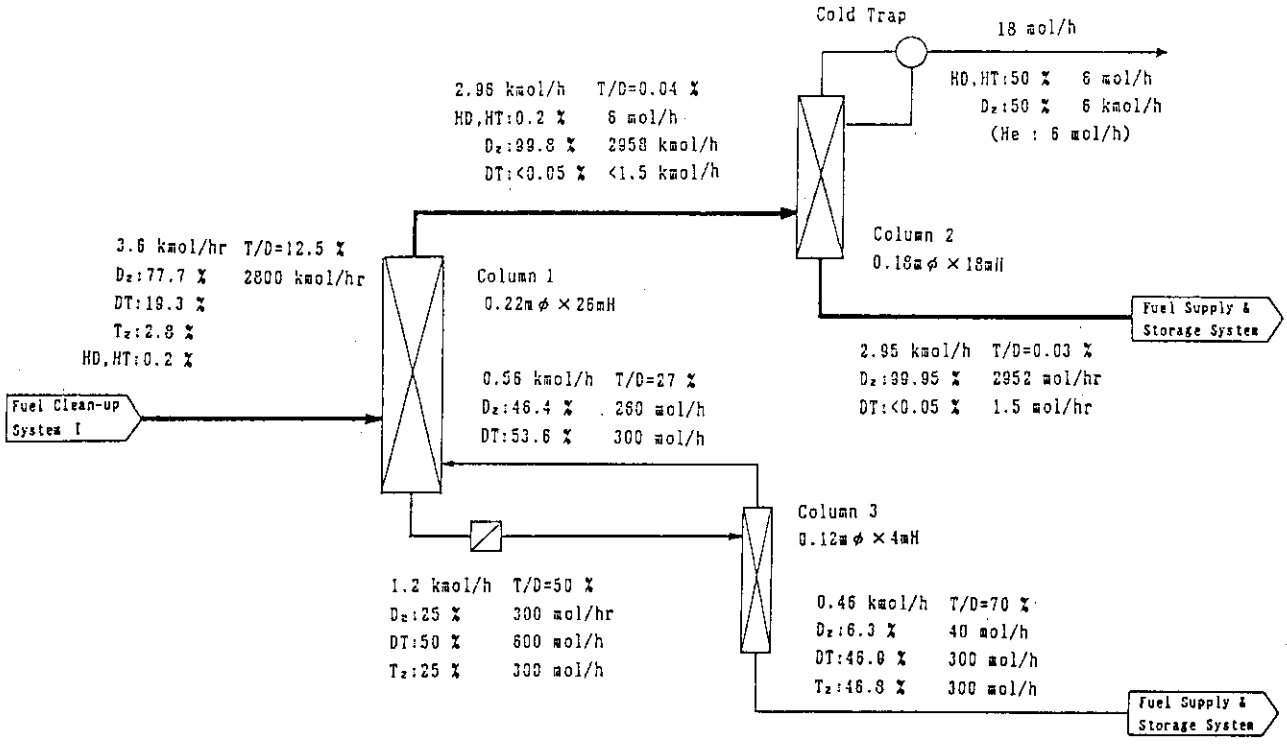

Fig. 13.4.2 Case 1 flow diagram.

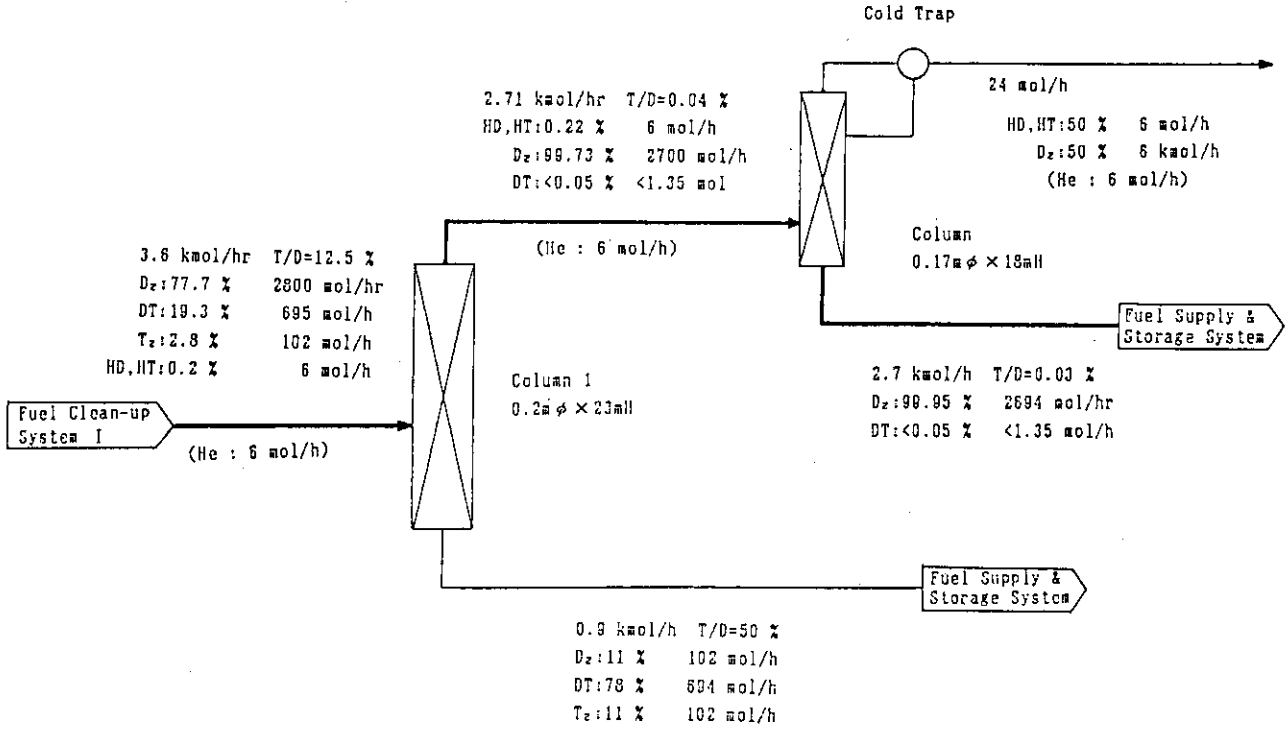

Fig. 13.4.3 Case 2 flow diagram.

13.5 Future problems

Principal future problems in the SSTR fuel circulation system include the following items.

(1) Development of main exhaust pump, fore pump of plasma exhaust system

In order to lower the pressure in the exhaust port, it is required to enhance the performance of the main exhaust pump, and develop its fore pump.

(2) Clarification of quantity and composition of impurities in plasma exhaust gas

In order to design the fuel clean-up system more adequately, it is necessary to clarify the quantities and composition of impurities in the plasma exhaust gas.

(3) Reduction of impurity level in plasma exhaust gas

By reducing the impurity level of the plasma exhaust gas, it is possible to simplify the structure of the fuel clean-up system and isotope separation system.

(4) Reduction of tritium inventory of entire fuel circulation system

Including reduction of the quantity of the gas to be treated, it is necessary to plan, aiming at reduction of the tritium inventory.

14. Power supply system/Control system

14.1 Power supply system

14.1.1 Toroidal field coil power supply

1) Introduction

Toroidal field coil power supply (TFCPS) provides electric power required for the toroidal field coil (TFC) of SSTR. As the TFC is super-conductive and the current in the TFC is kept constant during the operation, the capacity of the TFCPS is small. Magnetic energy stored in the TFC, however, is so large (more than 100GJ) that the capacity of quench protection system becomes very large. Resistance of the DC current feeder has to be low because the out put of the TFCPS is low voltage and high current.

Table 14.1.1 shows main parameters of TFC.

2) Quench protection system

Current in the TFC has to be decreased as rapid as possible when quench occurs in the TFC. Electric power required to decrease the current in the TFC is very large because of high current and high inductance, so that it is not realistic to provide this power by converters. Consequently, DC circuit breaker (DCCB) together with dump resistor is adopted for the quench protection system.

Recovery voltage required for significant quench protection exceeds the withstand voltage of insulation system of the TFC, if the quench protection system consists of only one DCCB. To reduce recovery voltage, DCCB and TFC are connected alternately as shown in Fig. 14.1.1 and all the DCCBs are opened at the same time when quench protection is necessary. This configuration has the following merits;

a) Recovery voltage per one DCCB is reduced to 1/16.
(Insulation level of TFC is also reduced)
b) If one of the DCCBs should fail to be opened, TFC current could be dumped with the rest of DCCBs without causing any current imbalance among the TFCs.

Recovery voltage per one DCCB is determined to be 20kV considering acceptable temperature rise of the TFC. Resistance of the dump resister is;

20kV/81kA=0.247ohm

Heat capacity of the dump resistor is;

136.5GJ/16=8.53GJ

Then, time constant of TFC current decrease is;

41.6H/0.247/16=10.5Sec

Ratings of the quench protection system are summarized as follows;

DCCB	DC 20kV - 81kA	16 units
Dump resistor	8.53GJ - 0.247ohm DC 20kV - 81kA	16units

3) DC power supply

TFCs are connected in series and magnetized by one DC power supply.

The DC power supply and the quench protection system are located in the power supply building which is distant from the TOKAMAK. Configuration as shown in Fig. 14.1.1 requires two DC current feeder for each one of the TFCs between power supply building and the TOKAMAK. As these DC current feeders are connected in series, resistance of the feeders causes large energy consumption and degrades total plant efficiency. From this point, super-conducting DC current feeder is required.

If resistance of the DC feeder is negligibly low, voltage rating of the DC power supply is determined by magnetization time of the TFC. Assuming that the TFC is magnetized to its rated current within 24 hours, required voltage Ed of the DC power supply is;

$$Ed = (81kA \times 41.6H)/(24 \times 3600Sec) = 39V$$

DC power supply will consist of thyristor converter. The converter will be 24 pulse system in order to reduce out put voltage ripple and to reduce harmonic current to its power source. As the out put of the converter is low voltage and high current, four sets of three phase bridge converters will be connected in parallel to realize 24 pulse system.

One line diagram of the TFCPS is shown in Fig. 14.1.2.

14.1.2 Poloidal field coil power supply

1) Introduction

Poloidal field coil power supply (PFCPS) provides electric power required for the poloidal field coils (PFCs) of SSTR to produce and maintain the plasma current and to control plasma position and cross section shape. The PFCs are super-conductive. The currents in the PFCs have to be controlled according to the operation scenario. The capacity of the PFCPS is large and required power vary in time.

2) Effect of current in vacuum vessel induced at initial plasma production

The vacuum vessel has a double-thin-walled-structure and its resistance is relatively low. Therefore, initial plasma production might be affected by error field produced by toroidal current in the vacuum vessel which is induced by plasma break down voltage. Effect of current in vacuum vessel is examined modeling the vacuum vessel with 14 loop coils.

Table 14.1.2 shows time variation of induced current in the vacuum vessel during initial plasma production phase of t=0Sec to t=3Sec together with PFC current pattern. Error field produced by current in the vacuum vessel at t=0.5Sec and t=3.0Sec are calculated respectively. Results are shown in Table 14.1.3. Contours of error field are shown in Fig. 14.1.3. Error field at t=3.0Sec is approximately uniform vertical field of 200Gauss and its direction is opposite to equilibrium vertical field produced by PFC current.

As a result, induced current in the vacuum vessel acts as a time delay element to equilibrium vertical field and will not produce serious error field that disables initial plasma production.

3) Estimation of power demand

Electric power demand of the PFC is estimated based on the operation scenario which is described in Chapter 4. Table 14.1.4 shows current pattern of the PFC derived from the operation scenario and the number of turns of the PFC based on the design in Chapter 6. Initial magnetization time of the PFC is chosen to be 100Sec so that required voltage for magnetization is relatively low compared to the voltage required for plasma operation. Table 14.1.5 shows calculated voltage pattern required to the PFCPS out put.

Capacities of the DC power supply for each one of the PFCs are derived form Tables 14.1.4 and 14.1.5, and they are shown in Table 14.1.6. Total capacity of the DC power supplies which is calculated from peak current and peak voltage of each of the PFCs is 900MW approximately. In order to reduce the total capacity, time interval between t=20Sec and the beginning of the steady state can be doubled compared to the operation scenario in chapter 4. In that case, total capacity will be reduced by 20% as shown in Table 14.1.7.

Voltage pattern shown in Table 14.1.5 is for "preprogrammed control" which controls the current in the PFCs according to current pattern defined by the operation scenario. However, Plasma could change its parameters for various causes and the PFCPS has to control position and shape of the plasma within the acceptable limit. In this design,

required power for the PFCPS to control the plasma is estimated considering the following case:

The PFCPS has to be able to change the current in each of the PFCs from the value at steady state to the value required for the equilibrium at poloidal beta increment by 0.1 within two seconds.

Ampere-turns of the PFC required for plasma equilibrium at poloidal flux of -140VSec which is the value at steady state are calculated in the case of poloidal beta of 0.1 and 2.0. Results are shown in Fig. 14.1.4. Change in ampere-turns of the PFC required for poloidal beta increment by 0.1 is assumed to be nineteenth of the deference between the two cases above. Voltage necessary for the DC power supplies to accomplish the ampere-turn change of the PFCs in two seconds are calculated as shown in Table 14.1.8.

4) Configuration of the power supply system

High out put voltage of the DC power supplies is required in the period from the beginning of initial plasma production to the beginning of steady state (t=0-100Sec). During the period of steady state, voltage only for plasma control which is derived in the previous section is necessary. From this point, it is considered to have the following demerits to provide the DC power supplies of ratings in Table 14.1.7 and operate them fully in all the time.

a) Energy loss in the PFCPS in steady state is large.
b) Large reactive power for the DC power supplies is required in steady state.

In order to minimize the demerits described above , DC power supplies in the PFCPS are divided into two kinds of DC power supply connected in series and are operated according to the following principles.

-DC power supply the maximum out put voltage of which is necessary in the period before t=20S is composed of two kinds of DC power supply connected in series. Voltage rating of one is decided according to the highest voltage required in the period after t=20Sec. The other provides necessary voltage in the period before t=20Sec. The latter is operated in by-pass-pair mode (BPP) after t=20Sec.

-DC power supply the maximum out put voltage of which is necessary in the period after t=20S is composed of two kinds of DC power supply connected in series. Voltage rating of one is decided according to the voltage required for plasma control in the steady state operation. The other provides necessary voltage in the

period before the beginning of steady state operation (t=100Sec). The latter is operated in BPP after the period in which high voltage is required.

Ratings of the DC power supplies for the PFCPS according to the principles above are shown in Tables 14.1.9 and 14.1.10. Operation pattern of these power supplies are shown in Fig. 14.1.5.

AC power required for the DC power supplies which are operated in BPP in the steady state is provided by motor-generators which are isolated from commercial grid, because its peak value and fluctuation are both very large. AC power required for the other DC power supplies is derived from commercial grid.

AC power demand in the PFCPS which is composed as described above are calculated. Thyristor converters are adopted for the DC power supplies. Impedance of the converter transformers is assumed to be 20% and 20 degrees is also assumed for minimum delay angle of the thyristor converters. The results are shown in Figs. 14.1.6 and 14.1.7.

Configuration of the PFCPS is shown in Fig. 14.1.8.

Another way to reduce total capacity of the DC power supplies required in the period of initial plasma production and current lump up, is to utilize DCCB combined with a resistor to provide a part of the high voltage which is necessary at initial plasma production between t=0Sec and t=3Sec. If high voltage is provided utilizing DCCBs in the DC power supply for No3(5U), 4(4U), 5(3U), 8(1L), 10(3L) and 11(4L) PFCs, for example, total capacity of the DC power supply required for initial plasma production and current lump up which is shown in Table 14.1.10 can be reduced to 492MW.

14.1.3 List of equipment

1) TFCPS		Quantity
1)Converter system		
Thyristor converter	790kW-DC39V-20.25kA	4
Converter transformer	3.0MVA-6.6kV/54Vx2	2
2)Quench protection system		
DCCB	DC20kV-81kA	16
Dump resistor	0.247ohm-8.53GJ	16

3)Miscellaneous		
S.C. current feeder	350m-32feeders	1 Set
Switchgears	6.6kV-600A	1 Set

2)PFCPS		Quantity
1)Motor generator system		
Generator	250MVA-18kV-3GJ	2
Moter	10,000kW-11kV	2
Liquid rheostat		2
Thyristor scherbius		2
Exciter		2
Auxiliary		2 Sets
2)Converter system		
#7U thyristor converter	1.4MW-DC1997V-0.7kA	4
	23.5MW-DC1997V-11.7kA	4
	8.3MW-DC708V-11.7kA	4
#7U converter transformer	61.9MVA-18kV/1932Vx2	2
	22.0MVA-18kV/685Vx2	2
#6U thyristor converter	1.6MW-DC152V-10.4kA	4
	1.8MW-DC152V-11.8kA	4
#6U converter transformer	4.8MVA-18kV/147Vx2	2
#5U thyristor converter	27.3MW-DC2811V-9.7kA	4
	5.2MW-DC531V-9.7kA	4
#5U converter transformer	72.0MVA-18kV/2718Vx2	2
	13.6MVA-18kV/514Vx2	2
#4U thyristor converter	15.8MW-DC2247V-7.0kA	4
	1.9MW-DC272V-7.0kA	4
#4U converter transformer	41.6MVA-18kV/2172Vx2	2
	5.1MVA-18kV/263Vx2	2
#3U thyristor converter	8.2MW-DC1163V-7.0kA	4
	1.3MW-DC1163V-1.13kA	4
	407kW-DC362V-1.13kA	4

#3U converter transformer	21.6MVA-18kV/1125Vx2	2
	1.1MVA-18kV/350Vx2	2
#2U Thyristor converter	4.8MW-DC607V-7.9kA	4
	3.3MW-DC607V-5.4kA	4
	1.7MW-DC310V-5.4kA	4
#2U converter transformer	12.6MVA-18kV/587Vx2	2
	4.5MVA-18kV/300Vx2	2
#1U thyristor converter	5.6MW-DC727V-7.7kA	4
	5.9MW-DC727V-8.2kA	4
	3.8MW-DC464V-8.2kA	4
#1U converter transformer	15.6MVA-18kV/703Vx2	2
	10.0MVA-18kV/449Vx2	2
#1L thyristor converter	10.6MW-DC1498V-7.0kA	4
	13.4MW-DC1498V-8.9kA	4
	3.9MW-DC434V-8.9kA	4
#1L converter transformer	35.3MVA-18kV/1449Vx2	2
	10.2MVA-18kV/420Vx2	2
#2L thyristor converter	4.7MW-DC613V-7.5kA	4
	4.4MW-DC613V-7.2kA	4
	1.7MW-DC237V-7.2kA	4
#2L converter transformer	12.2MVA-18kV/593Vx2	2
	4.5MVA-18kV/230Vx2	2
#3L thyristor converter	7.1MW-DC1004V-7.0kA	4
	1.1MW-DC1004V-1.1kA	4
	520kW-DC495V-1.1kA	4
#3L converter transformer	18.7MVA-18kV/971Vx2	2
	1.4MVA-18kV/479Vx2	2
#4L thyristor converter	13.0MW-DC1562V-8.3kA	4
	2.8MW-DC335V-8.3kA	4
#4L converter transformer	34.3MVA-18kV/1511Vx2	2
	7.4MVA-18kV/324Vx2	2

#5L thyristor converter	10.7MW-DC1553V-6.9kA	4
	300kW-DC44V-6.9kA	4
#5L converter transformer	28.3MVA-18kV/1502Vx2	2
	0.8MVA-18kV/42Vx2	2
#6L thyristor converter	1.1MW-DC755V-1.4kA	4
	7.5MW-DC755V-9.8kA	4
#6L converter transformer	19.6MVA-18kV/731Vx2	2
#7L thyristor converter	1.3MW-DC4312V-0.3kA	4
	39.9MW-DC4312V-9.3kA	4
	11.2MW-DC1205V-9.3kA	4
#7L converter transformer	105.4MVA-18kV/4170Vx2	2
	29.5MVA-18kV/1166Vx2	2

3)Quench protection system

#7U DCCB	DC20kV-46.9kA	1
#7U dump resistor	0.426ohm-0.99GJ	1
#6U DCCB	DC20kV-47.0kA	1
#6U dump resistor	0.426ohm-0.29GJ	1
#5U DCCB	DC20kV-38.8kA	1
#5U dump resistor	0.515ohm-0.33GJ	1
#4U DCCB	DC20kV-28.1kA	1
#4U dump resistor	0.712ohm-0.33GJ	1
#3U DCCB	DC20kV-28.1kA	1
#3U dump resistor	0.712ohm-0.36GJ	1
#2U DCCB	DC20kV-31.4kA	1
#2U dump resistor	0.637ohm-0.37GJ	1
#1U DCCB	DC20kV-32.5kA	1
#1U dump resistor	0.615ohm-0.40GJ	1

#1L DCCB	DC20kV-35.6kA	1
#1L dump resistor	0.562ohm-0.40GJ	1
#2L DCCB	DC20kV-30.1kA	1
#2L dump resistor	0.664ohm-0.43GJ	1
#3L DCCB	DC20kV-28.1kA	1
#3L dump resistor	0.712ohm-0.37GJ	1
#4L DCCB	DC20kV-33.1kA	1
#4L dump resistor	0.604ohm-0.32GJ	1
#5L DCCB	DC20kV-27.4kA	1
#5L dump resistor	0.730ohm-1.50GJ	1
#6L DCCB	DC20kV-39.3kA	1
#6L dump resistor	0.509ohm-0.66GJ	1
#7L DCCB	DC20kV-37.0kA	1
#7L dump resistor	0.541ohm-2.50GJ	1

4)Miscellaneous

Switchgears	18kV-1200A-28feeders	1Set
Switchgears	18kV-3000A-24feeders	1Set
S.C. current feeder	350m-28feeders	1Set

14.1.4 R&D requirements

The power supply system will be realized with some extension of present technologies. However, to optimize the system design and to reduce the space for the system, following R&D activities will be required.

1) Confirm operation limit of the plasma

Capacity of the PFCPS is decided by following factors:

-Voltage required at initial plasma production

-Rate of plasma current increment

-Plasma control capability in the steady state

Therefore, to clarify the operation limit on these factors is necessary to optimize the configuration of the PFCPS.

2) Increase the current conducting capacity of DCCB

Size of the DCCB is decided according to the current conducting capacity both in TFCPS and PFCPS.In order to reduce the space for this equipment, investigation to increase the current conducting capacity is required.

3) Increase the energy capacity of dump resister

To reduce the space required for dumping resistor, resistive element with large heat capacity has to be developed. Low inductive connection of these elements has also to be developed.

4) Develop super conducting current feeder

To reduce the loss in the power supply system and to improve total plant efficiency, DC current feeders between the coils and the power supply equipments has to be super conductive. Conductor itself will be developed for TFC and PFC. Optimization, however, will be necessary in cooling method, mechanical support structure, etc.

Table 14.1.1 Main parameters of TF coils

Number of coils	16
Total inductance	41.6H
Operating current	81kA
Total stored energy	136.5GJ

Table 14.1.2 Induced current in vacuum vessel at initial plasma production

(A) Coil current pattern (Units: MAT)

Coil No. \ TIME(S)	0.0	0.5	1.0	1.5	2.0	3.0
1 (7U)	0.13	0.13	0.13	0.14	0.14	0.14
2 (6U)	0.62	0.82	1.01	1.21	1.40	1.79
3 (5U)	5.14	5.10	5.06	5.02	4.98	4.90
4 (4U)	8.45	7.67	6.89	6.12	5.34	3.78
5 (3U)	8.45	7.81	7.18	6.54	5.90	4.63
6 (2U)	8.45	7.99	7.53	7.08	6.62	5.70
7 (1U)	8.45	8.45	8.45	8.45	8.44	8.44
8 (1L)	8.45	8.38	8.32	8.25	8.18	8.05
9 (2L)	8.45	8.22	7.99	7.76	7.53	7.07
10 (3L)	8.45	8.15	7.85	7.56	7.26	6.66
11 (4L)	8.45	8.14	7.83	7.53	7.22	6.60
12 (5L)	5.08	5.01	4.93	4.86	4.78	4.63
13 (6L)	-0.07	0.01	0.08	0.16	0.23	0.38
14 (7L)	0.61	0.43	0.24	0.06	-0.13	-0.50

(B) Induced current in vacuum vessel (Units: kA)

Coil No. \ TIME(S)	0.0	0.5	1.0	1.5	2.0	3.0
V1	-4.3	21.5	34.4	45.2	55.9	68.8
V2	-5.4	-16.1	-6.5	4.8	15.0	29.0
V3	-0.4	-2.2	-1.2	0.0	0.5	1.9
V4	-4.3	36.6	59.1	71.6	81.7	91.4
V5	-2.7	75.3	96.8	104.8	111.6	116.9
V6	-2.7	67.2	91.4	103.5	110.2	116.9
V7	-2.1	38.7	62.4	75.3	81.7	88.2
V8	-2.1	30.1	53.8	63.4	71.0	76.3
V9	-2.1	38.7	59.1	67.7	74.6	81.7
V10	-2.1	40.9	55.9	65.6	71.0	76.3
V11	-4.3	30.1	53.8	67.7	77.4	88.2
V12	-4.3	8.6	29.0	45.2	54.8	68.8
V13	-5.4	21.5	41.9	58.1	68.8	84.9
V14	-5.4	7.5	22.6	36.6	46.2	60.2

Table 14.1.3 Error field produced by current induced in vacuum vessel at initial plasma production

Sample point			Error field(at t=0.5S)		
No.	R (m)	Z (m)	Br (Gauss)	Bz (Gauss)	|B| (Gauss)
1	5.5	0.9	−24.2	7.6	25.4
2	6.5	0.9	−5.2	6.1	8.0
3	7.5	0.9	8.6	9.5	12.8
4	6.5	−4.0	2.5	26.4	26.5
5	6.5	−3.0	−2.7	29.7	29.8
6	6.5	−2.0	−3.0	29.0	29.2
7	6.5	−1.0	−3.9	25.4	25.7
8	6.5	0.0	−5.3	17.5	18.3
9	6.5	1.0	−5.0	4.6	6.8
10	6.5	2.0	−2.3	−11.9	12.1
11	6.5	3.0	0.7	−27.1	27.1
12	6.5	4.0	−2.9	−39.4	39.5

Sample point			Error field(at t=3.0S)		
No.	R (m)	Z (m)	Br (Gauss)	Bz (Gauss)	|B| (Gauss)
1	5.5	0.9	−3.4	153.0	153.0
2	6.5	0.9	20.7	158.3	159.6
3	7.5	0.9	39.2	167.5	172.1
4	6.5	−4.0	36.5	224.3	227.3
5	6.5	−3.0	15.9	219.1	219.6
6	6.5	−2.0	11.0	208.7	209.0
7	6.5	−1.0	12.2	195.2	195.6
8	6.5	0.0	15.4	177.9	178.6
9	6.5	1.0	21.4	155.8	157.3
10	6.5	2.0	29.5	129.7	133.0
11	6.5	3.0	33.0	101.6	106.8
12	6.5	4.0	13.9	65.2	66.5

Table 14.1.4 Current pattern of PF coils

Time(S) / Coil No.	-100	0	3	20	40	50	80	100	Number of turns
1 (7U)	0.0	0.8	2.8	-11.0	-17.9	-13.4	-16.8	-45.5	140
2 (6U)	0.0	27.5	32.5	41.7	13.1	5.3	-47.0	-3.7	36
3 (5U)	0.0	32.1	18.3	32.8	38.8	31.2	36.4	28.1	196
4 (4U)	0.0	28.1	14.9	14.5	15.4	12.2	10.1	4.8	300
5 (3U)	0.0	28.1	25.4	24.0	18.2	16.5	5.2	-4.5	300
6 (2U)	0.0	28.1	31.4	27.2	17.1	11.6	-13.7	-21.7	300
7 (1U)	0.0	28.1	30.7	14.9	-0.2	-2.4	-32.6	-30.3	300
8 (1L)	0.0	28.1	17.3	10.3	-13.9	-7.3	-35.5	-35.6	300
9 (2L)	0.0	28.1	30.1	21.9	5.3	2.9	-16.1	-28.6	300
10 (3L)	0.0	28.1	25.4	23.0	16.8	15.2	10.4	-4.2	300
11 (4L)	0.0	33.1	20.6	13.3	14.2	14.5	16.0	8.4	300
12 (5L)	0.0	7.8	9.4	11.5	15.1	19.5	27.4	25.2	528
13 (6L)	0.0	5.5	3.9	-5.7	-22.5	-28.4	-39.3	-6.5	120
14 (7L)	0.0	1.2	-1.0	-0.1	-4.2	-4.6	-16.3	-36.2	270
Plasma	0.0	0.0	500	2,000	5,000	5,000	10,000	12,000	1

Table 14.1.5 Required voltage pattern of PF coils

Coil No. \ Time(S)	-100～0	0～3	3～20	20～40	40～50	50～80	80～100	100～
1 (7U)	136	123	-891	-660	367	-469	-1,997	-12
2 (6U)	52	-49	8	-123	-49	-152	-24	-1
3 (5U)	298	-3,342	483	87	-531	-20	-386	7
4 (4U)	238	-2,519	39	-46	-272	-140	-272	2
5 (3U)	263	-1,163	-70	-240	-242	-354	-362	-2
6 (2U)	267	-6	-243	-415	-307	-607	-294	-6
7 (1U)	267	-155	-506	-606	-113	-727	-106	-8
8 (1L)	266	-1,498	-389	-783	195	-682	-171	-9
9 (2L)	266	-495	-340	-613	-27	-476	-433	-8
10 (3L)	263	-1,004	-211	-306	-18	-188	-495	-1
11 (4L)	246	-1,897	-223	-69	94	3	-336	2
12 (5L)	586	242	83	184	1,597	683	-645	7
13 (6L)	139	-744	-454	-755	-315	-425	614	-2
14 (7L)	281	-3,286	-357	-1,458	-153	-1,908	-4,312	-9

Table 14.1.6 Ratings of converters for PF coil power supply

(in the case of base operation scenario)

Coil No.	Forward converter rating						Reverse converter rating					
1 (7U)	5.6	MW -	1997	V -	2.8	kA	93.7	MW -	1997	V -	46.9	kA
2 (6U)	6.4	MW -	152	V -	41.7	kA	7.2	MW -	152	V -	47.0	kA
3 (5U)	129.7	MW -	3342	V -	38.8	kA	———					
4 (4U)	70.8	MW -	2519	V -	28.1	kA	———					
5 (3U)	32.7	MW -	1163	V -	28.1	kA	5.3	MW -	1163	V -	4.5	kA
6 (2U)	19.1	MW -	607	V -	31.4	kA	13.2	MW -	607	V -	21.7	kA
7 (1U)	22.4	MW -	727	V -	30.7	kA	23.7	MW -	727	V -	32.5	kA
8 (1L)	42.1	MW -	1498	V -	28.1	kA	53.4	MW -	1498	V -	35.6	kA
9 (2L)	18.5	MW -	613	V -	30.1	kA	17.6	MW -	613	V -	28.6	kA
10 (3L)	28.3	MW -	1004	V -	28.1	kA	4.3	MW -	1004	V -	4.2	kA
11 (4L)	62.8	MW -	1897	V -	33.1	kA	———					
12 (5L)	43.8	MW -	1597	V -	27.4	kA	———					
13 (6L)	4.2	MW -	755	V -	5.5	kA	29.7	MW -	755	V -	39.3	kA
14 (7L)	5.2	MW -	4312	V -	1.2	kA	159.6	MW -	4312	V -	37.0	kA
	Total capacity of converters						898.2 MW					

Table 14.1.7 Ratings of converters for PF coil power supply (Rate of plasma current lump up is 1/2 of base operation scenario after t=20s)

Coil No.	Forward converter rating							Reverse converter rating						
1 (7U)	2:9	MW -	1004	V -	2.8	kA		47.1	MW -	1004	V -	46.9	kA	
2 (6U)	3.5	MW -	82	V -	41.7	kA		3.9	MW -	82	V -	47.0	kA	
3 (5U)	129.7	MW -	3342	V -	38.8	kA		———						
4 (4U)	70.8	MW -	2519	V -	28.1	kA		———						
5 (3U)	32.7	MW -	1163	V -	28.1	kA		5.3	MW -	1163	V -	4.5	kA	
6 (2U)	9.6	MW -	306	V -	31.4	kA		6.7	MW -	306	V -	21.7	kA	
7 (1U)	15.6	MW -	506	V -	30.7	kA		16.5	MW -	506	V -	32.5	kA	
8 (1L)	42.1	MW -	1498	V -	28.1	kA		53.4	MW -	1498	V -	35.6	kA	
9 (2L)	14.9	MW -	495	V -	30.1	kA		14.2	MW -	495	V -	28.6	kA	
10 (3L)	28.3	MW -	1004	V -	28.1	kA		4.3	MW -	1004	V -	4.2	kA	
11 (4L)	62.8	MW -	1897	V -	33.1	kA		———						
12 (5L)	22.0	MW -	801	V -	27.4	kA		———						
13 (6L)	4.1	MW -	744	V -	5.5	kA		29.3	MW -	744	V -	39.3	kA	
14 (7L)	4.0	MW -	3286	V -	1.2	kA		121.6	MW -	3286	V -	37.0	kA	
	Total capacity of converters							744.3 MW						

Table 14.1.8 Required voltage for PF coil current control in 2S at plasma parameter change $\Delta\beta p=0.1$

Time(S) / Coil No.	PF coil current difference for $\Delta\beta p=0.1$	Required control voltage
1 (7U)	-45.5 → -46.9	-708
2 (6U)	-3.7 → 0.7	87
3 (5U)	28.1 → 28.1	104
4 (4U)	4.8 → 4.8	78
5 (3U)	-4.5 → -4.3	157
6 (2U)	-21.7 → -21.0	310
7 (1U)	-30.3 → -28.9	464
8 (1L)	-35.6 → -34.3	434
9 (2L)	-28.6 → -28.1	237
10 (3L)	-4.2 → -4.3	57
11 (4L)	8.4 → 8.1	-11
12 (5L)	25.2 → 25.0	44
13 (6L)	-6.5 → -4.1	645
14 (7L)	-36.2 → -37.0	-1,205
Notes	Units:kA	Units:V

Table 14.1.9 Ratings of converters for PF coil power supply (Converters used in the steady state)

Coil No.	Forward converter rating	Reverse converter rating
1 (7U)	——	33.2 MW - 708 V - 46.9 kA
2 (6U)	6.4 MW - 152 V - 41.7 kA	7.2 MW - 152 V - 47.0 kA
3 (5U)	20.6 MW - 531 V - 38.8 kA	——
4 (4U)	7.7 MW - 272 V - 28.1 kA	——
5 (3U)	——	1.7 MW - 362 V - 4.5 kA
6 (2U)	——	6.8 MW - 310 V - 21.7 kA
7 (1U)	——	15.1 MW - 464 V - 32.5 kA
8 (1L)	——	15.5 MW - 434 V - 35.6 kA
9 (2L)	——	6.8 MW - 237 V - 28.6 kA
10 (3L)	——	2.1 MW - 495 V - 4.2 kA
11 (4L)	11.1 MW - 335 V - 33.1 kA	——
12 (5L)	1.2 MW - 44 V - 27.4 kA	——
13 (6L)	4.2 MW - 755 V - 5.5 kA	29.7 MW - 755 V - 39.3 kA
14 (7L)	——	44.6 MW - 1205 V - 37.0 kA
	Total capacity of converters	213.4 MW

Table 14.1.10 Ratings of converters for PF coil power supply (Converters used at initial plasma production and current lump up)

Coil No.	Forward converter rating	Reverse converter rating
1 (7U)	5.6 MW - 1997 V - 2.8 kA	93.7 MW - 1997 V - 46.9 kA
2 (6U)	——	——
3 (5U)	109.1 MW - 2811 V - 38.8 kA	——
4 (4U)	63.2 MW - 2247 V - 28.1 kA	——
5 (3U)	32.7 MW - 1163 V - 28.1 kA	5.3 MW - 1163 V - 4.5 kA
6 (2U)	19.1 MW - 607 V - 31.4 kA	13.2 MW - 607 V - 21.7 kA
7 (1U)	22.4 MW - 727 V - 30.7 kA	23.7 MW - 727 V - 32.5 kA
8 (1L)	42.1 MW - 1498 V - 28.1 kA	53.4 MW - 1498 V - 35.6 kA
9 (2L)	18.5 MW - 613 V - 30.1 kA	17.6 MW - 613 V - 28.6 kA
10 (3L)	28.3 MW - 1004 V - 28.1 kA	4.3 MW - 1004 V - 4.2 kA
11 (4L)	51.7 MW - 1562 V - 33.1 kA	——
12 (5L)	42.6 MW - 1553 V - 27.4 kA	——
13 (6L)	——	——
14 (7L)	5.2 MW - 4312 V - 1.2 kA	159.6 MW - 4312 V - 37.0 kA
	Total capacity of converters	810.4 MW

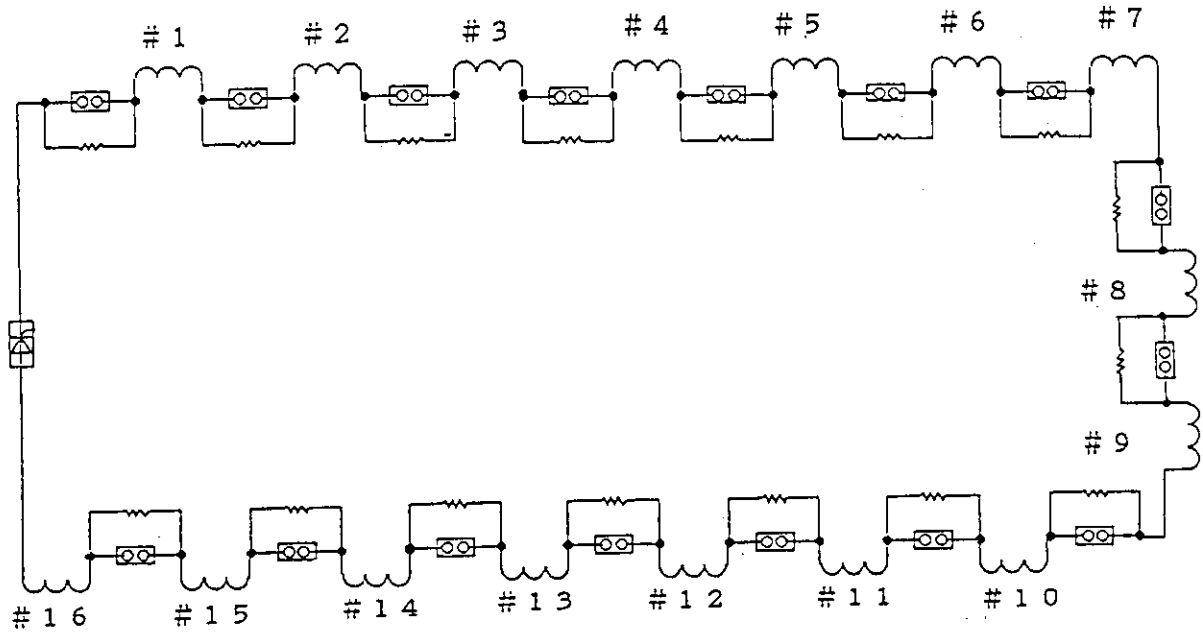

Fig. 14.1.1 Quench protection circuit configuration for TF coil.

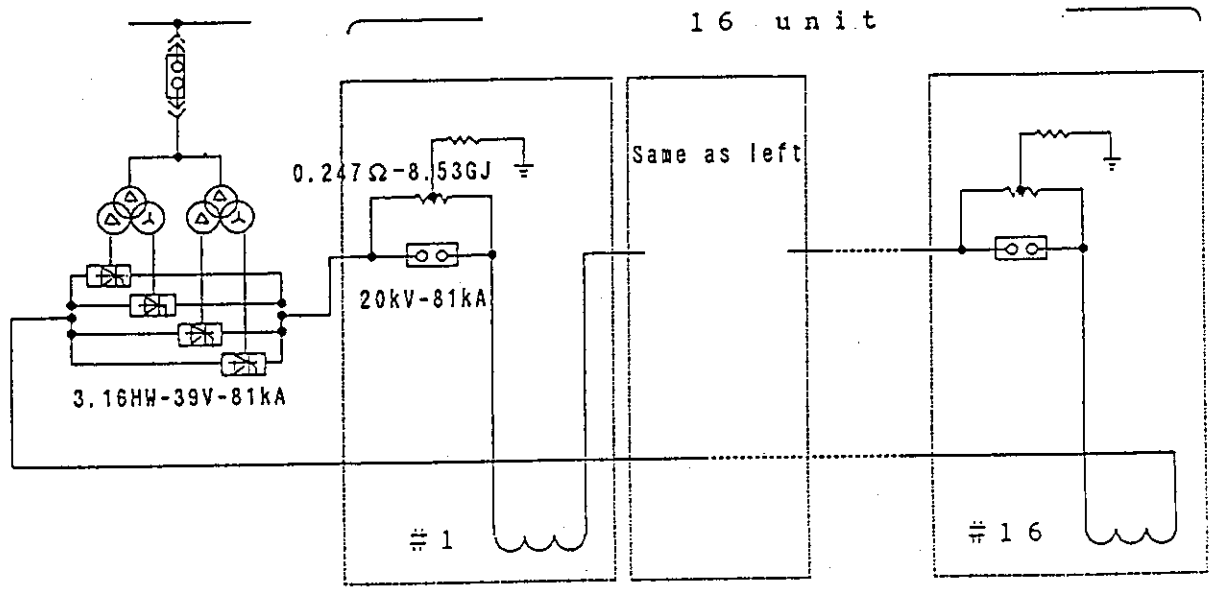

Fig. 14.1.2 Configuration of TF coil power supply.

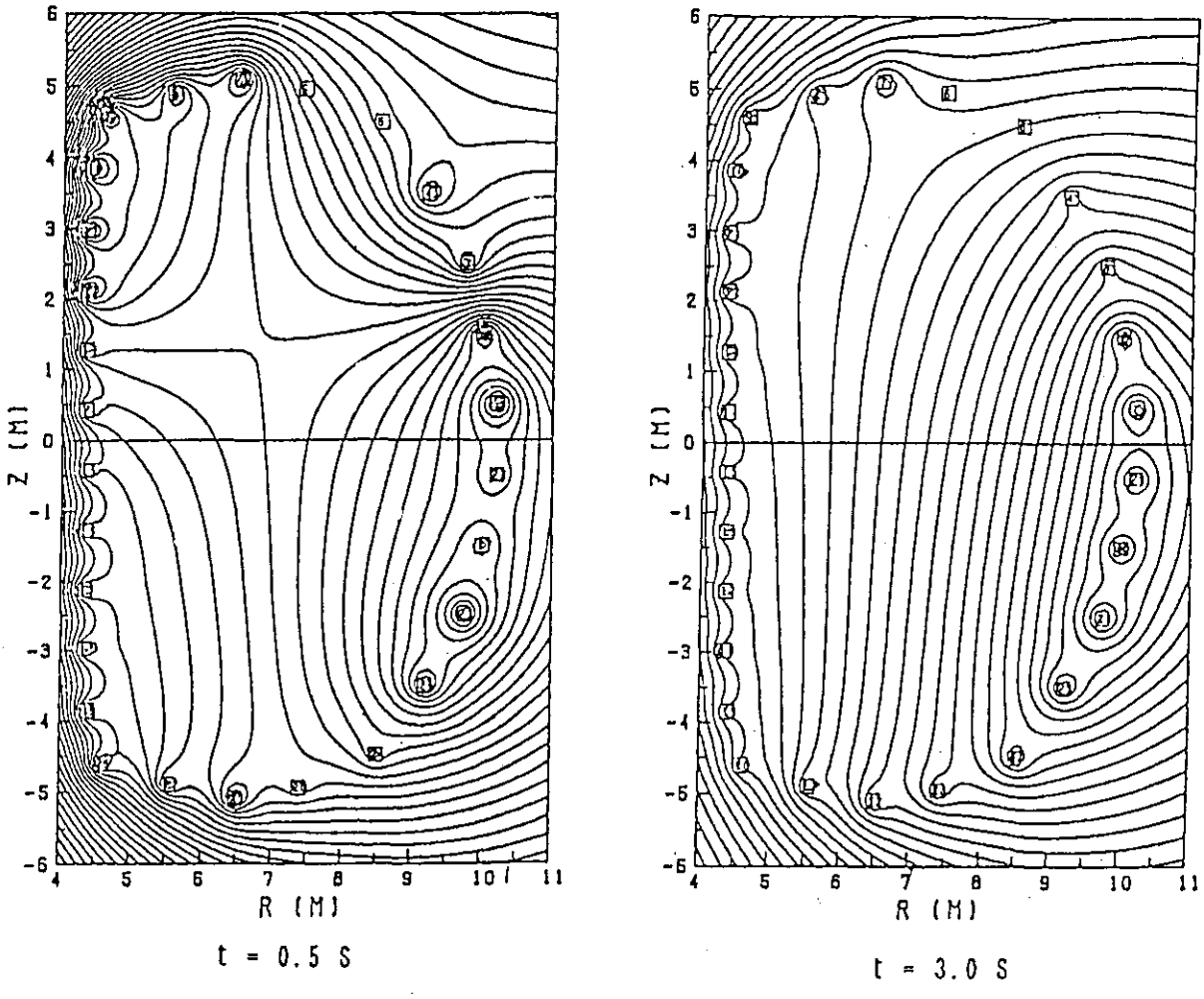

Fig. 14.1.3 Error field produced by current in vacuum vessel which is induced at initial plasma production.

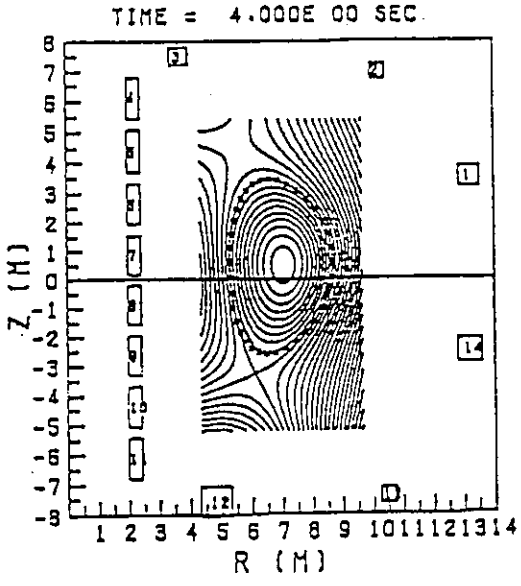

***** COILS *******

NO.	CURRENT(A)
1	-2.724E 06
2	-2.961E 06
3	5.265E 06
4	1.259E 06
5	-2.216E 06
6	-1.017E 07
7	-1.653E 07
8	-1.768E 07
9	-1.124E 07
10	-4.129E 05
11	3.662E 06
12	1.490E 07
13	-5.794E 06
14	-6.029E 06

$\beta p = 0.1$

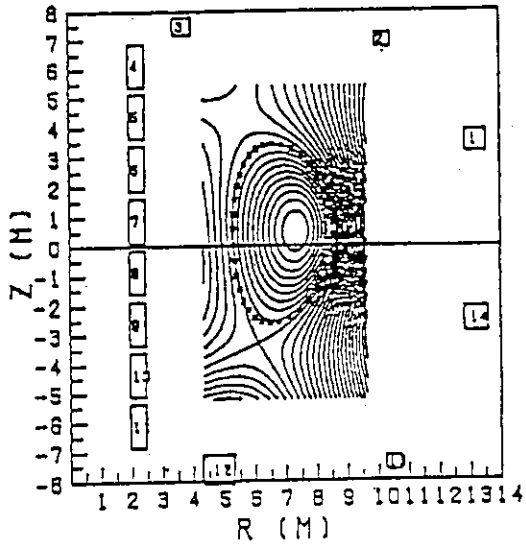

***** COILS ********

NO.	CURRENT(A)
1	-6.363E 06
2	-8.872E 04
3	5.897E 06
4	1.676E 06
5	-9.502E 05
6	-5.995E 06
7	-8.549E 06
8	-1.021E 07
9	-8.165E 06
10	-8.546E 05
11	2.767E 06
12	1.376E 07
13	-9.094E 05
14	-9.677E 06

$\beta p = 2.0$

Fig. 14.1.4 PF coil current required for equilibrium at βp=0.1 and βp=2.0.

Coil No.	Converter No.	AC input	Cuennt direction	Time(S) -100	0	3	20	40	50	80	100
1 (7U)	PS1-12	Comm	Reverse	GB			BPP				DB
	PS1-21	HG	Forward	DB			GB				
	PS1-22	HG	Reverse	GB			BPP				
2 (6U)	PS2-11	Comm	Forward	DB						GB	
	PS2-12	Comm	Reverse	GB						DB	
3 (5U)	PS3-11	Comm	Forward	DB							
	PS3-21	HG	Forward	BPP	DB		BPP				
4 (4U)	PS4-11	Comm	Forward	DB							
	PS4-21	HG	Forward	BPP	DB		BPP				
5 (3U)	PS5-12	Comm	Reverse	GB						BPP	DB
	PS5-21	HG	Forward	DB							GB
	PS5-22	HG	Reverse	GB						DB	BPP
6 (2U)	PS6-12	Comm	Reverse	GB						BPP	DB
	PS6-21	HG	Forward	DB							GB
	PS6-22	HG	Reverse	GB						DB	BPP
7 (1U)	PS7-12	Comm	Reverse	GB				BPP			DB
	PS7-21	HG	Forward	DB				GB			
	PS7-22	HG	Reverse	GB				DB			BPP
8 (1L)	PS8-12	Comm	Reverse	GB				BPP			DB
	PS8-21	HG	Forward	DB				GB			
	PS8-22	HG	Reverse	GB				DB			BPP
9 (2L)	PS9-12	Comm	Reverse	GB						BPP	DB
	PS9-21	HG	Forward	DB							GB
	PS9-22	HG	Reverse	GB						DB	BPP
10(3L)	PS10-12	Comm	Reverse	GB						BPP	DB
	PS10-21	HG	Forward	DB							GB
	PS10-22	HG	Reverse	GB						DB	BPP
11(4L)	PS11-11	Comm	Forward	DB							
	PS11-21	HG	Forward	BPP	DB		BPP				
12(5L)	PS12-11	Comm	Forward	DB							
	PS12-21	HG	Forward	DB							BPP
13(6L)	PS13-11	Comm	Forward	DB				GB			
	PS13-12	Comm	Reverse	GB				DB			
14(7L)	PS14-12	Comm	Reverse	GB			BPP				DB
	PS14-21	HG	Forward	DB			GB				
	PS14-22	HG	Reverse	GB			DB				BPP

Fig. 14.1.5 Operation pattern of converters for PF coil power supply.

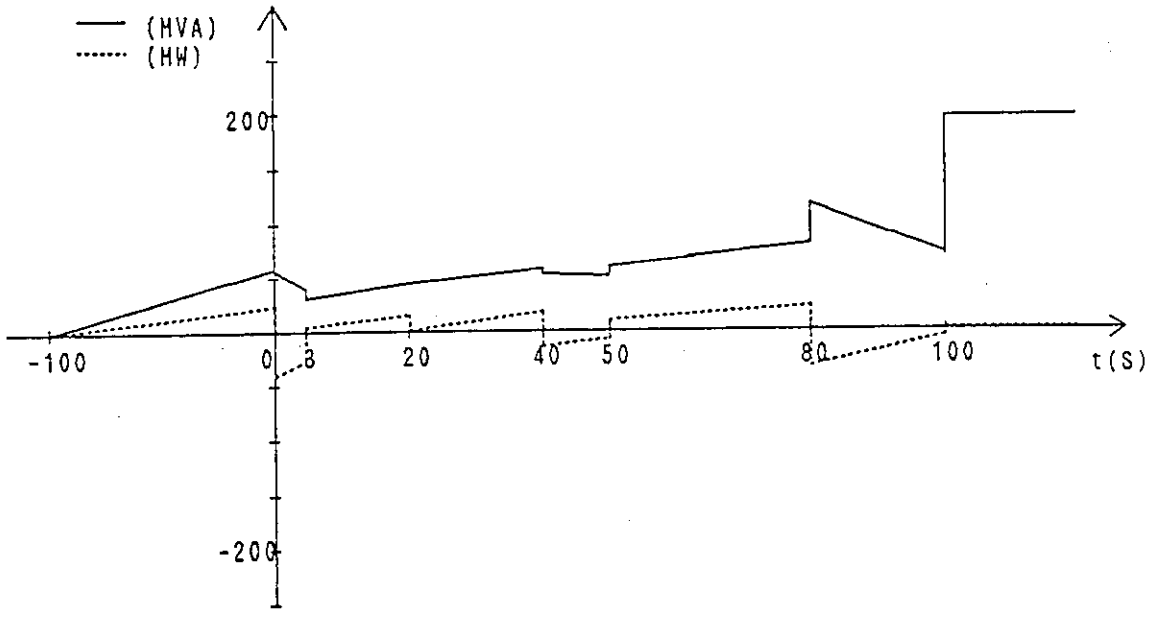

Fig. 14.1.6 Demand of PF coil power supply to the commercial line.

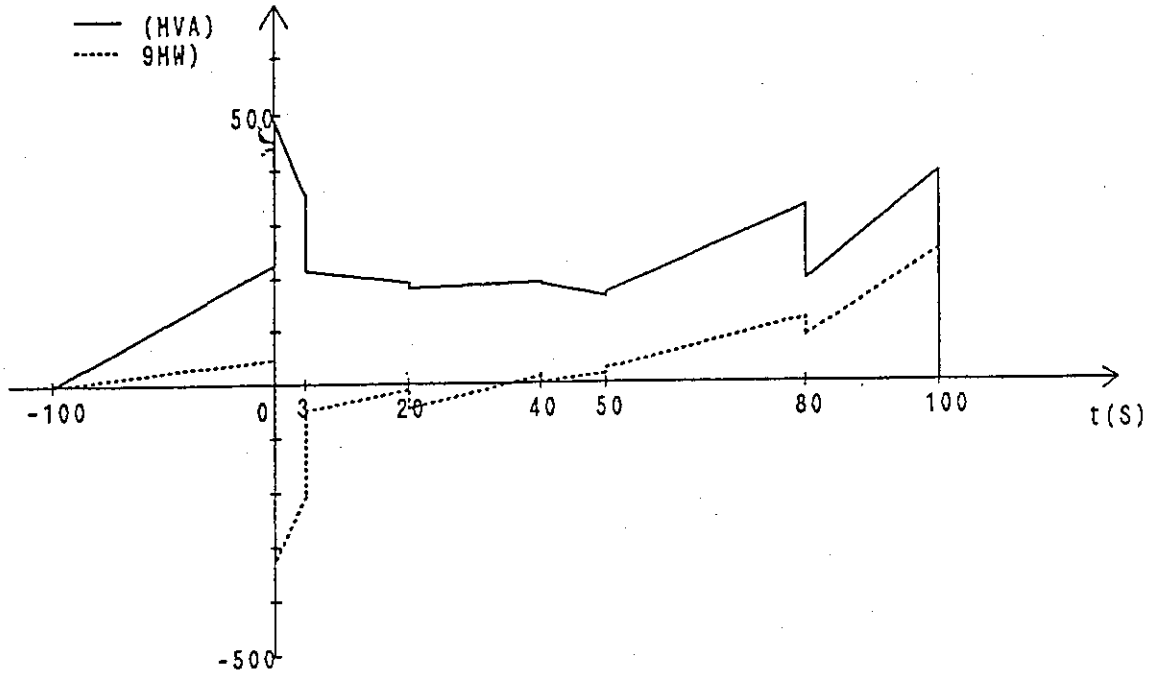

Fig. 14.1.7 Demand of PF coil power supply to the MG system.

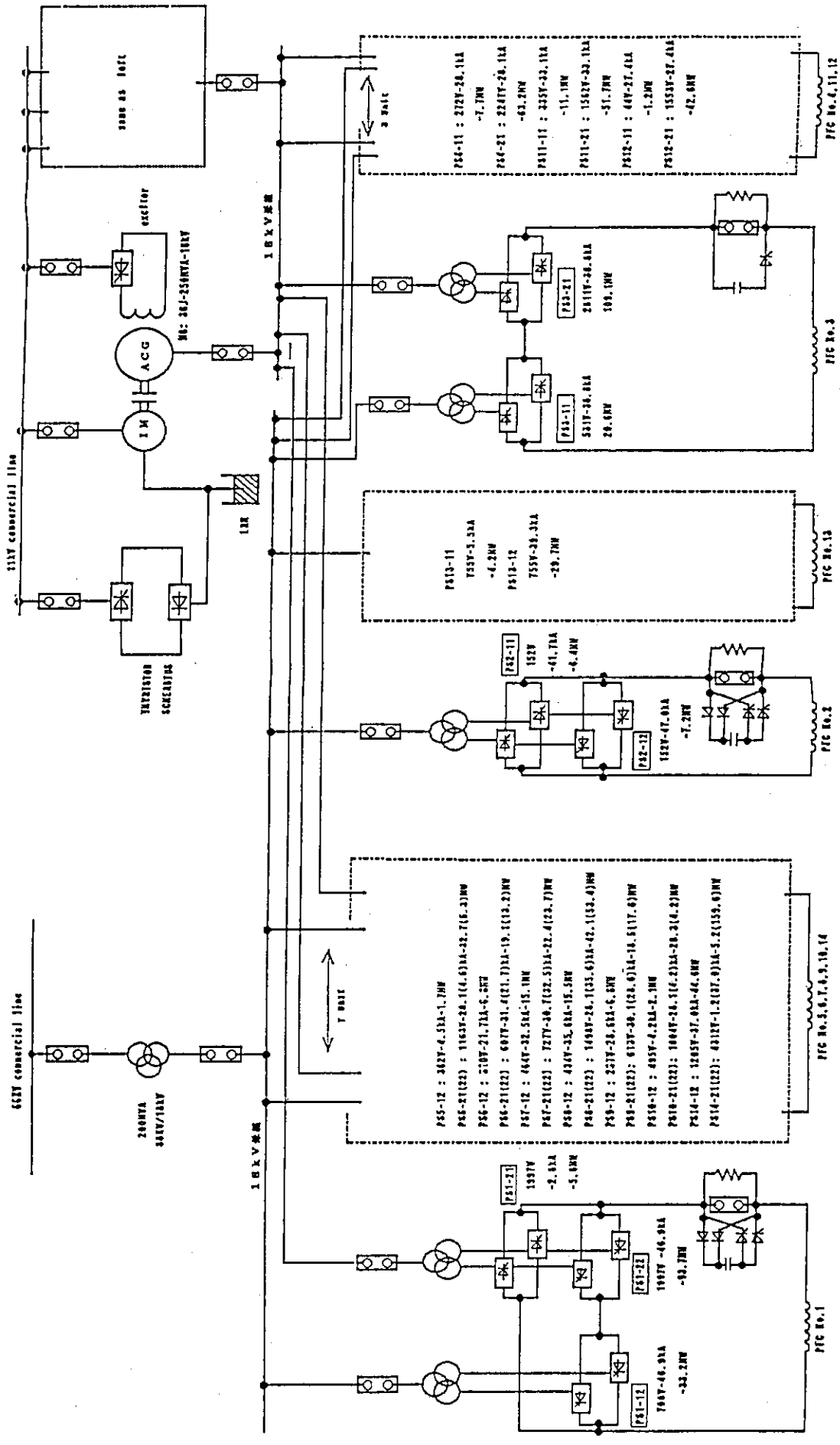

Fig. 14.1.8 Configuration of PF coil power supply.

14.2 Control and instrumentation system

14.2.1 Control system

Control system of SSTR is to process the data and to administrate the total plant in its operation, control, instrumentation and protection. It is composed of the central control system and the local control systems.

Local control systems are, for example, as follows:

-TOKAMAK system control system
-Fuel control system
-Coil power supply control system
-NBI control system
-Power plant control system
-Cooling system control system
-Refrigeration control system
-Substation control system

Central control system synthesizes the local control systems and harmonizes their total operation. Central control system consists of central control panel, processing and communication system, timing system, plant interlock system and their auxiliaries. Central control panel is composed of control panel and central console. Processing and communication system is a core of the central control system and is divided into three subsystems; operation control system, plasma control system and plant monitoring system. Task of operation control system is to control the start up and shut down and to maintain the steady state operation of SSTR in coordination with the power plant control system. Plasma control system controls plasma position and shape through hybrid poloidal field control based on the data from in-core and plasma instrumentation system and commands the NBI control system and the fuel control system based on the informations on plasma temperature, density, plasma current, fusion reaction rate, etc. Plant monitoring system collects and processes plant data and inspects the status of the plant and its equipments. Timing system provides reference signals in order to synchronize the control of the plant especially at its start up and shut down. Plant interlock system controls total plant shut down and/or transition of plant status safely in the case of non-standard situation. It consists of hard wired logic.

Fig. 14.2.1 shows configuration of SSTR control system.

14.2.2 Instrumentation

Main role of the SSTR instrumentation system is considered to be as follows;

A. Instrumentation for plant operation
B. Instrumentation for automatic/manual control
C. Instrumentation for safety function on an abnormal and an accidental condition

More specifically, the following six items are needed for the SSTR instrumentation system in referring to light-water type power plant, etc.

1) Instrumentation system for core plasma
2) Instrumentation system for monitoring main process data
3) Instrumentation system for controlling reactor output and various process data
4) Instrumentation system for safety protection system
5) Radiation monitoring system
6) Process computer

Instruments for the item 1), for example, consists of neutron monitoring system and magnetic measurements system. Neutron monitoring system, which corresponds to nuclear instrumentation monitoring system for LWR, will be designed to monitor neutron flux over a range of 10 decades for plasma burning control. Electromagnetic measurement system is considered to be one of the most important plasma monitoring system to control plasma shape, position and PF-coil system. The items 2) and 3) above correspond to process instrument (temperature, pressure, output, etc.) in usual plants. In order to make clear what kinds of measurement items and instruments are needed for SSTR plant control, more detailed and specific design of SSTR will be needed. Especially,

a) R&D of plasma burning control
b) Design Study for specific burning control system based on item a) are indispensable.

Requirements for the items 4) and 5) strongly depend on the level of the safety standard and safety function required for SSTR as a "fusion plant". As for the item 6), ideally, the control and data processing system is centralized. However, it is required for SSTR computer system to acquire and process large amount of the data compared with common plants. Moreover,fast data processing time will be required for fusion power plant like SSTR. For example, the data processing time during start-up and shutdown will be less than 10ms. Therefore the system will have a hierarchical structure and it will be necessary to localize sub-system in order to provide local control functions or local processing for the monitoring data.

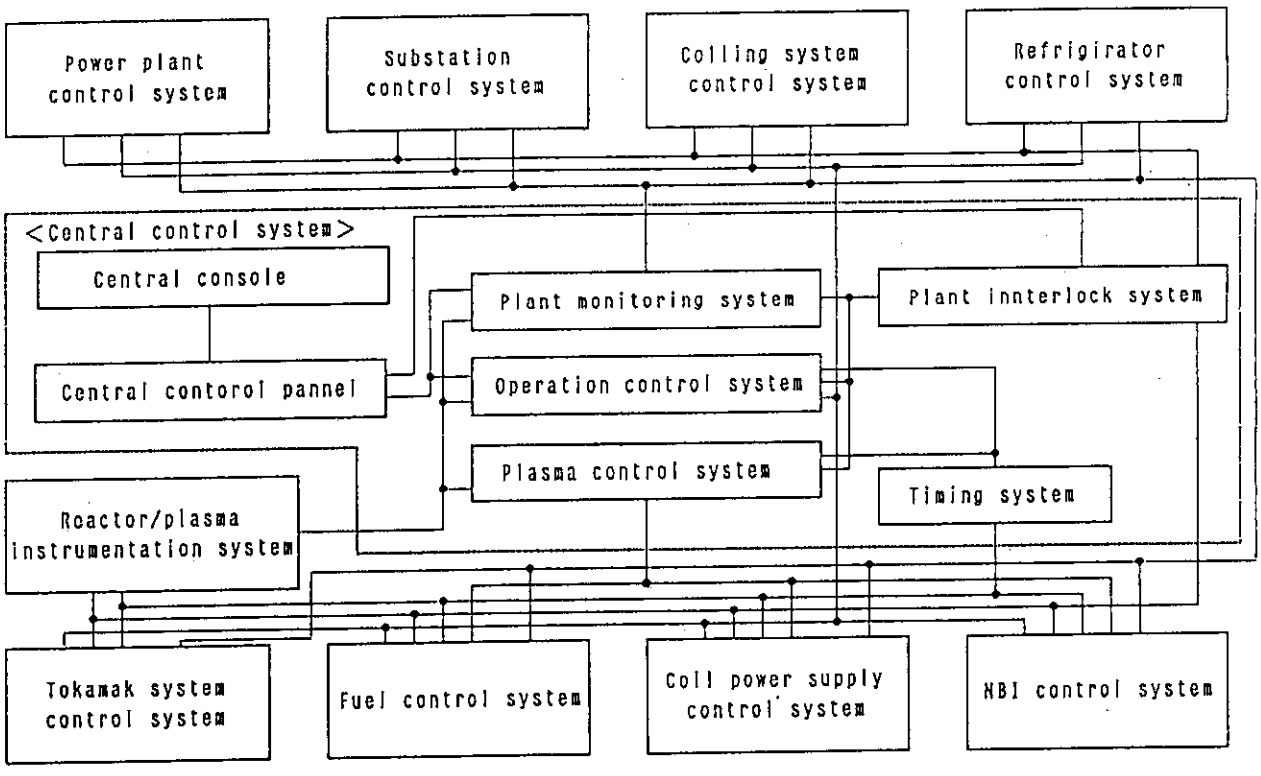

Fig. 14.2.1 Configuration of SSTR control system.

15. Pellet Injector Systems

15.1 Introduction

The gas-puffing method is the most common general fueling method used in most of present fusion devices. Recently, various pellet injectors, which can drive solid hydrogen isotopes into plasmas, have been developed, and fueling experiments have been carried out on pellet injectors. As a result of injection experiments combined with heating experiments, it has also been reported that plasma performance is improved.

In large fusion devices such as FER and ITER, there are plans to use both pellet fueling method and gas-puffing method. In particular, phased operations corresponding to the ramp-up and burning phases will be considered as part of the pellet fueling operation scenario. For example, requirements for pellet injectors in ITER are as follows: 2 ~ 5 km/s x 1 ~ 2 Hz for the ramp-up phase, 1 ~ 2 km/s x ~ 5 Hz for the burning phase.

However, many development subjects are required for pellet injectors, related to the enlargement of fusion devices, the long-burning operation and the improvement of plasma performance in the future. In particular, it is important to develop engineering technologies to speed up the injection velocity, high repetition injection and steady formation of the frozen pellets. In addition, the explanation of the pellet ablation mechanism is also thought to be important to optimize the design of the pellet injector.

In this chapter, we have investigated the injection method, which satisfies the requirements of the pellet injector in the Steady State Tokamak Reactor (SSTR), in the light of the present engineering level of pellet injectors. The basic features and operation scenarios have also been investigated, and R&D subjects concerning the SSTR pellet injector have been proposed.

15.2 Basic Features

The basic performance of the SSTR pellet injector, the acceleration method of the frozen pellet and the basic specifications are investigated in the following sub-sections.

15.2.1 Requirements to the SSTR pellet injector

The SSTR is a steady state reactor, and its design concept is characterized by a higher toroidal field, a larger aspect ratio and a lower plasma current compared with other

reactor concepts. Another particular feature is that 75 % of the plasma total current is driven by the bootstrap current. Therefore, the external current driven by the NBI and the RF becomes small, and plasmas can be compacted so that a high density plasma is attainable.

Here, to sustain stationary burning, plasma source particles must be supplied to core plasmas steadily and efficiently. Gas-puffing method will first of all be considered as a steady fueling method. However, in terms of particle deposition efficiency and the influence on plasma facing components, there seem to be some problems in the gas-puffing method. For example, it is questionable whether gas-puffing can supply fuel particles beyond the scrape-off layer. Moreover, the gas-puffing method has the disadvantage of enhancing sputtering erosion of plasma facing components.

Therefore, the pellet fueling method is believed to be applicable to the SSTR, and the SSTR pellet injector should be designed with an emphasis on higher reliability and easier maintenance.

15.2.2 Comparison of pellet injectors

Based on the following pellet fueling requirements, we have examined injection methods.

1) Supply of fuel particles at least inside the scrape-off layer.
2) A steady injection of a large amount of fuel particles into the plasmas.
3) Prevention of impurities introduced into the core plasmas.
4) A low tritium inventory.
5) Ease of tritium processing.
6) High reliability and simple mechanism.
7) Ease of maintenance and long life span

Based on the requirments 1 and 2), a centrifugal injection method and a repeating pneumatic injection method are suitable for the SSTR pellet injector because of a lower injection velocity, a stationary injection and a high-repetition rate injection. The present status and engineering problems involved in both methods are summarized in Table 15.2.1.

The injection velocity and injection accuracy of the pneumatic injector is superior to those of the centrifugal injector. However, exhaust systems for propellant gases are expected to become larger in order to prevent the mixing of impurities into the core plasmas as much as possible. The durability of the fast opening valve is also a key issue in the

pneumatic injector. In the centrifugal injector, propellant gases are not used to accelerate a pellet so that the exhaust systems are more compact than those of the pneumatic injector. Therefore, the total systems of the centrifugal injector are believed to be more compact than those of the pneumatic injector. Since the centrifugal injector is supposed to satisfy the requirements 6 and 7), the centrifugal method is chosen for the SSTR pellet injector when low velocity injection is applied.

15.2.3 Basic specifications

The specifications for the SSTR pellet injector are investigated in this section.

(1) Number of fuel particles

The number of fuel particles are estimated based on the following assumptions.

1) The particle confinement time is assumed to be 0.5 sec.

2) The average plasma density and plasma volume are assumed to be 1.4×10^{20} m^{-3} and 730 m^3, respectively.

The total number of plasma particles is given by

$$N_P = \langle n \rangle \times V_P \cong 1 \times 10^{23},$$

where $\langle n \rangle$ and V_P are the average plasma density and plasma volume.

Therefore, the fuel particles per unit time and the molecular numbers per unit time are estimated as follows;

$$N = N_P/\tau_P = 2 \times 10^{23} \text{ [1/sec]},$$

$$Q_{DT} = N_P/N_A/2 = 0.166 \text{ [mol/sec]},$$

where N and Q_{DT} are the fuel particles and molecular numbers per unit time, and N_A is Avogadro's number.

(2) Formation of frozen pellets

The pellet parameters and the basic requirements for pellet formation are investigated.

1) Pellet parameters

The pellet size should be determined by considering the loads on the injector and the influence on the core plasmas. For example, a large-size pellet is advantageous for pellet penetration and reducing loads, while it seems not to be so good influence on plasmas. Here, on the basis of the calculation results in Sec. 15.3, the repetition rate is required to be 45 Hz to supply the required particles, where the value of 45 Hz includes particle losses during flight in guide tube and during pellet formation in feeder.

The main pellet parameters are summarized as follows;

pellet size	:	5 mm-diameter and 5 mm-long
repetition rate	:	45 Hz
injection velocity	:	1 km/sec

2) Refrigerator capacity

The capacity of the refrigerator to form solid hydrogen isotopes can roughly be estimated from the cooling-down capacity from gas phase to solid phase and the thermal invasion from the external.

For simplicity, the average enthalpy of deuterium and tritium required to cool down from 300 K to 10 K is used to calculate the cooling capacity. Then, the cooling capacity Dq_{DT} is given by

$$\Delta q_{DT} = 1.2 \times Q_{DT} \cdot H_{DT} = 1610 \text{ [W]},$$

where the factor of 1.2 is the safety margin, and H_{DT} is the average value of the enthalpy.

The thermal invasion Δq_E from the external is given by

$$\Delta q_E = L \cdot \Delta q + \alpha = 60 + \alpha \ (\sim 50) \text{ [W]},$$

where we assume that the thermal invasion per unit length of pipe Δq is 3 W/m, and that the cooling pipe has a total length L of 20 m, and a represents another thermal invasion through the flexible tubes, connectors and valves.

Therefore, the total capacity of the refrigerator is about 3 kW if it is multiplied by a safety factor of 1.5.

3) Piston velocity for extruding pellet filament

The extruding velocity of about 225 mm/sec is required to generate fourty-five 5 mm-long pellets per unit time. Since the maximum attainable velocity is expected to be about 40 mm/sec from current experiments on the filament extruding. Therefore, at least six injectors are necessary to satisfy the injection requirments.

Here, if the inner diameters of the filament generator and the pellet feeder are designed to be 9 mm and 5 mm, respectively, it will be possible to reduce the number of injectors from 6 to 2, not failed to supply the necessary fuel particles, so that the total systems will be compacted. Then, the effective piston velocity of the extruder will be about 34.7 mm/sec.

To confirm the performance of the extruder with the special nozzle, we will need to

go on the studies on forming conditions of the frozen filament and investigate the mechanical loads on the piston driver and the bellows.

4) Formation time for the frozen filament

The liquefied fuel gas, which is generated through the liquefaction device, is introduced into the cryogenic extruder and is solidified to form the frozen filament.

The solidification time is roughly estimated by the following formula :

$$T_i = r^2 L / 4 \cdot K \cdot C \cdot \theta = 58.5 \text{ [sec]},$$

where T_i is the solidification time, r the diameter of the filament, L the filament length, K the thermal diffusivity, C the specific heat of the frozen filament, and θ the temperature difference.

The total formation time, including the time required to liquefy the fuel gas and supply the liquid fuel to the extruder, will be about 120 sec.

5) Frozen filament extruder

The frozen filament is assumed to be 1500 mm long, so that it takes about 43.2 sec. to completely extrude the frozen filament.

Since the total formation time for the frozen filament is about 120 sec., four extruders must be set up in each injector to gain the time required to form the filament. The extruding scenario will be described in Sec. 15.4.3.

Table 15.2.1 Present status of pneumatic pellet injector and centrifuge pellet injector

	PNEUMATIC INJECTOR	CENTRIFUGE INJECTOR
PELLET SIZE (mm)	MAX. 6.0 ϕ x 6.0 L [JET]	MAX. 1.3 ϕ X 1.3 L [Tore Supra]
PELLET VELOCITY (km/sec)	MAX. 2.3 for H_2 pellet [JT-60] (4.0 ϕ x 4.0 L)	MAX. 0.8 for D_2 pellet [Tore Supra] (1.3 ϕ x 1.3 L)
REPETITION RATE (Hz)	~5 for 2.7 ϕ x 2.7 L [JET]	30~40
INJECTION PRECISION	Good [±1.2° (JT-60)]	Not so good [±1.5°~±2.0°(4.0°)]
VACUUM EXHAUST SYSTEM	Very large Because of using propellant gas	Very small Only pellet evapolation gas in pellet feeder and guide tube
MIXTURE OF IMPURITY GAS INTO MAIN PLASMA	A little (Propellant gas)	Not a serious problem
MAIN COMPONENTS OF PELLET INJECTOR	Cryogenic extruder Fast opening valve Pellet chambering Propellant gas Supply fuel gas supply	Cryogenic extruder Accelerator (Rotor/Motor) Pellet feeder Fuel gas supply
MAIN SYSTEM COMPONENTS	Pellet injector Large expanding chamber Large pumping system Control system	Pellet injector Small pumping system Control system
DURABILITY OF KEY COMPONENT	Fast opening valve (Life cycles : ~10^6)	Bellows in extruding driver (Life cycles : ~10^5)

15.3 Estimation of the penetration depth

The penetration depth can be calculated by using the simplified calculation code[1].

15.3.1 Analysis model

Various theoretical models of pellet ablation have been proposed ; however, those models have not yet been sufficiently verified by experiments.

To evaluate the penetration depth, we use the neutral shielding ablation model proposed by Milora and Foster. The incident energy flux of the electron is assumed to be effectively shielded by neutral clouds around the pellet surface, which are formed by the vaporized pellet materials. This ablation model includes the effect of the ablated particles on the bulk plasmas, what is called the self-limiting ablation model.

15.3.2 Analysis conditions

To calculate the penetration depth, we have assumed the following plasma parameters and pellet parameters.

(1) Plasma parameters
1) Circular cross section plasma
2) Major radius and minor radius : 7 [m] and 1.7 [m]
3) The density and temperature profiles : As shown in Fig. 15.3.1 and 15.3.2, the parabolic profile such as $[1-(r/a)^2]^n$ is assumed for the bulk plasma, where the value of the index-n are 0.5 and 1.5 for density and temperature profiles, respectively. The density and temperature in the scrape-off layer are assumed to change linearly.
4) The density and the temperature at the plasma center : 2×10^{20} [m^{-3}] and 34 [keV]

(2) Pellet parameters
1) The horizontal injection
2) The D-T mixture pellet : effective atomic mass number 2.5
3) The pellet size : 5 mm ϕ x 5 mm L, 6 mm ϕ x 6 mm L, 8 mm ϕ x 8 mm L,
4) pellet velocity : 1.0 km/sec, 1.5 km/sec, 2.0 km/sec.

15.3.3 Results

The relation between the penetration depth and pellet parameters is shown in Fig.

15.3.3. Figs. 15.3.4 and 15.3.5 represent the particle source density profile and the temperature modification, respectively.

From these results, even a 5 mm ϕ x 5 mm L pellet with a velocity of 1 km/sec can be driven beyond the scrape-off layer, and the range of $\Delta n/n$ (the ratio of the particle source density to the local bulk plasma density) is estimated to be from 1.2 (for a 5 mm ϕ x 5 mm L pellet) to 3.0 (for a 8 mm ϕ x 8 mm L pellet) in case of the injection velocity of 1km/sec. As reference, the range of $\Delta n/n$ is from 1.0 to 2.6 in case of the injection velocity of 2 km/sec. In our calculation, the effect of repetitive injections has not been taken into account.

The above results of a single pellet injection indicate that the density perturbation could be decreased with a smaller pellet injected at a higher velocity. However, it would be difficult to supply the large amount of particles with small pellets by means of a hyper-velocity injector at the current technological level.

As previously mentioned, the centrifugal pellet injector is the primary candidate for the SSTR pellet injector to steadily supply the fuel particles. The pellet velocity in the centrifugal injector depends on the rotor performance and the mechanical strength of the hoop in the accelerator. The pellet size must be determined by considering the soundness of the pellet during acceleration and the influence on the bulk plasma.

A large pellet has the advantage of reducing loads on the machines, while has the disadvantage of the soundness and the influence on the bulk plasma. From a view of the influence on the plasmas, we primarily choose a moderate-size pellet (a 5 mm ϕ x 5 mm L pellet), and an injection velocity of 1.0 km/sec is proposed to reduce the mechanical loads on both the pellet and the accelerator.

Hereafter, we will proceed to perform detailed analyses on pellet ablation and plasma transport, and will need to optimize the design of the pellet injector.

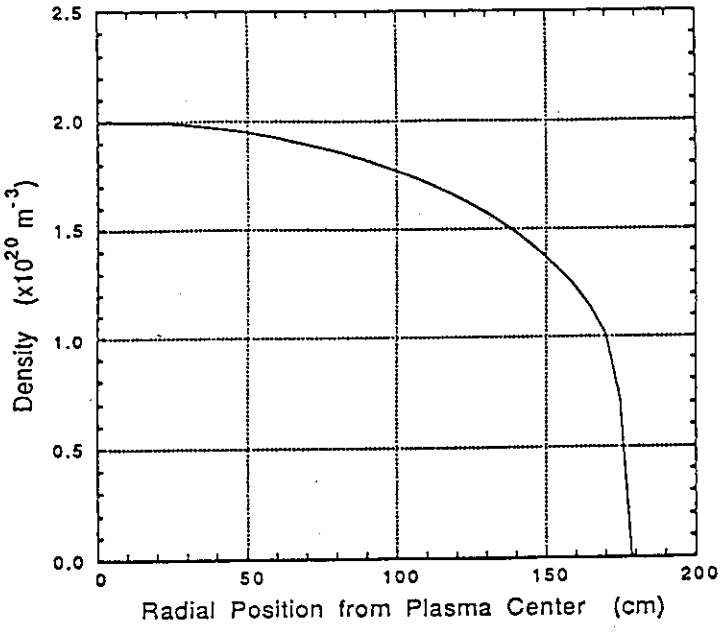

Fig. 15.3.1 Initial density profile.

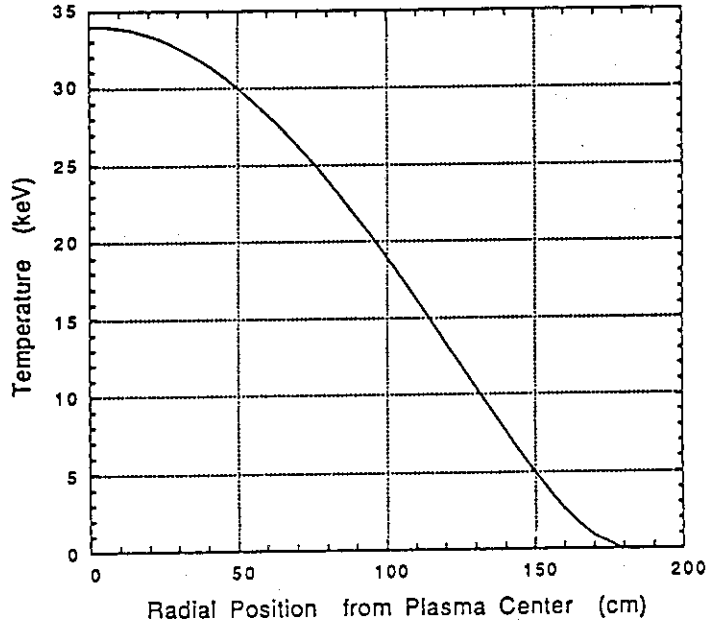

Fig. 15.3.2 Initial temperature profile.

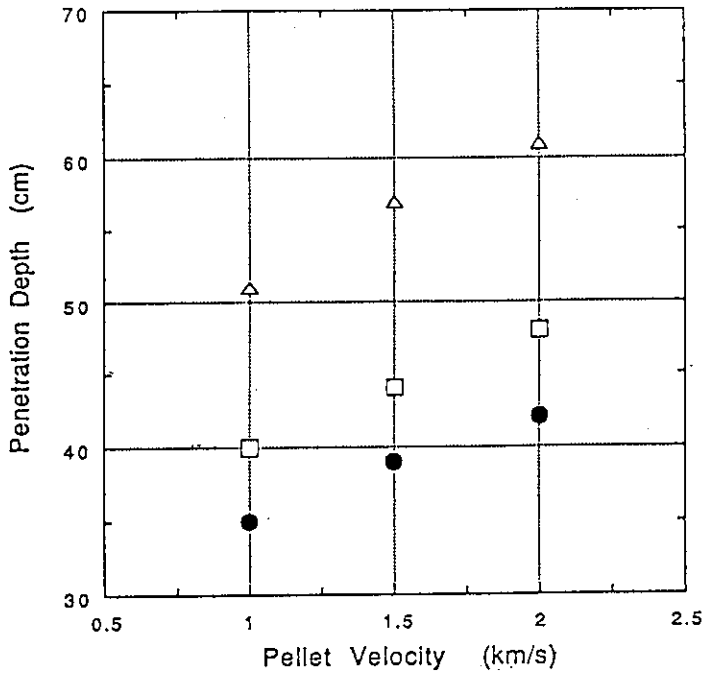

Fig. 15.3.3 Pellet velocity vs penetration depth.

The closed-circle represents the calculation results for the case of 5mm x 5mmL pellet, and the opened-square and triangle for the cases of 6mm x 6mmL and 8mm x 8mmL pellets, respectively.

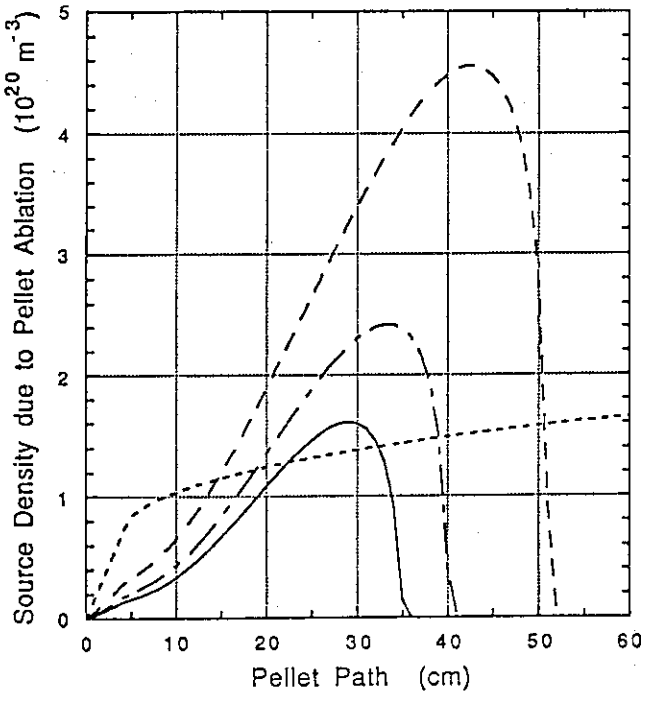

Fig. 15.3.4 Source density profile along pellet path.

The solid line represents the increase of density for the case of 5mm x 5mmL pellet, and the dashed-dotted and dashed lines for the cases of 6mm x 6mmL and 8mm x 8mmL pellets, respectively. As reference, the initial density profile is overwritten with the dotted line.

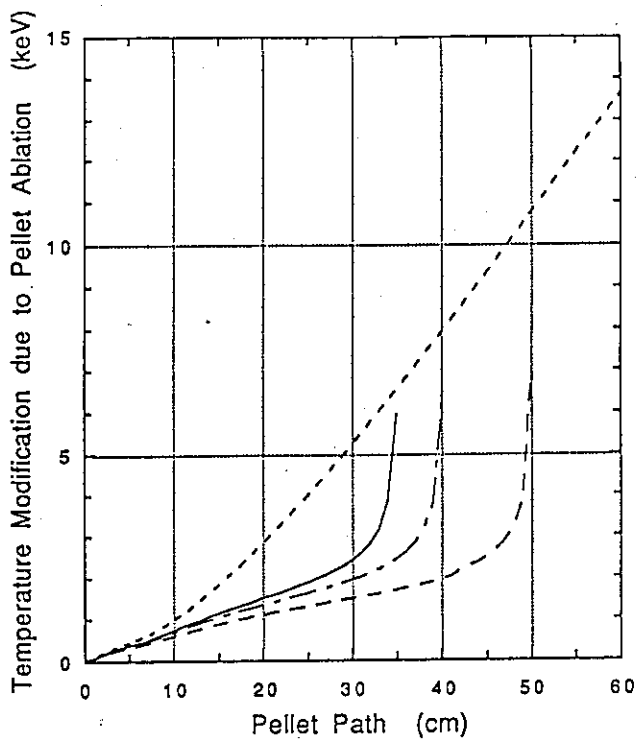

Fig. 15.3.5 Temperature profile along pellet path.

The solid line represents the temperature modification for the case of 5mm x 5mmL pellet, and the dashed-dotted and dashed lines for the cases of 6mm x 6mmL and 8mm x 8mmL pellets, respectively. As reference, the initial temperature profile is overwritten with the dotted line.

15.4 Main components and operation scenarios

15.4.1 Main system components

The SSTR injector systems mainly consist of a pellet injector, vacuum exhausting systems, cooling systems, fuel gas supply systems, control and measurement systems and remote maintenance systems. To handle potential problems which may arise with very important components, we will prepare backup systems. The main injector components are summarized in Table 15.4.1, and the schematic figure of the injector is shown in Fig. 15.4.1.

15.4.2 Layout plan

The SSTR injector is set up in conditioned room, where the behavior of tritium is monitored all the time. The layout plan is shown in Fig. 15.4.2. Double backup systems are adopted to steadily supply fuel particles, so that six injectors are set up in the room. Two injectors are used for the usual operation, two are always on stand-by for trouble in the operating injectors, while the other two are prepared as spare machines to replace the trouble machines. The backup machines of main vacuum exhaust systems are provided for the only injectors on stand-by.

The space between the apparatuses is as great as possible so that the machines can be maintained by remote handling. All the cables and pipes are connected with joints so that they can be attacked and detached easily.

15.4.3 Operation scenario

(1) Pellet injection cycles

The pellets are injected due to operating two main injectors alternately to reduce the loads on the extruders. The injection scenarios are illustrated in Fig.15.4.3.

(2) Formation cycles of the frozen filament

Four extruders are set up in each injector and operated alternately. The operation period between the cycles has 160 seconds (40 sec. for injection and 120 sec. for filament formation). The extruding and forming scenarios of the frozen filament are summarized in Fig. 15.4.4.

(3) Injector replacement cycles

To maintain the machines, the injector must be replaced according to the expected

life span of its various parts. An estimation of the life of the key parts is summarized in Table 15.4.2. The life span of the bellows in the piston driver hold the key to replacement of the injector and that of the bellows is about 120 days. Fig. 15.4.5. shows the replacement scenarios.

Table 15.4.1 Main system components of pellet injector

COMPONENT	NUMBER	REMARKS
PELLET INJECTOR	2 for OPERATION 2 for BACKUP 2 for ALTERNATIVE	· Repetition rate : 22.5 Hz/each · Extruder: 4/each injector · Piston speed: 34.7 mm/sec
VACUUM EXHAUST SYSTEM	1 for 4 Cryogenic chambers 1 for each pellet injector 2 for alternative	· Exhaust system for cryogenic chambers is required for thermal insulation · Exhaust system for each injector is used for exhausting pellet evaporation
COOLING SYSTEM	4 for each pellet injector	· Generation of solid hydrogen isotopes by L-He
GAS SUPPLY SYSTEM	1	· Supply of fuel gases
CONTROL & MEASUREMENT SYSTEM	1	· Measurement of pellet condition · Control of cooling temperature · Control of repetition rate
REMOTE MAINTENANCE	1	· Detachment and replacement by manipulator and crane

Table 15.4.2 Estimation of life span of mechanisms

MECHANISM	SPECIFICATION	LIFE SPAN
EXTRUDING PISTON (BELLOWS)	120 sec/cycle (720 cycles/day)	LIFE CYCLES 100,000 138 days
PELLET FEEDING MECHANISM	22.5 Hz (486,200 times/days)	LIFE TIMES 100,000,000 205 days
ROTOR	12,000 r.p.m.	LIFE TIME 5,000 Hr. 208 days

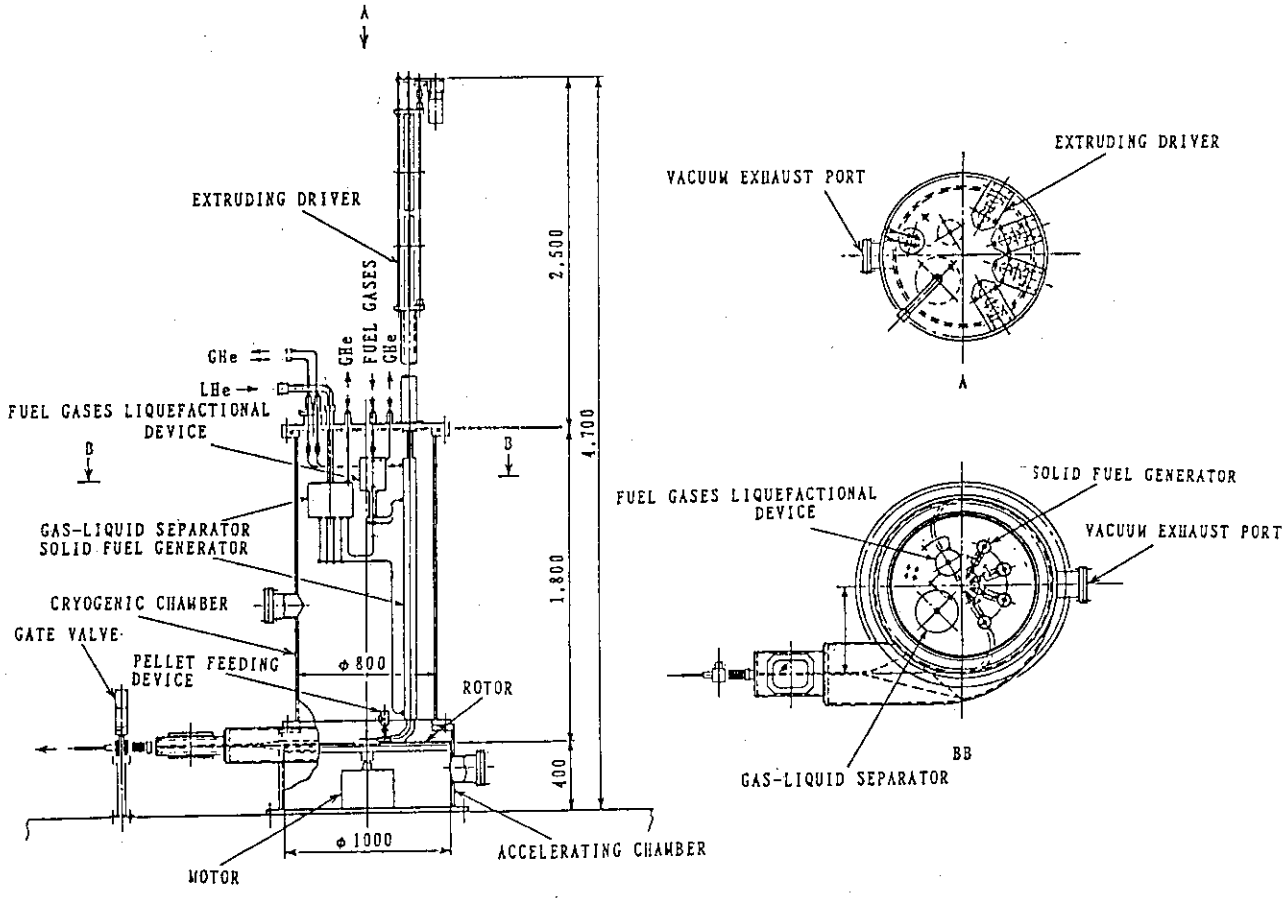

Fig. 15.4.1 Pellet injection construction figure.

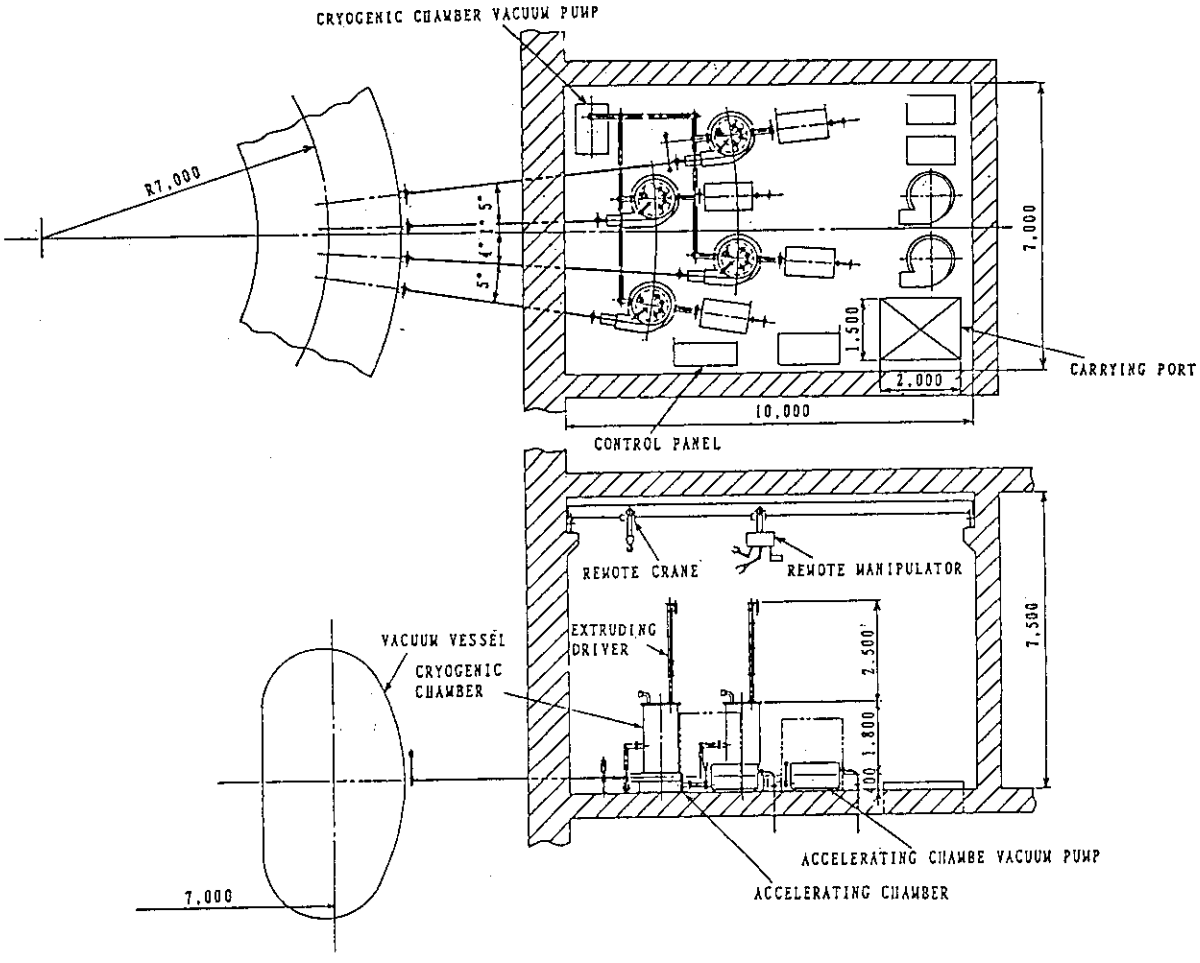

Fig. 15.4.2 Layout of pellet injector system.

PELLET INJECTOR	TIME / OPERATION	1 SECOND [45Hz]
No. 1 (22.5 Hz)	EXTRUDING	
	PELLET FEEDING	
No. 2 (22.5 Hz)	EXTRUDING	
	PELLET FEEDING	

Fig. 15.4.3 Pellet injection timing.

PELLET INJECTOR	EXTUDER	1st 40sec	2nd 40sec	3rd 40sec	4th 40sec
No. 1	A	EXTRUDING		GENERATING	
	B		EXTRUDING		GENERATING
	C	GENERATING		EXTRUDING	
	D		GENERATING		EXTRUDING
No. 2	A	EXTRUDING		GENERATING	
	B		EXTRUDING		GENERATING
	C	GENERATING		EXTRUDING	
	D		GENERATING		EXTRUDING

Fig. 15.4.4 Solid hydrogen generating and extruding cycle.

PELLET INJECTOR	1st 4months	2nd 4months	3rd 4months	4th 4months
No. 1, 2	OPERATING	MAINTENANCE	ALTERNATION	BACKUP
No. 3, 4				
No. 5, 6				
No. 7, 8				

Fig. 15.4.5 Regular substitution cycles of pellet injectors.

15.5 Tritium inventory and consumption

15.5.1 Premises

1) Although six injectors are set up in the room, the fuel materials are always loaded into the only four injectors including the two injectors on stand-by.

2) The fuel gases are liquefied by liquefaction devices before being introduced into the cryogenic extruder. The only four liquefaction devices are filled with the fuel materials.

15.5.2 Tritium inventory

The volume of the filament generators per injector is given by

$$(\pi/4) \times (0.9)^2 \times 150 \times 4 = 38.2 \ [cm^3],$$

and the volume of the liquefaction devices and introduction lines is given by

$$(\pi/4) \times 5^2 \times 20 + (p/4) \times (0.625)^2 \times 30 = 402 \ [cm^3].$$

Here, the densities of the liquid and solid tritium are assumed to be 0.251 g/cm^3 and 0.308 g/cm^3, respectively, and the composition ratio of the fuel pellet is assumed to be 50/50 of D/T. The tritium inventory per injector is estimated to be

$$0.5 \times (402 \times 0.251 + 38.2 \times 0.308) \cong 57 \ [g],$$

so that the total tritium inventory during the operation is about 230 g in the room.

15.5.3 Tritium consumption

The total volume of injected pellets is given by

$$(\pi/4) \times (0.5)^2 \times 0.5 \times 45 = 4.42 \ [cm^3/sec],$$

so that the consumption of the tritium is estimated by assuming D/T = 50/50 as follows :

$$0.5 \times 0.308 \times 4.42 \cong 0.7 \ [g/sec] = 2.52 \ [kg/h].$$

15.6 Research and Development

There seem to be two directions to develop the pellet injector. One is to establish injector systems which can steadily supply fuel particles. In this case, the steady formation technique of solid hydrogen isotopes is a key issue. The other is to develop a hyper-velocity injector, which has a potentiality to improve the plasma performance.

(1) For a steady pellet injector (a centrifugal pellet injector)

1) Optimization of the extruder to steadily generate the frozen filament
2) Establishment of a technique to generate large pellets
3) Optimization of the accelerating characteristics of the centrifugal injector
4) Establishment of a feeding mechanism to cut the filament
5) Establishment of a technique to form the D-T mixture pellet

(2) To improve the plasma profile

A hyper-velocity injector, which is believed to be useful for burning and controlling impurities will also be needed in the future to improve fueling efficiency. Therefore, the following R&D item is proposed to confirm availability of the hyper-velocity injector.

1) An explanation of the relationship between particle transport and pellet penetration.

References

(1) W.A. Houlberg et al.; ORNL/TM-6549 (January, 1979).

16. ECH System

16.1 Introduction

The ECH system reduces the breakdown voltage for plasma production, supplements heating, and saves on volt-seconds during start-up. The ECH system has the following specifications.

Frequency:	250 GHz
Injected power:	5 MW
Pulse length:	CW
Injection mode:	Ordinary mode from the outboard side
Injection position:	R = 7 m, Z = -1 m
Injection angle:	15° with respect to normal of the toroidal field

Because the magnetic field along the plasma axis is 9 T high, a frequency of 250 GHz is needed. This required frequency is relatively high compared to that in conventional systems..

16.2 System Outline

The ECH system consists of millimeter wave sources, a power supply, transmission lines, and an antenna module. Fig. 16.2.1 shows a block diagram of the system, and Table 16.2.1 lists the main components.

Millimeter wave sources with output power levels of 1 MW are needed to satisfy certain physical requirements. Possible candidates for the required 250-GHz, 1-MW, CW source are the whispering-gallery-mode (WGM) gyrotron, the quasi-optical (QO) gyrotron, the cyclotron auto-resonance maser (CARM), and the free electron laser (FEL).

The WGM gyrotron is a conventional cylindrical gyrotron similar to the TE_{0n} (n = 2, 3) mode gyrotron used at frequencies of 30-70 GHz. The WGM gyrotron differs, however, in that its cavity has a relatively large diameter. Moreover, the gyrotron employs a TE_{mn} (m >> n, n = 1, 2) whispering-gallery mode so as to reduce mode competition and power density on cavity walls due to ohmic losses. We expect that the WGM gyrotron currently under development will achieve 100-140 GHz, 1 MW, and CW. Recently, short-pulse (0.5-ms) power levels of 1 MW and long-pulse (500-ms) power levels of 400 kW have been obtained at 140 GHz.

The QO gyrotron uses a quasi-optical resonator such as the Fabry-Perot resonator. Because of its larger resonator, a higher output power capability is expected. Short-pulse

power levels of 300 kW at 100 GHz have been achieved, but the efficiency is lower than that of the WGM gyrotron.

At present, the WGM gyrotron is the most promising candidate as a 250-GHz, 1-MW, CW source, so for the time being it will be used as the reference source. Although a power input of only 5 MW is required, because of transmission losses, 6 MW of RF power are actually needed. Thus, 6 gyrotrons will be installed.

Assuming that the efficiency of the reference 1-MW gyrotron is the same as that of gyrotrons available today (that is, 30%-35%), the power supply should provide each tube with a beam voltage of 80-100 kV, a regulation value of 0.1%, and a beam current of about 40 A. The power supply unit consists of a high voltage DC power supply, a filter, a crowbar and a regulator tube. Since each unit will be capable of supplying 2 gyrotrons with beam voltage, 3 units will be installed.

6 gyrotrons and 3 regulator tubes will be installed in a gyrotron room about 440 m^2 in area. This room will also contain power supplies for gyrotron magnets, facilities to cool tubes cryogenically and distribute water, magnet coils and windows, and gyrotron loads. Except for those used for the regulator tubes, the power supply units will be installed in the ECH power supply room, which will be about 580 m^2 in area.

The choice of concepts for low-loss transmission of high-power millimeter waves depends on the gyrotron output mode. If the reference source WGM gyrotron has a built-in quasi-optical converter, linearly polarized Gaussian beams will be emitted. There are two ways to achieve low-loss transmission in this Gaussian TEM_{00} mode: one way is to use a closed corrugated circular metal waveguide that propagates in HE_{11} mode; the other is to use a quasi-optical mirror waveguide that propagates the Gaussian beam.

Given a corrugated waveguide with a slot depth of about $\lambda/4$ (λ : free-space wavelength), the field distribution in HE_{11} mode approximates that of the Gaussian distribution, and this mode loss is theoretically less than the TE_{01} mode loss in a waveguide with smooth walls. The Gaussian beam emitted from the gyrotron is coupled into the HE_{11} mode with an efficiency of about 98% by focusing the beam on the waveguide aperture. Assuming that the allowable maximum electric field strength is 10 kV/cm, the waveguide diameter required for 1-MW transmission is more than 60 mm. As the waveguide diameter is enlarged, the ohmic loss is lowered, but losses brought about by conversion to spurious modes due to curvature and tilts at junctions increase scaling with a/λ (a : waveguide radius).

At an aluminum waveguide diameter of 88.9 mm, the maximum electric field strength is about 7 kV/cm, and the ohmic attenuation is about 4×10^{-5} dB/m (0.1% loss per 100 m). Using an oversized waveguide diameter makes it possible to use low-loss mitre bends. The expected loss when using a Cu-mirror 90° mitre bend in an 88.9 mm diameter waveguide is about 0.4%.

The quasi-optical transmission system would transmit the Gaussian beams from the gyrotrons using focusing reflector mirrors. The required diameter of the mirrors increases with mirror separation due to diffraction. For a mirror-to-mirror separation of 5 m, each transmission line must have mirrors 20 cm in diameter. The mirror waveguide also needs an RF shield that surrounds the beam line. Therefore, the quasi-optical transmission system must be large, but it is capable of handling high power ratings. Assuming that the beam radius at the beam waist is 5 cm and the allowable maximum electric field strength is 10 kV/cm, the system will be capable of carrying about 5 MW of power. Therefore, this system makes it possible to reduce the number of beam lines by combining beams from gyrotrons.

Mirror losses are expected to be 0.5% - 0.6%. This value includes ohmic and diffraction losses as well as losses due to misalignment and shape imperfections. The transmission losses of the above two systems are on the same order, and the choice of reference system depends on the results of future research and development. Like the gyrotron window, however, the RF window near the tokamak will support only 1 MW. Therefore, when using a quasi-optical system, the combined beam should be divided again, further complicating the system. For this reason, we will use the corrugated waveguide system as the reference transmission system. But because the waveguide system cannot focus RF beams on a fixed position in the plasma, the quasi-optical system will be used for the injection antenna system.

Table 16.2.1 Main equipment list

(1) Millimeter wave sources		
Gyrotron	250 GHz, 1 MW, CW	6 tubes
(2) Power supply		
Beam power supply	100 kV - 40 A	3 units
Anode power supply	40 kV - 10 mA	6 units
Heater power supply	60 V - 10 A	6 units
Magnet power supply	100 A	6 units
(3) Transmission lines		
Corrugated waveguide	f88.9 mm	6 lines
(4) Antenna module		
Multi-face reflector	60x90 cm	1
Flat mirror	30x45 cm	2
Curved mirror	60x90 cm	1
(5) Vacuum pump		
Turbomolecular pump		2 pumps
(6) Control system		
Control and monitoring of gyrotrons		

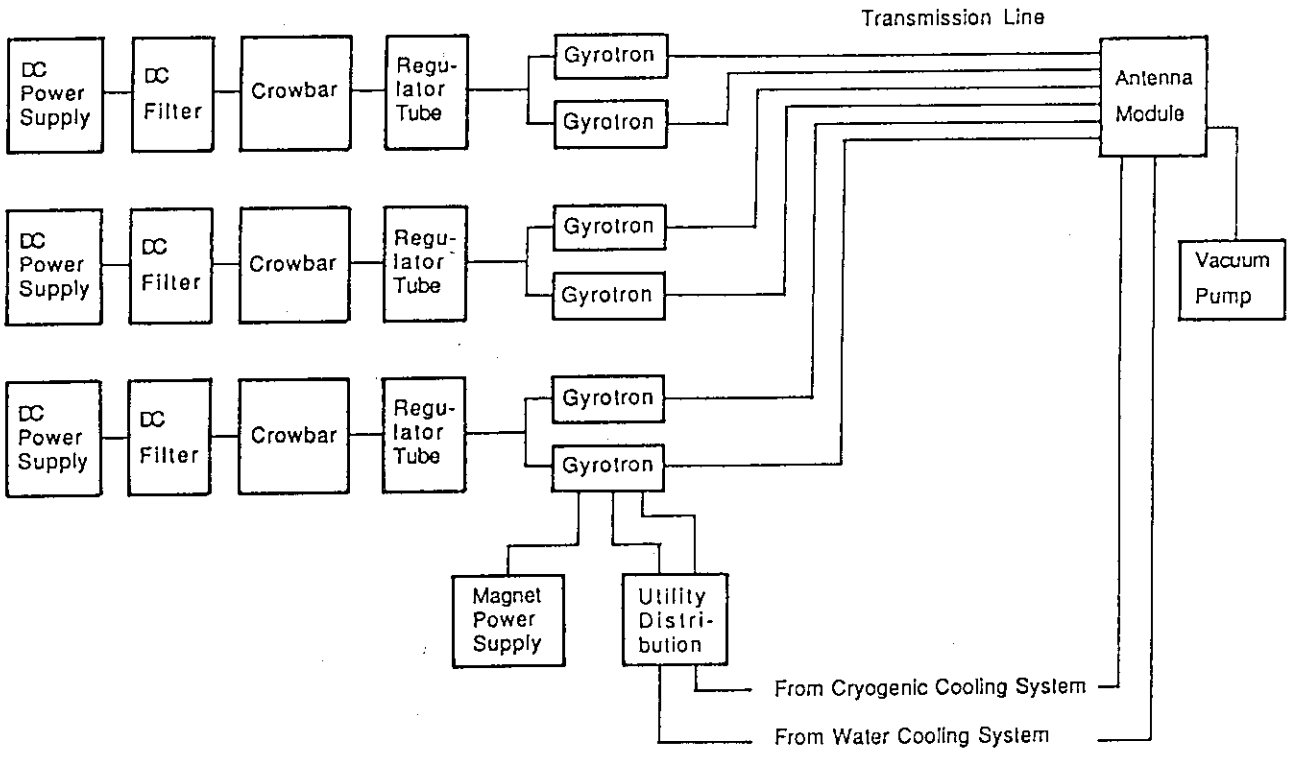

Fig. 16.2.1 Block diagram of ECH system.

16.3 Antenna Module

The antenna module will supply RF power, which will be transmitted through the corrugated waveguides, to the required position in the plasma using quasi-optical focusing mirrors. The port dimension should be as small as possible so as to reduce the nuclear radiation and the escape of tritium and neutrals. The reflectors of the antenna module should also be far away from the plasma to minimize possible damage to the mirror surface. Therefore, all the reflectors will be installed outside the cryostat.

Figures 16.3.1 and 16.3.2 show a schematic of the antenna module. The millimeter wave beams radiated from the waveguide ends following the windows will be injected into the plasma, after bending by means of four reflector mirrors for the purpose of effective neutron shield. The injection angle must be about 15° with respect to the normal of the magnetic field in the horizontal direction. Since the required injection position is 1 m below the equatorial plane, an oblique launch is proposed with a 10°-angle in the vertical direction so as to avoid interference with the duct and other structures.

The beams radiated from the waveguide ends are made to converge on the flat mirror by means of a multiface reflector. This reflector is made up of 2x3 mirrors, each of which is 30x30 cm in size. Thus the total dimension of the reflector is 60x90 cm. The converged beams are reflected by two flat mirrors, and are focused and injected into the required position in the plasma by mean of a curved focusing mirror. Both flat mirrors are 30x45 cm in size, and the dimensions of the focusing mirror are 60x90 cm. The material used for the reflectors should be resistant to sputtering and radiation damage and should also have good electrical and thermal conductivity. Sputtering erosion is especially problematic for the last reflector, so the surface coating of the material should contain Tungsten or Molybdenum to ensure a low sputtering yield.

The thickness of the shield is 60 cm inside the cryostat and 1 m outside the cryostat. The containment structure of the reflectors has a screening wall with a relatively small hole between two flat mirrors. Since the ECH system will be operated only during plasma production and start-up, a neutron shutter installed at the duct end will be used as a shield against nuclear radiation; the shutter will be closed when the device is not running. A large gate valve is installed in front of the neutron shutter to facilitate maintenance.

The antenna module is pumped by two vacuum pumps (not shown in the figures).

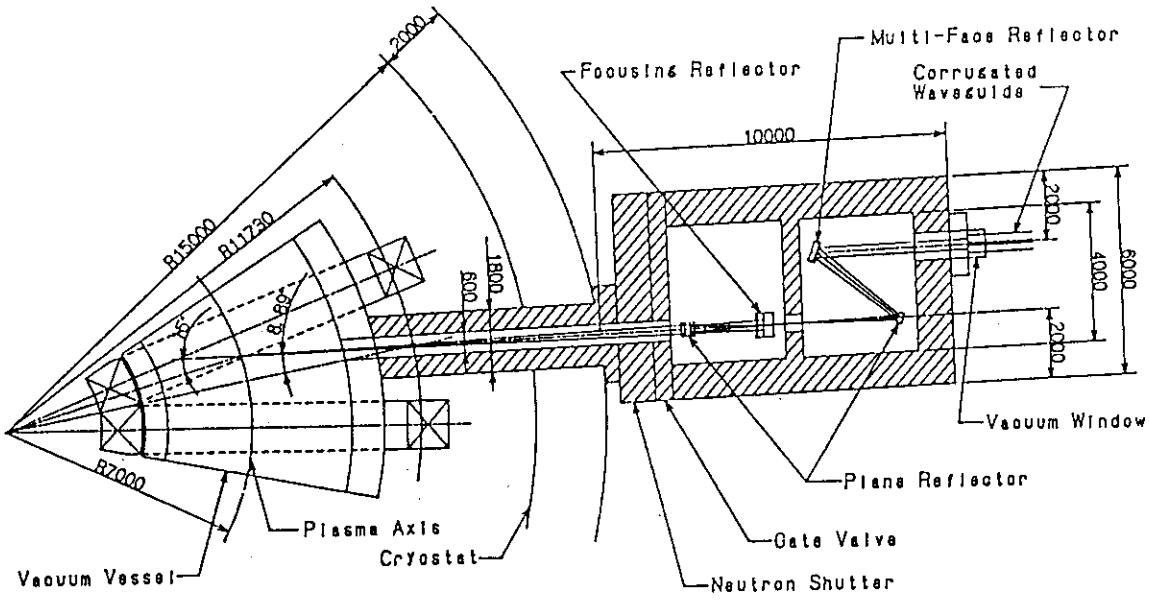

Fig. 16.3.1 Schematic of ECH antenna module (horizontal cross-sectional view).

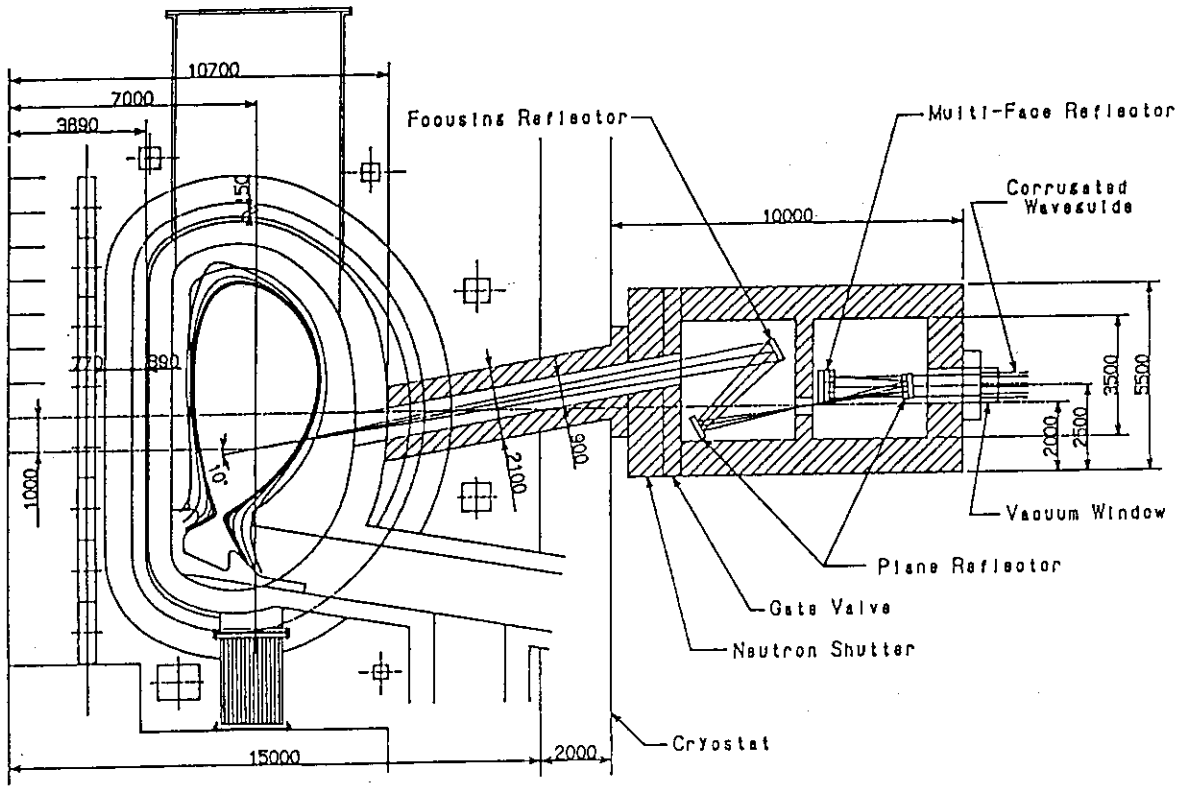

Fig. 16.3.2 Schematic of ECH antenna module (vertical cross-sectional view).

16.4 System Efficiency

The estimated efficiencies for each component are as follows:

Power supply :	95%
Sources :	30% - 35%
Transmission line :	85%

Thus the total system efficiency is about 26%. Although the efficiency of the reference gyrotrons is assumed to be the same as that of gyrotrons currently available, the value may improve to as high as 50% if development of depressed collectors proceeds as planned. If gyrotron efficiency does improve to this level, the total system efficiency will be 40% or more.

16.5 Future Topics for Research and Development

1) Development of an efficient 250-GHz, 1-MW, CW gyrotron

The gyrotron is a key component in the ECH system that will require further development. The main problems to be solved are as follows.

(1) Optimization of the cavity wall loading

A large diameter cavity is needed to reduce the wall loading. Because of the higher frequency, a higher-order whispering-gallery mode of higher order that in today's gyrotrons or a volume mode (TE_{mn} : m >>n, n > 2) may be used in future gyrotron models. Whichever mode is used, it must be optimized while taking mode competition into account.

(2) Optimization of the collector

To reduce the amount of heat absorbed by the collector, it may be possible to use a quasi-optical convertor that separates the RF and the electron beam. It will also be necessary to develop an efficient quasi-optical converter and optimize the collector shape.

(3) Optimization of gyrotron efficiency

High gyrotron efficiency can be achieved by optimizing the gun and developing a depressed collector.

(4) Development on the output window

A cryogenically cooled window will be needed. Development studies are now underway.

2) Development of a low-loss transmission line

Further developments will be needed to obtain a low-loss corrugated waveguide. Waveguide components, the alignment structure, and the cooling structure will also require development.

3) Development of antenna reflectors

Antenna reflectors must use materials that are resistant to sputtering and swelling.

4) Development of the window

The RF window in the antenna module must become capable of withstanding radiation damage as well as 1 MW of power.

5) Study on antenna module maintenance

Reflector and window maintenance procedures must be researched.

The closed-circle represents the calculation results for the case of 5mm x 5mmL pellet, and the opened-square and triangle for the cases of 6mm x 6mmL and 8mm x 8mmL pellets, respectively.

The solid line represents the increase of density for the case of 5mm x 5mmL pellet, and the dashed-dotted and dashed lines for the cases of 6mm x 6mmL and 8mm x 8mmL pellets, respectively. As reference, the initial density profile is overwritten with the dotted line.

The solid line represents the temperature modification for the case of 5mm x 5mmL pellet, and the dashed-dotted and dashed lines for the cases of 6mm x 6mmL and 8mm x 8mmL pellets, respectively. As reference, the initial temperature profile is overwritten with the dotted line.

17. Plant Buildings

17.1 Conditions

(1) General Conditions

When deciding on the dispositions of buildings and equipment in the plant, the type of power plant and geographical conditions, geological conditions, earthquake conditions, and water supply conditions should be determined in advance. These conditions will change as the related technologies become more advanced. We planned the dispositions of buildings and equipment in the plant in accordance with the conditions shown in Table 17.1.1. Auxiliary facilities and equipment are shown in Table 17.1.2. The equipment was determined in each phase of evaluation phase. However, the actual dispositions were based on plans.

(2) Determination of the containment vessel type

According to the preliminary evaluation of the equipment dispositions, it became clear that the inner diameter of the containment vessel should be 55 to 60 m. When part of the blanket cooling pipes is broken, the inner pressure of the containment vessel will rise. However, this situation is affected by the design conditions, which will be determined in future.

Although the increase in internal pressure is currently unknown, we feel that the degree is the same as or equal to that of a light-water reactor.

The internal pressure ranges from 2 to 3 kg/cm^2. When steel plates are used, the thickness of the shield wall will become 60 to 70 mm (depending on the material type), and so the cost will increase. Moreover, the mounting position of the swinging crane in the doom section will become large enough to withstand its weight.

Given these estimations, we planned to build the containment vessel using ferroconcrete, which is less expensive than steel plates.

Steel plates whose thickness is approx. 4.5 mm will line the inner wall of the containment vessel so as to prevent gas leaks. However, if excellent heat-resistant resin films can be developed, they may be used instead.

Table 17.1.1 Conditions for study of plant layout

Number of Plant	1
Electrical Power	apporox. 1,100MW
Reactor Type	Steady State Tokamak Reactor (SSTR)
Generator Type	Steam Turbine Driven Generator
Steam Generator	Vertical Type Primary Side:Blanket Coolant Secondary Side: Feedwater and Saturated Steam
Auxiliary	Based on Table 17.1.2
Containment Type	Concrete Containment
Geographical Condition	Turning on Flat Place
Earthquake Condition	Domestic Average(S1=apporox.200gal)
Final Source of Radiation of Heat	Sea Water

Table 17.1.2(1) List of facilities and equipments for SSTR plant

Building Name	Facility Name	Number	Floor(F)
Nuclear Fusion Reactor Building(Main Building)			
In Containment	Fusion Reactor	1	3
	Pellet Injection Unit	1	3
	ECH	1	3
	Steam Generator	4	3
	Primary Coolant Pump	4	3
	Pressurizer	1	3
	Pressurizer Relief Tank	1	3
Out of Containment	NBI	2	3
	NBI Inverter	1	2
	NBI Inverter D.C. Power Supply	1	1
	Helium Pump Unit	1	1
	Purity,Isotope Separation and Storage Facility	1	4
	Tritium Removal System	1	4
	Tritium Safety System	1	4
	Heating,Ventilating and Air-Conditioning System	1	5,6
	Main Control Room		5
	Primary Makeup Water Tank	1	3
	Emergency Core Cooling System	2	1,2
	Residual Heat Removal System	2	1,2
	Containment Spray System	2	1,2
	Volume Control System	1	2
	Component Cooling System	1	3
	Feed Water Heater Exchanger	1	3
	Safeguard Switch Gear	1	4
	D.C. Power Supply	1	3
	Vital Power Supply System	1	3
	ECH Power Supply	1	2
	ECH Gyrotron	1	2

Table 17.1.2(2) List of facilities and equipments for SSTr plant

Building Name	Facility Name	Number	Floor(F)
Turbine building	Deaerator	1	4
	Steam Turbine (TC6F52)	1	3
	Electrical Generator	1	3
	Moisture Separetor Reheater	1	3
	Feed Water Heater	1	2
	Condenser	1	1,2
	Turbine Driven Feed Water Pump	2	1
	Feed Water Booster Pump	2	1
	Condensate Pump	3	1
Cryogenics Building	Helium Liquefaction System	1	1
Electrical Building	Fusion Reactor Coil Power Supply System	1	1,4
	Fusion Reactor Component Switch System	1	2,3,5
	Vital D.C. Power Supply System	1	1
	Vital A.C. Power Supply System	1	1
Emergency Diesel Generator Building	Emergency Diesel Generator System	2	1
Switch Gear Yard	Circuit Breaker	1	
	Disconnecting Switch,etc.	1	
Transformer Division	Main Transformer	1(outdoors)	
	House Transformer	1(outdoors)	
	Emergency Transformer	1(outdoors)	

17.2 Disposition of Buildings

17.2.1 Basic conception of buildings

The plant consists of several buildings. Buildings are classified according to the following considerations:

* Presence/absence of radiation of the equipments
* Functional concentration of the equipments
* Earthquake resistance of the equipments
* Restrictions on structural strength of the buildings

These items are discussed below.

(1) Grouping the presence of radiation:

A shielding wall is needed if radiation is present, and the building's structure will depend on how thick the shielding wall is. When radiation is present in the building, access control is required through an access control room. Moreover, an extra floor drain system and air conditioning system must be installed for the radiation area.

Buildings should be designed according to whether radiation is present or absent. If such grouping is unreasonable, the radiation area should be partitioned in each building.

(2) Grouping by functional centralization:

Piping and wiring can be designed efficiently if equipment is centralized by function. Moreover, functional centralization makes equipment maintenance and inspection convenient. Thus, the centralization of electrical equipment will be possible, too.

(3) Grouping by earthquake resistance criteria:

The earthquake-resistance design of the buildings depends on earthquake-resistance classes of the equipment to be installed. If the equipments whose earthquake resistance is of the same class are installed closely each other, the buildings can be designed efficiently. Normally, the groupings of equipment by earthquake-resistance and functional centralization overlap.

(4) Restrictions on structural strength:

If the buildings are designed in accordance with the following criteria, problems that might otherwise arise in the later detail evaluation stages can mostly be avoided.

(i) The overall length of each building should be around 100 m to prevent deformation by earthquakes.

(ii) The best shape for buildings is a square. If the building is rectangular, the longer side should be less than twice the shorter side.

(iii) The overall height of each earthquake-resistant building should be 60% to 80% of the shorter side.

17.2.2 Outline of the buildings

The equipment of the entire plant was disposed by reasonably grouping them into several buildings in accordance with the basic conception of the buildings. Table 17.2.1 gives an outline of the buildings.

17.2.3 Dispositions of Buildings

Figure 17.2.1 shows the plant building disposition where the major buildings shown in Table 17.2.1 are disposed on a site prepared on flat land. Figure 17.2.2 shows a bird's eye view.

The nuclear fusion reactor building is adjacent to the turbine building so as to minimize the length of the main steam pipe. With this disposition, the administration building, access control building, and emergency diesel generator building can be functionally disposed. In other words, it is convenient for the workers (operators) to access the administration, turbine, and access-control buildings which are adjacent. In addition, the access-control building should be adjacent to the nuclear fusion reactor building. On the other hand, since the access-control building does not need a shielding wall, it is disposed as a building independent from the nuclear fusion reactor building.

Since the electrical building does not need a shielding wall and the height of each floor can be lower than that of the machine room, it can be inexpensively built as a separate building from the nuclear fusion reactor building. The electrical building is independent from the nuclear fusion reactor building. Since the electrical building is functionally close to the nuclear fusion reactor building, the two are adjacent to each other. In the present plan, they are connected by a 7 m-wide road. However, depending on the arrangement between the wiring plan and the building plan, the road may be deleted from the plan.

The switch gear yard, auxiliary boiler area, waste storage building, and so forth are disposed so that their functions and the spaces can be effectively used. The sea water circulation pipes (2 pipes with an inner diameter of 4 m) for cooling the condensers of steam turbine should be routed to the turbine building. The site on which the above

buildings and equipment are located will be approx. 450 m x 400 m once expansions are made.

Table 17.2.1 Outline of Major Buildings of The Plant

Building Name	Size (Length xWidth xHight,m)	Radioactivity	Structure
Containment	Inner Diam. 56m x Outer Hight 97.7m	Presence	Ferroconcrete
Nuclear Fusion Reactor Building	140x112x69	Presence * /Absence	Ferroconcrete
Electrical Building	119x77x42	Absence	Steel Frame Ferroconcrete
Turbine Building	125x50x40	Absence	Steel Frame and Light Panel
Emergency Diesel Generator Building	30x25x15	Absence	Ferroconcrete
Access Control Building	30x30x8	Absence	Steel Frame Ferroconcrete
Administrating Building	50x25x10	Absence	Steel Frame and Light Panel
Cryogenics Building	70x57x21	Absence	Steel Frame and Light Panel
Blanket Maintenance Building	70x60x50	Presence /Absence	Steel Frame Ferroconcrete

* There is no radioactivity about one-third rooms of the building,which are NBI power supply room,main control room and etc.

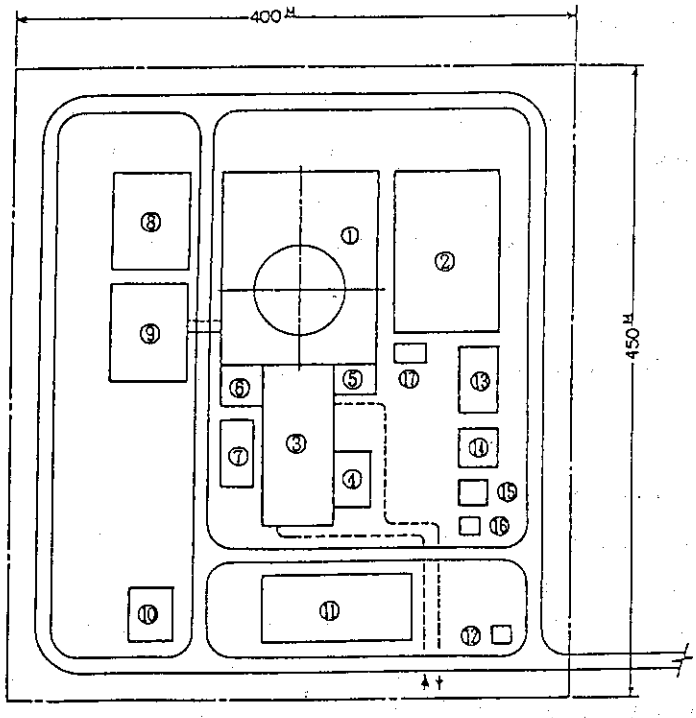

① NUCLEAR FUSION REACTOR BUILDING
② ELECTRICAL BUILDNG
③ TURBINE BUILDING
④ TRANSFORMER AREA
⑤ EMERGENCY DIESEL GENERATOR BUILDING
⑥ ACCESS CONTROL BUILDING
⑦ ADMINISTRAITING BUILDING
⑧ CRYOGENICS BUILDING
⑨ BLANKET MAINTENANCE BUILDING
⑩ WASTE STRAGE BUILDING
⑪ SWITCH GEAR YARD
⑫ GUARD HOUSE
⑬ DISCHARGE WATER TREATMENT AREA
⑭ FEED WATER TREATMENT AREA
⑮ AUXILIARY BOILER AREA
⑯ OIL TANK AREA
⑰ OIL TANK AREA

Fig. 17.2.1 Plant building arrangement.

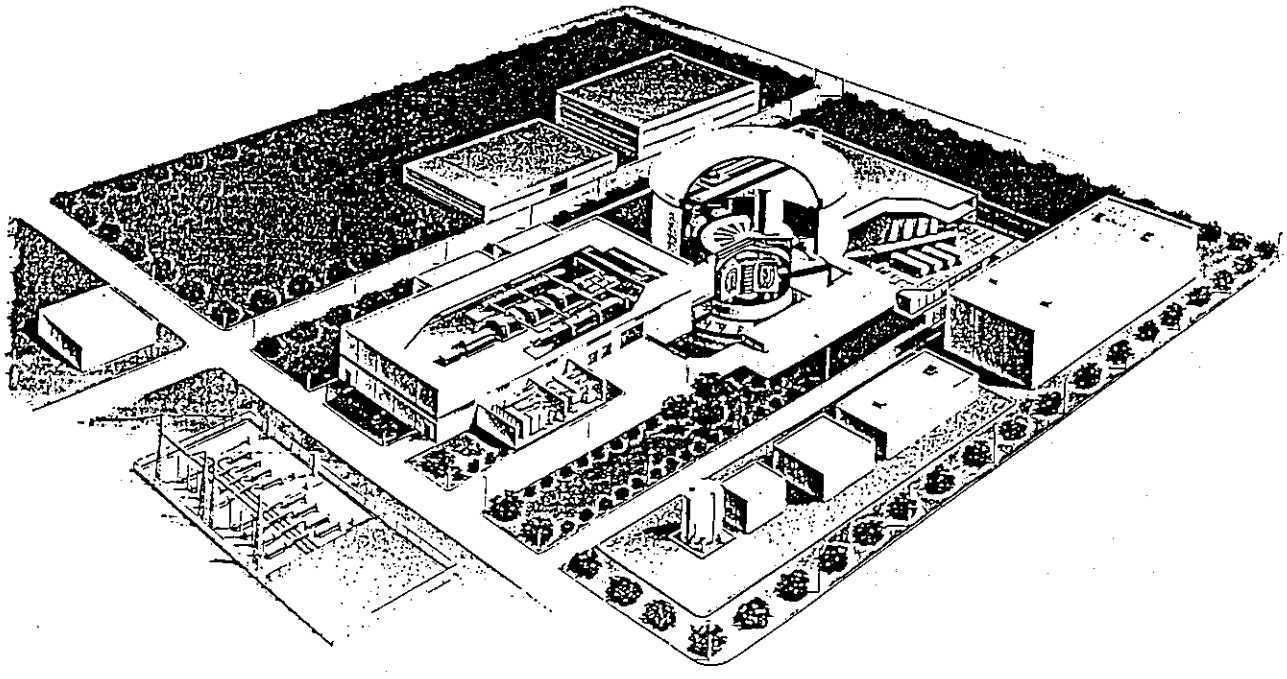

Fig. 17.2.2 Bird's-eye view of SSTR power station.

17.3 Disposition of Equipment in Buildings

(1) Dispositions in the nuclear fusion reactor building

The containment vessel should be disposed at the center of the nuclear fusion reactor building in terms of the earthquake resisting design. However, NBI should be disposed, the main steam pipe should be as short as possible, and the building should be as small as possible. thus, the containment vessel is disposed with some degree of eccentricity.

Figures 17.3.1 (1/7) to 17.3.1 (7/7) show the equipment dispositions in the nuclear fusion reactor building.

In the containment vessel, a vacuum vessel is disposed at the center, while steam generators, primary coolant pumps, pressurizer, pellet injection unit, ECH unit, maintenance space, and so forth are disposed around the vacuum vessel in a ring shape. Two steam generators are set up across from two other steam generators so as to balance the flow rate of the cooling system. The steam generators, primary coolant pumps, and primary coolant main pipes are disposed inside the wall. In the room under the vacuum vessel, the vacuum pump and cable separating room are disposed.

On the operation floor over the vacuum vessel, a blanket handling equipment can be used. A swinging crane will be installed at the proper height.

In the nuclear fusion reactor building equipment other than the containment vessel is generally grouped depending on whether radiation is present or absent. Below the NBI room, power equipment is disposed. The equipment relating to the turbine generating system is disposed in the turbine building. Heating,ventilating & air conditioning system (HVAC), which is large in structure but light in weight, is disposed on an upper floor for ventilation.

(2) Disposition of the electrical building

Since the electrical building does not house radioactive equipment, it does not need a shielding wall. Thus, the structure of the electrical building can be light. Although ready access to the building is required, management of radiation is not necessary. Thus, periodical maintenance of the building will be simple.

A vibrating PFC motor generator is disposed on the lowest floor of the electrical building. Other electrical equipment — a TFC power conversion element, a PFC power conversion element, a TFC power protection element, and a PFC power protection element — is disposed on the second to fifth floors (including the lowest floor).

The HVAC is disposed on part of the fifth floor and on the sixth floor of the electrical building.

(3) Disposition of the turbine building

The structure of the thermal power generators is basically the same as that of the nuclear fusion reactors except that thermal power generators use overheated steam and this nuclear fusion reactor plant drives turbine generators with saturated steam.

Since the pressure of the saturated steam used in the nuclear fusion reactor plant is low, its specific volume is large. In addition, since the steam enthalpy is small, a large amount of steam is required. Thus, large turbines are needed to process the steam. The turbines are composed of one high-pressure turbine room and three low-pressure turbine rooms. Since the main steam pipe connects to the high pressure turbine, it is disposed on the nuclear fusion reactor building side. In addition, on the turbine operation floor, two large moisture separation heaters are disposed on both sides of the turbine

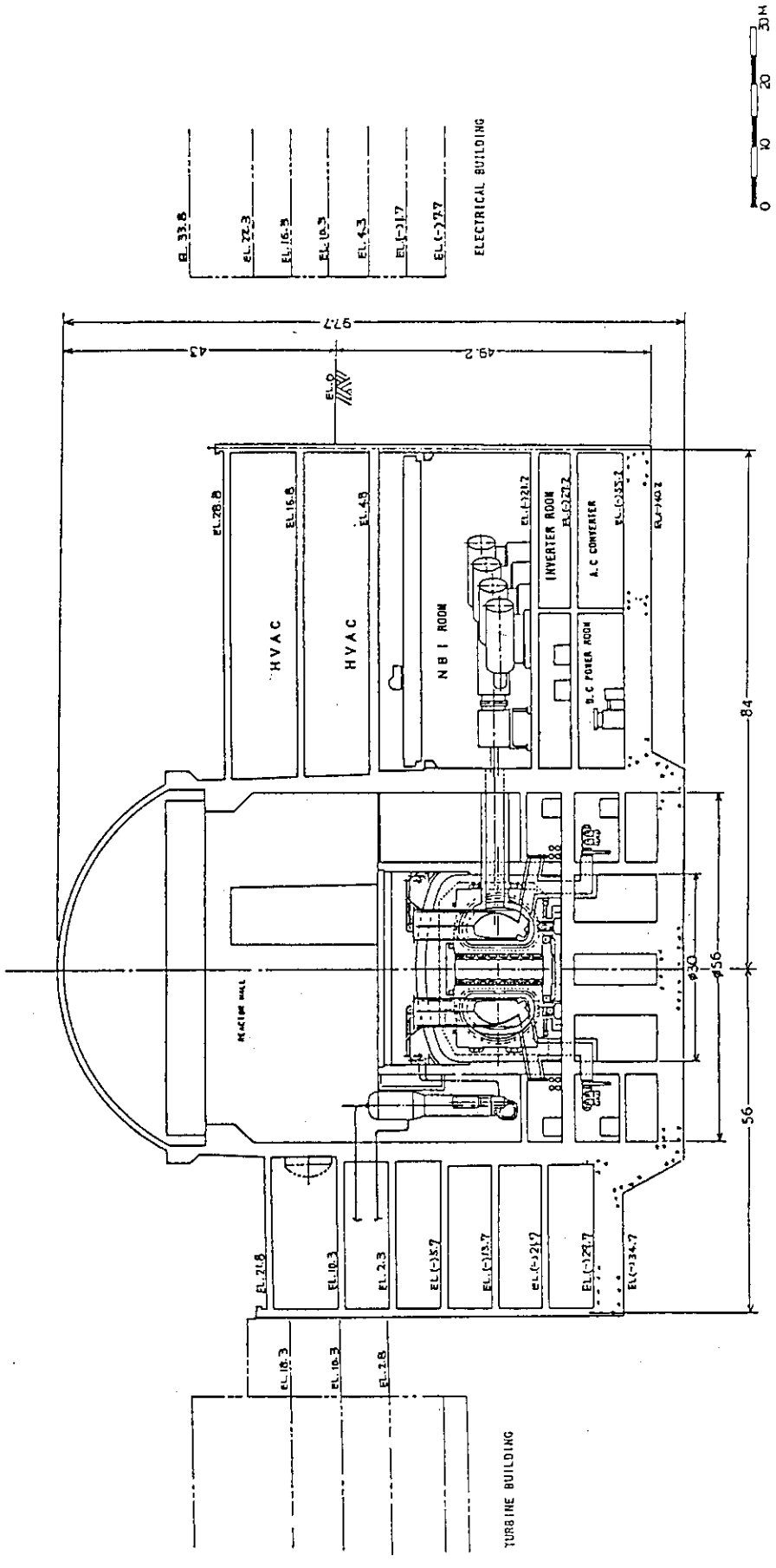

Fig. 17.3.1 General arrangement (1/7).

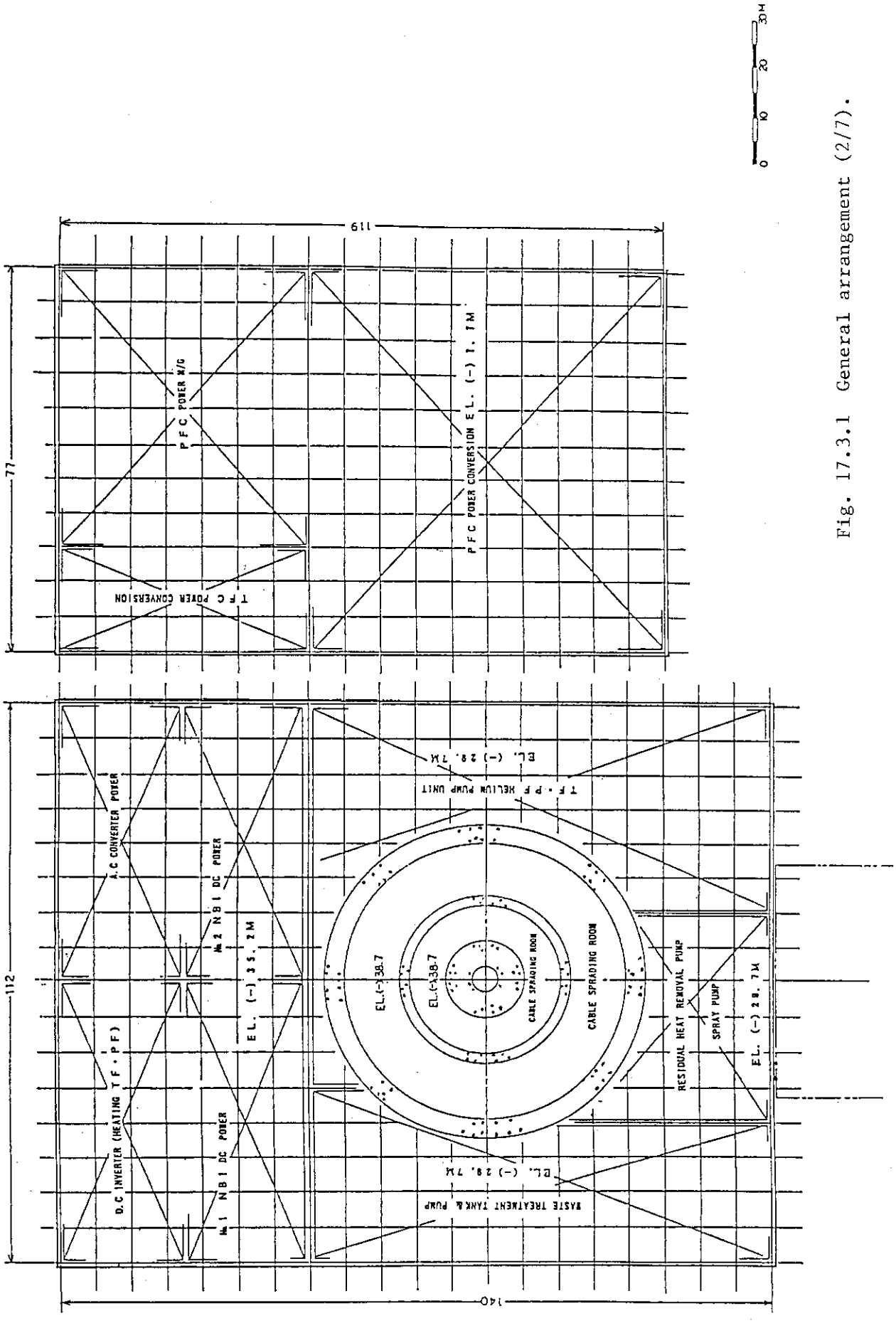

Fig. 17.3.1 General arrangement (2/7).

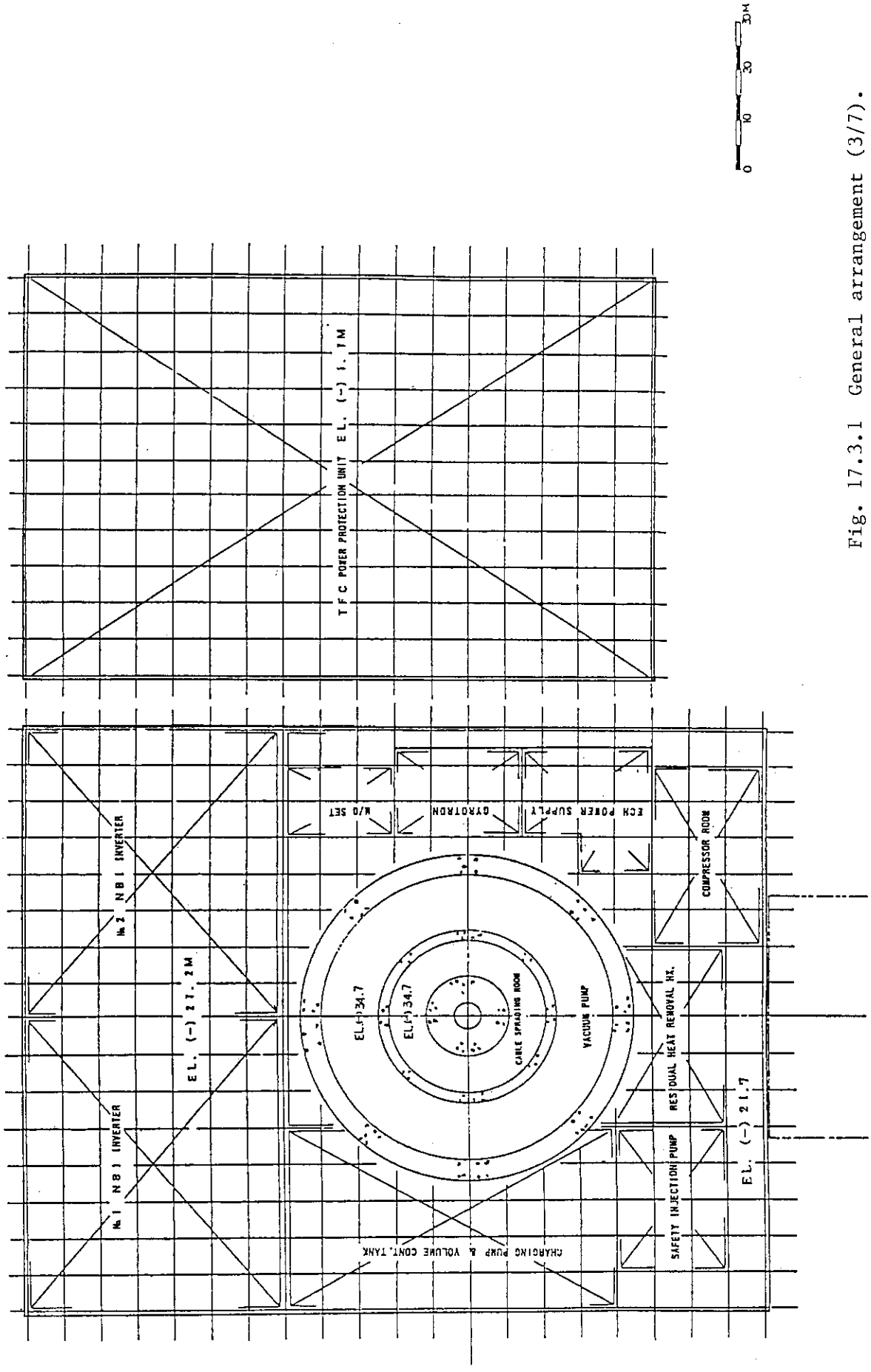

Fig. 17.3.1 General arrangement (3/7).

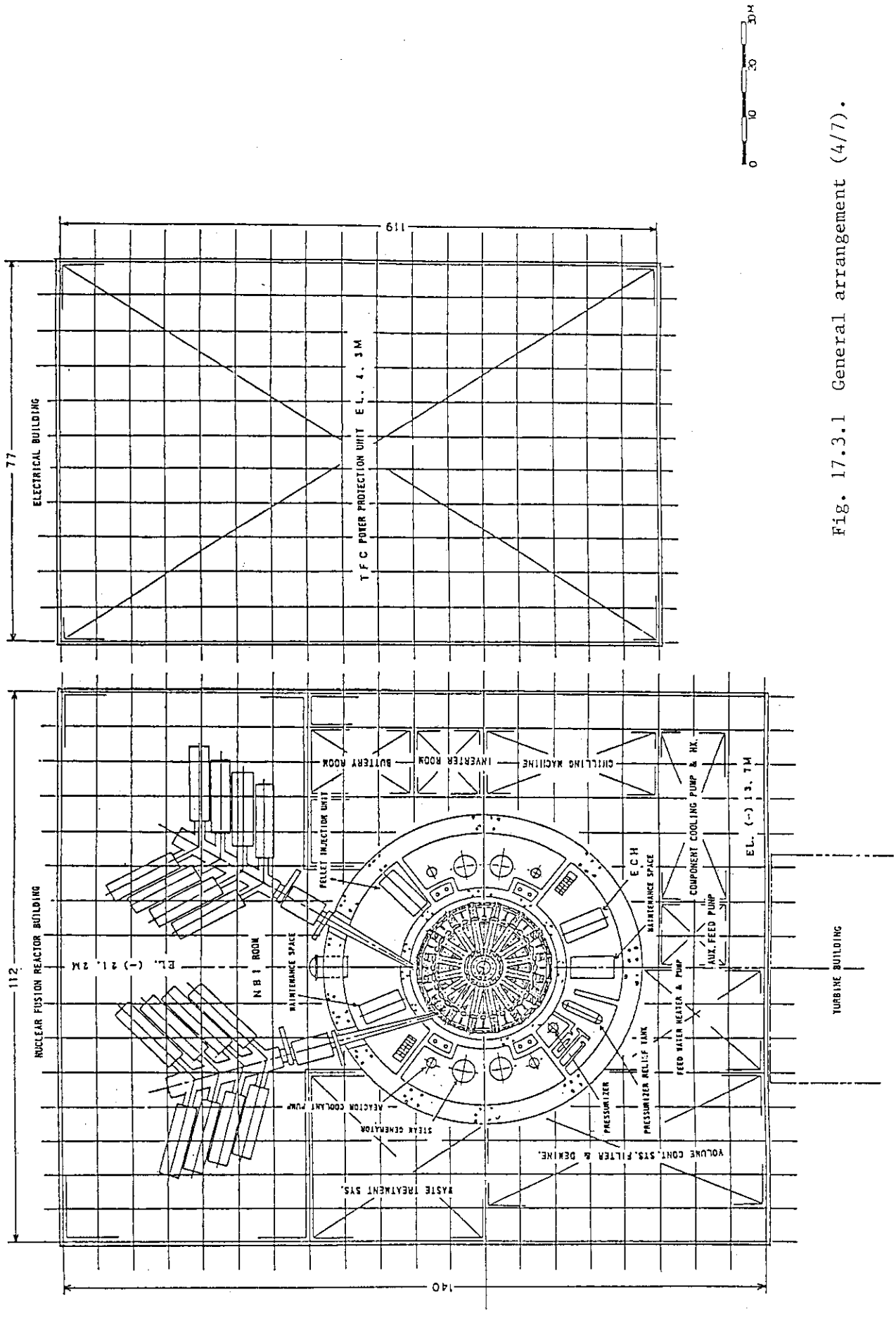

Fig. 17.3.1 General arrangement (4/7).

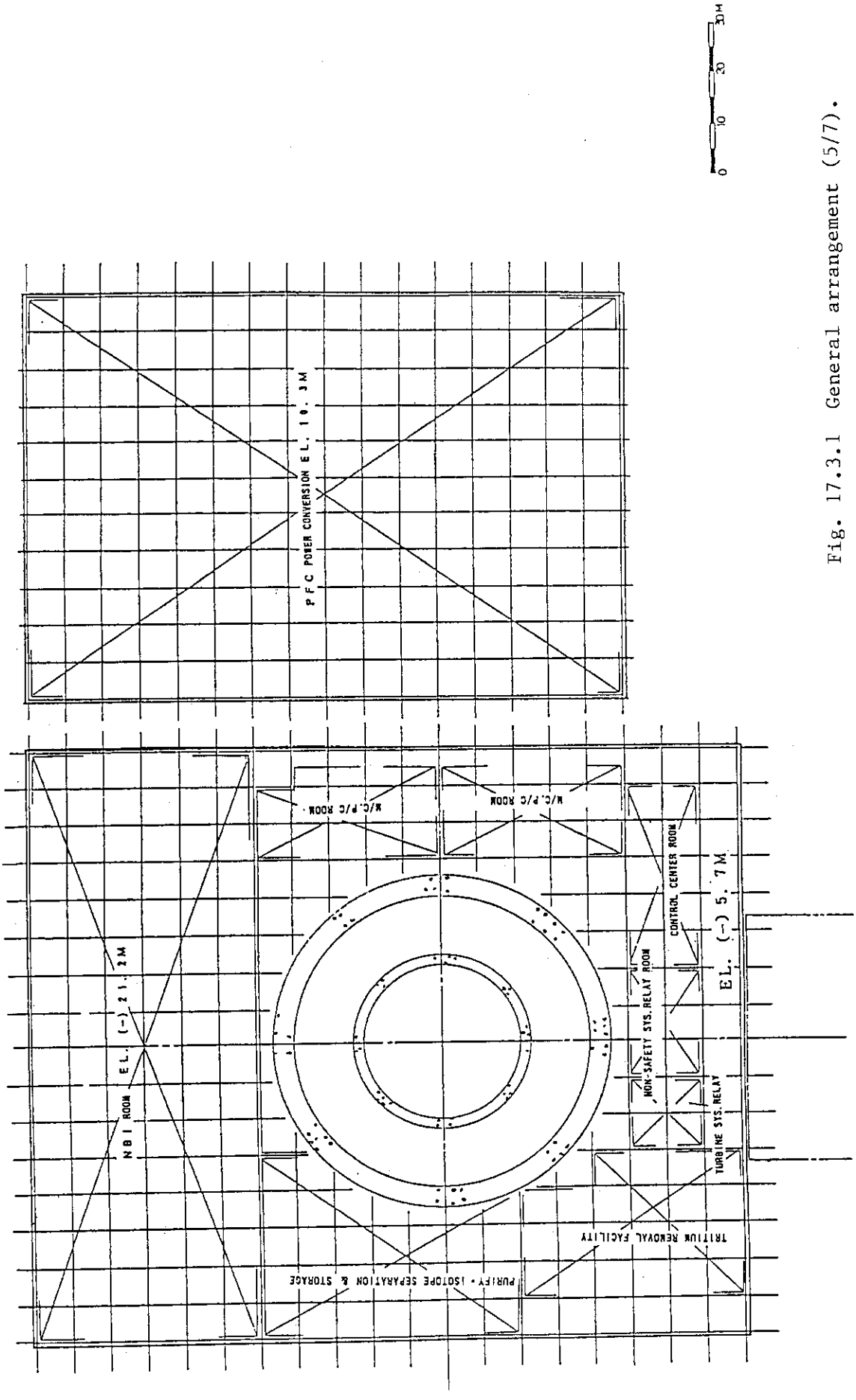

Fig. 17.3.1 General arrangement (5/7).

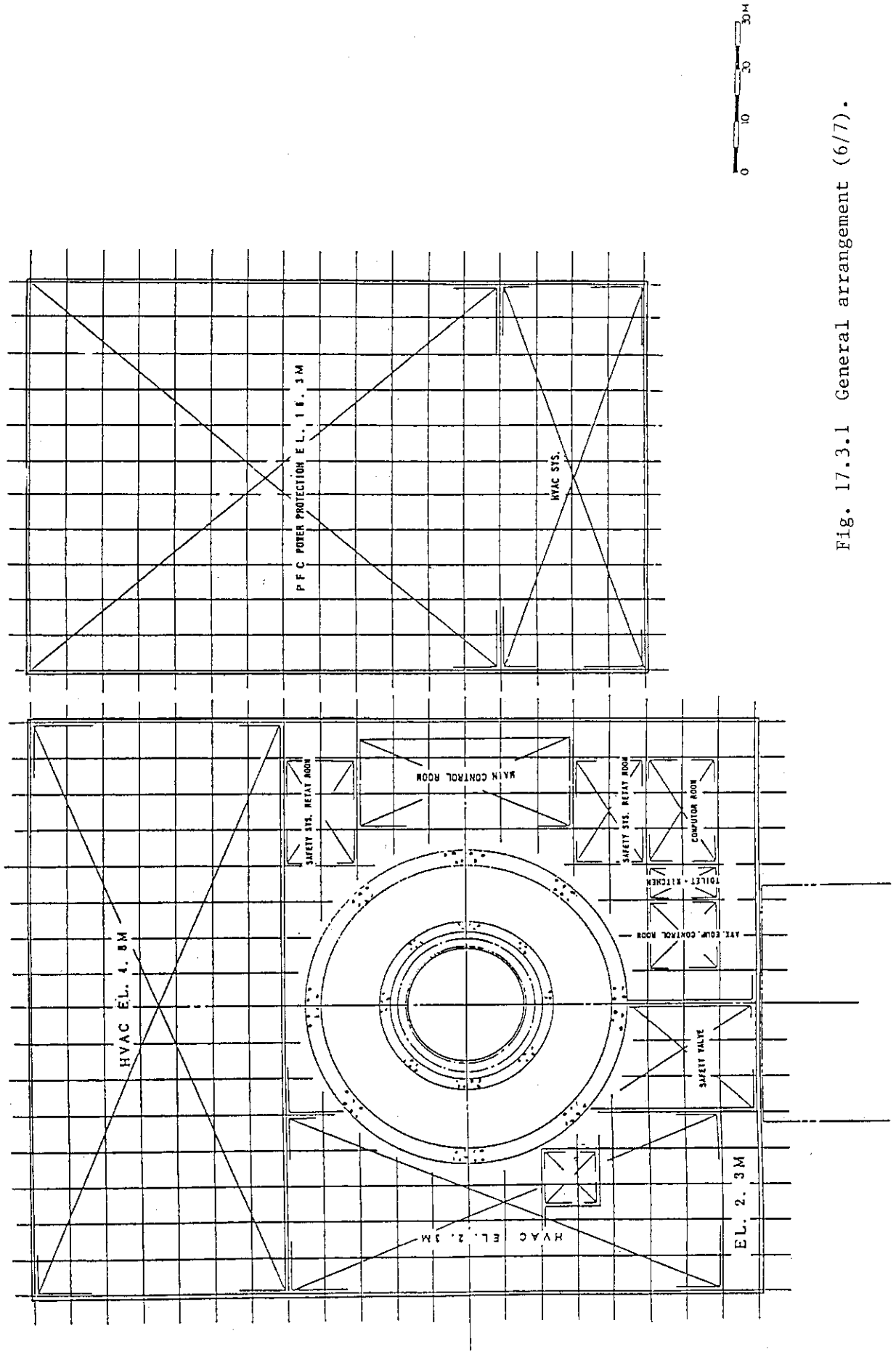

Fig. 17.3.1 General arrangement (6/7).

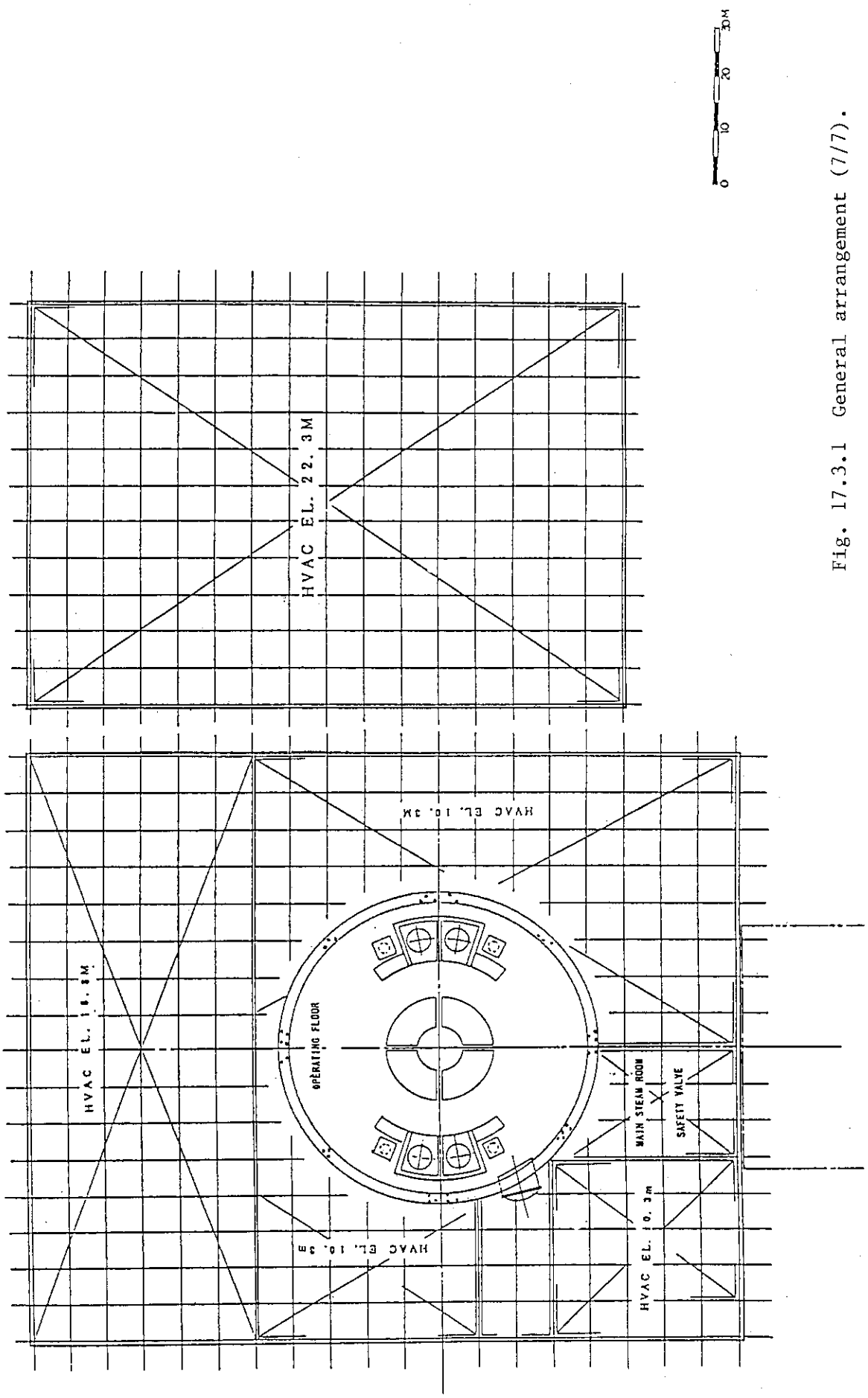

Fig. 17.3.1 General arrangement (7/7).

17.4 Items to be researched in the future

With the present study, we could have made the conception of overall disposition of the plant. However, through the following studies, the accuracy of the plan should be improved to the level of plan schematics.

(1) To improve the accuracy of the disposition by means of external views of the equipment with intermediate accuracy.

(2) To improve the accuracy of the disposition by evaluating the routes of the major pipings, ducts, trays, and so forth.

(3) To improve the accuracy of the disposition by clarifying the conception of the blanket handling equipment.

(4) To determine detailed items for the building structure, including the upper structure of the secondary vacuum room.

18. Safety and Environmental Aspects

18.1 Safety approach

A fusion reactor is much safer than a fission reactor because of the following inherent features:

1) It does not have a criticality accident.
2) Reaction products from the D-T fusion reaction are neutron and helium so that fission products or actinides are not present in a fusion reactor.
3) Decay heat density is lower than in case of fission core so that its removal is relatively easy.

A safety consideration of SSTR is described considering the above inherent features.

Major concerns in fusion reactor safety come from the 14 MeV neutrons generated as a result of the D-T fusion reaction, the tritium used as the fuel, and the activation products from the neutron interaction with materials constituting the reactor components.

Radiation doses to the general public outside the reactor site boundary and personnel of the reactor plant should be minimized based on the ALARA principle. The doses by the 14 MeV neutrons and gamma rays during operation and abnormal states will be minimized by the proper radiation shielding technique. Special attention should be paid to take account of the numerous penetrations and ducts existing in the shielding structures of a fusion reactor.

Tritium inventory should be reduced as much as possible and the components with large amount of tritium are made to possess multiple barriers for tritium containment. Usually this is accomplished by the device boundary, glove box or some similar secondary containment and the room or building installing the component. For the secondary containment and the room or building with components with large tritium inventory, inert gas/atmospheric detritiation systems are provided to deal with tritium leakage. Leak tight joints and valves are employed for the tritium loops with special permeation reducing measures, as required, as in the case of high temperature components. In view of the fact that tritium is flammable, proper measures are taken to avoid the tritium combustion condition and explosion protection is provided. In case of off-normal events such as earthquakes or power loss, the components are made to achieve tritium containment mostly by isolation, passively as much as possible.

As for the activation products produced by the neutrons, the quantity is large but the most will be contained forever within the metals and a process for their full mobilization is inconceivable. However, a partial mobilization could occur by the following processes:

1)Activated corrosion products in the coolant of the primary cooling system, which will come from cooling tube material/coolant interaction in the first wall and blanket and divertor.
2)Activated dust in the plasma chamber produced by the erosion and sputtering of the plasma facing components.
3)In case of highly unlikely, extreme condition of air ingress into the vacuum vessel and contacting with very high temperature plasma facing material, the volatilization of the metals could be considered.

It has been found that the volatilization of tungsten divertor plate is the most serious cause of accidental dose to the public in the ITER safety analysis[1].

In addition to activated solids, there are some activation products in form of liquid and gases. They are;

1)Activation of the coolant itself.
2)Inert gas surrounding penetration ducts.
3)High voltage insulating gas for the neutral beam injector.

The normal effluent dose from these sources have been evaluated for ITER and found to be sufficiently small[5].

On the other hand, by selecting the low activation materials these activation products could be reduced.

18.2 Radioactive inventory

Major tritium inventory distribution in SSTR is shown in Table 18.2.1. Large uncertainty exists for the tritium inventory in the beryllium in the blanket and only an estimated value is shown. The total inventory became about 5 kg (5×10^7 Ci).

The of activation products is about 10^6 Ci per 1 MW of fusion power at shutdown as shown in Fig. 18.2.1 for the time evolution of induced activity as the function of time after shutdown after a continuous operation of 1 year. The total inventory of activation products becomes about 3×10^9 Ci at shutdown which is about 60 times larger than that of tritium. However most of the inventory is in the form of metal which is difficult to be mobilized for release.

Figure 18.2.1 shows that the total induced activity reduces by about six orders of magnitudes in 100 years after shutdown, because the reduced activation ferritic steel F82H has been used as the structural material for the first wall and blanket. The use of F82H should result in reducing the radwaste management problems but its implications is yet to be quantified.

Table 18.2.1 Tritium inventory distribution in SSTR

Name of System	Tritium Inventory	Reference.
Blanket Li_2O Be	300 g 800 g	Section 7.2.1
Isotope Separation System	1200 g	Section 13.4
Piping	300 g	Section 13.4
Storage	2000 g	
Pellet Injector	230 g	Section 15.5.2
Total	4830 g	

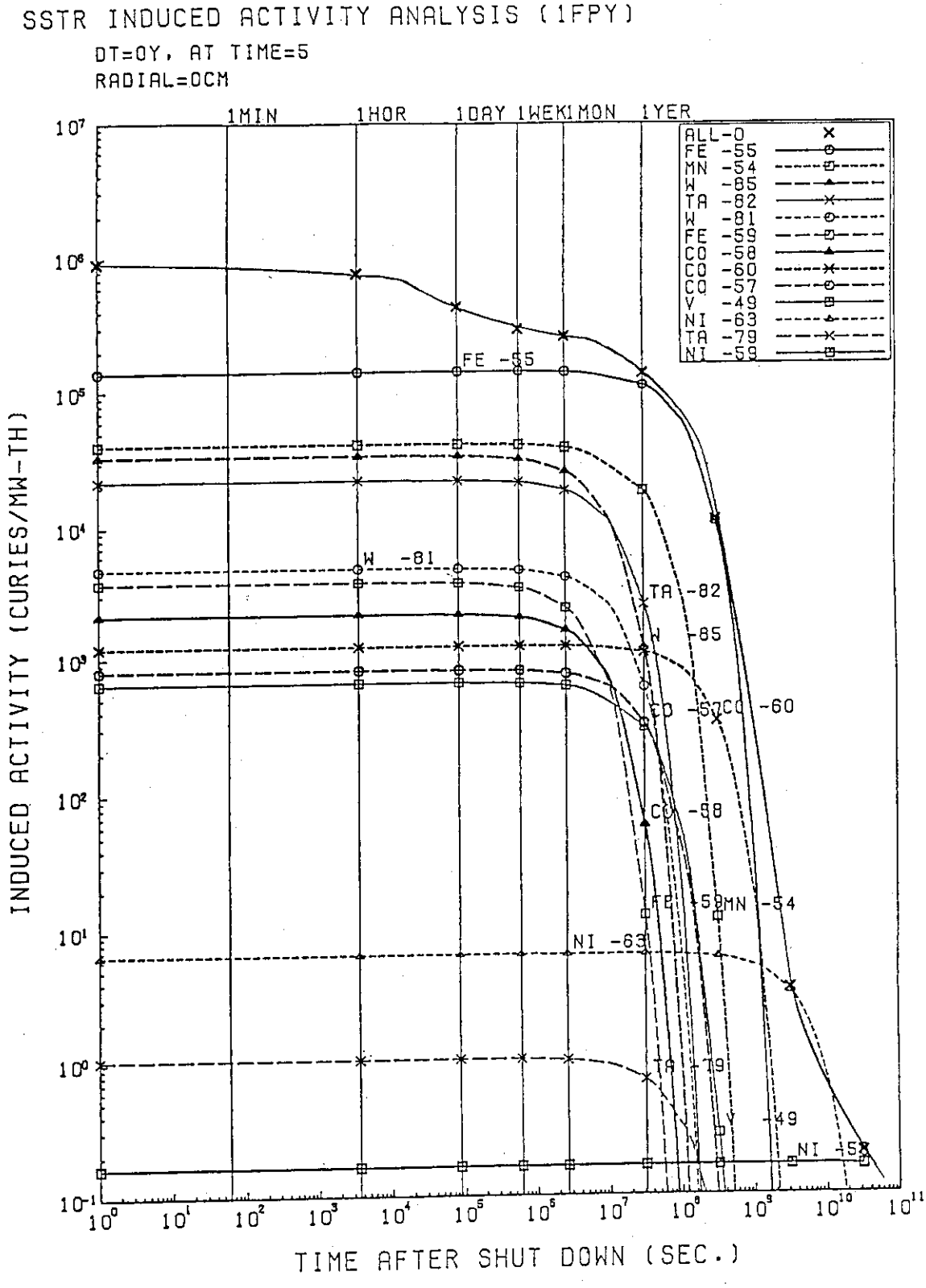

Fig. 18.2.1 Time evolution of total induced activity per unit fusion power of the SSTR after 1 full power year operation.

18.3 Radioactive material release

In the safety evaluation of the Fusion Experimental Reactor (FER)[2], major tritium leakage path during operation is identified to be the implanted tritium in the divertor and first wall which permeates through the structures to the coolant, and to leak into the reactor room with the coolant leakage. Tritium leakage into the coolant have been evaluated. The leakage with and without tritium barriers are shown in Table 18.3.1. It can be seen that tritium barrier is necessary for and first wall and blanket.

Table 18.3.1 Tritium leakage into coolant in SSTR

Name of System	Tritium Leakage into coolant w/o T-Barrier	Tritium leakage into coolant with T-Barrier	Reference
First wall	21 g/d	<1 g/d	Section 7.3.6
Blanket	15 g/d	<1 g/d	Section 7.3.6
Divertor	0.3 g/d	-	Section 8.8
Total	36 g/d	<1 g/d	

18.4 Safety considerations

In the present design of SSTR, most emphases are placed on its realization and hence it is not optimized in terms of achieving high level of safety. Basic design decisions related to safety of SSTR are as follows:

1)Material selections are made to minimize radioactive inventory and potential energy in components.

2)Multi-boundaries are provided to prevent the release of radioactive materials into the reactor room and environment.

3)For the prevention of the radioactivity release and propagation of accidents, passive safety measures relying on natural phenomena should be used as much as possible rather than on active safety features using power sources and human control. Some of the safety considerations made in the SSTR design are described in the following.

The reduced activation ferritic steel (RAF) called F82H [3], which is being developed by JAERI and NKK Corp., has been selected as the structural material for the first wall and blanket where the activation problem is most severe. The use of F82H in place of usual austenitic steel such as Type-316 should result in a considerable reduction of long term radioactive waste management cost. As described in chapter 7, the division of the blankets into two layers is also effective in reducing the amount of radwaste.

A solid breeder instead of liquid lithium metal has been selected to minimize stored chemical energy inventory. The area of concern in terms of safety is the interaction of hot pressurized water and the solid breeder. The use of double-walled cooling tube and placing the welded parts out of the blanket vessel are considered to reduce the probability of the breeder/water interaction. In addition, the pressure relief valve for the blanket vessel to limit the propagation of the failure to the other blanket vessels, is being considered.

The primary cooling system is designed to provide natural circulation in the event of loss of flow accident in the primary cooling system. The vacuum vessel will be surrounded by the nitrogen inert gas area to prevent air in-leakage and the possible interaction of air and the hot surface of the plasma facing components in the vacuum vessel.

18.5. Safety research and developments

Many safety research and development needs have been identified in the ITER safety analysis. The R&D needs evolved from the SSTR design study are described here.

1)Low activation materials

In order to reduce the radiation dose during the maintenance operations and to ease the radwaste problem, development of low activation materials is needed.

2)Tritium containing barrier

Tritium permeation into the high temperature cooling water through the first wall and blanket is very large so that some tritium barrier is needed to reduce the permeation amount. Furthermore, the tritium barrier is also needed in the steam generator to reduce the amount of tritium transferring to the secondary steam be minimized.

3)Corrosion reduction by primary coolant

In order to reduce the activated corrosion products, water chemistry control measures to reduce the production of corrosion products should be developed.

References

(1) J. Raeder et al., ITER Safety, ITER Documentation Series, No.36, IAEA (1991)

(2) Y. Seki, H. Iida, T. Honda, Conceptual Design Study of Fusion Experimental Reactor (FY86FER) -Safety-, JAAERI-M Report 87-111 (1987)

(3) M.Tamura, et al., J. Nucl. Materials, 155-157 (1988) 620-625.

19. Economical Feasibility

19.1 Introduction

Economical competitiveness against present power plants such as light water reactor, coal/oil/LNG fired power plants and fast breeder reactor is required in order to serve a tokamak fusion power reactor to a practical use. There are some examples in the past on the economical feasibility of fusion. But they are not based on the actual manufacturing achievements such as JT-60. A cost estimation of the SSTR is presented in this chapter taking account of the experiences in JT-60 and of the conceptual design study of the ITER (International Thermonuclear Experimental Reactor). The cost evaluation strongly depends on the methodology. So we intended to describe basic parameters which are important for the cost evaluation. In this concept study, special attention is paid on the simpleness and reliability of the manufacturing processes. So the manufacturing period could be minimized. Based on the following cost estimation, cost of electricity of the SSTR is ~1.5 times that of light water reactor (without decommissioning cost). So it is shown that fusion has a potential as a power source if we consider future possibility of the price hike for the fossil materials. Considering the energy security requires multiple energy sources, it is timely to demonstrate the power generation by fusion in the near future.

The cost of electricity in Japan is relatively high because there are few energy resources in Japan. The light water reactor provides significant electricity and the rationalization of the design is pursued to reduce the cost and to improve its safety. Moreover, oil/coal/LNG fired power plant must be reduced in the future due to its production of CO_2 and political uncertainty in the near east. So the fusion reactor could be a candidate of the alternate of oil/coal/LNG fired power plant. Moreover, fusion reactor has small amount of D/T fuel in the core burning plasma (only 0.4g and the burn up time constant of 30 second) which assures the intrinsic safety of fusion for the nuclear burst. In such a sense, fusion could have a national public acceptance. Japanese fission technologies is now in the top level among the world and provide many fission power plants. So a combination of the fission reactors (thermal and fast breeder reactors) and the fusion reactors can form the best mixture of the energy source in the next century.

In the next section, a summary will be given on the cost of electricity for various sources of electricity in Japan. The construction cost estimation for the SSTR is described in section3. Operation cost and cost of electricity are given in section 4.

19.2 Status of electric power sources and cost of electricity in Japan

Electric power is supplied mainly with steam plants, fission reactors and hydro power plants in Japan. Fig. 19.2.1 shows a history of the annual power generation (achievement) in Japan. As seen in the figure, electric power consumption increases linearly with fiscal year and it reaches up to 666.8TWh. Power demand in 2010 is reported to be 1.6 times present power supply even if we made a significant effort on the power saving. Shares of various power sources have changed year by year. For example, share of the oil fired plant which was a dominant power source in 1970's decreases and the share of fission and LNG power plants becomes large recently. As an economical measure of various power sources, cost of electricity (total cost per kWh) is used. A cost evaluation in FY1987 is shown in Table 19.2.1. The costs of electricity (COE) for LWR, COAL, OIL and LNG are 10.43yen/kWh, 11.63yen/kWh, 10.89yen/kWh and 11.03yen/kWh, respectively. The COE for fission reactor may be further decreased and the fission is thought to be a cheapest energy source.

The COE is divided into those from capital cost, fuel cost and operation cost. The capital cost is total cost to build the plant which includes the cost of land and the interest. Fuel cost includes the cost of OIL, COAL, LNG, nuclear fuel rods, etc. For the fusion reactor, it includes the cost of replaceable blanket and deuterium. The operation cost includes personnel expenses, repairing expenses and miscellaneous expenses. In the fission reactor, fraction of the capital cost is large. Fuel cost becomes large for the OIL/LNG fired plants.

Construction cost of the LWR is about 350Gyen/1GWe output and the cost of the power plant (primary cooling system and turbine generator) is ~100Gyen. Construction cost of the LWR has a large variation and can be 2.5 times the average value. The COE for the power plants starting its operation in FY2000 is estimated for LWR (7.59-10.57yen/kWh),COAL (10.23-11.89yen/kWh), OIL (14.74-15.28yen/kWh) and LNG (14.03-14.76yen/kWh), respectively[1]. In this estimation, fuel unit cost of 34 $/barrel was used for the OIL.

The development of fast breeder reactor (FBR) which has a long history of research and development as a promising goal of fission is now in a stage of the operation of a proto type reactor (FUGEN) and a design of the DEMO reactor is being conducted. The cost of electricity of FBR is estimated to be 1.35 times the LWR. With a significant growth of the electric power demand, the share of the FBR together with the LWR will increase in the next century if we must decrease the coal/oil/LNG fired plants in order to reduce biological

effects. On the other hand, special efforts are required to get "public acceptance" for LWR and FBR. We consider that the fusion has better acceptability and it is required to demonstrate a production of fusion energy in the near future. Continuous construction of the experimental reactor, DEMO reactor and commercial reactor will be needed to start commercial utilization of the fusion power plant around 2040.

(1) I. Maeda, Energy, No10 (1987)18.

Table 19.2.1 Estimated cost of electricity for various power sources (start operation in FY1986) (Yen/kWh)[1]

	LWR	COAL	OIL	LNG
Capital	6.27	5.57	3.25	4.46
Operation	2.16	2.25	1.07	1.35
Fuel	2.00	3.81	6.57	5.22
Total	10.43	11.63	10.89	11.03

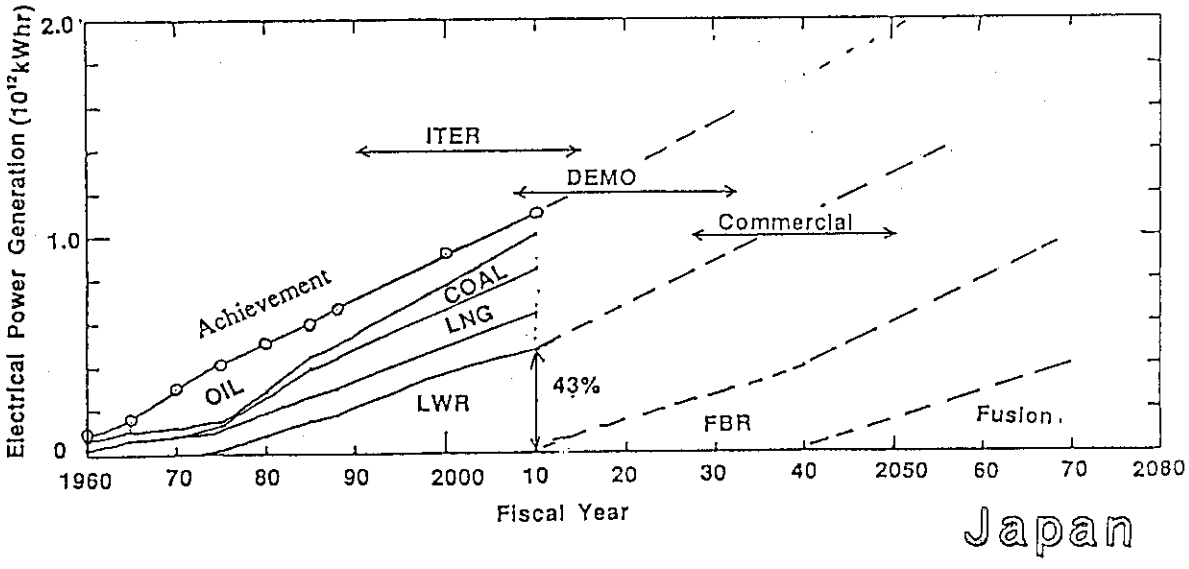

Fig. 19.2.1 Achievement and long term need for power generation.

19.3 Estimation of the SSTR construction cost.

As a power plant, the SSTR consists of tokamak equipment, heating and current drive system, He refrigeration system, fuel system, HVAC system, power supply system, control and diagnostic system, operation and maintenance equipments, power plant system, site and buildings. In this construction cost, interest during the construction period and profit are included.

19.3.1 Cost break down of the SSTR construction

Cost break down of the SSTR is shown as follows,

Tokamak		34.1%
	Toroidal field coils	(43.7%)
	Poloidal field coils	(12.4%)
	SC assemble cost	(3.5%)
	Vacuum vessel	(15.2%)
	Blanket	(15.5%)
	Divertor	(4.1%)
	Assemble cost (V,B,D)	(5.6%)
Heating and current drive system		8.3%
	N-NBI system	(88%)
	ECH system	(12%)
Cryogenic system		3.5%
HVAC system		4.2%
Fuel system		3.3%
Power supply		5.6%
Control and diagnostics system		3.3%
Maintenance equipments		1.7%
Steam generator, turbine		13.9%
Building and site		8.3%
Interest during construction		8.8%
Profit		5.0%
Total		100% (720Gyen)

Total construction cost of a fusion reactor is ~2 times that of LWR, but the operation cost and the fuel cost is relatively low by which fusion can have an economical competitiveness against other energy sources.

19.3.2 Superconducting coils

It is fairly difficult to estimate the cost of superconducting coils because there are few commercial products in which large amount of the superconductor is used. For example, total filament weight of the superconductor for the SSTR is 1400ton. But total annual production rate of the superconductor is only 100ton/year which is mainly manufactured for the medical use.

There are four types of superconductors for the SSTR, namely 16.5T $(N_bT_i)_3S_n$ conductor for the toroidal field coil, 5T NbTi conductor for the second grading of the toroidal field coil, 7T and 5.5T NbTi superconductors for the poloidal field coils. There are many characteristics of the SSTR superconductors. At first, a simple cable-in-conduit conductor is adopted in the SSTR which enables to reduce the manufacturing cost of the conductor. For the 16.5T toroidal field coil, a special winding concept is adopted which enables the grading into two conductors (16.5T and 5T). With this concept, 30% of the conductor can be made with cheaper NbTi conductor which also contribute to the cost reduction. Total electromotive force of the poloidal field coils is fairly small by the selection of moderate plasma current (12MA) and the single null divertor. And the use of the low resistance vacuum vessel reduces the AC loss and enables to adopt a simple structure for the poloidal conductor. These points also contribute to the cost reduction.

The diameter of the 16.5T $(N_bT_i)_3S_n$ superconductor is 50mm including the insulator. In this conductor, 972 filaments with the diameter of 1.05mm (Cu/nonCu=2.1) are contained. The material cost of the conductor is estimated from the total filament weight of 700ton. The manufacturing processes of the conductor are material (Nb+Bz) processing into the ~1mm diameter filaments with stabilizing Cu, twisting, conduit formation and cabling. Total length of the $(N_bT_i)_3S_n$ conductor is 98km (=34m x 180 turns x 16) and reaches the level of mass production.

The 5T NbTi superconductor for the toroidal field coil is believed to be manufactured with around half price of the $(N_bT_i)_3S_n$ conductor. The diameter of the conductor is 36mm including the insulator. In this conductor, 972 filaments with the diameter of 0.86mm (Cu/nonCu=4.1) are contained. The material cost of the conductor is estimated from the total filament weight of 300ton. Manufacturing processes are almost same as those for the (NbTi)3Sn conductor except for the initial process. Total length of the NbTi conductor is 38km (=37m x 64turns x 16).

The coil cases, advanced disks and the shear panels are made of new cryogenic steel called JN1. The unit cost of JN1 is about two times that of usual SUS. Total weight of the structural components (cases, disks and shear panels) are 8240ton and the material cost is easily calculated. We estimated the process cost of the structural components in proportion to the weight with the unit cost of 3Myen/ton taking account of the simple structure of the components. The weight of one toroidal coil is ~600ton (six times that of JT-60) and total weight is 11200ton.

Poloidal conductors consists of 7T NbTi conductors(CS coil) and 5.5T NbTi conductors(EF coil). Both are cable-in-conduit conductors and the operation current is 40kA. The diameter of the CS conductor is 34mm and 972 filaments having 0.84mm diameter (Cu/nonCu=1.5) are contained in the conductor. The diameter of the EF conductor is 30mm and 108 filaments having 2.2mm diameter (Cu/nonCu=7.5) are contained in the conductor. Total length of the conductors are 33.2km for CS coil and 64.7km for EF coil. Total weight of the filaments is 370tons. The EF conductor may be somewhat cheaper than CS conductor, but the coil diameter is ~26m and the manufacturing supports are large. The conductors are set in the JN1 conduit and the total weight of the poloidal coils are 2550ton including the spacer and the support.

Other parts necessary for the superconducting coil system are current leads ((16+14)x2 for TFC and PFC), power cables ((16+14)x2), 80°K shield, piping, valves and diagnostics and control system. The total length of 200m is assumed for the power cable.

Construction cost at the site consists of those for assembly and testing. The tokamak machine is assembled using the large side cranes during the construction of the building. Total weight of a toroidal coil and 1/16 shield integrated vacuum vessel is 880ton and is close to the crane capacity used for the LWR construction. In general, the plant is cheaper for higher completeness in the factory because longer period is usually required for the assembly in the site due to poor circumstances. So we assumed that a toroidal coil and a sector of the vacuum vessel is integrated in the factory to reduce the assemble cost at the site. Such a philosophy is effective for all components. For example, the vacuum vessel and poloidal field coils are assembled at the site and the welding is also made at the site in JT-60U which leads to the increase of the assemble cost although such processes are unavoidable due to the topological constraint in JT-60U.

19.3.3 Shield integrated vacuum vessel

The vacuum vessel and the shield in the SSTR are integrated and the structure is extremely simplified. As shown in Table 9.3.2, weight ratio for the main chamber and the ports are 4 : 6 (it should be noted that weight reduction of the ports is not optimized in the present design). And the total weight of the vessel is 11000ton. The vacuum vessel is made of austenic stain less steel (SUS316) and the material cost is easily obtained. Same unit cost for the processing used in the toroidal coil is assumed for the vacuum vessel considering its simpleness. In the site, 16 vessel units and ports are welded and various piping works are made.

19.3.4 Blanket

In contrast to the vacuum vessel, the fraction of the material cost is high for the blanket. Table 19.2.2 shows weight break down of the blanket.

Table 19.2.2 Weight break down of the blanket

	replaceable blanket	permanent blanket
Structural materials(ferritic steel)	250ton	250ton
Breeding materials(Li2O)	50ton	160ton
Neutron multiplier(Be)	110ton	
Vertical port plug	470ton	

Material costs of the neutron multiplier (Be) and the tritium breeding material ($L_{i2}O$) share a large portion of the total cost. The beryllium is highly expensive and the material cost of the Be is 1/4 of the total cost. Moreover, unit material cost of $L_{i2}O$ is slightly less than a half of Be. So the material cost of $L_{i2}O$ becomes slightly less than 1/4 of the total cost. On the other hand, the material cost of the ferritic steel is very small even with total weight of 1280ton. The structure of the blanket and the piping are fairly complicated a high reliability is required. So the processing unit cost may be much higher than that of the vacuum vessel. At the site, installation to the vacuum vessel and pipe connection to the ring header are major works.

19.3.5 Divertor

The divertor consists of the divertor plate ($53m^3$, 360ton) and removable shield ($380m^3$,2450ton). Most of the components are made of SUS and the material cost is only

20% of the total cost. A weight reduction is pursued to reduce the activated materials such as Mo. Unit processing cost of vacuum vessel is used for the divertor. At the site, installation to the vacuum vessel and pipe connection to the ring header are major works.

19.3.6 Heating and current drive system

The heating and current drive system consists of NNBI system (2MeV, 60MW, CW) for heating and current drive, and ECH system (250GHz,5MW,CW) for preionization/ initial heating. As a large scale achievement of the NBI system, deuterium beam injector (120kV,40MW) has been developed for JT-60U. But it should be noted that this system uses positive ion sources and the system efficiency is not so good. NNBI system to be installed to JT-60U in 1994 (500kV,10MW) is the first large scale development in the world. There are many cost reduction points of the NNBI system for the SSTR. Adoption of the Cockcroft-Walton type accelerator clears off the high voltage cablings. Attainment of the high system efficiency more than 50% becomes possible by the plasma neutralizing cell. The reduction of the extraction current with the high beam energy (~1120A in JT-60 and ~80A in the SSTR) reduces the cost of the ion sources and the pumping capacity. The attainment of the low operation pressure (0.3Pa) of the ion source also reduces the capacity of the pumping system significantly (total pumping speed of 1750m^3/sec).

The power supply system consists of the high voltage DC power supplies using the Cockcroft-Walton multi step rectifier, the invertor/convertor system supplying the 10kHz/600V AC power to the rectifier and the ion source power supply.

The ECH system has low system efficiency as described in Chapter 16. And the cost per unit injection power becomes relatively high.

19.3.7 Cryogenic system

The He refrigeration load for the SSTR during the current ramp up phase is larger than that for the steady state phase. Total cryogenic load (37kW) during the current ramp up phase consists of the load for the superconductors (AC loss, heat transfer from the current leads, nuclear heating; total 33.7kW) and the load for the pellet injector (3.75kW). On the other hand, AC loss disappears in the steady state phase and the cryogenic load is reduced to 15.6kW. Furthermore, there are 8600 liter/hr liquefaction load and 80°k thermal shield load (refrigeration load of 130kW at 80°k). This cryogenic system adopted the forced flow cooling using the super critical He flow. So the there is a large thermal

load in the ultra low temperature circulation pump which almost double the thermal load. So the total power supply to the cryogenic system becomes ~20MW during the steady state operation.

19.3.8 HVAC system

The design of the HVAC system is not made in this study. And the cost is guessed from other estimates.

19.3.9 Fuel system

The fuel system of the SSTR consists of a tritium circulation system (tritium inventory of 1.5kg), tritium recovery system from the primary cooling water (1g/day), pellet injector (600mol/hr) and the tritium storage system (tritium inventory of 2kg).

19.3.10 Power supply system

The power supply system of the SSTR includes poloidal and toroidal power supplies. The poloidal power supply has thyristor convertor capacity of 970MW and the transformer capacity of 1140MVA due to its high power factor. This capacity is required in the initial current build up phase. So the power is delivered from two 3GJ,250MVA motor generators and the 200MVA line grid. The capacity of these power supplies is smaller than that of JT-60 power supplies (motor generator of 8GJ,1100MVA, thyristor convertor of 1GW and transformer of 2GVA). But the power supply system is designed for the pulsed operation. So, for example, the weight of the transformer will be doubled for the steady state operation.

The DC circuit breakers and the quench protection resistors are important components of the system. Especially, total energy of the toroidal field coil system is 135GJ. And the weight of the SUS quench protection resistors is 1400ton. The DC circuit breakers for the quench protection are 16 units 81kA,20kV DC breakers for toroidal coils and 14 units 40kA,20kV DC breakers for the poloidal coils.

19.3.11 Control and diagnostics system

In this study, designs of the control and diagnostics system are not made. So the estimation from other design and the experience of JT-60 was made.

19.3.12 Maintenance equipments

Because there is no armor tiles in the SSTR, the main functions of the maintenance system are the coating and monitoring of the first wall.

19.3.13 Steam generator, primary cooling pipes and turbine generator

These equipments becomes slightly bigger than those used for the commercial pressurized water reactors.

19.3.14 Building and site

The site of the SSTR is in the sea shore. And basic works such as sea port construction, land readjustment, road construction, etc should be made. The reactor building becomes fairly compact for the DEMO reactor.

19.3.15 Interest

The fusion reactor is an expensive machine and a long term budget with low interest rate should be supplies to the private company. Here, we assumed that a first plasma is possible 5.5 years after the main contract.

19.4 Operation cost and cost of electricity

19.4.1 Service life and availability

The service lifes of the power stations are 35years for hydro power station, 15years for steam power station and 16years for nuclear power station. There is no definition of the service life for the fusion reactor. Here, we use 16years of the nuclear power station for the fusion reactor. For the steam and nuclear power stations, maintenance is made every two years for the steam turbine and annual maintenance is made for the boiler and the reactor vessel. In the fission reactor, 90-100 days are spent on the maintenance. In the SSTR, it will be possible to replace the divertors and the replaceable blankets within 100 days. So we assume 70% availability for the COE estimation. Annual operation hours corresponding to 70% availability are 6132 hours. And, the annual power generation is 6623GWh.

19.4.2 Estimation of the operation cost

The personal expense for 100 employees is ~1.8Gyen which corresponds to ~0.27yen/kWh. As a repair cost, the replacement of the damage sections of the divertor plates, ion sources, pellet injector and the power supplies. We estimated that these operation costs are 9Gyen/year which corresponds to ~1.4yen/kWh. In total, the contribution of the operation cost to the COE is ~1.7yen/kWh.

19.4.3 Estimation of the fuel cost

The fuel cost of the fusion reactor is the cost of the replaceable blankets. The outboard blankets are periodically replaced every two years. The inboard blankets are periodically replaced every four years. We add up 11Gyen every year for this replacement which corresponds to the 1.7yen/kWh. Here the recovery of the Li_2O and Be from the used blankets is highly desirable.

19.4.4 Estimation of the cost of electricity

From the construction cost estimate of the SSTR in section 19.3.1, the contribution to the COE from the capital cost is 12.6yen/kWh if we plan to repay 90% of the total construction cost within 16 years assuming annual interest rate of 6%. So the total COE including contributions from operation and fuel costs is 16yen/kWh. On the other hand, the COE becomes 11.5yen/kWh if we use the service life of 30years and the availability of 85%. Then the fusion has an ecomomical competitiveness against the steam power plants and the advantage of the fusion will be enhanced in the future.

20 Study Conclusions

An overall concept of SSTR has been studied and its feasibility in the near future has been shown. It has been shown that a tokamak machine comparable to ITER in size can become a steady state power reactor capable of generating ~1GW of electricity with a plant efficiency of ~30%. Here, the critical issues for a feasibility of SSTR are briefly summarized.

20.1 Plasma Characteristics

The SSTR plasma produces a fusion reaction power of 3000 MW, with a major radius of 7 m, a minor radius of 1.7 m and an ellipticity of 1.85.

The plasma current was suppressed at a relatively low value of 12 MA, in order to keep down a required power for current drive and keep up a fusion power multiplication factor Q. The plasma temperature was selected at a relatively high value of 17 keV for a high efficiency of current drive. A relatively high electron density of 1.4×10^{20} m $^{-3}$ and the relatively low plasma current led to a high value of poloidal beta. Consequently, a bootsrap current constituted up to 75 % of the total plasma current. The rest 25 % of the plasma current was driven by high energy neutral beam injection based on negative ion sources(NNBI). The required beam energy and injection power for NNBI were 2 MeV and 45 MW, respectively. The SSTR plasma condition required a high toroidal field of 9 T on a plasma axis, which corresponds to a maximum field strength of 16.5 T in a toroidal field coil conductor.

The energy confinement time of 1.4 s was required for sustaining the plasma temperature and density of 17 keV and 1.4×10^{20} m $^{-3}$ with the total heating power(α heating and neutral beam injection) of 660 MW. This confinement time corresponded to a improvement factor of 1.8 for Goldston scaling law, and 2.0 for ITER89 power law.

The MHD instabilities in the SSTR plasma were classified in three categories, which were caused by a plasma internal pressure, a plasma current profile and a plasma ellipticity, respectively, It was confirmed by ERATO-J code that an operation at high safety factor of q_{95}=5.0 and low toroidal beta of 2.5 % suppressed the ideal ballooning instabilities and the internal kink instabilities. That confirmation was carried out on the assumption of the appropriate current profile. It was also confirmed by ACCOME code that the appropriate current profile was realized by the neutral beam injection. The plasma vertical position instability caused by plasma ellipticity was considerably suppressed by an eddy current on in-vessel conducting structure by the plasma vertical motion. After the eddy current decayed, the plasma vertical position was controlled by active control coil system made of normal

conductor, which was partitioned for each torus sector and located behind each renewable outboard blanket module.

20.2 High Field Toroidal Coil

The high field toroidal coil system is the key component, which supported the SSTR concept. A combination of $(NbTi)_3Sn$ and NbTi superconductors was adopted in order to produce the field strength of 16.5 T. The current density of $(NbTi)_3Sn$ employed in this design was 600 A/mm^2 at the field strength of 16.5 T. An "advanced disk" type was introduced for coil winding structure in order to improve a transmission of electromagnetic force from conductors to structural elements. The winding pack consisted of 20 disks. The circular shape conductors were heat-treated in dummy disk having the same grooves as the real disks. Then, they were installed into half circle grooves of the real disks without bending stress.

The maximum membrane stress of 80 kg/mm^2 and the maximum bending stress of 27 kg/mm^2 were generated in the coil supporting structure. The design stress intensity of the newly developed Japanese cryogenic steel JN-1 is 80 kg/mm^2. According to the design code of ASME Section III, the generated stresses satisfied the design criteria.

20.3 High Energy Neutral Beam Injector(NBI)

The neutral beam injection(NBI) system was required to inject deuterium neutral beams with 2 MeV and 60 MW to drive 25% fraction of the total plasma current. The NBI system consisted of two beamline modules. Each beamline module had eight ion sources which delivered a maximum neutral beam injection power of 5 MW per ion source. In the beamline design, the ion beams from each ion source were deflected magnetically and guided to the plasma neutralizer. This concept made it possible to mount many small ion sources in the beamline. The small source was expected to mitigate the R&D risk for the 2 MeV acceleration power supply. As the acceleration power supply, a Cockcroft Walton type DC high voltage generator which eliminated the large high voltage transmission line was the most promising.

The most important feature of the NBI system was that the total system efficiency was higher than 50 %. This high system efficiency was realized by adopting an efficient negative ion generator coupled with an efficient electrostatic accelerator and also a plasma neutralizer. The negative ion generator was of a volume-surface type which produced a dense negative ions at an operating pressure of source as low as 0.3 Pa. The electrostatic accelerator

had high transmission efficiency and high power supply system efficiency compared to the RF acceleration system. The plasma neutralizer had high efficiency of around 85 %.

20.4 Torus Structure and Blanket Structure

One of the most critical issues for designing the torus structure was the selection of an appropriate torus one-turn resistance. It was found that the one-turn resistance of 4 μΩ was acceptable from viewpoints of a plasma breakdown and current rise. The toroidally uniform resistance of 4 μΩ corresponds to a torus structure equivalent to 20 cm thickness. Thus, the vacuum vessel and shield were integrated to form a double-walled structure filled with insulated stainless steel block and water.

The blanket consisted of a solid breeder in pebble bed structure. Beryllium was used as a neutron multiplier. The thicknesses of blanket vessel required 50 cm ~ 60 cm to obtain the breeding ratio more than unity. The blanket vessel was divided into the permanent vessel and the renewable vessel. A renewable vessel thickness of 20 cm was just decided from both viewpoints of neutron fluence reduction and fuel burn-up, in order to make the lifetime of the rear(permanent) blanket more than 30 years without replacement. The renewable blanket vessel was electrically insulated at the end wall by using a functionally gradient material(FGM) made of ceramics sandwiched by the ferritic steel. This FGM concept was calculated to be significantly effective in reducing the electromagnetic force on the blanket vessel. Therefore, it was sufficient to hook or thrust the renewable blanket vessel on or in the permanent vessel, like a fuel rod handling of a fission reactor. Consequently, the renewable blanket was not expected to contribute to the passive control of plasma vertical position instability. Each renewable blanket sector was segmented into three modules and replaced from the vertical port every two years.

20.5 Heat Flux to Divertor Plate and First Wall

Power handling was found to be the important issue for SSTR. Most of the kinetic energy of neutrons was deposited in the blanket vessel. An α-heating power and a current drive power, however, were removed from the first wall and the divertor plate. The total plasma heating power is 660MW which comes from α heating (600MW) and NBI(60MW). The heat load to the divertor plate was more serious, because the power flow into the divertor region was evaluated to be more than 400MW. The divertor heat load is estimated for various scrape-off densities. When the scrape-off density was $8\times10^{19}m^{-3}$, the peak heat flux to the divertor plate was $10MW/m^2$ when 80% of the total heating power was radiated

from main plasmas and divertor plasmas. A divertor plasma temperature was then lowered to ~10 eV.

More than half of the heating power (~55% , 374MW) was radiated in the divertor plasma due to remote radiative cooling effect. In order to realize such a radiative divertor plasma, impurities in high density divertor plasmas and degrading the effective particle confinement time were needed. Two-dimensional divertor code simulation showed that a combination of the strong divertor gas puff with powdery Fe enhanced the remote radiative cooling and the heat flux(conduction and radiation) to the divertor plate was ~10MW/m^2. In this case, iron impurities did not flow into the main plasma due to strong friction force by the fuel ion.

20.6 Concluding Remarks

This design study clarified an example of the goal of fusion research and the technological base was not so far from our present knowledge. We believe that the engineering basis of SSTR will be established soon after the construction of the experimental reactor.